SAMPLE PREPARATION AND 2D SOLID STATE NUCLEAR MAGNETIC RESONANCE STUDIES OF THE FP–HAIRPIN CONSTRUCT OF THE HIV GP41 PROTEIN

By

Matthew J. Nethercott

A DISSERTATION

Submitted to
Michigan State University
In partial fulfillment of the requirements
for the degree of

DOCTOR OF PHILOSOPHY

Chemistry

2012

ABSTRACT

SAMPLE PREPARATION AND 2D SOLID STATE NUCLEAR MAGNETIC RESONANCE STUDIES OF THE FP–HAIRPIN CONSTRUCT OF THE HIV GP41 PROTEIN

By

Matthew J. Nethercott

The Human Immunodeficiency Virus (HIV) is an enveloped retrovirus responsible for causing the Acquired Immunodeficiency Syndrome (AIDS) in humans. The virus vesicle's membrane contains the gp120/gp41 protein expressed on the outside of the virus, which is responsible for recognizing and fusing the virus vesicle with the target cell, creating a fusion pore leading to infection of the target cell. Currently there are no high resolution structures for the gp41 protein's fusion peptide (FP) during the infection process. Solid state nuclear magnetic resonance (SSNMR) spectroscopy provides the ability to obtain high resolution structural information for proteins in their native environment.

This dissertation project required the development of a practical methodology for creating isotopically labeled FP–Hairpin where the labels are located in the FP region of a gp41 protein construct. Synthetically made FP23(linker) containing isotopic ^{13}C, ^{15}N labels and recombinantly expressed Hairpin in *E. coli* bacteria were ligated together using the native chemical ligation (NCL) reaction to produce the 115 residue FP–Hairpin construct in ~20% yield and 2 weeks time. FP–Hairpin allows for the study of the FP domain of gp41 in a lipid

membrane environment in the post fusion, low energy six helix bundle (SHB) formation. Using 2D SSNMR experiments with selectively placed isotopic labels in the FP region provided the ability to probe secondary and tertiary structure of the protein in a membrane environment.

Major results of this project are (1) the development of methodology to produce the 115 residue FP-Hairpin with isotopic labels using the NCL reaction and (2) SSNMR studies of the FP-Hairpin in lipid membrane environments. FP-Hairpin sample preparation time was reduced from 2 months to 2 weeks and NCL efficiency was improved from ~4% to ~20% yields. SSNMR was used to probe the secondary and tertiary structure of the FP-Hairpin protein in lipid membrane environments by using 2D ^{13}C-^{13}C experiments at magnetic fields of 9.4 T and 21.1 T. Results from the SSNMR experiments showed that with the 21.1 T instrument and the E–free probe, ^{13}C peak signal to noise per scan was 5–fold higher and linewidths 2–fold narrower than that which was obtained at the 9.4 T instrument and non E-free probe. Time savings of at least 50% were obtained at 21.1 T compared to the 9.4 T instrument. Prior to this work, the 21.1 T magnet had not been utilized to any great extent by the Weliky group.

Thus this project can be summed up as a proof of concept project which highlights sample preparation and SSNMR work that previously had not been attempted. By utilizing the SSNMR experiments it was determined that the FP–Hairpin construct can have both the helical and β-strand secondary structure in the FP region in the presence of cholesterol containing membranes. The β-strand conformation agrees with the previous work for FP peptides. However, the tertiary structure was not the same, as Alanine–6 and Glycine–10 were observed to have cross peaks in the FP23 peptide at long mixing times, which were absent in the FP–Hairpin construct, suggesting that the registry of the two constructs FP23 and FP–Hairpin are different.

To my parents Gerald and Carol, and my brother Daniel.

Acknowledgements

I would like to acknowledge and thank my advisor Dr. Weliky for all the support, help, and guidance that he has provided over the course of my Ph.D. career. Though my career he has been very positive and supportive of my research projects. He has allowed me the ability to present my work at several conferences as posters and talks, which I greatly appreciate. His support and guidance has help secure funding from various travel grants and from the College of Natural Science's Continuation Fellowship. The project that I was given has been quite challenging over the past five years, but very rewarding as well, and I appreciate the challenge. Dr. Weliky has allowed me to mentor several undergraduate students as well. All of these experiences have helped me develop as a scientist and a person.

Facilities and staff at Michigan State University (MSU) which played a pivotal role in my research included the MSU Mass Spectrometry Facility, Max. T. Rogers NMR Facility and the MSU Biomolecular NMR facility. They have provided me the ability to accomplish my SSNMR research projects. I greatly appreciate the help that I received from Mr. Kermit Johnson and Dr. Dan Holmes of the Max T. Rogers NMR facility and also Dr. Jochem Struppe from Bruker Biospin (Bricilla, MA). Assistance from Dr. Struppe provided the ability to fully utilize the 21.1 T (900 MHz) NMR and E–free probe. Dr. Struppe also collected data for a sample with the 700 MHz NMR and E-free probe which is presented in Chapter 4 for one of my samples. I am also grateful to Dr. Shivani Ahuja who was always willing to help answer my questions with

experiments and data processing associated with the 900 MHz NMR. I also want to thank my committee, Dr. John McCracken, Dr. Kevin Walker, and Dr. Jim Geiger for all their help and guidance during my Ph.D. career. Their advice and suggestions were helpful in driving my project forward.

Finally, I would like to thank the Weliky group, both past and present for all their support and help during my Ph.D. career. Help from former graduate students Dr. Wei Qiang, Dr. Yan Sun, Dr. Zhaoxiong "Norm" Zheng, Dr. Jaime Curtis–Fisk, Mr. Scott Schmick, Mrs. Erica Vogel, Mr. Li Xie, Mrs. Koyeli Banerjee, Mrs. Punsisi Ratnayake, and Post–docs Dr. Kelly Sackett and Dr. Charles Gabrys were essential to me for this project. Help from Mr. Douglas R. Kindra as an undergraduate student was quite beneficial in preparing large quantities of the Hairpin protein. Finally I would like to thank all my friends and family that have been there and supported me through this process in obtaining my Ph.D.

TABLE OF CONTENTS

LIST OF TABLES

LIST OF FIGURES

Figure 4–9: ^{13}C CP ramp experiment at 21.1 T for FP–Hairpin with UA6/UG10 labeling in the FP region in a POPC/POPG/Chol lipid membrane environment. Approximately 1 μmole of protein was added to lipid vesicles at pH 3. The spectrum is the result of 4096 acquisitions and 100 Hz of Gaussian line broadening. The spectrum was acquired at a nominal temperature of –23 °C as measured at the thermocouple, and 12 kHz spinning frequency. Spinning sidebands are marked by (*). The (x) is at δ = 131.9 ppm corresponding to the aromatic region of the ^{13}C spectrum. This signal at 131.9 ppm is not observed in the pH 7 samples, so it is likely that it arises from a protonated side chain / aromatic residue of the protein or is due to cholesterol. One possibility of observing the signal at 21.1 T and not 9.4 T is due to the increased ^{13}C peak signal to noise per scan at the higher field. This signal is also observed ^{13}C CP ramp experiment using dynamic nuclear polarization which is presented in Appendix II. DNP has also provided ~39–fold peak signal to noise per scan enhancement with microwave irradiation of the sample compared no microwave irradiation, which is why the 131.9 ppm chemical shift is observed in the DNP ^{13}C CP experiment. 205

Figure 4–10: 2D DARR ^{13}C–^{13}C spectra at 21.1 T of FP–Hairpin with uniform ^{13}C, ^{15}N labeling at Ala–6 and Gly–10 in the FP region in an 8:2:5 molar ratio of POPC/POPG/Chol in a lipid membrane environment at ~33:1 lipid to protein ratio. The protein and lipid vesicles were prepared as described in Chapter 2's "Membrane Lipid Preparation, Method B" section. (A) The 50 ms mixing time spectrum shows the intra–residue cross peaks. (B) The f_2 slice corresponding to the Ala $^{13}C\beta$ β–strand conformation from f_1 = 23.5 ppm is marked by the red arrow in (A). There were 256 t_1 points and 128 scans summed per t_1 point in a total time of ~14 hrs. Assignments are listed as assignment in f_2 – assignment in f_1. 100 Hz of Gaussian line broadening was applied to each dimension. 207

Figure 4–11: 2D DARR ^{13}C–^{13}C spectra at 21.1 T of FP–Hairpin with uniform ^{13}C, ^{15}N labeling at Ala–6 and Gly–10 in the FP region in an 8:2:5 molar ratio of POPC/POPG/Chol in a lipid membrane environment at ~33:1 lipid to protein ratio. The protein and lipid vesicles were prepared as described in Chapter 2's "Membrane Lipid Preparation, Method B" section. (A) The 500 ms mixing time spectrum shows the intra–residue cross peaks, however no inter–residue cross peaks were observed in this sample between A6 / G10 consistent with the other FP–Hairpin work presented in Chapters 3 and 4. (B) The f_2 slice corresponding to the Ala $^{13}C\beta$ β–strand conformation from f_1 = 23.5 ppm is marked by the red arrow in (A). There were 256 t_1 points and 320 scans summed per t_1 point in a total time of ~46 hrs. Assignments are listed as assignment in f_2 – assignment in f_1. 200 Hz of Gaussian line broadening was applied to each dimension. 208

Figure AI–17: 2D NCO experiment for U–NAL. (A) The carbonyl region of the 2D experiment, where the predominate peak is the acetyl ^{13}CO for U–NAL. A slight peak for the Leu ^{13}CO is also seen. (B) The aliphatic region of the 2D plot where the Leu ^{13}Cα carbon is observed. No other ^{13}C peaks are observed in the 2D plot. The slices presented in (C) and (D) correspond to the red arrows in the 2D plot in (A) and (B). The slice was taken at the ^{15}N chemical shift of 128.0 ppm. The Leu ^{13}CO peak is hardly observable in (C). The 2D results are consistent with the 1D NCO results for Figure 4–20B. The chemical shifts are presented in Table AI–6. 25 Hz of Gaussian line broadening was applied to each dimension. ..325

Figure AI–18: The 2D NCA experiment for FP–Hairpin UA6/UG10 prepared at pH 3 with ~1 μmole of protein in a lipid membrane consisting of an 8:2:5 molar ratio of POPC/POPG/Chol. 300 Hz of Gaussian line broadening was applied to each dimension. (A) The 2D NCA plot, where the Ala–6 ^{15}N/^{13}Cα and the Gly–10 ^{13}Cα/^{15}N cross peaks are observed. (B) The slice corresponding to the Ala–6 ^{15}N chemical shift of 125 ppm. The chemical shifts of the cross peaks are presented in Table AI–5. The Ala–6 ^{13}Cβ peak is observed in the slice (B), however it is not seen in the 2D plot due to the chosen contour levels. Lowering the contour levels of the 2D plot would result in the spectrum being filled with noise. The 2D plot is the result of 128 scans per t_1 point, with 128 t_1 points and a 2 s recycle delay. The raw and processed data are listed in Table AIV–6. Parameters for the 2D experiment are presented in Table AI–5. 326

Figure AI–19: Pulse sequence for the Bruker 3D NCACX experiment at 21.1 T. The magnetization is initially prepared by a π/2 pulse on ^{1}H, after a delay (t_1) the magnetization is selectively cross polarized from the ^{1}H→^{15}N nuclei. After a second delay (t_2), the magnetization is selectively cross polarized from the ^{15}N→^{13}Cα nuclei with a tangent ramp for the ^{13}C nuclei (see Figure 2–10 for more information). The transverse magnetization is then rotated to the Z axis by a ^{13}C π/2 pulse where a third delay (t_3) exchanges the magnetization among the nearby ^{13}C nuclei. Following the t_3 mixing, the ^{13}C magnetization is rotated back to the transverse plane by a ^{13}C π/2 pulse and then detection occurs on the ^{13}C channel. This variant of the pulse sequence uses a PDSD mixing for the t_3 period. A DARR t_3 period can also be used by applying ^{1}H rf during the t_3 mixing time if desired, much like the 2D ^{13}C–^{13}C experiment (Figure 2–13B). 329

Figure AI–20: Visual presentation of the 3D box. For the experiments discussed here, the F1 dimension is the ^{15}N chemical shift, the F2 dimension is the ^{13}C chemical shift, and the F3 dimension is the ^{13}C chemical shift. The 2D planes obtained from the 3D experiments corresponding to the F1–F2 or the F2–F3 can be visually seen in the cube. The F1–F2 plane

LIST OF ABBREVIATIONS AND SYMBOLS

1D	one dimensional
$^{13}C_{lab}$	^{13}C label
$^{13}C_{NA}$	^{13}C natural abundance
$^{15}N_{lab}$	^{15}N label
$^{15}N_{NA}$	^{15}N natural abundance
2D	two dimensional
3D	three dimensional
A	absorbance
AA	amino acid
ACN	Acetonitrile
AIDS	acquired immunodeficiency syndrome
AMS	ammonium sulfate
BCA	bicinchoninic acid
BF_x	base frequency of nucleus "x"
BMWS	broad molecular weight standards
B_0	static external magnetic field
BP	bearing pressure

Buffer A	100 % DDW / 0.1 % TFA; for RP–HPLC
Buffer B	90 % ACN / 10 % DDW / 0.1 % TFA; for RP–HPLC
Cα	alpha carbon
Cβ	beta carbon
CD	circular dichroism
Chol	cholesterol
CHR	C–terminal heptad repeat
CO	carbonyl
CP	cross polarization
CS	chemical shift
CSA	chemical shift anisotropy
CW	continuous wave
d	delay (Bruker software variable)
Da	Dalton
DARR	dipolar assisted rotational resonance
dB	decibel
DC	dipolar coupling
DCM	dicholormethane
DCP	double cross–polarization
DDW	degassed deionized water
DEPBT	3–(Diethoxyphosphoryloxy)–1,2,3–benzotriazin–4(3H)–one
DIEA	*N*,*N*–diisopropylethylamine
DMF	*N*,*N*–dimethylformamide

DNP	dynamic nuclear polarization
DP	drive pressure
DSC	differential scanning calorimetry
DTPC	1,2–di–O–tetradecyl–*sn*–glycero–3–phosphocholine
DTPG	1,2–di–O–tetradecyl–*sn*–glycero–3–phospho–*rac*–(1–glycerol) sodium salt
DTT	dithiothreitol
E	efficiency
E_c	conservative electric field
E. coli	*Escherichia coli*
E–free	electric field free probe design
EM	electron microscopy
ENV	envelope
EPL	expressed protein ligation
ESI	electrospray ionization
FID	free induction decay
FP	fusion peptide
FP23/FP34	first 23 or first 34 residues of N–terminal fusion peptide
FPH / FP-HP	FP-Hairpin construct
FT	Fourier transform
FWHM	full width at half maximum
GdCl	guanidinium chloride
GM	Gaussian multiplication
gp	glycoprotein

gp41	HIV fusion protein
HEPES	N–(2–hydroxyethyl)piperazine–N'–2–ethanesulfonic acid
HF	hydrofluoric acid
HFP	HIV fusion peptide
HIV	human immunodeficiency virus
HP	expressed gp41 NHR + minimal loop + CHR
HPLC	high performance liquid chromatography
HP–MPER	expressed gp41 HP + MPER domain
Hz	hertz
IPTG	isopropyl–β–D–1–thiogalactopyranoside
IR	infrared
KBr	potassium bromide
kDa	kilodalton
LB	line broadening
LBm	Luria Bertani broth media
LGR	loop gap resonator
LSNMR	liquid state NMR
LUV	large unilamellar vesicles
MALDI	matrix assisted laser desorption ionization
MAS	magic angle spinning
MES	2–(*N*–morpholino)ethanesulfonic acid
MESNA	2–mercaptoethanesulfonic acid
MHz	megahertz

mM	millimolar
MPAA	4–mercaptophenylacetic acid
MPER	membrane proximal external region
MW	microwaves
MWCO	molecular weight cutoff
N70	gp41 FP + NHR
NCA	$^{1}H \rightarrow {}^{15}N \rightarrow {}^{13}C\alpha$ DCP
NCL	native chemical ligation
NCO	$^{1}H \rightarrow {}^{15}N \rightarrow {}^{13}CO$ DCP
NHR	N–terminal heptad repeat
NMR	nuclear magnetic resonance
N–PHI	N–terminal pre–hairpin intermediate
ord	order for baseline correction
P	pulse (Bruker software variable)
P0	zero order phase correction (nmrDraw)
P1	first order phase correction (nmrDraw)
PCR	polymerase chain reaction
PDB	protein data bank
PDSD	proton driven spin diffusion
PHI	pre–hairpin intermediate
PI	Phosphatidylinositol
PL	power level (Bruker software variable)
Pop	population

poly	polynomial baseline correction
POPC	1–palmitoyl–2–oleoyl–*sn*–glycero–3–phosphocholine
POPE	1–palmitoyl–2–oleoyl–*sn*–glycero–3–phosphoethanolamine
POPG	1–palmitoyl–2–oleoyl–*sn*–glycero–3–[phospho–*rac*–(1–glycerol)]
POPS	1–palmitoyl–2–oleoyl–*sn*–glycero–3–[phospho–L–serine]
ppm	parts per million
PS	phase (nmrDraw)
REDOR	rotational echo double resonance
rf	radio frequency
RP–HPLC	reverse phase high performance liquid chromatography
rpm	revolution per minute
S_{CP}	signal from cross polarization spectrum
S_F	signal from filtered spectrum
SHB	six helix bundle
SR	spectrum reference (value in Hz, used in Bruker software)
SSB	spinning sideband
SDS	sodium dodecyl sulfate
SDS–PAGE	sodium dodecyl sulfate polyacrylamide gel electrophoresis
SPPS	solid phase peptide synthesis
SSNMR	solid state nuclear magnetic resonance
SUV	small unilamellar vesicle
t–Boc	tert–butyloxycarbonyl
TCEP	tris(2–carboxyethyl)phosphine hydrochloride

TFA	trifluoroacetic acid
THF	tetrahydrofuran
T_m	melting temperature
TM	transmembrane domain
TP	transpose (nmrDraw)
TOTAPOL	1–(TEMPO–4–oxy)–3–(TEMPO–4–amino)propan–2–ol
TPPM	two pulse phase modulation
U–NAL	uniformly labeled N–acetyl–leucine
ZF	zero filling (nmrDraw)
δ	chemical shift
ε	molar extinction coefficient
τ	mixing time
π	180° pulse
π/2	90° pulse

Chapter 1:

Introduction

What is HIV?

The Human Immunodeficiency Virus (HIV) [1] is a retrovirus responsible for the acquired immunodeficiency syndrome (AIDS) disease in humans. As of 2007, approximately 33.2 million people worldwide were infected with HIV, and 2.1 million deaths had occurred in 2007 from HIV.[1] The virus is surrounded by a membrane that contains glycoprotein spikes of gp160 which are proteolytically cleaved into two non–covalently associated glycoproteins, gp120 and gp41.[2] Gp120 shrouds the gp41 protein from the outside environment and is responsible for recognizing and binding to the CD4 receptors and chemokine coreceptors CXCR4 or CCR5.[2] Binding of these receptors results in causing conformational changes which expose the gp41 protein which allow it to insert into the host cell membrane.

Figure 1–1 [3] highlights the infection process as studied using electron microscopy (EM). First, the virus comes into close proximity of the host cell where gp120 is recognized by the surface receptor CD4. A conformational change occurs exposing the gp41 fusion protein which inserts into the host cell's membrane and draws the two membranes close together. As fusion progresses a fusion pore is created which expands allowing for the transfer of the contents from the virus to host cell. As the fusion pore expands the gp41 folds back into the six helix bundle (SHB) to support the pore and stabilize it from collapsing.[4] At the end of the fusion process, the fusion pore is opened up and stabilized by the gp41 SHB formation.

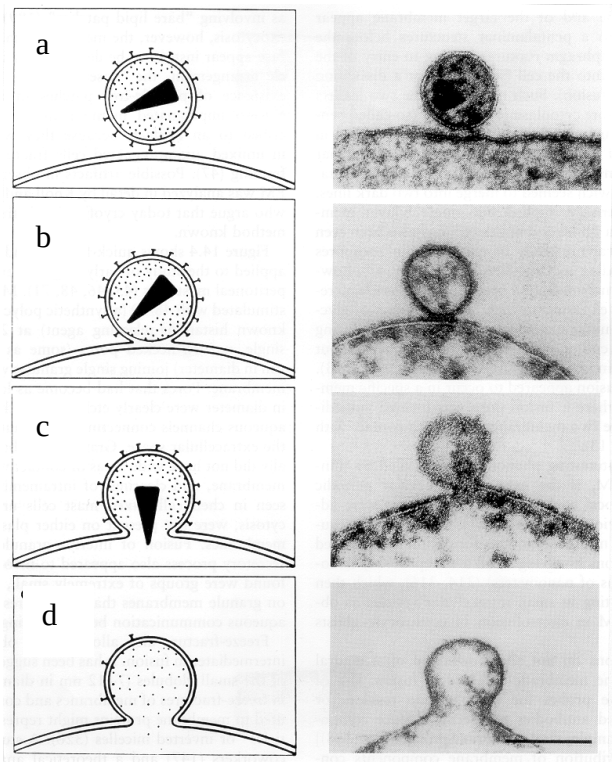

Figure 1–1: The time line for fusion of the viral vesicle to the host cell membrane. (a) The viral vesicle's gp120 subunit binds to the host cell's CD4 receptor. (b) After conformation changes to gp120, gp41 is exposed and is inserted into the host cell's lipid membrane to begin the fusion process. (c) The fusion pore has been created, and gp41 has folded back into the SHB formation to support the fusion pore, allowing it to expand, and the viral RNA (black triangle) can pass through the pore and enter the host cell. (d) Infection of the host cell is completed.[3]

Membrane Fusion

Gp41 is implicated in the membrane fusion process, causing the merging of the virus and host cell membranes. The HIV fusion protein gp41 is classified as a Class I fusion protein, meaning that the protein is a trimer, and has a N–terminal fusion peptide.[5] For the viral vesicle of HIV to infect a host cell, the membranes of the host cell and viral membrane must first fuse and create a fusion pore. This process is catalyzed by the gp41 protein located on the surface of the virus vesicle which is shrouded by the gp120 protein.[5] After binding of gp120 to multiple receptors a conformational change occurs exposing the gp41 protein with its N–terminal fusion peptide.[5] Figure 1–2A shows the initial gp120/gp41 complex consisting of three subunits of each protein. Gp41's fusion peptide sequence is very hydrophobic and will insert in the host cell's lipid membrane creating the pre–hairpin intermediate (PHI), as seen in Figure 1–2B. The FP domain of gp41 corresponding to the first 16 amino acid residues will form an antiparallel β–sheet structure while the rest of the ectodomain remains outside of the lipid membrane.[6-9] The FP domain creates a fusion pore which expands allowing for the passage of the viral material from the virus to the host cell. The extended PHI will have the CHR domain fold back and pack antiparallel to the NHR domain forming the SHB and remaining on the exterior of the membrane surface as seen in Figure 1-2. Folding of the gp41 protein into the SHB formation drives the expansion of the fusion pore, which then will stabilize and support the pore from collapse.[4] The FP domain will remain in the membrane interior, separate from the folded SHB which will be located on the membrane exterior. The SHB is composed of the antiparallel NHR and CHR domains stabilizes the fusion pore created by the FP domain. The SHB will arrest membrane fusion and stabilize the fusion pore as seen in Figure 1-2C. The full length HXB2 strand of HIV's protein sequence is presented in Figure 1-2D and is color coded to match with the structures

drawn in Figures 1-2B and 1-2C. Studies have shown that the PHI conformation lasts up to 15 minutes, making it one area of drug research for targeting the NHR or CHR domains which would prevent successful formation of gp41's SHB and preventing the fusion pore from enlarging.[10]

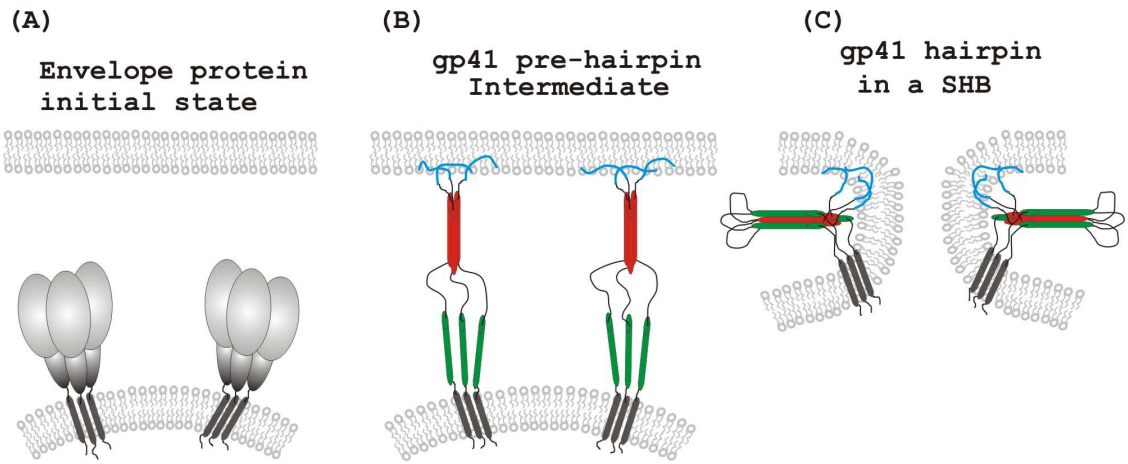

Figure 1–2: HIV fusion model. (A→B) After binding of HIV's gp120 protein to target cell receptor proteins, gp41 is activated and binds the target cell membrane in the Pre–Hairpin structure. The final state (C) is fused membranes with a fusion pore and gp41 in the Hairpin structure. (D) Full amino acid sequence for the HXB2 gp41 construct. The regions are color coded to match the model presented in (B) and (C). Reproduced with permission from Vogel et al.[11] The different membrane structures presented here will be related to the EM pictures presented in Figure 1-1 below. For interpretation of the references to color in this and all other figures, the reader is referred to the electronic version of this dissertation.

The different structures presented in Figure 1-2 correlate with the electron microscopy images of Figure 1-1 in the following way: First, Figure 1-2A correlates with Figure 1-1a where the virus vesicle is approaching the host cell and the receptor and co-receptors on the host cell will recognize the gp120 protein resulting in a conformational change exposing the gp41 protein. Proceeding from Figure 1-2A → 1-2B, the gp120 protein has undergone a conformation change exposing the gp41 protein, which then inserts in the host cell's membrane. This is observed in the EM image of Figure 1-1b. The EM image in Figure 1-1b also illustrates that the initial lipid mixing of the viral and host cell membranes is occurring called hemifusion, which is not shown in Figure 1-2B. Figure 1-2B → 1-2C provides structures which correspond to the post lipid mixing of the viral and host cell membranes, creation, enlargement, and stabilization of the fusion pore, and folding of the gp41 intermediate into the final SHB formation while the FP domain is still inserted into the lipid membranes. These steps are illustrated by Figure 1-1c → 1-1d where the images show the fusion pore formation and ability to transfer the viral RNA genetic material (Figure 1-1: black triangle) from the viral capsid through the fusion pore and into the host cell.

As presented in Figures 1-2B and 1-2C, the FP domain is the blue line from residues 1-16 and the apolar region from 17-22. The red helix corresponds to the NHR domain of residues 23-84 followed by a loop from residues 85–106 and finally the green helix spans residues 107–194 which contains the CHR and the membrane proximal external region (MPER) domains. The black tube extending through the viral membrane (bottom) is the transmembrane domain anchor. The green helix shown in Figures 1-2B and 1-2C is not a continuous helix for the CHR and MPER domains as depicted. Buzon and co-workers report that the MPER domain is highly helical with continuous helical structure from residues 628 to 676 followed by a 90° bend at

residue Asn 677 placing the remaining residues of 678-683 perpendicular to the membrane.[12] The continuous helix of residues 628 – 676 incorporates the CHR and all but the last 7 residues of the MPER domain. Their basis for this 90° bend is based off of crystallography of the HR1/HR2 complex containing the MPER domain.[12]

The fusion peptide has been extensively studied by Weliky and co–workers over the past decade.[6-9, 13-29] From this work a better understanding of the structure of the FP region embedded in membranes has been obtained. Forward progress has also been made in the study of larger domains of the HIV gp41 protein by Weliky and co–workers to determine structure and function relationships using solid state nuclear magnetic resonance (SSNMR), fluorescence, circular dichroism (CD), and differential scanning calorimetry (DSC).[11, 30-35]

Gp41 is an interesting protein to study due to the lack of high resolution structures and also the desire to understand how this protein catalyzes membrane fusion. SSNMR has the ability to provide these high resolution structures of gp41 in a lipid membrane environment which can not be achieved by X–ray crystallography. Determination of high resolution secondary and tertiary structures for key intermediates along the fusion pathway in a native lipid environment is one main area where SSNMR can be utilized.

Function of gp41 Constructs

Lipid mixing experiments were performed to develop an understanding of the fusion of peptides and proteins with lipid membranes. Lipid mixing is an experiment where two populations of lipid vesicles, one set with labeled fluorescent and quenching lipids and one set without fluorescent lipids are mixed in a 1:9 ratio in solution to which a protein or peptide is then added.[14] The addition of the protein or peptide will then cause the two populations of vesicles

to fuse, becoming larger and spread the fluorescently labeled lipid away from the quencher lipid. By increasing the distance between the fluorescent lipid and the quencher lipid, an emission signal will be observed due to resonant energy transfer.[36] Detection of the emission signal is done by monitoring the emission wavelength of λ = 530 nm.[36] Lipid mixing experiments allow for probing the ability of a peptide or a protein to fuse lipid membranes, and to determine the rate and extent of membrane fusion. The lipid mixing experiments are correlated with the membrane fusion process of gp41 which are presented in Figures 1-1b and 1-1c.

Lipid mixing experiments were performed with gp41 constructs of various oligomerization states to try and elucidate a structure – function relationship between oligomerization state and rate of membrane fusion. Lipid mixing assays have shown that for the FP region, oligomerization state is directly tied to rate of lipid mixing, where FP monomer < FP dimer < FP trimer where the FP dimer and FP trimer were chemically cross–linked.[23]

The oligomerization state is relevant to the rate of fusion of lipids as a chemical cross–linked FP trimer induced an ~40–fold increase in lipid mixing as compared to its monomer.[23, 27] In comparison, a peptide "N70" corresponding to the first 70 residues of HIV containing the FP and the NHR region was found to assemble into discrete trimers and also aggregates of trimers, and induce lipid mixing at a much greater rate than the FP23.[30, 37, 38] The trimeric assembly of N70 is due to the NHR coil-coiled region, and the aggregates of trimers are due to the FP region of N70.[30, 38] Notably, neither of these peptides contain the hairpin structure of the SHB.

Two new gp41 constructs termed "Hairpin" and "FP–Hairpin" showed quite different results compared to chemically cross–linked FPs and "N70" for lipid mixing. The Hairpin construct represents the SHB without the FP domain or native loop and the FP–Hairpin construct

had the FP region chemically ligated to the N–terminus of the Hairpin protein.[30, 31, 35] Work with both of these constructs has shown that the formation of the SHB halts lipid mixing at pH 7.[30] For example, addition of the FP34 construct to membrane vesicles induced lipid mixing that was subsequently arrested when FP–Hairpin was added at a later time, suggesting that the SHB structure abolishes lipid mixing.[30] It is likely that the role of the SHB is to stabilize the lipid membranes after fusion has completed.[30]

Research by Markosyan and co-workers probed the SHB formation for gp41 in an attempt to correlate pore formation with SHB formation. They discovered that bundle formation occurs after the fusion pore has formed, suggesting that the SHB is used to stabilize the fusion pore against collapse.[4] These studies were done following a temperature jump protocol that initially maintained the temperature at 4°C where no pore formation occurred, followed by increasing the temperature to 37°C using a laser to heat the cell solution which resulted in pore formation which was detected by calcein dye transfer through the fusion pore.[4] Two main findings from this research were: (1) Allowing the solution to cool from 37°C to 4°C resulted in the ability of gp41 to maintain small pores for up to 15 minutes before closing irreversibly.[4] (2) By binding of the synthetic peptides N36 or C34 to the CHR or NHR respectively, the gp41 protein was not able to fold back into a SHB, preventing the enlarging of the fusion pore.[4] This was observed visually by the lack of dye transfer through the fusion pore, and the authors suggest that any pores that were created prior to binding of the peptides would eventually close irreversibly as was observed by maintaining the cell solution at 4°C.[4] The results from this earlier work showed that the formation of the SHB is not completed by the time the pore forms, as observed by the stabilization of the small pores. The formation of the SHB structure however

was thought imperative to enlarge and stablize the fusion pore.[4] The data highlight the folding of gp41 from the extended pre-hairpin intermediate to the SHB formation is essential to the stabilization and maintenance of the fusion pore. The data also suggests that peptides that target the extended PHI state, such as T-20 or C34, bind to the NHR and prevent the gp41 protein from folding into the SHB.[4]

Drug Targeting for gp41

Targeted regions of the HIV gp41 protein include the NHR with use of synthetic CHR peptides such as T-20 or C34.[39, 40] There is a window of ~15 minutes between when gp120 and CD4 interact and the six helix bundles. It is during which time that the intermediate states of gp41 can be targeted.[10] Binding of the CHR peptides to the NHR domain of gp41 while it is fully extended in the pre–hairpin intermediate state will prevent gp41 from folding into the SHB, preventing fusion pore formation and stabilization.[4, 39-42] One of the best anti–HIV drugs T–20 also known as Enfuvirtide or Fuzon, is cost prohibitive with a year supply costing ~$20,000.[42] Figure 1-3 compares the amino acid sequence of the HXB2 amino acid sequence for the CHR domain of gp41 with the amino acid sequence of C34 and T-20. T-20 corresponds to a 36 residue portion of the CHR domain of gp41, allowing it to pack against the NHR region of gp41 creating a SHB while in the PHI state. C34 corresponds to 34 residues of the CHR domain which will also bind to the NHR domain. As seen in Figure 1-3, there is overlap between C34 and T-20, with the main difference being the starting and ending locations for the two peptides. The SHB formation between NHR and either T-20 or C34 will trap gp41 in the extended state, preventing the completion of the fusion pore, and preventing the transfer of genetic material from the viral capsid to the host cell.[4]

```
Residue: 117                  137                  157
          |                    |                    |
   CHR: TTWMEW DREINNYTSL IHSLIEESQN QQEKNEQELL ELDKWASLWN WF
   C34: --WMEW DREINNYTSL IHSLIEESQN QQEKNEQELL ---------- --
  T-20: ------ ------YTSL IHSLIEESQN QQEKNEQELL ELDKWASLWN WF
```

Figure 1–3: The amino acid sequence for the C-heptad repeat (CHR) domain of the HXB2 gp41 sequence and the amino acid sequence for the anti-HIV synthetic peptides C34 and T-20. The two synthetic peptides are derived from the CHR domain of gp41. Sequences and layout adopted from reference [43].

A different drug target domain is the membrane proximal exterior region (MPER) which is a short segment consisting of ~22 residues (662–683) located between the CHR domain and the transmembrane (TM) segments of gp41.[44] This domain is incorporated in the green helix presented in Figure 1-2B. The MPER domain is highly conserved across the HIV-1, HIV-2, and SIV sequences which is one reason the MPER domain is being targeted for drug development.[44] Targeting this conserved MPER region by broadly neutralizing antibodies can be affective at simultaneously neutralizing multiple strains of HIV at one time. Currently, the broadly neutralizing antibodies are being designed to straddle the helix-hinge-helix motif which is common between the HIV and SIV sequences.[44] As discussed previously, the HR2/MPER domain was crystallized by Buzon and co-workers shows that the MPER is at a right angle to the CHR domain and the membrane.[12]

Mutational Studies of gp41

Mutational studies were performed to understand the importance of the fusion peptide and how mutations in the FP sequence affect the fusion process. Mutations in the FP region with V2E, L9R, and A15E have been studied before.[45, 46] The V2E mutation swaps the nonpolar hydrophobic valine to a negatively charged hydrophilic glutamic acid residue and is one of the

most common mutations studied.[45, 46] The V2E mutation has been studied by syncytium formation [45, 46], SSNMR [8], lipid mixing assays [47], and viral infection studies [47, 48].

Syncytium formation is when cells fuse to form large cells with many nuclei.[49] Gp41 syncytium formation occurs when infected CD4 cells start producing the viral proteins which then migrate to the membrane where they will stick out of the cell making it possible to fuse with a healthy cell, creating the large multi–nuclei syncytia.[49] Syncytium formation is significant as it is correlated with the rapid progression of HIV to AIDS.[50]

The FP V2E mutant does not induce lipid mixing of membrane vesicles and SSNMR studies show that it is located on the membrane surface.[8, 9, 51] Syncitia and virus infection studies of gp41 with the FP V2E mutant have shown that this mutant is inaffective at fusing membranes and infecting host cells.[45-47]

Mutational studies have also been carried out on the NHR (HR1) domain of gp41. Due to the lack of high resolution structures of the gp120–gp41 interaction and NHR being a highly affective drug target, alanine scanning mutagenesis has been used to understand the protein–protein interactions.[52] The alanine scanning mutagenesis studies systematically changed residues to alanine one at a time in the HR1 domain to determine the affects of the mutation on viral entry using a luciferase-based assay.[52] Measuring the intensity of light observed from the luciferase assay will relate proportionally to the viral entry activity.[52] The alanine mutation studies found that the gp41 protein's HR1 domain is sensitive to mutations resulting in the protein becoming inaffective at fusing membranes.[52] The mutation results of the HR1 domain correlate well with the mutagenesis studies of the FP region, discussed above. The mutations in either the fusion peptide domain or the HR1 domain provide evidence that membrane fusion can be disrupted by mutations in these regions, resulting in the inability to completely fuse the viral

and host cell membranes which would prevent the complete formation of the viral fusion pore and prevent the transfer of genetic material from the viral capsid to the host cell.

Structure Determination of gp41 Constructs

Structures by Nuclear Magnetic Resonance

Research has provided data on the structure and function of the FP region. Structurally, the FP region has been studied using liquid state NMR (LSNMR), solid state NMR (SSNMR), and Fourier Transformed Infrared (FTIR) with ^{13}C and ^{15}N labeled amino acids. The HIV fusion peptide (FP) consist of the first ~20 residues of the N–terminus of gp41.[13] The FP domain is hydrophobic enabling its ability to insert into lipid membranes. Studies from the past ~10 years have focused mainly on the FP region in order to understand the fusion process. Several reasons for this are (1) the FP region being ~20 residues which can easily be synthesized by solid phase peptide synthesis (SPPS). (2) The FP peptides induce vesicle fusion which can be monitored via lipid mixing assays.[9] (3) Isotopic labeling of the FP is easily achieved for peptides made by SPPS. (4) Peptide model systems are easier to study than the whole protein system in their ability to be quickly produced, straight forward purification, and ability to selectively label at specific residues whereas production of a whole protein would result in the possibility of low protein yields, complicated purification schemes, and complicated labeling schemes where one can not selectively label a specific residue.[53] Studying peptides allows for developing model systems to answer specific question, such as the HFP's role in membrane fusion or the structural motif of HFP in lipid membranes as two examples.[7, 9, 13, 15, 16, 51, 54] These model systems can then be applied to understanding how larger domains or the whole protein interact with the lipid membranes in the case of gp41.

Liquid state characterization of the FP region in a micelle solution resulted in an alpha helical structure assignment from residues Ile4 to Met19.[55] SSNMR experiments were performed in a lipid membrane environments with ~30 mol % cholesterol incorporated into the lipid membranes, which is biologically relevant for the HIV virus and host cell membrane composition.[56] In contrast to the LSNMR experiments, SSNMR experiments of the FP region in membranes containing biologically relevant cholesterol resulted in a β–strand structure for residues Ala-1 – Gly-16.[7, 9, 14, 51] The FP was shown to have a mix of alpha helical and β–strand conformations in cholesterol depleted membranes.[15, 16, 54]

SSNMR studies of the gp41 fusion peptide determined that fusion peptides form antiparallel arrangements with tertiary structural contacts between A6 / G10 and F8/L9.[7] Work from the Weliky group using SSNMR studies to probe the registry of the HFP's showed that at most, 15% of the registries were in a parallel arrangement.[9] Quantitative SSNMR studies showed that predominantly the HFP forms an antiparallel arrangement in cholesterol containing membranes with at least half the peptides in the 16→1/1→16 and 17→1/1→17 overlap registries.[9, 18]

Because of this conflicting data between the liquid state and solid state NMR along with the lack of high resolution crystal structures of the FP region, SSNMR can be employed as a valuable tool for providing the ability to study the peptide or protein in the context of the native lipid membrane environment. SSNMR can provide high resolution structures of proteins in their native environments such as lipid membranes or proteins which are not able to be crystallized due to their conformational flexibility. Recently larger systems of the 115 residue construct FP–Hairpin containing the FP, N–heptad repeat (NHR), six residue minimal linker, and C–heptad repeat (CHR) have been studied by SSNMR to determine the structure of the FP region in

membranes in the context of the low energy folded state of the SHB.[30] This work has shown that the FP region of FP–Hairpin adopts both α–helical and β–strand conformations in cholesterol containing and cholesterol depleted lipid membrane environments.[31]

Crystal Structures

A major goal of this research is to determine the structure and function of the gp41 protein in the context of the native membrane environment. No crystal structures of the native gp120/gp41 complex or of the gp41 FP region exist. There are crystal structures for HIV gp41 representing the SHB formation[2, 12, 57-60] and of the SIV gp41 protein's SHB formation[61, 62], but none for this exact construct of "Hairpin" and none that contain the fusion peptide region. The current crystal structures represent the final folded state of gp41 in the low energy SHB formation which has three NHR peptides packed in parallel in a central core and three CHR peptides packed antiparallel to the NHR domains forming a trimer of heterodimers.

Push to Larger gp41 Constructs

As the progress on understanding the FP region continues it is important to push forward to understand the other parts of the gp41 domain and what role they play in membrane fusion. Model peptides have been an essential starting point for understanding how the gp41 FP region interacts with lipid membranes and in development of secondary and tertiary structural models for the FP region. However, the gp41 protein consists of more than just the FP region, and thus larger constructs like "N70", "Hairpin", and "FP–Hairpin" are the next steps in understanding how the domains of gp41 affect the fusion process between the virus vesicle and the host cell membranes. The larger constructs of the gp41 protein need to be produced either by recombinant

expression in *E. coli* or by a combination of SPPS and expression in *E. coli*. The "N70" construct corresponds to the first 70 residues of the FP + NHR domains, which has been shown to associate into trimers and larger aggregated oligomers.[37] N70 also has the ability to bind synthetic CHR peptides and form a SHB.[37] Two separate constructs of a 34-mer and a 36–mer peptide are ligated together using the native chemical ligation (NCL) reaction to create the "N70" molecule.[37] A third way to create larger domains is a combination of SPPS and recombinant protein expression. For the "FP–Hairpin" construct, FP23 is synthesized by SPPS and the 92 residue "Hairpin" is expressed recombinantly in *E. coli*.[30, 31] The NCL reaction ligates the two fragments together creating the FP–Hairpin construct.[30, 31] This approach has several key benefits with the main one being control over the isotopic labeling in the FP region.

Magic Angle Spinning for SSNMR

What are MAS and NMR?

NMR stands for nuclear magnetic resonance which is a technique that makes use of the magnetic properties of nuclei which have a non zero spin quantum number (K) by probing the splitting of the energy levels in a static magnetic field.[63] Examples include ^{1}H, ^{13}C, and ^{15}N which all have spin quantum numbers of K = 1/2, whereas ^{12}C has a spin quantum number of K = 0, and can not be probed by NMR. Solid state NMR (SSNMR) allows for the study of samples which are in the solid physical state. The samples are packed into a rotor and placed in a large magnetic field. The research that will be presented in Chapters 3 and 4 used 4 mm rotors (outer diameter) and either a 9.4 T, 16.5 T, or 21.1 T static magnetic field (B_0). Simply placing the solid sample in the magnetic field is not enough to obtain high resolution spectra. For solid

samples such as the proteins in lipid membranes that will be presented, the sample needs to be rotated about a specific angle of 54.7° with respect to the magnetic field direction, called the magic angle in order to average out the chemical shift anisotropy (CSA). Rotation of the sample about this angle is done by passing a gas flow of compressed air or nitrogen gas over the drive tip of the rotor, which is in the form of a turbine. There are three gas flows in the probe, the drive gas, the bearing gas, and the variable temperature (VT) gas. The bearing gas acts like a cushion for the rotor to sit in. The drive gas passes over the turbine, causing the rotor to rotate while being suspended by the cushion of bearing gas. The VT gas flows over the stator and sample and is used to control the temperature at which the stator and sample are at. Adjusting the gas flows will result in the ability to spin the 4 mm rotor up to ~15 kHz. The rotor is located in the stator, which is where the rf coils are located and is near the top of the NMR probe. The NMR probe is inserted into the magnet from below, and will position the stator and sample in the uniform static magnetic field. In the following subsections, the theory behind SSNMR will be introduced.

NMR Theory

NMR probes the differences in energy levels that are observed when a non zero spin quantum number is placed in a magnetic field.[63] The sample in the static, uniform magnetic field will be split into a low and high energy state, resulting in the sample having a net magnetization, where the magnetization is defined by Equation 1-1:

$$\mathbf{M} = \sum_i \mu_i \tag{1-1}$$

M is the magnetization resulting from the vector sum of the magnetic moments (μ_i). The magnetic moment is intrinsic to the sample, and is defined by Equation 1-2:

$$\boldsymbol{\mu} = \gamma\hbar\mathbf{I} \tag{1-2}$$

$\boldsymbol{\mu}$ is the magnetic moment vector, γ is the gyromagnetic ratio of the nuclei and **I** is the spin angular momentum of the nuclei.[64] The gyromagnetic ratio is different for each nuclear isotope, and can be found in various reference books. Equation 1-3 defines γ as the product of the nuclear g-factor (g_N) and the nuclear magneton (μ_N), and the reduced Planck's constant ($h/2\pi$):

$$\gamma = \frac{(g_N \mu_N)2\pi}{h} \tag{1-3}$$

Combining Equations 1-1 and 1-2 results in the magnetization being defined by Equation 1-4:

$$\mathbf{M} = \sum_i \gamma\hbar\mathbf{I}_i \tag{1-4}$$

Which is the product of the angular momentum of nucleus "i" ($\mathbf{I}_i$) and the gyromagnetic ratio (γ) for a nucleus. The net magnetization (**M**) interacting with the static magnetic field (B_0) is defined by Equation 1-5 where the "$\otimes$" means take the cross product, **a*b***cos(ϕ) of the two vectors, where ϕ is the angle between the two vectors:

$$\mathbf{M} \otimes \mathbf{B} \tag{1-5}$$

Equation 1-6 defines the applied magnetic field (B_0) with B_0 being the magnitude and **z** being the vector direction along the z axis.

$$\mathbf{B} = (B_0)\mathbf{z} \tag{1-6}$$

To determine the precession of the net magnetization about the magnetic field, the time derivative of Equation 1-5 needs to be determined, resulting in Equation 1-7:

$$\frac{d}{dt}\mathbf{M} = \gamma(\mathbf{M} \otimes \mathbf{B}) \tag{1-7}$$

The magnetization will precess about the magnetic field at the frequency (ω_0) of Equation 1-8:

$$\omega_0 = \gamma B_0 = 2\pi f_0 \tag{1-8}$$

The frequency (f_0) of Equation 1-8 is the Larmor precession frequency, and it is dependant on the nuclei's gyromagnetic ratio and the static field strength of the magnetic field.

The NMR Hamiltonian

The total Hamiltonian for a multinuclear spin system is the following:

$$\hat{H} = \hat{H}_{Ze} + \hat{H}_{D} + \hat{H}_{Q} + \hat{H}_{CS} + \hat{H}_{J} \tag{1-9}$$

Where $\hat{H}_{Ze}$ is the Zeeman Hamiltonian, $\hat{H}_{D}$ is the dipolar coupling Hamiltonian, $\hat{H}_{Q}$ is the quadrupolar Hamiltonian, $\hat{H}_{CS}$ is the chemical shielding Hamiltonian, and $\hat{H}_{J}$ is the J-coupling Hamiltonian.[65] The quadrupolar term is only present for spins greater than 1/2 (K > 1/2), for the cases being considered at present with K = 1/2, the $\hat{H}_{Q}$ term will be neglected. Energy is determined from the Hamiltonian by using the time independent Schrödinger Equation, where in Equation 1-10 $\hat{H}$ is the Hamiltonian operator, Ψ is a wavefunction, and E is the energy.

$$\hat{H}\Psi = E\Psi \tag{1-10}$$

E is an eigenvalue of the Hamiltonian equation.

Zeeman Hamiltonian

The Zeeman Hamiltonian is defined by Equation 1-11:

$$\hat{H}_{Ze} = -\hat{\boldsymbol{\mu}} \bullet \mathbf{B}_0 = -\gamma \hbar B_0 m \tag{1-11}$$

Where $\hat{\boldsymbol{\mu}}$ is the magnetic moment operator defined by Equation 1-12, and "$\bullet$" means the dot product of the two terms, and m is the spin quantum number discussed below. The Zeeman Hamiltonian describes the splitting of the nuclear spin in the magnetic field.

$$\hat{\boldsymbol{\mu}} = \gamma \hbar \hat{\mathbf{I}} \tag{1-12}$$

$\hat{\mathbf{I}}$ is the spin operator. When the nuclei are placed in a magnetic field, the spins will be split into different energy levels. The number of spin states is related to the spin quantum number (K) by Equation 1-13:

$$\text{Total number of spin states} = 2K + 1 \tag{1-13}$$

For the K = 1/2 nuclei spin, such as ^{1}H, ^{13}C, or ^{15}N, Equation 1-13 results in 2 different spin states. The individual spin states are defined by the quantum number m, where m is defined by Equation 1-14:

$$m = -K, -K+1, \ldots, K-1, K \tag{1-14}$$

The allowed spin states for K = 1/2 are m = +1/2 and m = -1/2 using Equation 1-14.[66] Using Equation 1-15 for the Zeeman Hamiltonian, the spin quantum numbers of m will result in the two spin states of Equations 1-16a and 1-16b.

$$H_{Ze} = -\gamma \hbar B_0 m \tag{1-15}$$

For m = +1/2, the Zeeman Hamiltonian will equal Equation 1-16a, for the m = -1/2, the Zeeman Hamiltonian will be equal to Equation 1-16b:

$$H_{Ze} = -\frac{1}{2}\gamma\hbar B_0 \tag{1-16a}$$

$$H_{Ze} = \frac{1}{2}\gamma\hbar B_0 \tag{1-16b}$$

Equation 1-16b with the spin state of -1/2 results in being the higher energy state. Equation 1-17 results in determining the difference in the two energy states.

$$\Delta E = E_{-1/2} - E_{1/2} = \gamma\hbar B_0 \tag{1-17}$$

The difference in the two energy states (+1/2 and -1/2) is linear and depends on the gyromagnetic ratio (γ) and the applied magnetic field strength (B_0). The larger the static field strength or the larger the gyromagnetic ratio, the greater the energy separation between the spin states.

At equilibrium, the population difference between the two spins states is not zero, but rather is governed by the Boltzmann distribution (p_j^*) which is the fractional population of the "j^{th}" state, Q is the total population and is presented in Equation 1-18:

$$p_j^* = \frac{e^{-E_j/kT}}{\sum_{j=1}^{n}\left(e^{-E_j/kT}\right)} = \frac{e^{-E_j/kT}}{Q} \tag{1-18}$$

E_j is the energy of the "j^{th}" state, k is the Boltzmann constant, and T is temperature in Kelvin. The denominator of Equation 1-18 is the partition function, which sums over all possible states for the system from 1 to n, and is denoted by Q.[67] Equation 1-18 yields the fractional population which has energy of E_j for the system.

$$Q = \sum_{j=1}^{n} \left(e^{-E_j / kT} \right) \tag{1-19}$$

At equilibrium the relative populations between the lower energy (+1/2 spin state) and higher energy (-1/2 spin state) can be determined from Equation 1-20.

$$\frac{p_{-1/2}}{p_{+1/2}} = e^{-(E_{-1/2} - E_{+1/2})/kT} \tag{1-20}$$

The Chemical Shift and Chemical Shift Hamiltonian

Nuclei do not all feel the same magnetic field as a result of their chemical shifts being spread out over a range of values. The cause of the different chemical shifts is shielding, which is defined by Equation 1-21:

$$B_{tot} = B_0(1-\sigma) \tag{1-21}$$

σ is called the shielding constant, and this value will vary according to the electronic environment.[68]

The chemical shift (δ) is defined by Equation 1-22:

$$\delta = \left(\frac{\gamma}{2\pi} \right) B_0 \left(\boldsymbol{\sigma}_{ref} - \boldsymbol{\sigma} \right) / \upsilon_{RF} \tag{1-22}$$

Where $\boldsymbol{\sigma}$ and $\boldsymbol{\sigma}_{ref}$ are the chemical shielding of the sample and the reference compound respectively, and υ_{RF} is the operating frequency of the spectrometer. The chemical shift of a sample is related to the isotropic and anisotropic chemical shifts, presented next.

The anisotropic chemical shift (δ_{CSA})is defined by Equation 1-23:

$$\delta_{CSA} = \delta_{11}\cos^2\theta_{11} + \delta_{22}\cos^2\theta_{22} + \delta_{33}\cos^2\theta_{33} \tag{1-23}$$

δ_{11}, δ_{22}, and δ_{33} are the "principal value" of the NMR chemical shifts corresponding to the principal axes, and θ_{11}, θ_{22}, and θ_{33} are the angles between the respective principal axis and the external magnetic field.[68] Figure 1-4A illustrates the principal axis system in relation to the external magnetic field. One example is the ^{13}CO of N-acetyl leucine (NAL) which has principal axis values of 246 ppm, 201 ppm, and 87 ppm for the δ_{11}, δ_{22}, and δ_{33} chemical shifts.[16] The chemical shift anisotropy is the dependence of the chemical shift on the orientation of the functional groups (i.e. ^{13}CO) relative to the external magnetic field direction.[68] The principal axis is a 3D orthogonal axis system fixed relative to the functional group and is determined from a single crystal. If one knows the orientation of the functional group(s) relative to the crystal axes and the orientation of the crystal axes relative to the external magnetic field direction, one can determine experimentally both the principal values and principal axis of a functional group.[68]

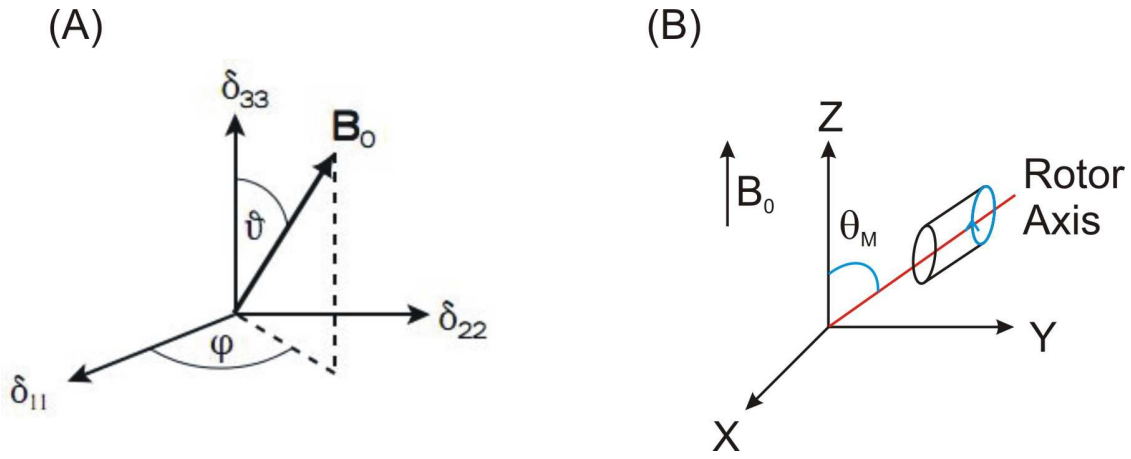

Figure 1-4: (A) MAS picture depicting the principal axes system, obtained from reference [69]. The δ_{11}, δ_{22}, δ_{33} are the principal axis with respect to the external magnetic field (B_0). φ and υ are the angles between the external magnetic field and the principal axis in spherical coordinates. (B) Schematic view of the rotor placed in the stator with the Z axis parallel to the external magnetic field (B_0). The rotor is placed at $\theta_M = 54.7^{\circ}$ with respect to the magnetic field. Rotation of the sample in the rotor is about the magic angle in relation to the static magnetic field shown by the blue arrow on the end of the rotor cylinder.

When the chemical shift anisotropy is not averaged out, a powder pattern of all possible orientations of the functional group in the magnetic field is obtained, as shown in Figure 1-5a. Rotating the sample about the magic angle, as depicted in Figure 1-4B results in the ability to average out the anisotropic interactions, resulting in obtaining the isotropic chemical shift (δ_{iso}), and spinning sidebands. The isotropic chemical shift is defined by Equation 1-24:

$$\delta_{iso} = 1/3\ (\delta_{11} + \delta_{22} + \delta_{33}) \qquad (1\text{-}24)$$

Using Equation 1-24 and the principal axis values from the above example with ^{13}CO of NAL results in the ^{13}CO's δ_{iso} = 1/3 (246 ppm + 201 ppm + 87 ppm) = 178 ppm.

The Dipolar Coupling Hamiltonian

Magic angle spinning (MAS) is a technique used in solid state NMR where the solid sample is packed into a rotor and is placed in a magnetic field at an angle of 54.7° with respect to the applied magnetic field (B_0). The rotor is then rotated around at kHz frequencies by blowing nitrogen gas over the drive tip's turbine fins. MAS is also used in SSNMR to average out the affects of dipolar couplings between nuclei.[66] The dipolar Hamiltonian equation is:

$$\hat{H}_D = -\left(\frac{\mu_o}{4\pi}\right)\frac{\gamma_I \gamma_S \hbar}{R_{IS}^3}\left(3\cos^2\theta_{IS} - 1\right)\hat{I}_Z \hat{S}_Z \qquad (1\text{–}25)$$

where γ_I and γ_S are the gyromagnetic ratios of spins I and S respectively, μ_o is the permittivity of free space, R_{IS} is the inter nuclear distance vector between the two nuclei and the angle θ_{IS} is the angle between the inter nuclear vector and the applied magnetic field. $\hat{I}_Z$ and $\hat{S}_Z$ are the spin operators of the nuclei I and S respectively. When a π pulse of rf is applied to the system, the spin operators will change signs due to π pulses rotating the magnetization by 180°. SSNMR experiments such as rotational echo double resonance (REDOR) make use of this property of the dipolar Hamiltonian which makes it possible to selectively reintroduce the dipolar coupling by have a non-zero dipolar coupling value during a rotor period. This will be discussed more in Appendix I in terms of the REDOR experiment. Spinning the sample about the angle θ_M will result in all components of the inter nuclear vectors which do not lie at this angle with respect to B_0 being averaged to zero.[66] The components that are collinear with the spinning axis will result in zero dipolar coupling as the term $3\cos^2\theta_{IS}$-1 will equal zero.[66]

The J-Coupling Hamiltonian

The final Hamiltonian to consider is the J-coupling Hamiltonian. J-coupling is a through bond coupling between two nuclei.[66, 68] J-coupling depends on molecular structure and is independent of the magnetic field strength.[66] J-coupling can be defined by Equation 1-26, which shows that there is no magnetic field dependence on the J-coupling which is why it can not be removed by MAS and remains a constant value in Hz even with differing magnetic field strength.

$$\hat{H}_J = h \sum_{i<j} (\mathbf{I}_i \bullet \mathbf{J}_{ij} \bullet \mathbf{I}_j) \tag{1-26}$$

In Equation 1-26, $\hat{H}_J$ is the J-coupling Hamiltonian, $\mathbf{I}_i$ is the nuclear spin of the i^{th} nucleus, $\mathbf{I}_j$ is the nuclear spin of the j^{th} nucleus, and $\mathbf{J}_{ij}$ is the interaction tensor, which is a value in hertz describing the spin-spin interaction between spin $\mathbf{I}_i$ and $\mathbf{I}_j$.[64] The values for J-coupling between two directly bonded ^{13}C's are small, typically ~50 Hz.[64, 68] The splitting from J-coupling can usually be observed in liquid state NMR due to the narrow linewidths of only a few hertz, whereas in SSNMR the linewidths are much broader, on the order of several hundred hertz, and the J-coupling will be within the linewidth of the peak.

Magic Angle Spinning

Placing the a sample in the magnetic field and rotating it about the magic angle, as depicted in Figure 1-4B will result in averaging out the chemical shift anisotropy term in the

H_{CS} Hamiltonian. However, spinning will not remove the splitting affects from the Zeeman Hamiltonian, isotropic chemical shift, or the J–coupling terms.[66] The most beneficial aspect of MAS is the fact that it averages out the CSA and dipolar coupling of the sample, resulting in narrower lines at the isotropic chemical shifts. A slight draw back to MAS is the need to spin at a frequency which is 2-3 times larger than the CSA to completely average out the CSA. Not spinning fast enough results in the appearance of spinning sidebands in the spectrum, which will be presented next in the subsection "Spinning sidebands from magic angle spinning".

What would be most convenient in SSNMR experiments would be to obtain narrow ^{13}C resonance signals like those obtained in LSNMR. In order to achieve this, one must spin the sample at kHz frequencies. MAS is done experimentally by spinning a rotor containing the sample about the $\theta_{MAS} = 54.7^{\circ}$ axis with respect to the magnetic field, which breaks up the powder pattern from the chemical shift anisotropy (CSA) of Equation 1-22 resulting in the isotropic chemical shift, defined by Equation 1-23. A powder pattern is shown in Figure 1-5a. The orientation of the ^{13}CO functional group with respect to the external magnetic field results in the observed powder pattern. Figure 1-5 illustrates the affect of placing a sample in a static magnetic field. In Figure 1-5a, no rotation of the sample occurs, resulting in the observed powder pattern. As the spinning frequency is increased the CSA is averaged out, resulting in the observation of the isotropic chemical shifts and spinning sidebands. The powder pattern for the ^{13}CO would look similar to what is shown in Figure 1-5a between 100 to 250 ppm. The highest peak in the powder pattern will be associated with the most likely orientation in the magnetic field. Spinning the sample about the magic angle axis results in obtaining the isotropic chemical

shifts, as defined by Equation 1-23 along with increased peak signal to noise of the spectrum.[66]

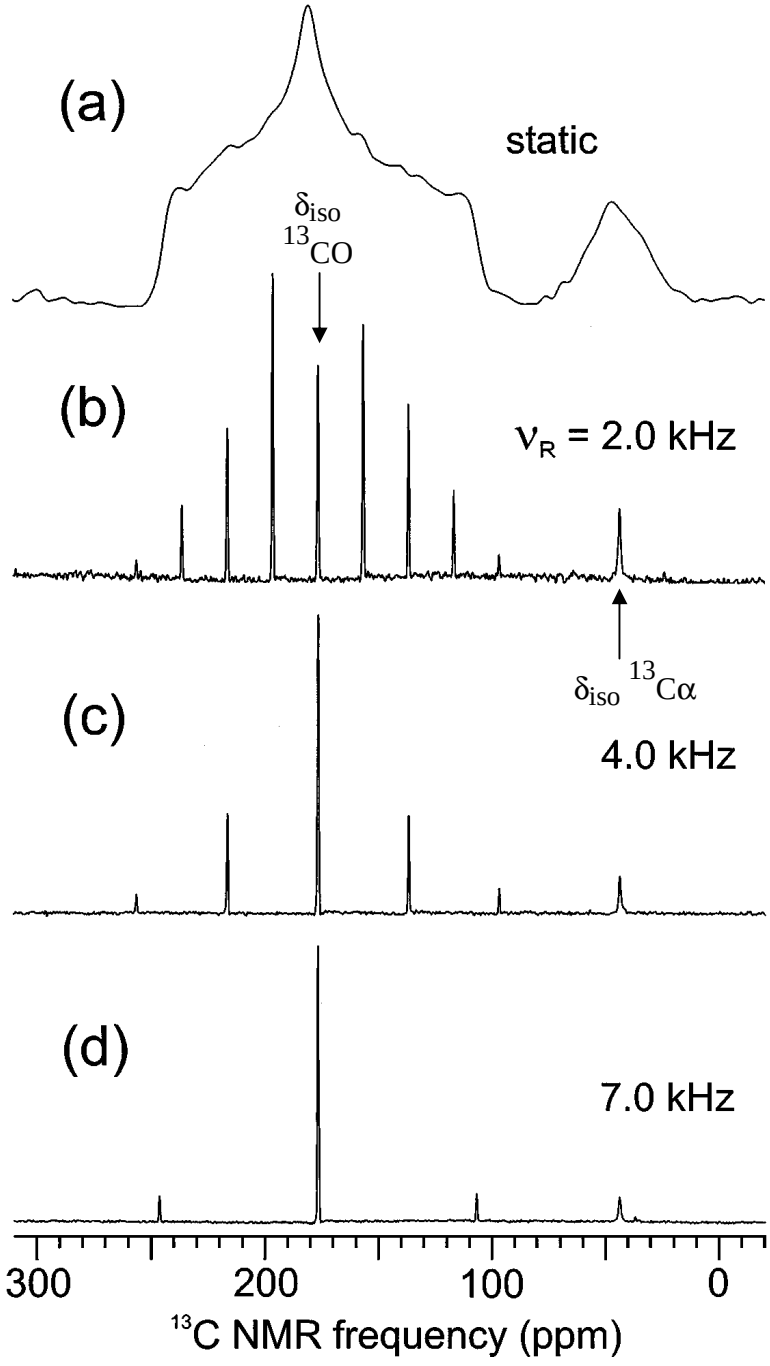

Figure 1-5: (a) Powder pattern of a glycine sample, no spinning. (b) Sample spun at 2 kHz, (c) Sample spun at 4 kHz and (d) sample spun at 7 kHz all about the magic angle. Spinning the sample averages out the CSA of the sample, resulting in the observation of the isotropic chemical shift and the spinning sidebands in the spectrum. Adapted from reference [70]. δ_{iso} will not change with spinning frequency. The δ_{iso} ^{13}CO and δ_{iso} ^{13}Cα are marked in (b).

The signal per scan will remain the same because you are not changing the amount of sample present, instead what is occurring is that the total integrated area of the peak is being condensed into a smaller region of the NMR spectrum, resulting in the increased peak signal to noise ratio for the ^{13}C nuclei. The peak signal to noise of the spectrum is enhanced by spinning because the anisotropy is eliminated and the isotropic chemical shift is obtained resulting in a narrow (30 – 300 Hz) peak centered on the isotropic chemical shift versus the 40 kHz broad peaks when not spinning. The total integrated area will be conserved between a non spinning sample and a sample being spun at a frequency of several kHz.[70] The isotropic chemical shift will be a narrower and more intense peak than the peak in the powder pattern, however the total integrated area will remain constant. The spinning frequency needs to be on the order of 3-4 times larger than the CSA of the sample in order to only obtain signals at the isotropic chemical shifts.[63] The CSA span for the ^{13}CO nuclei of NAL is defined by Equation 1-27.

$$\text{Span} = \delta_{33} - \delta_{11} \tag{1-27}$$

For NAL, the span of the CSA is (246 ppm – 87 ppm) or 159 ppm. Operating a 9.4 T spectrometer, the ^{13}C frequency is ~100 MHz, resulting in the ^{13}CO CSA to be 15.9 kHz. Typical values for the anisotropy for the aliphatic, aromatic, and carbonyl ^{13}C groups are 30 ppm, 180 ppm, and 150 ppm.[71] The frequency range at 9.4 T would be 3 kHz, 18 kHz, and 15 kHz for the aliphatic, aromatic, and carbonyl carbons, whereas at 21.1 T the frequency would be ~7 kHz, 40 kHz, and 34 kHz for the aliphatic, aromatic, and carbonyl carbons. Spinning speeds of 10 – 12 kHz are possible for the 4 mm rotor used in the Weliky lab at 9.4 T, and spinning speeds of up to 15 kHz are possible with the 4 mm rotor for the 21.1 T spectrometer. Spinning speeds of 12 kHz at 9.4 T will result in spinning at a frequency which is four times larger than

the aliphatic CSA, and on the order of the ^{13}C CSA for the carbonyl and aromatic carbons resulting in the spectrum's lack of spinning sidebands with the 9.4 T spectrometer . At 21.1 T, the spinning speeds of 12 – 15 kHz are much greater than the CSA of the aliphatic carbons, resulting in the lack of any observable spinning sidebands in the spectrum. However, the ^{13}CO CSA is ~2-3 times greater than the spinning frequency of the sample, which will result in the observation of the spinning sidebands for the ^{13}CO resonances in the spectrum. The mathematical explanation for the observation of the spinning sidebands and there location is presented in the subsection "Spinning sidebands from magic angle spinning".

Spinning sidebands from magic angle spinning

The following description is used to define the isotropic chemical shift and observation of spinning sidebands at integral frequencies separated from the isotropic chemical shift. The initial equations were taken from Stejskal and Memory [64], whereas I performed the derivation from one step to another.

The Zeeman Hamiltonian (H_{Ze}), previously defined by Equation 1-15 is presented here in Equation 1-28:

$$\hat{H}_{Ze} = \sum_i \frac{h}{2\pi} \boldsymbol{\sigma}_{izz} I_{iz} \mathbf{B}_0 \tag{1-28}$$

Where $\boldsymbol{\sigma}_{izz}$ is chemical shift tensor, I_{iz} is the spin operator, and $\mathbf{B}_0$ is the applied external magnetic field. The principal axis definition is Equation 1-29:

$$\sigma_{izz} = \sigma_{i1}\cos^2\theta_{i1} + \sigma_{i2}\cos^2\theta_{i2} + \sigma_{i3}\cos^2\theta_{i3} \tag{1-29}$$

The $\cos^2\theta$ is a directional cosine term. Sample rotation with respect to the principal axis is defined by Equation 1-30 where β is the angle of sample rotation axis with respect to the applied magnetic field (B_0) , χ_{ip} is the angle of the sample rotation axis with respect to the principal axis, ψ_{ip} is the initial azimuthal angle, and ω_r is the angular frequency:

$$\cos\theta_{ip} = \cos\beta\cos\chi_{ip} + \sin\beta\sin\chi_{ip}\cos(\omega_r t + \psi_{ip}) \tag{1-30}$$

Combining Equations 1-28, 1-29, and 1-30 yields Equation 1-31:

$$\hat{H}_{Ze} = \frac{h}{2\pi}\sum_i(\sigma_{i1}\cos^2\theta_{i1} + \sigma_{i2}\cos^2\theta_{i2} + \sigma_{i3}\cos^2\theta_{i3})I_{iz}\mathbf{B}_0 \tag{1-31}$$

Equation 1-31 can be simplified to Equation 1-32:

$$\hat{H}_{Ze} = \hbar\sum_i\sum_{p=1}^{3}(\sigma_{ip}\cos^2\theta_{ip})I_{iz}\mathbf{B}_0 \tag{1-32}$$

By definition of Equation 1-33, the $\cos^2\theta$ term can be determined, which is Equation 1-34 and simplified in Equation 1-35, where α is some angle.

$$\cos^2(\alpha) = \cos(\alpha) * \cos(\alpha) \tag{1-33}$$

$$\cos^2\theta_{ip} = \begin{pmatrix}[\cos\beta\cos\chi_{ip} + \sin\beta\sin\chi_{ip}\cos(\omega_r t + \psi_{ip})] \\ *[\cos\beta\cos\chi_{ip} + \sin\beta\sin\chi_{ip}\cos(\omega_r t + \psi_{ip})]\end{pmatrix} \tag{1-34}$$

Resulting in:

$$\cos^2\theta_{ip} = \begin{pmatrix}\cos^2\beta\cos^2\chi_{ip} + \sin^2\beta\sin^2\chi_{ip}\cos^2(\omega_r t + \psi_{ip}) \\ +2\cos\beta\cos\chi_{ip}\sin\beta\sin\chi_{ip}\cos(\omega_r t + \psi_{ip})\end{pmatrix} \tag{1-35}$$

Combining Equations 1-35 with 1-32 yields Equation 1-36:

$$\hat{H}_{Ze} = \hbar \sum_i \sum_{p=1}^{3} \begin{pmatrix} (\sigma_{ip}[\cos^2\beta\cos^2\chi_{ip} + \sin^2\beta\sin^2\chi_{ip}\cos^2(\omega_r t + \psi_{ip}) \\ + 2\cos\beta\cos\chi_{ip}\sin\beta\sin\chi_{ip}\cos(\omega_r t + \psi_{ip})])I_{iz}B \end{pmatrix} \quad (1\text{-}36)$$

From Equation 1-36, only time dependent parts are we concerned with from Equation 1-36, which are presented in Equations 1-37a and 1-37b:

$$\sin^2\beta\sin^2\chi_{ip}\cos^2(\omega_r t + \psi_{ip}) \quad (1\text{-}37a)$$

$$2\cos\beta\cos\chi_{ip}\sin\beta\sin\chi_{ip}\cos(\omega_r t + \psi_{ip}) \quad (1\text{-}37b)$$

Which will be simplify to Equations 1-38a and 1-38b:

$$A\cos^2(\omega_r t + \psi_{ip}) \quad (1\text{-}38a)$$

$$C\cos(\omega_r t + \psi_{ip}) \quad (1\text{-}38b)$$

Where A is a constant defined by Equation 1-38c:

$$\text{A} = \sin^2\beta\sin^2\chi_{ip} \quad (1\text{-}38c)$$

And C is a constant defined by Equation 1-38d:

$$\text{C} = 2\cos\beta\cos\chi_{ip}\sin\beta\sin\chi_{ip} \quad (1\text{-}38d)$$

First, let's evaluate Equation 1-38a for the time dependence of the frequency of rotation. Using Equation 1-39 where again α is some value:

$$\cos^2\alpha = \frac{1}{2}(1 + \cos(2\alpha)) \quad (1\text{-}39)$$

Which is a double angle formula, and substituting in Equation 1-38a into 1-39, yields Equation 1-40:

$$\cos^2(\omega_r t + \psi_{ip}) = \frac{1}{2}\left(1 + \cos(2(\omega_r t + \psi_{ip}))\right) \quad (1\text{-}40)$$

Using Euler's formula of Equation 1-41, one can rewrite the time dependant part into Equation 1-42 where α is some value:

$$\cos\alpha = \frac{e^{i\alpha} + e^{-i\alpha}}{2} \tag{1-41}$$

$$\begin{aligned} &\frac{1}{2}[1+\cos((2\omega_r t + 2\psi_{ip})] \\ &= \frac{1}{2}\left(1+\left(\frac{e^{i(2(\omega_r t+\psi_{ip}))} + e^{-i(2(\omega_r t+\psi_{ip}))}}{2}\right)\right) \end{aligned} \tag{1-42}$$

From Equation 1-42, one sees that the only time dependant part to be concerned with are the terms of $\exp(i*2\omega_r t)$ and $\exp(-i*2\omega_r t)$, which be changed to $\exp(i(-2\omega_r t))$. From these two terms, it can be seen that oscillations are at $\pm 2\omega_r$; and one knows that the rotation frequency (f_r) in Hertz is defined as Equations 1-43a and 1-43b where ω_r is the angular frequency in radians per second, which can converted to Hz by the 2π factor.

$$\omega_r = 2\pi * f_r \tag{1-43a}$$

$$(\omega_r / 2\pi) = f_r \tag{1-43b}$$

From Equations 1-42 and 1-43, it is observed that $\pm 2 * f_r = \omega_r/2\pi$, which is ± 2 times the spinning frequency in Hz.

Looking back at Equation 1-38b, one can now look at the time dependence for this equation, which can be taken directly to the exponential form of cosine, shown in Equation 1-44 by using Equation 1-41:

$$\cos((\omega_r t+\psi_{ip})] = \left(\frac{e^{i((\omega_r t+\psi_{ip}))} + e^{-i((\omega_r t+\psi_{ip}))}}{2} \right) \tag{1-44}$$

From Equation 1-44, the only time dependant part is the terms of $\exp(i\omega_r t)$ and $\exp(-i\omega_r t)$, which can be rewritten as $\exp(i(-\omega_r t))$. From these two terms one gets that the spinning sidebands will be observed at $\pm f_r = \omega_r/2\pi$ which is ±1 the spinning frequency in Hz.

It is thus shown that the spinning sidebands will be observed at $\pm n(\omega_r/2\pi)$, where n = 1 or 2 and $(\omega_r/2\pi)$ is the frequency of rotation in Hz from the isotropic chemical shift of Equation 1-36. The spinning sidebands will be observed on either side of the isotropic chemical shift by the difference in spinning frequency.

Cross Polarization

Cross polarization is a technique commonly used with MAS and allows for polarization transfer from the abundant spin of ^{1}H to the dilute spins in a system, such as ^{13}C or ^{15}N.[66] The net magnetization (polarization) is defined as Equations 1-1 and 1-45:

$$\mathbf{M} = \sum_i \mu_i \tag{1-45}$$

Cross polarization typically requires the Hartmann–Hahn condition of Equation 1-46:

$$\gamma_I \mathbf{B}_{1I} = \gamma_S \mathbf{B}_{1S} \tag{1–46}$$

where γ_I is the gyromagnetic ratio of the I spin (^{1}H), $\mathbf{B}_{1I}$ is the rf spin locking field of the I spin, γ_S is the gyromagnetic ratio of the S spin (^{13}C), and $\mathbf{B}_{1S}$ is the rf spin locking field of the S spin.[72] The rf spin locking fields maintain the ^{1}H magnetization in the transverse plane following the ^{1}H $\pi/2$ pulse during the contact time between the two spins ^{1}H and ^{13}C.[72] Matching the $\mathbf{B}_1$ fields between the two nuclei allows for polarization transfer from the ^{1}H→^{13}C nuclei during the contact time by the heteronuclear dipolar couplings of the ^{1}H and the ^{13}C nuclei.

There are two main benefits of using cross polarization from the ^{1}H nuclei to the dilute spins of ^{13}C or ^{15}N nuclei. First, cross polarization allows for theoretically a 4-fold increase in ^{13}C signal to be obtained which is determined from the ratio of the ^{1}H and ^{13}C gyromagnetic ratios as (γ_{1H}/γ_{13C}) from Equation 1-46.[66] The magnitudes of the magnetic moments ($\boldsymbol{\mu}$) of the two nuclei (^{13}C and ^{1}H) are different, with the ^{1}H being ~4 times larger than the ^{13}C, which results in the theoretical 4-fold increase in the ^{13}C signal from the ^{1}H→^{13}C CP step. Cross polarization occurs via the heteronuclear dipole couplings between the ^{1}H and the ^{13}C spin systems. The second benefit from cross polarization is that shorter recycle delays between acquisitions can be used when cross polarizing from the ^{1}H nuclei as opposed to directly polarizing on the low gamma nuclei of ^{13}C and ^{15}N. The recycle delay between acquisitions is dependant on the T_1 relaxation of the nuclei, and ^{13}C and ^{15}N have longer T_1's than the ^{1}H

nuclei. The T_1 relaxation time for the ^{1}H are ~0.5 s,[73] whereas the T_1 relaxation time for the ^{13}C and ^{15}N nuclei can be ~2 - 7 s or longer.[74, 75]

The spin-lattice relaxation time, T_1, describes the recovery of the M_z magnetization back to the initial magnetization (M_0), and is defined by Equation 1-47.[76] The spin-spin relaxation time, T_2, describes the decay of the transverse (M_{xy}) magnetization and is defined by Equation 1-48.[76]

$$\frac{d}{dt}M_z = \frac{-(M_z - M_0)}{T_1} \tag{1-47}$$

$$\frac{d}{dt}M_{xy} = \frac{-M_{xy}}{T_2} \tag{1-48}$$

With cross polarization one is only concerned with allowing the ^{1}H magnetization to return to thermal equilibrium after the each acquisition.[72] The short ^{1}H recycle delay (1 s) compared to the ^{13}C recycle delay (3 – 5 s) then allows for acquiring ~3 – 5 times more scans per unit of time resulting in higher summed signal for the ^{13}C or ^{15}N nuclei by using CP compared to direct polarization. The CP and MAS techniques are essential to the 1D and 2D SSNMR experiments presented in this dissertation as each experiment uses a CP step from the abundant ^{1}H spin system to either the ^{13}C or the ^{15}N nuclei.

Using SSNMR to Determine Protein Structures

The field of SSNMR for structure determination has developed tremendously over the past decade, resulting in the ability to determine structures of proteins in native environments that are comparable to the quality of crystal structures from X–ray crystallography. Through use of multidimensional NMR experiments, Castellani and co–workers were able to determine the structure of the 62 residue α–spectrin Src–homology 3 domain in a micro-crystalline state using a 17.6 T (750 MHz ^{1}H frequency) spectrometer.[77, 78] The incorporation of ^{13}C and ^{15}N isotopic labels throughout the protein allowed for determination of ^{13}C–^{13}C contacts and ^{15}N–^{15}N contacts using different pulse sequences such as 2D ^{13}C-^{13}C PDSD.[77] Secondary structure of the different residues can be obtained from the chemical shifts of the ^{13}C and ^{15}N labels and comparing the experimental chemical shifts to a database of known chemicals shifts, such as RefDB [79]. The ^{13}C-^{13}C and ^{15}N-^{15}N contacts allow for determining the tertiary structure which will then determine the global fold of the protein.[77] Pauli and authors do not directly state the linewidths associated with the ^{13}C and ^{15}N peaks, only that narrow linewidths were obtained for the for the well ordered globular part of the protein.[78] Pauli does mention that their linewidths are in agreement with previous results for the reaction center of a bacterium *Rhodobacter sphaeroides* transmembrane complex.[78] The ^{13}C linewidths reported for the *Rhodobacter sphaeroides* transmembrane complex by Fischer and co-workers were ~30 Hz in a 9.4 T field [80], and by van Rossum et al. were between 30 and 80 Hz in a 9.4 T field [81] suggesting that narrow linewidths can be obtained for a well ordered sample.

Castellani and co-workers[77] and Pauli and co-workers[78] used different isotopic labeling schemes to obtain the 3D structure of the α–spectrin Src–homology 3 domain from the 2D ^{13}C-^{13}C and the 2D ^{15}N-^{15}N experiments. Supplementing the media during expression of the protein with the following labeling allowed for obtaining differential ^{13}C and ^{15}N labeling through the 62 residue protein. The labeling schemes from the labeled glucose where either (i) [U-^{13}C] glucose with $^{15}NH_4Cl$; (ii) [1,3–^{13}C] glucose with $^{15}NH_4Cl$; or (iii) [2-^{13}C] glucose with $^{15}NH_4Cl$.[77, 78] Labeling scheme (i) allows for U-^{13}C, ^{15}N labeling of the protein, which can then be used to determine the short range ^{13}C-^{13}C and ^{15}N-^{15}N contacts from 2D experiments. The problem with this labeling scheme is the dipolar truncation can occur from the directly bonded ^{13}C-^{13}C nuclei which have strong dipolar coupling signals and will suppress the weak dipolar coupling signals from long distance ^{13}C-^{13}C interactions.[82] Labeling scheme (ii) and (iii) limit the amount of dipolar truncation that can occur because ^{12}C will be incorporated in the expressed protein that is being labeled which will break up the ^{13}C spin system, minimizing the dipolar truncation. By minimizing dipolar truncation, the observation of long distance (< 7Å) can be observed since the strong dipolar couplings are minimized, allowing for the observation of the weaker dipolar couplings of the system.[82] The incorporation of the ^{12}C nuclei also prevents the relaying of the polarization thru the ^{13}C spin system as would be observed in labeling scheme (i).[77] All three label schemes incorporated the $^{15}NH_4Cl$ salt which allows for the ^{15}N labeling of the protein. The six ^{15}N-^{15}N constraints were determined from a single 2D

^{15}N-^{15}N PDSD experiment with a 4 s mixing time, resulting in long range distances of 3 – 6 Å.[77] The labeled protein sample was also diluted with naturally abundant protein in a 80:20 ratio of unlabeled to labeled protein, likely in an attempt to observe long distance interactions while minimizing dipolar truncation.[77, 78]

The 2D ^{13}C-^{13}C and the ^{15}N-^{15}N experiments resulted in the assignment of residues 7 – 61 of the 62 residues.[78] The authors were not able to make assignments for residues 1 – 6 or 62 due to the flexibility of the N- and C-terminus of the protein.[78] Flexibility in the N- and C-terminal is suggested by Pauli and co-workers due to strongly attenuated signals or absent signals in the solid state NMR spectrum.[78] Pauli and co-workers suggest that the motions of the protein in these two regions could be interfering with the ^{1}H decoupling and that the cross polarization of these residues is also weak, resulting in signals that would show up in the spectrum as low intensity, broad lines.[78] The most probable reason for the lack of observable resonances is that due to the flexibility of the N- and C-terminus.[78] The flexibility of the terminus can result in inefficient cross polarization which would result in a lack of observable peaks.[78] The flexibility also allows for many orientations to be present in the sample, which would result in the resonances being broadened compared to the sharp resonances which had been obtained for the well structured portion of the protein.[78] These broad resonances of the terminal residues could contribute to the lack of observable signals.[78] One possible solution would be to lower the temperature at which the spectra were collected provided that this will not adversely affect the protein sample by denaturation or causing the sample to become non-functional. The spectra were acquired at a sample temperature of 278 K.[78]

A huge benefit of SSNMR is the ability to study proteins in native environments. Examples include the determination of secondary and tertiary structure for the FP region of gp41 in membrane environments [7, 14-16, 18, 20, 83] and structure determination of the Alzheimer's β–amyloid fibrillar protein.[84, 85] SSNMR has lead to structural models for these proteins; such models were not able to be determined by X–ray crystallography as they were not able to be crystallized. Development of multidimensional NMR experiments have allowed for backbone walks which can correlate the $^{15}N_j$ to the $^{13}CO_j$ resonances through the $^{13}C\alpha_j$ side chain or the $^{13}C\alpha_j$ to the $^{13}CO_{j-1}$ resonance through the $^{15}N_j$ resonance, resulting in the sequential assignments of all the ^{13}C and ^{15}N resonances in the backbone of the peptide or protein. The assignments of side chains can be performed from the 2D ^{13}C-^{13}C experiments of uniformly labeled samples or from 3D experiments which utilize the double cross polarization (DCP) step in the pulse sequence. The DCP experiments first prepare the magnetization on the ^{1}H nuclei before transferring the polarization from $^{1}H \rightarrow ^{15}N$ in the first cross polarization step. In the second cross polarization step, the magnetization is selectively transferred between the $^{15}N \rightarrow ^{13}C\alpha$, where the $^{13}C\alpha$ is directly bonded to the ^{15}N nuclei. Comparison of the isotropic chemical shift from the filtered spectrum to known shifts for the $^{13}C\alpha$ nuclei can be used to determine secondary structure. For the 2D ^{13}C-^{13}C experiments using uniformly ^{13}C, ^{15}N labeled samples the off diagonal cross peaks at 50 ms exchange time will correlate all of the ^{13}C-^{13}C intra-residue spin systems providing chemical shifts for the ^{13}C nuclei which can be used to determine secondary structure from a known distribution of chemical shifts. ^{15}N assignments

can be made by 2D ^{15}N-^{13}C correlation experiments where the ^{15}N is correlated to the ^{13}CO or the ^{13}Cα residue within a residue.

Probe improvements such as minimizing the electric field applied to the sample by directing it away with lowE resonators (E–free) [86-88], scroll coils [87, 89], and cross–coils [87, 90] have allowed investigators the ability to study lossy samples which are samples with high salt concentrations that are highly conductive. The ability to study lossy samples is important because these samples more closely resemble the actual cellular environment for biological samples. Progress in rotor and probe development has led to development of 1.3 mm rotors which have the ability to spin up to 70 kHz.[91, 92] The ability to spin up to 70 kHz will result in maximizing the signal of the δ_{iso} peak and minimizing or eliminating spinning sidebands at the cost of reduced sample volume.[93] It has been shown that at spinning frequencies greater than 40 kHz the applied decoupling frequencies can be 10 – 15 kHz.[91] Application of low rf frequencies results in less sample heating, which is important since sample heating can potentially denature a biological protein sample by dehydration. These developments have propelled SSNMR to complete structure determination of fully labeled proteins [77], determining structural changes as a result of drug binding or pH changing conditions at binding sites [94], and determining structures of insoluble protein aggregates such as the amyloid fibrils [84]. Chapter 4 will present a more in depth look at the benefits of probe development in the context of the FP–Hairpin studies at high magnetic fields.

My Contributions

This dissertation is a proof of concept project and biotechnology development. The main accomplishments are the ability to produce the "Hairpin" and "FP–Hairpin" proteins in a routine fashion and in high yields in short periods of time (2 weeks or less) while studying the FP–Hairpin construct by SSNMR. The constructs are highly relevant to understanding the fusion process as well as the final folded state of gp41. This work proved that FP–Hairpin could be studied by SSNMR and expands the gp41 constructs to larger systems. These constructs had not been previously synthesized. The utility of the native chemical ligation allows probing the FP region using selective NMR labeling in terms of the larger, folded SHB final fusion formation.

The work in this dissertation highlights the ability to efficiently produce the large 115 residue FP–Hairpin construct containing isotopic labels in high yield and purity for SSNMR studies. Sample preparation of "FP–Hairpin" was reduced from ~2 months to ~2 weeks resulting from the optimization of expression, purification of the Hairpin construct, and optimization of the NCL reaction creating FP–Hairpin.

Finally, SSNMR studies were done at different fields. The work greatly benefited from a high field (21.1 T, 900 MHz ^{1}H frequency) NMR spectrometer along with a 4 mm MAS E–free probe. At 21.1 T the ^{13}C resonances had a 5–fold increase in ^{13}C peak signal to noise per scan and an ~11-fold increase in the total integrated area of the ^{13}C peaks and will be discussed in Chapter 4. A two–fold narrowing of the linewidths in ppm units was also achieved at 21.1 T relative to 9.4 T. The narrower resonances obtained at 21.1 T relative to 9.4 T in ppm units for the 2D ^{13}C–^{13}C NMR experiments allowed for unambiguous assignments of cross peaks. The increased ^{13}C peak signal to noise per scan with the 21.1 T spectrometer allowed for the less

signal averaging time per sample which was on average between 33 – 50% less signal averaging time for the 2D experiments at 21.1 T compared to the 9.4 T spectrometer. Chapter 2 will present the methods for sample preparation along with results for the optimization of the native chemical ligation. Chapter 3 highlights solid state NMR experiments performed at 9.4 T, and the high field SSNMR work will be presented in Chapter 4. The major conclusions and future work are presented in Chapter 5. Appendix I contains supplemental data for FP-Hairpin when studied in the presence of CuEDTA and also projects at 21.1 T not included in Chapter 4. Appendix II details two side projects for FP-Hairpin: (1) A sample prepared to be studied by dynamic nuclear polarization; (2) Attempts at crystallizing Hairpin and FP-Hairpin with collaborators at Arizona State University. Appendix III presents a "how to guide" for using the Bruker 21.1 T (900 MHz NMR) spectrometer, and Appendix IV lists the data locations for all of the SSNMR data files, both raw and processed from the 9.4 T, 16.5 T, 21.1 T, and DNP experiments.

REFERENCES

References

1. Joint United Nations Programme on HIV/AIDS. and World Health Organization., *AIDS epidemic update December 2006*. 2006, Geneva, Switzerland: Unaids. 96.

2. Weissenhorn, W., et al., *Atomic structure of the ectodomain from HIV-1 gp41.* Nature, 1997. **387**(6631): p. 426-30.

3. Grewe, C., A. Beck, and H.R. Gelderblom, *HIV: early virus-cell interactions.* J Acquir Immune Defic Syndr, 1990. **3**(10): p. 965-74.

4. Markosyan, R.M., F.S. Cohen, and G.B. Melikyan, *HIV-1 envelope proteins complete their folding into six-helix bundles immediately after fusion pore formation.* Mol. Biol. Cell., 2003. **14**(3): p. 926-938.

5. White, J.M., et al., *Structures and mechanisms of viral membrane fusion proteins: Multiple variations on a common theme.* Critical Reviews in Biochemistry and Molecular Biology, 2008. **43**(3): p. 189-219.

6. Qiang, W., J. Yang, and D.P. Weliky, *Solid-state nuclear magnetic resonance measurements of HIV fusion peptide to lipid distances reveal the intimate contact of beta strand peptide with membranes and the proximity of the Ala-14-Gly-16 region with lipid headgroups.* Biochemistry, 2007. **46**(17): p. 4997-5008.

7. Qiang, W., M.L. Bodner, and D.P. Weliky, *Solid-state NMR spectroscopy of human immunodeficiency virus fusion peptides associated with host-cell-like membranes: 2D correlation spectra and distance measurements support a fully extended conformation and models for specific antiparallel strand registries.* J Am Chem Soc, 2008. **130**(16): p. 5459-71.

8. Qiang, W., Y. Sun, and D.P. Weliky, *A strong correlation between fusogenicity and membrane insertion depth of the HIV fusion peptide.* Proc Natl Acad Sci U S A, 2009. **106**(36): p. 15314-9.

9. Schmick, S.D. and D.P. Weliky, *Major Antiparallel and Minor Parallel beta Sheet Populations Detected in the Membrane-Associated Human Immunodeficiency Virus Fusion Peptide.* Biochemistry, 2010. **49**(50): p. 10623-10635.

10. Jacobs, A., et al., *HIV-1 envelope glycoprotein-mediated fusion and pathogenesis: Implications for therapy and vaccine development.* Vaccine, 2008. **26**(24): p. 3026-3035.

11. Vogel, E.P., et al., *Solid-State Nuclear Magnetic Resonance (NMR) Spectroscopy of Human Immunodeficiency Virus gp41 Protein That Includes the Fusion Peptide: NMR Detection of Recombinant Fgp41 in Inclusion Bodies in Whole Bacterial Cells and Structural Characterization of Purified and Membrane-Associated Fgp41.* Biochemistry, 2011. **50**(46): p. 10013-10026.

12. Buzon, V., et al., *Crystal Structure of HIV-1 gp41 Including Both Fusion Peptide and Membrane Proximal External Regions.* PLoS Pathogens, 2010. **6**(5): p. e1000880.

13. Yang, J., et al., *Solid state NMR measurements of conformation and conformational distributions in the membrane-bound HIV-1 fusion peptide.* J Mol Graph Model, 2001. **19**(1): p. 129-35.

14. Yang, J., C.M. Gabrys, and D.P. Weliky, *Solid-state nuclear magnetic resonance evidence for an extended beta strand conformation of the membrane-bound HIV-1 fusion peptide.* Biochemistry, 2001. **40**(27): p. 8126-37.

15. Wasniewski, C.M., et al., *Solid-state nuclear magnetic resonance studies of HIV and influenza fusion peptide orientations in membrane bilayers using stacked glass plate samples.* Chem Phys Lipids, 2004. **132**(1): p. 89-100.

16. Zheng, Z., et al., *Conformational flexibility and strand arrangements of the membrane-associated HIV fusion peptide trimer probed by solid-state NMR spectroscopy.* Biochemistry, 2006. **45**(43): p. 12960-75.

17. Yang, J., et al., *Application of REDOR subtraction for filtered MAS observation of labeled backbone carbons of membrane-bound fusion peptides.* J Magn Reson, 2002. **159**(2): p. 101-10.

18. Yang, J. and D.P. Weliky, *Solid-state nuclear magnetic resonance evidence for parallel and antiparallel strand arrangements in the membrane-associated HIV-1 fusion peptide.* Biochemistry, 2003. **42**(40): p. 11879-90.

19. Gabrys, C.M., J. Yang, and D.P. Weliky, *Analysis of local conformation of membrane-bound and polycrystalline peptides by two-dimensional slow-spinning rotor-synchronized MAS exchange spectroscopy.* J Biomol NMR, 2003. **26**(1): p. 49-68.

20. Yang, R., J. Yang, and D.P. Weliky, *Synthesis, enhanced fusogenicity, and solid state NMR measurements of cross-linked HIV-1 fusion peptides.* Biochemistry, 2003. **42**(12): p. 3527-35.

21. Bodner, M.L., et al., *Temperature dependence and resonance assignment of C-13 NMR spectra of selectively and uniformly labeled fusion peptides associated with membranes.* Magnetic Resonance in Chemistry, 2004. **42**(2): p. 187-194.

22. Yang, J., et al., *Oligomeric beta-structure of the membrane-bound HIV-1 fusion peptide formed from soluble monomers.* Biophys J, 2004. **87**(3): p. 1951-63.

23. Yang, R., et al., *A trimeric HIV-1 fusion peptide construct which does not self-associate in aqueous solution end which Has 15-fold higher membrane fusion rate.* Journal of the American Chemical Society, 2004. **126**(45): p. 14722-14723.

24. Gabrys, C.M. and D.P. Weliky, *Chemical shift assignment and structural plasticity of a HIV fusion peptide derivative in dodecylphosphocholine micelles.* Biochim Biophys Acta, 2007. **1768**(12): p. 3225-34.

25. Zheng, Z., W. Oiang, and D.P. Weliky, *Investigation of finite-pulse radiofrequency-driven recoupling methods for measurement of intercarbonyl distances in polycrystalline and membrane-associated HIV fusion peptide samples.* Magnetic Resonance in Chemistry, 2007. **45**: p. S247-S260.

26. Bodner, M.L., et al., *13C-13C and (15)N-(13)C correlation spectroscopy of membrane-associated and uniformly labeled human immunodeficiency virus and influenza fusion peptides: amino acid-type assignments and evidence for multiple conformations.* J Chem Phys, 2008. **128**(5): p. 052319.

27. Qiang, W. and D.P. Weliky, *HIV fusion peptide and its cross-linked oligomers: efficient syntheses, significance of the trimer in fusion activity, correlation of beta strand conformation with membrane cholesterol, and proximity to lipid headgroups.* Biochemistry, 2009. **48**(2): p. 289-301.

28. Tristram-Nagle, S., et al., *HIV fusion peptide penetrates, disorders, and softens T-cell membrane mimics.* J Mol Biol, 2010. **402**(1): p. 139-53.

29. Gabrys, C.M., et al., *Nuclear magnetic resonance evidence for retention of a lamellar membrane phase with curvature in the presence of large quantities of the HIV fusion peptide.* Biochimica Et Biophysica Acta-Biomembranes, 2010. **1798**(2): p. 194-201.

30. Sackett, K., et al., *Hairpin folding of HIV gp41 abrogates lipid mixing function at physiologic pH and inhibits lipid mixing by exposed gp41 constructs.* Biochemistry, 2009. **48**(12): p. 2714-22.

31. Sackett, K., et al., *Comparative analysis of membrane-associated fusion peptide secondary structure and lipid mixing function of HIV gp41 constructs that model the early pre-hairpin intermediate and final hairpin conformations.* J Mol Biol, 2010. **397**(1): p. 301-15.

32. Curtis-Fisk, J., et al., *Solid-state NMR structural measurements on the membrane-associated influenza fusion protein ectodomain.* J Am Chem Soc, 2007. **129**(37): p. 11320-1.

33. Curtis-Fisk, J., R.M. Spencer, and D.P. Weliky, *Isotopically labeled expression in E-coli, purification, and refolding of the full ectodomain of the influenza virus membrane fusion protein.* Protein Expression and Purification, 2008. **61**(2): p. 212-219.

34. Curtis-Fisk, J., R.M. Spencer, and D.P. Weliky, *Native conformation at specific residues in recombinant inclusion body protein in whole cells determined with solid-state NMR spectroscopy.* J Am Chem Soc, 2008. **130**(38): p. 12568-9.

35. Sackett, K., A. TerBush, and D.P. Weliky, *HIV gp41 six-helix bundle constructs induce rapid vesicle fusion at pH 3.5 and little fusion at pH 7.0: understanding pH dependence of protein aggregation, membrane binding, and electrostatics, and implications for HIV-host cell fusion.* European Biophysics Journal with Biophysics Letters, 2011. **40**(4): p. 489-502.

36. Struck, D.K., D. Hoekstra, and R.E. Pagano, *Use of resonance energy transfer to monitor membrane fusion.* Biochemistry, 1981. **20**(14): p. 4093-4099.

37. Sackett, K. and Y. Shai, *The HIV-1 gp41 N-terminal heptad repeat plays an essential role in membrane fusion.* Biochemistry, 2002. **41**(14): p. 4678-4685.

38. Sackett, K., Y. Wexler-Cohen, and Y. Shai, *Characterization of the HIV N-terminal fusion peptide-containing region in context of key gp41 fusion conformations.* J. Biol. Chem., 2006. **281**(31): p. 21755-21762.

39. Kilby, J.M., et al., *Potent suppression of HIV-1 replication in humans by T-20, a peptide inhibitor of gp41-mediated virus entry.* Nat. Med., 1998. **4**(11): p. 1302-1307.

40. Bai, X., et al., *Impact of the enfuvirtide resistance mutation N43D and the associated baseline polymorphism E137K on peptide sensitivity and six-helix bundle structure.* Biochemistry, 2008. **47**(25): p. 6662-6670.

41. Bewley, C.A., et al., *Design of a novel peptide inhibitor of HIV fusion that disrupts the internal trimeric coiled-coil of gp41.* J Biol Chem, 2002. **277**(16): p. 14238-14245.

42. Liu, S., S. Wu, and S. Jiang, *HIV entry inhibitors targeting gp41: from polypeptides to small-molecule compounds.* Curr Pharm Des, 2007. **13**(2): p. 143-162.

43. McGillick, B.E., et al., *Origins of Resistance to the HIVgp41 Viral Entry Inhibitor T20.* Biochemistry, 2010. **49**(17): p. 3575-3592.

44. Sun, Z.-Y.J., et al., *HIV-1 broadly neutralizing antibody extracts its epitope from a kinked gp41 ectodomain region on the viral membrane.* Immunity, 2008. **28**(1): p. 52-63.

45. Freed, E.O., D.J. Myers, and R. Risser, *Characterization of the fusion domain of the human immunodeficiency virus type 1 envelope glycoprotein gp41.* Proc Natl Acad Sci U S A, 1990. **87**(12): p. 4650-4.

46. Freed, E.O., et al., *A mutation in the human immunodeficiency virus type 1 transmembrane glycoprotein gp41 dominantly interferes with fusion and infectivity.* Proc. Natl. Acad. Sci. U. S. A., 1992. **89**(1): p. 70-74.

47. Kliger, Y., et al., *Fusion peptides derived from the HIV type 1 glycoprotein 41 associate within phospholipid membranes and inhibit cell-cell Fusion. Structure-function study.* J. Biol. Chem., 1997. **272**(21): p. 13496-13505.

48. Elson, H.F., D.S. Dimitrov, and R. Blumenthal, *A TRANSDOMINANT MUTATION IN HUMAN-IMMUNODEFICIENCY-VIRUS TYPE-1 (HIV-1) ENVELOPE GLYCOPROTEIN GP41 INHIBITS MEMBRANE-FUSION WHEN EXPRESSED IN TARGET-CELLS.* Molecular Membrane Biology, 1994. **11**(3): p. 165-169.

49. Watkins, B.A., et al., *Syncytium formation induced by human immunodeficiency virus type 1 isolates correlates with affinity for CD4.* Journal of General Virology, 1997. **78**: p. 2513-2522.

50. Dejong, J.J., et al., *Minimal Requirements for the Human-Immunodeficiency-Virus Type-1 V3 Domain to Support the Syncytium-Inducing Phenotype – Analysis by Single Amino-Acid Substitution.* Journal of Virology, 1992. **66**(11): p. 6777-6780.

51. Pereira, F.B., et al., *Permeabilization and fusion of uncharged lipid vesicles induced by the HIV-1 fusion peptide adopting an extended conformation: dose and sequence affects.* Biophys. J., 1997. **73**(4): p. 1977-1986.

52. Sen, J., et al., *Alanine Scanning Mutagenesis of HIV-1 gp41 Heptad Repeat 1: Insight into the gp120-gp41 Interaction.* Biochemistry, 2010. **49**(24): p. 5057-5065.

53. Nieva, J.L. and A. Agirre, *Are fusion peptides a good model to study viral cell fusion?* Biochimica Et Biophysica Acta-Biomembranes, 2003. **1614**(1): p. 104-115.

54. Rafalski, M., J.D. Lear, and W.F. DeGrado, *Phospholipid interactions of synthetic peptides representing the N- terminus of HIV gp41.* Biochemistry, 1990. **29**(34): p. 7917-7922.

55. Jaroniec, C.P., et al., *Structure and dynamics of micelle-associated human immunodeficiency virus gp41 fusion domain.* Biochemistry, 2005. **44**(49): p. 16167-16180.

56. Brugger, B., et al., *The HIV lipidome: A raft with an unusual composition.* Proceedings Of The National Academy Of Sciences Of The United States Of America, 2006. **103**(8): p. 2641-2646.

57. Chan, D.C., et al., *Core structure of gp41 from the HIV envelope glycoprotein.* Cell, 1997. **89**(2): p. 263-273.

58. Tan, K.M., et al., *Atomic structure of a thermostable subdomain of HIV-1 gp41.* Proceedings Of The National Academy Of Sciences Of The United States Of America, 1997. **94**(23): p. 12303-12308.

59. Shu, W., H. Ji, and M. Lu, *Interactions between HIV-1 gp41 core and detergents and their implications for membrane fusion.* J. Biol. Chem., 2000. **275**(3): p. 1839-1845.

60. Shi, W., et al., *Structural characterization of HIV gp41 with the membrane-proximal external region.* J Biol Chem, 2010. **285**(31): p. 24290-8.

61. Caffrey, M., et al., *Three-dimensional solution structure of the 44 kDa ectodomain of SIV gp41*. Embo J, 1998. **17**(16): p. 4572-4584.

62. Yang, Z.N., et al., *The crystal structure of the SIV gp41 ectodomain at 1.47 angstrom resolution.* Journal of Structural Biology, 1999. **126**(2): p. 131-144.

63. Duer, M.J., *Solid-state NMR spectroscopy : principles and applications*. 2002, Malden, MA: Blackwell Science. xvii, 567 p.

64. Stejskal, E.O. and J.D. Memory, *High resolution NMR in the solid state : fundamentals of CP/MAS*. 1994, New York: Oxford University Press. xii, 189 p.

65. Chuang, I.S. and G.E. Maciel, *NMR Characterization of Complex Organic Resins*, in *Annual Reports on NMR Spectroscopy*, G.A. Webb, Editor. 1994, Academic Press. p. 169-286.

66. Pochapsky, T.C. and S.S. Pochapsky, *NMR for Physical and Biological Scientists*. 2007, New York: Taylor & Francis Group. 372.

67. Dill, K.A. and S. Bromberg, *Molecular driving forces : statistical thermodynamics in chemistry and biology*. 2003, New York: Garland Science. xx, 666 p.

68. Weliky, D.P. *Chemistry 988 Lecture Notes*. [website containing pdf file of notes] May 3, 1999 [cited 2011 19 December 2011]; Available from: http://www2.chemistry.msu.edu/courses/CEM988NMR/cem988nmr.htm.

69. Schurko, R. *Introduction to Solid State NMR*. [website containing pdf file on notes] [cited 2012 28 Jan 2012]; Available from: http://mutuslab.cs.uwindsor.ca/schurko/ssnmr/ssnmr_schurko.pdf.

70. Tycko, R., *Biomolecular solid state NMR: Advances in structural methodology and applications to peptide and protein fibrils.* Annual Review of Physical Chemistry, 2001. **52**: p. 575-606.

71. Haeberlen, U., *Solid State NMR in High and Very High Magnetic Fields*, in *NMR at Very High Field*, P. Diehl, et al., Editors. 1991, Springer-Verlag. p. 143 - 168.

72. Evans, J.N.S., *Biomolecular NMR spectroscopy*. 1995, Oxford ; New York: Oxford University Press. xvi, 444 p.

73. Balbach, J.J., et al., *Probing hydrogen bonds in the antibody-bound HIV-1 gp120 V3 loop by solid state NMR REDOR measurements.* J Biomol NMR, 2000. **16**(4): p. 313-27.

74. Lewandowski, J.z.R., et al., *Measurement of Site-Specific 13C Spin−Lattice Relaxation in a Crystalline Protein.* Journal of the American Chemical Society, 2010. **132**(24): p. 8252-8254.

75. Giannini, D.D., et al., *Carbon-13 and nitrogen-15 spin-lattice relaxation (T1) and nuclear Overhauser enhancement (NOE) measurements for acetamide and N,N-dimethylacetamide.* Journal of the American Chemical Society, 1975. **97**(12): p. 3416-3419.

76. Wink, D.J., *Spin-lattice relaxation times in 1H NMR spectroscopy.* Journal of Chemical Education, 1989. **66**(10): p. 810.

77. Castellani, F., et al., *Structure of a protein determined by solid-state magic-angle-spinning NMR spectroscopy.* Nature, 2002. **420**(6911): p. 98-102.

78. Pauli, J., et al., *Backbone and side-chain C-13 and N-15 signal assignments of the alpha-spectrin SH3 domain by magic angle spinning solid-state NMR at 17.6 tesla.* Chembiochem, 2001. **2**(4): p. 272-281.

79. Zhang, H.Y., S. Neal, and D.S. Wishart, *RefDB: A database of uniformly referenced protein chemical shifts.* Journal of Biomolecular Nmr, 2003. **25**(3): p. 173-195.

80. Fischer, M.R., et al., *Carbon-13 magic angle spinning NMR study of the light-induced and temperature-dependent changes in Rhodobacter sphaeroides R26 reaction centers enriched in [4'-13C]tyrosine.* Biochemistry, 1992. **31**(45): p. 11038-11049.

81. van Rossum, B.J., et al., *13C MAS NMR evidence for structural similarity of L162YL mutant and Rhodobacter sphaeroides R26 RC, despite widely different cytochrome c2-mediated re-reduction kinetics of the oxidized primary donor.* Spectrochimica Acta Part A: Molecular and Biomolecular Spectroscopy, 1997. **53**(12): p. 2201-2208.

82. Bayro, M.J., et al., *Dipolar truncation in magic-angle spinning NMR recoupling experiments.* The Journal of Chemical Physics, 2009. **130**(11): p. 114506-8.

83. Bodner, M.L., *Solid state nuclear magnetic resonance of the HIV-1 and influenza fusion peptides associated wtih membranes*. 2006, Michigan State University: East Lansing, MI.

84. Petkova, A.T., et al., *A structural model for Alzheimer's beta-amyloid fibrils based on experimental constraints from solid state NMR.* Proceedings Of The National Academy Of Sciences Of The United States Of America, 2002. **99**(26): p. 16742-16747.

85. Wickramasinghe, N.P., et al., *Nanomole-scale protein solid-state NMR by breaking intrinsic (1)H T(1) boundaries.* Nature Methods, 2009. **6**(3): p. 215-218.

86. Gor'kov, P.L., et al., *Using low-E resonators to reduce RF heating in biological samples for static solid-state NMR up to 900 MHz.* Journal of Magnetic Resonance, 2007. **185**(1): p. 77-93.

87. Gor'kov, P.L., W.W. Brey, and J.R. Long, *Probe Development for Biosolids NMR Spectroscopy*, in *Encyclopedia of Magnetic Resonance*. 2007, John Wiley & Sons, Ltd.

88. McNeill, S.A., et al., *A low-E magic angle spinning probe for biological solid state NMR at 750 MHz.* Journal of Magnetic Resonance, 2009. **197**(2): p. 135-144.

89. Stringer, J.A., et al., *Reduction of RF-induced sample heating with a scroll coil resonator structure for solid-state NMR probes.* Journal of Magnetic Resonance, 2005. **173**(1): p. 40-48.

90. Doty, F.D., et al., *Using a cross-coil to reduce RF heating by an order of magnitude in triple-resonance multinuclear MAS at high fields.* Journal of Magnetic Resonance, 2006. **182**(2): p. 239-253.

91. Weingarth, M., G. Bodenhausen, and P. Tekely, *Low-power decoupling at high spinning frequencies in high static fields.* Journal of Magnetic Resonance, 2009. **199**(2): p. 238-241.

92. Hu, B., et al., *Broad-band homo-nuclear correlations assisted by 1H irradiation for bio-molecules in very high magnetic field at fast and ultra-fast MAS frequencies.* Journal of Magnetic Resonance, 2011. **212**(2): p. 320-329.

93. Thompson, L.K., *Solid-state NMR studies of the structure and mechanisms of proteins.* Current Opinion in Structural Biology, 2002. **12**(5): p. 661-669.

94. Cady, S.D., et al., *Structure of the amantadine binding site of influenza M2 proton channels in lipid bilayers.* Nature, 2010. **463**(7281): p. 689-692.

Chapter 2:

Experimental

Materials

S–Trityl–β–mercaptopropionyl–p–Methyl–Benzhydrylamine resin with a loading of 0.88 meq/g was purchased from Peptides International (Louisville, KY). Boc amino acids were purchased from Novabiochem. 3–(Diethoxyphosphoryloxy)–1,2,3–benzotriazin–4(3H)–one (DEPBT) was purchased from Chemprep (Wellington, FL). The bicinchoninic acid (BCA) assay and tris(2–carboxyethyl)phosphine hydrochloride (TCEP) were purchased from Pierce (Rockford, IL). 1–palmitoyl–2–oleoyl–*sn*–glycero–3–phosphocholine (POPC), 1–palmitoyl–2–oleoyl–*sn*–glycero–3–[phospho–*rac*–(1–glycerol)] sodium salt (POPG), 1,2–di–*O*–tetradecyl–*sn*–glycero–3–phosphocholine (DTPC), 1,2–di–*O*–tetradecyl–*sn*–glycero–3–phoso–*rac*–(1–glycerol) sodium salt (DTPG), and cholesterol were purchased from Avanti Polar Lipids, Inc. (Alabaster, AL). Uniformly labeled ^{13}C, ^{15}N alanine and glycine were purchased from Cambridge Isotope Labs (Andover, MA) and were Boc–protected using literature methods.[1] Isopropyl–β–D–1–thiogalactopyranoside (IPTG) was purchased from Anatrace (Maumee, OH). Di–t–butyl–dicarbonate, dithiothreitol (DTT), N–(2–hydroxyethyl)piperazine–N'–2–ethanesulfonic acid (HEPES), sodium formate, 4–mercaptophenylacetic acid (MPAA), 2–mercaptoethanesulfonate (MESNA), and TCEP were purchased from Sigma (St. Louis, IL). All other reagents were of analytical grade.

Sample Preparation of Hairpin and FP–Hairpin

Synthesis and Purification of Peptides

The FP23(linker) corresponds to the consensus sequence of gp41 and was adapted from the HXB2 strain of HIV–1 residues 512 – 534, (S534A)–thioester.[2, 3] FP23(linker) was synthesized by solid phase peptide synthesis (SPPS) with the sequence AVGIG**A**LFL**G** FLGAAGSTMG ARA–linker, where A6 and G10 were uniformly ^{13}C, ^{15}N labeled.

Synthesis of FP23(linker) was done using the t–Boc methodology[4] that was adapted to our needs. 700 mg of resin was swollen in dichloromethane (DCM) for ~1 hr and subsequently washed 3x with DCM prior to trityl group removal. Trityl group removal was accomplished with 2 x 4 minute washes of 95 : 2.5 : 2.5 of trifluoroacetic acid (TFA) : distilled water (DDW) : triisopropylsilane (TIS). After deprotection of the trityl group, the resin was washed with 5 x 1–2 minute DCM solutions followed by 3 x 1–2 minute washes of the 5% *N*,*N*–Diisopropylethylamine (DIEA) solution. After the 5% DIEA washings, the resin was ready for coupling with amino acids.

Pre–reaction of the next amino acid was done for ~1 hr in the dark. A 2x molar equivalents of the coupling reagent (DEPBT) relative to the amino acid was used. DEPBT and amino acid (AA) were dissolved to a final concentration of 0.35 – 0.40 M in tetrahydrofuran (THF) for the AA. After pre–reaction was completed the solution was neutralized with pure DIEA.

Standard t–Boc synthesis conditions are as follows: (1) Before starting washes, start pre–reacting next AA. (2) Rinse resin with 5 x 1 minute DCM washes, (3) deprotect N–terminus of peptide chain in two cycles using 50% TFA / 48% DCM / 2% anhydrous–anisole solution for 1 minute and then for 12 minutes. (4) Wash resin with 5 x 1 minute DCM washes, (5) neutralize

resin with 2–3 washes of 5% DIEA solution for 1 – 2 minutes. (6) Add pure DIEA (1:1 molar ratio of DIEA:DEPBT) to pre–reacted AA, (7) add in pre–reacted AA and start coupling in the reaction vessel. Repeat steps 1 – 7 for each amino acid that will be added. Typically a 5–fold molar excess of AA is used relative to the resin except for labeled amino acids where a 3–fold molar excess was used. The first coupling of alanine to the resin used a 10–fold molar excess and reacted for ~7 hrs before preforming steps 1, 2, 6, and 7 of the cycle followed by a second coupling reaction with alanine. Suggested coupling times are: 3 hrs for L12, G13, A14, A15, M19, G20 and A23; 4 hrs for G3, I4, A21, and R22; 5 hrs for G5, A6, L9, G10, G16; 7 – 8 hrs for A1, V2, S17 and T18; and 8 – 10 hrs for L7, F8 and F11. No attempt was made to optimize coupling times. Labeled amino acids were typically reacted for longer times than the minimum suggested coupling times. A6 and G10 were reacted for 8.5 – 10.5 hrs each. After completion of the peptide sequence, steps 2 – 6 were performed followed by 3 – 5 extra DCM washings of the resin. The resin was then allowed to dry under a stream of N_2 gas in the reaction vessel for 1 hour before being placed in a vacuum desiccator overnight to ensure the resin was fully dried. Once dry, the resin was weighed and shipped out for HF cleavage at either Midwest Bio–tech, Inc. (Fishers, IN) or Peptides International (Louisville, KY).

700 mg of resin produced 520 mg of crude peptide which after HPLC purification yielded ~260 mg of pure FP23(linker). FP23(linker) was purified by RP–HPLC on a Vydac C18 (Hesperia, CA) with a multistep gradient using a water / acetonitrile (ACN) gradient containing 0.1% TFA. Buffer A was 100% DDW / 0.1% TFA (v/v) and Buffer B was 90% ACN / 10% DDW / 0.1% TFA (v/v/v). Table 2–1 lists the gradients used for HPLC purification of FP23. The sum of the percent Buffer A and the percent Buffer B always adds to 100%. Only Buffer B's percentage is shown as that was the condition which could be changed. Purified FP23(linker)

with isotopic labeling was confirmed by mass spectrometry (m/z = 2201 Da) and quantified using the bicinchoninic acid assay. Purified peptide was lyophilized and stored in a conical tube under an argon environment at 4 °C until needed. The argon environment was created by gently blowing argon gas over the tube containing the sample for 30 – 60 s and then sealing the tube with a lid and parafilm.

Table 2–1: Purification gradients for gp41 constructs by RP–HPLC where Buffer A was 100% DDW / 0.1% TFA and Buffer B was 90% ACN / 10% DDW / 0.1% TFA.

FP23 C18 prep.		**Hairpin C18 prep.**		**FP–Hairpin C18 prep.**		**FP–Hairpin C18 semi–prep.**	
Time (min)	**Buffer B**	**Time** (min)	**Buffer B**	**Time** (min)	**Buffer B**	**Time** (min)	**Buffer B**
t = 0.0	25 %	t = 0.0	15 %	t = 0.0	15 %	t = 0.0	15 %
t = 3.5	39 %	t = 5.0	45 %	t = 6.0	45 %	t = 5.0	40 %
t = 53.5	64 %	t = 30.0	70 %	t = 36.0	75 %	t = 45.0	80 %
t = 65.0	64 %	t = 35.0	90 %	t = 39.0	75 %	t = 49.0	80 %
t = 68.0	25 %	t = 40.0	90 %	t = 42.0	15 %	t = 52.0	15 %
		t = 45.0	15 %				
Flow rate:	6 mL / min					2 mL / min	

Expression and Purification of Hairpin

The *Escherichia coli* (*E. coli*) used to express the N47(L6)C39 protein termed "Hairpin" was a kind gift from Dr. Kelly Sackett. Detailed information on the microbiology has been previously reported for the Hairpin construct in reference [2]. The N47(L6)C39 fragment corresponds to residues 535(M535C) to 581 of the N–Heptad repeat (NHR) followed by a six residue minimal loop (SGGRGG) and residues 628 to 666 for the C–Heptad repeat (CHR) from the HXB2 strain of HIV–1. The M535C point mutation was required for the NCL reaction at the

N–terminal end of NHR.[2] Figure 2–1 contains the surrounding DNA sequence (in italics) and the DNA for the protein sequence of the Hairpin construct with the start codon (ATG) and the stop codons TGA TAG. Figure 2–1 also presents the protein sequence for the 92 residue Hairpin construct expressed by *E. coli* and beneath the corresponding non–italicized DNA sequence.

GACGTCGCATGCTCCCGGCCGCCATGGCCGCGGGATTATCCCGCGAAATTAATACGACT
CACTATAGGGGAATTGTGAGCGGATAACAATTCCCCTCTAGAAATAATTTTGTTTAACT
TTAAGAAGGAGATATACAT
ATGTGCACGCTGACGGTACAGGCCAGACAATTATTGTCTGGTATAGTGCAGCAGCAG
C T L T V Q A R Q L L S G I V Q Q Q
AACAATTTGCTGAGGGCTATTGAGGCGCAACAGCATCTGTTGCAACTCACAGTCTGG
N N L L R A I E A Q Q H L L Q L T V W
GGCATCAAGCAGCTCCAGGCAAGAATCCTGTCTGGTGGCCGTGGCGGTTGGATGGAG
G I K Q L Q A R I L S G G R G G W M E
TGGGACAGAGAAATTAACAATTACACAAGCTTAATACACTCCTTAATTGAAGAATCG
W D R E I N N Y T S L I H S L I E E S
CAAAACCAGCAAGAAAAGAATGAACAAGAATTATTGGAATTAGATAAATGG**TGATAG**
Q N Q Q E K N E Q E L L E L D K W
GGATCCTAATGAATTAGATAAATGGCATCACCATCACCATCACTGATAGGGATCCTAAG
GAATTAGTAAATGGCATCACCATCACCATCACTGATAGGGATCCTAAGGAATTAGATAA
ATGGCATCACCATCACCATCACTGATAGGGATCCTAATCACTAGTGCGGCCGCCTGCAG
GTCGACCATATGGGAGAGCTCCCCACGCGTTGGATGCATAGCTTGAGTATTCTATAGT

Figure 2–1: DNA sequence and protein sequence for the 92 residue gp41 construct "Hairpin" expressed in *E. coli* cells. The DNA codons encoding for the protein have the amino acid underneath it. The surrounding DNA is in italics. ATG (in red) is the start codon, TGC is the first residue corresponding to the N–terminal cysteine residue, and the two stop codons (in red) are TGA TAG segment at the end of the non–italic sequence.

Hairpin was expressed in BL–21 *E. coli* cells containing the pGEMT plasmid, which are grown up overnight to an OD_{600} of ~6 in 1 L of Luria Bertani broth media (LBm) containing 100 mg/L of ampicillin. After overnight growth, the cell suspension is pelleted at 7,000 rpm (~9,000g) for 10 – 15 min using a Sorvall RC6 SLC–4000 rotor (Thermo–Fisher Scientific, Wilmington, DE). Cell pellets from 2 L of growth are resuspended in a fresh liter of LBm

containing ampicillin and allowed to grow for ~1 hr before induction with IPTG. Induction lasted ~4 hrs before harvesting by centrifugation. Expression and induction were done at 37°C with yields of ~10 – 12 grams of wet cells/L culture, which were stored at –20°C until needed.[2, 5, 6]

Purification of the Hairpin construct was done in glacial acetic acid (HOAc). Approximately 120 mL of glacial acetic acid was used to resuspend 10 grams of cells in a plastic 250 mL beaker. The beaker and cell solution were placed in an ice bath, and the cells were lysed by tip sonication with cycles of 30 s on / 30 s off for 10 minutes at 70% amplitude. The lysis solution was centrifuged at 20,000 rpm (~48,000g) using an ss–34 rotor (Thermo–Fisher) for 20 minutes at 16°C to pellet out the cell debris and insoluble proteins. The decanted supernatant solution was dialyzed overnight against TFA:water (1:2000 v/v) and 150 µM DTT using a 3.5 kDa MWCO Spectra/Por 3 dialysis tubing (Spectrum Labs, Rancho Dominguez, CA).[5] The post dialysis Hairpin solution was ~400 mL which was concentrated to ~60 mL using a 10 kDa MWCO Vivacell 100 concentrator (Viva Products Inc., Littleton, MA) under ~5 atmospheres of N_2 gas at room temperature and no centrifugation. The concentrated protein solution had TCEP and ACN added to it, for final concentrations of 2 mM TCEP and ~15% ACN (v/v). The concentrated protein solution was tip sonicated 5 s on / 2 s off for 30 s at 50 % amplitude before being purified on a C18 RP–HPLC preparative column using a multistep gradient between Buffer A and Buffer B which is presented in Table 2–1.[5] Tip sonication worked well to break up any globular protein that occurred during the concentration step. Hairpin eluted as a single peak as shown in Figure 2–2, and all HPLC collections of Hairpin were pooled together, and the ACN was removed under a stream of N_2 gas. Typical volumes were ~300 mL from the HPLC

reduced to ~60 mL prior to lyophilization. Hairpin's identity was confirmed by MALDI mass spectrometry and SDS–PAGE, quantified by A_{280} measurements and secondary structure checked by circular dichroism (CD) spectroscopy.[2] 50 mg of purified Hairpin obtained from 1 L of expression was estimated to be ~95% pure by SDS–PAGE, as seen in Figure 2–3. The lyophilized pellet was centrifuged at ~1,000g for 3 – 5 min and stored under an argon atmosphere at 4 °C until needed.

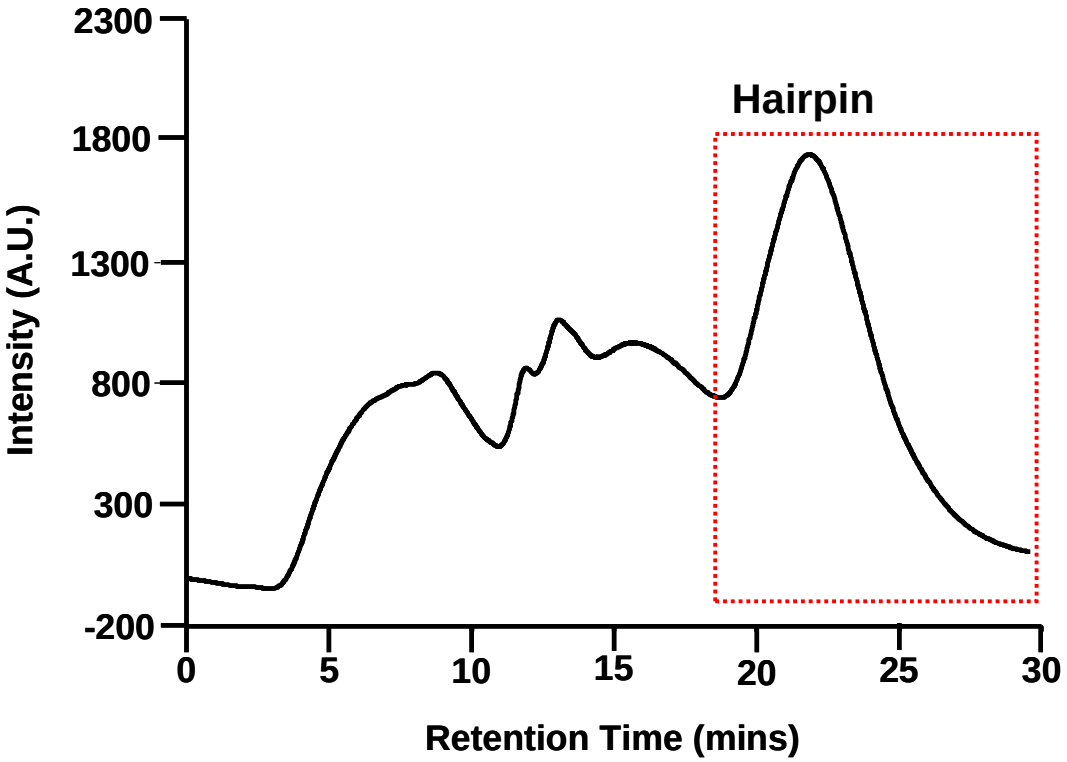

Figure 2–2: A typical HPLC purification of Hairpin. The absorbance at λ = 280 nm was observed. Hairpin elutes between 18 – 30 minutes (red dotted box) on the C18 preparative column.

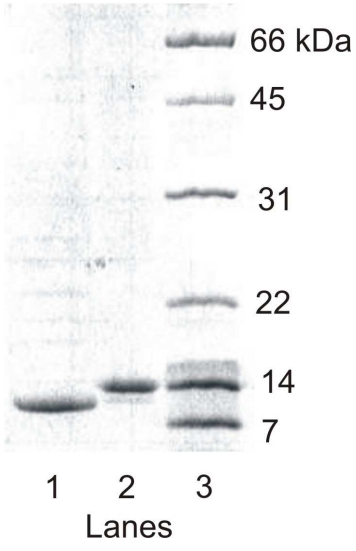

Figure 2–3: SDS–PAGE gel showing Hairpin, FP–Hairpin and broad molecular weight standards (Lanes 1 – 3 respectively). A clear gel shift is observed between Hairpin and FP–Hairpin confirming that a new construct has been synthesized. 2 µg of sample were loaded in each lane. Hairpin = 10.7 kDa; FP–Hairpin = 12.8 kDa.

Solubilization of Hairpin in different lysing solutions was attempted, however none of the solutions were able to solubilize Hairpin to the extent which glacial acetic acid could. Solubilization was attempted with the following solutions: 50 mM Tris, pH 7.3; 10% acetic acid; degassed water with 0.1% TFA; 8 M Urea; lyse in glacial acetic acid, basify with NaOH to precipitate Hairpin; and finally lyse with glacial acetic acid, dilute to 10% HOAc and try to precipitate by addition of 5 M NaOH. It was thus determined that Hairpin in the bacteria was in inclusion bodies that were best solubilized with the glacial acetic acid.

Native Chemical Ligation (NCL)

The native chemical ligation (NCL) reaction is a protocol that allows for the reaction of two unprotected peptides to create one longer peptide.[7–11] The reaction shown in Figure 2–4 requires that the C–terminal of one peptide have a thioester and that the N–terminal of the other peptide contain a free cysteine residue. By reacting the two peptides together, an intermediate C – S bond will form linking the two peptides which will re–arrange and under go an S – N shift, creating the new C – N peptide bond and the final larger protein construct.

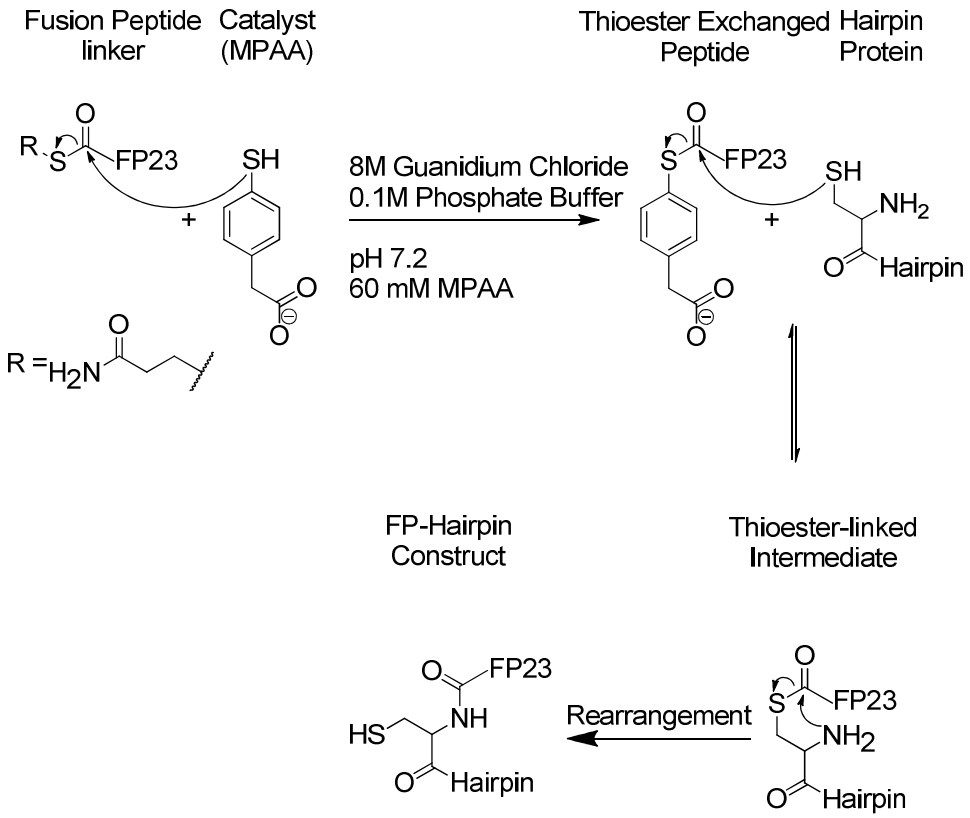

Figure 2–4: Native chemical ligation scheme. Hairpin is the 92 residue fragment from recombinant *E. coli* expression, FP23 is the fragment made via t–Boc methodology solid phase peptide synthesis. FP23 and Hairpin are ligated together to create the final product, FP–Hairpin.

Figure 2–4 illustrates the native chemical ligation reaction pathway. The first step is the pre–reaction between the catalyst and the FP23(linker). Once pre–reaction of the FP23(linker) is complete, the N–terminal cysteine domain (Hairpin) is introduced and reacted with the thioester exchanged peptide creating the intermediate C – S bonded protein. After rearrangement, the final protein construct (FP–Hairpin) is created containing a new peptide bond.

NCL was first introduced in 1994 by Dawson and co–workers.[7] The practical limit of SPPS is ~50 amino acids after which poor yields occur due to the formation of secondary structure which causes the N–terminus to become hindered and inaccessible to the new amino

acid being added.[8, 9] This limit excludes the creation of larger proteins synthetically, instead requiring them to be produced recombinantly. With NCL the door has been opened to allow for connecting together smaller synthetically created fragments to produce proteins of up to ~200 residues extending the range, size and applicability of the synthetic SPPS methodology.[12] One of the benefits of the NCL is that internal cysteines can be present, as they will not react with the thioester since it can not undergo the S – N shift.[13] The t–Boc methodology for SPPS has been used to create the thioester containing peptide as opposed to Fmoc methodology until recently since the use of piperidine in the Fmoc methodology will cleave the thioester – resin linkage.[13, 14] Recent work has resulted in the development of Fmoc–thioester resins which are stable to piperidine.[15, 16] Fmoc based SPPS is similar to the t–Boc methodology however using the Fmoc protocol, cleavage from the resin would be safer and quicker than the t–Boc methodology since the t–Boc protocol cleavage of the peptide thioester from the resin is accomplished with liquid HF which is very dangerous and only available in specialized labs. Fmoc cleavage can be performed in any lab as the cleavage cocktail contains chemicals that are available in most laboratories.[15]

The use of a thiol catalyst has shown to increase the rates of the NCL reaction along with the extent of the ligation reducing the time required to reach completion.[10, 17] Studies with model peptides detailing the time of reactions for a specific dipeptide sequence have been performed.[12] The affect of the catalyst used has also been studied.[10] These studies served as a starting point for the optimization of the FP–Hairpin ligation reaction.

Initial yields for the FP–Hairpin ligation were ~5% using the 2–mercaptoethanesulfonate (MESNA) catalysts and required several days at room temperature to reach said yield. A paper by Johnson and Kent highlighted a new catalyst 4–mercaptophenylacetic acid (MPAA) which

could increase yields, is highly water soluble, is an excellent leaving group, and lacks the pungent odor normally associated with sulfur containing compounds such as β–mercaptoethanol.[10] Table 2–2 highlights the results of test ligations to determine the best conditions for the FP–Hairpin system with all comparisons relative to the 30 mM MENSA final concentration reaction. An immediate 4–fold improvement was obtained by switching catalysts from MESNA to MPAA while maintaining a 30 mM final concentration. Yields in Table 2–2 were determined by quantifying the area under the HPLC curve using the 280 nm wavelength chromatograph. The ratio of the FP–Hairpin peak to the total area of Hairpin and FP–Hairpin was then used to compare the different reactions. The larger the ratio of FP–Hairpin to total area, the more product that was present. Johnson and Kent also showed that increasing the MPAA concentration resulted in higher yields.[10] For the FP–Hairpin system the best result was obtain from a final concentration of 30 mM MPAA which is highlighted in Table 2–2 along with other concentrations of MPAA. While other conditions were tested as shown in Table 2–2 nothing was as affective or as reproducible as the change in catalysts. Attempts to perform the reaction at higher temperatures failed to produce consistent results when scaled up to larger ligations. As a result ligations were preformed at room temperature.

The NCL reaction was performed in 6 M or 8 M guanidium chloride solution to increase the solubility of the reacting peptides, thereby allowing the use of higher peptide concentrations which could accelerate the ligation reactions.[8] For the FP–Hairpin ligation the concentration of guanidium chloride was increased from 6 M to 8 M to obtain a more denatured Hairpin protein at the N–terminal which could reduce the steric hindrance for the ligation reaction.

Previously, creation of smaller peptides such as N70 have used the NCL and the 2–mercaptoethanesulfonate (MENSA) catalyst.[18] Best results for FP–Hairpin from the test

ligations were room temperature incubation at pH 7.2 with 30 mM MPAA catalyst which consistently produced 20% yields.

Steric hindrance from the C–terminal amino acid should also be considered. It has been shown that all 20 amino acids can be ligated in the X–Cys combination, where X represents the C–terminal residue.[12] Testing of the time of reaction was also performed. Model ligations using the Ala – Cys dipeptide were shown to be complete within 10 hrs in the literature.[12] This dipeptide is the same as the one in the FP–Hairpin system, and alanine is one of the least sterically hindered amino acids.

Table 2–2: Yields from NCL test ligations and the relevant conditions.

Rxn	Catalyst [a]	Temp [b]	Area FP-HP [c]	Total Area [d]	FP-HP / Total Area [e]	Ratio Yield Compared to Rxn. 1 [f]	Other Conditions
1	30 mM MESNA	RT	171.02	3545.52	0.0482	1.000	Standard Reaction
2	30 mM MESNA	42 ^{o}C	299.12	3746.00	0.0799	1.655	
3	30 mM MPAA	RT	631.52	3620.53	0.1744	3.616	
4	30 mM MPAA	42 ^{o}C	414.04	1673.31	0.2474	5.130	
5	100 mM MPAA	RT	159.69	1807.48	0.0883	1.832	
6	100 mM MPAA	42 ^{o}C	316.85	1666.55	0.1901	3.942	
7	225 mM MPAA	RT	59.99	1507.77	0.0398	0.825	
8	100 mM MPAA	RT	207.30	3145.70	0.0659	1.366	Recovered HP
9	100 mM MPAA	RT	118.56	2152.62	0.0551	1.142	2 : 1 ratio peptide : protein
10	100 mM MPAA	RT	76.52	1771.20	0.0432	0.896	2 days RT, then –20 ^{o}C
11	100 mM MPAA	RT	72.07	3806.95	0.0189	0.392	Pre–react peptide and MPAA 9 hrs
12	30 mM MESNA	RT	196.60	3793.61	0.0518	1.074	Boiled sample first
13	30 mM MESNA	RT	170.77	3381.64	0.0505	1.047	Tip sonicated throughout day
14	30 mM MESNA	RT	181.85	3665.19	0.0496	1.029	Stirred reaction
15	30 mM MESNA	RT	69.87	3778.35	0.0185	0.383	Dissolved HP pellet with peptide solution
16	30 mM MESNA	RT	80.87	3811.48	0.0212	0.440	0.5 mM final [protein] & [peptide]

Table 2-2 (cont'd)

a = final concentration of catalyst in ligation reaction

b = Temperature that reaction was performed at ± 3 °C. RT = room temperature.

c = Integrated area under the HPLC profile peak for λ = 280 nm wavelength for the FP–HP peak. Area units are mAu*mins.

d = Integrated area under the HPLC profile for HP and FP–HP added together.

e = Ratio of the area for FP–HP divided by the total area of HP and FP–HP.

f = Ratio of yield for each reaction compared to yield for the standard reaction (Rxn. 1).

To determine the time requirement for the FP–Hairpin ligation, small 100 μL aliquots were withdrawn at 1, 3, 6, 12 hrs, 1, 2, 3, 4, 5, and 6 days after co–mixing of the FP23(linker) and Hairpin reactants, quenched, and stored at –80 °C until all the aliquots could be purified. Quenching of the ligation is discussed below. The reaction had been incubated at 55–57 °C for 6 days. The pH of the reaction was monitored after each withdrawal and was found to be consistent between pH 7.2 – 7.4 for the first 72 hrs, after which an increase to pH 7.5 – 7.6 was observed. RP–HPLC was used to monitor the reaction showing that after ~2 days the FP–Hairpin reaction had reacted equilibrium. Table 2–3 shows the results of the time test.

From the data, 24 – 48 hrs was optimal for the reaction to proceed, after which mostly oxidized product was observed and yields did not increase. After 72 hrs yields decreased and oxidized product was more prevalent. One possible explanation for the increased oxidized product is that the TCEP reducing agent is not particularly stable in phosphate buffers at neutral pH and as the time increased for the reaction there was no more TCEP present.[19]

Table 2–3: Time study of the native chemical ligation reaction for the FP–Hairpin construct.

Time (hrs)	Aliquot (μL)	Area HP [a]	FPH P1	FPH P2	Total FPH	Total Area	FPH / Total Area
1	274.2	231.67	6.76	55.06	61.82	293.49	0.2106
3	145.9	209.80	7.65	54.01	61.66	271.46	0.2271
6	145.9	213.40	8.69	54.79	63.48	276.88	0.2293
12	145.9	208.81	12.34	51.48	63.82	272.63	0.2309
24	145.9	186.68	13.02	35.93	48.95	235.63	0.2077
48	145.9	202.83	17.02	29.11	46.13	248.96	0.1853
72	145.9	220.22	19.12	24.48	43.60	263.82	0.1653

[a] = Integrated area under the HPLC profile peak for λ = 280 nm wavelength for each peak. Area units are mAu*mins.

In Table 2–3 the area under the peaks for Hairpin and FP–Hairpin were quantified using the λ = 280 nm wavelength chromatograph. Initially FP–Hairpin had a small peak that developed at an earlier retention time followed by a larger second peak at a slightly later retention time. Mass spectroscopy confirmed that both peaks were FP–Hairpin and that the early one was likely oxidized which can be reduced with TCEP reducing agent. As can be seen in Table 2–3, as reaction time proceeded, the first peak becomes more substantial until it is nearly half of the total area for the FP–Hairpin peak. To gauge the reaction progress, the total area of FP–Hairpin was divided by the area of Hairpin and FP–Hairpin, similar to Table 2–2. The ratio shows that an approximate 20% yield was achieved within 1 hr at the high temperature and no further increase in yield was obtained.

Small scale tests of the NCL ligation helped define optimal conditions for FP–Hairpin production. These conditions, along with optimization of Hairpin purification contributed significantly in reducing sample preparation time from 2 months to 2 weeks and producing pure

multi–milligram quantities of the 115 residue FP–Hairpin construct in the high yields needed for biophysical characterization and SSNMR experiments.

From the test ligations, it was found that the best parameters were to use higher concentration of the FP23(linker) and the Hairpin, change catalysts to 30 mM MPAA final concentration, and allow the reaction to proceed at room temperature for 1 – 2 days. Ligations preformed with these changes routinely produced 20% yields of pure FP–Hairpin after purification and refolding. While 20% yield is less than reported in literature for model ligations, the reaction is able to consistently provide enough protein in a timely manner for SSNMR experiments. Consequently, this also highlights the fact that a large asymmetric protein of 115 residues can be created by a 23–mer and a 92–mer, where the 92–mer was recombinantly expressed. To my knowledge this is the first time such an asymmetric protein complex was created, as previous ligations tended to be more evenly balanced in fragment size. Figure 2–5 highlights the different domains for gp41, specifically the FP23, Hairpin and the FP–Hairpin constructs which are relevant to the research presented here.

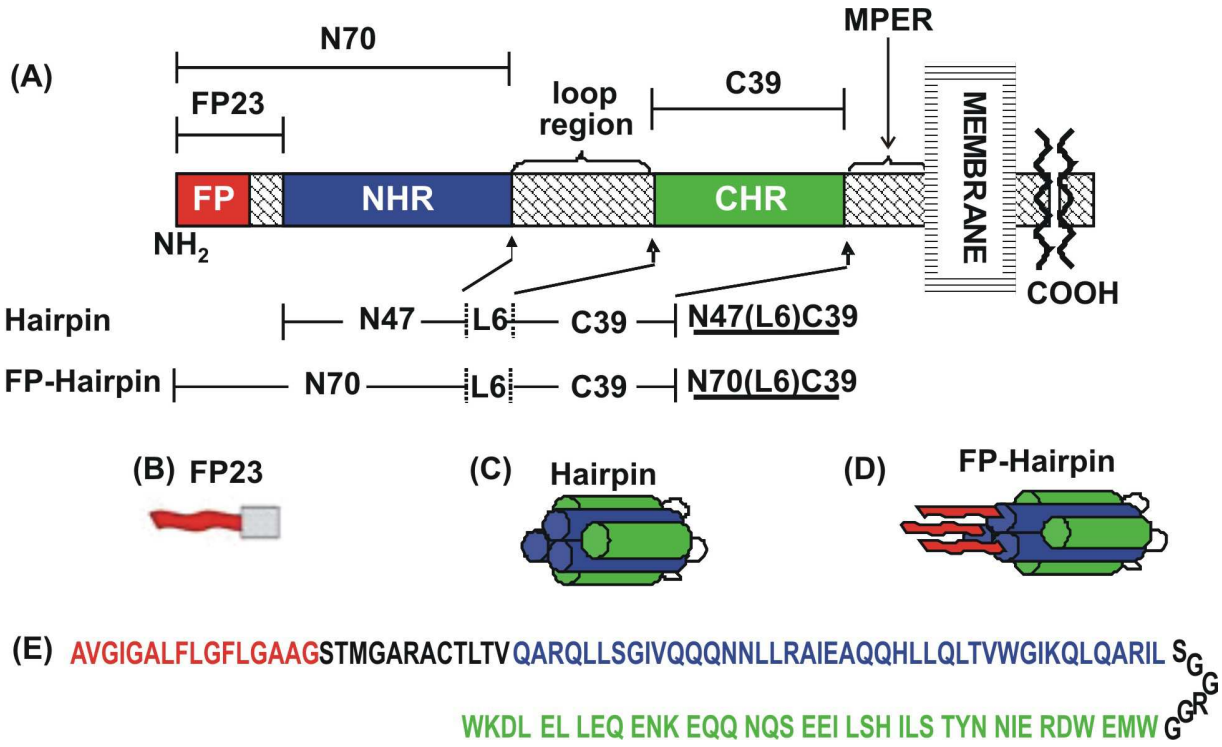

Figure 2–5: (A) Schematic diagram of the domains of the gp41 construct showing the different functional domains with colors corresponding to the structures and amino acid residues below for each construct. (B) Representation of the structure of the FP23 in free solution, (C) Representation of six helix bundle structure of FP–Hairpin which is formed after the native chemical ligation (NCL) of FP23 and Hairpin, and (D) Representation of Hairpin structure with the associated amino acid sequence. (E) Amino acid sequence that is color coded to match up with the domains (A).[2, 5, 20]

Preparation of FP–Hairpin by Native Chemical Ligation Protocol

Initial ligation conditions for FP–Hairpin were: 0.3 mM FP23(linker) and 0.3 mM Hairpin dissolved in a degassed solution of 6 M GdCl, with 0.1 M phosphate buffer at pH 7.2. FP23(linker) was pre–reacted with 60 mM MESNA and 2 mM TCEP reducing agent for 60 minutes. The FP23(linker) solution was tip sonicated for 30 s at 40% amplitude with cycles of 5 s on / 2 s off and then rested for 10 minutes before repeating the cycle. After pre–reacting the

FP23(linker), Hairpin was dissolved in the ligation buffer, tip sonicated for 30 s at 40% amplitude with cycles of 5 s on / 2 s off, and then co–mixed with the pre–reacted FP23(linker) solution. The co–mixed solution was subjected to another round of sonication and the pH adjusted with 5 M NaOH to pH 7.2 The ligation was blanketed with an inert atmosphere of argon gas, sealed, and allowed to react for 3 – 14 days before quenching and purification of the reaction resulting in ~5% yields of FP–Hairpin.

Optimized ligation conditions for FP–Hairpin were: FP23(linker) and Hairpin initially dissolved at 1.2 mM concentration in a degassed solution of 8 M GdCl with 0.1 M phosphate buffer at pH 7.2. FP23(linker) was pre–reacted with 60 mM MPAA and 2 mM TCEP reducing agent for 30 – 60 minutes. The FP23(linker) solution was tip sonicated for 30 s at 40% amplitude with cycles of 5 s on / 2 s off and then rested for 10 minutes before repeating the cycle. After FP23(linker) pre–reaction, Hairpin was dissolved in the ligation buffer, tip sonicated for 30 s at 40% amplitude with cycles of 5 s on / 2 s off, and co–mixed with pre–reacted FP23(linker) solution. The co–mixed solution was then subjected to another round of sonication, and the pH was adjusted with 5 M NaOH to pH 7.2. The ligation was blanketed with argon gas, sealed, and allowed to react for 1 – 2 days before quenching and purification of the reaction resulting in ~20% yields.

The FP–Hairpin ligation reaction was initially quenched by addition of 12% β–mercaptoethanol, acidified by addition of 1.5% (v/v) of formic acid, addition of 75 mM TCEP (final concentration) and addition of 15% ACN (v/v) to the reaction vessel. Initially the β–mercaptoethanol was used to stop the NCL reaction from continuing to react, however this step was subsequently removed from the workup protocol in order to recover useable FP23(linker). FP23(linker) without the thioester exchanged β–mercaptoethanol could possibly be used again in

another NCL reaction. β–mercaptoethanol is a poor leaving group, resulting in an inability to exchange with the MPAA catalyst again in another NCL reaction. The quenched ligation was portioned out and injected on the RP–HPLC for purification using a semi–preparative YMC C4 column (Waters, Milford, MA) or a preparative C18 column from Vydac. Narrower peaks were achieved with the C4 column, however more material could be loaded and purified at once with the C18 column. For testing of ligation conditions the C4 column was used. When large volumes were purified the C18 column was chosen. FP–Hairpin was purified using a multistep gradient between Buffer A and Buffer B, with the gradients presented in Table 2–1. Pure FP–Hairpin elutes separately from unreacted Hairpin material but co–elutes with residual FP23(linker) as seen in Figure 2–6. The collected FP–Hairpin fractions were pooled together with 200 μM TCEP and 20 mM sodium formate added so that after removal of ACN these concentrations were obtained. The volume was generally reduced by a factor of 3 – 4, leaving ~50 mL of FP–Hairpin solution for dialysis. Dialysis was used to refold FP–Hairpin, remove any residual ACN, and also remove the co–eluted FP23(linker). Refolding was confirmed experimentally by CD spectroscopy. If the FP–Hairpin was not refolded or the sample still contained impurities such as FP23(linker) or guanidium chloride then the CD spectra would not be consistent with the spectra presented in Figure 2–7. The salt would cause a distorted signal in the 190 – 200 nm range and the FP23(linker) would affect the overall helicity of the protein sample. FP23(linker) and FP–Hairpin co–mixed would likely provide a $[\Theta]_{222nm}$ value closer to 0 x 10^3 deg cm^2 $dmol^{-1}$ than the experimentally determined value of $[\Theta]_{222nm}$ = –24.9 x 10^3 deg cm^2 $dmol^{-1}$ in 20 mM sodium formate buffer at pH 3.[2] Mass spectroscopy was used to confirm that FP–Hairpin after dialysis did not contain FP23(linker).[2, 5, 20] Dialysis was done in 20 or 50 mM sodium formate, 200 μM TCEP, pH 3.0 and 3 L of volume at 4 °C for 3 days with daily buffer

changes.[2, 5] Dialyzed FP–Hairpin was quantified using the A_{280} absorbance with the molar extinction coefficient ε = 23,490 cm^{-1} M^{-1} and MW = 12.822 kDa, concentrated to ~80 μM with a 10 kDa MWCO spin concentrator and stored under argon gas at 4 °C until used.

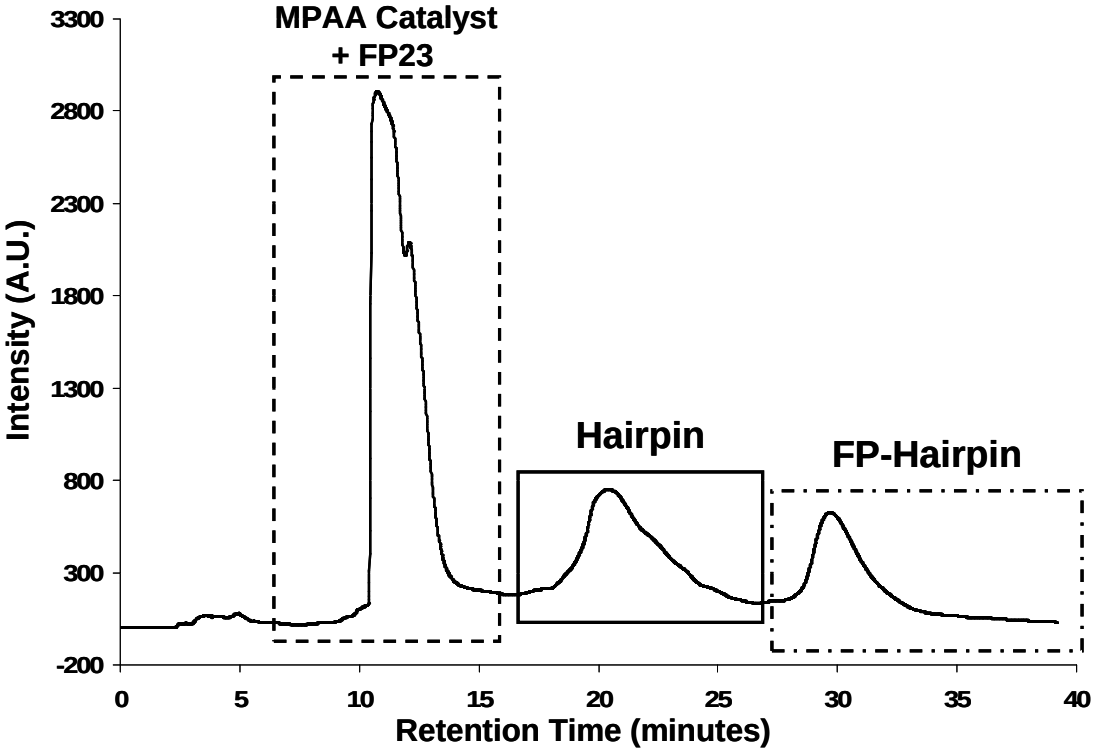

Figure 2–6: A typical HPLC purification of FP–Hairpin UA6/UG10 by observing the λ= 280 nm wavelength. Clear resolution is observed between all peaks. The FP23 has no A_{280} absorbance, and therefore is not seen here, however it is predominant in the dashed box region for the catalyst and continues to co–elute all the way through the FP–Hairpin peak. FP23 that co–eluted with FP–Hairpin is removed by dialysis. The dashed line represents the region where the catalyst and FP23 elute, the solid line represents where Hairpin elutes, and the dash dot line represents the region where the FP–Hairpin elutes. MALDI mass spectrometry was used to determine assignments.

FP–Hairpin was generally used within 1 week after dialysis. Mass spectrometry and SDS–PAGE were used to confirm FP–Hairpin mass and purity.[2, 5, 20] CD spectroscopy was used to confirm refolding and to determine the global secondary structure. Quantification was performed on a NanoDrop Spectrophotometer (Thermo Fisher Scientific; Wilmington, DE) and was the averaged result from 3 – 5 separate readings. Figure 2–3 shows a gel of Hairpin and FP–Hairpin with molecular weight standards. A clear gel shift is observed for FP–Hairpin and no Hairpin reactant is present in the FP–Hairpin sample shown in Figure 2–3. Approximately equal amounts of protein were loaded in the two lanes.

Hairpin and FP–Hairpin Characterization

CD spectra were acquired on a Chirascan CD spectrometer (Applied Photophysics Limited, Leatherhead, U.K.) with a 0.5 nm increment and 2 s averaging time between 190 – 260 nm. Thermal melts for Hairpin and FP–Hairpin were monitored at λ = 222 nm over a temperature range of 5 – 100 $^{\circ}$C.[2] Protein was dissolved in 20 mM sodium formate buffer at pH 3 with 200 μM TCEP.

Figure 2–7A shows the CD spectra for 25 μM Hairpin and 26 μM FP–Hairpin in the formate buffer prior to thermal melts. CD spectra for Hairpin and FP–Hairpin after the thermal melts were identical to pre–melt spectra and are overlaid in Figure 2–7A. Figure 2–7B shows the melts preformed in the formate buffer for 25 μM Hairpin and 26 μM FP–Hairpin. Figure 2–7C show thermal melts of Hairpin which were preformed in 6 M and 8 M GdCl at pH 7, with 0.1 M phosphate buffer and 200 μM TCEP. Hairpin was 22 μM and 26 μM in the 6 M and 8 M GdCl solutions respectively. Determination of the helicity of the constructs was done using $[\Theta]_{222nm}$ = –33.0 x 10^3 deg cm^2 $dmol^{-1}$ for 100% helicity.[2, 21, 22] Hairpin was ~99% helical with

$[\Theta]_{222nm}$ = –32.6 x 10^3 deg cm^2 $dmol^{-1}$ and FP–Hairpin was ~75% helical with a $[\Theta]_{222nm}$ = –24.9 x 10^3 deg cm^2 $dmol^{-1}$ in 20 mM sodium formate buffer at pH 3.[2] The lower helicity in FP–Hairpin is likely due to the addition of the FP region adopting a β–strand/sheet conformation. The nearly 100% helicity for the Hairpin construct is consistent with crystal structures of gp41 with antiparallel coiled–coiled structures.[23–27]

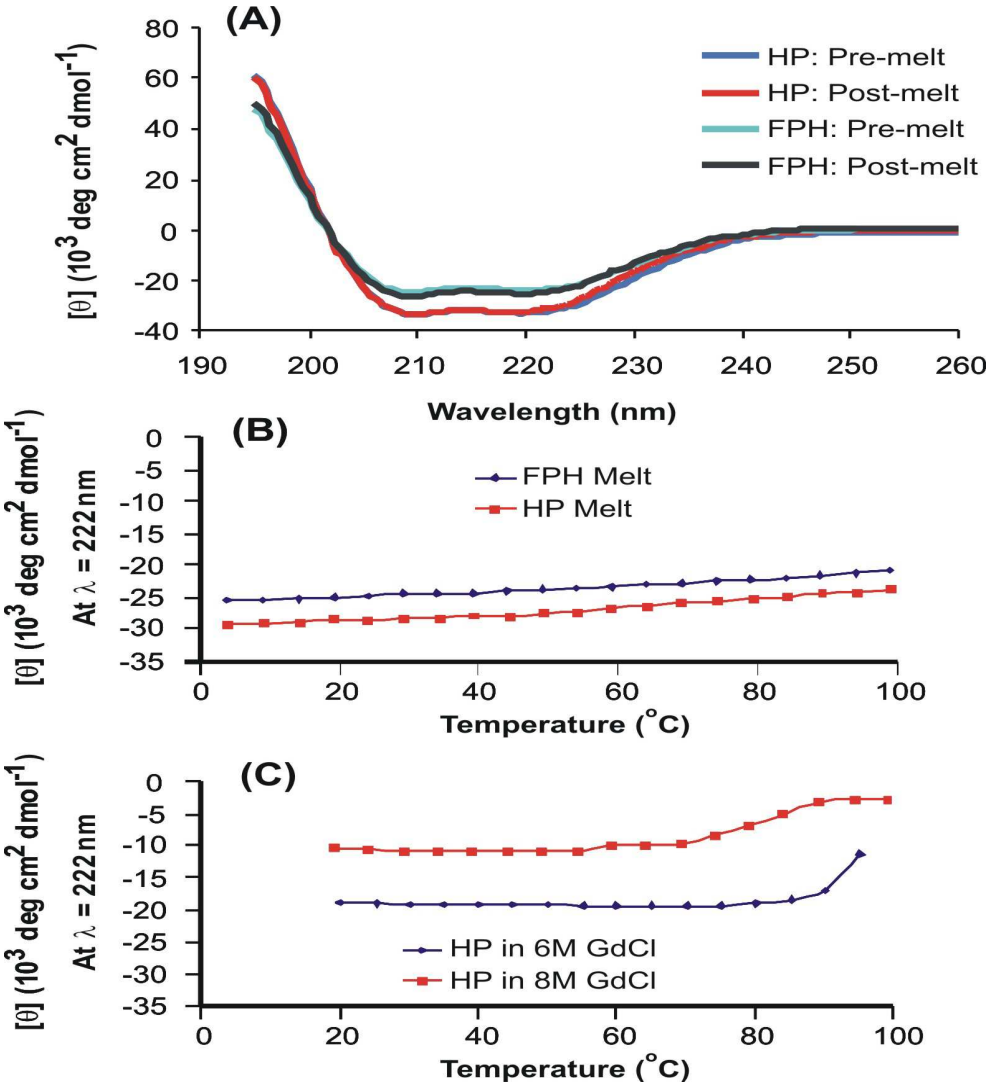

Figure 2–7: (A) Far–UV CD spectra of Hairpin and FP–Hairpin in 20 mM sodium formate buffer, pH 3 with 200 μM TCEP. For Hairpin, the pre–melt spectrum (blue) and post–melt spectrum (red) overlay each other with minimal deviation between 220–240 nm. For FP–Hairpin the pre–melt spectrum (black) and the post–melt spectrum (light blue) are overlay nearly exact with no significant deviation between the two spectra. This highlights that the proteins are not affected by heating up to 100 °C. (B) Thermal melts of Hairpin and FP–Hairpin in the sodium formate buffer while observing the λ = 222 nm wavelength. The concentration of Hairpin was 25 μM and FP–Hairpin was 26 μM for both A and B. No thermal transition up to 100 °C was observed. (C) Thermal melts (λ = 222 nm) of Hairpin in 6 M and 8 M GdCl. The 6 M GdCl solution shows the start of a thermal transition around 95 °C where as the 8 M GdCl solution shows a thermal transition around 85 °C. Neither construct melts below 100 °C in non–denaturing buffer solution. Concentration of Hairpin was 22 μM in the 6 M GdCl and 26 μM in the 8 M GdCl solutions, both solutions were at pH 7 with 100 mM phosphate buffer and 200 μM reducing agent was TCEP.

Hairpin and FP–Hairpin are highly thermostable proteins, as exhibited with melting temperatures (T_m) exceeding 100°C which is significantly higher than physiological conditions. Hairpin in the 6 M guanidium chloride solution showed the onset of a thermal melt at ~95°C. In the 8 M guanidium chloride solution, the T_m is ~85°C. Figure 2–7C confirms that Hairpin in the NCL solutions of either 6 M or 8 M guanidium chloride solution does not under go a thermal transition below 85°C, allowing for the use of elevated temperatures to facilitate the ligation reaction.

Gp41 constructs presented in Table 2–4 highlight the thermostability of the six helix bundle (SHB) formation. Interestingly, Hairpin and FP–Hairpin's thermal transition needed to be measured by differential scanning calorimetry (DSC) in 20 mM formate buffer, pH 3.0 and 200 μM TCEP to ascertain their T_m values.[5]

Table 2–4: Thermostability of various gp41 constructs in either a trimer assembly or a SHB formation.

Peptide Construct	T_m (°C)	Number of Residues	Notes
N36/C34	58	70	Free peptides [18]
17 – 70	82	54	
N70/C34	81	104	
N70	45	70	First 70 residues [2]
N36/C34	62	70	Free peptides [24]
N34(L6)C28	70	68	Minimal Linker [24]
N51/C43	90	94	Free peptides [24, 28]
N47(L6)C39 {Hairpin}	112.4, 111.4	92	Measured via DSC [5]
N70(L6)C39 {FP–Hairpin}	111.3, 111.0	115	Measured via DSC, Minimal linker. [5]
HIV gp41(540–665)	106	125	Lacks FP, pH 3.0, non–reduced [29]
HIV gp41(540–665)	105	125	Lacks FP, pH 3.0 + reduced [29]
HIV gp41(540–665)	109	125	Lacks FP, pH 8.0 [29]
gp41 (536–669)	110.4, 119.5	133	Non–reduced, no FP, native loop, pH 2.8. [30]
gp41 (536–669)	109.1	133	Reduced, no FP, native loop, pH 2.8. [30]
Ectodomain (512–684)	> 125	172	Contains FP, no definitive peak seen via DSC when heated to 125 °C. [31]
E–core (546–684)	70	138	Lacks FP, contains loop and MPER. [31]
Core (538–665)	104.6	127	Measured via DSC. [31]

As Table 2–4 highlights, various constructs of gp41 range in T_m's from 58 °C to above 125 °C. Some of the constructs contain the native loop, others have a minimal loop, and a few are simply co–mixed NHR and CHR constructs, which all form the stable SHB. From the tabulated data, the addition of either the minimal linker or the native loop adds considerable thermostability to the gp41 constructs compared to the SHB's formed from the free peptides. The

other significant point from Table 2–4 is that once the SHB is formed it is thermodynamically stable, requiring temperatures at least 20 °C higher than physiological conditions for the unfolding transition to occur.

Membrane Lipid Preparation

Membrane lipids were prepared following previously published protocols from the Weliky group.[2, 5, 32] Briefly, an 8:2:5 molar ratio of POPC:POPG:Chol or a 4:1 molar ratio of POPC:POPG lipids were massed out and dissolved in chloroform. Chloroform was removed under a stream of N_2 gas, and then the lipids were placed in a vacuum desiccator overnight to remove residual solvent. Lipids were re–dissolved in chloroform from the stock container, portioned out, and again chloroform was removed under a stream of N_2 gas. Samples were place in the vacuum desiccator overnight. Two methods for preparing the lipids are described below. Preparation of 200 nm diameter LUV's were prepared through freeze thaw cycles and extrusion through a polycarbonate membrane with 200 nm pore diameter. [33, 34] A loss of 20% was assumed in the extruder.[34] The POPC and POPG lipids were predominantly used for the lipid sample preparations and contained natural abundance ^{13}CO in the ester linkage. Two samples were prepared with the DTPC and DTPG lipids which were equivalent to the POPC and POPG lipids except that they were ether linked instead, and did not contain the natural abundant ^{13}CO in the lipids. The samples with the DTPC and DTPG lipids were prepared in the same manor as the POPC and POPG lipids as discussed above.

Method A

A lipid fraction was hydrated with 25 mM HEPES buffer at pH 7.4 to a 10 mM concentration and gently vortexed for ~15 minutes. The hydrated mixture was then subjected to 5 freeze – thaw cycles in liquid nitrogen before being extruded 19 times through a filter with 200 nm diameter pores. The lipid vesicles were diluted to 1.8 mM with 25 mM HEPES pH 7.4 buffer. 80 μM FP–Hairpin in 20 mM sodium formate buffer pH 3 was added dropwise to the stirring vesicle solution while monitoring the pH. The pH of the protein – lipid vesicle solution was maintained near pH 7.0 with the addition of 25 or 100 mM HEPES pH 7.4 aliquots. After all the FP–Hairpin was added, the solution was allowed to stir at room temperature for 30 minutes before placement at 4 °C overnight. Protein – lipid complexes deposited on the bottom of the conical tube, which were centrifuged for 3 – 5 min at ~4,000g and 4 °C to pellet the complex. The supernatant was decanted and the protein – lipid pellet was lyophilized. Almost all solid state NMR samples were prepared following this method.

Method B

A lipid fraction was hydrated with 20 mM sodium formate buffer at pH 3 to a concentration of 10 mM and gently vortexed for ~15 minutes. The hydrated mixture was then subjected to 5 freeze – thaw cycles in liquid nitrogen before being extruded 19 times through a 200 nm pore. The lipid vesicles were diluted to 1.8 mM with 20 mM sodium formate pH 3 buffer. 200 μM FP–Hairpin in 20 mM sodium formate pH 3 was added dropwise to the stirring vesicle solution. The pH of the protein – lipid vesicle solution was maintained near pH 3.0. After all the FP–Hairpin was added, the solution was allowed to stir at room temperature for 30 minutes before placement at 4 °C overnight. Protein – lipid complexes deposited on the bottom of

the conical tube and then centrifuged for ~ 3 – 5 min at ~4,000g and 4 °C to pellet the complex. The supernatant was decanted and the protein – lipid pellet was lyophilized. Unbound FP–Hairpin will not pellet under these conditions since it is still soluble in the 20 mM sodium formate pH 3 buffer and can be separated from the protein – lipid complex that contains bound FP–Hairpin. The pH swap protocol was initially developed by Dr. Kelly Sackett.

Solid State NMR Sample Preparation

Dialyzed and refolded FP–Hairpin was quantified and then concentrated prior to addition to lipid vesicles. Sample preparation using Method A typically had FP–Hairpin at 80 µM in 20 mM sodium formate, pH 3 and 150 µM TCEP reducing agent and Method B had FP–Hairpin concentrated to 200 µM in the same buffer. After the protein – lipid complex was pelleted, lyophilization was used to remove excess water. The lyophilized pellet was placed in an 1.7 mL eppendorf tube and rehydrated with 30 – 50 µL of deionized water. The rehydrated pellet was mixed using the sealed end of a capillary tube until a homogenous mixture was achieved. The sample was frozen with liquid N_2, and transferred to the rotor via the capillary tube or spatula. Once on the open end of the 4 mm rotor, the sample was packed down into the rotor using the packing tool. During this time the sample would warm and become fluid. The sample and rotor were submerged into liquid N_2 to freeze the sample again. Once all the sample was packed in the central 2/3 of the rotor, the top spacer was added and the whole rotor was submerged in liquid N_2 to maintain a frozen state for the protein – lipid mixture. The sample was maintained at –20 °C until being transferred to the NMR.

Solid State Nuclear Magnetic Resonance Experiments and Experimental Details

^{13}C spectra were externally referenced to the methylene resonance of adamantane at 40.5 ppm in accordance with IUPAC standards.[35, 36] ^{15}N chemical shifts were indirectly referenced from referenced ^{13}C spectra using the ratio of the ^{13}C and ^{15}N gyromagnetic ratios.[36] Briefly, ^{15}N referencing requires knowledge of the base frequency (BF) of ^{13}C and ^{15}N along with the spectrum reference (SR) value for ^{13}C. First determine the BF_{13C} of the referenced ^{13}C experiment and then determine the BF_{15N} in the ^{15}N experiment. The BF_{13C} and the SR_{13C} values are used with Equation 2–1 to obtain the corrected ^{13}C frequency (V_{13C}). It is important to maintain the sign associated with the SR_{13C} value.

$$BF_{13C} + SR_{13C} = V_{13C} \quad (2–1)$$

$$V_{13C} * 0.402979946 = \mu_{15N} \quad (2–2)$$

$$\mu_{15N} – BF_{15N} = SR_{15N} \quad (2–3)$$

Equation 2–2 uses the ratio of gyromagnetic ratios of ^{13}C and ^{15}N ($\gamma_{15N}/\gamma_{13C}$) to get 0.402979946, which is multiplied by the V_{13C} to give you the corrected frequency for the ^{15}N spectrum, μ_{15N}.[36] Equation 2–3 is used to determine the SR value in MHz for the ^{15}N spectrum. Convert the SR_{15N} value from MHz to Hz by multiplying by 10^6.

Chemical shifts for referenced spectra were compared to the RefDB database which contains the average and standard deviation of chemical shifts as determined from ~309 entries from PDB files containing 3D coordinates.[37] Secondary structures from the PDB files were directly calculated using a computer program that used peptide geometry to determine the secondary structure assignment, allowing for residues to be classified as helices, β–strand, and "coil" regions.[37] Comparison of the database chemical shifts to the experimentally determined chemical shifts allowed for characterizing the secondary structure for the spectra as either helical or β–strand for the $^{13}C\alpha$, $^{13}C\beta$, ^{13}CO, and ^{15}N chemical shifts. NMR spectra were acquired on a 9.4 T (400 MHz ^{1}H frequency) spectrometer (Varian Infinity Plus, Agilent Technologies, Palo Alto, CA) using a 4 mm MAS probe in $^{1}H/^{13}C/^{15}N$ triple resonance configuration. High field data was acquired on a 21.1 T (900 MHz ^{1}H frequency) Bruker Advance spectrometer (Billerica, MA) equipped with a 4 mm MAS E–free probe in $^{1}H/^{13}C/^{15}N$ triple resonance configuration. A sample was sent to Dr. Jochem Struppe at Bruker BioSpin (Billerica, MA) for analysis on a 16.5 T (700 MHz ^{1}H frequency) Bruker Advance spectrometer. NMR frequencies were tuned to 400.8 MHz and 100.2 MHz for ^{1}H and ^{13}C on the 9.4 T instrument, 899.8 MHz, 226.3 MHz, and 91.2 MHz for ^{1}H, ^{13}C, and ^{15}N respectively for the 21.1 T instrument and 700.1 MHz and 175.0 MHz for ^{1}H and ^{13}C on the 16.5 T instrument.

Nominal cooling temperatures as measured at the thermocouple were –50 °C with the 9.4 T instrument and –23 °C for the high field instruments. The thermocouple was located about 1" away from rotor in the probe for the 9.4 T instrument and in the flow of the cooling gas.[38] The

thermocouple for the E-free probe design is located on the post supporting the stator and is directly in the path of the bearing and VT gas flow (Brian Andrew, Bruker Biospin Corp., personal communication). The thermocouple is therefore ~1" away from the rotor for the E–free probe used at 16.5 T and 21.1 T and in the flow of the cooling gas. Previous work from Bodner et al showed a threefold improvement in ^{13}C integrated area was obtained at –50°C sample temperatures when compared to 20°C.[39] The chemical shifts at –50°C were similar to those acquired at 20°C temperatures.[39]

All Bruker data and all 2D Varian SSNMR data were processed using the nmrDraw software unless otherwise stated.[40, 41]

The Rabi frequency is the frequency of population oscillations for a given atomic transition, such as from the spin up to the spin down state of a nuclei. The Rabi frequency is determined by Equation 2–4, where γ_H is the gyromagnetic ratio of proton, B_1^H is the B_1 field defined by Equation 2–5.[42]

$$\nu_r = \frac{\varpi_r}{2\pi} = \frac{\gamma_H B_1^H}{h} \tag{2–4}$$

The B_1^H field is determined from 4 times the 90° pulse length which generates a full 360° or 2π rotation of the magnetization from the pulse. The B_1^H field is the strength of the ^1H rf field.[42]

$$B_1^H \text{ field} = \frac{1}{4*\left(\frac{\pi}{2}\right)_{1H}} \tag{2–5}$$

where $(\pi/2)_{1H}$ is the 90° pulse in microseconds for a ^{1}H nucleus, but can be extended to any nucleus and 90° pulse. The Rabi frequency can be calculated for any nucleus using Equation 2–4, and will provide the frequency in units of hertz.

^{13}C CP Ramp

The ^{13}C cross polarization ramp experiment allows for acquiring both isotopically labeled and natural abundance signal from the protein and lipids in the sample. Figure 2–8 illustrates the ^{13}C CP pulse sequence at (A) 9.4 T or (B) 16.5 T and 21.1 T. The difference between the two pulse sequences is whether the ramp is applied on the ^{1}H or the ^{13}C channel during the cross polarization step. The Bruker pulse sequences have the ramp on the proton channel whereas the Varian (Agilent) has the ramp on the ^{13}C channel.

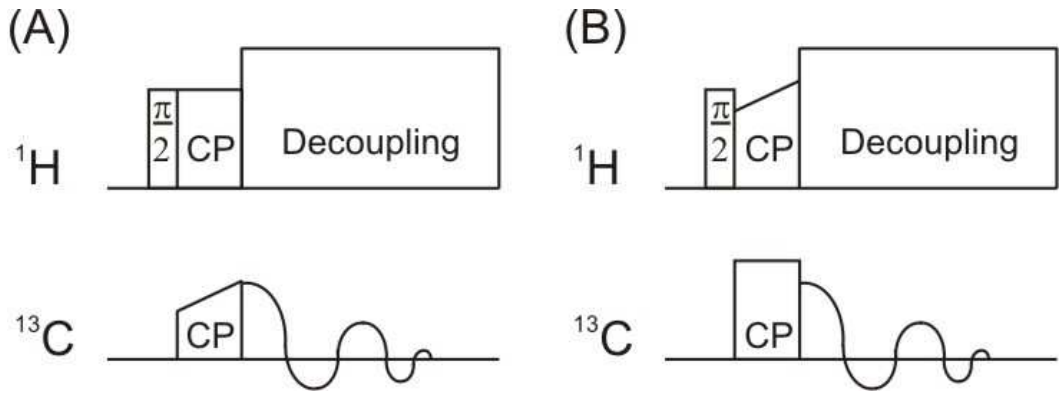

Figure 2–8: Pulse sequence for the ^{13}C cross polarization experiments performed at (A) 400 MHz NMR and (B) 700 and 900 MHz instruments. Transverse magnetization is prepared on the ^{1}H nuclei with a $\pi/2$ pulse, then transferred to ^{13}C nuclei via cross polarization followed by acquisition on the ^{13}C channel while decoupling the protons.

A $\pi/2$ pulse on the proton channel rotates the proton magnetization from the Z axis to the transverse plane, followed by a cross polarization matching condition using a ramp to transfer magnetization from the $^{1}H \rightarrow {}^{13}C$ nuclei followed by detection on the ^{13}C channel. Ramping the CP allows for matching the wide range of ^{13}C nuclei in the sample. This is due to the ^{13}CO carbons having a higher frequency than the $^{13}C\alpha$ and $^{13}C\beta$ carbons. Ramping the ^{13}C CP allows for establishing the various Hartman–Hahn conditions for the different ^{13}C which can then equally excite all the ^{13}C nuclei. Equation 2–6 is the Hartmann–Hahn condition which was previously presented and explained in Chapter 1 section "Magic Angle Spinning for SSNMR" subsection "Cross Polarization" with Equation 1–46.

$$\gamma_I \mathbf{B}_{1I} = \gamma_S \mathbf{B}_{1S} \tag{2–6}$$

By matching the conditions in Equation 2–6, the magnetization can be transferred from nucleus I to nucleus S to such as from ^{1}H to ^{13}C. The transmitter offset is where the center of the excitation pulse is located. For the proton and carbon channels the offsets were 5 ppm and 100 ppm respectively. Typical parameters for the ^{13}C CP experiment are similar to those used in the 2D ^{13}C–^{13}C correlation experiments discussed below.

Phase cycling was used in all solid state NMR experiments. Phase cycling is the process of acquiring data with different pulse and receiver phases, which are changed in a definitive way over a number of scans.[43] Phase cycling is used to suppress spectral artifacts, which when summed together will have differing phases that cancel each other out.[43] The phase cycling at 9.4 T was different than at 16.5 T and 21.1 T. The Agilent 9.4 T ^{13}C CP ramp had the following

phase cycling: ^{1}H π/2 pulse was x, –x; and the receiver phase cycling was: –x, x, y, –y. For the Bruker 16.5 T and the 21.1 T ^{13}C CP experiment, the ^{1}H π/2 pulse was y, –y and the receiver phase cycling was: x, –x, –x, x, y, –y, –y, y.

^{15}N CP Ramp

The ^{15}N CP ramp is similar to the ^{13}C CP ramp discussed above. The main difference is that cross polarization occurs between ^{1}H→ ^{15}N, and that the transmitter offset is located at ~110 ppm for ^{15}N and 8 ppm for ^{1}H for the amide proton, which is where the center of the excitation pulse is located. Figure 2–9 illustrates the pulse sequence for the ^{15}N CP experiment performed using the 21.1 T NMR.

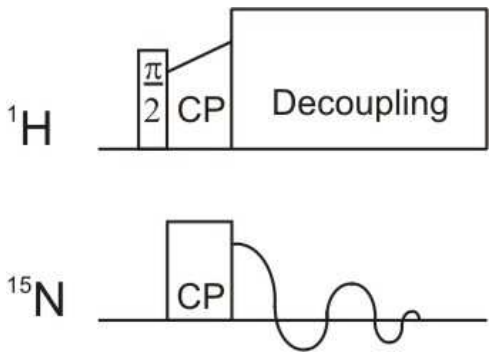

Figure 2–9: Pulse sequence for the ^{15}N cross polarization experiments performed with the 21.1 T spectrometer. Transverse magnetization is prepared on the ^{1}H nuclei with a π/2 pulse, then transferred to ^{15}N nuclei via cross polarization followed by acquisition on the ^{15}N channel while decoupling the protons.

A π/2 pulse on the proton channel rotates the proton magnetization from the Z axis to the transverse plane, followed by a cross polarization matching condition (Equation 2–6) using a ramp to transfer magnetization from the $^{1}H \rightarrow {}^{15}N$ nuclei and then detection on the ^{15}N channel. Ramping the CP allows for matching the wide range of ^{15}N nuclei in the sample as described previously for the ^{13}C CP Ramp. Table 2–5 lists the typical parameters for the 1D ^{15}N CP ramp experiment at 21.1 T. The phase cycling for the ^{15}N CP experiment was: ^{1}H π/2 pulse: y, –y; receiver phase cycling was: x, –x, –x, x, y, –y, –y, y.

Table 2–5: Typical parameters for the ^{15}N cross polarization experiment at 21.1 T

Parameter	Parameter Name	21.1 T Value
$\pi/2$ pulse ^{1}H	P3	4. 66 μs
$\pi/2$ power level ^{1}H	PL12	2 dB (53.6 kHz)
^{1}H CP condition	PL2	–0.8 dB (74.0 kHz)
^{15}N CP condition	PL1	0.40 dB (64.5 kHz)
^{1}H decoupling	PL12	53.6 kHz
CP time	P15	2.2 ms
Acquisition time	AQ	12.8 ms
Temperature	–	250 K
MAS frequency	cnst31	12 kHz
Recycle delay	D1	3 s
^{15}N offset location	O1P	110 ppm
^{1}H transmitter offset	O2P	6 – 7 ppm
Dwell time	DW	12.5 μs

1D NCA / NCO Selective filtering

Figure 2–10 illustrates the pulse sequence for the one dimensional $^{1}H \rightarrow ^{15}N \rightarrow ^{13}C$ double cross polarization (DCP) experiment.[44] For the NCA experiment the ^{13}C transmitter is set to ~50 ppm which is near the $^{13}C\alpha$ / $^{13}C\beta$ region of the spectrum. Magnetization is selectively transferred from the $^{15}N \rightarrow ^{13}C\alpha$ nuclei using Rabi frequencies of ~35 – 50 kHz. The Hartmann–Hahn match from Equation 2–6 between the fields of the ^{15}N and the $^{13}C\alpha$ nuclei will result in the transfer of the polarization preferentially between the $^{15}N \rightarrow ^{13}C\alpha$ nuclei compared to the

$^{15}N \rightarrow {}^{13}CO$ nuclei with the 35 – 50 kHz frequency through dipole – dipole interactions. Under the matching of the Hartmann–Hahn conditions and the selected Rabi frequency, the $^{15}N–{}^{13}C\alpha$ is well matched whereas the $^{15}N–{}^{13}CO$ frequencies are not well matched, as can be visually observed in Figure 2–11. Figure 2–11 shows that the 30 kHz frequency (± 15 kHz from the transmitter) centered on 50 ppm for the NCA experiment does not extend to the ^{13}CO region. The ^{13}CO to $^{13}C\alpha$ chemical shifts are ~30 kHz, which is approximately double the transfer frequency of the NCA experiment. Figure 2–11 illustrates the resonance offset of the spectrum along with an illustration of how the pulse length affects the spectrum. Equation 2–7 defines the total spectral frequency (ω), ω_0 is the Larmor frequency, and $\omega_{CS}(\theta,\phi)$ is the chemical shift frequency in spherical coordinates.

$$\varpi = \varpi_0 + \varpi_{CS}(\theta,\phi) \tag{2–7}$$

Selective transfer of magnetization from the $^{15}N–{}^{13}C\alpha$ thus occurs due to the frequency overlap. The NCO experiment has the ^{13}C transmitter set to ~165 ppm and magnetization is selectively transferred from the $^{15}N \rightarrow {}^{13}CO$ nuclei using the same principles as discussed for the NCA experiment. This time, the frequency overlap between the $^{15}N–{}^{13}CO$ is well matched resulting in selective transfer from the $^{15}N \rightarrow {}^{13}CO$ and the $^{15}N \rightarrow {}^{13}C\alpha$ condition is not sufficiently matched due to the large frequency difference between the ^{13}CO and $^{13}C\alpha$ nuclei, which is ~30 kHz at 21.1 T.

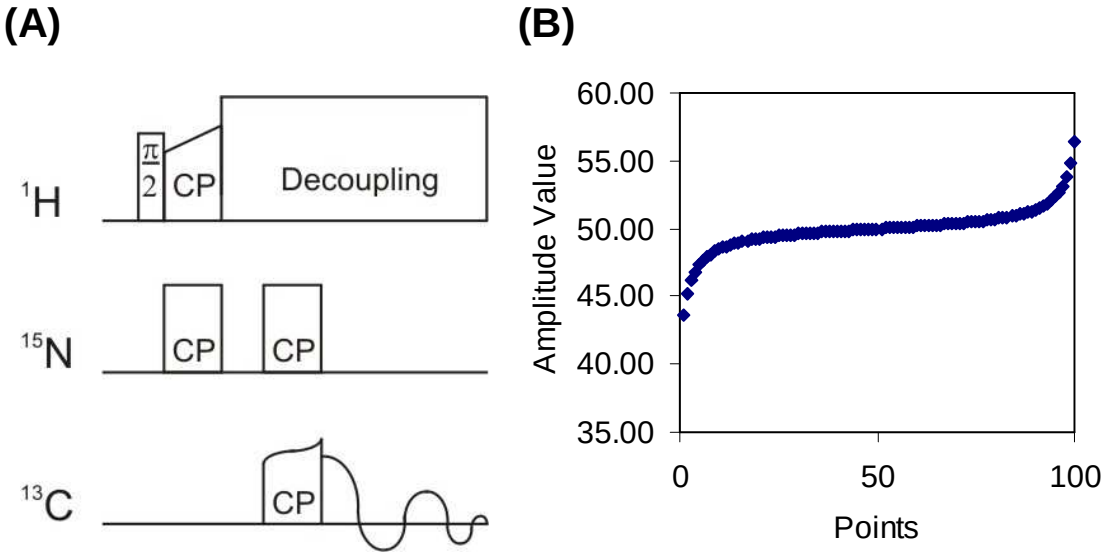

Figure 2–10: (A) Pulse sequence for the one dimensional double cross polarization (DCP) experiment. Transverse magnetization is prepared on the ^{1}H channel, then transferred to the ^{15}N nuclei via cross polarization. The magnetization is then selectively transferred to the nearby ^{13}C nuclei via the second cross polarization step and the signal is detected on the ^{13}C channel. For the $^{1}H \rightarrow {}^{15}N \rightarrow {}^{13}C\alpha$ experiment, the ^{13}C transmitter is set to ~50 ppm. For the $^{1}H \rightarrow {}^{15}N \rightarrow {}^{13}CO$ experiment, the ^{13}C transmitter is set to ~165 ppm. A short delay of 1 μs occurs between the ^{1}H–^{15}N and ^{15}N – ^{13}C cross polarization steps. For the 2D heteronuclear correlation experiment, this delay corresponding to the t_1 value and will be incremented between slices. (B) Illustrated tangent ramp for cross polarization between the ^{15}N–^{13}C nuclei.

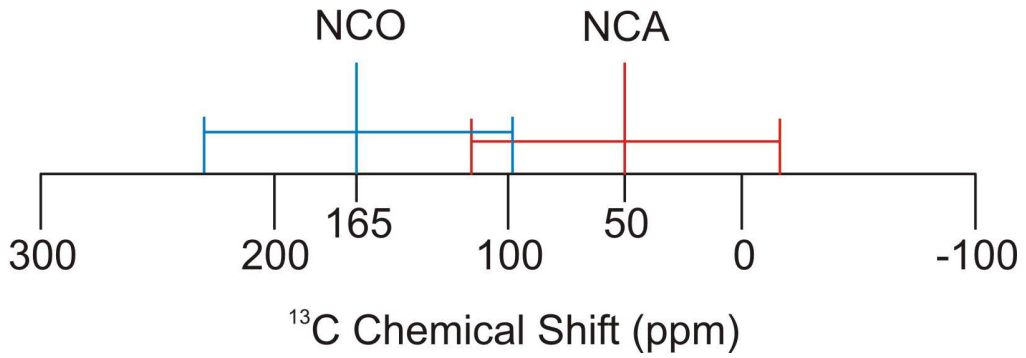

Figure 2–11: Illustration of the ^{13}C scale, and affect at 900 MHz for the NCA / NCO experiments. The transmitter location for the NCA and NCO experiment are marked by the red and blue spike at 50 and 165 ppm respectively. The pulse in both experiments generates a 30 kHz frequency range, which is centered on either 50 ppm (NCA) or 165 ppm (NCO) experiment. The pulse centered will excite equally on both sides of the transmitter location 15 kHz. For the NCA experiment at 900 MHz, the chemical shift range will be from ~116 ppm to –16 ppm. For the NCO experiment, the chemical shift range will be from ~231 ppm to 99 ppm. The total ^{13}C frequency range (0 to 200 ppm) is 45 kHz. As is shown above, there is minor overlap at the edge of the NCA / NCO experiment, however that overlap region does not contain signals of interest to these experiments. The total separation between the 50 ppm and the 165 ppm transmitter is ~26 kHz.

The 1D NCA and NCO experiments are selective filtering experiments as the magnetization transfer conditions are matched to the specific nuclei of interest. The matching conditions for the NCA experiment are setup so that the $^{13}C\alpha$ will be matched to the ^{15}N and not other ^{13}C in the sample using Equation 2–6. For the NCO experiment, the ^{15}N nuclei are matched to the ^{13}CO nuclei and not other ^{13}C nuclei in the sample using Equation 2–6.

The magnetization is first prepared from the optimized ^{15}N CP conditions, allowing for transfer of magnetization from the proton to the ^{15}N nuclei. For the NCA experiment, the magnetization is selectively transferred from the ^{15}N nuclei to directly bonded ^{13}Cα using a shaped ramp (Figure 2–10B) which filters out all other ^{13}C signal from natural abundance or from isotopic labels. This is accomplished by setting the ^{13}C offset near the resonance of the ^{13}Cα nuclei, ~50 ppm. For the NCO experiment, magnetization is transferred from a ^{15}N nuclei to the directly bonded ^{13}CO nuclei, which is accomplished by setting the ^{13}C offset to ~165 ppm, see Figure 2–11. The 1D NCA experiment has worked quite well on protein samples, as will be highlighted in Chapter 4, whereas the NCO experiment has only worked on the setup sample U–NAL, which will be discussed further in Chapter 4. Typical parameters include are listed in Table 2–6. Figure 2–10B illustrates the tangent ramp (tan_CN.100) used for the ^{15}N–^{13}C cross polarization step. The ramp is composed of 100 steps varying the amplitude, which starts at ~43.57 and ends at ~56.42. The step time will vary depending on the ^{15}N – ^{13}C contact time, P16. For the NCA experiment the time between steps is ~46 μs and ~47 μs for the NCO experiment based on the parameters listed in Table 2–6. The phase cycling for the 1D NCA / NCO double cross polarization experiments were: ^{1}H π/2 pulse: y, –y; and the receiver phase cycling was: x, –y, –x, y, –x, y, x, –y.

Table 2–6: Typical parameters for the 1D NCA or NCO double cross polarization experiment using Bruker's Topspin notation.

Parameter	Parameter Name	NCA Experiment	NCO Experiment
P3	^{1}H $\pi/2$	3 μs	3 μs
P15	^{1}H→^{15}N contact time	2 ms	4.2 ms
PL12	^{1}H decoupling	–2.2 dB (83.3 kHz)	–2.2 dB (83.3 kHz)
O2P	^{1}H offset	7 ppm	7 ppm
O3P	^{15}N offset	110 ppm	110 ppm
O1P	^{13}C offset	50 ppm	165 ppm
P16	^{13}C→^{15}N contact time	4.6 ms	4.7 ms
–	AQ length	15 ms	15 ms
PL2 PL3	Pow level ^{1}H–^{15}N	–0.6 dB (69.3 kHz) ^{1}H 2.0 dB (45.8 kHz) ^{15}N	–0.7 dB (70.1 kHz) ^{1}H 2.0 dB (45.8 kHz) ^{15}N
PL5 PL1	Pow level ^{15}N–^{13}C	4.6 dB (38.0 kHz) ^{15}N 3.0 dB (45.8 kHz) ^{13}C	4.8 dB (37.2 kHz) ^{15}N 3.0 dB (45.8 kHz) ^{13}C
spnam1	Tangent ramp	Tan_CN.100	Tan_CN.100
D1	Recycle Delay	3 s	3 s
DW	Dwell Time	7.350 μs	7.350 μs
TD	Time Domain points	2048	2048

2D ^{13}C–^{13}C PDSD and DARR Experiments

The 2D ^{13}C–^{13}C correlation experiment allows for the observation of magnetization exchange between the spin states of nuclei. The basis of the 2D ^{13}C–^{13}C experiment is that after the magnetization is first cross polarized from the $^{1}H \rightarrow {}^{13}C$ nuclei in the transverse plane followed by a $\pi/2$ ^{13}C pulse to rotate the ^{13}C magnetization to the longitudinal axis. The ^{13}C magnetization will then mix between the different ^{13}C nuclei via dipole – dipole interactions. Finally the ^{13}C magnetization will be rotated back to the transverse plane for detection by a ^{13}C $\pi/2$ pulse.

During the mixing period, the spin states of α and β for the two nuclei will then under go flip flop at the same time to conserve the net magnetization, and will in the process be exchanging the magnetization between different nuclei, as shown in Figure 2–12. The resulting exchange in the magnetization from $\alpha \rightarrow \beta$ or $\beta \rightarrow \alpha$ will result in an off diagonal cross peak defined by (f_2, f_1) which corresponds to the exchange between the two nuclei. The diagonal cross peaks are the result of the magnetization starting and ending on the same nuclei, or rather the nuclei only interacting with itself. The off diagonal cross peaks are observed when the magnetization which started on one nuclei is transferred to a different nuclei during the mixing time. The off diagonal cross peaks are the result of transfer of the magnetization through the ^{13}C spin network via spin diffusion, which occurs with the ^{13}C–^{13}C dipole couplings.[45] Changing of both states at the same time for the two spins results in the oscillation of the magnetization between the two spins, resulting in the off diagonal cross peaks.[45]

The ^{13}C spin diffusion rate is dependant on the concentration of the ^{13}C label in the sample.[46] In proton driven spin diffusion (PDSD), the protons drive the ^{13}C diffusion during the exchange time.[46] Natural spin diffusion without ^{1}H decoupling during mixing time allows the ^{1}H–^{13}C dipolar couplings the ability to produce a resonance shift that cancels the chemical shift difference ($\omega_A - \omega_B$) making ^{13}C spin diffusion possible.

Equation 2–8 is the transition probability for two spins going from the α to the β state.[46]

$$P_{if}(t) = \frac{1}{2}\pi\left(g_0^{AB}\right)\left(\omega_A - \omega_B\right)\omega_D^2 t \qquad (2\text{–}8)$$

In Equation 2–8, ($\omega_A - \omega_B$) is the chemical shift difference between the two ^{13}C nuclei, ω_D is the dipolar coupling between the two spins, A and B. For the 2D ^{13}C–^{13}C experiments, ω_D will be the ^{13}C–^{13}C dipolar coupling. The g_0^{AB} term is the cross correlation function, and is related to the line shape and is determined by the ^{1}H–^{13}C couplings.[46] The $g_0^{AB}(\omega_A - \omega_B)$ function is the bottleneck of spin diffusion process as it is a fixed area.[46] The cross correlation function having a fixed area results in the following issue: (i) If the function is to have a broad width, then the intensity will need to be small. (ii) If the intensity is to be maximal, then the width will be minimal. For a large chemical shift difference of ($\omega_A - \omega_B$) a broad difference of the cross correlation function will be needed, however this will result in a small intensity for the cross correlation function. Condition (ii) with a small chemical shift difference will result in allowing the cross correlation function to be narrower and more intense.

Figure 2–12A illustrates the process of spin diffusion between spin up and spin down states. Figure 2–12B illustrates a simplistic 2D spectrum where the lines represent spins and the circles in the 2D plot represent the interaction between the two spins.

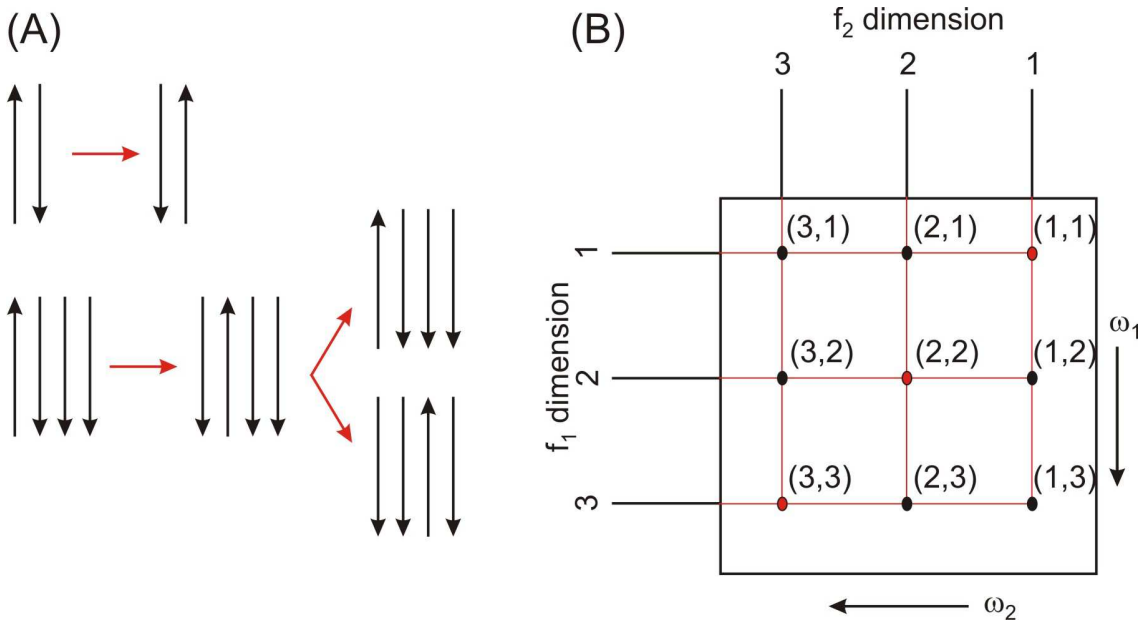

Figure 2–12: (A) Graphical representation of spin diffusion. In the two state system, the spin up and spin down will change to the spin down and spin up configuration at the same time resulting the conservation of the total net magnetization. In the second example with four spins, after the first step the spin diffusion has two options of which way to continue with the spin diffusion process. (B) Explanation of the 2D cross peaks, listed in the convention of (f_2, f_1). Red circles are the diagonal cross peaks, which are merely the spin interacting with itself. The valuable information is obtained from the off diagonal cross peaks which are different spins exchanging their magnetization with each other, resulting in the off diagonal cross peaks. For example, (2,3) results in the magnetization initially residing on nucleus 3 prior to the mixing time period. During the mixing time, spin diffusion occurs, resulting in the exchange of magnetization with the nearby nuclei of spin 2, and establishing the (2,3) cross peak. The magnetization is exchanged via dipolar couplings.[45]

Two variants of this pulse sequence are the proton driven spin diffusion (PDSD) experiment [47] and the dipolar assisted rotational resonance (DARR) experiment [48, 49] which is also known as radiofrequency–assisted diffusion (RAD) [50]. During the mixing period in the PDSD experiment no ^{1}H radio frequency (rf) is applied, whereas in the DARR/RAD experiment there is a low frequency ^{1}H rf field applied which is equal to the spinning frequency. The ^{1}H–^{13}C dipolar couplings can produce a resonance shift that cancels the chemical shift difference ($\omega_A - \omega_B$) and thus makes ^{13}C spin diffusion possible.[46]

Spin diffusion is a process by which magnetization is transferred from one nucleus to a second nucleus via dipolar coupling. The 2D ^{13}C–^{13}C experiments will mix the magnetization between nearby ^{13}C nuclei. In the PDSD experiment, the magnetization exchange is mediated by the ^{1}H–^{13}C dipolar couplings, during the ^{13}C–^{13}C mixing time. These experiments are done under MAS with spinning frequencies of 8 – 12 kHz. The MAS spinning will introduce a time dependence into the Hamiltonian, which will average out some of the dipolar interactions.[51] MAS spinning at these frequencies is not sufficient to fully average out the ^{13}C–^{13}C, ^{1}H–^{13}C, and ^{1}H–^{1}H dipolar couplings which are ~20 kHz, ~20 – 30 kHz, and 50 – 100 kHz respectively.[42, 46, 52] The residual ^{13}C dipolar coupling will result in the spin diffusion of the ^{13}C magnetization to other ^{13}C nuclei during the mixing period, resulting in the off diagonal ^{13}C cross peaks in a 2D spectrum.

Under PDSD, the ^{13}C spin diffusion is a slow process due to the dilute concentration of the ^{13}C spins. One way to speed up the spin diffusion process is to apply ^{1}H rf equal to the spinning frequency of the MAS rotor. Techniques that apply this are the DARR and RAD experiments. The incorporation of the rf frequencies during mixing will result in reintroducing the ^{1}H–^{13}C dipolar coupling, enhancing the spin diffusion process. By applying the ^{1}H rf the ^{13}C linewidths will be broadened from the ^{1}H–^{13}C dipolar couplings, resulting in more overlap of the ^{13}C resonances during the mixing period of the rotor cycle. When the two ^{13}C spins are at resonance, the transfer of magnetization can occur, as shown in Figure 2–14. During the ^{13}C exchange time, the magnetization will be exchanged between neighboring ^{13}C nuclei via dipole – dipole interactions.

Reintroducing the ^{1}H–^{1}H interaction results in a homogenous broadening of the ^{13}C resonances by both the ^{1}H–^{13}C and the ^{1}H–^{1}H interactions during the mixing time period.[48] Broadening the ^{13}C resonances will allow for more overlap between the ^{13}C spins during the exchange time, resulting in greater exchange of magnetization between directly bonded ^{13}C spins (50 ms mixing time) and through space ^{13}C spins (500 ms mixing time). Figure 2–14 depicts the variation of the ^{13}C frequencies during a rotor period for the exchange of magnetization between two nuclei in the mixing time. The condition for exchange between the two nuclei via dipolar couplings are that the two spins are at resonance with each other, as is depicted in Figures 2–14B to 2–14D. Broadening of the ^{13}C resonances results in more overlap

of the two chemical shifts during the rotor period, which will result in more magnetization which can transfer between the two nuclei. The two nuclei need to be in resonance in order for the transfer of magnetization to occur.

Due to spinning frequencies of 10 – 12 kHz for these samples, it is possible to apply the low frequency ^{1}H rf for long periods of time without damaging the probe. The PDSD pulse sequence is shown in Figure 2–13A and the DARR pulse sequence is shown in Figure 2–13B. There are four main parts to this experiment: (1) preparation, (2) evolution, (3) mixing, and (4) detection.

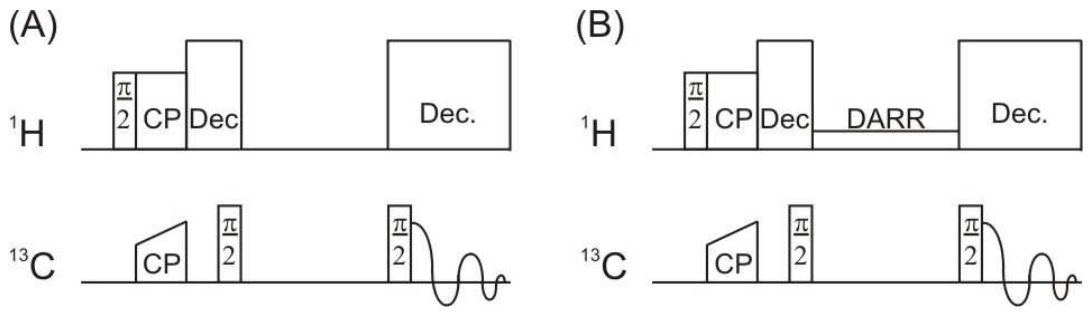

Figure 2–13: Pulse sequence for the 2D ^{13}C – ^{13}C experiments. (A) 2D proton driven spin diffusion (PDSD) experiment and (B) the dipolar assisted rotation resonance (DARR) experiment. Transverse magnetization is prepared on the ^{1}H nuclei and rotated with a $\pi/2$ pulse from the Z–axis to the X–Y plane, then transferred to ^{13}C nuclei via cross polarization. The ^{13}C $\pi/2$ pulse rotates the magnetization from the X–Y plane to the –Z axis, followed by a mixing period of either 50 or 500 ms. After the mixing period the ^{13}C magnetization is rotated back to the X–Y plane by a ^{13}C $\pi/2$ pulse followed by acquisition on the ^{13}C channel while high power decoupling is applied on the ^{1}H channel.

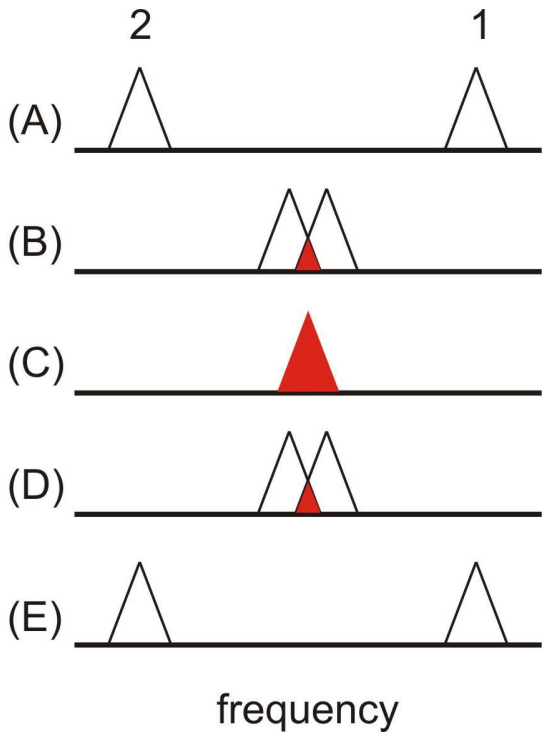

Figure 2–14: Illustration of the exchange of magnetization during the mixing time period for the 2D ^{13}C–^{13}C exchange experiments. (A) Spins 1 and 2 are separated by a frequency of $(\omega_2 - \omega_1)$ at the start of the rotor period. (B) During the rotation of the rotor period, the spins are closer in frequency, resulting in the overlap of the two spins as highlighted by the red triangle. (C) Both spins are in resonance with each other, resulting in maximum overlap of their resonance frequencies and ensuring maximum exchange of the magnetization. (D) As the rotor period continues, the spins now start to move off resonance with each other, diminishing the overlap between them until finally (E) the two spins are back to their starting point condition. Broad lines ensure maximum overlap between the two spins whereas narrow lines will result in less time for the two spins to be in resonance, reducing the transfer of magnetization between the spin system.

Optimal conditions for the ^{13}C CP Ramp experiment are used to setup the 2D experiment. The magnetization is first prepared on the protons by applying a $\pi/2$ pulse which rotates the magnetization from the Z axis to the transverse plane. Next, a cross polarization from the proton to the ^{13}C nuclei occurs. Magnetization on the ^{13}C nuclei in the transverse plane is

rotated to the longitudinal axis by a ^{13}C $\pi/2$ pulse and the magnetization is allowed to exchange with the neighboring ^{13}C nuclei during the mixing time τ. After mixing, a ^{13}C $\pi/2$ pulse rotates the magnetization back to the transverse plane and the ^{13}C signal is acquired. As seen in Figure 2–13, high power decoupling is applied on the proton channel after CP from $^{1}H \rightarrow {}^{13}C$ and during acquisition of the signal, but is not applied during the mixing period. High power decoupling is a simple technique used to remove the ^{1}H–^{13}C dipolar broadening, which is ~20 kHz.[45, 53] All optimized parameters for the PDSD experiment are from the ^{13}C CP experiment. The DARR experiment requires optimizing the ^{1}H rf field during mixing as the only additional step.

The direct dimension is the ^{13}C signal that is detected after mixing and the indirect dimension is acquired by incrementing the t_1 evolution time located between the CP step and the first ^{13}C $\pi/2$. Typically 256 or 300 increments (t_1 points) were acquired on the Bruker and Varian instruments respectively. Short mixing times of 50 ms were used to establish the intra–residue connectivity and long mixing times of 500 ms or 1 s where used to probe the inter–residue connectivities and tertiary structure up to ~7 Å in distance.[54]

Typical parameters are listed in Table 2–7 for the 2D ^{13}C–^{13}C experiments. The initial t_1 value was 0 μs and the increment was either 25 μs, 27.7 μs, or 17.7 μs for the 9.4 T, 16.5 T, and 21.1 T experiments respectively. The t_1 of 25 μs results in a spectral width of 40 kHz at 9.4 T. The t_1 of 27.7 μs for the 16.5 T resulted in a sweep width of 36.0 kHz. The t_1 of 17.7 μs for the

21.1 T resulted in a sweep width of ~56.5 kHz. The t_1 values at 16.5 T and 21.1 T were not the same as the t_1 value at 9.4 T due to the frequency range that needed to be excited. At 9.4 T, the t_1 of 25 μs results in a spectral width of 40 kHz (~400 ppm). At 16.5 T or 21.1 T, the same t_1 value produces a spectral width of 40 kHz but the chemical shift range corresponds to ~227 ppm or ~176 ppm, respectively. As the ^{13}C chemical shift range covers ~200 ppm, the t_1 incremental value needs to be adjusted to produce a spectral width which would completely cover this range. If the spectral width does not fully cover the ^{13}C chemical shift range, then folding over of the spectral window can occur resulting in overlap of the peaks or peaks appearing at unexpected chemical shifts.

The phase cycling for the 9.4 T was different from the 16.5 T and 21.1 T spectrometers. The 9.4 T phase cycling was: ^{1}H π/2 pulse: x; first ^{13}C π/2 pulse: x, –x; second ^{13}C π/2 pulse: x, x, y, y, –x, –x, –y, –y; and the receiver phase cycling was: x, –x, y, –y, –x, x, –y, y. For the DARR experiments, the ^{1}H decoupling was the y phase. The 16.5 T and the 21.1 T experiments had the following phase cycling: ^{1}H π/2 pulse: y, –y; first ^{13}C π/2 pulse: x, x, x, x, x, x, x, x, –x, –x, –x, –x, –x, –x, –x, –x; second ^{13}C π/2 pulse: x, x, –x, –x, y, y, –y, –y; and the receiver phase cycling was: x, –x, –x, x, y, –y, –y, y, –x, x, x, –x, –y, y, y, –y. For the DARR experiments the ^{1}H decoupling was the x phase.

Table 2–7: Typical parameters for the 2D ^{13}C–^{13}C experiments at either 9.4 T, 16.5 T, or 21.1 T.

Parameter [a]	**Parameter Name**	**9.4 T**	**16.5 T**	**21.1 T**
pw90H ; P3	^{1}H $\pi/2$	3.88 or 5.0 μs	2.5 μs	3.0 or 3.25 μs
ct ; P15	CP contact time	1.5 or 2.6 ms	2 ms	2 ms
aHdec ; PL12	^{1}H decouple	85 kHz	100 kHz	83.3 kHz
pw90X ; PL11	^{13}C $\pi/2$	4.7 or 5.0 μs	4.0 μs	4.0 or 5.0 μs
tau ; L10	Mixing time	50 & 500 ms	50 ms	50 & 500 ms
aqtm ; AQ	AQ time	20.48 ms	19.67 ms	9.06 ms
ampmin, ampmax ; PL1	CP ramp conditions ^{13}C	43.7 – 58.3 kHz	–	–
aHcp ; PL2	CP ramp condition ^{1}H	–	80 – 100 kHz	66.7 – 83.3 kHz
SW ; SWH	Sweep width	40 kHz	36 kHz	56.5 kHz
DW2 ; IN_F	t_1 increment	25 μs	27.7 μs	17.7 μs
PD ; D1	Recycle delay	1 s	1.5 s	1.5 s
temp ; –	Temperature	–50 °C	–23 °C	–23 °C
speed ; cnst31	MAS	10 kHz	12 kHz	12 kHz
– ; TD	t_1 points	300	256	256
NA ; NS	ns / t_1	256	128	64
aHdspin ; PL14	DARR frequency	10 or 12 kHz	0 kHz	12 kHz

a = Parameter name for Varian is listed first and the Bruker parameter is listed second. They are separated by the semi–colon.

Conclusions

The significant results from this chapter are (1) creation of two gp41 constructs; and (2) characterization of the two gp41 constructs. The gp41 construct of Hairpin is now easily expressed and purified by RP–HPLC resulting in yields of ~50 mg pure protein / liter of expression. Efficiency of the native chemical ligation to produce the FP–Hairpin was increased 4–fold by switching to the MPAA catalyst. Test ligations to determine the optimal conditions for the NCL reaction were preformed resulting in determining that the reaction reaches equilibrium within 48 hrs at room temperature. From the combined optimization of Hairpin and FP–Hairpin, sample preparation for SSNMR analysis was significantly reduced from 2 months to 2 weeks.

Gel electrophoresis of Hairpin and FP–Hairpin constructs in Figure 2–3 show clean monomer molecular weights for the Hairpin and FP–Hairpin constructs. A clear gel shift is observed between the two constructs, and estimates of 95% purity are concluded from the gel. CD spectroscopy was used to determine the overall secondary structure of Hairpin and FP–Hairpin in Figure 2–7A, which showed that in formate buffer Hairpin is nearly 100% helical, consistent with SHB formation. FP–Hairpin has reduced helicity, which is consistent with the addition of the FP region that can adopt a β–strand/sheet conformation, thus lowering the overall helicity of protein. CD spectroscopy was used to confirm that the FP–Hairpin protein had been refolded after HPLC purification. Thermal melts of Hairpin and FP–Hairpin are presented in Figure 2–7B by monitoring the λ = 222 nm wavelength indicated that neither gp41 construct undergo a thermal transition below 100 $^{\circ}$C. Differential scanning calorimetry of the two constructs was employed to determine the T_m's of the two constructs, which were 111 $^{\circ}$C and

112 °C for FP–Hairpin and Hairpin respectively.[5] Both of these proteins show thermal stability consistent with other gp41 constructs listed in Table 2–4.

Finally, this chapter highlights the background work that was required for the project just to make one SSNMR sample. None of the work presented in Chapters 3 or 4 could have been accomplished without the significant investment in optimization of the sample production. Not only was time saved by performing optimizations of expression, purification, and the ligation but money was also saved. Money savings were obtained from the reduced loss of isotopically labeled FP23(linker) along with solvent for the RP–HPLC purifications of Hairpin and FP–Hairpin.

REFERENCES

References

1. Harris, R.B. and I.B. Wilson, *Tert–Butyl Aminocarbonate (Tert–Butyloxycarbonyloxyamine) – a New Acylating Reagent for Amines.* International Journal of Peptide and Protein Research, 1984. **23**(1): p. 55–60.

2. Sackett, K., et al., *Hairpin folding of HIV gp41 abrogates lipid mixing function at physiologic pH and inhibits lipid mixing by exposed gp41 constructs.* Biochemistry, 2009. **48**(12): p. 2714–22.

3. Schmick, S.D. and D.P. Weliky, *Major Antiparallel and Minor Parallel beta Sheet Populations Detected in the Membrane–Associated Human Immunodeficiency Virus Fusion Peptide.* Biochemistry, 2010. **49**(50): p. 10623–10635.

4. Merrifield, R.B., L.D. Vizioli, and H.G. Boman, *Synthesis of the antibacterial peptide cecropin A (1–33).* Biochemistry, 1982. **21**(20): p. 5020–5031.

5. Sackett, K., et al., *Comparative analysis of membrane–associated fusion peptide secondary structure and lipid mixing function of HIV gp41 constructs that model the early pre–hairpin intermediate and final hairpin conformations.* J Mol Biol, 2010. **397**(1): p. 301–15.

6. Curtis–Fisk, J., R.M. Spencer, and D.P. Weliky, *Isotopically labeled expression in E. coli, purification, and refolding of the full ectodomain of the influenza virus membrane fusion protein.* Protein Expr Purif, 2008. **61**(2): p. 212–9.

7. Dawson, P.E., et al., *Synthesis of proteins by native chemical ligation.* Science, 1994. **266**(5186): p. 776–9.

8. Dawson, P.E. and S.B.H. Kent, *Synthesis of native proteins by chemical ligation.* Annual Review of Biochemistry, 2000. **69**: p. 923–960.

9. Macmillan, D., *Evolving strategies for protein synthesis converge on native chemical ligation.* Angewandte Chemie–International Edition, 2006. **45**(46): p. 7668–7672.

10. Johnson, E.C. and S.B. Kent, *Insights into the mechanism and catalysis of the native chemical ligation reaction.* J Am Chem Soc, 2006. **128**(20): p. 6640–6.

11. Canne, L.E., S.J. Bark, and S.B.H. Kent, *Extending the applicability of native chemical ligation.* Journal Of The American Chemical Society, 1996. **118**(25): p. 5891–5896.

12. Hackeng, T.M., J.H. Griffin, and P.E. Dawson, *Protein synthesis by native chemical ligation: expanded scope by using straightforward methodology.* Proc Natl Acad Sci U S A, 1999. **96**(18): p. 10068–73.

13. David, R., M.P. Richter, and A.G. Beck–Sickinger, *Expressed protein ligation. Method and applications.* Eur J Biochem, 2004. **271**(4): p. 663–77.

14. Muralidharan, V. and T.W. Muir, *Protein ligation: an enabling technology for the biophysical analysis of proteins.* Nat Methods, 2006. **3**(6): p. 429–38.

15. Raz, R. and J. Rademann, *Fmoc–Based Synthesis of Peptide Thioesters for Native Chemical Ligation Employing a tert–Butyl Thiol Linker.* Organic Letters, 2011. **13**(7): p. 1606–1609.

16. Zheng, J.–S., et al., *Fmoc Synthesis of Peptide Thioesters without Post–Chain–Assembly Manipulation.* Journal of the American Chemical Society, 2011. **133**(29): p. 11080–11083.

17. Dawson, P.E., et al., *Modulation of reactivity in native chemical ligation through the use of thiol additives.* Journal Of The American Chemical Society, 1997. **119**(19): p. 4325–4329.

18. Sackett, K., Y. Wexler–Cohen, and Y. Shai, *Characterization of the HIV N–terminal fusion peptide–containing region in context of key gp41 fusion conformations.* J. Biol. Chem., 2006. **281**(31): p. 21755–21762.

19. Thermo Scientific Pierce. *TCEP–HCl*. 2011 [cited 2011 12 September 2011]; information on the use of TCEP]. Available from: http://www.piercenet.com/products/browse.cfm?fldID=02051012.

20. Sackett, K., A. TerBush, and D.P. Weliky, *HIV gp41 six–helix bundle constructs induce rapid vesicle fusion at pH 3.5 and little fusion at pH 7.0: understanding pH dependence of protein aggregation, membrane binding, and electrostatics, and implications for HIV–host cell fusion.* European Biophysics Journal with Biophysics Letters, 2011. **40**(4): p. 489–502.

21. Greenfield, N. and G.D. Fasman, *Computer Circular Dichroism Spectra for Evaluation of Protein Conformation.* Biochemistry, 1969. **8**(10): p. 4108–&.

22. Chen, Y.H., J.T. Yang, and K.H. Chau, *Determination of the helix and beta form of proteins in aqueous solution by circular dichroism.* Biochemistry, 1974. **13**(16): p. 3350–9.

23. Weissenhorn, W., et al., *Atomic structure of the ectodomain from HIV–1 gp41*. Nature, 1997. **387**(6631): p. 426–30.

24. Chan, D.C., et al., *Core structure of gp41 from the HIV envelope glycoprotein.* Cell, 1997. **89**(2): p. 263–273.

25. Tan, K., et al., *Atomic structure of a thermostable subdomain of HIV–1 gp41*. Proc. Natl. Acad. Sci. U. S. A., 1997. **94**(23): p. 12303–12308.

26. Buzon, V., et al., *Crystal Structure of HIV–1 gp41 Including Both Fusion Peptide and Membrane Proximal External Regions.* PLoS Pathogens, 2010. **6**(5): p. e1000880.

27. Shi, W., et al., *Structural characterization of HIV gp41 with the membrane–proximal external region.* J Biol Chem, 2010. **285**(31): p. 24290–8.

28. Lu, M., S.C. Blacklow, and P.S. Kim, *A trimeric structural domain of the HIV–1 transmembrane glycoprotein.* Nat Struct Biol, 1995. **2**(12): p. 1075–82.

29. Jacobs, A., C. Simon, and M. Caffrey, *Thermostability of the HIV gp41 wild–type and loop mutations.* Protein Pept Lett, 2006. **13**(5): p. 477–480.

30. Krell, T., et al., *HIV–1 gp41 and gp160 are hyperthermostable proteins in a mesophilic environment – Characterization of gp41 mutants.* European Journal of Biochemistry, 2004. **271**(8): p. 1566–1579.

31. Lev, N., et al., *Conformational Stability and Membrane Interaction of the Full–Length Ectodomain of HIV–1 gp41: Implication for Mode of Action.* Biochemistry, 2009. **48**(14): p. 3166–3175.

32. Yang, J., C.M. Gabrys, and D.P. Weliky, *Solid–state nuclear magnetic resonance evidence for an extended beta strand conformation of the membrane–bound HIV–1 fusion peptide.* Biochemistry, 2001. **40**(27): p. 8126–37.

33. Hope, M.J., et al., *Production of Large Unilamellar Vesicles by a Rapid Extrusion Procedure – Characterization of Size Distribution, Trapped Volume and Ability to Maintain a Membrane–Potential* Biochimica Et Biophysica Acta, 1985. **812**(1): p. 55–65.

34. Olson, F., et al., *Preparation of Liposomes of Defined Size Distribution by Extrusion Through Polycarbonate Membranes.* Biochimica Et Biophysica Acta, 1979. **557**(1): p. 9–23.

35. Morcombe, C.R. and K.W. Zilm, *Chemical shift referencing in MAS solid state NMR.* Journal of Magnetic Resonance, 2003. **162**(2): p. 479–486.

36. Bodner, M.L., et al., *13C–13C and (15)N–(13)C correlation spectroscopy of membrane–associated and uniformly labeled human immunodeficiency virus and influenza fusion peptides: amino acid–type assignments and evidence for multiple conformations.* J Chem Phys, 2008. **128**(5): p. 052319.

37. Zhang, H.Y., S. Neal, and D.S. Wishart, *RefDB: A database of uniformly referenced protein chemical shifts.* Journal of Biomolecular Nmr, 2003. **25**(3): p. 173–195.

38. Bodner, M.L., *Solid state nuclear magnetic resonance of the HIV–1 and influenza fusion peptides associated wtih membranes*. 2006, Michigan State University: East Lansing, MI.

39. Bodner, M.L., et al., *Temperature dependence and resonance assignment of C–13 NMR spectra of selectively and uniformly labeled fusion peptides associated with membranes.* Magnetic Resonance in Chemistry, 2004. **42**(2): p. 187–194.

40. States, D.J., R.A. Haberkorn, and D.J. Ruben, *A Two–Dimensional Nuclear Overhauser Experiment with Pure Absorption Phase in 4 Quadrants.* Journal of Magnetic Resonance, 1982. **48**(2): p. 286–292.

41. Delaglio, F., et al., *NMRPIPE – A Multidimensional Spectral Processing System Based on UNIX Pipes.* Journal of Biomolecular Nmr, 1995. **6**(3): p. 277–293.

42. Weliky, D.P. *Chemistry 988 Lecture Notes*. [website containing pdf file of notes] May 3, 1999 [cited 2011 19 December 2011]; Available from: http://www2.chemistry.msu.edu/courses/CEM988NMR/cem988nmr.htm.

43. Rule, G.S. and T.K. Hitchens, *Fundamentals of protein NMR spectrosopy*. Focus on structural biology. 2006, Dordrecht: Springer. xxvi, 530 p.

44. Baldus, M., et al., *Cross polarization in the tilted frame: assignment and spectral simplification in heteronuclear spin systems.* Molecular Physics, 1998. **95**(6): p. 1197–1207.

45. Duer, M.J., *Solid–state NMR spectroscopy : principles and applications*. 2002, Malden, MA: Blackwell Science. xvii, 567 p.

46. Schmidt–Rohr, K. and H.W. Spiess, *Multidimensional Solid–State NMR and Polymers*. 2'nd ed. 1994, San Diego: Academic Press.

47. Szeverenyi, N.M., M.J. Sullivan, and G.E. Maciel, *Observation Of Spin Exchange By Two–Dimensional Fourier–Transform C–13 Cross Polarization–Magic–Angle Spinning.* Journal Of Magnetic Resonance, 1982. **47**(3): p. 462–475.

48. Takegoshi, K., S. Nakamura, and T. Terao, *13C–1H dipolar–assisted rotational resonance in magic–angle spinning NMR.* Chemical Physics Letters, 2001. **344**(5–6): p. 631–637.

49. Takegoshi, K., S. Nakamura, and T. Terao, *13C–1H dipolar–driven 13C–13C recoupling without 13C rf irradiation in nuclear magnetic resonance of rotating solids.* Journal of Chemical Physics, 2003. **118**(5): p. 2325–2341.

50. Morcombe, C.R., et al., *Diluting abundant spins by isotope edited radio frequency field assisted diffusion.* Journal of the American Chemical Society, 2004. **126**(23): p. 7196–7197.

51. Grommek, A., B.H. Meier, and M. Ernst, *Distance information from proton–driven spin diffusion under MAS.* Chemical Physics Letters, 2006. **427**(4–6): p. 404–409.

52. Ernst, M. *Heteronuclear Spin Decoupling in Magic–Angle–Spinning Solid–State NMR*. 2008 [cited 2012 28 Jan 2012]; pdf on webpage of a presentation]. Available from: http://www.enc–conference.org/portals/0/TutorialErnst2008.pdf.

53. Pochapsky, T.C. and S.S. Pochapsky, *NMR for Physical and Biological Scientists*. 2007, New York: Taylor & Francis Group. 372.

54. Castellani, F., et al., *Structure of a protein determined by solid–state magic–angle–spinning NMR spectroscopy.* Nature, 2002. **420**(6911): p. 98–102.

Chapter 3:

Studying FP–Hairpin by Solid State NMR Using a 9.4 T Spectrometer

Introduction

This chapter focuses on the solid state NMR (SSNMR) work preformed using a 9.4 T spectrometer. FP–Hairpin with uniformly labeled ^{13}C, ^{15}N alanine–6 (UA6) and glycine–10 (UG10) bound to either a PC/PG/Chol or PC/PG lipid membrane composition were studied. Different protein loadings were used in an attempt to probe the secondary and tertiary structure of the FP region of the FP–Hairpin protein construct along with determining the loading affect on secondary structure.

The objective of the work with FP–Hairpin was to determine the secondary structure and tertiary contacts of the FP region for FP–Hairpin. By using the UA6/UG10 labeling in the FP–Hairpin sample one can be able to determine secondary structure at those residues from chemical shift measurements and also determine whether the tertiary structure for FP–Hairpin contained the same A6 / G10 contacts as the FP23 peptides.

Previous Work Using FP23 Peptides

FP23 represents the 23 N–terminal residues of the gp41 sequence denoted the FP domain. The Weliky group has focused on studying this construct, probing the oligermization state along with determining secondary and tertiary structures using various SSNMR techniques.[1–5] Previous work showed that when FP23 inserted into lipid membranes containing cholesterol

FP23 adopts predominantly β–strand secondary structure for residues A1 – G16.[1, 6, 7] In lipid membranes lacking cholesterol, the FP adopts both helical and β–strand conformations.[8–10] Lipid to protein ratios also affected the observed secondary structure, with higher protein loadings favoring the β–strand conformation.[5, 10–12]

The tertiary structure of FP in lipid membranes has been probed by the 2D ^{13}C–^{13}C experiments along with distance measurements by 1D rotation echo double resonance (REDOR) experiment with ^{13}CO (carbonyl) and ^{15}N isotopic labeling in the fusion peptide.[1, 3, 9] Recent work from Qiang et al. [13] showed that by using the $^{1}H/^{13}C/^{31}P$ REDOR pulse sequence and also the $^{1}H/^{13}C/^{19}F$ REDOR pulse sequence membrane location could be established.[13] The $^{1}H/^{13}C/^{31}P$ REDOR allowed for probing the ^{31}P–^{13}CO distances between the lipid head group and the peptide's ^{13}CO label, establishing which residues made contact near the surface of the membrane. The ^{19}F isotopic label was located at either the C5 or the C16 carbon on the lipid acyl chain which probed the depth of insertion of a particular ^{13}CO labeled residue.[13]

Work by Qiang, Bodner, and Weliky [7] used FP23 with UA6/UG10 labeling to probe tertiary structure. From the 2D ^{13}C–^{13}C experiment shown in Figure 3–1A the intra–residue assignments of cross peaks can be made from the 10 ms mixing time since it only allows the magnetization to exchange between the directly bonded ^{13}C nuclei.[7] The 1000 ms mixing time employed for Figure 3–1B is used to probe the inter–residue assignments. The slice shown in Figure 3–1C corresponds to the alanine $^{13}C\beta$ β–strand chemical shift of f_1 = 23.5 ppm of Figure

3–1A. The slice shown in Figure 3–1D corresponds to the alanine $^{13}C\beta$ β–strand chemical shift of f_1 = 23.5 ppm of Figure 3–1B.

The 1000 ms mixing time experiment showed unique inter–residue A6 / G10 cross peaks between the Gly$^{13}C\alpha$/Ala$^{13}C\beta$, Gly^{13}CO/Ala$^{13}C\beta$, Ala$^{13}C\beta$/Gly$^{13}C\alpha$, and Ala$^{13}C\beta$/Gly^{13}CO for FP23 UA6/UG10 which are labeled in green in Figure 3–1B.[7] The slice in Figure 3–1D shows the Gly $^{13}C\alpha$ peak observed for the Gly$^{13}C\alpha$/Ala$^{13}C\beta$ cross peak. The unique A6 / G10 cross peaks help define the tertiary structure of FP23 peptides in the lipid membrane environment. The 2D ^{13}C–^{13}C experiment allows for probing ^{13}C–^{13}C distances of up to 5–6 Å.[7, 14] The chemical shifts for the unique inter–residue cross peak correspond to the β–strand conformation. From this work, it was determined that the FP23 peptide forms an antiparallel β–sheet assembly with overlap between the A6 and G10 residues. The A6 and G10 overlap could be from either the G16→A1/A1→G16 or the S17→A1/A1→S17 residue antiparallel registries.[7, 15] Evidence for this antiparallel overlap of strands is from $^{1}H/^{13}C/^{15}N$ REDOR experiments and 2D ^{13}C–^{13}C experiments with 1000 ms mixing times that provide the ability to probe distances of 5 – 6 Å.[7, 15] Initial work by Qiang and co–workers suggested that the antiparallel arrangement of strands were 50 – 60%.[7] Recent work by Schmick and Weliky support the antiparallel arrangement of strands with their SSNMR evidence from the $^{1}H/^{13}C/^{15}N$ REDOR experiments putting an upper bound of ~85% antiparallel arrangement of the FP23 peptides in a lipid membrane environment.[15] The data for the two antiparallel registries were also supported by other inter–strand interactions of A6 / G10, A6/F11, and I4/G13.[7]

Assignments for conformations were based off of known values for the ^{13}C chemical shift distributions of helical and β–strand conformations.[16] The helical (H) and β–strand (β) peak chemical shift ± standard deviation for Ala $^{13}C\alpha$ are H: 54.8 ± 1.1 ppm and β: 51.5 ± 1.5 ppm, $^{13}C\beta$ are H: 18.3 ± 0.9 ppm and β: 21.1 ± 2.1 ppm, and for ^{13}CO are H: 179.4 ± 1.3 ppm and β: 176.1 ± 1.5 ppm. The helical and β–strand chemical shifts ± standard deviation for Gly $^{13}C\alpha$ are H: 46.9 ± 1.1 ppm and β: 45.2 ± 1.2 ppm, and for ^{13}CO are H: 175.5 ± 1.2 ppm and β: 172.6 ± 1.6 ppm.

The FP work was the initial step towards building high resolution secondary and tertiary models of the gp41 protein in a lipid membrane environment during the early membrane fusion step when the fusion peptide initially inserts into the lipid membrane and establishes a tertiary structure prior to creating and opening of the fusion pore. In regards to lipid mixing, the FP23 peptides cause lipid mixing of the lipid vesicles, as observed by fluorescence spectroscopy. It has been shown that the addition of FP–Hairpin or Hairpin to the protein and lipid vesicle solution after the start of lipid mixing results in the halting any further lipid mixing.[17] This suggests that the FP–Hairpin construct is the post lipid mixing conformation for the gp41 protein. The work with FP–Hairpin construct will be used to elucidate the secondary and tertiary structures of the fusion peptide domain in the context of the final folded SHB state of the gp41 construct.

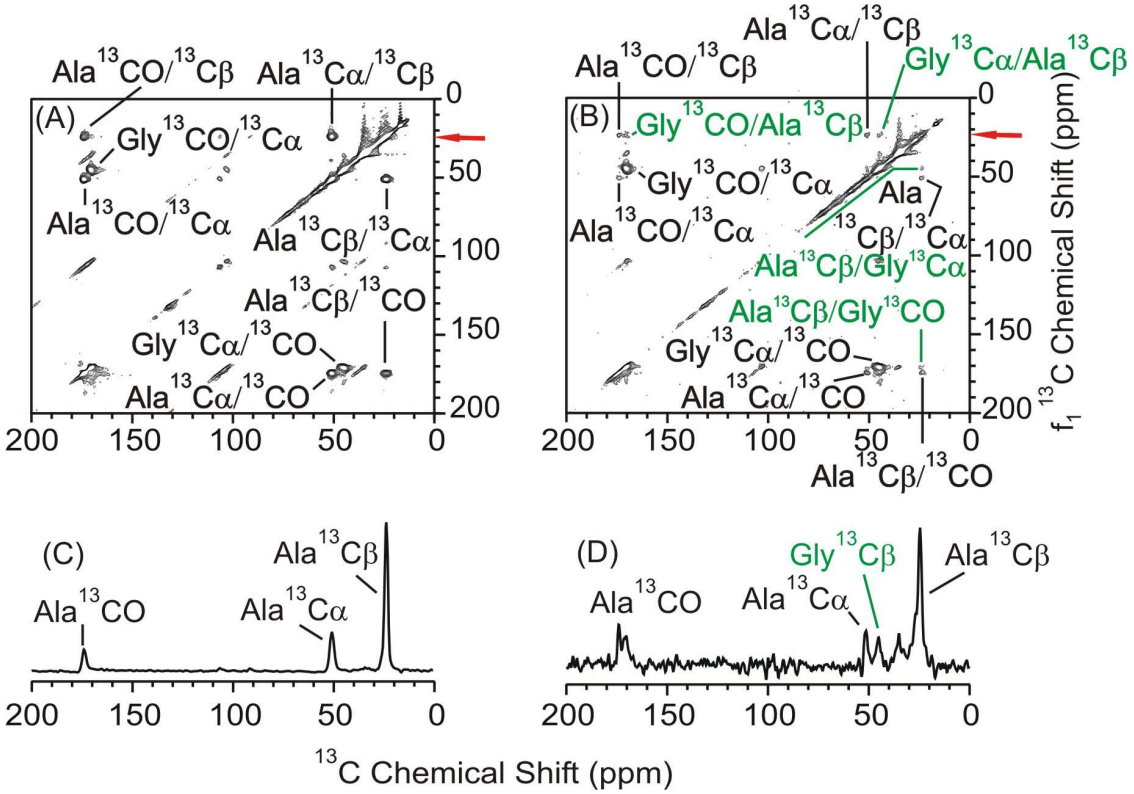

Figure 3–1: 2D PDSD ^{13}C–^{13}C spectra at 9.4 T of FP23 with uniform ^{13}C, ^{15}N labeling at Ala–6 and Gly–10 in the FP region inserted into a cholesterol containing lipid membrane environment. (A) The 10 ms mixing time spectrum shows only the intra–residue cross peaks while in (B) the 1000 ms mixing time spectrum shows the intra–residue assignments in black and the Ala–6/Gly–10 inter–residue cross peaks in green for the peptide. (C) is the f_2 slices corresponding to the Ala $^{13}C\beta$ β–strand conformation from f_1 = 23.5 ppm marked by red arrows in (A) and (D) is the f_2 slices corresponding to the Ala $^{13}C\beta$ β–strand conformation from f_1 = 23.5 ppm marked by red arrows in (B). The 1000 ms mixing time in (B) shows a cross–peak for A6 / G10, which is observable in the slice below in (D). The total number of acquisitions were (A) 102,400 and (B) 204,800. Assignments are listed as assignment in f_2 – assignment in f_1. 100 Hz of Gaussian line broadening was applied to each dimension. Data was adapted from reference.[7]

Initial SSNMR Studies for FP–Hairpin in Cholesterol Containing Membranes

Initial SSNMR studies for FP–Hairpin were performed with ~0.4 μmoles of the FP–Hairpin protein with UA6/UG10 labeling consistent with work for FP23. Figure 3–2 is the 50 ms data for FP–Hairpin UA6/UG10 associated with the cholesterol containing membranes at ~40:1 lipid to protein loading. Approximately 0.4 μmoles of FP–Hairpin was added to ~16 μmoles of lipids in an 8:2:5 molar ratio of DTPC:DTPG:Chol. Two distinct conformations of helical and β–strand are observed for intra–residue assignments. The slice through the Ala $^{13}C\beta$ chemical shift of f_1 = 23.5 ppm shows that the peak signal to noise for the cross peaks is approximately 10.6, 1.9, and 1.5 for the Ala $^{13}C\beta$, $^{13}C\alpha$, and ^{13}CO respectively. The peak signal to noise ratio for the ^{13}C signals were determined by first measuring the signal intensity of the ^{13}C resonance peak to the baseline to determine the peak signal intensity. Measuring the peak to peak intensity of the noise was done for determining the noise intensity. The signal intensity divided by the noise intensity yielded the peak signal to noise ratio for the ^{13}C peak. Figure 3–2 is from ~45 hrs of signal averaging. An attempt to acquire data for the 1000 ms mixing time experiment proved unsuccessful and the spectrum is shown in Figure 3–3. Only the Gly ^{13}CO/Gly $^{13}C\alpha$ and the Gly $^{13}C\alpha$/Gly ^{13}CO intra–residue cross peaks were observable. This data was acquired in ~85 hrs. The weak peak signal to noise resulted in the lack of observable cross peaks which is highlighted in Table 3–1. Longer mixing times of 500 ms or 1000 ms were not feasible due to the limited amount of protein present and the weak peak signal to noise ratios which would result in having to signal averaging for several weeks. The lipids used in this experiment were DTPC/DTPG/Chol in an 8:2:5 molar ratio. These lipids are ether rather than ester linked, lacking

the ^{13}CO natural abundance. Previous work for FP23 trimer showed that the ether and ester linked lipids do not affect the chemical shifts of the FP residues.[9]

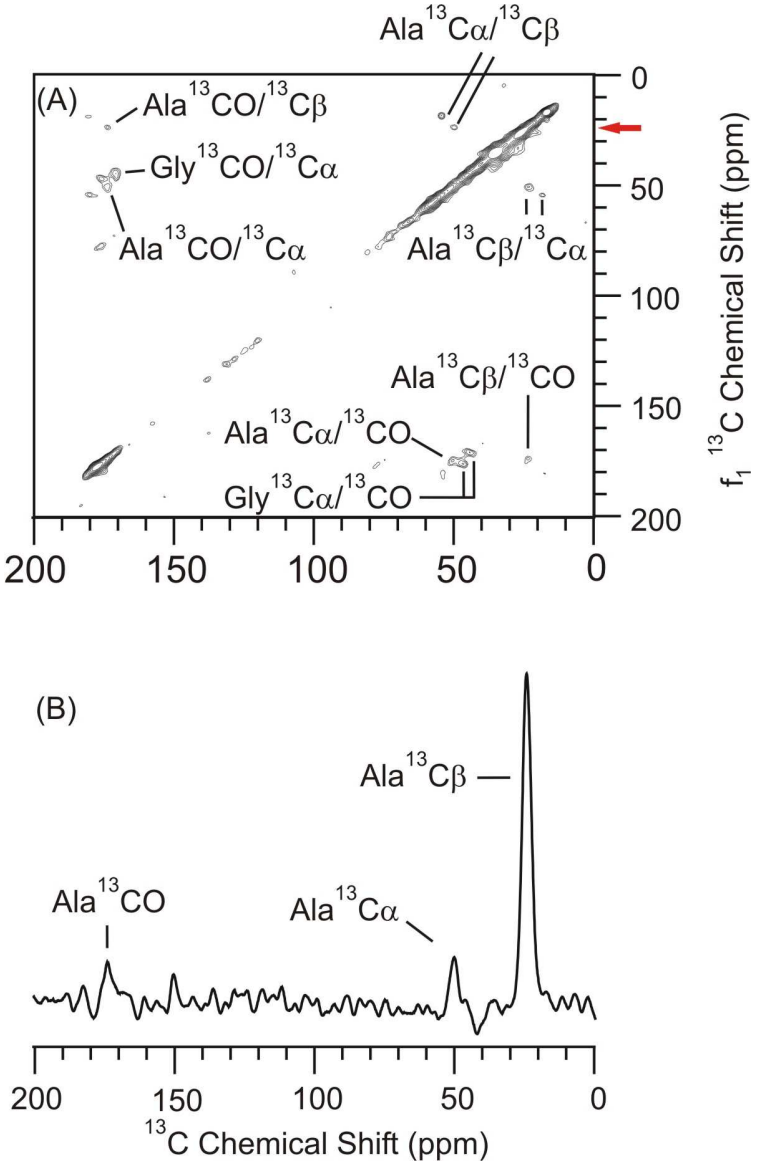

Figure 3–2: 2D DARR ^{13}C–^{13}C spectra at 9.4 T of FP–Hairpin with uniform ^{13}C, ^{15}N labeling at Ala–6 and Gly–10 in the FP region in a DTPC/DTPG/Chol lipid membrane environment at ~40:1 lipid to protein ratio. (A) The 50 ms mixing time spectrum shows only the intra–residue cross peaks. (B) The f_2 slice corresponding to the Ala $^{13}C\beta$ β–strand conformation from f_1 = 23.5 ppm is marked by the red arrow in (A). There were 318 t_1 points and 512 scans summed per t_1 point in a total time of ~45 hrs. Assignments are listed as assignment in f_2 – assignment in f_1 convention. 200 Hz of Gaussian line broadening was applied to each dimension.

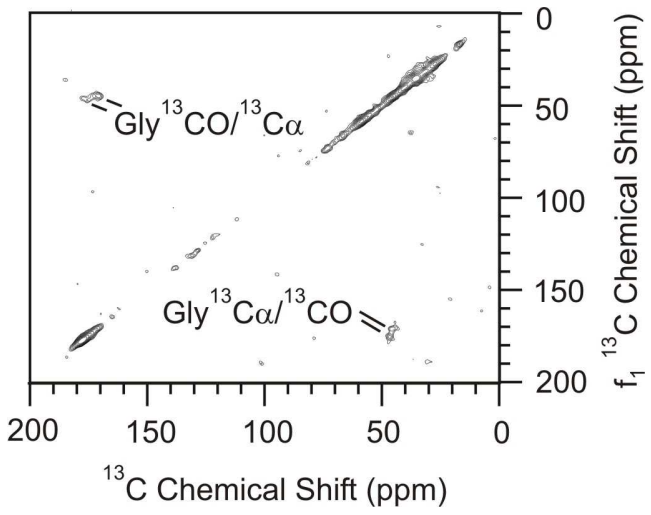

Figure 3–3: 2D DARR ^{13}C–^{13}C spectra at 9.4 T of FP–Hairpin with uniform ^{13}C, ^{15}N labeling at Ala–6 and Gly–10 in the FP region in a DTPC/DTPG/Chol lipid membrane environment at ~40:1 lipid to protein ratio. The 1000 ms mixing time spectrum shows only two cross peaks above the noise level corresponding to the Gly–10 residue with the helical and β–strand chemical shifts. There were 300 t_1 points and 512 scans summed per t_1 point in a total time of ~85 hrs. Assignments are listed as assignment in f_2 – assignment in f_1 convention. 200 Hz of Gaussian line broadening was applied to each dimension. No other cross peaks were observed if the contours were lowered. Lowering of the contours swamped the spectra with noise, resulting in the inability to distinguish the cross peaks from the noise peaks.

A second sample was prepared using ~1 μmole of FP–Hairpin with UA6/UG10 labeling which was added to POPC/POPG/Chol membranes at a lipid to protein loading of ~25:1. Figure 3–4 highlights the 2D ^{13}C–^{13}C DARR experiment with the 50 ms mixing period for intra–residue assignments. The POPC/POPG/Chol lipid composition contains the ester linked lipids which will contribute to the natural abundance ^{13}CO signal. However, this natural abundance (NA) will only be seen in the ^{13}C CP ramp experiment and the diagonal of the 2D ^{13}C–^{13}C experiment.

The affect of the natural abundance on the 2D spectrum for the off diagonal cross peaks is negligible for the follow reasons. The natural abundance of ^{13}C ($^{13}C_{NA}$) is only 1.1%, and the labeled signal for the ^{13}C ($^{13}C_{lab}$) of alanine–6 and glycine–10 is 100%. Consider the following three interactions: (1) A $^{13}C_{lab}$–$^{13}C_{lab}$ interaction; (2) A $^{13}C_{NA}$–$^{13}C_{NA}$ interaction; (3) A $^{13}C_{lab}$–$^{13}C_{NA}$ interaction. In condition (1), the probability will be 1 x 1 = 1. For condition (2), the probability will be $(0.011)^2 = 1.21 \times 10^{-4}$. For condition (3), the probability will be $1 \times 0.011 = 1.1 \times 10^{-2}$. From this, the labeled signal will dominate by 2 – 4 orders of magnitude. As a specific example, consider the 25:1 lipid to protein loading sample containing ~1 μmole of labeled protein, and ~25 μmoles of lipids. The off diagonal cross peaks that arise from the label – label interaction will have a probability of 1, as defined by condition (1) above. The off diagonal cross peaks that arise from the $^{13}C_{lab}$ – $^{13}C_{NA}$ will have a probability of 1.1×10^{-2} as defined by condition (3) above. From this, it is likely that the off diagonal cross peaks resulting from the $^{13}C_{NA}$–$^{13}C_{NA}$ condition will have the smallest intensity, and the $^{13}C_{lab}$–$^{13}C_{NA}$ intensity will

have a possibility to exist in the 2D spectra. The off diagonal cross peaks from the $^{13}C_{lab}$–$^{13}C_{NA}$ interactions will have a different chemical shift from the $^{13}C_{lab}$–$^{13}C_{lab}$, resulting in separation between off diagonal cross peaks.

Two conformations were observed for the intra–residue cross peaks at the ~25:1 loading. The 50 ms data was acquired in ~68 hrs and yielded more ^{13}C signal from the sample due to the increased amount of protein present in the sample. The cross peaks are more intense for the 25:1 sample due to the ~1.5x higher peak signal to noise ratio compared to the ~40:1 sample of Figure 3–2. The peak signal to noise ratio for the Ala $^{13}C\beta$, $^{13}C\alpha$, and ^{13}CO were 15.3, 2.0, and 2.4 respectively. The 40:1 loading of Figure 3–2 had a peak signal to noise ratio of 1.5 for the Ala ^{13}CO whereas the Ala ^{13}CO peak of the 25:1 loading sample had a peak signal to noise ratio of 2.4, which is ~1.6x higher. The Ala ^{13}CO peak shown in Figure 3–4B appears more structured than in Figure 3–2B, likely due to the increased peak signal to noise of the cross peak and also the higher protein loading of the sample.

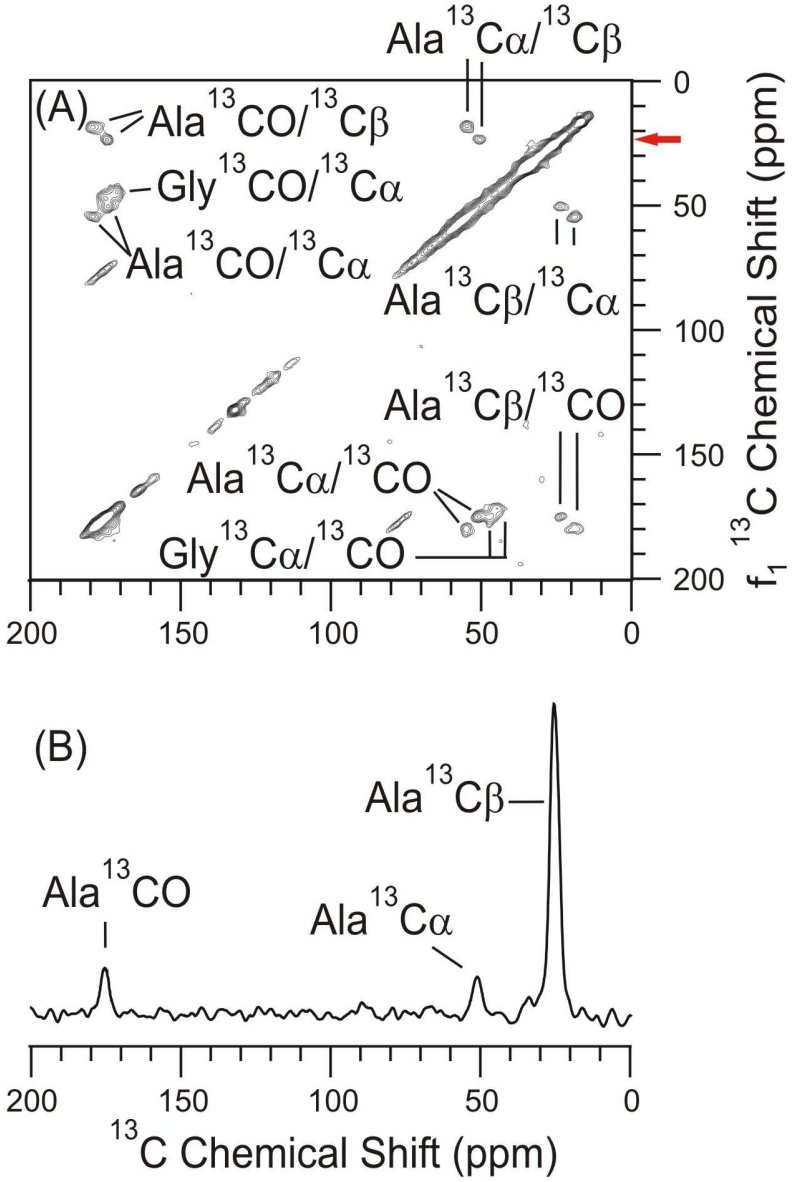

Figure 3–4: 2D DARR ^{13}C–^{13}C spectra at 9.4 T of FP–Hairpin with uniform ^{13}C, ^{15}N labeling at Ala–6 and Gly–10 in the FP region in a POPC/POPG/Chol lipid membrane environment at ~25:1 lipid to protein ratio. (A) The 50 ms mixing time spectrum shows only the intra–residue cross peaks. (B) The f_2 slice corresponding to the Ala $^{13}C\beta$ β–strand conformation from f_1 = 23.5 ppm is marked by the red arrow in (A). There were 300 t_1 points and 768 scans summed per t_1 point in a total time of ~68 hrs. Assignments are listed as assignment in f_2 – assignment in f_1. 200 Hz of Gaussian line broadening was applied to each dimension.

Favorable results from Figure 3–4 suggested that it would be possible to perform the 500 ms mixing time experiment probing for any A6 / G10 cross peak interactions to determine tertiary structure. The data was acquired using block averaging with each block being ~32 hrs. The 500 ms mixing time experiment shown in Figure 3–5 was acquired in 192 hrs. 200 Hz of Gaussian line broadening was applied to each dimension.

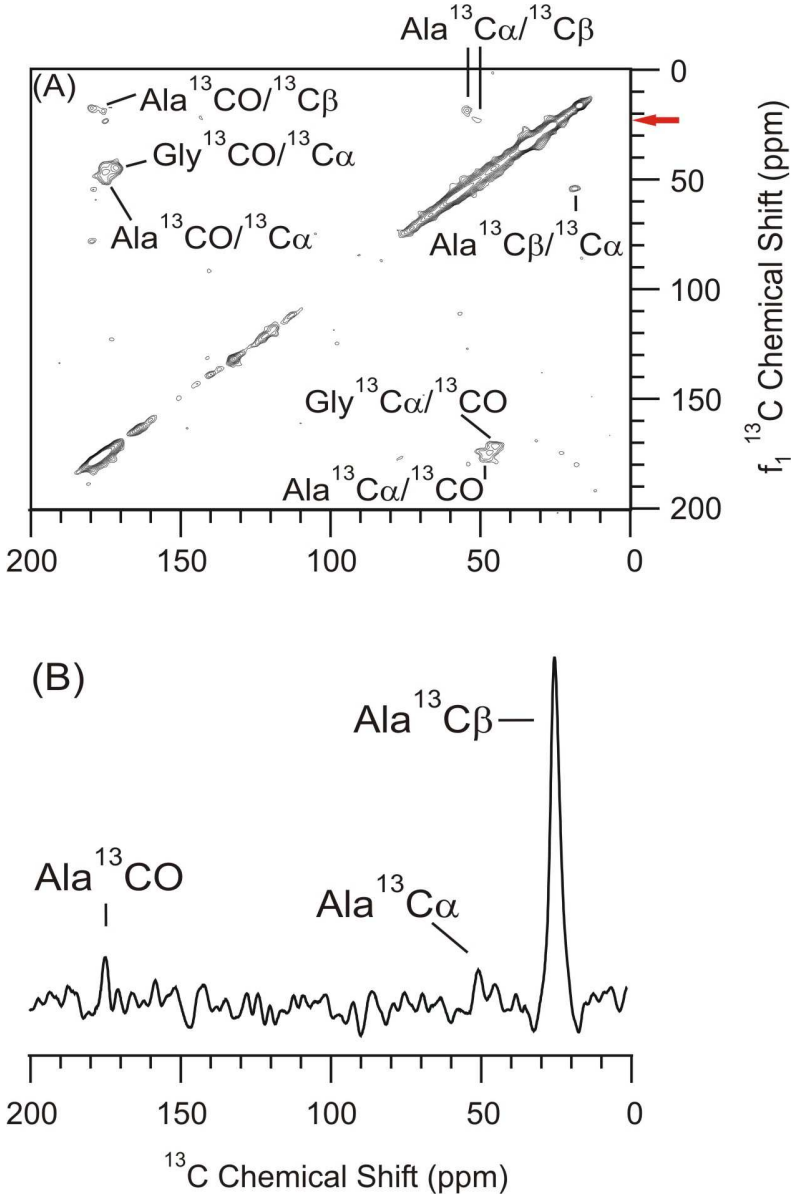

Figure 3–5: 2D DARR ^{13}C–^{13}C spectra at 9.4 T of FP–Hairpin with uniform ^{13}C, ^{15}N labeling at Ala–6 and Gly–10 in the FP region in a POPC/POPG/Chol lipid membrane environment at ~25:1 lipid to protein ratio. (A) The 500 ms mixing time spectrum shows the intra–residue cross peaks, however no inter–residue cross peaks were observed in this sample between A6–G10. (B) The f_2 slice corresponding to the Ala $^{13}C\beta$ β–strand conformation from f_1 = 23.5 ppm is marked by the red arrow in (A). There were 300 t_1 points and 1536 scans summed per t_1 point in a total time of ~192 hrs. Assignments are listed as assignment in f_2 – assignment in f_1. 200 Hz of Gaussian line broadening was applied to each dimension.

Figure 3–5 only contains intra–residue assignments, which were assigned previously from the 50 ms mixing time experiment. Two conformations are present in the spectra, however they are of reduced intensity compared the 50 ms mixing time of Figure 3–4A. No unique A6 / G10 cross peaks were observed for this sample, suggesting the possibility that the FP region of FP–Hairpin adopts a different tertiary structure in the final folded SHB formation compared to the FP23 peptides. Further work to support this hypothesis will be presented in this chapter and Chapter 4. Figure 3–5B is the slice from Figure 3–5A corresponding to the f_1 = 23.5 ppm chemical shift of alanine $^{13}C\beta$ β–strand peak. From the slice only the Ala $^{13}C\beta$, $^{13}C\alpha$ and ^{13}CO are identifiable with peak signal to noise ratios of 8.4, 0.9, and 1.1 respectively. No peak for the glycine $^{13}C\alpha$ carbon is observed in the slice. The peak signal to noise of the off diagonal peaks are weak ($^{13}C\alpha$, ^{13}CO) suggesting that either longer signal averaging time, more sample, or more Gaussian line broadening should be used. Since the peak signal to noise ratio increases as the square root of the number of scans, in order to double the current peak signal to noise ratio would require signal averaging for four times as long which is ~32 days! This is not feasible nor is it an efficient use of spectrometer time. The best option was to pack more sample into the rotor.

FP–Hairpin in Cholesterol Depleted Membranes

Two samples of FP–Hairpin with UA6/UG10 labeling were also prepared in cholesterol depleted membranes. A 40:1 lipid to protein loading sample was prepared in DTPC:DTPG and a 25:1 lipid to protein loading sample was prepared in POPC:POPG membranes where the molar ratio of lipids were 4:1 of PC:PG. Figure 3–6 illustrates the 40:1 loading in the cholesterol

depleted membranes. The ~40:1 loading sample contained ~0.4 μmoles of FP–Hairpin with UA6/UG10 labeling. Similar to the ~40:1 loading sample of Figure 3–2, these data were acquired in ~45 hrs and suffers from weak peak signal to noise for the cross peaks. The sample for Figures 3–2 and 3–6 were prepared at the same time. Due to the weak peak signal to noise of the sample, no 500 ms or 1000 ms mixing time experiments were performed. The peak signal to noise ratio was 10.7, 2.8, and 2.5 for the Ala $^{13}C\beta$, $^{13}C\alpha$, and ^{13}CO peaks in the slice of Figure 3–6B.

Table 3–1 contains the tabulated data for the chemical shifts (CS) and the populations (Pop) for the 40:1 loading of FP–Hairpin in the ether linked lipid membranes. Data for the 50 ms DARR experiment was determined from either Figure 3–2 for the cholesterol containing membranes or Figure 3–6 for the cholesterol depleted membranes. The populations were determined using Equation 3–1:

$$\left(\frac{\text{Intensity}\left(\text{Ala}^{13}C\alpha/^{13}C\beta \text{ peak} \right)_{H}}{\text{Intensity}\left(\text{Ala}^{13}C\alpha/^{13}C\beta \right)_{H} + \text{Intensity}\left(\text{Ala}^{13}C\alpha/^{13}C\beta \right)_{\beta s}} \right) \times 100 \qquad (3–1)$$

where the populations of the intra–residue assignment were determined from the intensity of the helical (H) and β–strand (βs) cross peaks for the specific intra–residue assignment.

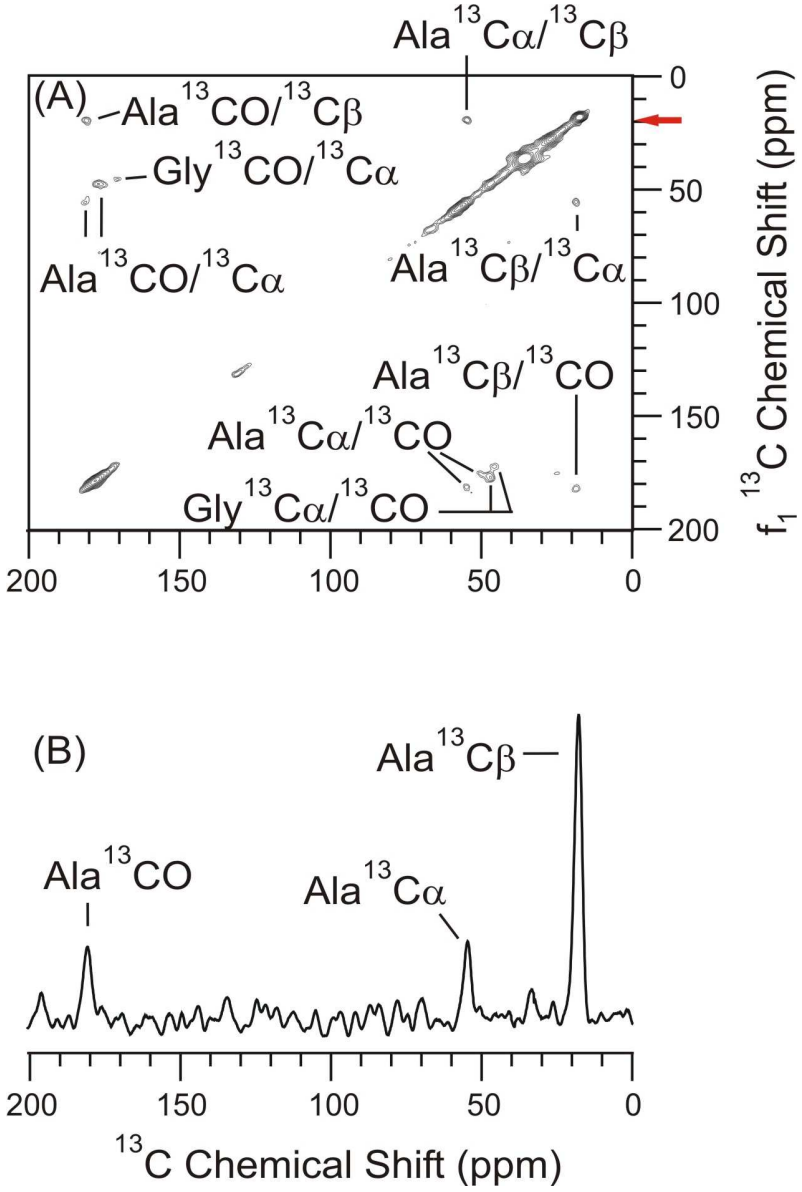

Figure 3–6: 2D DARR ^{13}C–^{13}C spectra at 9.4 T of FP–Hairpin with uniform ^{13}C, ^{15}N labeling at Ala–6 and Gly–10 in the FP region in a DTPC/DTPG lipid membrane environment at ~40:1 lipid to protein ratio. (A) The 50 ms mixing time spectrum shows only the intra–residue cross peaks. (B) The f_2 slice corresponding to the Ala $^{13}C\beta$ helical conformation from f_1 = 18.6 ppm is marked by the red arrow in (A). There were 300 t_1 points and 512 scans summed per t_1 point in a total time of ~45 hrs. Assignments are listed as assignment in f_2 – assignment in f_1. 200 Hz of Gaussian line broadening was applied to each dimension.

Table 3–1: Chemical shift (CS) and relative populations (Pop) for the FP–Hairpin UA6/UG10 sample with loading at 40:1 in cholesterol containing and cholesterol depleted membranes with shifts reported as the (f_2, f_1) convention.

Loading		**40 : 1**				**40 : 1**	
Composition		**DTPC / DTPG / Chol**				**DTPC / DTPG**	
Field		**9.4 T**				**9.4 T**	
Pulse Sequence		**DARR**				**DARR**	
Mixing Time		**50 ms**		**1000 ms**		**50 ms**	
Assignment		**CS**	**Pop (%)**	**CS**	**Pop (%)**	**CS**	**Pop (%)**
A Cα / A Cβ	**Helix**	54.7, 18.8	57.8	–	–	54.6, 18.6	–
	β–sheet	50.2, 24.1	42.2	–	–	–	–
A Cα / A CO	**Helix**	–	–	–	–	54.8, 180.8	52.5
	β–sheet	50.7, 175.3	–	–	–	50.1, 174.9	47.5
A Cβ / A CO	**Helix**	–	–	–	–	18.4, 181.7	–
	β–sheet	23.8, 174.5	–	–	–	–	–
A CO / A Cα	**Helix**	180.7, 54.8	48.0	–	–	181.5, 55.1	–
	β–sheet	174.4, 50.9	52.0	–	–	–	–
A CO / A Cβ	**Helix**	–	–	–	–	181.0, 18.8	–
	β–sheet	174.2, 24.0	–	–	–	–	–
A Cβ / A Cα	**Helix**	18.5, 54.8	47.2	–	–	18.5, 54.8	–
	β–sheet	23.5, 51.0	52.8	–	–	–	–
G Cα / G CO	**Helix**	47.0, 176.9	50.1	46.8, 175.7	55.7	47.0, 176.8	61.5
	β–sheet	44.7, 171.6	49.9	45.8, 171.4	44.3	45.8, 171.8	38.5
G CO / G Cα	**Helix**	176.1, 47.4	47.3	175.9, 47.1	39.9	177.1, 46.8	61.5
	β–sheet	171.3, 45.0	52.7	171.1, 44.7	60.1	170.7, 44.8	38.5

Average populations and their standard deviations for the 40:1 DTPC/DTPG/Chol sample with the 50 ms data in Table 3–1 are reported below. The Ala–6 residue is 51.0 ± 5.9 % helical and 49.0 ± 5.9 % β–strand conformation. The Gly–10 residue is 48.7 ± 2.0 % helical and 51.3 ± 2.0 % β–strand conformation. The average populations and their standard deviations for the 40:1 DTPC/DTPG sample with the 50 ms data in Table 3–1 are presented below. The Ala–6 residue is 52.5% helical and 47.5% β–strand conformation. Standard deviation is not reported due to the sample size of N = 1. The Gly–10 residue is 61.5 ± 0.0 % helical and 38.5 ± 0.0 % β–strand conformation. The standard deviation (σ) was calculated using Equation 3–2, where N is the number of data points, x_j is data point j, and $\bar{x}$ is the average.

$$\sigma = \left(\frac{\sum_{j=1}^{N} (x_j - \bar{x})^2}{N-1} \right)^{1/2} \qquad (3\text{–}2)$$

The populations of the helical and β–strand conformation for FP–Hairpin UA6/UG10 at 40:1 lipid to protein loading in the PC/PG/Chol lipid membranes overlap within 1σ of each other for both the alanine–6 and the glycine–10 residues. The populations determined for the alanine–6 and the glycine–10 residues overlap within 1σ of each other which means that there is no significant difference between the populations between the two residues.

For the FP–Hairpin UA6/UG10 sample in the PC/PG lipid membranes at 40:1 lipid to protein loading, the populations of the helical and β–strand conformation at alanine–6 overlap

with the populations determined for the same sample in PC/PG/Chol lipid membrane environment. No standard deviation was determined for this residue due to the sample size of N=1. The glycine–10 residue has average populations which are significantly higher for the helical conformation than the β–strand conformation. The glycine–10 residue conformation in PC/PG lipid membranes populations do not overlap within 1σ of the populations determined for the sample in PC/PG/Chol lipid membranes. However, both samples were observed to contain the helical and β–strand conformation with no clear difference on the populations of the conformation based on the different lipid membrane compositions.

Table 3–1 contains data for the attempt at performing the 1000 ms mixing time experiment for the ~40:1 lipid to protein loading in cholesterol containing membranes. The 2D ^{13}C–^{13}C spectrum was shown in Figure 3–3. From the table and the spectrum, it is shown that most of the cross peaks were not detectable due to the weak peak signal to noise of the sample. Data for the 50 ms experiments in cholesterol containing membranes are from Figure 3–2 and cholesterol depleted membranes from Figure 3–6.

Figure 3–7 illustrates the 25:1 lipid to protein loading in the cholesterol depleted membranes. Previous work with the FP23 had shown that in cholesterol depleted membranes there are two conformations observable where as in cholesterol containing membranes FP23 was predominantly β–strand.[12] For FP–Hairpin in cholesterol depleted membranes, there is a mix of the two conformations favorably corresponding to work from FP23. The peak signal to noise ratio were 15.7, 3.3 and 4.6 for the Ala $^{13}C\beta$, $^{13}C\alpha$ and ^{13}CO peaks presented in Figure 3–7B.

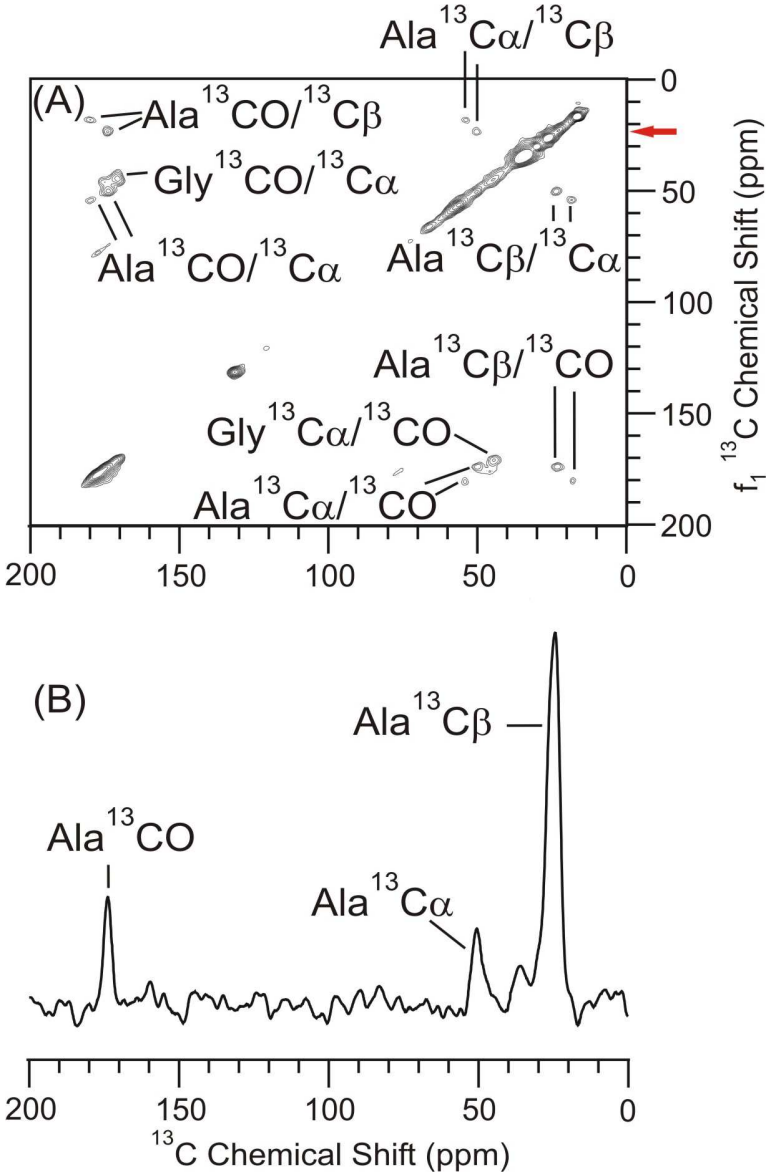

Figure 3–7: 2D DARR ^{13}C–^{13}C spectra at 9.4 T of FP–Hairpin with uniform ^{13}C, ^{15}N labeling at Ala–6 and Gly–10 in the FP region in a POPC/POPG lipid membrane environment at ~25:1 lipid to protein ratio. (A) The 50 ms mixing time spectrum shows only the intra–residue cross peaks. (B) The f_2 slice corresponding to the Ala $^{13}C\beta$ β–strand conformation from f_1 = 23.5 ppm is marked by the red arrow in (A). There were 300 t_1 points and 768 scans summed per t_1 point in a total time of ~68 hrs. Assignments are listed as assignment in f_2 – assignment in f_1. 200 Hz of Gaussian line broadening was applied to each dimension.

Figure 3–8 illustrates the results of the 500 ms mixing time for the POPC/POPG membranes. After ~128 hrs of signal averaging the data shows peak signal to noise ratio of 7.0, 2.1, and 1.8 for the Ala $^{13}C\beta$, $^{13}C\alpha$, and ^{13}CO peaks in Figure 3–8B. Lowering the contour levels of the 2D plot in Figure 3–8A would result in significant noise being displayed. Instead of continuing to signal average with this sample, a decision to prepare a FP–Hairpin sample containing ~2 μmoles (~24 mg) of protein in cholesterol containing membranes was pursued. The cholesterol containing membranes are more biologically relevant than the cholesterol depleted membranes presented in Figures 3–6 to 3–8.

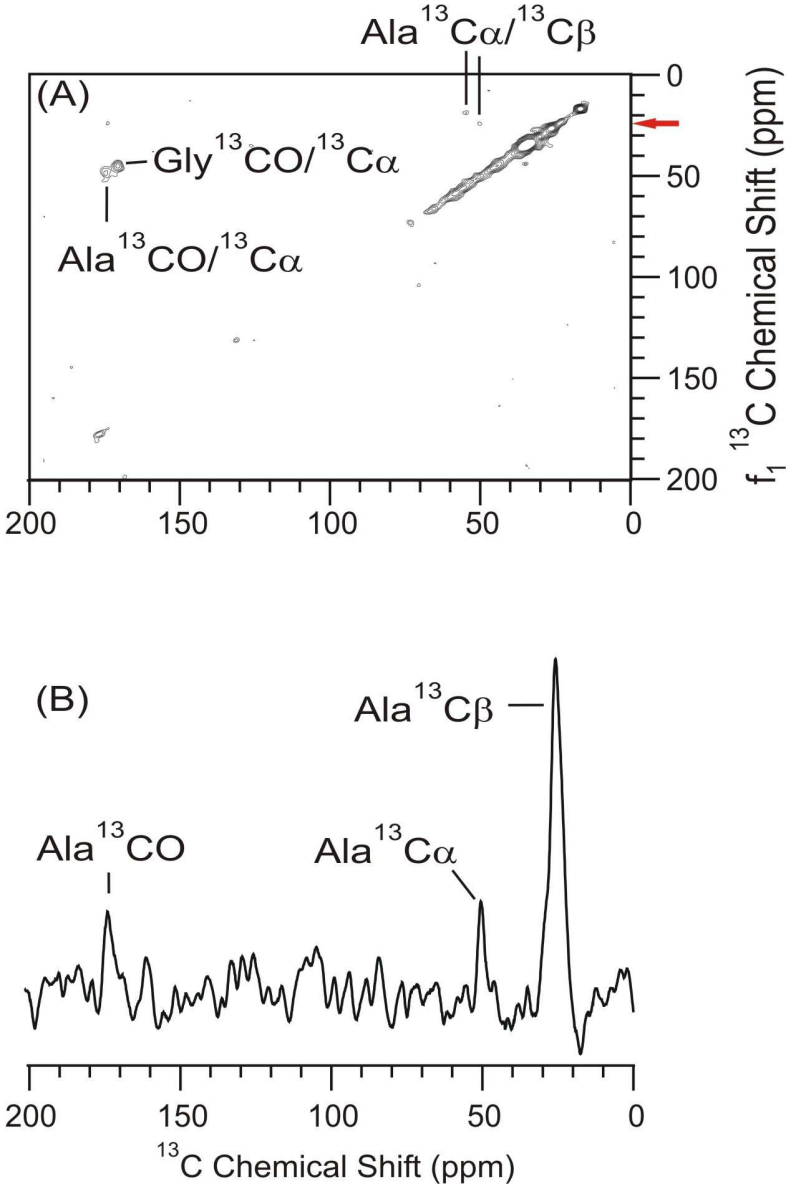

Figure 3–8: 2D DARR ^{13}C–^{13}C spectra at 9.4 T of FP–Hairpin with uniform ^{13}C, ^{15}N labeling at Ala–6 and Gly–10 in the FP region in a POPC/POPG lipid membrane environment at ~25:1 lipid to protein ratio. (A) The 500 ms mixing time spectrum shows the intra–residue cross peaks, however no inter–residue cross peaks were observed in this sample between A6–G10. (B) The f_2 slice corresponding to the Ala ^{13}Cβ β–strand conformation from f_1 = 23.5 ppm is marked by the red arrow in (A). There were 300 t_1 points and 1024 scans summed per t_1 point in a total time of ~128 hrs. Assignments are listed as assignment in f_2 – assignment in f_1. 200 Hz of Gaussian line broadening was applied to each dimension.

Figure 3–9 compares the 50 ms 2D ^{13}C–^{13}C experiments for FP–Hairpin in (A) cholesterol depleted and (B) cholesterol containing membranes for the 25:1 loading sample corresponding to the $^{13}C\alpha/^{13}C\beta$ region. The spectra for the two samples are the result of the same number of acquisitions performed under the same experimental conditions and sample preparation was the same for both samples aside from cholesterol concentration.

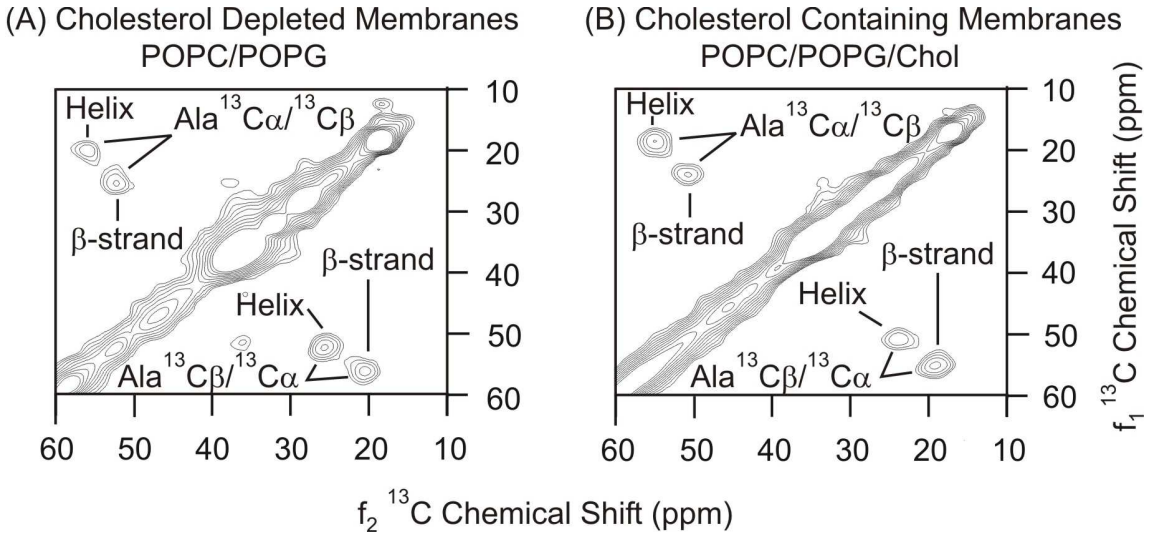

Figure 3–9: Comparison between POPC/POPG and POPC/POPG/Chol lipid membranes. FP–Hairpin UA6/UG10 in (A) cholesterol depleted membranes and (B) cholesterol containing membranes. The loading was ~25:1 lipid to protein ratio for both samples. From the 2D DARR ^{13}C–^{13}C 50 ms mixing time experiment it is evident that at these loadings, there is no dependence on cholesterol affecting secondary structure of the fusion peptide portion of the FP–Hairpin construct. There were 300 t_1 points and 768 scans summed per t_1 point using a 9.4 T magnet. 200 Hz of line broadening was applied to each dimension. The percentage of each population was determined from the average of the $^{13}C\alpha/^{13}C\beta$ and $^{13}C\beta/^{13}C\alpha$ peak intensities, and calculated by Equation 3–1.

Comparing the intensity of the cross peaks for the Ala $^{13}C\alpha/^{13}C\beta$ and the $^{13}C\beta/^{13}C\alpha$ conformations, it can be determined a relative percentage of the helical and β–strand conformations. In the POPC/POPG lipid membranes, there is an approximate 46.9% / 53.1% ± 2.0% mix of the helical and β–strand conformations. This is not surprising as the FP23 peptide in cholesterol depleted membranes also exhibited both helical and β–strand conformations.[8, 9] For FP–Hairpin in POPC/POPG/Chol, it is a 57.6% / 42.4% ± 2.3% mix for the helical and β–strand conformations.

The data for the populations determined from the 25:1 lipid to protein loading samples in PC/PG/Chol lipid membrane environments for Ala–6 and Gly–10 fit well within 1σ of the data for the 40:1 lipid to protein loading sample in either the PC/PG/Chol or the PC/PG lipid membrane environment. The data for populations of the Ala–6 residue at the 25:1 lipid to protein sample in PC/PG lipid membranes fit well the results from the 40:1 lipid to protein sample. The populations determined for the Gly–10 residue do not fit well with the populations from the 40:1 lipid to protein sample in PC/PG lipid membranes. One possible reason is that the 40:1 lipid to protein sample in the PC/PG lipid environment had ~1.5x lower peak signal to noise of the cross peaks than the 25:1 lipid to protein loading sample in PC/PG lipid membranes did. The data for the 25:1 loading in my opinion is more reliable since the peak signal to noise ratios are higher for the cross peaks than those of the 40:1 loading samples.

Previous work with FP23 showed that in cholesterol containing membranes the FP23 peptide was predominantly β–strand conformation.[8, 9] For FP–Hairpin presented here, practically equal quantities of the two conformations are observed for the cholesterol depleted and cholesterol containing membranes. This suggests that there is little to no dependence on

secondary structure of the FP domain of FP–Hairpin with regards to cholesterol content of the membranes.

Table 3–2 contains the tabulated data for the chemical shifts and populations of the 25:1 loading of FP–Hairpin in the POPC/POPG/Chol and the POPC/POPG lipid membrane environments at both the 50 ms and 500 ms mixing time. The populations were determined as discussed for Table 3–1 using Equation 3–1. Data for the POPC/POPG/Chol membrane sample with a 50 ms or 500 ms mixing time were determined from Figures 3–4 and 3–5 respectively. Data for FP–Hairpin in the POPC/POPG lipid membrane composition was determined from Figures 3–7 and 3–8 for the 50 ms and 500 ms mixing times respectively. All four spectra had 200 Hz of Gaussian line broadening applied to each dimension.

Table 3–2: Chemical shift (CS) and relative populations (Pop) for the FP–Hairpin UA6/UG10 sample with loading at 25:1 in cholesterol containing and cholesterol depleted membranes with shifts reported as the (f_2, f_1) convention.

Loading		**25 : 1**				**25 : 1**			
Composition		**POPC / POPG / Chol.**				**POPC / POPG**			
Field		**9.4 T**				**9.4 T**			
Pulse Sequence		**DARR**				**DARR**			
Mixing Time		**50 ms**		**500 ms**		**50 ms**		**500 ms**	
Assignment		**CS**	**Pop (%)**	**CS**	**Pop (%)**	**CS**	**Pop (%)**	**CS**	**Pop (%)**
A Cα / A Cβ	**Helix**	55.0, 18.5	55.9	54.3, 19.0	59.8	54.0, 18.0	48.3	55.1, 19.0	53.1
	β–strand	50.8, 24.0	44.1	51.3, 23.7	41.2	50.2, 23.4	51.7	50.4, 24.0	46.9
A Cα / A CO	**Helix**	55.1, 179.9	41.1	54.1, 180.3	38.3	54.2, 181.0	40.8	–	–
	β–strand	50.9, 175.0	58.9	49.7, 174.8	61.7	50.0, 174.3	59.2	–	–
A Cβ / A CO	**Helix**	19.9, 180.0	46.0	17.9, 180.7	51.6	18.1, 180.5	40.7	–	–
	β–strand	23.8, 175.1	54.0	22.9, 175.2	48.4	23.3, 174.2	59.3	–	–
A CO / A Cα	**Helix**	179.6, 54.9	45.0	178.9, 55.2	33.3	179.9, 54.4	31.8	–	–
	β–strand	174.6, 50.8	55.0	174.9, 50.9	66.7	173.9, 50.0	68.2	175.4, 49.0	–
A CO / A Cβ	**Helix**	179.6, 19.0	51.9	179.5, 17.8	52.4	179.9, 18.0	42.4	–	–
	β–strand	174.8, 24.1	48.1	174.9, 24.0	47.6	174.0, 23.4	57.6	–	–
A Cβ / A Cα	**Helix**	19.1, 55.1	59.2	18.5, 54.8	–	18.5, 54.0	45.5	–	–
	β–strand	23.9, 50.8	40.8	–	–	23.7, 50.2	54.5	–	
G Cα / G CO	**Helix**	47.3, 175.1	53.4	46.9, 174.8	47.3	46.5, 176.2	36.1	–	–
	β–strand	45.0, 171.8	46.6	44.7, 171.7	52.7	44.5, 171.2	63.9	–	–
G CO / G Cα	**Helix**	174.0, 47.3	46.9	174.9, 47.0	44.0	175.0, 46.2	39.7	–	–
	β–strand	171.7, 45.0	53.1	171.1, 45.1	56.0	170.8, 44.4	60.3	171.0, 45.1	–

Average populations and their standard deviations for the 25:1 POPC/POPG/Chol sample with the 50 ms data in Table 3–2 are reported below. The Ala–6 residue is 49.9 ± 7.0 % helical and 50.1 ± 7.0 % β–strand conformation. The Gly–10 residue is 50.1 ± 4.6 % helical and 49.9 ± 4.6 % β–strand conformation. The average populations and their standard deviations for the 25:1 POPC/POPG sample with the 50 ms data in Table 3–2 are presented next. The Ala–6 residue is 41.6 ± 5.6 % helical and 58.4 ± 5.6 % β–strand conformation. The Gly–10 residue is 37.9 ± 2.5 % helical and 62.1 ± 2.5 % β–strand conformation. Equation 3–2 was used to calculate the standard deviation.

The FP–Hairpin UA6/UG10 sample at 25:1 lipid to protein loading in PC/PG/Chol lipid membranes showed that the population of the Ala–6 and Gly–10 residues with a helical conformation overlap within 1σ of each other. The population with β–strand conformation at the residues Ala–6 and Gly–10 also are within 1σ of each other, suggesting that there is no significant difference in the populations within 1σ. For the PC/PG lipid membrane environment with FP–Hairpin at a 25:1 lipid to protein loading, the Ala–6 and Gly–10 residues overlap within 1σ for the populations of the helical conformation. The β–strand conformation for Ala–6 and Gly–10 overlap within 1σ as well.

When comparing the Ala–6 residue in PC/PG/Chol to the Ala–6 residue in the PC/PG lipid membranes, the populations both overlap within 1σ. When comparing the Gly–10 residues between the PC/PG/Chol and PC/PG lipid membrane environments, the populations do not overlap within 1σ. As the Ala-6 residues had more cross peaks that could be used to determine their average and standard deviation, the data suggests that no significant difference between the PC/PG/Chol and PC/PG lipid membrane environment exists for the FP domain of the FP–

Hairpin construct. These results are consistent with the 40:1 lipid to protein loading previously presented.

FP–Hairpin 15:1 Loading System in Cholesterol Containing Membranes

The ~15:1 lipid to protein loading system was designed to address the three main concerns that were presented from the 40:1 and 25:1 lipid to protein loading samples. Those points were (1) weak peak signal to noise of the cross peaks, (2) two conformations for an intra–residue assignment and (3) long signal averaging times. The 15:1 lipid to protein loading sample was prepared in biologically relevant cholesterol containing membranes. The 15:1 lipid to protein loading sample contained ~2 μmoles of FP–Hairpin protein with the UA6/UG10 isotopic labeling scheme. By loading this amount of protein into the lipid membranes, I was trying to favor one conformation, the β–strand as opposed to the split conformation observed for the other samples. It was previously shown with FP23 that increasing the loading of the protein concentration favored the β–strand conformation.[5, 10–12] The increased protein content of the system would result in more ^{13}C signal, increased peak signal to noise ratios, and obtaining one conformation which would result in the need for less signal averaging time.

The data presented in Figure 3–10 is for the 50 ms 2D ^{13}C–^{13}C PDSD experiment for the 15:1 lipid to protein sample at 9.4 T. Figure 3–10A shows that the cross peaks for each intra–residue assignment favor the β–strand conformation significantly more than the helical conformation. The slice presented in Figure 3–10B is for the Ala $^{13}C\beta$ β–strand chemical shift of f_1 = 23.5 ppm. Figure 3–10 has 100 Hz of Gaussian line broadening applied to each dimension

and was acquired in ~23 hrs. The peak signal to noise ratio for the Ala $^{13}C\beta$, $^{13}C\alpha$, and ^{13}CO peaks for the slice are 16.4, 6.1, and 5.4 respectively.

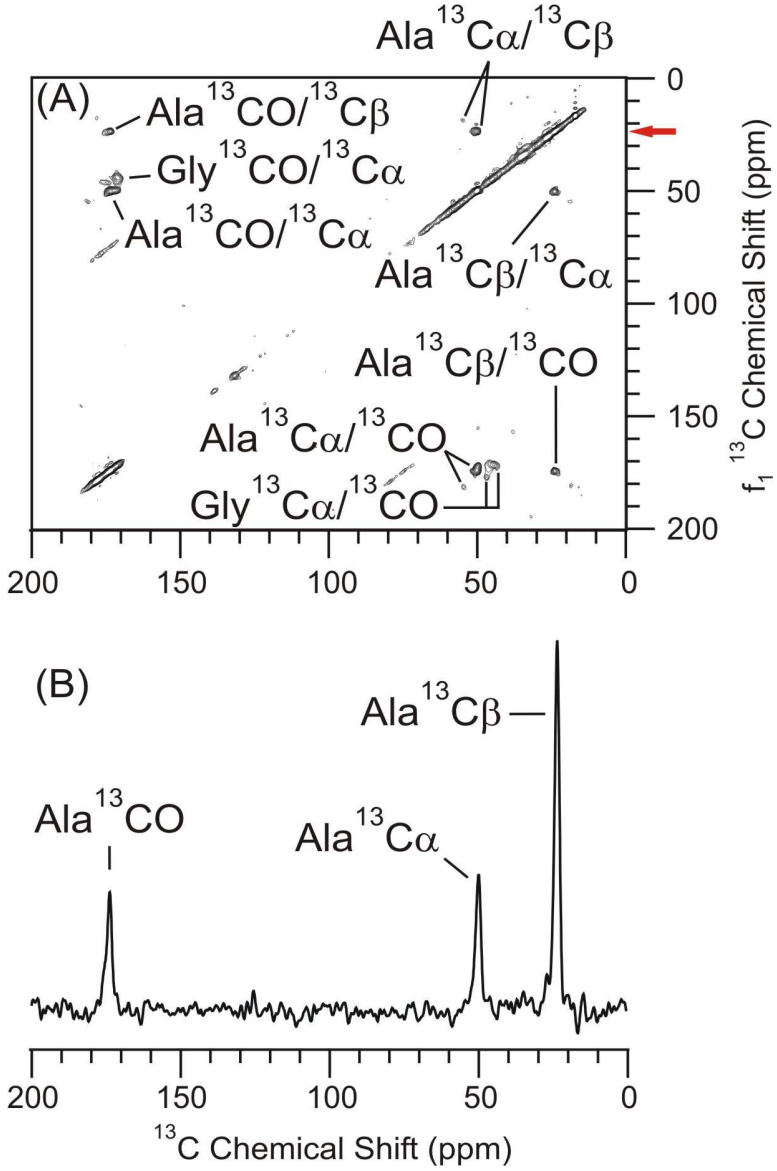

Figure 3–10: 2D PDSD ^{13}C–^{13}C spectra at 9.4 T of FP–Hairpin with uniform ^{13}C, ^{15}N labeling at Ala–6 and Gly–10 in the FP region in a POPC/POPG/Chol lipid membrane environment at ~15:1 lipid to protein ratio. (A) The 50 ms mixing time spectrum shows the intra–residue cross peaks. (B) The f_2 slice corresponding to the Ala $^{13}C\beta$ β–strand conformation from f_1 = 23.5 ppm is marked by the red arrow in (A). There were 300 t_1 points and 256 scans summed per t_1 point in a total time of ~23 hrs. Assignments are listed as assignment in f_2 – assignment in f_1. 100 Hz of Gaussian line broadening was applied to each dimension.

The 500 ms mixing time experiment was performed and is displayed in Figure 3–11 using the PDSD pulse sequence. This data was acquired in ~64 hrs and has 200 Hz of Gaussian line broadening applied to each dimension. The β–strand cross peak is still the predominant conformation observed for the intra–residue assignments. The slice in Figure 3–11B corresponds to the Ala ^{13}Cβ β–strand conformation with a f_1 = 23.5 ppm chemical shift and shows that the peak signal to noise for the peaks are 8.3, 4.3, and 4.3 for the Ala ^{13}Cβ, ^{13}Cα, and ^{13}CO. No unique inter–residue alanine–6 / glycine–10 cross peaks are observed in the 2D spectrum. In order to confirm that there are no inter–residue alanine–6 / glycine–10 cross peaks for this sample the 2D ^{13}C–^{13}C DARR sequence was used which can probe ^{13}C–^{13}C inter–nuclear distances up to 7 Å.[14] Also, this sample was analyzed using a high field, 21.1 T NMR spectrometer, with the data being presented in Chapter 4.

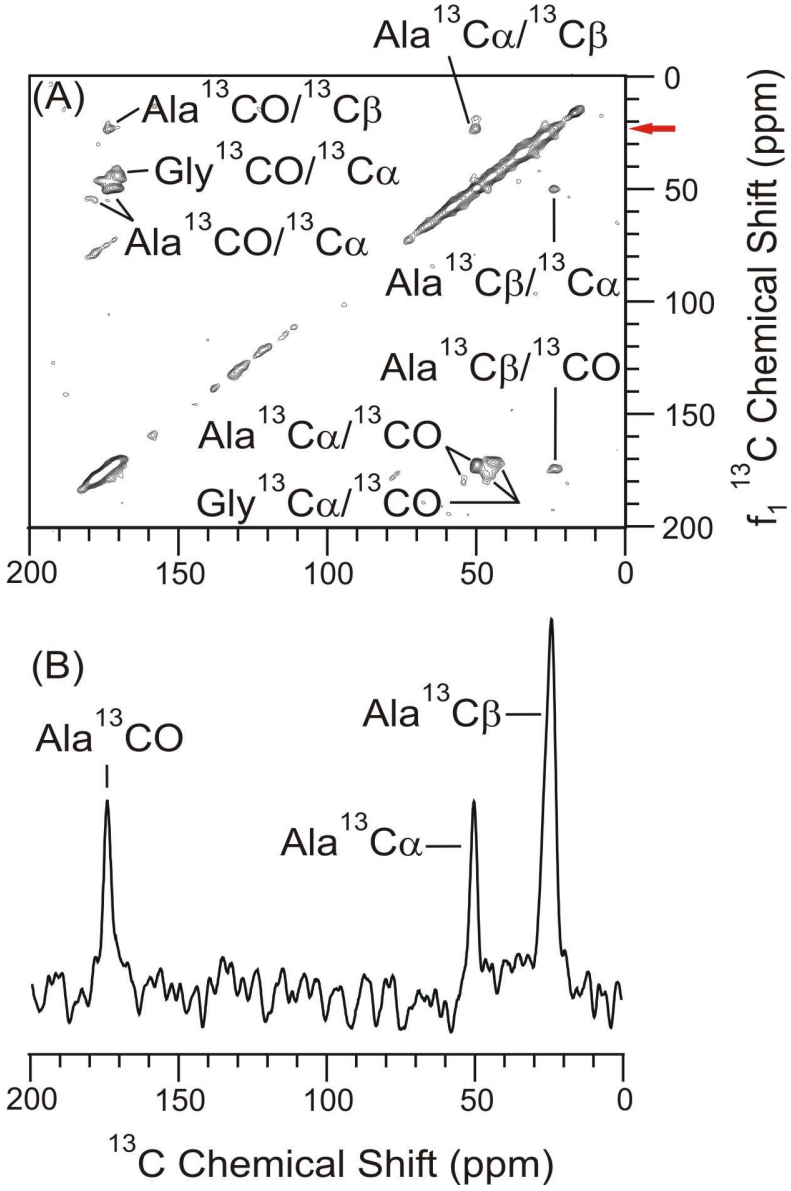

Figure 3–11: 2D PDSD ^{13}C–^{13}C spectra at 9.4 T of FP–Hairpin with uniform ^{13}C, ^{15}N labeling at Ala–6 and Gly–10 in the FP region in a POPC/POPG/Chol lipid membrane environment at ~15:1 lipid to protein ratio. (A) The 500 ms mixing time spectrum shows the intra–residue cross peaks, however no inter–residue cross peaks were observed in this sample between A6–G10. (B) The f_2 slice corresponding to the Ala $^{13}C\beta$ β–strand conformation from f_1 = 23.5 ppm is marked by the red arrow in (A). There were 300 t_1 points and 512 scans summed per t_1 point in a total time of ~64 hrs. Assignments are listed as assignment in f_2 – assignment in f_1. 200 Hz of Gaussian line broadening was applied to each dimension.

The DARR experiment was performed using a sample rotation frequency of 12 kHz and a 12 kHz ^{1}H decoupling field applied during the mixing time period of either 50 ms or 500 ms. There was no other difference between the PDSD and DARR experimental conditions. Figure 3–12 is the 50 ms mixing time DARR experiment, which was acquired in ~23 hrs and had 100 Hz of Gaussian line broadening applied to each dimension. Figure 3–13 is the 500 ms mixing time DARR experiment. In both spectra, peak signal to noise ratios of ~3 or greater were obtained for the cross peaks. In Figure 3–13, as in Figure 3–11 only the intra–residue cross peaks are observed and no unique inter–residue alanine–6 / glycine–10 cross peaks are seen. Figure 3–13 is the result of ~128 hrs of signal averaging to obtain high peak signal to noise for the cross peaks. The slice in Figure 3–12B corresponds to the Ala $^{13}C\beta$ β–strand conformation at f_1 = 23.5 ppm. The peak signal to noise is 12.7, 3.7, and 3.2 for the Ala $^{13}C\beta$, $^{13}C\alpha$, and ^{13}CO cross peaks of Figure 3–12B. Figure 3–13B corresponds to the Ala $^{13}C\beta$ β–strand conformation at f_1 = 23.5 ppm. The peak signal to noise is 10.6, 3.9, and 2.8 for the Ala $^{13}C\beta$, $^{13}C\alpha$, and ^{13}CO cross peaks of Figure 3–13B.

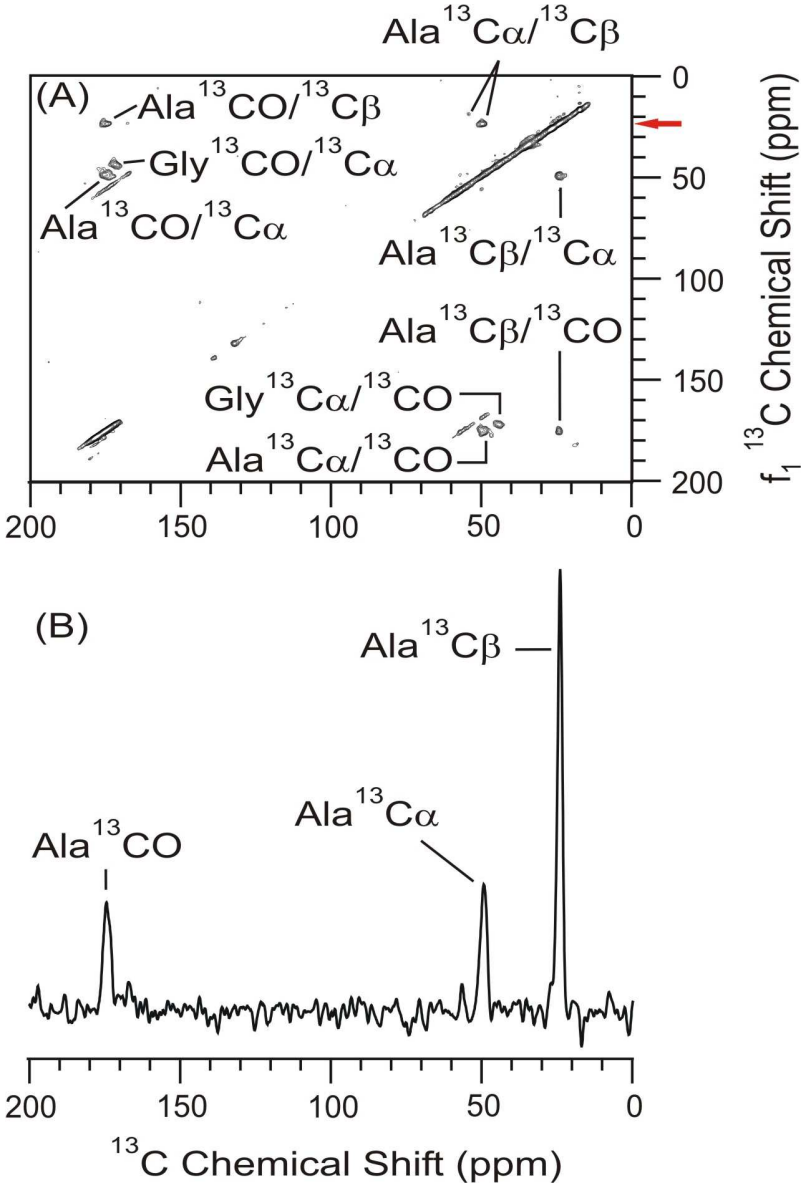

Figure 3–12: 2D DARR ^{13}C–^{13}C spectra at 9.4 T of FP–Hairpin with uniform ^{13}C, ^{15}N labeling at Ala–6 and Gly–10 in the FP region in a POPC/POPG/Chol lipid membrane environment at ~15:1 lipid to protein ratio. (A) The 50 ms mixing time spectrum shows the intra–residue cross peaks. (B) The f_2 slice corresponding to the Ala $^{13}C\beta$ β–strand conformation from f_1 = 23.5 ppm is marked by the red arrow in (A). There were 300 t_1 points and 256 scans summed per t_1 point in a total time of ~23 hrs. Assignments are listed as assignment in f_2 – assignment in f_1. 100 Hz of Gaussian line broadening was applied to each dimension. The MAS and DARR frequencies were 12 kHz.

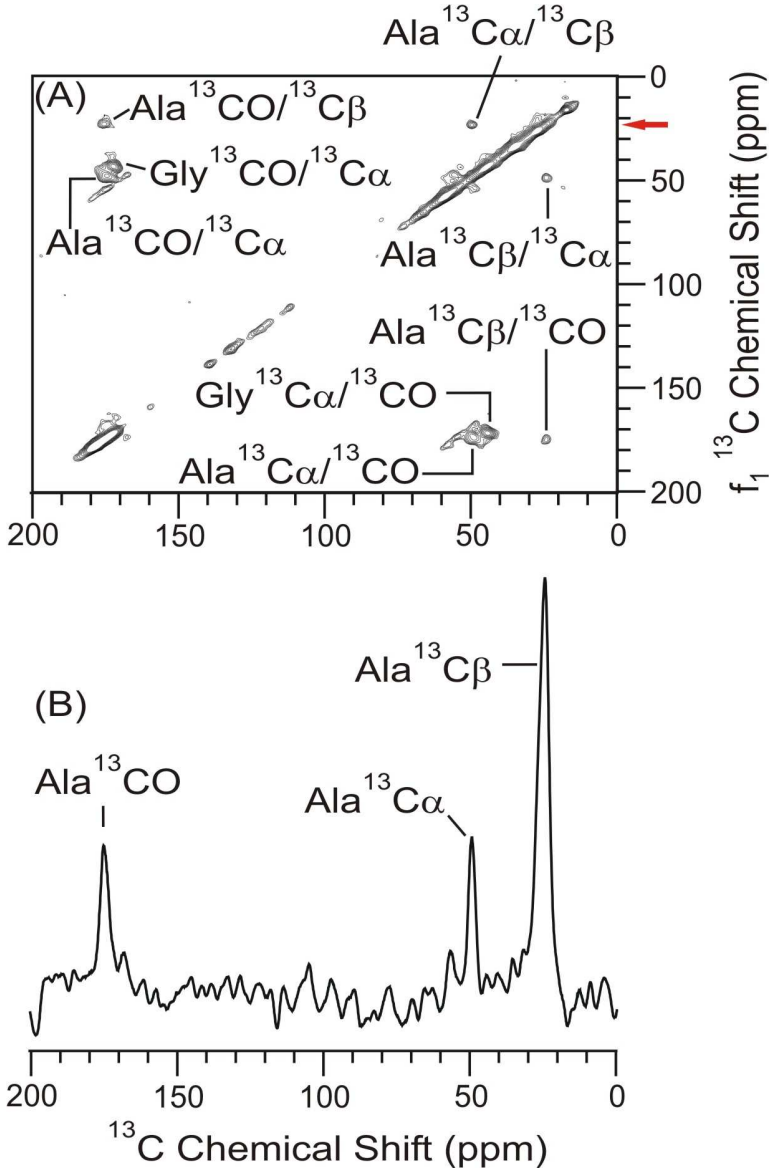

Figure 3–13: 2D DARR ^{13}C–^{13}C spectra at 9.4 T of FP–Hairpin with uniform ^{13}C, ^{15}N labeling at Ala–6 and Gly–10 in the FP region in a POPC/POPG/Chol lipid membrane environment at ~15:1 lipid to protein ratio. (A) The 500 ms mixing time spectrum shows the intra–residue cross peaks, however no inter–residue cross peaks were observed in this sample between A6–G10. (B) The f_2 slice corresponding to the Ala $^{13}C\beta$ β–strand conformation from f_1 = 23.5 ppm is marked by the red arrow in (A). There were 300 t_1 points and 1024 scans summed per t_1 point in a total time of ~128 hrs. Assignments are listed as assignment in f_2 – assignment in f_1. 200 Hz of Gaussian line broadening was applied to each dimension. The MAS and DARR frequencies were 12 kHz.

The data for the chemical shifts (CS) and the populations (Pop) for both the PDSD and the DARR experiments for the FP–Hairpin UA6/UG10 15:1 lipid to protein loading sample are presented in Table 3–3. Data for the 50 ms and 500 ms DARR experiment were determined from Figures 3–12 and 3–13 respectively. The PDSD 50 ms and 500 ms data were determined from Figures 3–10 and 3–11 respectively. The 50 ms data for both the DARR and the PDSD experiment are consistent, showing ~70 – 85% β–strand conformation and chemical shifts that are consistent between the two experiments.

The data for the 500 ms mixing time are consistent with the 50 ms mixing time for the PDSD experiment in both the chemical shifts and the relative populations of helical and β–strand. The chemical shifts obtained from the DARR and PDSD 500 ms experiments are consistent between both experiments and with previous work for FP–Hairpin. The populations were not determined for the DARR experiment due to limited signal averaging resulting in few helical cross peaks being observed above the noise level for the Ala–6 and Gly–10 residues.

Table 3–3: Chemical shift (CS) and relative populations (Pop) for the FP–Hairpin UA6/UG10 sample with loading at 15:1 in cholesterol containing membranes at 9.4 T with the shifts reported as the (f_2, f_1) convention. Comparison of DARR and PDSD spectra.

15:1 Loading of FP–Hairpin in POPC / POPG / Chol Membranes									
Field		**9.4 T**				**9.4 T**			
Pulse Sequence		**DARR**				**PDSD**			
Mixing Time		**50 ms**		**500 ms**		**50 ms**		**500 ms**	
Assignment		**CS**	**Pop (%)**	**CS**	**Pop (%)**	**CS**	**Pop (%)**	**CS**	**Pop (%)**
A Cα / A Cβ	**Helix**	53.9, 18.9	23.2	–	–	–	–	–	–
	β–strand	49.4, 23.7	76.8	49.2, 23.8	–	50.2, 23.7	–	50.3, 23.6	–
A Cα / A CO	**Helix**	–	–	–	–	54.6, 181.1	13.5	54.2, 180.2	12.7
	β–strand	49.4, 175.0	–	48.5, 173.9	–	50.2, 173.6	86.5	49.8, 172.4	87.3
A Cβ / A CO	**Helix**	–	–	–	–	–	–	–	–
	β–strand	23.8, 175.3	–	23.8, 175.0	–	23.9, 173.9	–	23.5, 174.3	–
A CO / A Cα	**Helix**	–	–	–	–	–	–	178.6, 55.4	11.6
	β–strand	175.4, 48.7	–	174.3, 48.2	–	172.9, 50.0	–	172.2, 49.9	88.4
A CO / A Cβ	**Helix**	–	–	–	–	–	–	–	–
	β–strand	175.2, 23.7	–	174.9, 23.4	–	173.8, 23.7	–	174.0, 23.8	–
A Cβ / A Cα	**Helix**	–	–	–	–	–	–	–	–
	β–strand	23.8, 49.1	–	23.8, 49.1	–	23.9, 50.3	–	23.9, 50.4	–
G Cα / G CO	**Helix**	46.4, 177.3	30.8	46.0, 176.2	21.5	46.8, 176.8	35.2	46.6, 176.2	32.0
	β–strand	43.9, 171.9	69.2	43.9, 171.8	78.5	44.3, 171.2	64.8	44.3, 171.3	68.0
G CO / G Cα	**Helix**	–	–	–	–	174.8, 46.4	27.8	176.2, 46.7	31.8
	β–strand	171.7, 43.7	–	172.0, 43.7	–	171.5, 44.1	72.2	171.1, 44.5	68.2

Average populations and their standard deviations for the FP–Hairpin UA6/UG10 sample with the 15:1 lipid to protein ratio in POPC/POPG/Chol lipid membrane environment using the 50 ms mixing time and DARR sequence are presented in Table 3–3. The Ala–6 residue is 23.2% helical and 76.8% β–strand conformation. The Gly–10 residue is 30.8% helical and 69.2% β–strand conformation. The standard deviation of the populations for the Ala–6 and Gly–10 residues were not able to be determined due to the sample size of N=1. The average populations and their standard deviations for the FP–Hairpin UA6/UG10 sample at 15:1 lipid to protein loading with the 50 ms mixing time and the PDSD experiment were determined from data in Table 3–3. The Ala–6 residue is 13.5% helical and 86.5% β–strand conformation. The Gly–10 residue is 31.5 ± 5.2 % helical and 68.5 ± 5.2 % β–strand conformation. No standard deviation could be determined for the populations of the helical and β–strand conformations for the Ala–6 residue due to N=1. The Gly–10 had N=2, so the standard deviation for the helical and β–strand conformation could be determined using Equation 3–2.

Comparison of the DARR vs. PDSD pulse sequence for populations of the helical and β–strand conformation for the Ala–6 and Gly–10 residues suggests a general agreement between the two sequences. For Ala–6, the helical populations are ~14% and ~23% for the PDSD and the DARR experiment respectively. The standard deviation was not able to be determined for these samples, the average helical and β–strand populations are within 10% of each other. For the Gly–10 residue, the helical conformation was ~30% for both the PDSD and the DARR experiment, suggesting that there is no significant difference between the two experiments. Both experiments have predominantly β–strand conformation for the off diagonal cross peaks for the 15:1 lipid to protein loading.

Figure 3–14 highlights a direct comparison of the 500 ms PDSD and DARR experiments performed at 12 kHz spinning frequency. The ^{1}H decoupling during the mixing time was either 0 or 12 kHz for (A) and (B) respectively. Slices shown in Figure 3–14C and 3–14D correspond to the Ala ^{13}Cβ β–strand chemical shift at f_1 = 23.5 ppm. From Figure 3–14 there are no major difference between the two experiments. 12 kHz was not an optimal spinning frequency as seen by the spectra where the spinning sidebands are not well separated from the off diagonal cross peaks near the ^{13}Cα/^{13}CO and ^{13}CO/^{13}Cα region. Experiments were also performed under mismatched DARR and spinning frequencies, with a sample rotation of 10 kHz and the ^{1}H DARR frequency of 12 kHz. No difference was observed compared to matching DARR and spinning frequencies as seen in Figures 3–15 and 3–16 for the 50 ms and 500 ms data. The peak signal to noise ratios in Figure 3–14C and 3–14D are very similar, with the Ala ^{13}Cβ, ^{13}Cα, and ^{13}CO peaks having peak signal to noise ratios of 7.7, 3.5, and 3.3 in Figure 3–14C and the ratios were 7.5, 3.0, and 3.1 in Figure 3–14D.

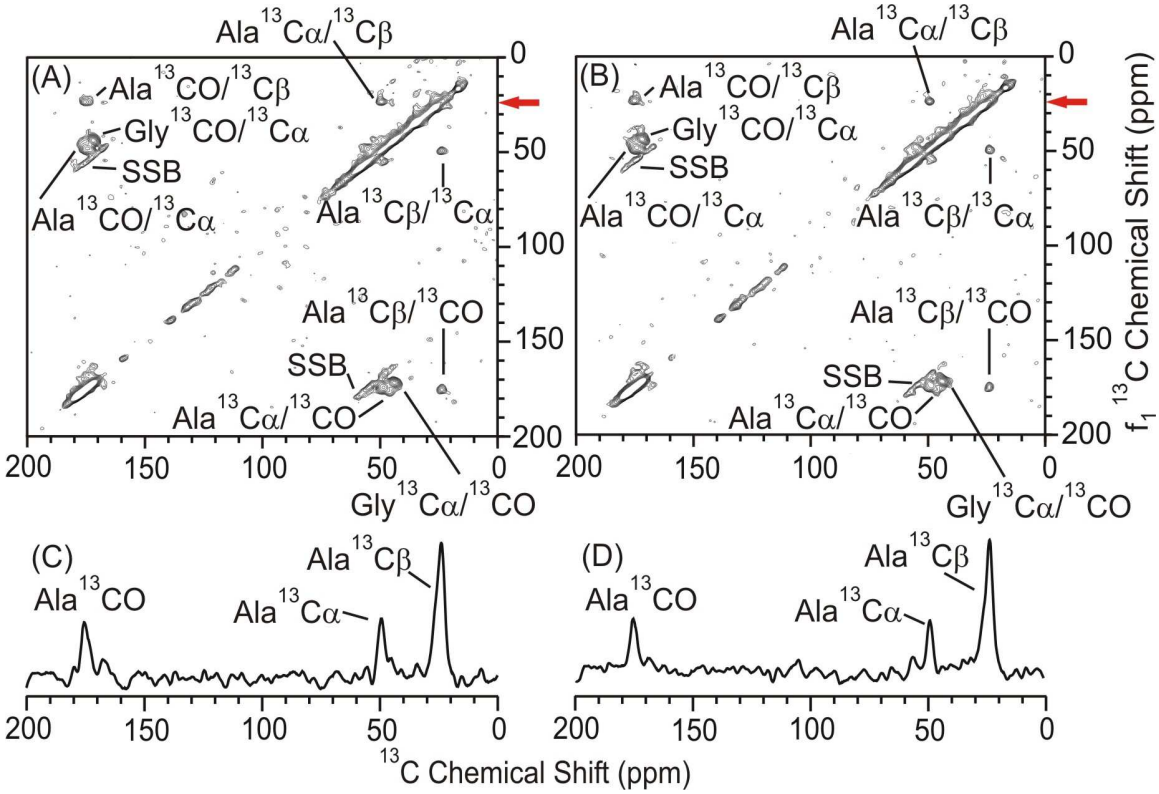

Figure 3–14: Comparison between the (A) 2D PDSD and (B) 2D DARR ^{13}C–^{13}C data from FP–Hairpin UA6/UG10 at 15:1 loading in a POPC/POPG/Chol lipid membrane environment with a 500 ms mixing time. (C) The f_2 slice corresponding to the Ala $^{13}C\beta$ β–strand conformation from f_1 = 23.5 ppm is marked by the red arrow in (A). (D) The f_2 slice corresponding to the Ala $^{13}C\beta$ β–strand conformation from f_1 = 23.5 ppm is marked by the red arrow in (B). Assignments are listed as assignment in f_2 – assignment in f_1. MAS was 12 kHz in both (A,B) and the DARR frequency was 0 and 12 kHz during the mixing period in (A) and (B) respectively. There were 300 t_1 points and 1024 scans summed per t_1 point in a total time of ~128 hrs for each spectrum. Spinning sidebands are labeled as SSB. 200 Hz of Gaussian line broadening was applied to each dimension for the two spectra.

Figures 3–15 and 3–16 are the miss–matched conditions of 12 kHz ^{1}H DARR and 10 kHz MAS frequencies. Figure 3–15 is the 50 ms exchange time used to determine the intra–residue assignment and Figure 3–16 is the 500 ms exchange time. Data for the chemical shifts and the populations determined under the miss–matched conditions are presented in Table 3–4.

The slice in Figure 3–15B corresponds to the Ala ^{13}Cβ β–strand conformation at f_1 = 23.5 ppm with the peak signal to noise ratios of 19.1, 8.3, and 8.1 for the Ala ^{13}Cβ, ^{13}Cα, and ^{13}CO cross peaks. Figure 3–16B corresponds to the Ala ^{13}Cβ β–strand conformation at f_1 = 23.5 ppm with the peak signal to noise ratios of 7.7, 4.0, and 3.8 for the Ala ^{13}Cβ, ^{13}Cα, and ^{13}CO cross peaks of Figure 3–16B. The data agrees well with the data presented for the 2D ^{13}C–^{13}C PDSD or DARR experiment where the DARR and the spinning frequencies were the same.

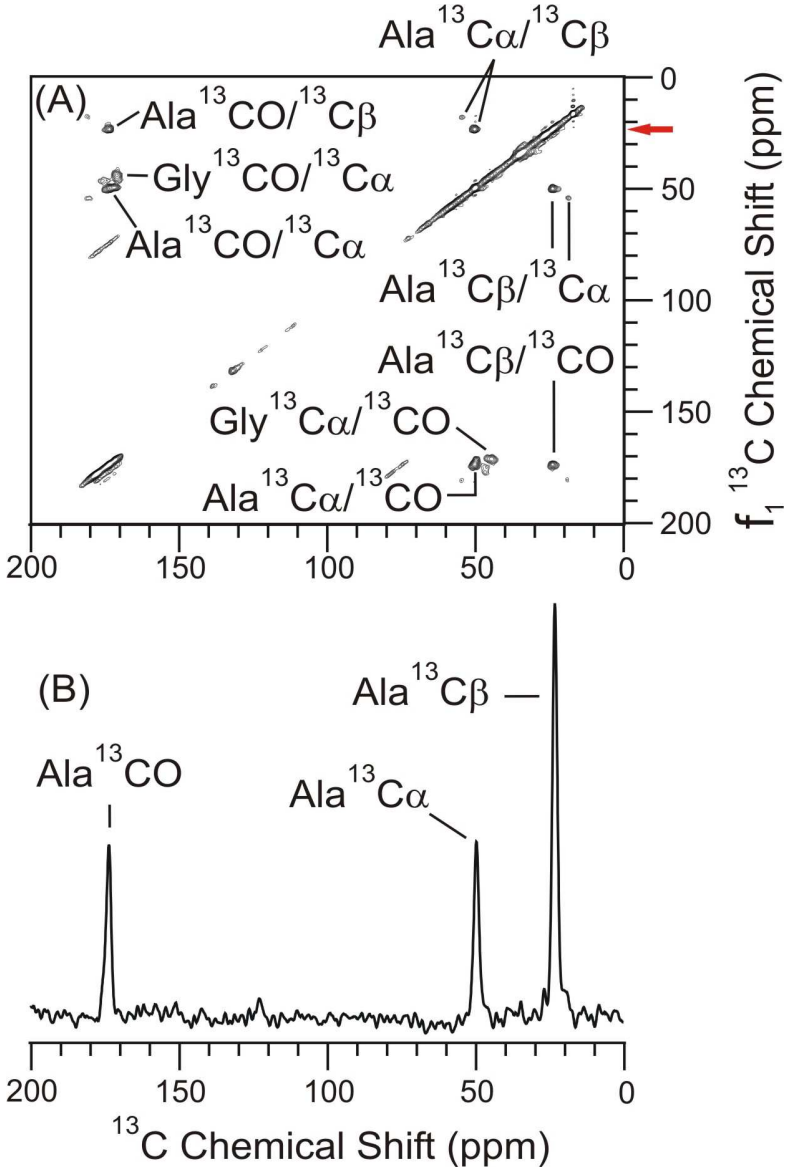

Figure 3–15: 2D DARR ^{13}C–^{13}C spectra at 9.4 T of FP–Hairpin with uniform ^{13}C, ^{15}N labeling at Ala–6 and Gly–10 in the FP region in a POPC/POPG/Chol lipid membrane environment at ~15:1 lipid to protein ratio. (A) The 50 ms mixing time spectrum shows the intra–residue cross peaks. (B) The f_2 slice corresponding to the Ala $^{13}C\beta$ β–strand conformation from f_1 = 23.5 ppm is marked by the red arrow in (A). There were 300 t_1 points and 512 scans summed per t_1 point in a total time of ~45 hrs. Assignments are listed as assignment in f_2 – assignment in f_1. 100 Hz of Gaussian line broadening was applied to each dimension. The MAS frequency was 10 kHz and DARR frequency was 12 kHz.

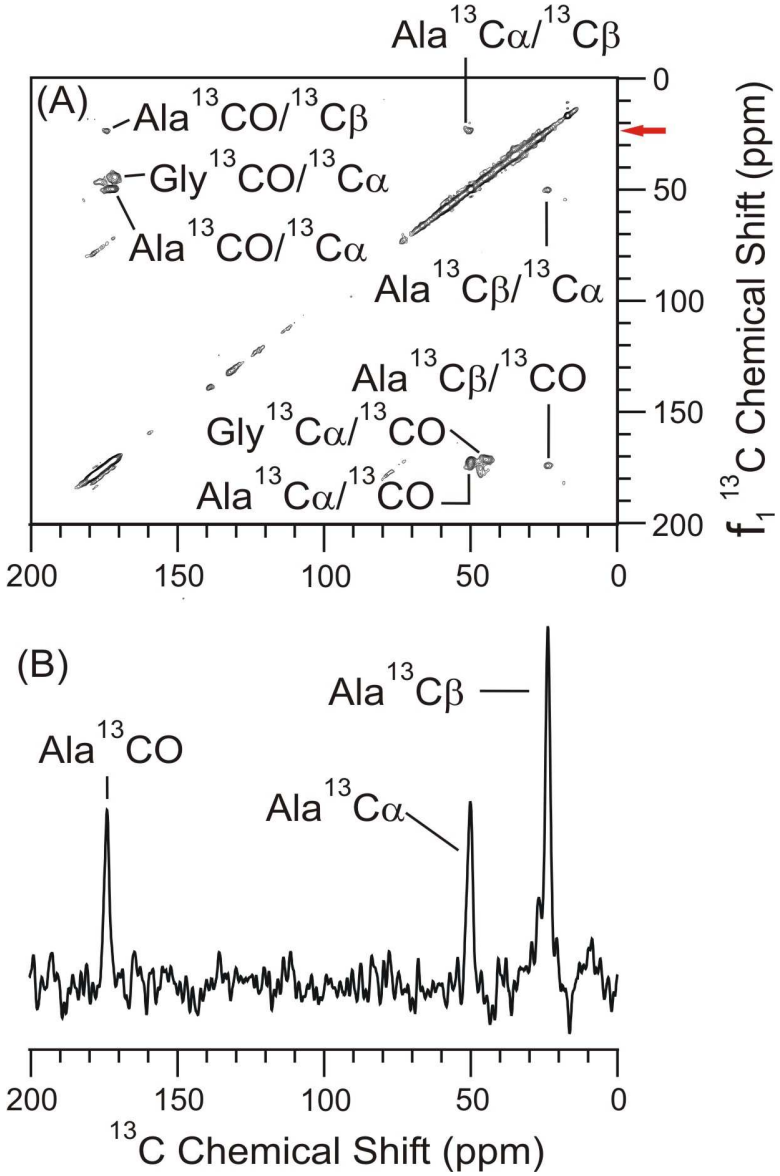

Figure 3–16: 2D DARR ^{13}C–^{13}C spectra at 9.4 T of FP–Hairpin with uniform ^{13}C, ^{15}N labeling at Ala–6 and Gly–10 in the FP region in a POPC/POPG/Chol lipid membrane environment at ~15:1 lipid to protein ratio. (A) The 500 ms mixing time spectrum shows the intra–residue cross peaks, however no inter–residue cross peaks were observed in this sample between A6–G10. (B) The f_2 slice corresponding to the Ala $^{13}C\beta$ β–strand conformation from f_1 = 23.5 ppm is marked by the red arrow in (A). There were 300 t_1 points and 768 scans summed per t_1 point in a total time of ~96 hrs. Assignments are listed as assignment in f_2 – assignment in f_1. 100 Hz of Gaussian line broadening was applied to each dimension. The MAS frequency was 10 kHz and DARR frequency was 12 kHz.

Table 3–4: Chemical shift (CS) and relative populations (Pop) for the FP–Hairpin UA6/UG10 sample with loading at 15:1 in cholesterol containing membranes for miss–matched DARR and spinning frequencies. The shifts are reported using the (f_2, f_1) convention.

Loading		**15 : 1**			
Composition		**POPC / POPG / Chol.**			
Field		**9.4 T**			
Conditions		**MAS = 10 kHz DARR = 12 kHz**			
Mixing Time		**50 ms**		**500 ms**	
Assignment		**CS**	**Pop (%)**	**CS**	**Pop (%)**
A Cα / A Cβ	**Helix**	54.5, 18.2	18.5	–	–
	β–strand	50.2, 23.8	81.5	45.5, 23.6	–
A Cα / A CO	**Helix**	54.73, 181.1	11.2	–	–
	β–strand	50.2, 173.8	88.8	49.9, 172.2	–
A Cβ / A CO	**Helix**	18.9, 180.8	14.6	–	–
	β–strand	23.9, 173.9	85.4	23.9, 174.2	–
A CO / A Cα	**Helix**	180.8, 54.7	12.4	–	–
	β–strand	173.7, 50.2	87.6	172.0, 49.9	–
A CO / A Cβ	**Helix**	181.1, 18.1	15.5	–	–
	β–strand	173.8, 23.8	84.5	174.0, 23.8	–
A Cβ / A Cα	**Helix**	18.5, 54.6	18.7	–	–
	β–strand	23.8, 50.4	81.3	23.8, 50.3	–
G Cα / G CO	**Helix**	46.5, 176.3	29.1	46.7, 176.6	27.9
	β–strand	44.4, 171.5	70.9	44.9, 171.3	72.1
G CO / G Cα	**Helix**	176.2, 47.0	26.2	176.2, 46.8	26.5
	β–strand	171.2, 44.4	73.8	171.3, 44.5	73.5

The 50 ms data was determined from Figure 3–15 and the 500 ms data was determined from Figure 3–16. The average population ± the standard deviation were calculated for the 50 ms sample with a MAS frequency of 10 kHz and a ^{1}H DARR frequency of 12 kHz. Ala–6 was 15.2 ± 3.1 % helical and 84.8 ± 3.1 % β–strand. The Gly–10 residue was 27.7 ± 2.1 % helical and 72.3 ± 2.1 % β–strand. The populations of helical and β–strand conformations for alanine–6 and glycine–10 do not overlap within 1 σ of each other, however the residues are consistent in that they both clearly favor the β–strand conformation. A complete comparison of the data is presented in Table 3–5 where the samples, their lipid to protein loadings, and their populations (average ± standard deviation) are all presented. As can be seen by the data presented, a miss–matched DARR and MAS condition will still provide correct data about the populations and chemical shifts of the spin systems. Work by Takegoshi and co–workers has also shown that slight misadjustments of the ^{1}H rf field and the MAS frequency are not crucial.[18]

Table 3–5: Comparison of all the populations determined for the FP–Hairpin UA6/UG10 samples with the 2D ^{13}C–^{13}C 50 ms mixing time experiments presented in Chapter 3 with their loadings and populations of the helical and β–strand conformations in a lipid membrane environment.

Sample Experiment	Lipid	Ala–6 Helical ± σ	Ala–6 β–strand ± σ	Gly–10 Helical ± σ	Gly–10 β–strand ± σ
40:1 DARR	PC/PG /Chol	51.0 ± 5.9 %	49.0 ± 5.9 %	48.7 ± 2.0 %	51.3 ± 2.0 %
40:1 DARR	PC/PG	52.5 ± N.D. %	47.5 ± N.D. %	61.5 ± 0.0 %	38.5 ± 0.0 %
25:1 DARR	PC/PG /Chol	49.9 ± 7.0 %	50.1 ± 7.0 %	50.1 ± 4.6 %	49.9 ± 4.6 %
25:1 DARR	PC/PG	41.6 ± 5.6 %	58.4 ± 5.6 %	37.9 ± 2.5 %	62.1 ± 2.5 %
15:1 DARR	PC/PG/ Chol	23.2 ± N.D. %	76.8 ± N.D. %	30.8 ± N.D. %	69.2 ± N.D. %
15:1 PDSD	PC/PG/ Chol	13.5 ± N.D. %	86.5 ± N.D. %	31.5 ± 5.2 %	68.5 ± 5.2 %
15:1 Miss–match	PC/PG/ Chol	15.2 ± 3.1 %	84.8 ± 3.1 %	27.7 ± 2.1 %	72.3 ± 2.1 %

In Table 3–5, N.D. refers to not determined, and that occurred if the sample size was N=1 for that conformation. The populations for the miss–matched FP–Hairpin 15:1 lipid to protein loading sample for Ala–6 is in agreement with the data for the PDSD experiment. For Gly–10, the populations determined from the DARR, PDSD, and the miss–matched DARR experiment are all within one standard deviation of each other, which is a good agreement.

Conclusions

2D ^{13}C–^{13}C experiments with either the PDSD or the DARR pulse sequence were performed on five different FP–Hairpin UA6/UG10 samples with different lipid to protein loadings. Samples contained the isotopic labeling in the FP domain. The initial work of ~40:1 lipid to protein loading in cholesterol containing membranes or cholesterol depleted membranes

were performed using ~0.4 μmoles of protein. These experiments suffered from poor peak signal to noise in the off diagonal cross peaks for the 50 ms mixing time and observation of the helical and β–strand conformation for the Ala–6 and Gly–10 residues. Figure 3–3 is the spectra for the 1000 ms mixing time experiment for the 40:1 sample with the data presented in Table 3–1. The 1000 ms mixing time was not feasible for this sample due to the lack of peak signal to noise for the ^{13}C resonances which resulted in the lack of observable cross peaks for this sample.

The second group of samples were the 25:1 lipid to protein loadings in either cholesterol containing or cholesterol depleted lipid membrane environments contained ~1 μmole of protein each. Populations and chemical shift results at the 25:1 and 40:1 lipid to protein loadings were observed for the α–helical and β–strand conformations of the intra–residue assignments, however the 25:1 samples had better peak signal to noise ratios for the cross peaks due to the increased protein content and ~50% longer signal averaging time. The ~25:1 loading samples contained ~1 μmole of FP–Hairpin, yet still required long signal averaging times to produce high peak signal to noise ratios for the cross peaks with a 50 ms mixing time spectrum acquired in ~3 days or with a 500 ms mixing time spectrum acquired in ~8 days. The 500 ms experiment did not contain any unique inter–residue cross peaks between the alanine–6 / glycine–10 residues like the ones observed in the FP23 spectra with the same labeling scheme. The observed secondary structure of FP–Hairpin in either cholesterol containing or cholesterol depleted membranes was a mix of the helical and β–strand conformations for both the 40:1 and the 25:1 lipid to protein loadings, suggesting that cholesterol does not affect the secondary structure of the fusion peptide region of FP–Hairpin in the same manner as just the FP23 peptide when prepared at neutral pH. One possible reason is that the SHB appendage attached to the FP domain in FP–Hairpin affects the FP domain's registry. This will be discussed in more detail in Chapter 4. The FP–Hairpin

protein having both the helical and β–strand conformations in cholesterol depleted membranes agrees with previous work for FP23 in cholesterol depleted membranes.[8–10] However, FP23 adopts predominantly β–strand conformation in cholesterol enriched membranes, which was not observed for FP–Hairpin. It appears that the loading affect of going from 40:1 to 25:1 does not significantly alter the distribution of secondary structures of FP–Hairpin, which is different than that of FP23.[10, 11]

A possible reason for observing both the helical and β–strand conformation at the Ala–6 and Gly–10 residues could be that some of the FP domain of FP–Hairpin protein is not completely membrane inserted. The protein which is not inserted into the membrane is precipitated due to the sample preparation buffer conditions. As will be discussed in more detail in Chapter 4 and Appendix I, it is possible that the β–strand conformation is the membrane inserted protein and that the helical conformation corresponds to the precipitated protein form of the Ala–6 and Gly–10 residues. Chapter 2 presented the sample preparation protocol for preparing the protein – lipid vesicles, where the protein was at pH 3 and the vesicles were at pH 7. A recent study from Sackett and co–workers in 2011 discovered that the FP–Hairpin protein was not soluble at pH 7.[19] Chapter 4 will present a sample of FP–Hairpin UA6/UG10 which was prepared at pH 3 and then pH swapped to pH 7 and was studied by SSNMR to avoid precipitated protein.

The fifth sample contained ~2 μmoles of FP–Hairpin with UA6/UG10 labeling in cholesterol containing membranes at ~15:1 lipid to protein mole ratio. 2D ^{13}C–^{13}C experiments with this sample resulted in an increased ^{13}C signal with a predominantly β–strand conformation and high peak signal to noise of the cross peaks, which resulted in shorter signal averaging times.

The 2D ^{13}C–^{13}C PDSD and DARR 500 ms experiments did not contain any unique inter–reside alanine–6 / glycine–10 cross peaks like those observed for FP23 with the same labeling scheme.[7] This suggests that the FP–Hairpin's fusion peptide region adopts a different tertiary structure when the SHB is formed compared to the FP23 in the lipid membrane environment. Chapter 4 will present high field SSNMR data to support the claim that FP–Hairpin's FP domain adopts a different tertiary structure compared to the FP23 peptide and provide possible explanations for the adoption of the different tertiary structure of the FP domain.

REFERENCES

References

1. Yang, J., C.M. Gabrys, and D.P. Weliky, *Solid–state nuclear magnetic resonance evidence for an extended beta strand conformation of the membrane–bound HIV–1 fusion peptide.* Biochemistry, 2001. **40**(27): p. 8126–37.

2. Yang, R., J. Yang, and D.P. Weliky, *Synthesis, enhanced fusogenicity, and solid state NMR measurements of cross–linked HIV–1 fusion peptides.* Biochemistry, 2003. **42**(12): p. 3527–35.

3. Yang, J. and D.P. Weliky, *Solid–state nuclear magnetic resonance evidence for parallel and antiparallel strand arrangements in the membrane–associated HIV–1 fusion peptide.* Biochemistry, 2003. **42**(40): p. 11879–90.

4. Yang, J., et al., *Oligomeric beta–structure of the membrane–bound HIV–1 fusion peptide formed from soluble monomers.* Biophys J, 2004. **87**(3): p. 1951–63.

5. Yang, R., et al., *A trimeric HIV–1 fusion peptide construct which does not self–associate in aqueous solution and which has 15–fold higher membrane fusion rate.* J Am Chem Soc, 2004. **126**(45): p. 14722–3.

6. Bodner, M.L., *Solid state nuclear magnetic resonance of the HIV–1 and influenza fusion peptides associated wtih membranes*. 2006, Michigan State University: East Lansing, MI.

7. Qiang, W., M.L. Bodner, and D.P. Weliky, *Solid–state NMR spectroscopy of human immunodeficiency virus fusion peptides associated with host–cell–like membranes: 2D correlation spectra and distance measurements support a fully extended conformation and models for specific antiparallel strand registries.* J Am Chem Soc, 2008. **130**(16): p. 5459–71.

8. Wasniewski, C.M., et al., *Solid–state nuclear magnetic resonance studies of HIV and influenza fusion peptide orientations in membrane bilayers using stacked glass plate samples.* Chem Phys Lipids, 2004. **132**(1): p. 89–100.

9. Zheng, Z., et al., *Conformational flexibility and strand arrangements of the membrane–associated HIV fusion peptide trimer probed by solid–state NMR spectroscopy.* Biochemistry, 2006. **45**(43): p. 12960–75.

10. Rafalski, M., J.D. Lear, and W.F. DeGrado, *Phospholipid interactions of synthetic peptides representing the N– terminus of HIV gp41*. Biochemistry, 1990. **29**(34): p. 7917–7922.

11. Qiang, W., J. Yang, and D.P. Weliky, *Solid–state nuclear magnetic resonance measurements of HIV fusion peptide to lipid distances reveal the intimate contact of beta strand peptide with membranes and the proximity of the Ala–14–Gly–16 region with lipid headgroups.* Biochemistry, 2007. **46**(17): p. 4997–5008.

12. Qiang, W. and D.P. Weliky, *HIV fusion peptide and its cross–linked oligomers: efficient syntheses, significance of the trimer in fusion activity, correlation of beta strand conformation with membrane cholesterol, and proximity to lipid headgroups.* Biochemistry, 2009. **48**(2): p. 289–301.

13. Qiang, W., Y. Sun, and D.P. Weliky, *A strong correlation between fusogenicity and membrane insertion depth of the HIV fusion peptide.* Proc Natl Acad Sci U S A, 2009. **106**(36): p. 15314–9.

14. Castellani, F., et al., *Structure of a protein determined by solid–state magic–angle–spinning NMR spectroscopy.* Nature, 2002. **420**(6911): p. 98–102.

15. Schmick, S.D. and D.P. Weliky, *Major Antiparallel and Minor Parallel beta Sheet Populations Detected in the Membrane–Associated Human Immunodeficiency Virus Fusion Peptide.* Biochemistry, 2010. **49**(50): p. 10623–10635.

16. Zhang, H.Y., S. Neal, and D.S. Wishart, *RefDB: A database of uniformly referenced protein chemical shifts.* Journal of Biomolecular Nmr, 2003. **25**(3): p. 173–195.

17. Sackett, K., et al., *Hairpin folding of HIV gp41 abrogates lipid mixing function at physiologic pH and inhibits lipid mixing by exposed gp41 constructs.* Biochemistry, 2009. **48**(12): p. 2714–22.

18. Takegoshi, K., S. Nakamura, and T. Terao, *13C–1H dipolar–assisted rotational resonance in magic–angle spinning NMR.* Chemical Physics Letters, 2001. **344**(5–6): p. 631–637.

19. Sackett, K., A. TerBush, and D.P. Weliky, *HIV gp41 six–helix bundle constructs induce rapid vesicle fusion at pH 3.5 and little fusion at pH 7.0: understanding pH dependence of protein aggregation, membrane binding, and electrostatics, and implications for HIV–host cell fusion.* European Biophysics Journal with Biophysics Letters, 2011. **40**(4): p. 489–502.

Chapter 4:

Solid State NMR Experiments Using High Magnetic Fields

Introduction

Solid state NMR experiments were carried out at high magnetic fields, using Bruker NMR spectrometers at 16.5 T and 21.1 T (700 and 900 MHz ^{1}H frequency) equipped with a 4 mm MAS E–free probe. Experiments performed at the high magnetic fields complement Chapter 3's work performed using a 9.4 T (400 MHz ^{1}H frequency) spectrometer equipped with a 4 mm MAS non E–free probe. This chapter also details new experiments performed at high magnetic fields which are not feasible at 9.4 T due to the lack of peak signal to noise per scan of the ^{13}C and ^{15}N nuclei compared to the higher fields and the E–free probe. The 1D ^{13}C CP and 2D ^{13}C–^{13}C PDSD / DARR experiments were performed at both 21.1 T and 9.4 T for FP–Hairpin UA6/UG10 in a POPC/POPG/Chol lipid membrane environment. The 1D double cross polarization (DCP) experiments of NCA and NCO along with the 1D ^{15}N CP were the new experiments performed at 21.1 T for the uniformly labeled N–acetyl leucine (U–NAL) setup compound and FP–Hairpin UA6/UG10. Three FP–Hairpin UA6/UG10 samples were studied, FP–Hairpin at 15:1 lipid to protein loading initially presented in Chapter 3 and two other samples with ~1 μmole of FP–Hairpin UA6/UG10 in an 8:2:5 mole ratio of POPC/POPG/Chol which was prepared at pH 3 following the Method B protocol presented in Chapter 2. The sample was

subsequently pH swapped to pH 7 and studied as well. The 15:1 lipid to protein sample will be presented first followed by the pH 3 and then the pH 7 swapped sample.

Assignments of the cross peaks in the 2D ^{13}C–^{13}C experiments were based off of the known ^{13}C peak chemical shift distributions of helical and β–strand conformations as previously described in Chapter 3.[1] The helical (H) and β–strand (β) peak chemical shift ± standard deviation for Ala $^{13}C\alpha$ are H: 54.8 ± 1.1 ppm and β: 51.5 ± 1.5 ppm, $^{13}C\beta$ are H: 18.3 ± 0.9 ppm and β: 21.1 ± 2.1 ppm, and for ^{13}CO are H: 179.4 ± 1.3 ppm and β: 176.1 ± 1.5 ppm and for Gly $^{13}C\alpha$ are H: 46.9 ± 1.1 ppm and β: 45.2 ± 1.2 ppm, and for ^{13}CO are H: 175.5 ± 1.2 ppm and β: 172.6 ± 1.6 ppm.[1]

2D ^{13}C–^{13}C Experiments at 21.1 T and 16.5 T for FP–Hairpin UA6/UG10

2D ^{13}C–^{13}C Experiments at 21.1 T

2D ^{13}C–^{13}C DARR experiments for FP–Hairpin UA6/UG10 at ~15:1 lipid to protein loading are shown in Figure 4–1 for the 50 ms mixing time and Figure 4–2 for the 500 ms mixing time. The intra–residue assignments for cross peaks were assigned from the 50 ms experiment. Intra–residue cross peaks were also observed in the 500 ms spectrum, however no alanine–6 / glycine–10 inter–residue cross peaks were observed. Peak signal to noise ratios for the Ala $^{13}C\beta$, $^{13}C\alpha$, and ^{13}CO cross peaks were 44.1, 23.7, and 14.9 respectively in Figure 4–1B from 256 t_1 points with 128 summed acquisitions per t_1 point. In comparison, the peak signal to noise ratios of the 50 ms experiment for the same FP–Hairpin sample at 9.4 T for the slice were

12.7, 3.7, and 3.2 for the Ala $^{13}C\beta$, $^{13}C\alpha$, and ^{13}CO cross peaks of Figure 3–12B acquired in 300 t_1 points with 256 summed acquisitions per t_1 point. Data at 9.4 T in Figure 3–12 was obtained in ~23 hrs and the data in Figure 4–1 were obtained in ~16 hrs at 21.1 T resulting in an approximately 4–fold increase in the ^{13}C peak signal to noise ratio being obtained in ~7 hrs less time and ~42% less acquisitions at 21.1 T than 9.4 T for the same sample.

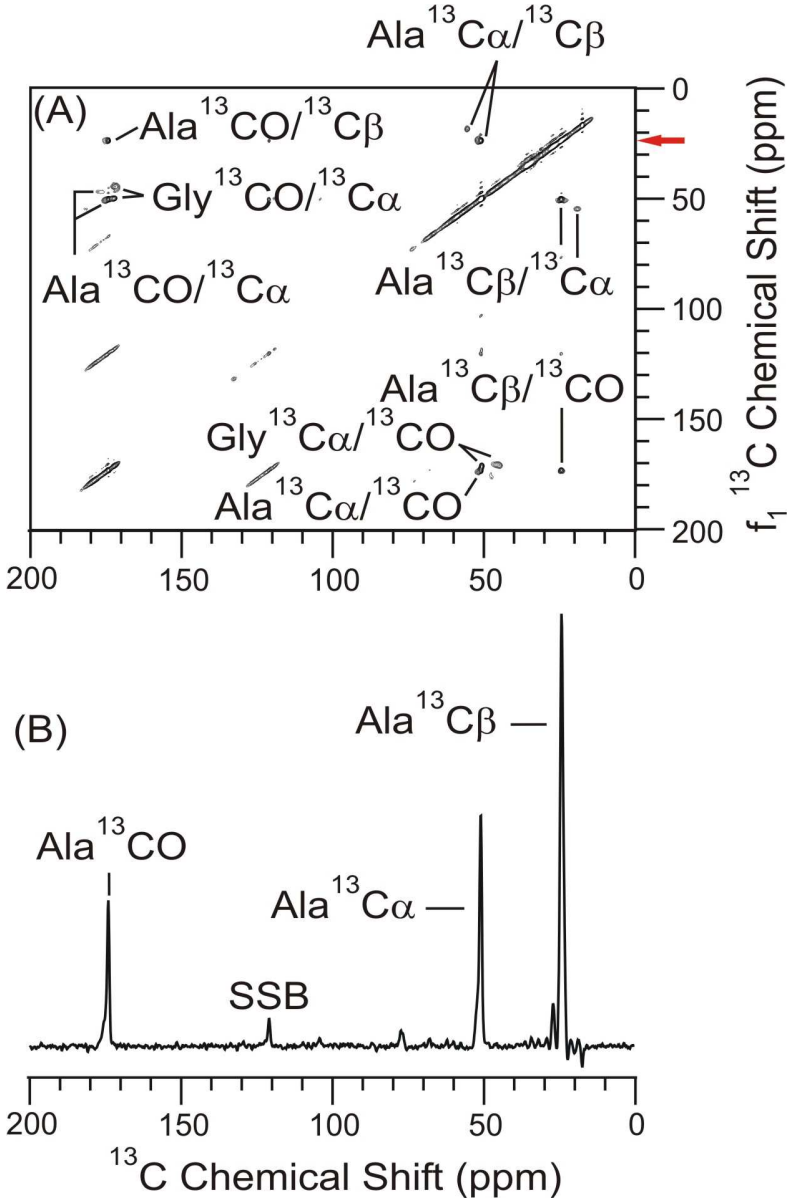

Figure 4–1: 2D DARR ^{13}C–^{13}C spectra at 21.1 T of FP–Hairpin with uniform ^{13}C, ^{15}N labeling at Ala–6 and Gly–10 in the FP region in an 8:2:5 mole ratio of POPC/POPG/Chol in a lipid membrane environment at ~15:1 lipid to protein ratio. (A) The 50 ms mixing time spectrum shows the intra–residue cross peaks. (B) The f_2 slice corresponding to the Ala $^{13}C\beta$ β–strand conformation from f_1 = 23.5 ppm is marked by the red arrow in (A). There were 256 t_1 points and 128 scans summed per t_1 point in a total time of ~16 hrs. Assignments are listed as assignment in f_2 – assignment in f_1. 100 Hz of Gaussian line broadening was applied to each dimension. A spinning sideband for the ^{13}CO peak is labeled as SSB.

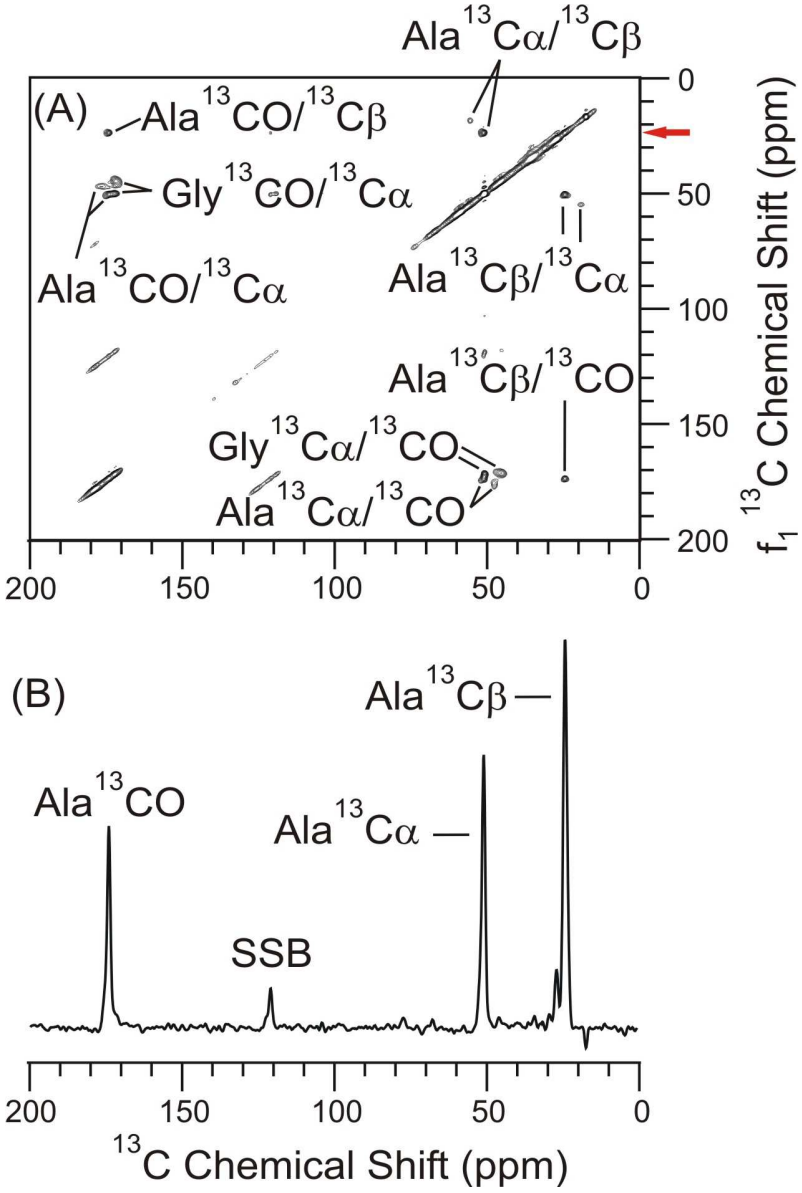

Figure 4–2: 2D DARR ^{13}C – ^{13}C spectra at 21.1 T of FP–Hairpin with uniform ^{13}C, ^{15}N labeling at Ala–6 and Gly–10 in the FP region in an 8:2:5 mole ratio of POPC/POPG/Chol in a lipid membrane environment at ~15:1 lipid to protein ratio. (A) The 500 ms mixing time spectrum shows the intra–residue cross peaks, however no inter–residue cross peaks were observed in this sample between A6 / G10. (B) The f_2 slice corresponding to the Ala $^{13}C\beta$ β–strand conformation from f_1 = 23.5 ppm is marked by the red arrow in (A). There were 256 t_1 points and 384 scans summed per t_1 point in a total time of ~55 hrs. Assignments are listed as assignment in f_2 – assignment in f_1. 200 Hz of Gaussian line broadening was applied to each dimension. A spinning sideband from the ^{13}CO peak is labeled as SSB.

Figure 4–2B has peak signal to noise ratios for the Ala $^{13}C\beta$, $^{13}C\alpha$, and ^{13}CO cross peaks of 37.7, 26.5, and 19.6 respectively at 21.1 T for the f_1 = 23.5 ppm chemical shift for the Ala $^{13}C\beta$ β–strand conformation. For the same sample and f_1 chemical shift at 9.4 T, the peak signal to noise ratios were 10.6, 3.9, and 2.8 presented in Figure 3–13B. The data in Figure 4–2 was acquired in half the time at 21.1 T (~55 hrs) as at 9.4 T (~128 hrs) and 32% less acquisitions at 21.1 T. The increased ^{13}C peak signal to noise per scan resulted in the data being acquired in fewer acquisitions at 21.1 T compared to the 9.4 T spectrometer providing significant spectrometer time savings. Time savings are beneficial for two reasons, one there is limited solids time available at the 21.1 T spectrometer. Second, it allows for more experiments to be performed or more samples to be studied in the same time frame.

No cross peaks between A6 / G10 are observed at 21.1 T with a 500 ms mixing time, confirming results from the 9.4 T data presented in Chapter 3 for the FP–Hairpin UA6/UG10 samples. This suggest that the FP region adopts a different tertiary structure compared to the FP23 peptides in the lipid membrane environment. The contacts between A6 / G10 are either not present in FP–Hairpin or they are farther than 5–6 Å away, which is the upper detection limit for the 2D ^{13}C–^{13}C experiment.[2, 3] There are two possible explanations for the lack of the A6 / G10 cross peaks. One, the FP region is pulled back by the SHB formation so that the A6 / G10 residues are not as close as they are in the FP23 peptide studies. A second possibility is that the FP splays outwards away from the A6 / G10 overlap. Both possibilities are visually presented in Figure 4–3.

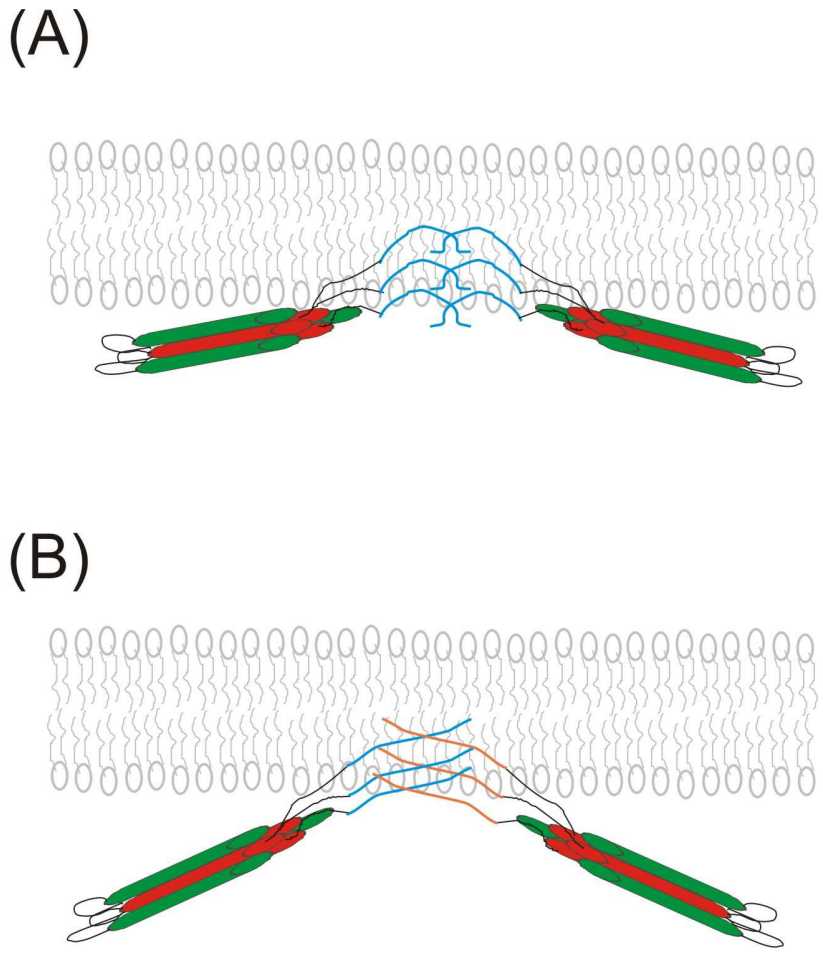

Figure 4–3: (A) The situation where antiparallel β–strands are present for the FP region (thick blue lines) with the L7/F8 overlap. This model is based off of the previous work for FP23 and also the L7/F8 contact for FP–Hairpin, and lack of A6 / G10 cross peaks. (B) The second scenario where there is an L7/F8 overlap, but the FP strands (blue and orange for visual distinction) overlap only at L7/F8 and splay outward into the lipid membrane. The red cylinder is the NHR, the green cylinder is the CHR, which for FP–Hairpin are connected by a six residue minimal linker. The FP β–strands are either (A) blue or (B) blue and orange, and are representative of residues 1–16. The black line connecting the NHR and the FP domain is consistent with residues 17 – 23 of the FP region, the NHR are residues 24 – 70, followed by residues 71–76 for the loop, and residues 77 – 115 for the CHR domain of FP–Hairpin construct.

In the first case presented in Figure 4–3A, the antiparallel β–sheets form when gp41 is in the PHI conformation. As gp41 folds into the SHB, the antiparallel β–sheets which are still established, are pulled backwards towards the SHB domain, disrupting the inter–strand contacts such as A6 / G10. There is no experimental NMR evidence for this claim yet, however SSNMR studies have shown β–strand chemical shifts for the FP region and also a L7/F8 stand crossing as probed by $^{1}H/^{13}C/^{15}N$ REDOR.[4] It would be beneficial to probe a gp41 construct which was in the PHI conformation and contained the UA6/UG10 labeling in the FP region and establish the presence or absence of the A6 / G10 cross peak by 2D $^{13}C–^{13}C$ experiments. Next, taking the same gp41 construct, try and shift from the PHI conformation to the FP–Hairpin conformation by folding the ectodomain of the NHR and CHR into the SHB formation and then probe for the A6 / G10 cross peaks using 2D $^{13}C–^{13}C$ experiments. This would yield insight into how the FP region is affected by the formation of the SHB.

Figure 4–3B presents a second way to explain the lack of A6 / G10 cross peaks in the 2D $^{13}C–^{13}C$ spectra with the 500 ms mixing time. First an antiparallel arrangement is established with strand crossings near L7/F8, as determined by $^{1}H/^{13}C/^{15}N$ REDOR.[4] As the FP–Hairpin protein has this bulky SHB formation, it will affect how the FP region is arranged. It might be possible that the FP region does not sit in a plane, but rather is positioned out of the plane of the β–sheet. Establishment of the strand crossings between L7/F8 suggests that the adjacent stands crisscross at those residues with the N–terminal residues pointed towards the membrane interior. There are two approaches to test this scenario. One is to do protein – protein distance measurements and the second is to perform protein – lipid distance measurements. The protein –

protein distance measurements can utilize the $^{1}H/^{13}C/^{15}N$ REDOR experiment to probe different labeling schemes for the ^{13}CO and ^{15}N positions along the FP backbone between positions 1 to 23 for the FP–Hairpin construct. The labels would be incorporated in the FP23(linker) peptide synthesized by SPPS. This method allows for the determination of the secondary structure of helical or β–strand at the ^{13}CO positions, and also allows for the detection of registries for the FP region of the FP–Hairpin construct. Similar work has been performed for the FP23 peptides to determine the arrangement of the β–strands and for inter–strand contacts between the antiparallel arrangements.[3, 5] Modeling of the REDOR build up curves of $\Delta S/S_0$ due to different dephasing times would then allow for fitting distances to determine the tertiary structural models of the FP region. The other approach to protein – protein measurements would be to uniformly label the protein sample, and then perform 2D $^{13}C–^{13}C$ experiments with various exchange times between 10 – 500 ms as previously done by Castellani and co–workers.[2] The cross peak intensity from the different mixing times will yield information on distance constraints. At the short mixing times, the directly bonded $^{13}C–^{13}C$ will be the most intense cross peaks observed. As the mixing time increases, cross peaks will develop between $^{13}C–^{13}C$ which are not directly bonded, such as $^{13}CO/^{13}C\beta$ and $^{13}CO/^{13}C\gamma$ to name two examples. The possibilty exists to perform 2D NCA / NCO heteronuclear experiments and then extend to 3D experiments for developing $^{15}N–^{13}C$ constraints. This wealth of data will provide both secondary and tertiary structures of the FP region of FP–Hairpin in a lipid membrane environment provided that one can obtain resolved cross peaks in the 2D experiments for the $^{13}C–^{13}C$ or $^{15}N–^{13}C$ cross peaks.

In the second case of protein – lipid experiments the $^{13}C–^{31}P$ or $^{13}C–^{19}F$ REDOR experiments could be performed to detect the distances between the FP domain backbone ^{13}CO nuclei and the ^{31}P head group of the lipid or the ^{19}F label on the acyl chain of the lipid at the C5 position. This has previously been preformed to determine the membrane location of the FP23 peptides in the membrane bilayer.[6] The problem with this approach is that the ^{19}F tend to form lipid rafts, and thus can not be 100% labeled.[6] The other problem is that with the dilute labeling of ^{19}F lipids, there is an issue with determining distances between ^{13}CO and ^{19}F residues reliably.[6] Again, build up curves obtained from $\Delta S/S_0$ REDOR data would be modeled to fit distances to the experimental data.

2D $^{13}C–^{13}C$ Experiments at 16.5 T

The FP–Hairpin UA6/UG10 15:1 lipid to protein loading sample was sent to Dr. Jochem Struppe at Bruker Biospin for analysis using a 16.5 T spectrometer (700 MHz ^{1}H frequency) equipped with a 4 mm MAS E–free probe similar to the probe used at 21.1 T. Performing the 1D ^{13}C CP ramp and the 2D $^{13}C–^{13}C$ PDSD experiment with a 50 ms mixing time at 16.5 T was done to determine if the peak signal to noise per scan enhancement observed at 21.1 T compared to 9.4 T of the FP–Hairpin UA6/UG10 sample with ~15:1 lipid to protein loading in a POPC/POPG/Chol lipid membrane environment was due to the E–free probe design, the higher field strength, or a synergy of the probe and field strength. The data from 16.5 T and 21.1 T data allows for comparison of the two field strengths whereas comparing the data from the 9.4 T and

the 16.5 T or 21.1 T fields allows for comparing the affect of the field and the probe design. Comparison of the integrated signal intensity was also considered and will be presented in the following section "Comparison of ^{13}C peak signal to noise per scan and linewidths at high magnetic fields".

Figure 4–4 is the 2D ^{13}C–^{13}C PDSD experiment with a 50 ms mixing time. The FP–Hairpin sample was packed in a 4 mm rotor, and experimental conditions between the 16.5 T and 21.1 T experiment were nearly identical. The peak signal to noise ratios in Figure 4–4B for the Ala $^{13}C\beta$, $^{13}C\alpha$, and ^{13}CO cross peaks were 22.0, 11.1, and 8.4 respectively. The data was acquired in ~16 hrs under similar conditions to the data from Figure 4–1 acquired at the 21.1 T spectrometer. Parameters for the 2D ^{13}C–^{13}C experiments at 16.5 T and 21.1 T are presented in Table 2–7.

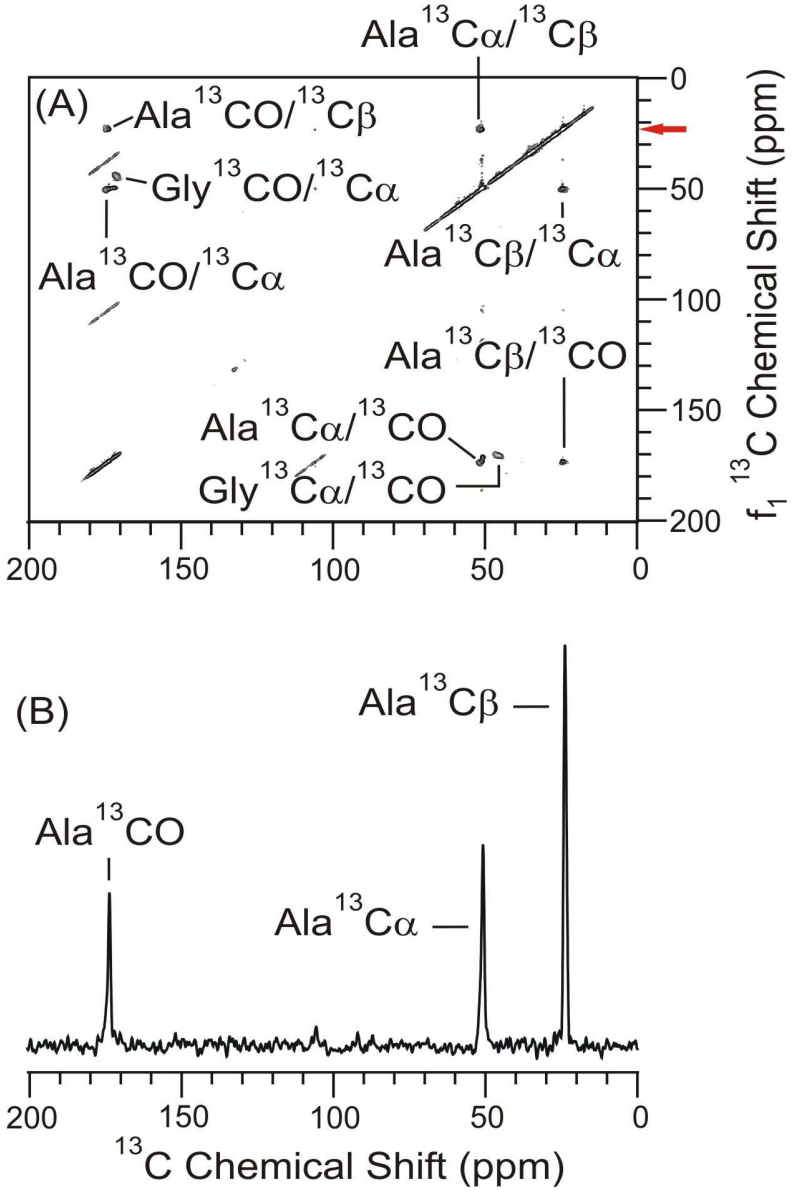

Figure 4–4: 2D PDSD ^{13}C – ^{13}C spectra at 16.5 T of FP–Hairpin with uniform ^{13}C, ^{15}N labeling at Ala–6 and Gly–10 in the FP region in an 8:2:5 molar ratio of POPC/POPG/Chol in a lipid membrane environment at ~15:1 lipid to protein ratio. (A) The 50 ms mixing time spectrum shows the intra–residue cross peaks. (B) The f_2 slice corresponding to the Ala $^{13}C\beta$ β–strand conformation from f_1 = 23.5 ppm is marked by the red arrow in (A). There were 256 t_1 points and 128 scans summed per t_1 point in a total time of ~16 hrs. Assignments are listed as assignment in f_2 – assignment in f_1. 100 Hz of Gaussian line broaden was applied to each dimension.

Table 4–1 contains the tabulated data for the chemical shifts (CS) and populations (Pop) of the 2D ^{13}C–^{13}C experiments at 21.1 T and 16.5 T. The 500 ms mixing time experiments were not performed using the 16.5 T instrument because the purpose of the experiments at 16.5 T with an E–free probe was to correlate the ^{13}C peak signal to noise per scan affect between the field and probe when comparing the 16.5 T and 21.1 T fields. We were not trying to probe for inter–residue assignments as there were no inter–residue cross peaks observed with the 500 ms mixing time using either the 9.4 T or 21.1 T spectrometer. The lack of A6 / G10 cross peaks at both 9.4 T and 21.1 T suggested that we would not expect to see the A6 / G10 cross peaks at 16.5 T either. The populations of the helical and β–strand conformations were determined as described in Chapter 3 by using the intensity of the cross peaks for the helical and β–strand chemical shifts of a specific intra–residue assignment and Equation 3–1.

Tabulated data for Table 4–1 were from Figure 4–1 and Figure 4–2 for the 21.1 T experiments with 50 ms and 500 ms mixing times and Figure 4–4 for the 16.5 T with a 50 ms exchange time. Gaussian line broadening was applied to each dimension of the 2D ^{13}C–^{13}C spectra. 100 Hz of line broadening were applied to the 50 ms spectra and 200 Hz of line broadening was applied for the 500 ms mixing time spectrum.

Table 4–1: Chemical shift (CS) and relative populations (Pop) for the FP–Hairpin UA6/UG10 sample with loading at 15:1 in cholesterol containing membranes at 16.5 T and 21.1 T with the chemical shifts reported as the (f_2, f_1) convention.

15:1 Loading of FP–HP in POPC / POPG / Chol. Membranes							
Field		**21.1 T**				**16.5 T**	
Pulse Sequence		**DARR**				**PDSD**	
Mixing Time		**50 ms**		**500 ms**		**50 ms**	
Assignment		**CS**	**Pop. (%)**	**CS**	**Pop. (%)**	**CS**	**Pop. (%)**
A Cα / A Cβ	**Helix**	55.6, 18.5	16.2	55.6, 18.5	15.1	–	–
	β–strand	51.1, 23.7	83.8	51.0, 23.7	84.9	51.0, 23.4	–
A Cα / A CO	**Helix**	–	–	–	–	–	–
	β–strand	51.1, 173.2	–	50.8, 171.5	–	51.0, 173.1	–
A Cβ / A CO	**Helix**	–	–	–	–	–	–
	β–strand	24.5, 173.3	–	24.5, 173.3	–	24.2, 173.2	–
A CO / A Cα	**Helix**	–	–	–	–	–	–
	β–strand	174.0, 50.4	–	173.0, 50.2	–	173.0, 50.0	–
A CO / A Cβ	**Helix**	–	–	–	–	–	–
	β–strand	174.0, 23.7	–	174.0, 23.7	–	173.9, 23.3	–
A Cβ / A Cα	**Helix**	19.2, 54.7	15.2	19.1, 54.7	14.4	–	–
	β–strand	24.5, 50.4	84.8	24.5, 50.4	85.6	24.2, 50.2	–
G Cα / G CO	**Helix**	47.5, 176.5	29.6	47.5, 176.3	32.9	–	–
	β–strand	45.4, 170.9	70.4	45.3, 170.9	67.1	45.2, 170.6	–
G CO / G Cα	**Helix**	177.4, 46.9	27.2	46.8, 176.3	26.1	–	–
	β–strand	171.8, 44.6	72.8	44.6, 171.6	73.9	171.5, 44.4	–

Average populations and their standard deviations for the FP–Hairpin UA6/UG10 ~15:1 lipid to protein loading sample in an 8:2:5 molar ratio of POPC/POPG/Chol in a lipid membrane environment for the 2D ^{13}C–^{13}C DARR experiment with a 50 ms mixing time at 21.1 T presented in Table 4–1 are reported below. The Ala–6 residue is 15.7 ± 0.7 % helical and 84.3 ± 0.7 % β–strand conformation. The Gly–10 residue is 28.4 ± 1.7 % helical and 71.6 ± 1.7 % β–strand conformation. The average populations and their standard deviations for the FP–Hairpin UA6/UG10 15:1 lipid to protein loading sample in a POPC/POPG/Chol lipid membrane environment for the 2D ^{13}C–^{13}C PDSD experiment with a 50 ms mixing time at 16.5 T in Table 4–1 were not determined due to the lack of observable helical signal at the presented contour levels. The standard deviation was calculated using Equation 3–2 as presented in Chapter 3's section "FP–Hairpin in Cholesterol Depleted Membranes". Table 4–2 compares the 9.4 T, 16.5 T, and the 21.1 T populations for the FP–Hairpin UA6/UG10 sample with ~15:1 lipid to protein loading in the POPC/POPG/Chol lipid membrane environment.

Table 4–2: Comparison of populations and standard deviations for the FP–Hairpin UA6/UG10 sample at 9.4 T, 16.5 T, and 21.1 T using the 2D ^{13}C–^{13}C pulse sequence and a 50 ms mixing time with either the PDSD or the DARR condition.

Sample / Residue	Ala–6 Helical	Ala–6 β–strand	Gly–10 Helical	Gly–10 β–strand
9.4 T DARR	23.2 ± N.D.	76.8 ± N.D	30.8 ± N.D	69.2 ± N.D
9.4 T PDSD	13.5 ± N.D	86.5 ± N.D.	31.5 ± 5.2	68.5 ± 5.2
16.5 T PDSD	N.D.	N.D.	N.D.	N.D.
21.1 T DARR	15.7 ± 0.7	84.3 ± 0.7	28.4 ± 1.7	71.6 ± 1.7

Table 4–2 presents a comparison of the populations for the alanine–6 and glycine–10 residues for FP–Hairpin UA6/UG10 at ~15:1 lipid to protein loading in a POPC/POPG/Chol lipid membrane environment as determined from the 9.4 T, 16.5 T, and 21.1 T data. The populations for the 9.4 T DARR and the 21.1 T DARR experiments are consistent for the glycine–10 residue. The helical populations at the 9.4 T and 21.1 T fit within 2σ of each other. The agreement with the β–strand population is also within 2σ of the average. If a standard deviation could be determined for the 9.4 T DARR data, then it is very likely that the populations at 9.4 T and 21.1 T for the glycine–10 residue would be within 1σ of each other. The 9.4 T data for the DARR and PDSD experiments are in good agreement for their populations of the Gly–10 residue. The populations of the 9.4 T PDSD experiment fit well within 1σ of the average of the populations for the 21.1 T data for the Gly–10 residue.

There is ~10% difference between the helical populations of the alanine–6 residue when the population was determined from the 2D ^{13}C–^{13}C DARR or the 2D ^{13}C–^{13}C PDSD experiment. The data for alanine–6 at 9.4 T using the PDSD sequence is consistent with the data from the 21.1 T spectrometer and the DARR experiment. The standard deviation of 0.7% is quite small, so it is likely that the standard deviation for the 9.4 T data would be between 2 – 5% based

on the standard deviations for the alanine–6 reside presented in Chapter 3 under different conditions. The alanine–6 data at 9.4 T with the PDSD experiment would then be within 1σ of the alanine–6 residue data at 21.1 T.

The results for the alanine–6 and glycine–10 residues suggest that the data from the high magnetic fields are able to better determine the populations for the residues than at the lower fields based on the smaller standard deviations. One possibility is that at 21.1 T, the increased peak signal to noise per scan results in being able to more accurately determine the intensity of the helical and the β–strand conformations by being able to better distinguish those signals from the noise signals. No populations were determined for the 16.5 T data due to observation of only the β–strand cross peaks in Figure 4–4 due to the chosen contour level.

Comparison of the ^{13}C peak signal to noise per scan, integrated ^{13}C signal, and ^{13}C linewidths at high magnetic fields

Affect of Field on ^{13}C Peak Signal to Noise per Scan for 1D CP Experiments

Figure 4–5 compares the 1D cross polarization experiment for FP–Hairpin UA6/UG10 with the ~15:1 lipid to protein loading at 9.4 T, 16.5 T, and 21.1 T. The spectra are scaled to the same noise level, and are the result of 512 acquisitions and the application of 50 Hz Gaussian line broadening each. Figure 4–5A was acquired at a nominal gas temperature of –50 °C as measured at the thermocouple, the same temperature under which all the spectra at 9.4 T were acquired. Figures 4–5B and 4–5C were acquired with a nominal gas temperature of –23 °C as measured at the thermocouple, consistent with the nominal temperature of the data acquired at 16.5 T and 21.1 T spectrometers. It is likely that sample temperatures were warmer than the

temperatures reported at the thermocouple due to (i) frictional heating from spinning, (ii) probe heating from rf pulses, (iii) use of ambient temperature N_2 gas for the drive and bearing control, and (iv) sample heating from the radiative electric field. Sample heating from the radiative electric field is a serious problem since the electric field will act like a microwave for a conductive sample causing the salt in the sample and charged residues to rotate contributing to the heating of the sample. This will then raise the sample temperature inside the rotor. Two solutions to the heating of the sample are to increase the delay time between pulses and/or lower the salt concentrations in the sample which will make the sample less conductive. Increasing the recycle delay will result in less signal per unit time being acquired and the need to signal average for longer periods of time. For biological protein samples where the salt concentration is relevant, reducing the concentration of salt will take the sample away from the biologically relevant conditions which one is trying to study the sample in.

Previous work by Bodner et al. showed that a three fold increase in the integrated ^{13}C peak signal to noise ratio per scan can be achieved by acquiring data at a sample temperature of –50 °C vs. 20 °C.[7] The 16.5 T and 21.1 T SSNMR experiments were performed at –23 °C as measured at the thermocouple and not colder because the BCU–Xtreme chiller unit could not readily attain temperatures colder than –23 °C while operating at a spinning frequency of 12 kHz. An affect of the limited cooling of the sample is that there is more motional averaging of the spectra at –23 °C vs. –50 °C, which will result in sharper lines, and are visible when comparing Figure 4–5A to Figures 4–5B and 4–5C. Comparison of the data suggests a 5–fold increase in ^{13}C peak signal to noise per scan at the 21.1 T spectrometer compared to the 9.4 T spectrometer.

Integrated areas of the 1D ^{13}C CP are presented in Table 4–4. Due to the probe difference between the solenoid and the E–free probe, there may be more sample heating at 9.4 T vs. 21.1 T. This is in agreement with visual observations where samples at 9.4 T appear dried out / dehydrated when the experiments are finished, whereas there is no evidence visually that the samples are dried out at 21.1 T after the experiments. Samples were not weighted before and after SSNMR experiment, which would be ideal for quantifying the dehydration of the sample. Visually, samples still seemed hydrated across a variety of types of samples at 21.1 T with an E–free probe. The actual temperature difference between the two fields is not currently known. Work by Gor'kov and co–workers has shown that the sample temperature is lower in an E–free probe than a solenoid probe for the same sample under the same experimental conditions at the same field.[8]

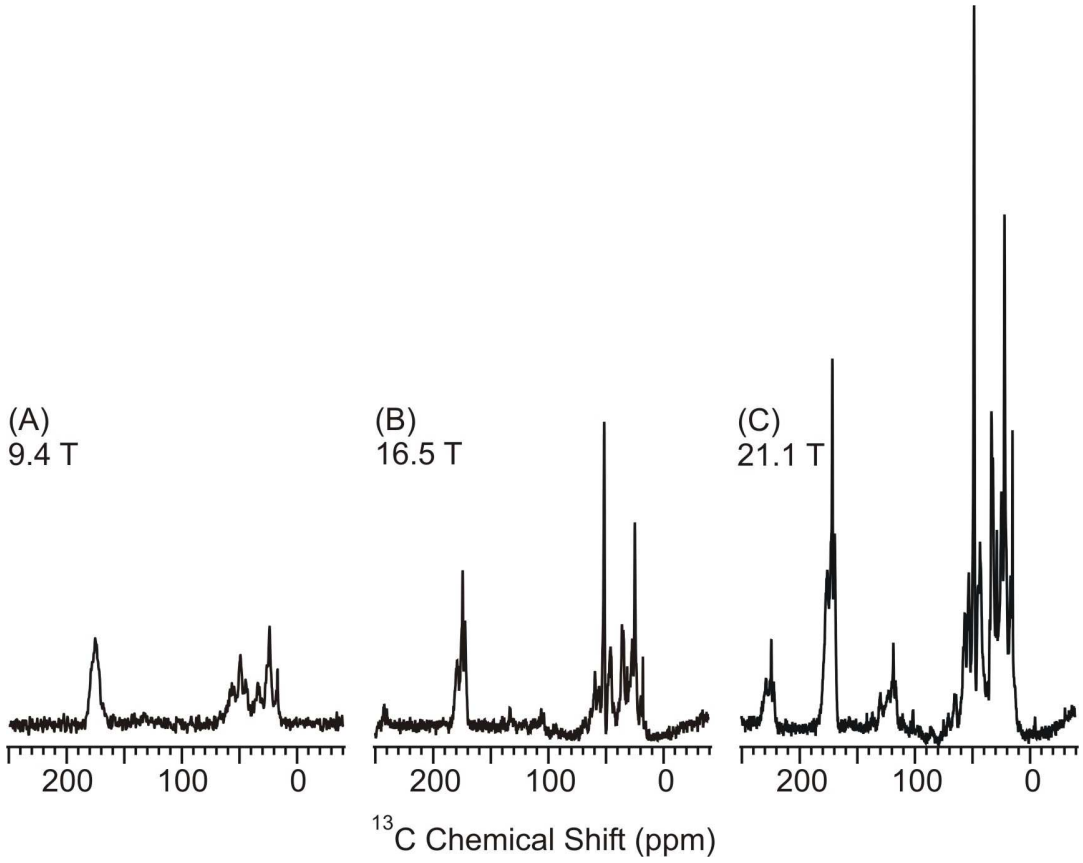

Figure 4–5: Comparison of the FP–Hairpin UA6/UG10 with a 15:1 lipid to protein sample loading in an 8:2:5 molar ratio of POPC/POPG/Chol in a lipid membrane environment at (A) 9.4 T, (B) 16.5 T, and (C) 21.1 T. The spectra were acquired using a ^{13}C CP experiment. The conditions between the three spectrometers were matched as close as possible for the experiments listed in Table 4–3. Spectra are the result of 512 acquisitions and 50 Hz of Gaussian line broadening each. Samples were cooled with nitrogen gas which had a nominal temperature of (A) –50 °C or (B, C) –23 °C as measured at the thermocouple. Sample rotation was 12 kHz for all samples. Table 4–4 presents the integrated area of the peaks. The spectra are scaled to the same horizontal axis in ppm units, and the same vertical peak to peak noise levels as well. The integrated area of the ^{13}C peaks are discussed below and presented in Table 4–4.

Figure 4–5 clearly illustrates the increased ^{13}C peak signal to noise per scan and the integrated area of the ^{13}C peaks at 21.1 T compared to 9.4 T. The two spectra were scaled to the same noise level and then comparisons between the ^{13}CO, $^{13}C\alpha$, and the $^{13}C\beta$ peaks vertical intensity were compared, resulting in an ~5–fold increase in ^{13}C peak signal to noise per scan at 21.1 T compared to 9.4 T. This fits well with the theoretical calculations presented below. By changing the field from 9.4 T to 21.1 T the increased ^{13}C peak signal to noise per scan will be related as the square of the change in fields, $(21.1\ T / 9.4\ T)^2$, yielding a ~5–fold increase in the ^{13}C peak signal to noise per scan. Two factors will contribute to this increase. First the static field strength B_0, will increase by the (21.1 T / 9.4 T) ratio of the fields, or 2.25. Second, the ^{13}C signal is proportional to the Boltzmann population difference and will also increase by this 2.25 ratio as well resulting in the squared dependence. By going to higher fields there are higher frequency (υ) photons which are available to excite the nuclei of the sample. These photons are related to the energy by Equation 4–1. Equation 4–2 relates the frequency and the static magnetic field, which when combined results in Equation 4–3 showing that the energy depends linearly on the gyromagnetic ratio (γ) and the field strength (B_0).

$$E = h * \upsilon \tag{4–1}$$

$$\upsilon = \gamma * B_0 \tag{4–2}$$

$$E = h * \gamma * B_0 \tag{4–3}$$

Previous claims for the increase in ^{13}C peak signal to noise per scan are that it scales as ratio of fields to the $B_0^{3/2}$ [9, 10], $B_0^{7/4}$ [11–13], and B_0^{2} [13, 14]. The expected increase in ^{13}C peak signal to noise per scan from a 9.4 T to 21.1 T field would be ~3.38, ~4.13, and ~5.06 if the increase in ^{13}C peak signal to noise per scan is proportional to the ratio of the fields being raised to the 3/2, 7/4, and 2 powers. For the change in fields from 16.5 T to 21.1 T the expected increase in ^{13}C peak signal to noise per scan is ~1.46, ~1.55, and ~1.65 if the increase in ^{13}C peak signal to noise per scan is proportional to the ratio of the fields being raised to the 3/2, 7/4, and 2 powers.

In order to confirm this hypothesis, one needs to compare the affect of the magnetic fields (B_0) directly using the same probe and the same sample. This is presented in Figure 4–5 (B) for the 16.5 T and (C) for the 21.1 T 1D ^{13}C CP experiments of FP–Hairpin UA6/UG10 at ~15:1 lipid to protein loading in an 8:2:5 molar ratio of POPC/POPG/Chol in a lipid membrane environment. Figures 4–5B and 4–5C compares only the different field strengths between the two experiments. The two spectra are scaled to the same noise level and are the result of 512 acquisitions and the application of 50 Hz of Gaussian line broadening each. Determining the field affect was done by comparison of the ^{13}CO, $^{13}C\alpha$, and $^{13}C\beta$'s vertical signal intensity from the ^{13}C CP spectra in Figure 4–5B and 4–5C with a common noise level. From this comparison the increased ^{13}C peak signal to noise per scan was determined to be ~2–fold higher at 21.1 T than at 16.5 T, suggesting that the ^{13}C peak signal to noise per scan increases as the square of the field ratio. Our results of ~2–fold increase are greater than the expected value of ~1.65–fold ^{13}C

increase by ~20%. Two possible sources for the higher than expected increase in ^{13}C peak signal to noise per scan is from the probe design or implementation of the ^{13}C CP experiment itself. If the setup of the ^{13}C CP at 16.5 T was not ideal then the 16.5 T spectrum would have less ^{13}C signal resulting in a greater than expected increase in ^{13}C peak signal to noise per scan between the two fields. Table 4–3 presents the parameters for the three spectra of Figure 4–5. Comparison of parameters in Table 4–3 shows that there is no significant variation between the 16.5 T and 21.1 T experiments aside from the decoupling fields at 16.5 T being ~100 kHz compared to ~83 kHz for the other spectra. Table 4–4 presents the integrated area for the 1D ^{13}C CP ramps at the three different fields. Comparison of 16.5 T to 21.1 T data provides a direct comparison of the affect of field on the integrated area. Comparison of the 9.4 T to the 16.5 T or the 21.1 T allows for comparison of the probe design and the field for the sample. Figure 4–6 shows the integration regions for the three spectra. The red dashed lines define the ^{13}CO and the ±1 SSB regions used for the integrated area of the ^{13}CO peak. The 9.4 T spectrum did not contain any observable spinning sidebands. The blue dash – dot – dash lines are the boundaries for the aliphatic region's integrated areas.

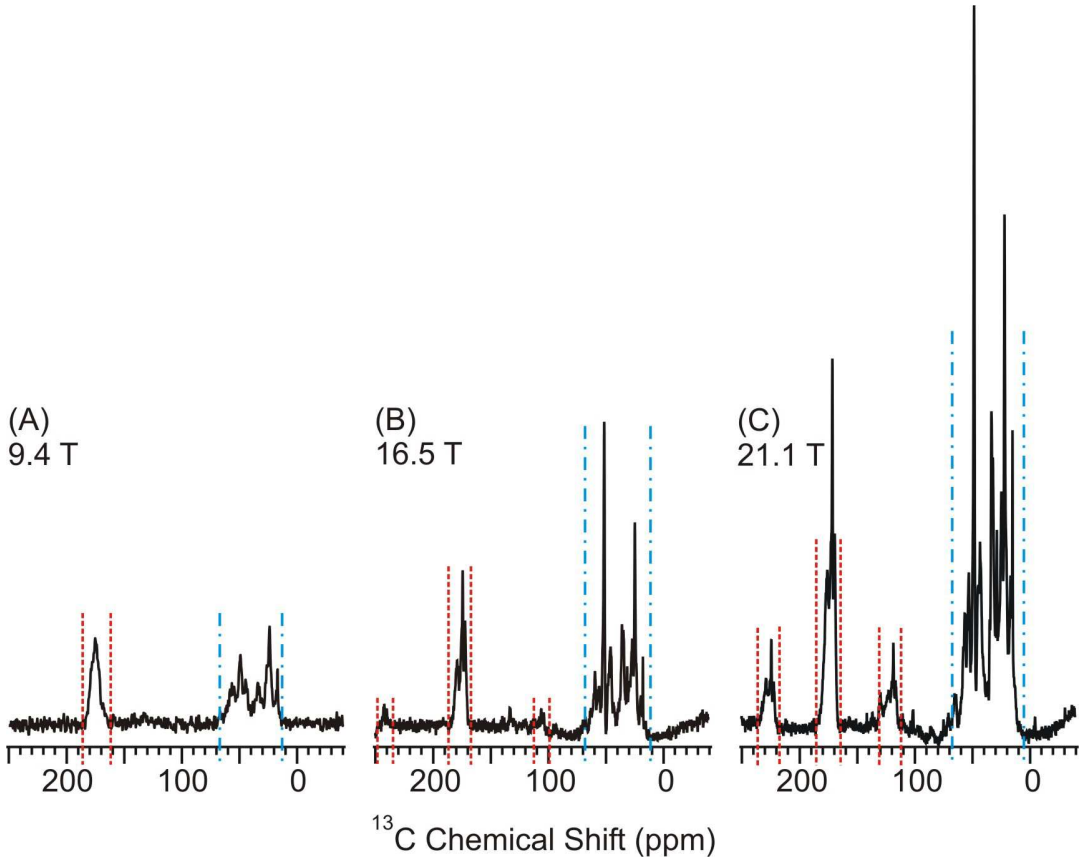

Figure 4–6: Comparison of the FP–Hairpin UA6/UG10 with a 15:1 lipid to protein sample loading in an 8:2:5 mole ratio of POPC/POPG/Chol in a lipid membrane environment at (A) 9.4 T, (B) 16.5 T, and (C) 21.1 T under the same conditions as presented in Figure 4–5. The red dashed lines correspond to the carbonyl region which was cut out and weighted on an analytical balance to determine the integrated area of the ^{13}C peaks. The ±1 spinning sidebands of the carbonyl region were also included in the integrated area for the carbonyl peak for the 16.5 T and 21.1 T spectra. The blue dash dot dash lines correspond to the aliphatic region which was cut out and weighted on an analytical balance. The results of the integrated signal for the peaks are presented in Table 4–4. Discussion of the method for determining the integrated area is also presented below.

As mentioned in Chapter 2, the ^{13}C CP pulse sequence for the 9.4 T spectrometer has the ramp on the ^{13}C channel whereas the 16.5 T and 21.1 T spectrometers have a ramp on the ^{1}H channel instead. The essential parameters are listed in Table 4–3, and are the ^{1}H pulse width to create a $\pi/2$ pulse (^{1}H PW) and the Rabi frequency associated with that pulse length. For the Bruker system the $\pi/2$ pulses are defined by a decibel (dB) value and the PL1 parameter, which is the power level to create the $\pi/2$ pulse. The contact time is the length of time that the CP between $^{1}H \rightarrow ^{13}C$ occurs. ^{1}H decoupling is the proton decoupling field that is applied during the detection of the ^{13}C magnetization. The acquisition time is the length of time to acquire a free induction decay (FID) and is defined as the product of the dwell time and the acquisition length. LB is the amount of Gaussian line broadening applied during processing of the spectrum, and MAS is the spinning frequency of the sample. The recycle delay is the length of time between acquiring successive acquisitions to allow for the ^{1}H magnetization to return to thermal equilibrium. The ^{13}C Rabi parameter is the condition for the ^{13}C nuclei during the cross polarization step.

Table 4–3: Comparing the ^{13}C CP conditions for the spectra at 9.4 T, 16.5 T, and 21.1 T of Figures 4–5 and 4–6 with the FP–Hairpin UA6/UG10 at ~15:1 lipid to protein loading.

Field **Parameters**	**9.4 T** **(Figure 4–5A)**	**16.5 T** **(Figure 4–5B)**	**21.1 T** **(Figure 4–5C)**
Sample	FP–Hairpin UA6/UG10 ~15:1 loading in POPC/POPG/Chol		
Temperature	–50 °C	–23 °C	–23 °C
Acquisitions	512	512	512
^{1}H PW (μs) **Rabi freq.**	5.20 48.1 kHz	2.50 100 kHz	3.00 83.3 kHz
^{1}H PL1	–	–3.1 dB	–2.2 dB
Contact Time	2.5 ms	2.0 ms	2.0 ms
^{1}H Decoupling	81.9 kHz	100 kHz	83.3 kHz
AQ Time	40.96 ms	15.05 ms	15.05 ms
LB (Hz)	50	50	50
MAS (kHz)	12	12	12
Recycle delay	2 s	2 s	2 s
^{13}C Rabi **PL2**	50 – 60 kHz Ramp –	95.5 kHz –2.7 dB	71.7 kHz –0.90 dB

Table 4–4 provides a comparison of the integrated intensity for the 1D ^{13}C CP ramp experiments at 9.4 T, 16.5 T, and 21.1 T with the integrated regions listed below the areas. For the carbonyl region, the spinning sidebands of the ^{13}CO which are observed at 16.5 T and 21.1 T were added into the total carbonyl intensity. No distinguishable spinning sidebands were present in the 9.4 T spectrum. Data for Table 4–4 were determined from Figures 4–5 and 4–6. Figure 4–6 highlights the regions that were used to determine the integrated ^{13}C signal.

The integrated ^{13}C signal was determined by the following protocol. First, the three spectra which had 512 acquisitions each were processed with 50 Hz of Gaussian line broadening. The 9.4 T data was processed using the spinsight software and the 16.5 T and 21.1 T data were processed using nmrDraw. The three spectra were exported as postscript files which were opened in CorelDraw. All three spectra were scaled to the same horizontal scale between –40 to 250 ppm. This range was chosen for two reasons. First, the 16.5 T and 21.1 T sweep width were ~300 ppm, covering the ^{13}C chemical shift range of –40 to 250 ppm. The 9.4 T data had a larger sweep width, covering a larger ^{13}C chemical shift range. Second, the –40 to 250 ppm range included the aliphatic region, the carbonyl region, and the ±1 spinning sidebands for the carbonyl region. For the determination of the carbonyl integrated signal, the 21.1 T spectrum was scaled to the maximum possible value that still fit on the page in landscape orientation. The 16.5 T and the 9.4 T spectra were then scaled to the same peak to peak noise levels as the 21.1 T spectrum in CorelDraw. Vertical lines shown in Figure 4–6 were added to the spectra for the carbonyl region and the spinning sidebands to define the integration limits. A baseline was also applied to all three spectra which ran parallel to the chemical shift axis and defined the bottom of the ^{13}C carbonyl and SSB peaks. The three spectra were printed on separate pages, and the peaks of interest were carefully cut out using a razor blade by tracing the peak between the defined boundaries. Once all the ^{13}CO and spinning sidebands were cut out, they were weighted on the analytical balance with 0.1 mg sensitivity. The masses of the 9.4 T, 16.5 T, and 21.1 T carbonyl regions are presented in Table 4–4.

Determining the integrated area for the aliphatic region was preformed in the same manor as for the carbonyl region, with the following differences. For the aliphatic region, the 21.1 T

spectrum was scaled to the most intense aliphatic peak possible while still staying on one page with the landscape orientation. The 9.4 T and 16.5 T were scaled to the same peak to peak noise level as the 21.1 T spectrum. The spectra were printed off on separate pages of paper, and then the peaks were carefully cut out using a razor blade between the integration boundaries and by tracing of the ^{13}C peaks. There were no observable ±1 spinning sidebands corresponding to the aliphatic region for any of the three spectra. Table 4–4 presents the integrated areas for the aliphatic regions of the three spectra.

Table 4–4 presents the masses of the peaks from the 9.4 T, 16.5 T, and 21.1 T spectra. The ppm units are constant at all fields, however the frequency values change as a function of field strength. To account for the differences in frequencies, the mass of the paper for the 16.5 T peaks was multiplied by the ratio of the (16.5 T / 9.4 T) field, and the 21.1 T masses were multiplied by the ratio of the (21.1 T / 9.4 T) field. From this conversion, the integrated areas of the ^{13}C peaks can be directly compared between the three fields while keeping the frequency the same for all three spectra.

Table 4–4: Comparison of the integrated areas of the 1D ^{13}C CP experiment for FP–Hairpin UA6/UG10 at ~15:1 lipid to protein loading in an 8:2:5 molar ratio of POPC/POPG/Chol in a lipid membrane environment as determined at 9.4 T, 16.5 T, and 21.1 T.

Carbon Signal	**9.4 T**	**16.5 T**	**21.1 T**
	Measured Mass of Cut Out Spectra (mg)		
Aliphatic ^{13}C region	25.2	48.7	123.4
^{13}CO and SSB region	16.3	31.1	89.1
	Constant Frequency Corrected Mass (mg)		
Aliphatic ^{13}C region	25.2	85.5	277.0
^{13}CO and SSB region	16.3	54.6	200.0
Ratio of 21.1 T / 9.4 T	Aliphatic: 11.0 CO: 12.3	Average ratio 21.1 T / 9.4 T	11.6
Ratio of 21.1 T / 16.5 T	Aliphatic: 3.24 CO: 3.66	Average ratio 21.1 T / 16.5 T	3.45
Ratio of 16.5 T / 9.4 T	Aliphatic: 3.35 CO: 3.39	Average ratio 16.5 T / 9.4 T	3.37

Table 4–4 presents the integrated area data for the 9.4 T, 16.5 T, and the 21.1 T spectra for the ^{13}C CP experiment with 512 acquisitions for FP–Hairpin UA6/UG10 with an 15:1 lipid to protein loading in the 8:2:5 molar ratio of POPC/POPG/Chol lipid membranes. The mass of the cut out peaks are listed as the "measured mass of cut out spectra" in Table 4–4. The "constant frequency corrected mass" corresponds to the mass of the cut out spectra multiplied by the ratio of fields of (16.5 T / 9.4 T) or (21.1 T / 9.4 T) for the 16.5 T and 21.1 T spectra respectively. The ratio of the integrated areas are presented in Table 4–4 for the aliphatic and the carbonyl regions

along with the average of the two regions. From Table 4–4, the average ratio of the integrated areas for the (21.1 T / 9.4 T), (21.1 T / 16.5 T), and the (16.5 T / 9.4 T) are 11.6, 3.37, and 3.45 respectively. If the integrated area scales as the 3/2, 7/4, or the 2 of the field, the expected values would be 3.36, 4.12, and 5.04 for the (21.1 T / 9.4 T); 1.45, 1.54, and 1.64 for the (21.1 T / 16.5 T) data; and 2.33, 2.68, and 3.08 for the (16.5 T / 9.4 T) data. The average for the (21.1 T / 9.4 T) data and the (21.1 T / 16.5 T) are both double the expected value for the squared dependence of the field. The average for the (16.5 T / 9.4 T) is only ~12% greater than the expected value for the squared dependence on the field. This suggests that the E–free probe design is a significant factor in increasing the total integrated area of the ^{13}C peaks.

Narrower Linewidths at High Magnetic Fields

Figure 4–7 compares the 1D slices from the 2D ^{13}C–^{13}C experiments at 9.4 T, 16.5 T, and 21.1 T for the FP–Hairpin UA6/UG10 with a ~15:1 lipid to protein loading sample in POPC/POPG/Chol lipid membranes. The f_2 slices are from the Ala $^{13}C\beta$ β–strand chemical shift at f_1 = 23.5 ppm. These slices are aligned vertically to highlight the narrowing of the linewidths with increasing magnetic field strength. The full width at half maximum (FWHM) intrinsic linewidths were measured with no line broadening applied, and the results are presented in Table 4–5. The spectra in Figure 4–7 are scaled to the same vertical intensity as opposed to the same noise level as scaling of spectra to a common noise level would result in a larger vertical intensity by ~2x for the 16.5 T and by ~5x for and 21.1 T spectra compared to the 9.4 T spectra due to the increased peak signal to noise per scan at the higher

magnetic fields. A common vertical intensity allows for clear visualization of linewidths of the cross peaks which is more informative for the linewidth comparisons presented here.

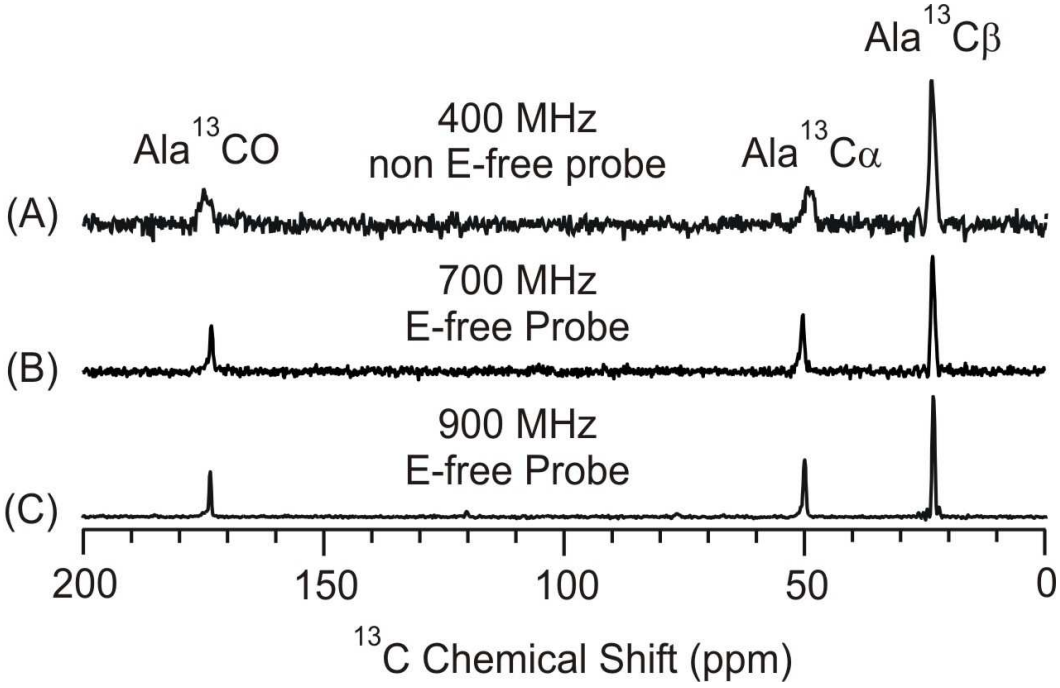

Figure 4–7: Comparison of linewidth at 400 (9.4 T), 700 (16.5 T) and 900 MHz (21.1 T) for the FP–Hairpin uniform ^{13}C, ^{15}N labeled Ala–6 and Gly–10 sample in a POPC/POPG/Chol lipid membrane environment with ~2 μmoles of protein at ~15:1 lipid to protein loading. (A) A f_2 slice from the 2D DARR ^{13}C–^{13}C spectrum for 50 ms mixing time at 400 MHz without an E–free probe setup corresponding to the Ala ^{13}C β β–strand conformation at f_1 = 23.5 ppm. (B) A f_2 slice from the 2D PDSD ^{13}C–^{13}C spectrum for 50 ms mixing time at 700 MHz with an E–free probe setup corresponding to the Ala ^{13}C β β–strand conformation at f_1 = 23.5 ppm. (C) A f_2 slice from the 2D DARR ^{13}C–^{13}C spectrum for 50 ms mixing time at 900 MHz with an E–free probe setup corresponding to the Ala ^{13}Cβ β–strand conformation at f_1 = 23.5 ppm. The slices are representative of the increased ^{13}C peak signal to noise ratio per scan, narrower linewidths, and decreased signal averaging time achieved at higher magnetic fields. No line broadening was applied during processing of the spectra. The intrinsic linewidths are presented in Table 4–5. (A) There were 300 t_1 points and 256 scans summed per t_1 point in ~23 hrs, (B) there were 256 t_1 points and 128 scans summed per t_1 point in ~16 hrs, and (C) there were 256 t_1 points and 64 scans summed per t_1 point in ~7 hrs. Spectra in (A) were acquired at a nominal gas temperature of –50 °C while the spectra in (B, C) were acquired at a nominal gas temperature of –23 °C as measured at the thermocouple. The same sample was used for all three experiments.

Table 4–5: Measurements of intrinsic linewidths at the full width at half maximum (FWHM) of the f_2 slices in hertz and ppm units when no line broadening was applied to the FP–Hairpin UA6/UG10 at ~15:1 lipid to protein loading sample in an 8:2:5 mole ratio of POPC/POPG/Chol in a lipid membrane environment at different magnetic fields, taken from the f_1 = 23.5 ppm slice of the Ala $^{13}C\beta$ β–strand cross peak of Figure 4–6.

Field (T) [a]	Cα		Cβ		CO	
	Hz	ppm	Hz	ppm	Hz	ppm
9.4	140.7	1.41	136.3	1.36	122.6	1.22
16.5	141.1	0.80	165.1	0.94	118.1	0.67
21	157.8	0.70	141.2	0.62	125.4	0.55

a = The ^{13}C frequencies at 9.4 T, 16.5 T, and 21.1 T result in 1 ppm equaling 100.2, 175.0, and 226.3 Hz respectively.

The FWHM intrinsic linewidths were measured for the Ala $^{13}C\beta$ β–strand slices of f_1 = 23.5 ppm at the three fields using the CorelDraw software. The ppm values were determined by direct comparison of linewidth in inches compared to the chemical shift scale for each spectrum in inches. The Hz values were determined by converting from ppm to Hz using the operating frequency of ^{13}C for each field. The ^{13}C operating frequencies at 9.4 T, 16.5 T, and 21.1 T fields resulted in 1 ppm equaling 100.2, 175.0, and 226.3 Hz respectively.

Table 4–5 shows that the FWHM values in hertz were consistent between the magnetic fields varying by < 10% for most samples. By maintaining a consistent value in Hz between the fields, a two fold reduction in ppm linewidth at higher fields was observed. The narrower linewidths at 21.1 T compared to 9.4 T allowed for the unambiguous assignments of the resolved cross peaks at high magnetic fields. This is valuable for the $^{13}C\alpha/^{13}CO$ and the $^{13}CO/^{13}C\alpha$ region.

Summing up the results of the data presented comparing the integrated area from the 1D ^{13}C CP ramps at 9.4 T, 16.5 T, and 21.1 T and the peak signal to noise per scan provides the following conclusions. The integrated peak area allowed for the direct comparison of the field and the probe design. The comparison of the peak signal to noise per scan allowed for comparison of the probe, the field, and the linewidth. Reviewing the results from Table 4–4 suggest that the E–free probe and the high magnetic fields result in an increased integrated area along with an increased peak signal to noise per scan ratios. From Table 4–5, it is shown that the FWHM values for the ^{13}C peaks are not more than 10% different between the fields. Considering that the linewidths are similar between the spectra, and the integrated areas are different, one observes a large increase in the peak signal to noise per scan at the 21.1 T field with an E–free probe design compared to lower fields or non E–free probe designs.

Comparison of Probe Designs: E–free vs. Solenoid Coil

As highlighted in the high field SSNMR data for FP–Hairpin samples at 21.1 T, impressive results were obtained at the higher magnetic fields, and one possible reason could be the difference in probe designs. Figure 4–8 illustrates the coil design inside the probes for the (A) non E–free probe (solenoid) and the (B) E–free probe design.

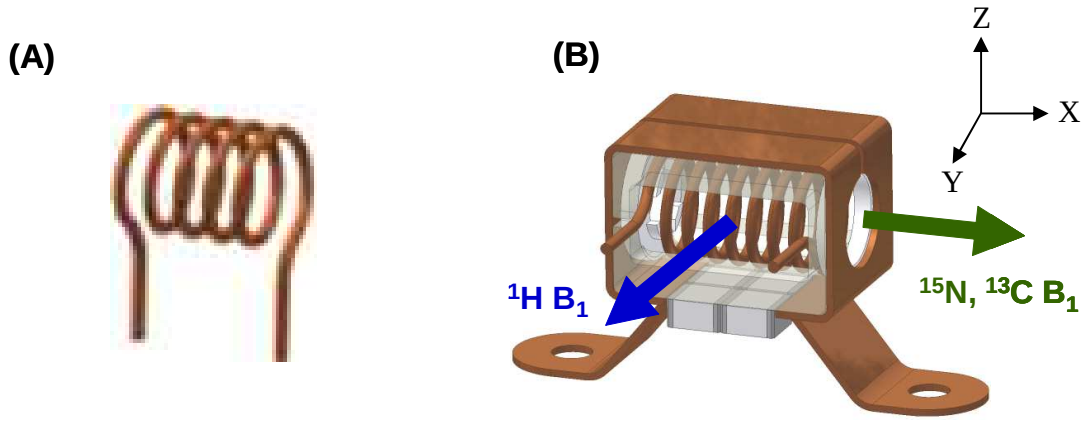

Figure 4–8: Coil designs for the solid state NMR probes used. (A) Solenoid coil used at 9.4 T for all nuclei and (B) the E–free probe's coil design with a loop gap resonator (LGR) used at 16.5 T and 21.1 T.[8, 15] The magnetic fields for the ^{1}H LGR coil and the ^{13}C/^{15}N solenoid are orthogonal in the E–free probe design. The ^{1}H field is produced along the Y–direction and the ^{13}C/^{15}N fields are produced along the X–direction.

Differences in Figure 4–8 are that the solenoid in (A) is tuned to both the ^{1}H and ^{13}C nuclei for double resonance or ^{1}H, ^{13}C, and ^{15}N nuclei for the triple resonance case on one solenoid coil. In Figure 4–8B the ^{1}H is tuned on the loop–gap resonator (LGR) and the low gamma nuclei of ^{13}C and ^{15}N are tuned on the solenoid coil. Second, the solenoid for the 9.4 T spectrometer only has 5 turns where as the solenoid coil in the E–free probe has 8 turns. For the E–free probe design, more turns can be used on the solenoid without the fear of arcing since the ^{1}H is tuned on a separate coil, the LGR. More turns on the solenoid coil can result in better peak signal to noise per scan for the low gamma nuclei.[8] Using the LGR for the ^{1}H frequency

channel results in reducing the electric field (E_c) due to the LGR's low–inductance and ability to apply lower currents to the LGR compared to a solenoid to obtain similar rf fields.[12] The coil design sets the magnetic field from the solenoid and LGR coils orthogonal to the each other as shown in Figure 4–8B, directing the conserved electric field away from the sample. The conserved electric field is orthogonal to the magnetic field. The LGR is made from a conductive plate which is placed in the magnetic field (B_0). If the resonator does not have a slit in the plate then the applied rf will cause eddy currents to develop. Eddy currents are induced electric currents created by the swirling of the conduction electrons caused by an induced current in a magnetic field. This will produce a magnetic field acting against the external magnetic field. By placing a slit down the length of the resonator and creating a gap, the resonator's loop is now broken which prevents induced currents from developing, resulting in the elimination of eddy currents.[16] The loop gap resonator's slit is essential to canceling of the eddy currents.[8, 12] Applying less current to the LGR coil will result in lowering the E_c.

To reduce the conservative field for a solenoid, the number of turns and the applied current thought the coil would need to be reduced, which would compromise the ability of the detection of the ^{13}C and ^{15}N low gamma nuclei.[17] It is also possible to reduce sample heating by reducing the sample conductivity. Lowering the salt concentration is not always ideal or possible, especially for the biological protein samples.[8] Reducing or removing the salt concentration in the protein sample being studied could result in affecting the sample's properties and stability.

Instead of reducing the conductivity of the sample to reduce sample heating, there are alternative coil design options which can minimize sample heating. The coil design that is used

in the Bruker E–free probe is the solenoid coil for low gamma nuclei and the LGR for the ^{1}H frequency shown in Figure 4–8B. Using two separate coils provides the ability to have individual circuits which can be optimized for each frequency range, 900 MHz for the ^{1}H and 225 MHz for the ^{13}C nuclei.[12] By having the solenoid coil inside the LGR, the solenoid coil will act as a partial Faraday shield for the sample by shielding the sample from the electric fields of the outer LGR coil, which can reduce heating of the sample.[8, 12] The magnetic fields generated by the solenoid and LGR can be designed to be orthogonal to each other which increases the channel isolation and therefore the efficiency.[12] The efficiency of the probe is proportional to the ratio of the input power to the probe coil divided by the total power inputted to the circuit.[18] Increasing the efficiency of the probe coil results in less power being lost to other parts of the circuit or as heat. Taken together, the development of the E–free probe with use of the LGR for the ^{1}H frequency channel and the solenoid for the low gamma ^{13}C and ^{15}N nuclei have contributed significantly to protecting biological samples by not dehydrating or destroying them from the rf at high magnetic fields, as well as increasing the low gamma nuclei peak signal to noise per scan as previously mentioned. The E–free probe technology results in the ability to study biological samples which can contain 100–300 mM concentrations of salt which was not feasible before due to sample heating at high magnetic fields caused by the electric fields from the rf pulses.[8]

Low pH Sample Preparation Technique for FP–Hairpin UA6/UG10

One question that developed from the work with the FP–Hairpin protein construct was why are two FP conformations of helical and β–strand observed in the cholesterol containing

membranes for the alanine–6 and glycine–10 residues? A possible explanation is that the sample contains protein that is membrane inserted and some protein which is not membrane inserted, but rather precipitated with the protein – lipid complex. The precipitated protein would correspond to a specific conformation of α–helical and the membrane inserted protein would correspond to the β–strand conformation for each of the alanine–6 and glycine–10 residues. The precipitated protein would have occurred during co–mixing of the protein solution at pH 3 with the lipid membranes which were at pH 7. The resulting sample containing the membrane inserted and the precipitated protein would be packed in the rotor. This is due to the precipitated protein not being able to be separated from the membrane associated lipid – protein sample at pH 7. In order to investigate the possibility that the precipitated protein in the sample results in the observation of the two conformations for each residue, a sample was prepared with the FP–Hairpin UA6/UG10 protein at pH 3, and the POPC/POPG/Chol lipid membranes in an 8:2:5 molar ratio. At pH 3 the FP–Hairpin protein is soluble and any non–membrane inserted protein can be separated by pelleting the protein – lipid complex and decanting the supernatant which will contain the non–membrane associated protein.[19] Lipid mixing assays with FP–Hairpin showed that lipid mixing occurs at pH 3 but that no lipid mixing occurred at physiological pH 7 in lipid membrane solutions.[19, 20]

The benefit of the pH 3 sample preparation protocol is that protein which does not insert into the lipid membrane at pH 3 will still be present in the supernatant after co–mixing of the protein and lipids followed by centrifugation. This allows for the separation of the unbound fraction from the membrane associated fraction. After centrifugation the supernatant is decanted, and can be quantified to determine the amount of protein still present in the supernatant, which allows for determining the amount of protein which is not membrane associated. The next two

sections of this chapter deal with the SSNMR data for FP–Hairpin UA6/UG10 at pH 3 and also pH swapped to pH 7, followed by a discussion of the results. The pH swapping procedure will be discussed in the section "pH swapped FP–Hairpin UA6/UG10 from pH 3 to pH 7 at 21.1 T". The sample used ~1 μmole of FP–Hairpin UA6/UG10 protein at ~33:1 lipid to protein loading in POPC/POPG/Chol in an 8:2:5 molar ratio of 200 nm lipid membranes and examined using the 21.1 T spectrometer equipped with a 4 mm MAS E–free probe. The same sample at pH 3 was used for the pH 7 studies by performing a pH swap of the sample.

pH 3.0 FP–Hairpin UA6/UG10 at 21.1 T

Figure 4–9 shows the ^{13}C CP ramp for the pH 3 sample preparation of ~1 μmole of FP–Hairpin with UA6/UG10 labeling at a field of 21.1 T using an E–free probe. The membrane composition was an 8:2:5 molar ratio of POPC/POPG/Chol. The ^{13}C CP was preformed to determine the ^{13}C signal intensity for the sample and also for the comparison to filtered spectra presented under the double cross polarization section.

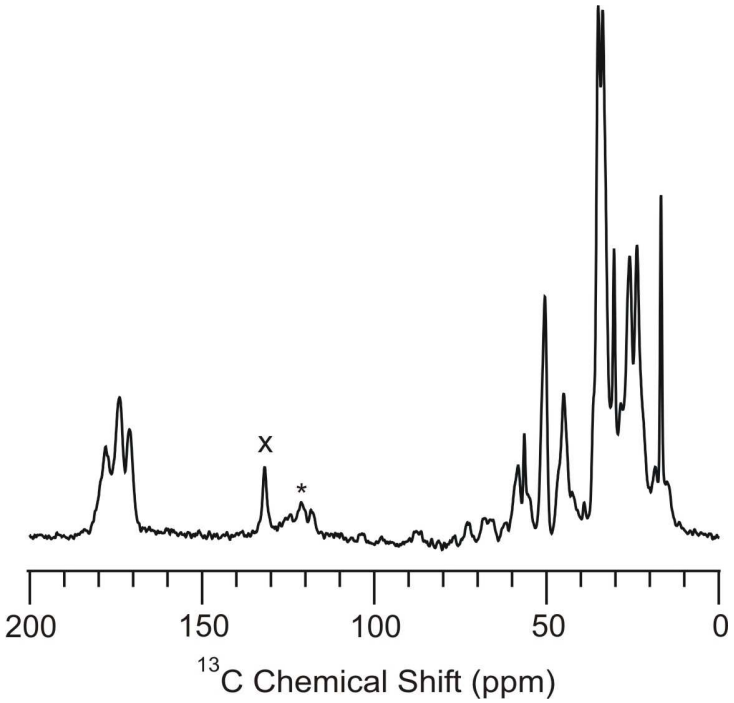

Figure 4–9: ^{13}C CP ramp experiment at 21.1 T for FP–Hairpin with UA6/UG10 labeling in the FP region in a POPC/POPG/Chol lipid membrane environment. Approximately 1 μmole of protein was added to lipid vesicles at pH 3. The spectrum is the result of 4096 acquisitions and 100 Hz of Gaussian line broadening. The spectrum was acquired at a nominal temperature of –23 °C as measured at the thermocouple, and 12 kHz spinning frequency. Spinning sidebands are marked by (*). The (x) is at δ = 131.9 ppm corresponding to the aromatic region of the ^{13}C spectrum. This signal at 131.9 ppm is not observed in the pH 7 samples, so it is likely that it arises from a protonated side chain / aromatic residue of the protein or is due to cholesterol. One possibility of observing the signal at 21.1 T and not 9.4 T is due to the increased ^{13}C peak signal to noise per scan at the higher field. This signal is also observed ^{13}C CP ramp experiment using dynamic nuclear polarization which is presented in Appendix II. DNP has also provided ~39–fold peak signal to noise per scan enhancement with microwave irradiation of the sample compared no microwave irradiation, which is why the 131.9 ppm chemical shift is observed in the DNP ^{13}C CP experiment.

Figure 4–10 is the 2D ^{13}C–^{13}C DARR experiment with a 50 ms mixing time for the pH 3 sample to determine the intra–residue assignments. All the displayed cross peaks fit well with the β–strand chemical shift, and no helical cross peaks are observed above the noise level. The f_2 slice of f_1 = 23.5 ppm chemical shift corresponding to the Ala $^{13}C\beta$ β–strand conformation is shown in Figure 4–10B. The peak signal to noise ratios of the slice from ~1 μmole of protein are quite impressive, where the Ala $^{13}C\beta$, $^{13}C\alpha$, and ^{13}CO are 20.5, 8.0, and 3.9 respectively. The data was acquired in ~14 hrs and had 100 Hz of Gaussian line broadening applied in each dimension.

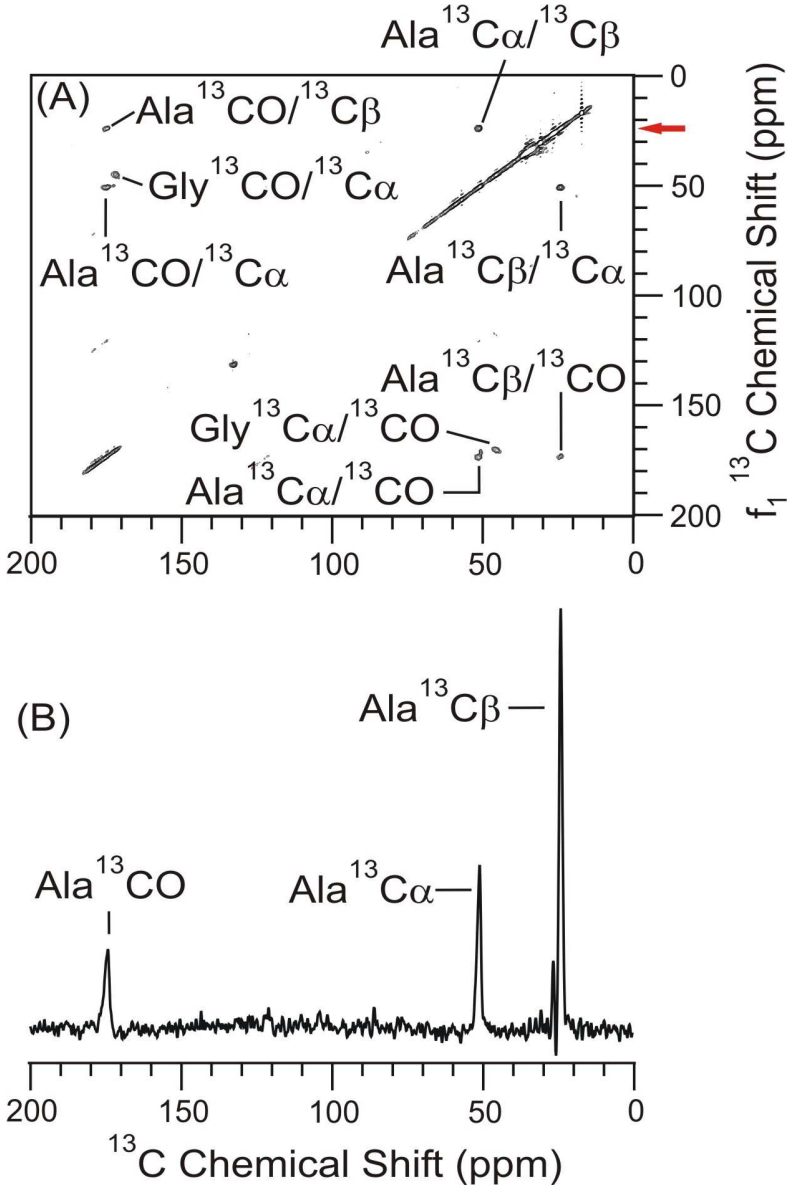

Figure 4–10: 2D DARR ^{13}C–^{13}C spectra at 21.1 T of FP–Hairpin with uniform ^{13}C, ^{15}N labeling at Ala–6 and Gly–10 in the FP region in an 8:2:5 molar ratio of POPC/POPG/Chol in a lipid membrane environment at ~33:1 lipid to protein ratio. The protein and lipid vesicles were prepared as described in Chapter 2's "Membrane Lipid Preparation, Method B" section. (A) The 50 ms mixing time spectrum shows the intra–residue cross peaks. (B) The f_2 slice corresponding to the Ala $^{13}C\beta$ β–strand conformation from f_1 = 23.5 ppm is marked by the red arrow in (A). There were 256 t_1 points and 128 scans summed per t_1 point in a total time of ~14 hrs. Assignments are listed as assignment in f_2 – assignment in f_1. 100 Hz of Gaussian line broadening was applied to each dimension.

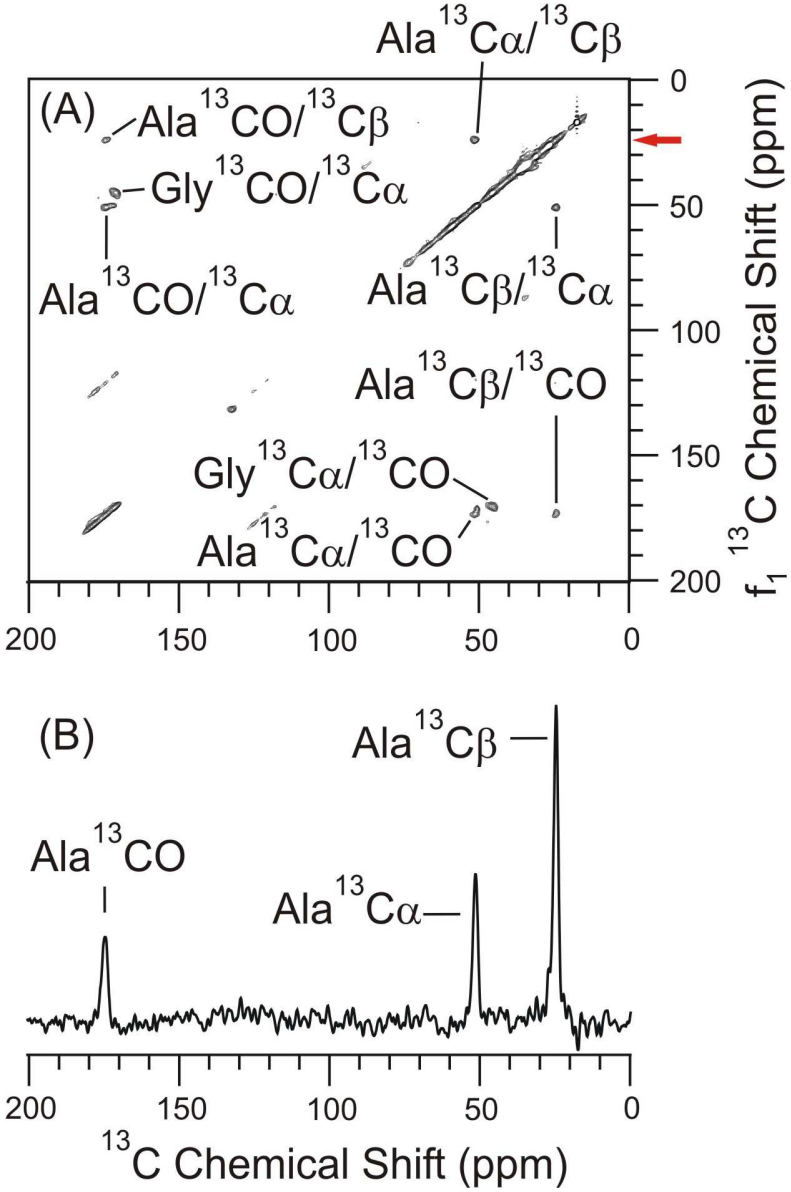

Figure 4–11: 2D DARR ^{13}C–^{13}C spectra at 21.1 T of FP–Hairpin with uniform ^{13}C, ^{15}N labeling at Ala–6 and Gly–10 in the FP region in an 8:2:5 molar ratio of POPC/POPG/Chol in a lipid membrane environment at ~33:1 lipid to protein ratio. The protein and lipid vesicles were prepared as described in Chapter 2's "Membrane Lipid Preparation, Method B" section. (A) The 500 ms mixing time spectrum shows the intra–residue cross peaks, however no inter–residue cross peaks were observed in this sample between A6 / G10 consistent with the other FP–Hairpin work presented in Chapters 3 and 4. (B) The f_2 slice corresponding to the Ala $^{13}C\beta$ β–strand conformation from f_1 = 23.5 ppm is marked by the red arrow in (A). There were 256 t_1 points and 320 scans summed per t_1 point in a total time of ~46 hrs. Assignments are listed as assignment in f_2 – assignment in f_1. 200 Hz of Gaussian line broadening was applied to each dimension.

Figure 4–11 is the 2D ^{13}C–^{13}C DARR experiment with a 500 ms mixing time acquired in ~46 hrs. The chemical shifts of the cross peaks fit well with the β–strand conformation. Intra–residue assignments are observed, however no unique alanine–6 / glycine–10 inter–residue assignments are observed which is consistent with previously presented FP–Hairpin UA6/UG10 work in Chapters 3 and 4. Figure 4–11B shows the f_2 slice corresponding to the Ala $^{13}C\beta$ β–strand chemical shift at f_1 = 23.5 ppm from Figure 4–11A. The peak signal to noise ratio for the $^{13}C\beta$, $^{13}C\alpha$, and ^{13}CO peaks were 12.5, 5.9, and 3.5 respectively. This data further supports the previous results for FP–Hairpin UA6/UG10 suggesting that relative to the FP23 peptides which lack the SHB, the FP region adopts a different tertiary structure compared to gp41 with the folded SHB appended to the FP region. Interestingly, with this sample preparation protocol the pH 3 sample only shows the β–strand conformation for FP–Hairpin's FP region suggesting that the α–helical conformation is due to precipitated protein and that the β–strand conformation is membrane inserted into the cholesterol containing membranes. The favoring of the β–strand conformation in cholesterol containing membranes for the alanine–6 and glycine–10 residues of FP–Hairpin fits well with previous data for FP23 peptides in cholesterol containing membranes where the residues of 1→16 of FP23 peptides were predominantly the β–strand conformation.[3, 5, 21–23]

pH Swapped FP–Hairpin UA6/UG10 from pH 3 to pH 7 at 21.1 T

The pH swap protocol involved unpacking the sample from the rotor and immersing the protein–lipid sample in ~1.5 mL of 100 mM HEPES buffer pH 7 in a 1.7 mL eppendorf tube to change the pH from 3 to ~7. After performing the pH swap the sample was centrifuged in the 1.7

mL eppendorf tube for 5 – 10 minutes at 16,000g using a microfuge. The solution was decanted from the 1.7 mL eppendorf tube and repacked into the rotor as described in Chapter 2's "Solid State NMR Sample Preparation" section. Figure 4–12 is the ^{13}C CP experiment for the pH 7 sample, which is directly comparable to the pH 3 sample in Figure 4–9 as the same conditions were used for the SSNMR experiment.

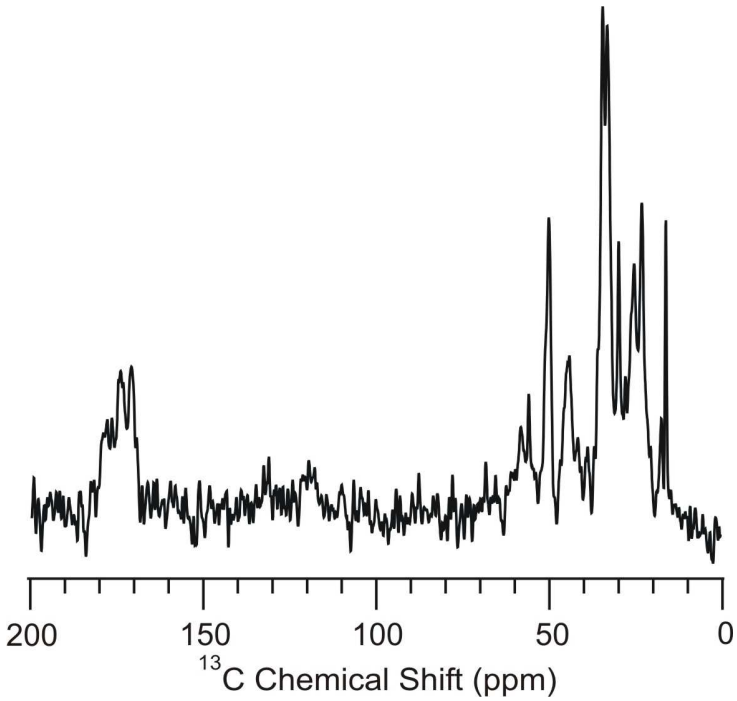

Figure 4–12: ^{13}C CP ramp experiment at 21.1 T for FP–Hairpin with UA6/UG10 labeling in the FP region in an 8:2:5 molar ratio of POPC/POPG/Chol in a lipid membrane environment. Approximately 1 μmole of protein was added to lipid vesicles at pH 3. After unpacking the rotor, the protein–lipid pellet was pH swapped in pH 7 buffer, vortexed, and centrifuged again. It is possible that some protein loss occurred by comparison of the ^{13}C CP of Figure 4–9 and the pH 7 sample ^{13}C CP experiment presented here. The spectrum is the result of 4096 acquisitions and 100 Hz of Gaussian line broadening. Data was acquired at a nominal temperature of –23 °C as measured at the thermocouple and 12 kHz spinning frequency.

Figure 4–13 shows the 2D ^{13}C–^{13}C DARR experiment with a 50 ms mixing time of the pH 7 swapped sample. The slice of Figure 4–13B is from the Ala $^{13}C\beta$ β–strand conformation at f_1 = 23.5 ppm. The peak signal to noise ratios for the Ala $^{13}C\beta$, $^{13}C\alpha$, and ^{13}CO peaks are 10.7, 4.3, and 2.1 respectively. Comparing the 2D ^{13}C–^{13}C DARR with a 50 ms mixing time results from Figure 4–10 and 4–13 shows that similar peak signal to noise ratios are obtained between the two samples at differing pH conditions suggested that a minimal loss of sample occurred from unpacking the rotor, performing the pH swap, and repacking the rotor. One possible reason for the difference in the ^{13}C CP ramps of Figures 4–9 and 4–12 may be due to the sample temperature of the pH 7 sample. It is possible that the sample within the rotor was not as frozen as the pH 3 sample had been when the ^{13}C CP ramp was acquired. Intra–residue cross peak assignments were assigned for the off diagonal cross peaks and still fit well to the predominantly β–strand conformation with no observable helical cross peaks.

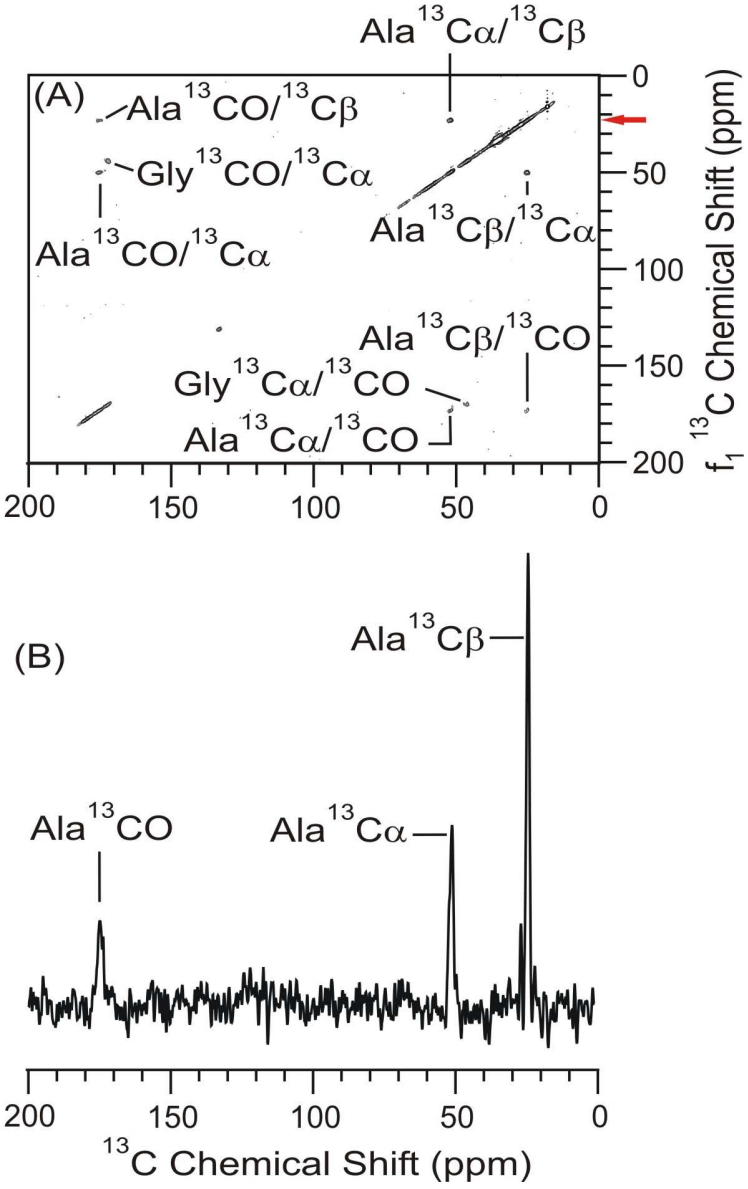

Figure 4–13: 2D DARR ^{13}C–^{13}C spectra at 21.1 T of FP–Hairpin with uniform ^{13}C, ^{15}N labeling at Ala–6 and Gly–10 in the FP region in an 8:2:5 molar ratio of POPC/POPG/Chol in a lipid membrane environment at ~33:1 lipid to protein ratio. The protein and lipid vesicles were prepared as described in Chapter 2's "Membrane Lipid Preparation, Method B" section at pH 3 and then pH swapped to pH 7. (A) The 50 ms mixing time spectrum shows the intra–residue cross peaks. (B) The f_2 slice corresponding to the Ala $^{13}C\beta$ β–strand conformation from f_1 = 23.5 ppm is marked by the red arrow in (A). There were 256 t_1 points and 128 scans summed per t_1 point in a total time of ~14 hrs. Assignments are listed as assignment in f_2 – assignment in f_1. 100 Hz of Gaussian line broadening was applied to each dimension.

Figure 4–14 is the 500 ms mixing time 2D ^{13}C–^{13}C DARR experiment for the pH swapped sample. Here, the same number of acquisitions for both the pH 7 and the pH 3 sample were performed and 200 Hz of Gaussian line broadening was applied to each dimension. The f_2 slice in Figure 4–14B corresponds to the Ala $^{13}C\beta$ β–strand conformation at f_1 = 23.5 ppm. The peak signal to noise ratios for the Ala $^{13}C\beta$, $^{13}C\alpha$, and ^{13}CO peaks are 6.1, 3.5, and 2.3 respectively. The chemical shifts align well with the β–strand conformation. No unique alanine–6 / glycine–10 inter–residue cross peaks were observed, consistent with the other FP–Hairpin UA6/UG10 samples previously presented in Chapter 3 and 4.

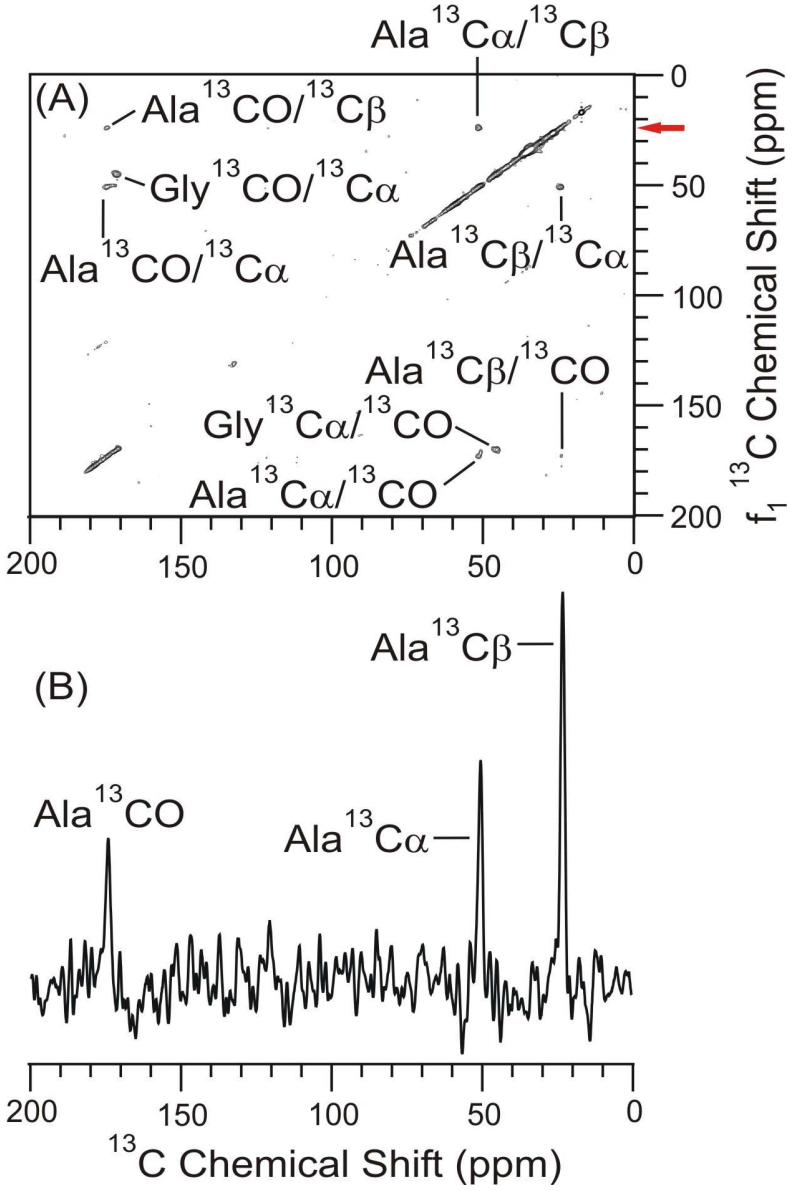

Figure 4–14: 2D DARR ^{13}C–^{13}C spectra at 21.1 T of FP–Hairpin with uniform ^{13}C, ^{15}N labeling at Ala–6 and Gly–10 in the FP region in an 8:2:5 molar ratio of POPC/POPG/Chol in a lipid membrane environment at ~33:1 lipid to protein ratio. The protein and lipid vesicles were prepared as described in Chapter 2's "Membrane Lipid Preparation, Method B" section at pH 3 and then pH swapped to pH 7. (A) The 500 ms mixing time spectrum shows the intra–residue cross peaks, however no inter–residue cross peaks were observed in this sample between A6 / G10. (B) The f_2 slice corresponding to the Ala $^{13}C\beta$ β–strand conformation from f_1 = 23.5 ppm is marked by the red arrow in (A). There were 256 t_1 points and 320 scans summed per t_1 point in a total time of ~46 hrs and assignments are listed as assignment in f_2 – assignment in f_1. 200 Hz of Gaussian line broadening was applied to each dimension.

Figure 4–15 shows the (A) pH 3 and (B) pH 7 swapped f_2 slices at f_1 = 23.5 ppm corresponding to the Ala $^{13}C\beta$ β–strand conformation of the 2D ^{13}C–^{13}C 50 ms DARR experiment at 21.1 T resulting from 256 t_1 points with 128 acquisitions per t_1 point in ~14 hrs. No line broadening was applied to the spectra which are scaled to approximately the same noise level. The spectra presented in Figure 4–15 were used to determine the FWHM values of the peaks presented in Table 4–6. The peak signal to noise ratios were determined for the peaks as previously described in Chapter 3. The peak signal to noise for the Figure 4–15A with the pH 3 sample for the $^{13}C\beta$, $^{13}C\alpha$, and ^{13}CO peaks are 14.2, 5.5, and 2.5 with no line broadening applied. The peak signal to noise for the Figure 4–15B with the pH 7 swapped sample for the $^{13}C\beta$, $^{13}C\alpha$, and ^{13}CO peaks are 7.2, 2.8, and 1.3 respectively with no line broadening applied. Comparison of the peak signal to noise ratio per scan ratios between the two spectra suggest that ~50% signal loss is observed with the pH 7 swapped sample. The integrated area for the signal is expected to remain constant if no protein is lost between the pH 3 and the pH 7 experiments. If the integrated area of the peaks remain constant, then for a factor of two reduction in signal intensity a corresponding increase in the FWHM linewidth value should be observed. Table 4–6 does not show such an increase in the FWHM value of the peaks, with the linewidths at pH 7 within ~10% of the linewidths at pH 3. One possible conclusion is that the sample losses protein due to the pH swap protocol. This would be consistent with the data from the comparison of the 1D ^{13}C CP's spectra at pH 3 (Figure 4–9) and pH 7 (Figure 4–12) for the pH swapped sample.

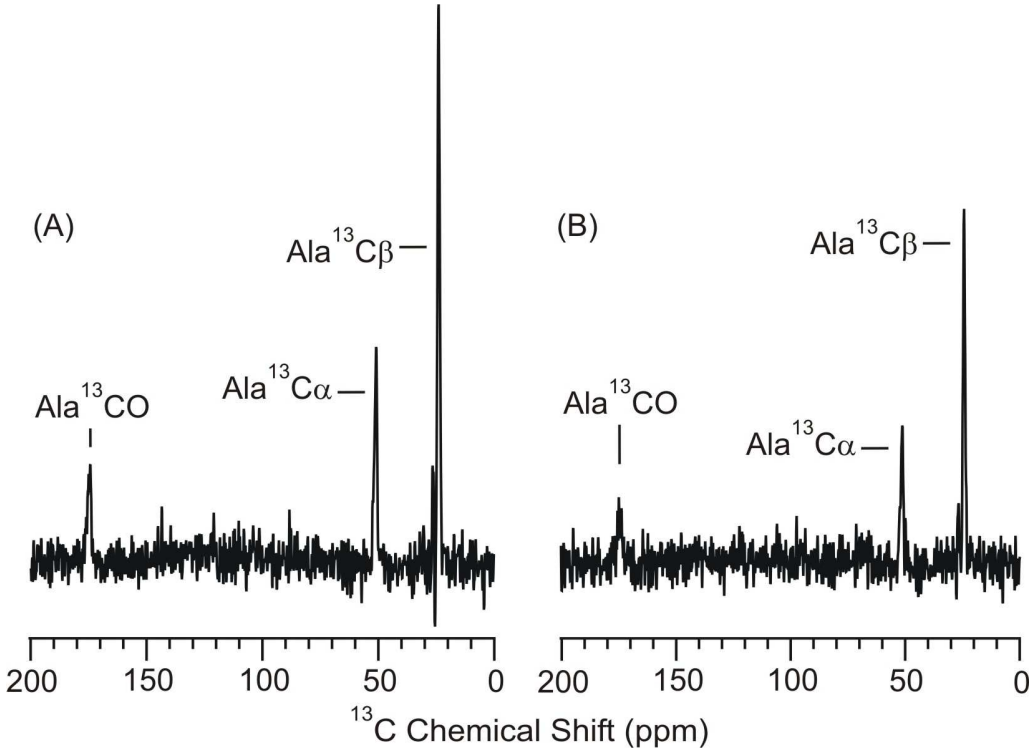

Figure 4–15: Comparison of the f_2 slices corresponding to the Ala ^{13}Cβ β–strand conformation from f_1 = 23.5 ppm from the 50 ms 2D ^{13}C–^{13}C spectra at either (A) pH 3 or (B) pH 7 samples. These slices are from Figures 4–10 and 4–13 respectively without application of line broadening. For the 2D spectrum, there were 256 t_1 points and 128 summed acquisitions per t_1 point. The spectra are scaled to a common noise level. No line broadening was applied to the spectra, and the FWHM linewidths are presented in Table 4–6. Comparison of the ^{13}C peak signal to noise ratios from the slices suggests that there is an ~50% reduction in peak signal to noise after performing the pH swap to the FP–Hairpin UA6/UG10 sample.

Table 4–6: Measurements of intrinsic linewidths at the full width at half maximum (FWHM) in hertz and ppm units when 0 Hz of line broadening is applied to the FP–Hairpin UA6/UG10 with ~33:1 lipid to protein loading sample at pH 3 and pH swapped to pH 7, which were obtained using a 21.1 T spectrometer and E–free probe, taken from the f_2 slice corresponding to the f_1 = 23.5 ppm chemical shift of the Ala $^{13}C\beta$ β–strand cross peak of Figure 4–15.

Sample	Cα		Cβ		CO	
	Hz	ppm	Hz	ppm	Hz	ppm
pH 3	339.0	1.50	303.3	1.34	446.1	1.97
pH 7	306.7	1.36	288.7	1.28	487.1	2.15

The linewidths for the pH 3 and pH 7 sample are approximately twice as large as the linewidths for the 15:1 sample presented in Table 4–5. One possible explanation for the wider linewidths for this sample is that there is only one conformation observed whereas the 15:1 sample had some helical conformation observed along with the β–strand conformation. The split conformation would result in dividing the integrated area into two separate peaks instead of one peak, which could reduce the FWHM values of the peaks. The FWHM linewidths differ by no more than ~10% between the pH 3 and pH 7 samples.

By preparing the sample at pH 3, only the β–strand conformation was observed for the Ala–6 and Gly–10 residues of FP–Hairpin in the 2D ^{13}C–^{13}C experiments. The sample was unpacked from the rotor, pH swapped to pH 7, and repacked in the rotor. The pH 7 sample still only had the β–strand conformation observed for the Ala–6 and Gly–10 residues of FP–Hairpin in the 2D ^{13}C–^{13}C experiments. From the pH swap experiments, the β–strand conformation of the Ala–6 and Gly–10 residues in the FP region for FP–Hairpin is likely due to the β–strand conformation being the membrane inserted conformation whereas the helical component may be from the precipitated protein. The preparation of the protein – lipid complex at pH 3 should

resolve the precipitated protein issue. Comparison of the pH swapped samples to the previous sample of 25:1 lipid to protein loading with ~1 μmole of FP–Hairpin, it is seen that only the β–strand conformation is observed. This suggests that sample preparation of how the protein is added to the lipid membranes is very important. The head to head comparison of the pH 7 preparation at 25:1 lipid to protein loading from Chapter 3 (Figures 3–4 and 3–5) and the pH 3 preparation which was then pH swapped to pH 7 shows only the β–strand conformation for the pH swapped sample, highlighting the possibility that the helical conformation is due to precipitated protein.

Also, this work was done with ~1 μmole of protein, similar to the amount used for the 25:1 lipid to protein loading work of Figures 3–4 and 3–5 for the 50 ms and 500 ms mixing time experiments in an 8:2:5 molar ratio of POPC/POPG/Chol in a lipid membrane environment. Using the E–free probe and the 21.1 T spectrometer, ~5–fold peak signal to noise per scan of the ^{13}C cross peaks were achieved with the 1 μmole of protein sample compared to similar samples at 9.4 T. The ~5–fold increase in peak signal to noise per scan was determined by comparing the slice of Figure 3–4B with a 25:1 lipid to protein loading of FP–Hairpin UA6/UG10 to the pH 3 and pH 7 swapped samples of Figures 4–10B and 4–13B, as all three samples contained ~1 μmole of FP–Hairpin UA6/UG10 in an 8:2:5 molar ratio of POPC/POPG/Chol lipid membranes. The slice presented in Figure 3–4B has peak signal to noise ratios for the ^{13}Cβ, ^{13}Cα, and ^{13}CO of 15.3, 2.0, and 2.4 from 300 t_1 points and 768 acquisitions per t_1 point. Dividing the peak signal to noise ratios of Figure 3–4B by the number of acquisitions (300*768), resulted in the peak signal to noise per scan for the specific ^{13}C peak. The determination of the peak signal to noise per scan for the ^{13}C peaks at 21.1 T data was done the same way using the data from

Figure 4–10B or Figure 4–13B for the pH 3 or the pH 7 data with a 50 ms mixing time, which had peak signal to noise ratios of 10.9, 4.3, and 2.1 in the pH 3 spectra and peak signal to noise ratios of 10.7, 4.3, and 2.1 for the pH 7 swapped spectra for the $^{13}C\beta$, $^{13}C\alpha$, and the ^{13}CO peaks from 256 t_1 points and 128 acquisitions per t_1 point. Dividing the peak signal to noise ratios for each ^{13}C peak by the number of acquisitions (256*128) resulted in the peak signal to noise per scan ratio at 21.1 T. The ratio of the 21.1 T / 9.4 T data resulted in a 4.9–fold increase in peak signal to noise per scan determination at 21.1 T compared to 9.4 T for the samples containing similar amount of the FP–Hairpin UA6/UG10 protein. The signal averaging time was reduced from 68 hrs to ~16 hrs for the 50 ms experiment and from 192 hrs to ~46 hrs for the 500 ms experiment with ~83% less acquisitions at 21.1 T. This is likely due to the ~5–fold increase in ^{13}C peak signal to noise per scan at the 21.1 T spectrometer discussed above and the increased ^{13}C integrated area for the peaks as well. Comparing the 50 ms data from Figure 3–4 of the ~25:1 lipid to protein loading sample of FP–Hairpin UA6/UG10 which was acquired in ~68 hrs to the pH 3 and pH 7 swapped 50 ms data presented in Figures 4–10 and 4–13 which were acquired in ~16 hrs each, spectra presented in Figures 4–10 and 4–13 are acquired in 75% less time at 21.1 T, with peak signal to noise ratio's of at least 2:1. Doubling the peak signal to noise of the 21.1 T spectra would require signal averaging for 4x as long, or ~64 hrs which is a reasonable amount of time, whereas doubling the peak signal to noise ratios of the 9.4 T spectra in Figure 3–4 would require 4x as long, or 272 hrs (~11 days) which is not a practical option. Signal averaging for 11 days for the 2D ^{13}C–^{13}C experiment is not a practical option at 9.4 T due to the costs associated with the spectrometer time and the cost of liquid nitrogen to cool the

sample. Also, as discussed in Chapter 3 with the 25:1 and 40:1 samples, long signal averaging times of up to 32 days would be required to obtain the 500 ms data set, which also is not a practical use of the spectrometer.

Combining the 21.1 T spectrometer and the E–free probe provided several benefits to the research. One of the benefits is the ability to study mass limited samples and obtain an ~5–fold increase in the ^{13}C peak signal to noise per scan at 21.1 T compared to the 9.4 T spectrometer. The increased peak signal to noise per scan and the greater integrated area resulted in time savings at 21.1 T of 33 – 75% compared to the 9.4 T spectrometer with a solenoid coil. A second benefit is the limited dehydration of the protein sample when using the E–free probe. The two benefits are ideal for the samples which were initial studied at 9.4 T using ~0.5 μmole and ~1.0 μmole of FP–Hairpin protein and required 3 – 8 days of signal averaging time for the 2D ^{13}C–^{13}C experiments.

Table 4–7 compares the tabulated data of the chemical shifts for the pH 3 and the pH 7 swapped samples. No populations were determined due to the lack of a distinguishable helical cross peak in the 2D ^{13}C–^{13}C spectra. Chemical shifts for the pH 3 and pH 7 swapped samples agree within ± 0.8 ppm of previously reported values for FP–Hairpin samples in Chapters 3 and 4. Two exceptions are the chemical shift of the Ala–6 ^{13}CO of the Ala $^{13}C\alpha/^{13}CO$ cross peak in Table 4–7 which is ~3 ppm lower than previously presented and the Gly–10 ^{13}CO chemical shift of the Gly $^{13}C\alpha/^{13}CO$ cross peak which is ~1.2 ppm lower than previously reported.

Table 4–7: Chemical shift (CS) and relative populations (Pop) for the FP–Hairpin UA6/UG10 sample initially prepared at pH 3.0 with a loading of ~33:1 in an 8:2:5 molar ratio of POPC/POPG/Chol in a lipid membrane environment at 21.1 T with the shifts reported as the (f_2, f_1) convention.

33:1 Loading of FP–HP in POPC / POPG / Chol. Membranes									
pH Condition		**Prepared at pH 3.0**				**Swapped to pH 7.0**			
Mixing Time		**50 ms**		**500 ms**		**50 ms**		**500 ms**	
Assignment		**CS**	**Pop (%)**	**CS**	**Pop (%)**	**CS**	**Pop (%)**	**CS**	**Pop (%)**
A Cα / A Cβ	**Helix**	–	–	–	–	–	–	–	–
	β–strand	51.0, 23.6	–	51.4, 23.7	–	51.3, 23.2	–	50.8, 23.8	–
A Cα / A CO	**Helix**	–	–	–	–	–	–	–	–
	β–strand	50.8, 172.6	–	51.3, 173.5	–	51.6, 173.5	–	50.8, 173.6	–
A Cβ / A CO	**Helix**	–	–	–	–	–	–	–	–
	β–strand	24.1, 173.3	–	24.3, 173.3	–	24.5, 173.2	–	23.5, 173.6	–
A CO / A Cα	**Helix**	–	–	–	–	–	–	–	–
	β–strand	174.6, 50.6	–	174.8, 50.7	–	174.8, 50.3	–	174.3, 50.8	–
A CO / A Cβ	**Helix**	–	–	–	–	–	–	–	–
	β–strand	174.5, 23.7	–	174.4, 23.6	–	174.3, 23.4	–	174.1, 23.7	–
A Cβ / A Cα	**Helix**	–	–	–	–	–	–	–	–
	β–strand	24.2, 50.5	–	24.4, 50.7	–	24.5, 50.2	–	23.8, 50.9	–
G Cα / G CO	**Helix**	–	–	–	–	–	–	–	–
	β–strand	45.5, 170.5	–	45.5, 170.6	–	45.6, 170.2	–	44.9, 170.7	–
G CO / G Cα	**Helix**	–	–	–	–	–	–	–	–
	β–strand	171.3, 45.0	–	171.5, 44.8	–	171.7, 44.4	–	171.0, 45.1	–

The 50 ms data had 100 Hz of Gaussian LB applied to each dimension and the 500 ms data had 200 Hz of Gaussian LB applied to each dimension during spectral processing. The data for the pH 3 sample at 50 ms and 500 ms mixing times were determined from Figures 4–10 and 4–11 respectively. The tabulated data for pH 7 swapped samples at 50 ms and 500 ms were determined from Figures 4–13 and 4–14 respectively.

FP23 with UA6/UG10 Labeling at 21.1 T

Michelle Bodner's sample of FP23 UA6/UG10 in LM3 lipid membranes which contained cholesterol was rehydrated with water and packed into a 4 mm MAS rotor for experiments using the 21.1 T spectrometer with a 4 mm MAS E–free probe. This sample was used to confirm that the inter–residue alanine–6 / glycine–10 cross peaks observed at 9.4 T with an 1000 ms exchange time were also observable at 21.1 T for the FP23 sample. The LM3 lipid combination is a 10:5:2:1:2:10 mole ratio of POPC/POPE/POPS/PI/Sphingomyelin/Cholesterol, which is a more accurate representation of the lipids present in the viral and host cell membranes.[3]

Figure 4–16 is the 50 ms mixing time spectrum and Figure 4–17 is the 500 ms mixing time spectrum for the 2D ^{13}C–^{13}C DARR experiments. The 50 ms data of Figure 4–16 is comparable to the 10 ms mixing time data of Figure 3–1A for establishing the intra–residue assignments. The data in Figure 4–17 is with the 500 ms mixing time as compared to the 1000 ms mixing time of Figure 3–1B. The spectra in Figure 4–17 clearly show that the inter–residue A6 / G10 cross peaks are still observed for the FP23 UA6/UG10 sample at 21.1 T which were previously observed with an 1000 ms mixing time using the 9.4 T spectrometer as seen in Figures 3–1B and 3–1D. Figure 4–18 shows slices corresponding to the inter–residue A6 / G10 cross peaks observed in Figure 4–17A.

Comparison of the intra–residue to the inter–residue cross peaks can provide an idea on the distance between the two strands. Castellani and co–workers present data for the inter–strand $^{13}C\alpha$ – $^{13}C\alpha$ cross peaks are due to distances of 4.6 – 5.4 Å, and that the cross peaks would first appear at an 100 ms mixing time period in the 2D ^{13}C–^{13}C experiments.[2] Cross peaks that arise from distances of up to 7 Å would be observed in the 500 ms spectra.[2] The distance constraint is a function of the integrated signal intensity as measured from cross peaks in the 50, 100, 200, and 500 ms mixing times in the 2D ^{13}C–^{13}C experiments.[2] Fitting the measured integrated area build up to the mixing time allows for predicating the distance constraint. The cross peak's intensity is proportional to the distance between nuclei as $1 / r^6$ which is how distances are determined in the NOESY spectra for liquid state NMR.[2, 24] Based on the spectra for FP23 at 500 ms mixing time, the inter–residue cross peaks for the Ala $^{13}C\beta$/Gly $^{13}C\alpha$ would fall within the 4.6 – 7 Å range, in agreement with previous work from Bodner and co–workers.[3] The cross peaks are present at the 500 ms mixing time, but not the 50 ms mixing time. To more accurately determine the distances for the A6 / G10 cross peaks, 2D ^{13}C–^{13}C spectra with 100 ms and 200 ms mixing times should be collected to determine the earliest time at which the inter–strand A6 / G10 cross peaks are observed. Correlating the cross peaks with the mixing time will provide a better constraint on the inter–strand distance measurement.

The inter–residue cross peaks at 21.1 T are smaller than the intra–residue cross peaks, as can be visually observed in Figure 4–17B or Figure 4–18. The Ala–6 $^{13}C\alpha$ peak's peak signal to noise ratio is 20.2, the Ala–6 $^{13}C\beta$ peak's peak signal to noise ratio is 31.9 in Figure 4–17B, with

a $^{13}C\beta$ / $^{13}C\alpha$ ratio of 1.6. The peak signal to noise ratio for the Gly–10 $^{13}C\alpha$ signal was 1.8 from Figure 4–17B. For the 9.4 T data for FP23 UA6/UG10 presented in Figures 3–1B and 3–1D, the Ala–6 $^{13}C\beta$, Ala–6 $^{13}C\alpha$, and the Gly–10 $^{13}C\alpha$ peak signal to noise were 8.8, 2.4, and 1.9 respectively. The ratio of the Ala–6 $^{13}C\beta$ / Gly–10 $^{13}C\alpha$ signal at 9.4 T was (8.8 / 1.9) which is ~4.6, where as at 21.1 T the ratio of the Ala–6 $^{13}C\beta$ / Gly–10 $^{13}C\alpha$ signal was (31.9 / 1.8) which is ~17.7, strongly favoring the Ala–6 $^{13}C\beta$ signal. The increased difference in the inter–residue cross peaks at 21.1 T is likely due to two items. First, the 2D ^{13}C–^{13}C data at 21.1 T had a 500 ms mixing time compared to the 9.4 T data which had an 1000 ms mixing time. The second possibility is that the distance between the two nuclei should be the same at both fields, but the frequency separation of the ^{13}C nuclei will be 2.25–fold larger at 21.1 T than at 9.4 T. The transfer of magnetization is proportional to the inverse of the distance to the sixth power ($1 / r^6$). At higher frequencies, there is less overlap in the linewidths of the nuclei during the mixing time. The overlap between the nuclei is what allows for the transfer of the magnetization from one nuclei to another. Therefore, if the linewidths in hertz do not change from 9.4 T to 21.1 T, but the field increases by a factor of 2.25, then the overlap between the ^{13}C nuclei will be reduced by the factor of 2.25. The reduced overlap between the two nuclei will reduce the magnetization exchange, resulting in smaller cross peaks for the inter–strand residues and larger ratios between the intra–residue to inter–residue cross peaks. One way to increase the magnetization transfer between the ^{13}C nuclei during the mixing time is to broaden the ^{13}C linewidths. By applying a ^{1}H field equal to the MAS spinning frequency during the mixing time,

the ^{13}C resonances will be broadened, facilitating the mixing between the ^{13}C nuclei as previously discussed in Chapter 2, section "2D ^{13}C–^{13}C PDSD and DARR Experiments". Broadening the linewidths will result in more overlap of the ^{13}C nuclei, and more transfer of the ^{13}C magnetization.

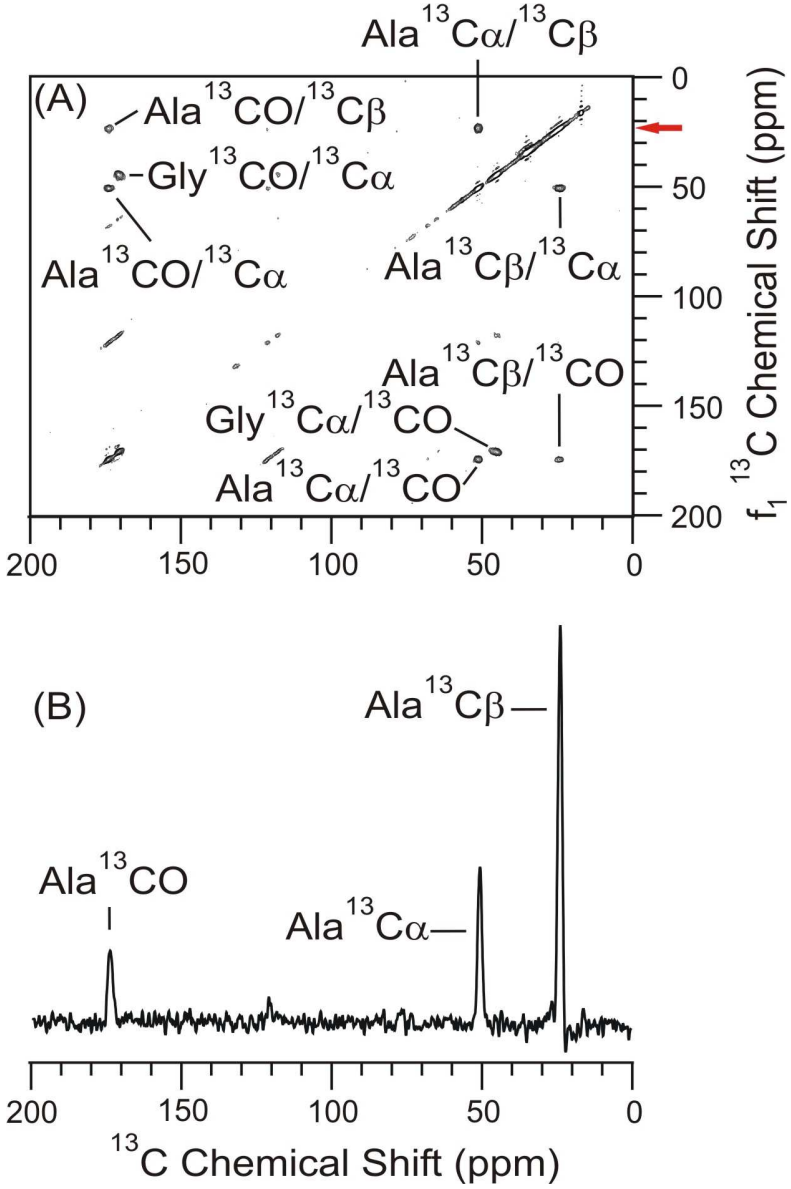

Figure 4–16: 2D DARR ^{13}C–^{13}C spectra at 21.1 T of FP23 with uniform ^{13}C, ^{15}N labeling at Ala–6 and Gly–10 in the FP region inserted into a cholesterol containing LM3 lipid membrane environment. (A) The 50 ms mixing time spectrum shows the intra–residue cross peaks. (B) The f_2 slice corresponding to the Ala $^{13}C\beta$ β–strand conformation from f_1 = 23.5 ppm is marked by the red arrow in (A). There were 256 t_1 points and 128 scans summed per t_1 point in a total time of ~14 hrs. Assignments are listed as assignment in f_2 – assignment in f_1. 100 Hz of Gaussian line broadening was applied to each dimension.

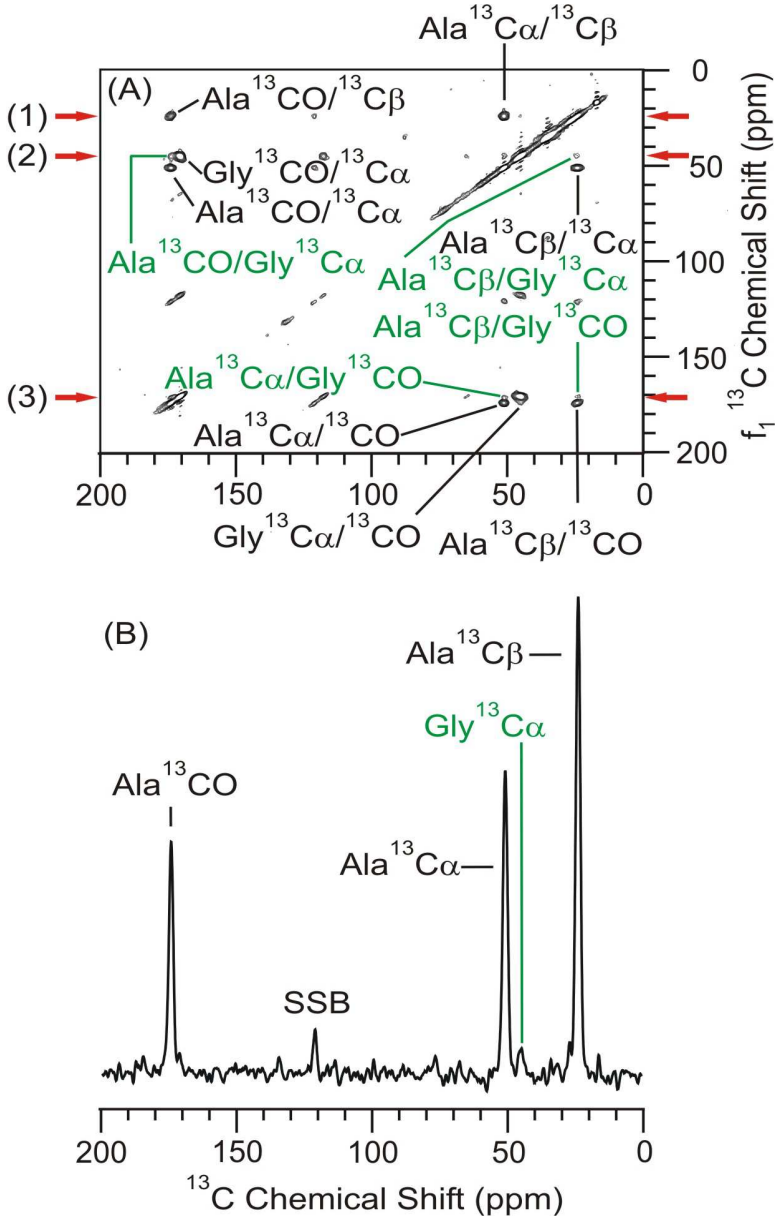

Figure 4–17: 2D DARR ^{13}C–^{13}C spectra at 21.1 T of FP23 with uniform ^{13}C, ^{15}N labeling at Ala–6 and Gly–10 in the FP region inserted into a cholesterol containing LM3 lipid membrane environment. (A) The 500 ms mixing time spectrum shows the intra–residue cross peaks in black and the unique Ala–6 / Gly–10 inter–residue cross peaks in green. (B) The f_2 slice corresponding to the Ala $^{13}C\beta$ β–strand conformation from f_1 = 23.5 ppm is marked by the red arrow numbered (1) in (A). There were 256 t_1 points and 960 scans summed per t_1 point in a total time of ~137 hrs. Assignments are listed as assignment in f_2 – assignment in f_1. 200 Hz of Gaussian line broadening was applied to each dimension. Spinning sidebands are labeled as SSB. The numbered f_2 slices corresponding to (1) f_1 = 23.5 ppm, (2) f_1 = 45.2 ppm, and (3) f_1 = 171.5 ppm show the inter–residue A6 / G10 cross peaks and are presented in Figure 4–18.

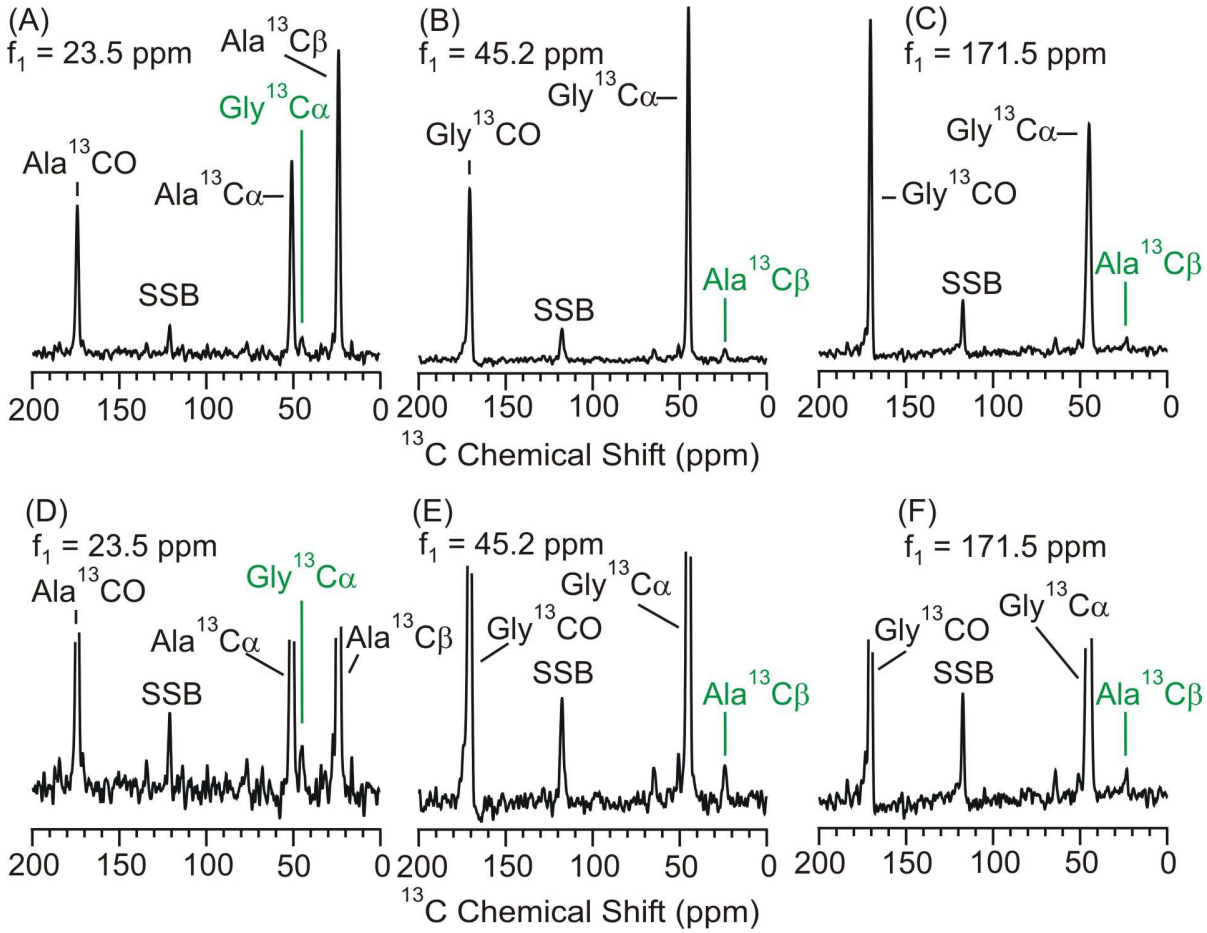

Figure 4–18: Additional slices from Figure 4–17 of FP23 UA6/UG10 with a 500 ms mixing time at 21.1 T. The slices were marked by the numbered arrows in Figure 4–17A. (A,D) The f_2 slice corresponding to the Ala ^{13}Cβ β–strand conformation from f_1 = 23.5 ppm is marked by the red arrow numbered (1) in Figure 4–17A. (B,E) The f_2 slice corresponding to the Gly ^{13}Cα β–strand conformation from f_1 = 45.2 ppm is marked by the red arrow numbered (2) in Figure 4–17A. (C,F) The f_2 slice corresponding to the Gly ^{13}CO β–strand conformation from f_1 = 171.5 ppm is marked by the red arrow numbered (3) in Figure 4–17A. All slices have an Ala–6 / Gly–10 inter–residue connection as can be seen by both alanine and glycine ^{13}C peaks in the slices. Slices shown in (D–F) are the blown up views of slices from (A–C). For ease of viewing the peaks corresponding to the ^{13}Cα and ^{13}CO were truncated to facilitate viewing of the inter–residue A6 / G10 cross peaks. The unique peaks for each slice are highlighted in green. All parameters are the same as those listed in Figure 4–17. Spinning sidebands for the ^{13}CO are labeled as SSB in the spectra.

Table 4–8: Chemical shift (CS) and relative populations (Pop) for the FP23 UA6/UG10 sample prepared in the LM3 cholesterol containing membranes at 21.1 T with the shifts reported as the (f_2, f_1) convention.

FP23 Dimer D at 21.1 T					
Lipids		**LM3**			
Mixing Time		**50 ms**		**500 ms**	
Assignment		**CS**	**Pop (%)**	**CS**	**Pop (%)**
A Cα / A Cβ	**Helix**	–	–	–	–
	β–strand	51.1, 23.7	–	50.9, 23.9	–
A Cα / A CO	**Helix**	–	–	–	–
	β–strand	51.1, 174.4	–	50.9, 174.7	–
A Cβ / A CO	**Helix**	–	–	–	–
	β–strand	23.8, 174.5	–	23.7, 174.7	–
A CO / A Cα	**Helix**	–	–	–	–
	β–strand	174.0, 50.9	–	174.0, 51.0	–
A CO / A Cβ	**Helix**	–	–	–	–
	β–strand	174.0, 23.6	–	174.1, 23.9	–
A Cβ / A Cα	**Helix**	–	–	–	–
	β–strand	24.0, 50.9	–	23.8, 51.1	–
G Cα / G CO	**Helix**	–	–	–	–
	β–strand	44.8, 171.0	–	44.7, 171.3	–
G CO / G Cα	**Helix**	–	–	–	–
	β–strand	170.8, 44.6	–	170.7, 44.9	–
A Cβ / G Cα	**Helix**	–	–	–	–
	β–strand	–	–	45.2, 24.1	–
A Cβ / G CO	**Helix**	–	–	–	–
	β–strand	–	–	23.1, 171.4	–
A Cα / G CO	**Helix**	–	–	–	–
	β–strand	–	–	50.8, 171.5	–
A CO / G Cα	**Helix**	–	–	–	–
	β–strand	–	–	174.2, 45.1	–

The data for Table 4–8 is derived from Figures 4–16 and 4–17 for the 50 ms and 500 ms mixing time spectra. The chemical shifts of Table 4–8 of all residues agree within ± 0.6 ppm of the previously reported values in reference [3]. Table 4–8 shows the intra–residue chemical shifts with the 50 ms and 500 ms mixing time along with the inter–residue A6 / G10 assignments which are not observed at 50 ms. The inter–residue A6 / G10 cross peaks are still observed with a long mixing time of 500 ms at 21.1 T, consistent with the 1000 ms data acquired previously at 9.4 T.[3] The intra–residue cross peaks agree with the β–strand chemical shifts of FP–Hairpin presented in Chapters 3 and 4.

The unique alanine–6 / glycine–10 cross peaks for FP23 are shown in green in Figure 4–17A. Observation of the A6 / G10 cross peaks confirms that the cross peaks are observable at 21.1 T supporting the lack of A6 / G10 cross peaks results for FP–Hairpin. FP23 UA6/UG10 was treated as a control at 21.1 T to confirm the presence of the alanine–6 / glycine–10 cross peaks. The conformation of the inter–residue cross peaks for FP23 UA6/UG10 was important because, as presented above, the ^{13}C frequency at 21.1 T is 2.25–fold greater than at 9.4 T. If no unique alanine–6 / glycine–10 cross peaks for FP23 were observed using the 21.1 T spectrometer, then there would be doubts about FP–Hairpin's lack of A6 / G10 cross peaks. Since the A6 / G10 inter–residue cross peaks are observed for FP23 at 21.1 T the lack of alanine–6 / glycine–10 inter–residue cross peaks for FP–Hairpin UA6/UG10 are a genuine result suggesting that the FP region adopts a different tertiary structure in FP–Hairpin than for the FP23 peptide. The slice shown in Figure 4–16B is from the Ala ^{13}Cβ β–strand chemical shift of f_1 = 23.5 ppm, and the peak signal to noise ratio for the peaks are 15.1, 5.9, and 2.9 for the Ala–6 ^{13}Cβ, ^{13}Cα, and ^{13}CO nuclei. The slice shown in Figure 4–17B is from the Ala ^{13}Cβ β–strand chemical shift of

f_1 = 23.5 ppm, and the peak signal to noise ratio for the peaks are 31.9, 20.2, and 15.6 for the Ala–6 $^{13}C\beta$, $^{13}C\alpha$, and ^{13}CO nuclei and 1.8 for the Gly–10 $^{13}C\alpha$ nuclei.

The slices presented in Figure 4–18 correspond to the f_2 slice of (A) the Ala $^{13}C\beta$ β–strand conformation from f_1 = 23.5 ppm, (B) the Gly $^{13}C\alpha$ β–strand conformation from f_1 = 45.5 ppm, (C) Gly $^{13}C\alpha$ β–strand conformation from f_1 = 171.5 ppm from the 2D ^{13}C–^{13}C DARR experiment with a 500 ms mixing time, presented in Figure 4–17A. The peak signal to noise ratios for Figure 4–18A are 24.8, 15.8, and 12.1 for the Ala–6 $^{13}C\beta$, $^{13}C\alpha$, and ^{13}CO nuclei and 1.5 for the Gly–10 $^{13}C\alpha$ nuclei. The peak signal to noise ratios for Figure 4–18B are 48.9, and 23.9 for the Gly–10 $^{13}C\alpha$ and ^{13}CO nuclei and 2.4 for the Ala–6 $^{13}C\beta$ nuclei. The peak signal to noise ratios for Figure 4–18C are 26.8 and 55.1 for the Gly–10 $^{13}C\alpha$ and ^{13}CO nuclei and 2.1 for the Ala–6 $^{13}C\beta$ nuclei. The peak signal to noise calculations were determined using the method presented in Chapter 3, section "Initial SSNMR Studies for FP–Hairpin in Cholesterol Containing Membranes". The peak signal to noise for the inter–residue contacts for the was determined from the expanded view presented in Figures 4–18D to 4–18F, resulting in a more accurate determination of the peak signal to noise ratio.

New Experiments at 21.1 T

Two new experiments performed at 21.1 T were the ^{15}N CP experiment, which is similar to ^{13}C CP and the double cross polarization (DCP) experiments for selective filtering of the ^{13}C nuclei. The double cross polarization experiments were either a NCA or NCO filtering method. The 1D ^{15}N CP and the 1D DCP experiments will be discussed below.

^{15}N Cross Polarization Experiment

Figure 4–19 illustrates the ^{15}N CP for (A) FP–Hairpin UA6/UG10 with a 15:1 lipid to protein loading and in an 8:2:5 molar ratio of POPC/POPG/Chol in a lipid membrane environment and (B) pH 3.0 sample preparation method in an 8:2:5 molar ratio of POPC/POPG/Chol in a lipid membrane environment. The ^{15}N CP experiment will detect all the ^{15}N signal in the sample. The ^{1}H→^{15}N cross polarization step is performed with the ^{1}H transmitter set to the amide proton of ~7 ppm and the amide ^{15}N of ~110 ppm. This is to selectively excite the amide nitrogens. The typical parameters for the ^{15}N CP are listed in Table 2–5. The ^{15}N CP will also contain natural abundance contributions from the ^{15}N nuclei present in the protein sample. The ^{15}N natural abundance is 0.37%. The protein contains predominantly amide nitrogens in the backbone, but will also contain some amine nitrogens in the side chains of certain amino acids such as arginine, asparagine, glutamine, histidine, lysine, and tryptophan which are all present in the FP–Hairpin construct. The nitrogens in the side chains will have a

different chemical shift by ~50 ppm upfield or downfield from the chemical shift range of the amide nitrogens.[25] The ^{15}N resonances of the side chains will only be naturally abundant. The chemical shift of the amine ^{1}H's is ~3 ppm, which is not near the carrier frequency for the ^{1}H which was placed at δ = 7 ppm. The location of the ^{1}H carrier frequency will result in limited polarization of the ^{1}H resonances which are not near the carrier frequency, resulting in limited $^{1}H \rightarrow {}^{15}N$ cross polarization of any natural abundant amines.

The ^{15}N CP will be composed of both the labeled ^{15}N signal ($^{15}N_{lab}$) and the natural abundance ^{15}N signal ($^{15}N_{NA}$) signal from the backbone amides. FP–Hairpin UA6/UG10 will contain two $^{15}N_{lab}$, one for alanine–6, and one for glycine–10 which are 100% labeled. The remaining FP–Hairpin protein will contain 113 backbone amides which are $^{15}N_{NA}$ at 0.37%. The ^{15}N signal in the CP experiment will then be the total of $^{15}N_{lab}$ + $^{15}N_{NA}$, which is 2 + (113*0.037), or 2.4181. ~82% of the ^{15}N CP signal will be from the $^{15}N_{lab}$ with the remaining signal contributed from $^{15}N_{NA}$ of the protein. The peak chemical shifts ± standard deviation for the amide ^{15}N of alanine are helical (H): 121.4 ± 2.4 ppm and β–strand conformation (β): 124.5 ± 4.4 ppm and for the glycine amide ^{15}N are H: 107.5 ± 2.7 ppm and β: 109.3 ± 3.9 ppm.[1] The determination of the peak chemical shifts were previously described in Chapter 2. The literature values for the chemical shift range of the amide ^{15}N for all the amino acids is between 105 – 128 ppm.[1]

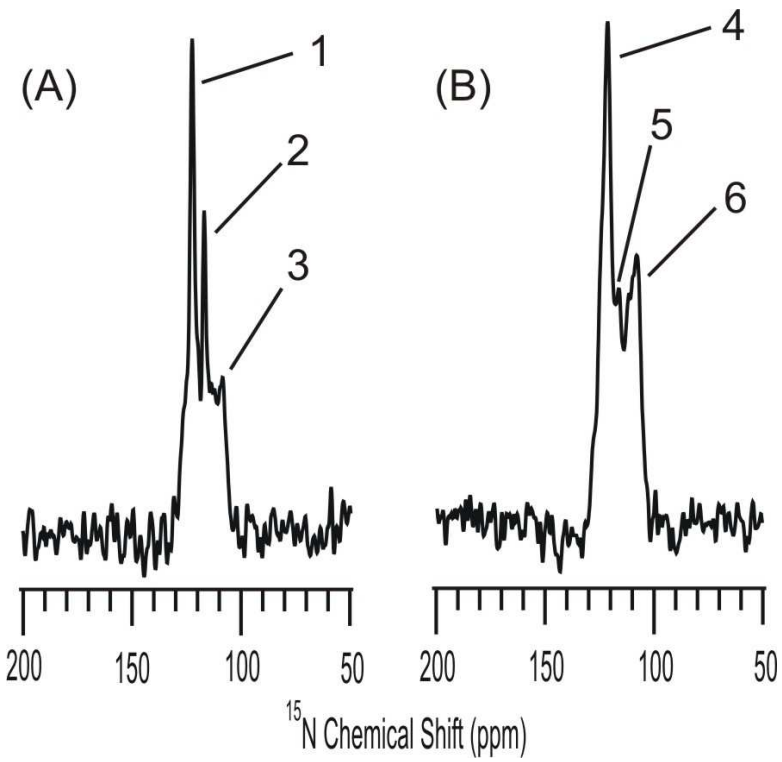

Figure 4–19: ^{15}N cross polarization experiments at 21.1 T using an E–free probe for FP–Hairpin with uniformly labeled Ala–6 and Gly–10 in the FP region in an 8:2:5 molar ratio of POPC/POPG/Chol in a lipid membrane environment. (A) The 15:1 lipid to protein loading sample was prepared by Method A and is at pH 7. (B) The ~33:1 lipid to protein loading sample was prepared by Method B and is at pH 3. Sample preparation was described in Chapter 2 in the sections "Membrane Lipid Preparation" and "Solid State NMR Sample Preparation". The number of acquisitions were (A) 2048 and (B) 4096. 100 Hz of Gaussian line broadening was applied to each spectrum. The spectra were acquired at a nominal temperature of –23 °C as measured at the thermocouple, with 12 kHz spinning frequency and a recycle delay of 3 seconds. The spectra were indirectly referenced from properly referenced ^{13}C spectra as described in the Chapter 2's section "Solid State Nuclear Magnetic Resonance Experiments and Experimental Details" and in Appendix III's section "Referencing the Spectrum". ~1.7 and ~3.5 hrs of signal averaging were required for (A) and (B) respectively. Table 4–9 lists the chemical shifts and FWHM of the peaks for the ^{15}N CP experiments. Peak assignments are likely: (A) Peaks 1–3: (1) Ala–6 β–strand, (2) Ala–6 helical, (3) Gly–10 β–strand. (B) Peaks 4–6: (4) Ala–6 β–strand, (5) Ala–6 helical, (6) Gly–10 β–strand based on the ^{15}N chemical shifts of the RefDB paper.[1]

The ^{15}N cross polarization allows for observation of all the ^{15}N isotopic label in the sample, which were incorporated at Ala–6 and Gly–10, along with any natural abundance signal. The strong ^{15}N signals are obtained for the two protein samples presented in Figure 4–19 suggesting that it is possible to perform experiments which require the ^{15}N label, such as the 1D double cross polarization or 2D heteronuclear ^{15}N–^{13}C correlation experiments at 21.1 T in a reasonable time of several hours to a couple of days.

Table 4–9: Peak chemical shifts and FWHM linewidths of the ^{15}N CP experiments from Figure 4–19 for the FP–Hairpin UA6/UG10 with either ~15:1 or ~33:1 lipid to protein loading in an 8:2:5 molar ratio of POPC/POPG/Chol lipid membrane environment.

Sample / Peak Number	^{15}N Chemical Shift	Assignment	FWHM Linewidth (Hz)
Fig. 4–19A	FP–Hairpin UA6/UG10 at ~15:1 lipid to protein loading		
1	122.3 ppm	Ala–6 ^{15}N β–strand	588.04 ± 16.48
2	116.8 ppm	Ala–6 ^{15}N helical	296.29 ± 19.90
3	108.3 ppm	Gly–10 ^{15}N β–strand	407.85 ± 18.20
Fig. 4–19B	FP–Hairpin UA6/UG10 at ~33:1 lipid to protein loading		
4	121.4 ppm	Ala–6 ^{15}N β–strand	690.32 ± 19.53
5	116.3 ppm	Ala–6 ^{15}N helical	628.54 ± 103.56
6	108.1 ppm	Gly–10 ^{15}N β–strand	622.72 ± 17.99

Assignments were based off of the spectra in Figure 4–19, which had 100 Hz of Gaussian line broadening applied during processing of the spectra in nmrDraw. The ^{15}N chemical shifts were determined from nmrDraw's peak picking function. The full width at half maximum (FWHM) values were determined from the spectra with 25 Hz of exponential multiplication line broadening applied during processing using the Topspin 3.0 software. The peaks were de–convoluted into separate sums of peaks resulting in the ability to measure the FWHM of the fittings with the Topspin 3.0 software. The use of the 25 Hz of exponential multiplication line broadening was to reduce the noise in the spectra and to smooth the peaks out slightly while minimizing any broadening to the peaks. Applying the 25 Hz of line broadening allowed for better fits as determined by visual inspection of the data of the generated de–convolution fits.

The linewidths for the FP–Hairpin UA6/UG10 ~15:1 lipid to protein loading sample were ~300 – 600 Hz, (3.3 – 6.5 ppm) with three distinguishable peaks corresponding to both helical and β–strand conformations. The linewidths for the FP–Hairpin UA6/UG10 sample at pH 3 were ~600 – 700 Hz, (6.8 – 7.6 ppm) for the FWHM values, and corresponded predominantly to the β–strand conformation for the Ala–6 and the Gly–10 residues. Peak 5 has a larger standard deviation associated with the FWHM value due to the peak being short and broad. Peak 5 corresponds to the Ala–6 helical conformation chemical shift for ^{15}N, and the reduced intensity of peak 5 compared to peak 2 is due to the FP–Hairpin protein having a predominantly β–strand conformation in the pH 3 sample preparation as observed in the 2D ^{13}C–^{13}C experiments where as the 15:1 lipid to protein sample contained some helical conformation that is likely due to the precipitated protein in the sample.

A possible explanation for the differences in FWHM linewidths of the ^{15}N spectra are that the pH 3 sample has a significant reduction in helical conformation (Figure 4–19B, peak 5) compared to the 15:1 lipid to protein loading sample (Figure 4–19A, peak 2). The reduction of the helical component is due to the sample preparation at pH 3 favoring the β–strand conformation and preventing the FP–Hairpin protein from precipitating. With all the Ala–6 and Gly–10 ^{15}N signal contributing to the β–strand conformation it will broaden the linewidths of the β–strand conformation. The integrated areas fit with the expected values for the amount of protein in the sample. From calculations, the total ^{15}N area for FP–Hairpin 15:1 lipid to protein loading was ~1.72 times greater than the pH 3 sample preparation of FP–Hairpin, which correlates well with the actually amount of protein in each sample. The 15:1 lipid to protein loading had ~2 μmoles of protein and the pH 3 sample had ~1 μmole of protein.

Double Cross Polarization Experiments at 21.1 T

Figure 4–20 illustrates the double cross polarization (DCP) experiment for uniformly ^{13}C, ^{15}N labeled N–acetyl leucine (U–NAL) compared to the ^{13}C CP experiment. Figure 4–20(A) is the chemical structure of U–NAL. Figure 4–20(B) is the 1D NCO double cross polarization experiment, (C) is the ^{13}C CP experiment and (D) is the 1D NCA double cross polarization experiment. The DCP pulse sequence was shown previously in Figure 2–10 for the $^{1}H \rightarrow {}^{15}N \rightarrow {}^{13}C$ experiment.[26] The NCO experiment transfers polarization from $^{1}H \rightarrow {}^{15}N_{j} \rightarrow {}^{13}CO_{j-1}$, where "j" and "j–1" are the specific residues. The NCA experiment

transfers the polarization from $^{1}H \rightarrow {}^{15}N_j \rightarrow {}^{13}C\alpha_j$, which is within the same residue. The typical parameters for the NCA and NCO experiments were presented in Table 2–6.

To determine the efficiency of the DCP experiment, the filtered spectrum is compared to the ^{13}C CP spectrum. The transfer efficiency (E) is measured by Equation 4–4:

$$E = S_f / S_{CP} \tag{4–4}$$

where S_f is the filtered signal intensity and S_{CP} is the ^{13}C CP signal intensity for the same number of acquisitions.[27] The transfer efficiency for the Leu ^{13}CO, acetyl ^{13}CO, and the Leu $^{13}C\alpha$ are 0.0767, 0.639, and 0.0950 respectively which were determined with Equation 4–4. A possible reason for the Leu ^{13}CO and Leu $^{13}C\alpha$ carbons being present is that there is transfer from the $^{1}H \rightarrow {}^{13}CO$ or $^{1}H \rightarrow {}^{13}C\alpha$ along with the selective $^{1}H \rightarrow {}^{15}N \rightarrow {}^{13}C$ transfer. Further investigation of the proper condition for the ^{13}C–^{15}N transfer needs to be performed.

Experiments were setup and tested on the model compound of U–NAL first before attempting on the protein sample. This is because U–NAL gave peak signal to noise ratios of ~100 in ~256 scans for the $^{13}C\alpha$ – $^{13}C\delta$ region of the ^{13}C CP, as observed in Figure 4–20C. From this, U–NAL yields a peak signal to noise of ~25:1 in 4 scans, making it possible to efficiently optimize the pulse program parameters. Due the high peak signal to noise per scan, optimization of parameters can be performed using setup samples with as few as 8 scans. For protein samples, minor adjustments can then be made to the optimized parameters of U–NAL. The double cross polarization pulse sequence has two CP steps. First, the $^{1}H \rightarrow {}^{15}N$, and then the $^{15}N \rightarrow {}^{13}C$ cross polarization step. Detection for the DCP experiment is done with the ^{13}C nuclei

which have ~2.5–fold higher sensitivity than the ^{15}N nuclei as calculated by the ratio of the ^{13}C and ^{15}N gyromagnetic ratios, $\gamma_{13C}/\gamma_{15N}$. The DCP experiment will allow for probing the secondary structure of the $^{13}C\alpha$ (NCA) or ^{13}CO (NCO) carbons of the labeled residue(s). The DCP experiments use a low frequency transfer of the polarization via the ^{15}N dipole – ^{13}C dipole to match the frequencies between the ^{15}N and ^{13}C nuclei in the $^{15}N \rightarrow {}^{13}C$ cross polarization step. The low frequency transfer of the magnetization is ~51 kHz which is less than the proton decoupling frequency of ~83 kHz that is being applied so the ^{1}H – ^{13}C Hartman – Hahn matching conditions are not satisfied. If the ^{1}H and ^{13}C Hartman – Hahn matching conditions were satisfied then ^{13}C spectrum would also contain signal from ^{13}C nuclei which were not the result of the ^{15}N – ^{13}C cross polarization step. Table 2–6 lists the parameters for the double cross polarization experiments for U–NAL and also for the FP–Hairpin UA6/UG10 protein construct.

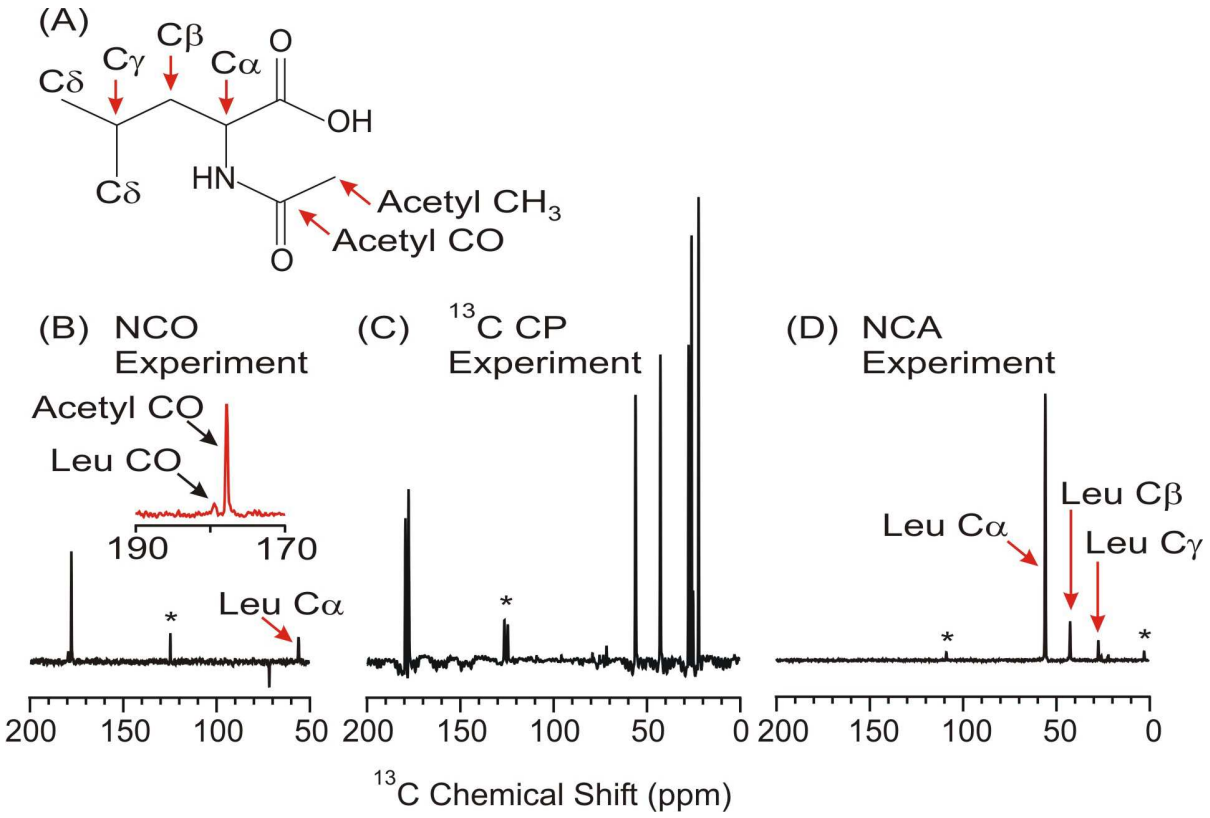

Figure 4–20: (A) Molecular structure of the uniformly labeled N–acetyl leucine (U–NAL) sample that was used for optimizing the double cross polarization experiments at 21.1 T. (B) Filtered spectrum from the 1D double cross polarization NCO experiment, (C) ^{13}C CP experiment of U–NAL, and (D) filtered spectrum from the 1D double cross polarization NCA experiment. Each spectrum is the result of 256 acquisitions and 50 Hz of Gaussian line broadening. The insert in Figure 4–20B is an expanded view of the 170 – 190 ppm range to better illustrate the Leu ^{13}CO and acetyl ^{13}CO signals. Data was acquired at a nominal temperature of –23 °C as measured at the thermocouple and 12 kHz spinning frequency using the 4 mm MAS E–free probe. Table 4–10 lists the chemical shifts for the ^{13}C peaks in Figure 4–20 (B–D). Spinning sidebands are shown as (*) in the spectra (B) for the acetyl ^{13}CO, (C) for the Leu ^{13}CO and acetyl ^{13}CO, and (D) the Leu ^{13}Cα.

Table 4–10: ^{13}C chemical shifts of the U–NAL spectra at 21.1 T presented in Figure 4–20 and comparison to Michelle Bodner's chemical shift measurements of U–NAL at 9.4 T.

^{13}C Chemical Shift (ppm)				
Carbon	**Figure 4–20B**	**Figure 4–20C**	**Figure 4–20D**	**Michelle Bodner [28]**
Acetyl CO	177.7	177.6	–	175.4
Acetyl CH_3	–	22.2	22.1	20.0
Leu CO	179.4	179.3	–	177.2
Leu Cα	56.0	56.1	55.9	53.8
Leu Cβ	–	42.7	42.6	40.5
Leu Cγ	–	27.6	27.5	25.5
Leu Cδ's	–	26.0	25.9	23.9

The U–NAL chemical shifts at 21.1 T are confirmed with those from Michelle Bodner at 9.4 T varying by ~2 ppm.[28] Michelle Bodner's chemical shifts were previously referenced to adamantane at 38.5 ppm in 2003, whereas the 21.1 T U–NAL spectra were referenced to 40.5 ppm. The difference between references is 2 ppm, correlating to the 2 ppm difference between the chemical shifts presented in Table 4–10. Correcting Michelle Bodner's U–NAL shifts by 2 ppm brings the U–NAL chemical shifts at both 9.4 T and 21.1 T to within 0.2 ppm, good agreement.

Shown in Figure 4–20B is the 1D double cross polarization NCO experiment where the directly bonded ^{13}CO of the acetyl group at 177.7 ppm is observed predominantly with a transfer efficiency of 0.639. A small peak at 179.4 ppm for the Leu ^{13}CO peak is observed with a transfer efficiency of 0.0767. The transfer efficiency was determined using Equation 4–4, with the comparison of the filtered signal of the DCP experiment compared to the ^{13}C CP of Figure 4–20C. Ideally, there will be no signal from the Leu ^{13}CO, and 100% signal retention for the

acetyl ^{13}CO peak. The Leu ^{13}Cα carbon is also observed near 56 ppm with a transfer efficiency of 0.0950, suggesting that the setup of the NCO experiment could be further optimized as not all the ^{13}Cα signal is being filtered out.

The DCP experiments performed using U–NAL were to optimize the parameters for the experiment before performing the DCP experiment with the FP–Hairpin UA6/UG10 protein sample. Shown in Figure 4–20C is the ^{13}C CP experiment with the same number of acquisitions as the DCP experiments. It was found that under these conditions, the transfer efficiency was 0.639 for the NCO and ~1 for the NCA experiments as determined from Figure 4–20 (B,D). Maximum efficiency is E = 1, which is when the filtered signal is equal to the signal from the ^{13}C CP signal. The DCP experiments will filter out all other ^{13}C nuclei except for the directly bonded to the ^{15}N. The selective transfer to either the ^{13}CO or the ^{13}Cα is achieved by placing the transmitter near the ^{13}CO (~165 ppm) or the ^{13}Cα (~50 ppm) nuclei and then transferring magnetization using a low frequency of ~51 kHz from the ^{15}N→^{13}C nuclei. By performing the magnetization transfer under the low frequency of ~51 kHz, the Hartman – Hahn matching conditions for the ^{15}N – ^{13}C are significantly removed from the high power decoupling Rabi frequency for ^{1}H of ~83 kHz. Not matching the ^{15}N – ^{13}C frequency to the decoupling frequency will result in eliminating the possibility of magnetization transfer from the ^{1}H→^{13}C nuclei through the dipole – dipole interactions. As seen in Figure 4–20B, selective filtering of the acetyl ^{13}CO is achieved as it is directly bonded by the ^{15}N–^{13}CO. The leucine ^{13}CO is only ~9% of the original signal in the filtered DCP experiment compared to the ^{13}C CP experiment.

The reason for the observation of the acetyl ^{13}CO signal and the lack of the leucine ^{13}CO signal in the double cross polarization NCO spectrum is due to the direct bonding of the acetyl ^{13}CO and the distance between the ^{15}N – ^{13}CO nuclei. The transfer rate of the magnetization is going to depend on the dipole – dipole interaction, and is related to the inverse of the distance raised to the sixth power ($1 / r^6$) between the two nuclei, where r is the inter–nuclear vector between the two nuclei.[24] Therefore, the acetyl ^{13}CO which is ~1.5 Å will have a higher transfer rate than the leucine ^{13}CO which is greater than 3 Å away from the ^{15}N nuclei through space.

For the NCA experiment of Figure 4–20D, the ^{13}Cα is observed and some ^{13}Cβ signal is also observed in the spectrum. The ^{13}Cβ signal chemical shift range is ~20 – 30 ppm, which are only separated by 3 to 7 kHz. The difference between the Leu Cα to Leu Cβ is ~3 kHz, the difference between the Leu Cα to Leu Cγ is ~6.4 kHz, and the difference between the Leu Cα to the Leu Cδ is ~6.8 kHz when the carrier frequency is placed at 50 ppm for the NCA experiment. Thus, the ^{13}Cβ carbons have the ability to match the ^{15}N→^{13}Cα transfer condition and be detected. From Figure 4–20D the transfer efficiency was measured as ~1.000, 0.127, and 0.065 for the Leu ^{13}Cα, Leu ^{13}Cβ, and Leu ^{13}Cγ nuclei respectively. As the distance between the ^{15}N and the ^{13}C nuclei increases, the transfer efficiency decreases, as observed with the ^{13}C peaks having less intensity. There are no ^{13}CO signals detected as there is a greater difference in frequency. The difference between the Leu Cα to Leu CO is 27.8 kHz and the Leu CO – Leu Cβ is ~31 kHz for those carbons.

Figure 4–21 illustrates the results for FP–Hairpin pH 3.0 sample preparation's 1D NCA experiment. Figure 4–21(A) shows the 1D ^{13}C CP experiment, (B) is the 1D NCA experiment and (C) illustrates the pathway of magnetization transfer for the experiment in regards to the protein backbone between residues G5 to F11. Figure 4–21(A,B) are the sum of 4096 acquisitions providing for direct comparison between the ^{13}C CP and the filtered double cross polarization signal. The red spectrum in Figure 4–21B is scaled to the same noise level as the ^{13}C CP spectrum in Figure 4–21A. The blue x10 spectrum in Figure 4–21B is a 10x scaling of the 1D NCA double cross polarization spectrum, which is provided for observing the linewidths of the filtered signals. The peak chemical shift is 50.5 ppm for the Ala–6 ^{13}Cα and 45.2 ppm for the Gly–10 ^{13}Cα peak in Figure 4–21B corresponding to the β–strand conformation.

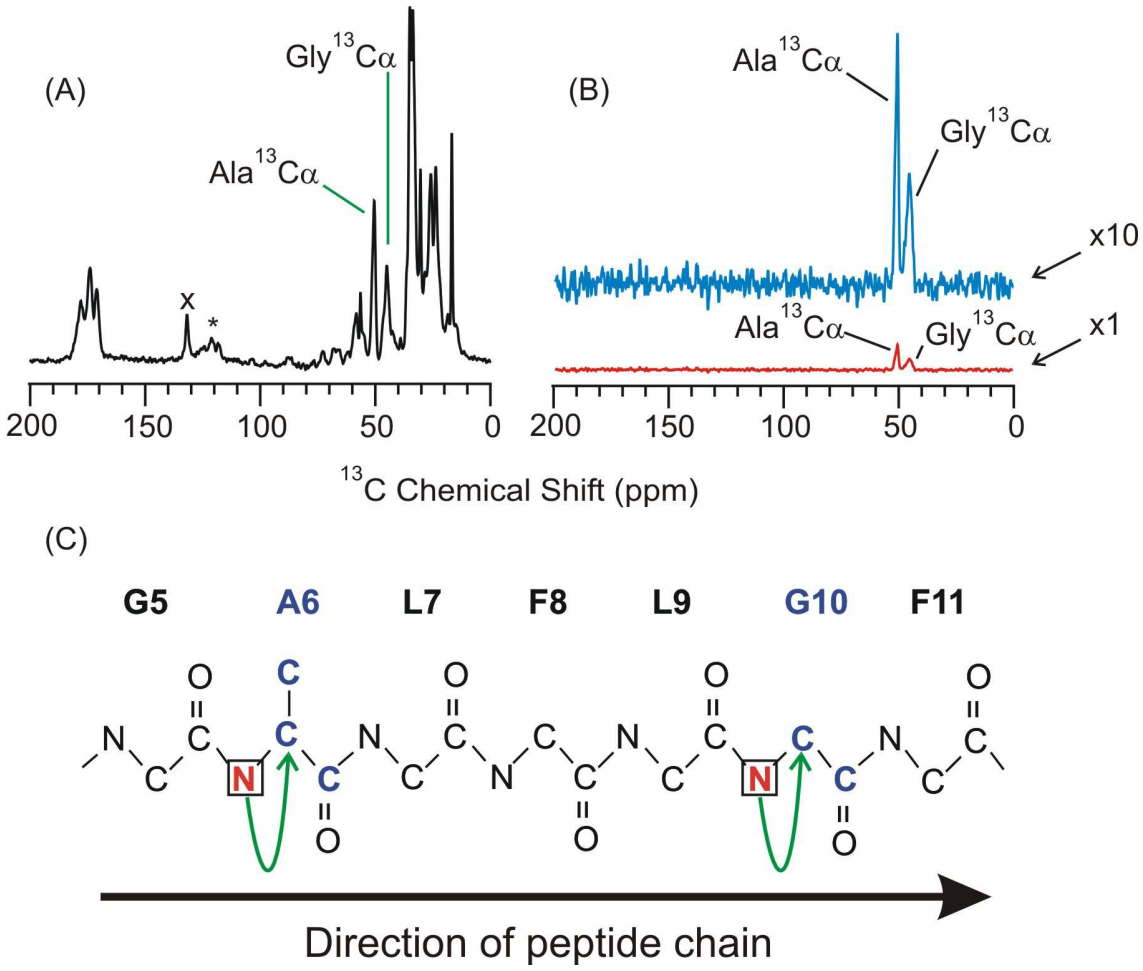

Figure 4–21: Comparison of ^{13}C CP experiment and the 1D NCA double cross polarization experiment for FP–Hairpin with uniform Ala–6 and Gly–10 labeling in the FP region in an 8:2:5 molar ratio of POPC/POPG/Chol in a lipid membrane environment. (A) ^{13}C CP of FP–Hairpin at ~33:1 loading sample using the pH 3.0 sample preparation method. (B) The corresponding 1D NCA double cross polarization experiment. Comparison of the 1D NCA experiments highlights the filtering by selectively transferring magnetization from ^{1}H → ^{15}N→ ^{13}Cα. Each spectrum is the result of 4096 acquisitions and application of 100 Hz Gaussian line broadening. (C) Graphical representation of the NCA experiment as applied to the FP backbone region. Magnetization is prepared on the ^{1}H nucleus and then transferred from the ^{1}H to the ^{15}N nuclei in the first cross polarization step. Next, the transfer of the magnetization from the ^{15}N to ^{13}C nuclei is performed with a cross polarization step of ~51 kHz Rabi frequency and a tangent ramp. The frequency is matched specifically for the ^{15}N to ^{13}Cα transfer eliminating transfer to the ^{13}CO and contributions from natural abundance ^{13}Cα nuclei. The chemical shift of δ = 131 ppm (x) was previously discussed in Figure 4–9. Spinning sidebands are marked by (*).

As discussed above for the model compound of U–NAL, the 1D DCP experiment allows for the selective filtering of the ^{13}C nuclei. For the FP–Hairpin UA6/UG10, the uniform labeling does not put a ^{15}N directly bonded to a ^{13}CO, therefore the NCO experiment was not performed. However, the labeling does allow for the NCA experiment to be performed which is presented in Figure 4–21. Figure 4–21A is the ^{13}C CP experiment and (B) is the 1D double cross polarization NCA experiment for FP–Hairpin UA6/UG10 which was prepared at pH 3. 4096 acquisitions were acquired for both the ^{13}C CP and the DCP experiment allowing for direct comparison of the transfer efficiency for this experiment. Figure 4–21B shows that the Ala $^{13}C\alpha$ and Gly $^{13}C\alpha$ peaks are observed for Ala–6 and Gly–10 with β–strand conformations. Only the $^{13}C\alpha$ signals were observed due to the transmitter offset of ~50 ppm. The NCA double cross polarization experiments used ~51 kHz Rabi frequency to transfer the polarization from the $^{15}N \rightarrow {}^{13}C$ nuclei. This was less than the ~83 kHz ^{1}H decoupling in the aim to avoid any signals arising from the direct $^{1}H \rightarrow {}^{13}C$ transfer. These conditions were used for the U–NAL sample in Figure 4–20 and the FP–Hairpin sample in Figure 4–21. Figure 4–21C graphically depicts part of the FP–Hairpin backbone chain, and shows the transfer of magnetization from the ^{15}N (red) to the ^{13}C (blue) via the arrow (green). As can be seen, it occurs at both the Ala–6 and Gly–10 residues.

The measured transfer efficiencies were 0.177 for Ala $^{13}C\alpha$ and 0.139 for Gly $^{13}C\alpha$ as determined by using the efficiency Equation 4–4. The spectra in Figure 4–21 (A, B) are

presented with a common noise level. The spectra in Figure 4–21A and the Figure 4–21B x1 (red) spectra are scaled to the same noise level. To determine the transfer efficiency of the Ala–6 $^{13}C\alpha$ in the DCP experiment, the signal of the ^{13}C CP was determined by measuring from the peak of the Ala–6 $^{13}C\alpha$ signal to the baseline of the signal. The same was done for the DCP filtered spectrum presented in Figure 4–21B (x1, red). The ratio of the filtered signal to the signal from the cross polarization experiment will provide the transfer efficiency, as defined by Equation 4–4. The same was done for the Gly–10 $^{13}C\alpha$ signal. Figure 4–21A marks the glycine $^{13}C\alpha$ β–strand and the alanine $^{13}C\alpha$ β–strand peaks used for determining the transfer efficiency. To better illustrate the filtered DCP spectrum a 10x expanded view is also provided. The FWHM linewidths of the Ala–6 $^{13}C\alpha$ and the Gly–10 $^{13}C\alpha$ peaks are 323 Hz (1.4 ppm) and 565 Hz (2.5 ppm) respectively, which were determined without applying line broadening the spectrum. The affect of the natural abundance signal on the filtered DCP spectrum will be presented along with a discussion on the upper limit to the transfer efficiency for the double cross polarization NCA experiment in terms of the FP–Hairpin UA6/UG10 protein system.

The following paragraph will discuss how the upper limit of the expected NCA signal for FP–Hairpin was determined. The FP–Hairpin UA6/UG10 sample at ~33:1 lipid to protein loading contained ~1 μmole of protein. Only the first 23 residues are being considered with the following assumptions. First, residues Ala–1 to Gly–16 are in the β–strand conformation based on previous work for FP23 [3, 5, 23] and current work for FP–Hairpin prepared with the pH 3 sample preparation protocol. Second, the ^{1}H is 100% abundant, Ala–6 and Gly–10 are 100% U–^{13}C, ^{15}N labeled, and the natural abundance for the alanine and glycine ^{13}C is 1.1% and for ^{15}N

is 0.37%. The total signal from the ^{13}C CP ramp for the alanine $^{13}C\alpha$ β–strand conformation is only from the alanines in the FP region of A1–G16, which contains 4 alanines. The glycine $^{13}C\alpha$ β–strand conformation is only from the glycine residues in the FP region of A1–G16, which contains 5 glycines. The final assumption is that the transfer of polarization in each step is ideal and 100%. The $^{1}H \rightarrow {}^{15}N$ transfer will be 100%, and the $^{15}N \rightarrow {}^{13}C\alpha$ transfer will be 100%, with both transfers being separate from each other. Two cases will be presented, one where only the labeled ^{13}C and ^{15}N are considered, neglecting any natural abundance contribution. The second case will consider both label and natural abundance contributions for the NCA experiment.

Case 1: Only considering the labeled component and ignoring the natural abundance from the ^{13}C and ^{15}N residues during the $^{15}N \rightarrow {}^{13}C\alpha$ transfer. The $^{1}H \rightarrow {}^{15}N$ will be 1, as it is assumed that 100% transfer between ^{1}H and ^{15}N occurs. The transfer to the $^{13}C_{lab}$ will also be 1, as the transfer is assumed to be 100%, resulting in the $^{13}C\alpha$ signal for either Ala–6 or Gly–10 to be (1 * 1) = 1 in the NCA filtered spectrum. The transfer efficiency is defined previously by Equation 4–4 and is the filtered signal divided by the ^{13}C CP signal. The ^{13}C CP has 4 alanine contributing to the Ala $^{13}C\alpha$ β–strand conformation, which results in the ^{13}C CP signal being the sum of the $^{13}C_{lab}$ + $^{13}C_{NA}$, which is 1 + (3*0.011) or 1.033 for the total ^{13}C signal. The Ala $^{13}C\alpha$ β–strand conformation should have an upper limit of 1 / 1.033, or 0.968 transfer efficiency. For glycine there are 5 residues, which will result in $^{13}C_{lab}$ + $^{13}C_{NA}$ equaling 1 + (4*0.11) or 1.044. The upper limit to the transfer efficiency for Gly–10 will be 1 / 1.044, or 0.958.

Case 2: Considering the labeling and the natural abundance contributions during the transfer from $^{15}N \rightarrow {}^{13}C\alpha$ cross polarization step. In this case, the protein will contain three $^{15}N_{NA}$ labels for alanine and four $^{15}N_{NA}$ labels for glycine between residues Ala–1 and Gly–16. Assuming 100% transfer efficiency, the ^{15}N total signal will be $^{15}N_{lab} + {}^{15}N_{NA}$. The transfer step of $^{15}N \rightarrow {}^{13}C\alpha$ can be broken down into four conditions.

Condition 1: $^{15}N_{lab} \rightarrow {}^{13}C_{lab}$ transfer, which was presented in case 1.

Condition 2: $^{15}N_{NA} \rightarrow {}^{13}C_{lab}$, which will be 0 as there are no labeled ^{13}C in the protein directly bonded to naturally abundant ^{15}N.

Condition 3: $^{15}N_{lab} \rightarrow {}^{13}C_{NA}$, which will be 0 as there are no labeled ^{15}N nuclei bonded to naturally abundant ^{13}C nuclei.

Condition 4: $^{15}N_{NA} \rightarrow {}^{13}C_{NA}$, which is possible if there are any ^{15}N and ^{13}C naturally abundant nuclei directly bonded. If there are directly bonded $^{15}N_{NA} - {}^{13}C_{NA}$ then this will also contribute to the filtered NCA signal. Considering that the probability that a $^{15}N_{NA} - {}^{13}C_{NA}$ pair to exist would be (0.0037 * 0.011) which is 4.1×10^{-5}, this signal will not affect the observed NCA filtered signal for either the Ala–6 or the Gly–10 $^{13}C\alpha$ residues with a β–strand conformation. Therefore, the $^{15}N_{NA} \rightarrow {}^{13}C_{NA}$ condition can be ignored.

Published transfer efficiencies for the DCP experiments are between 0.40 – 0.73 for powered samples of glycine or dipeptide systems.[26, 29–36] The glycine samples were either

uniformly labeled and then diluted to 10% (w/w) with natural abundance glycine or were 2–^{13}C, ^{15}N or 1–^{13}C, ^{15}N labeled glycine.[29] DCP has been previously used to study the ^{15}N–^{13}C heteronuclear coupling correlations, as it provides greater sensitivity than can be obtained by a single CP between the low–γ nuclei.[31] The transfer efficiency values for FP–Hairpin are lower than published efficiencies for peptides, however the U–NAL values fit well or better than the published reports. Further optimization of the DCP experiment tailored to the protein in a lipid environment could provide higher transfer efficiencies. It is likely that the NCA experiment is nearly optimized for the U–NAL sample in Figure 4–20 as the NCA efficiency value is ~1 for the Leu ^{13}Cα.

When working on setting up the NCO experiment, I found that transitioning from the U–NAL model compound to a lyophilized peptide of FP23(linker) with L7/F8 ^{13}CO/^{15}N labeling required that the DCP parameters needed to be adjusted. Specifically, the ^{1}H–^{15}N contact time, ^{15}N–^{13}C contact time, and the acquisition time were re–optimized for the lyophilized sample of FP23(linker) L7/F8. The acquisition time was reduced from 15.05 ms to 1.88 ms as the FID truncates before the end of a 15 ms acquisition time for FP23(linker) without the introduction of ringing in the spectrum, which occurs when a FID does not decay completely before ending the acquisition of the data. Attempts at performing the 1D NCO double cross polarization experiment using a FP–Hairpin sample with ^{13}CO at Met–19 and ^{15}N at Gly–20 in a lipid membrane environment failed to give any filtered ^{13}CO signal. The FP–Hairpin M19/G20 sample contained the directly bonded ^{13}CO–^{15}N and was prepared by Dr. Kelly Sackett. It is

possible that the lipid membrane environment at –23 °C is more fluid that the lyophilized peptide of FP23(linker) or U–NAL which were used to test the NCO double cross polarization experiment. The motional averaging from the fluid like environment of the lipid membranes could be the reason why no filtered signal is observed. 1D ^{13}C CP and ^{15}N CP ramps were acquired and showed strong signals for all samples that the NCO double cross polarization experiment were tested on. It is likely that the environmental conditions of the sample affect the DCP conditions. Further work to optimize the DCP conditions for NCA and NCO experiments for proteins may result in an increased transfer efficiency.

Conclusions

The major conclusions from Chapter 4's high field SSNMR work are presented here. SSNMR experiments at the high field of 21.1 T and an E–free probe resulted in an ~5–fold increase in ^{13}C peak signal to noise per scan and two fold decrease in linewidths in ppm units for the slices from the 2D ^{13}C–^{13}C experiments. Since the FWHM linewidths in hertz were of similar values at the different fields at seen in Table 4–5 the ppm value was reduced by a factor of 2 at the higher fields where 1 ppm equals ~226 Hz at 21.1 T and ~100 Hz at 9.4 T. Narrower linewidths in ppm units allowed for more resolution in assignments of the cross peaks using the 21.1 T spectrometer for the ^{13}CO/^{13}Cα and the ^{13}Cα/^{13}CO region. The 15:1 lipid to protein loading sample for FP–Hairpin UA6/UG10 still showed no unique inter–residue A6 / G10 cross peaks at 21.1 T, which is consistent with observations at 9.4 T.

A FP23 UA6/UG10 sample from Michelle Bodner did show unique inter–residue A6 / G10 cross peaks with a 500 ms mixing time at 21.1 T in Figures 4–17 and 4–18. This is

consistent with the previous 2D ^{13}C–^{13}C experiments with an 1000 ms mixing time for FP23 at 9.4 T.[3] Observation of the inter–residue A6 / G10 cross peaks at 21.1 T for FP23 supports the results that the FP domain of FP–Hairpin is different than the FP domain for just the FP23 peptides. Thus, FP–Hairpin genuinely has a different tertiary structure for the FP domain in the lipid membrane with the appendage of the folded SHB state than FP23 does in the lipid membrane environment which lacks the SHB.

The pH 3 sample preparation and subsequent pH swap to pH 7 work for FP–Hairpin resulted in a single β–strand conformation assignment of the secondary structure at the A6 and G10 residues in FP–Hairpin which was inserted into cholesterol containing membranes at ~33:1 lipid to protein ratio. The chemical shifts for these two samples were predominantly β–strand, and correlated well with previous work showing that the FP23 adopts a predominantly β–strand secondary structure in cholesterol containing membranes.[21, 22] The pH 3 sample was prepared with ~1 μmole of protein and was able to be studied by SSNMR experiments at 21.1 T due to the 5–fold increase in ^{13}C peak signal to noise per scan achieved at 21.1 T for the FP–Hairpin UA6/UG10 protein sample. The FP–Hairpin 25:1 lipid to protein loading sample in the same lipids of POPC/POPG/Chol presented in Chapter 3 would be comparable to this sample as both contained ~1 μmole of protein. For the FP–Hairpin sample at both pH 3 the peak signal to noise ratio was at least 3:1 and in the pH 7 sample the peak signal to noise of the off diagonal cross peaks were at least ~2:1 in ~14 hrs of signal averaging time. For the 500 ms mixing time experiments, the off diagonal intra–residue cross peaks were at least ~3:1 and for the pH 3 sample, and at least ~2:1 in ~46 hrs of signal averaging time. The pH 3 sample and the pH swap to pH 7 sample would not be feasible at the 9.4 T spectrometer as previously shown by the 25:1

lipid to protein loading sample of Figure 3–5. These samples would require signal averaging of ~3 days for the 50 ms exchange time and for ~8 days or longer for the 500 ms exchange time. While preparing the sample at pH 3 resulted in the elimination of the helical conformation for alanine–6 and glycine–10, compared to the previous work with FP–Hairpin, the data for both sample preparations still contained the β–strand conformation which is likely membrane inserted. The retention of the β–strand conformation of the alanine–6 and glycine–10 residues of the FP domain for FP–Hairpin are in agreement with work for FP23 which was membrane inserted in cholesterol containing lipid membranes. One possibility for the lack of the helical component using the pH 3 preparation is due to separating the protein which was not inserted into the membrane from the protein–lipid complex. The protein that was not inserted into the membrane will still be soluble at pH 3 in the supernatant after centrifugation to pellet the protein–lipid complex. Regardless of the sample preparation method, the 500 ms mixing time experiments showed that no A6 / G10 inter–residue cross peaks are observed for the three FP–Hairpin samples at 21.1 T presented in Chapter 4. The lack of A6 / G10 inter–residue cross peaks are consistent with all work for FP–Hairpin presented in this dissertation. The data therefore suggests that the FP domain of FP–Hairpin adopts a different tertiary structure in the lipid membrane environments due to the SHB appendage compared to the FP23 peptides lacking this SHB formation.

Two types of experiments that are not feasible to perform at 9.4 T because of the low gamma sensitivity were tested at 21.1 T. The experiments were the ^{15}N cross polarization experiment and the 1D NCA and NCO double cross polarization experiments. These experiments lay the ground work for future new experiments such as combining DCP filtering with distance measurements [29] or 2D ^{15}N–^{13}C heteronuclear correlations [30]. The transfer

efficiency of the 1D NCA experiment for the U–NAL setup compound was ~1 for the Leu $^{13}C\alpha$ and for the pH 3 sample of FP–Hairpin UA6/UG10 were 0.177 for Ala $^{13}C\alpha$ and 0.139 for the Gly $^{13}C\alpha$. The 1D NCO double cross polarization experiments were performed on U–NAL yielding ~0.638 transfer efficiency which fits well with the reported values for the double cross polarization experiments for NCO, but leaves room for improvement as well. This experiment was not tested on FP–Hairpin UA6/UG10 due to the labeling scheme. The NCO double cross polarization experiment was attempted on several protein samples containing the $^{13}CO_{j-1}$ and $^{15}N_j$ labeling scheme with no success. The motional averaging of the protein in the fluid like membrane environment is probably the reason why the NCO experiment did not work for FP–Hairpin M19/G20. More rigid samples that are in a powder form or experience less motional averaging by being at colder temperatures may get around this problem.

Finally, the E–free probe and higher magnetic fields greatly benefited this research. A 5–fold increase in ^{13}C peak signal to noise per scan was obtained by using the 21.1 T spectrometer, which is consistent with the theoretical prediction outlined in the section "Affect of Field on ^{13}C peak signal to noise per scan for 1D CP experiments". A two fold reduction in the linewidths in ppm units for the 2D ^{13}C–^{13}C experiments at high magnetic fields were beneficial to obtaining resolved peaks and provided unambiguous assignments of the off diagonal cross peaks. Comparison of the FP–Hairpin UA6/UG10 15:1 lipid to protein loading sample was studied at 16.5 T and 21.1 T resulted in observing a ~2–fold increase in ^{13}C peak signal to noise per scan being achieved between the two fields. While this is a higher increase than expected of ~1.65, the

data suggest that the ^{13}C peak signal to noise ratio per scan increases as the square of the field ratio. One possible explanation is that the optimized ^{13}C CP programs had different conditions as presented in Table 4–3 for decoupling. Regardless, the data fit well with the ratio of the fields having a squared dependence. Comparison of the integrated area between the 16.5 T and the 21.1 T ^{13}C CP experiments suggest that the probe design as well as the high magnetic fields contributes to the increased peak signal to noise per scan and the increased integrated area of the spectra. The increase in integrated area from 16.5 T increased by ~3.45–fold at 21.1 T for the same sample, which is double what was expected. This suggests that the probe provides a significant increase for the ^{13}C nuclei with the E–free probe design. Comparison of the total integrated area at 9.4 T to 21.1 T resulted in an average of ~11.6–fold increase in the total integrated area at 21.1 T compared to 9.4 T as presented in Table 4–4. This increase is ~2–fold greater than what was expected by going from 9.4 T to 21.1 T if the integrated area depends only on the square of the fields. Therefore, the probe design of the solenoid coil at 9.4 T to the E–free probe design at 21.1 T must also account for increasing the total integrated area of the ^{13}C peaks. The only other difference would be that the nominal temperature of the samples were –50 $^{\circ}$C and –23 $^{\circ}$C at 9.4 T and 21.1 T as measured by the thermocouple. It is likely that the sample temperatures are warmer than that as discussed in the section "Affect of Field on ^{13}C Peak Signal to Noise per scan for 1D CP Experiments" which could cause more motional averaging in the 16.5 T and 21.1 T spectra than in the 9.4 T spectra. Likely the main reason is due to the E–free probe design and the higher magnetic fields.

The E–free probe design used at the higher fields works well with the biological samples which can contain high salt concentrations. By reducing the conservative electric field, the sample is less likely to be heated as compared to a non E–free probe which does not minimize the conservative electric field. Sample heating can damage or destroy the precious protein sample and dehydration of the protein sample from heating can result in broader lines due to inhomogeneous line broadening.

REFERENCES

References

1. Zhang, H.Y., S. Neal, and D.S. Wishart, *RefDB: A database of uniformly referenced protein chemical shifts.* Journal of Biomolecular Nmr, 2003. **25**(3): p. 173–195.

2. Castellani, F., et al., *Structure of a protein determined by solid–state magic–angle–spinning NMR spectroscopy.* Nature, 2002. **420**(6911): p. 98–102.

3. Qiang, W., M.L. Bodner, and D.P. Weliky, *Solid–state NMR spectroscopy of human immunodeficiency virus fusion peptides associated with host–cell–like membranes: 2D correlation spectra and distance measurements support a fully extended conformation and models for specific antiparallel strand registries.* J Am Chem Soc, 2008. **130**(16): p. 5459–71.

4. Sackett, K., et al., *Residue specific secondary– and high resolution tertiary structure analysis of the HIV gp41 fusion peptide in constructs modeling fusion relevant gp41 conformations; implications for oligomerization of gp41 trimers.*

5. Schmick, S.D. and D.P. Weliky, *Major Antiparallel and Minor Parallel beta Sheet Populations Detected in the Membrane–Associated Human Immunodeficiency Virus Fusion Peptide.* Biochemistry, 2010. **49**(50): p. 10623–10635.

6. Qiang, W., Y. Sun, and D.P. Weliky, *A strong correlation between fusogenicity and membrane insertion depth of the HIV fusion peptide.* Proc Natl Acad Sci U S A, 2009. **106**(36): p. 15314–9.

7. Bodner, M.L., et al., *Temperature dependence and resonance assignment of C–13 NMR spectra of selectively and uniformly labeled fusion peptides associated with membranes.* Magnetic Resonance in Chemistry, 2004. **42**(2): p. 187–194.

8. Gor'kov, P.L., W.W. Brey, and J.R. Long, *Probe Development for Biosolids NMR Spectroscopy*, in *Encyclopedia of Magnetic Resonance*. 2007, John Wiley & Sons, Ltd.

9. Freeman, R. and J.B. Robert, *A Brieft History of High Resolution NMR*, in *NMR at Very High Field*, P. Diehl, et al., Editors. 1991, Springer–Verlag. p. 1–16.

10. Canet, D. and J.B. Robert, *Behaviour of the NMR Relaxation Parameters at High Fields*, in *NMR at Very High Field*, P. Diehl, et al., Editors. 1991, Springer–Verlag. p. 45–89.

11. McNeill, S.A., et al., *Optimizing ssNMR experiments for dilute proteins in heterogeneous mixtures at high magnetic fields.* Magnetic Resonance in Chemistry, 2007. **45**: p. S209–S220.

12. McNeill, S.A., et al., *A low–E magic angle spinning probe for biological solid state NMR at 750 MHz.* Journal of Magnetic Resonance, 2009. **197**(2): p. 135–144.

13. Fukushima, E. and S.B.W. Roeder, *Experimental Pulse NMR, A Nuts and Bolts Approach*. 1997, Reading, MA: Addison–Wesley Publishing Company.

14. Haeberlen, U., *Solid State NMR in High and Very High Magnetic Fields*, in *NMR at Very High Field*, P. Diehl, et al., Editors. 1991, Springer–Verlag. p. 143 – 168.

15. Brey, W.W., *Low–E Probe Development at the NHMFL*. 2009: Review of Instrumentation.

16. Halliday, D., R. Resnick, and J. Walker, *Fundamentals of physics*. 6th ed. 2001, New York: John Wiley & Sons.

17. Gor'kov, P.L., et al., *Using low–E resonators to reduce RF heating in biological samples for static solid–state NMR up to 900 MHz.* Journal of Magnetic Resonance, 2007. **185**(1): p. 77–93.

18. Mispelter, J., M. Lupu, and A. Briguet, *NMR probeheads for biophysical and biomedical experiments : theoretical principles & practical guidelines*. 2006, Hackensack, NJ: Imperial College Press ; Distributed by World Scientific. xiv, 596 p.

19. Sackett, K., A. TerBush, and D.P. Weliky, *HIV gp41 six–helix bundle constructs induce rapid vesicle fusion at pH 3.5 and little fusion at pH 7.0: understanding pH dependence of protein aggregation, membrane binding, and electrostatics, and implications for HIV–host cell fusion.* European Biophysics Journal with Biophysics Letters, 2011. **40**(4): p. 489–502.

20. Sackett, K., et al., *Hairpin folding of HIV gp41 abrogates lipid mixing function at physiologic pH and inhibits lipid mixing by exposed gp41 constructs.* Biochemistry, 2009. **48**(12): p. 2714–22.

21. Yang, J., C.M. Gabrys, and D.P. Weliky, *Solid–state nuclear magnetic resonance evidence for an extended beta strand conformation of the membrane–bound HIV–1 fusion peptide.* Biochemistry, 2001. **40**(27): p. 8126–37.

22. Bodner, M.L., *Solid state nuclear magnetic resonance of the HIV–1 and influenza fusion peptides associated wtih membranes*. 2006, Michigan State University: East Lansing, MI.

23. Qiang, W., J. Yang, and D.P. Weliky, *Solid–state nuclear magnetic resonance measurements of HIV fusion peptide to lipid distances reveal the intimate contact of beta strand peptide with membranes and the proximity of the Ala–14–Gly–16 region with lipid headgroups.* Biochemistry, 2007. **46**(17): p. 4997–5008.

24. Weliky, D.P. *Chemistry 988 Lecture Notes*. [website containing pdf file of notes] May 3, 1999 [cited 2011 19 December 2011]; Available from: http://www2.chemistry.msu.edu/courses/CEM988NMR/cem988nmr.htm.

25. Witanows.M, *NITROGEN NMR–SPECTROSCOPY.* Pure and Applied Chemistry, 1974. **37**(1–2): p. 225–233.

26. Baldus, M., et al., *Cross polarization in the tilted frame: assignment and spectral simplification in heteronuclear spin systems.* Molecular Physics, 1998. **95**(6): p. 1197–1207.

27. Yang, J., et al., *Application of REDOR subtraction for filtered MAS observation of labeled backbone carbons of membrane–bound fusion peptides.* J Magn Reson, 2002. **159**(2): p. 101–10.

28. Bodner, M.L., *Temperature dependence, structural plasticity, and resonance assignment of uniformly labeled HIV–1 fusion peptides associated with membranes*. 2003, Michigan State University. Dept. of Chemistry 2003. p. xi, 55 leaves.

29. Vogt, F.G., et al., *Measurement of Internuclear Distances in Solid–State NMR by a Background–Filtered REDOR Experiment.* Journal of Magnetic Resonance, 2000. **147**(1): p. 26–35.

30. Rienstra, C.M., et al., *2D and 3D 15N−13C−13C NMR Chemical Shift Correlation Spectroscopy of Solids: Assignment of MAS Spectra of Peptides.* Journal of the American Chemical Society, 2000. **122**(44): p. 10979–10990.

31. Schaefer, J., R.A. McKay, and E.O. Stejskal, *Double–cross–polarization NMR of solids.* Journal of Magnetic Resonance (1969), 1979. **34**(2): p. 443–447.

32. Baldus, M., et al., *Efficient15N–13C Polarization Transfer by Adiabatic–Passage Hartmann–Hahn Cross Polarization.* Journal of Magnetic Resonance, Series A, 1996. **118**(1): p. 140–144.

33. Sun, B.Q., et al., *3D 15N−13C−13C Chemical Shift Correlation Spectroscopy in Rotating Solids.* Journal of the American Chemical Society, 1997. **119**(36): p. 8540–8546.

34. Kehlet, C.T., et al., *Improving Solid–State NMR Dipolar Recoupling by Optimal Control.* Journal of the American Chemical Society, 2004. **126**(33): p. 10202–10203.

35. Bjerring, M. and N.C. Nielsen, *Solid–state NMR heteronuclear coherence transfer using phase and amplitude modulated rf irradiation at the Hartmann–Hahn sideband conditions.* Chemical Physics Letters, 2003. **382**(5–6): p. 671–678.

36. Christiansen, S.C., et al., *Sensitivity considerations in polarization transfer and filtering using dipole–dipole couplings: Implications for biomineral systems.* Solid State Nuclear Magnetic Resonance, 2006. **29**(1–3): p. 170–182.

Chapter 5:

Conclusions and Future Work

Conclusions

The research presented in this Ph.D. dissertation has laid the basis for future work in the Weliky group and others for studying proteins using SSNMR where the isotopic labels are to be specifically placed in one domain and then ligated to a second, possibly larger domain using the native chemical ligation protocol. There are three main benefits to the NCL methodology approach. (1) The isotopic labels are incorporated via the t–Boc methodology of SPPS and thus are placed exactly as intended without having to worry about scrambling or labeling every residue of a specific amino acid. Both possibilities can occur if the amino acids are fed to *E. coli* prior to expression. (2) This methodology provides a hybrid ability to create larger protein constructs with a selective labeling scheme from recombinant protein expression and SPPS. (3) Using the NCL reaction allows for easily studying mutations in the FP region in the context of a larger protein construct such as the FP–Hairpin construct which represents the post–fusion structure of gp41. Being able to employ SPPS to generate different FP sequences with mutations that can be ligated to the Hairpin domain will save time compared to having to express each new mutation individually in *E. coli*. Complete synthesis of the FP23 takes about 1.5 weeks, however by splitting the resin during synthesis one can allow for multiple labeling schemes to be completed at once, reducing the overall time of synthesis. In comparison, if the FP–Hairpin construct was to be expressed in *E. coli* and mutations to the FP region were to be studied the

following steps would have to occur. First, develop the DNA primers required for the new mutation, extract the DNA from the *E. coli* plasmid, perform a polymerase chain reaction (PCR) to incorporate the new mutation into the FP–Hairpin DNA, insert the mutated DNA into *E. coli* competent cells, grow up the mutant construct, and sequence the DNA from the mutant construct. If the mutation worked, one can try to express and purify the new construct. However, if the new mutation was not successful then this would require going back to the previous steps and trying again. If the purification does not work, then you need to figure out why and optimize it. It is likely that once a purification protocol for the FP–Hairpin construct which is completely expressed in *E. coli* is developed then the purification of the mutant construct(s) should be of similar conditions. All of these steps would have to be performed for each new mutation resulting in requiring weeks or months of time in order to prepare a new SSNMR sample compared to ~2 weeks for the chemical ligation approach. Mutational studies in the context of FP–Hairpin would best be performed by using the NCL approach, supporting the use of SPPS to generate the FP mutants and ligate the FP23–mer to the Hairpin construct. Currently there is no data on the FP–Hairpin construct's expression yields from *E. coli* bacteria in the Weliky group.

From the work presented in the dissertation, there are two main areas that the results can be grouped. First there was the development of the protein expression and sample preparation methodology. Second was the development of the solid state NMR studies of a large 115 residue construct with selective isotopic labeling to probe secondary and tertiary structures of the FP domain of the FP–Hairpin construct.

As discussed in Chapter 2, the first issue that needed to be addressed was protein production. The Hairpin construct expressed at high yields of 50 mg/L of purified protein, the time needed to purify that quantity of protein was initially on the order of days. The second issue

was that the NCL reaction was only ~5 % efficient, which would require ~400 mg of Hairpin and ~85 mg FP23(linker) of starting material, in a 1:1 molar ratio, just to achieve ~20 mg of FP–Hairpin for one SSNMR sample. After optimization of both the Hairpin production and purification along with optimization of the conditions for the NCL reaction, ~20 mg of FP–Hairpin can now be routinely created from ~100 mg Hairpin and ~21 mg FP23(linker) in a 1:1 molar ratio, resulting in ~20% yields. This optimization also resulted in reducing sample preparation time from ~2 months to ~2 weeks. Thus, a project that initially was not feasible due to time and materials is now feasible.

The other main focus of this dissertation was on the development and implementation of SSNMR studies of the FP–Hairpin construct. The work presented in Chapter 3 initially suffered from the protein production problem, leading to sample preparations that were 40:1 lipid to protein loadings. These samples contained ~6 mg (~0.4 μmole) of FP–Hairpin. Due to the low amount of protein in the samples, signal averaging was on the order of weeks to perform the 2D ^{13}C–^{13}C experiments of interest. After protein production was improved, higher loading samples of 25:1 lipid to protein loadings could be studied more readily. However, these samples with ~12 mg (~1 μmole) of protein still suffered from long signal averaging times of ~3 days for the 50 ms and ~8 days for the 500 ms 2D ^{13}C–^{13}C experiments at 9.4 T. Low peak signal to noise ratios of the ^{13}C cross peaks required the long signal averaging times using the 9.4 T spectrometer.

Significant findings for FP–Hairpin UA6/UG10 samples included the observation of both the helical and β–strand conformations in membranes which either contained or lacked the biologically relevant ~30 mole % cholesterol when prepared at neutral pH. From this finding, it was observed that for FP–Hairpin, the cholesterol in the lipid membrane does not affect the

populations of helical or β–strand of the FP domain at residues Ala–6 and Gly–10, which is in contrast to work with the FP23. For FP23, cholesterol containing membranes favored the β–strand conformation whereas cholesterol depleted membranes contained both the helical and β–strand conformations for the FP domain.[1, 2] Thus the same general secondary structure for the FP domain of FP–Hairpin in a cholesterol depleted membrane environment was observed compared to FP23. However, in the cholesterol containing membrane environment, the secondary structures of the FP domains for FP23 and FP–Hairpin do not show the same overall structure. The FP domain of FP23 was predominantly β–strand and the FP domain of FP–Hairpin was both β–strand and helical when prepared at neutral pH.[2] Different tertiary structure was also observed for FP–Hairpin by the lack of alanine–6 / glycine–10 inter–residue cross peaks in the 2D ^{13}C–^{13}C experiments with a 500 ms exchange time compared to FP23 UA6/UG10 with a 1000 ms exchange time.[3] As discussed in Chapter 4 and illustrated in Figure 4–3, the different tertiary structures and registries could be the result of two possibilities. (1) The FP region is pulled back by the SHB appendage, resulting in the Ala–6 / Gly–10 overlap being shifted so that they are farther away than the detectable 5 – 6 Å distance, and not fitting with the major populations of the 16→1/1→16 or the 17→1/1→17 antiparallel β–sheet registries, thus creating a new registry.[3, 4] (2) The FP domain of FP–Hairpin keeps certain inter–strand crossings such as L7/F8 [5], however the N–terminal end of the FP is then splayed away from the rest of the antiparallel strand of Figure 4-3.

For this research project, large quantities of protein were needed as illustrated by the point that the 40:1, 25:1 and 15:1 lipid to protein loadings contained ~0.4, 1, and 2 μmoles of protein respectively. The best results were obtained using at least 1 μmole of the FP–Hairpin protein. The FP–Hairpin protein is not the type of system where ~6 – 7 mg of protein will suffice

compared to the FP23 or FP34 peptides. This is because ~6 – 7 mg of FP–Hairpin is only ~0.4 – 0.5 μmoles of protein whereas 6 mg of FP23 is ~2.7 μmoles of protein which would result in nearly 5x as much label being present in the sample. Therefore to get more label in the sample for FP–Hairpin requires a larger amount of protein. It was found that at bare minimum ~24 mg (2 μmoles) of protein at 9.4 T or ~1 μmole at 21.1 T gave the best results.

The higher fields of 16.5 T and 21.1 T benefited the FP–Hairpin work because the increased peak signal to noise per scan at the higher fields with the E–free probe and narrower linewidths translated into time savings of at least 33 – 50% compared to results at 9.4 T spectrometer. Also, the increased peak signal to noise ratios and the narrower linewidths resulted in the observation of more resolved cross peaks in the 2D ^{13}C–^{13}C spectrum at 21.1 T compared to 9.4 T, especially in the $^{13}C\alpha$/^{13}CO and the ^{13}CO/$^{13}C\alpha$ regions.

A second sample of ~33:1 loading with ~1 μmole of FP–Hairpin protein was prepared at pH 3 using Method B from Chapter 2. From solubility studies by Sackett and co–workers, it was discovered that FP–Hairpin is not soluble in the pH 7 buffer which the SSNMR sample preparation was performed at.[6] The pH 3 sample analysis and pH swap to pH 7 sample had similar results for the 2D ^{13}C–^{13}C experiments as shown in Chapter 4. The goal of this work was to avoid any precipitated protein being present in the sample. The pH 3 and pH 7 data for this sample both showed β–strand chemical shifts in a POPC/POPG/Chol lipid membrane environment for the alanine–6 and glycine–10 labels in the FP domain. Comparing samples prepared by "Method B" at pH 3 and then pH swapped to pH 7 to the previous work of samples by "Method A" at pH 7 showed that the β–strand chemical shifts are in agreement between all samples. Comparison of the "Method A" and "Method B" sample preparation protocols supports

the hypothesis that the helical conformation observed for the alanine–6 and glycine–10 residues in the 2D ^{13}C–^{13}C spectra with POPC/POPG/Chol lipid membranes is likely due to precipitated protein. The helical conformation is not present in the "Method B" pH 3 sample preparation protocol where the FP–Hairpin protein does not precipitate, at pH 3 the unbound FP–Hairpin can be separated from the protein–lipid membrane complex since the protein will still be soluble in the buffer and not precipitate out which probably occurs using the neutral pH sample preparation as described in Chapter 4.

Three significant findings with the 21.1 T spectrometer were the following: (1) obtaining quality data; (2) discovering a five–fold increased ^{13}C peak signal to noise per scan with a two–fold decrease in linewidths in ppm units; and (3) ability to perform experiments such as the ^{15}N CP and double cross polarization NCA / NCO experiments which were not feasible on a 9.4 T spectrometer due to the low sensitivity of the ^{13}C and ^{15}N nuclei. This breakthrough has had three main impacts: (1) development of using the E–free probe to setup the ^{15}N CP and 1D NCO / NCA double cross polarization experiments which can be developed further into a combination of 2D and 3D experiments or also be coupled to the REDOR pulse sequence for distance measurements between ^{15}N–^{13}C nuclei. (2) Providing high peak signal to noise spectra and (3) making progress in the Weliky group SSNMR capabilities at high field. Use of the 900 MHz NMR resulted in time savings between 33 – 50% for signal averaging of biological protein samples, and providing better resolution in the cross peaks for the 2D spectra's $^{13}CO/^{13}C\alpha$ and $^{13}C\alpha/^{13}CO$ regions.

In summary research on the FP–Hairpin UA6/UG10 protein project has provided the building blocks for future work with FP–Hairpin and larger gp41 constructs. The significance of this project provides new insights into the production and characterization of the Hairpin and FP–Hairpin constructs of gp41 which represent the final folded state of the gp41 six helix bundle. Continued development of this work will allow for developing high resolution secondary and tertiary structural models of the FP domain of FP–Hairpin in a lipid membrane environment. The acquisition of secondary and tertiary structural information will compliment the information already known for the FP domain in lipid membrane environment for the FP23 peptides lacking the SHB appendage such as helical or β–strand conformation, membrane location, and registries of the antiparallel β–sheet structure.[3, 4, 7–10]

Future Work

Future work for this project can be divided up into three portions, (1) protein design, production, and characterization; (2) native chemical ligation; and (3) SSNMR spectroscopy. Advancements that were made in the production and characterization of FP–Hairpin, along with Hairpin provide proof that this project is a feasible Ph.D. research project. Once optimization of the protein production and NCL were complete, SSNMR samples could be readily obtained in a ~2 weeks as opposed to several months. I propose that the project continue in the following directions, highlighted below to extend our knowledge of the gp41 protein construct in both the post–fusion conformation (e.g. FP–Hairpin) and also the pre–fusion intermediate state (e.g. N70).

Protein Design, Production, and Characterization

The FP–Hairpin construct models the low energy post–fusion conformation of gp41. It is important to have atomic resolution structural information about this final conformation and also intermediate states to be able to understand how the viral infection process occurs at various time points. Development of different constructs would be created to obtain this goal. FP–Hairpin is only 115 residues and while it contains the FP, NHR, and CHR domains, it lacks the native loop, MPER, and TM domains. In order to extend the knowledge of gp41 in the final folded state, these missing regions should be added in, one at a time to develop even larger constructs. As the MPER domain is a relevant drug target, it may make the most sense to add this domain first, and then pursue the native loop and possibly the TM domain. Ideally one would be able to extend the FP–Hairpin construct from 115 residues to 171 residues which would represent the FP–CHR–loop–NHR–MPER domains correlating to residues 512 – 683 of the HIV gp41 ectodomain sequence.[11] The idea would be to express gp41 fragments corresponding to Hairpin–MPER; Hairpin–MPER with native loop; and Hairpin–MPER–TM with native loop; which will all still contain the N–terminal cysteine residue on the Hairpin domain which provides the ability to use the NCL reaction to ligate the FP domain onto the expressed constructs. FP could then be selectively labeled with isotopic NMR probes of ^{13}C and ^{15}N as has been used previously to probe secondary and tertiary structures of the FP region. After first confirming the ability to produce and study the new protein constructs, a new possibility would be to attempt uniformly labeling the entire protein and performing multidimensional SSNMR experiments to study the protein and obtain a structural model based on SSNMR constraints, much like the work by Castellani and co–workers.[12] Biophysical characterization with CD, SDS–PAGE, gel filtration

and crystallography would be important initial steps in characterizing the new constructs that can be carried out in concert with SSNMR experiments.

The other direction that the development of protein constructs could go towards would be development of a pre–hairpin intermediate (PHI) construct in order to elucidate structural information about gp41 intermediate state prior to the final folding into the SHB conformation. To create the N70 construct, I propose that the Hairpin construct is grown, expressed, and purified as previously described in Chapter 2. Using the Hairpin construct, a digest could be performed which will cleave Hairpin into two (or more) fragments with the main goal of obtaining the unfragmented NHR domain. Digestion of the Hairpin construct was calculated by using the ExPASy PeptideCutter website and the results are presented in Table 5–1.[13] From the 20 chemical or enzymatic conditions which produced cleavage sites, the top 6 conditions were chosen which had 3 or fewer cleavage sites minimizing the number of possible fragments that need to be separated after digestion.

Table 5–1: Possible digestions for Hairpin to create an "N70" type construct.

Enzyme / Chemical Condition	**Number of Cleave Sites**	**Residue Position of Cleavage [a]**
CNBr [14]	1	55
Thrombin [15]	1	51
Formic Acid [16]	2	58; 90
Asp–N endopeptidase [15]	2	57; 89
LysC [15]	3	40; 81; 91
LysN [15]	3	39; 80; 90

[a] = residue position corresponding to the 92 residue Hairpin sequence of gp41 presented in Chapter 2, Figure 2–1.

After further purification, the NHR domain could be ligated with FP23(linker) to create the N70 like molecule without having to synthesis the N47 domain. Two attractive reasons for this method of creating N70 are: (1) Hairpin expression and purification protocols are routine to do, yielding ~50 mg/L of pure protein. (2a) SPPS yields decrease as the number of residues increases, thus resulting in lower yields of pure protein. (2b) There is a large time investment into SPPS compared to letting *E. coli* bacteria produce the protein. Production of N70 in this route would still allow for selective incorporation of isotopic labels in the FP region as the FP23(linker) would be created using the t–Boc SPPS methodology. Tables 5–2 to 5–7 highlight the products of the six possible digestions listed in Table 5–1, followed briefly by the cleavage conditions for the protein. Purification of the fragments would require RP–HPLC due to the lack of C– or N–terminal tags.

Tables 5–2 to 5–7 are setup with the following titles and information: Site refers to the cleavage residue for Hairpin; Fragment (Frag.) refers to the fragment produced by cleavage at a specific residue; residues refers to the number of amino acids in the fragment; The expected MW and ε values were calculated by ExPASy [17] and are the molecular weight of the fragment and its molar extinction coefficient at 280 nm respectively. Domain refers to the parts of Hairpin that each fragment will contain such as: NHR for N–heptad repeat; CHR for C–heptad repeat; L6 for the six residue minimal linker loop; and uncleaved to mean the intact protein. Some entries are listed as ± x NHR ± y which means that the following: the fragment starts ± x residues N–terminally from the NHR domain and ends ± y residues C–terminally from the domain.

Table 5–2: CNBr chemical digestion products as determined by ExPASy PeptideCutter.

	Residues	Number of residues	Expected MW (Da/mol)	Expected ε (cm^{-1} mol^{-1})	Domain
Site 1: 55	1 – 55	55	6,138	11,500	NHR+L6+2CHR
Frag. 1:	56 – 92	37	4,602	12,660	–2 CHR
Frag. 2:	1 – 92	92	10,723	24,160	Uncleaved

Cleavage by the CNBr will result in two main fragments, with the NHR domain being 55 residues long, which when ligated to FP23(linker) will produce the "N78" construct. Using the cyanobromide cleavage, the Met – Glu peptide bond will be cleaved, resulting in the two fragments in Table 5–2.[13, 14] This is the only location in the Hairpin construct containing an Met residue as the N–terminal Met had been mutated to a Cys residue as a requirement for the NCL reaction. According to Schroeder and co–workers, only Met – Thr or Met – Ser cleavage sites resulted in partial or no cleavage.[14] Conditions for the cleavage are protein concentrations of 10 mg/mL in 75% TFA solution with the addition of 30x molar excess or more of the CNBr reagent.[14] The reaction takes place at room temperature for 15 minutes to 24 hrs, after which time the reaction was diluted with 10 volumes of water and lyophilized and then purified.[14] A more direct approach could be to dilute the reaction and subsequently purify the reaction mixture, as the volume should be ~100 mL or less. After purification, the fragments would need to be confirmed by mass spectrometry, quantified, and then could be used in the NCL reaction. One foreseeable problem would be if the cleaved products can not be separated due to formation of the SHB structure, the protein mixture may need to be dissolved in 8 M guanidium chloride and be subjected to ~80 $^{\circ}$C temperatures followed by purification. The GdCl will hopefully disrupt the SHB formation and the high temperatures as well will cause a denaturation of the SHB.

Table 5–3: Thrombin enzymatic digestion products determined by ExPASy PeptideCutter.

	Residues	Number of residues	Expected MW (Da/mol)	Expected ε (cm^{-1} mol^{-1})	Domain
Site 1: 51	1 – 51	51	5707	5810	NHR+partL6
Frag. 1:	52 – 92	41	5034	18350	partL6+CHR
Frag. 2:	1 – 92	92	10,723	24160	Uncleaved

Cleavage by use of the Thrombin enzyme results in two main fragments, with the NHR domain being 51 residues long, which when ligated to FP23(linker) would result in a "N74" construct. Thrombin will cleave the Arg – Gly bond in the loop. According to Gasteiger et al. for the Thrombin digest to work optimally, the Arg residue needs to have a glycine residue on either side of it.[13] The Arg residue in the loop is the only location that satisfies the G–R–G condition for the Hairpin construct. There are other Arg – Xaa pairings in Hairpin construct which may be cleaved, however not to any significant extent. The Thrombin enzyme can be performed in 50% acetonitrile buffer between pH 5 – 10.[15, 18] The enzyme can be purchased from Sigma–Aldrich, and more information can also be found on their website, reference [18]. Purification of the fragments, quantification, and ligation would be similar to the conditions previously described for the CNBr cleavage presented above.

Table 5–4: Formic acid chemical digestion products determined by ExPASy PeptideCutter.

	Residues	Number of residues	Expected MW (Da/mol)	Expected ε (cm^{-1} mol^{-1})	Domain
Site 1: 58	1 – 58	58	6,569	17,190	NHR+L6+5CHR
Site 2: 90	59 – 90	32	3,857	1,280	–5 CHR –2
Frag. 1:	59 – 92	34	4,172	6,970	–5 CHR
Frag. 2:	1 – 90	90	10,408	18,470	Full –2
Frag. 3:	91 – 92	2	332	5,690	Last 2 residues
Frag. 4:	1 – 92	92	10,723	24,160	Uncleaved

Cleavage by use of formic acid results in two main cleavage sites. The main fragment that will be used would be the cleaved protein at residue 58 corresponding to the Asp – Arg amino acid pair.[13, 16] The NHR domain being 58 residues long, which when ligated to FP23(linker) would result in a "N81" construct and contains the first 5 residues of the CHR domain. The formic acid cleavage condition requires dissolving the protein sample in formic acid, adding some DTT reducing agent for the cysteine residues and heating the sample to ~108 °C for 5 minutes to 4 hrs as the authors report that reaction overnight at room temperature did not cleave their protein samples.[16] The authors found that longer reaction times resulted in fewer missed cleavage sites.[16] After cleavage, the sample will need to be diluted with water and acetonitrile before purification can be performed. Purification, quantification, and ligation would be similar to the previously reported protocol for the CNBr chemical cleavage.

Table 5–5: Asp–N endopeptidase enzymatic digestion products determined by ExPASy PeptideCutter.

	Residues	Number of residues	Expected MW (Da/mol)	Expected ε (cm^{-1} mol^{-1})	Domain
Site 1: 57	1 – 57	57	6,454	17,190	NHR+L6+4CHR
Site 2: 89	58 – 89	33	3,973	1,280	–4 CHR –3
Frag. 1:	58 – 92	34	4,172	6,970	–4 CHR
Frag. 2:	1 – 89	89	10,293	18,470	Full –3
Frag. 3:	90 – 92	3	448	5,690	Last 3 residues
Frag. 4:	1 – 92	92	10,723	24,160	Uncleaved

Cleavage by using the Asp–N endopeptidase enzyme results in two main cleavage sites. The main fragment that will be used would be the cleaved protein at residue 57 corresponding to the Trp – Asp amino acid pair, where the Asp residue will become the N–terminal residue of the

unwanted cleaved product.[13] The NHR domain being 57 residues long, would result in the "N80" construct when ligated to the FP23(linker). It would contain the NHR, loop, and first 4 residues of the CHR domain. Cleavage conditions for Asp–N endopeptidase are 50 mM Tris–HCl, 2.5 mM $ZnSO_4$, pH 8, incubated at 37 °C.[15, 19] No reaction time was provided. This enzyme can be purchased at New England Biolabs, but is not recommend for protein cleavage, due to slow cleavage rate.[19]

Table 5–6: LysC enzymatic digestion products determined by ExPASy PeptideCutter.

	Residues	Number of residues	Expected MW (Da/mol)	Expected ε (cm^{-1} mol^{-1})	Domain
Site 1: 40	1 – 40	40	4,526	5,810	NHR –7
Site 2: 81	41 – 81	41	4,816	12,660	+7 NHR+L6 +CHR –12
Site 3: 91	82 – 91	10	1,230	–	–29 CHR –1
Frag. 1:	41 – 91	51	6,028	12,660	+7 NHR+L6 +CHR –1
Frag. 2:	41 – 92	52	6,214	18,350	+7 NHR+L6 +CHR
Frag. 3:	82 – 92	11	1,416	5,690	–29 CHR
Frag. 4:	1 – 81	81	9,324	18,470	Full –11 CHR
Frag. 5:	92	1	204	5,690	Last residue
Frag. 6:	1 – 92	92	10,723	24,160	Uncleaved

Cleavage by using the lysyl endopeptidase (LysC) enzyme results in two main cleavage sites, a 40 and an 81 residue peptides.[13] The main fragment that will be used would be the cleaved protein at residue 40 corresponding to the Lys – Gln amino acid pair.[13] The NHR domain being 40 residues long, which when ligated to FP23(linker) would result in a "N63" construct, and would be the second shortest constructs to model the PHI construct resulting from the digestion. The "N63" residue would lack the last 7 C–terminal residues of the NHR domain.

Possible cleavage conditions include incubation in water or buffer solution containing either 0.1% SDS or up to 4 M Urea.[20] The enzyme is also stable at pH 6 – 11 up to 30 °C and for 6 hrs.[20] No specific cleavage conditions were listed. It is likely that the Hairpin protein would be dissolved in 4 M urea near pH 7, followed by addition of the enzyme, and that the reaction would be done at room temperature for up to 6 hrs. Purification, identification, quantification, and ligation of the product to FP23(linker) to create "N63" would be done as previously described.

Table 5–7: LysN enzymatic digestion products determined by ExPASy PeptideCutter.

	Residues	Number of residues	Expected MW (Da/mol)	Expected ε (cm^{-1} mol^{-1})	Domain
Site 1: 39	1 – 39	39	4,398	5,810	NHR –9
Site 2: 80	40 – 80	41	4,816	12,660	+7 NHR+L6+ CHR–13
Site 3: 90	81 – 90	10	1,230	–	–28 CHR –2
Frag. 1:	40 – 92	53	6,342	18,350	+7 NHR+L6+ CHR
Frag. 2:	40 – 90	51	6,028	12,660	+7 NHR+L6+ CHR–2
Frag. 3:	81 – 92	12	1,544	5,690	–28 CHR
Frag. 4:	1 – 80	80	9,196	18,470	Full – 12CHR
Frag. 5:	91 – 92	2	332	5,690	Last 2 residues
Frag. 6:	1 – 92	92	10,723	24,160	Uncleaved
Frag. 7:	1 – 90	90	10408	18470	Full –2

Cleavage by using the peptidyl–Lys metalloendopeptidase (LysN) enzyme results in two main cleavage sites, a 39 and an 80 residue peptides.[13] The main fragment that will be used would be the cleaved protein at residue 39 corresponding to the Ile – Lys amino acid pair.[13] The NHR domain being 39 residues long, which when ligated to FP23(linker) would result in a "N62" construct, the smallest of the PHI constructs resulting from the digestion. The "N62" residue would lack the last 8 C–terminal residues of the NHR domain. A review of the literature

showed that Lys–C (Table 5–6) is readably used for digestions where one is trying to break the Lys – Xaa bond, and that this LysN enzymatic digestion is not very prevalent in the literature. A second issue would be location of this enzyme, which was not listed with Sigma, New England Biolabs, or Wako Pure Chemicals. Therefore using this enzyme would not be an ideal or practical route for Hairpin digestion.

From the presented cleavage reactions, the best chemical cleavage options appear to be either the CNBr chemical cleavage (Table 5–2) or the formic acid digestion (Table 5–4). These two choices were based on the ease with which the reaction can be performed, the preferential cleavage sites, and the reported results in the literature. While the digestions will not produce the exact N47 construct, they will produce constructs that are between 39 – 58 residues in length, which when ligated to the FP will create the N62 – N81 constructs, similar to the N70 construct. Ligation and purification for the ligated product would be done as previously described in Chapter 2 and described for the CNBr protocol. The best enzymatic condition was the Thrombin digest presented in Table 5–3 which will cleave the Arg–Gly peptide bond in the loop region.

Native Chemical Ligation

Work in this thesis highlights the ability to ligate together the FP and Hairpin constructs of 23 and 92 residues respectively, creating the 115 residue FP–Hairpin construct. By optimizing the NCL reaction, yields increased from 5% to 20%, proving that the FP–Hairpin construct was possible to create in quantities needed for SSNMR experiments. Future work with the NCL will be a two fold approach. First, NCL will be used to ligate together FP23 with the new, larger expressed constructs. Second, synthesis of the FP23(linker) should be modified so that the linker on the resin is actually the MPAA structure. The FP23(linker) will then have the best leaving

group possible, and no thiol linker exchange will need to occur to obtain the best leaving group. Work has shown that the preformed peptide–linker works faster than just a Cys–peptide.[21] While there is a linker already present on the resin, why not try and put MPAA as the linker instead ensuring that we have the most reactive thioester possible? Then no need for the pre–reaction of FP23(linker) and catalysts step which could be one reason why yields are limited to ~20% currently. There is a published literature method that details how to take the starting MBHA resin and modifying it to contain the MPAA structure as the linker, which can be created in house prior to synthesis of FP23.[22] FP23(linker) will still need to be sent out for HF cleavage for cleavage from the resin and cleavage of the arginine protecting group.

SSNMR Spectroscopy

The final aspect of the future work would be solid state NMR spectroscopy of the gp41 constructs. Previous work with the FP23–mer by Qiang and co–workers showed that inter–residue A6 / G10 cross peaks were observed at long mixing times.[3] These cross peaks corresponded to inter–strand contacts of the antiparallel β–sheets.[3] Work by Schmick and Weliky shows that the fusion peptide adopts several possible antiparallel registries, and not just one specific registry with the most predominant being the 16→1/1→16 and 17→1/1→17 antiparallel registries.[4] Further work to try and define the secondary and tertiary structure of the FP region in the context of the FP–Hairpin construct can be done with $^{1}H/^{13}C/^{15}N$ REDOR and 2D $^{13}C–^{13}C$ correlation experiments, which will highlight contacts that are ~7 Å or less distances obtainable at long mixing times of 500 ms.[3, 12] As highlighted in Chapter 4, the high field spectrometers with an E–free probe provided increased ^{13}C peak signal to noise per scan

and narrower linewidths which is important for bio–solids work. The increased ^{13}C peak signal to noise per scan allowed for 33 – 50% less signal averaging time, and the narrower linewidths allowed for unambiguous assignment of cross peaks. The E–free design also minimized dehydration of the sample and allows for samples containing high salt concentrations to be studied without requiring long recycle delays to minimize sample heating. The ability to perform ^{15}N experiments at high field will thus open the door to the selective filtering experiments and also to 2D ^{15}N–^{13}C correlation experiments. Other experiments such as the 1D double cross polarization NCA / NCO experiments can be combined with REDOR to perform distance measurements. The extension to 3D experiments using uniformly labeled samples is also a possibility.

REFERENCES

References

1. Wasniewski, C.M., et al., *Solid–state nuclear magnetic resonance studies of HIV and influenza fusion peptide orientations in membrane bilayers using stacked glass plate samples.* Chem Phys Lipids, 2004. **132**(1): p. 89–100.

2. Zheng, Z., et al., *Conformational flexibility and strand arrangements of the membrane–associated HIV fusion peptide trimer probed by solid–state NMR spectroscopy.* Biochemistry, 2006. **45**(43): p. 12960–75.

3. Qiang, W., M.L. Bodner, and D.P. Weliky, *Solid–state NMR spectroscopy of human immunodeficiency virus fusion peptides associated with host–cell–like membranes: 2D correlation spectra and distance measurements support a fully extended conformation and models for specific antiparallel strand registries.* J Am Chem Soc, 2008. **130**(16): p. 5459–71.

4. Schmick, S.D. and D.P. Weliky, *Major Antiparallel and Minor Parallel beta Sheet Populations Detected in the Membrane–Associated Human Immunodeficiency Virus Fusion Peptide.* Biochemistry, 2010. **49**(50): p. 10623–10635.

5. Sackett, K., et al., *Residue specific secondary– and high resolution tertiary structure analysis of the HIV gp41 fusion peptide in constructs modeling fusion relevant gp41 conformations; implications for oligomerization of gp41 trimers.*

6. Sackett, K., A. TerBush, and D.P. Weliky, *HIV gp41 six–helix bundle constructs induce rapid vesicle fusion at pH 3.5 and little fusion at pH 7.0: understanding pH dependence of protein aggregation, membrane binding, and electrostatics, and implications for HIV–host cell fusion.* European Biophysics Journal with Biophysics Letters, 2011. **40**(4): p. 489–502.

7. Qiang, W., Y. Sun, and D.P. Weliky, *A strong correlation between fusogenicity and membrane insertion depth of the HIV fusion peptide.* Proc Natl Acad Sci U S A, 2009. **106**(36): p. 15314–9.

8. Qiang, W. and D.P. Weliky, *HIV fusion peptide and its cross–linked oligomers: efficient syntheses, significance of the trimer in fusion activity, correlation of beta strand conformation with membrane cholesterol, and proximity to lipid headgroups.* Biochemistry, 2009. **48**(2): p. 289–301.

9. Qiang, W., J. Yang, and D.P. Weliky, *Solid–state nuclear magnetic resonance measurements of HIV fusion peptide to lipid distances reveal the intimate contact of beta strand peptide with membranes and the proximity of the Ala–14–Gly–16 region with lipid headgroups.* Biochemistry, 2007. **46**(17): p. 4997–5008.

10. Yang, J., C.M. Gabrys, and D.P. Weliky, *Solid–state nuclear magnetic resonance evidence for an extended beta strand conformation of the membrane–bound HIV–1 fusion peptide.* Biochemistry, 2001. **40**(27): p. 8126–37.

11. Buzon, V., et al., *Crystal Structure of HIV–1 gp41 Including Both Fusion Peptide and Membrane Proximal External Regions.* PLoS Pathogens, 2010. **6**(5): p. e1000880.

12. Castellani, F., et al., *Structure of a protein determined by solid–state magic–angle–spinning NMR spectroscopy.* Nature, 2002. **420**(6911): p. 98–102.

13. Gasteiger, E., et al. *Protein Identification and Analysis Tools on the ExPASy Server*. [website] 2011 [cited 2011 16 November 2011]; Available from: http://web.expasy.org/peptide_cutter/.

14. Schroeder, W.A., J.B. Shelton, and J.R. Shelton, *An examination of conditions for the cleavage of polypeptide chains with cyanogen bromide: Application to catalase.* Archives of Biochemistry and Biophysics, 1969. **130**(0): p. 551–555.

15. Keil, B.r., *Specificity of proteolysis*. 1992, Berlin ; New York: Springer–Verlag. ix, 336 p.

16. Li, A., et al., *Chemical Cleavage at Aspartyl Residues for Protein Identification.* Analytical Chemistry, 2001. **73**(22): p. 5395–5402.

17. Gasteiger, E., et al. *Protein Identification and Analysis Tools on the ExPASy Server*. [webpage] 2005 [cited 2011 19 December 2011]; Available from: http://web.expasy.org/protparam/.

18. Aldrich, S. *Thrombin Factor IIa*. [webpage] [cited 2011 21 December 2011]; Sigma Aldrich website – Thrombin]. Available from: http://www.sigmaaldrich.com/life–science/metabolomics/enzyme–explorer/analytical–enzymes/thrombins.html.

19. Biolabs, N.E. *Endoproteinase AspN*. [webpage] [cited 2011 21 December 2011]; Available from: http://www.neb.com/nebecomm/products/productP8104.asp.

20. Wako Pure Chemcial Industries, L. *Lysyl Endopeptidase (R)*. [webpage] [cited 2011 22 December 2011]; LysC enzymatic digestion]. Available from: https://www.e–reagentusa.com/cgi–bin/gx.cgi/AppLogic+ufg280disp_pr.ufg280disp_Main?now=1324560226910.

21. Bang, D., B.L. Pentelute, and S.B.H. Kent, *Kinetically controlled ligation for the convergent chemical synthesis of proteins.* Angewandte Chemie–International Edition, 2006. **45**(24): p. 3985–3988.

22. Bang, D., et al., *Direct on–resin synthesis of peptide–(alpha)thiophenylesters for use in native chemical ligation.* Organic Letters, 2006. **8**(6): p. 1049–1052.

APPENDICES

Appendix I:

Supplemental Data

Overview

This section contains supplemental material not previously presented in Chapters 1 – 5 of the dissertation. The data presented in this appendix can be divided up into six sections: (1) 9.4 T data for FP–Hairpin samples studied with the addition of CuEDTA; (2) 1D, 2D, and 3D experimental data for U–NAL and FP–Hairpin at 21.1 T; (3) REDOR at 9.4 T using either the $^{1}H/^{13}C/^{15}N$ or the $^{1}H/^{13}C/^{31}P$ experiments for FP34 or FP–Hairpin; (4) Scott Schmick's HFP V2E sample studied by $^{1}H/^{13}C/^{15}N$ REDOR at 21.1 T; (5) Erica Vogel's whole cell samples at 21.1 T; and (6) Collaboration with Dr. Ronny Priefer at Niagara University to provide SSNMR data for insoluble polymers. Each of these sections will be presented below.

Section 1: FP–Hairpin UA6/UG10 in POPC/POPG/Chol lipid membranes hydrated with copper EDTA (CuEDTA) solution

FP–Hairpin UA6/UG10 in an 8:2:5 molar ratio of POPC/POPG/Chol lipid membranes at ~25:1 lipid to protein ratio were prepared as previously described in Chapter 2's section "Membrane Lipid Preparation: Method A". Three types of samples were prepared: (1) FP–Hairpin UA6/UG10 at ~25:1 lipid to protein ratio which was previously studied by SSNMR (see Figure 3–4: 50 ms; Figure 3–5: 500 ms). (2) FP–Hairpin UA6/UG10 in an 8:2:5 molar ratio of

POPC/POPG/Chol lipid membranes at ~22:1 lipid to protein ratio which was prepared by Method A. Following preparation of this sample as previously described, the sample was then lyophilized and placed in an 1.7 mL eppendorf tube and then hydrated with ~1.5 mL of 10 mM CuEDTA, 5 mM MES, 10 mM HEPES pH 7.4 solution and gently vortex for several minutes. The sample was spun down again with a microfuge at 16,000g for 10 minutes, decanted, and packed into the 4 mm rotor. (3) The FP–Hairpin UA6/UG10 sample at ~22:1 lipid to protein loading was unpacked from the rotor, placed in an 1.7 mL eppendorf tube, re–hydrated with ~1.5 mL of the 10 mM CuEDTA, 5 mM MES, 10 mM HEPES pH 7.4 buffer, gently vortexed for several minutes and then centrifuged using the microfuge at 16,000g for 10 minutes. The sample was decanted and the pellet was repacked into the 4 mm rotor. Data from these three FP–Hairpin samples are presented in Figures AI–1 to AI–8 and file locations are presented in Table AIV–27 of Appendix IV. General parameters for the 2D ^{13}C–^{13}C experiments are listed in Table AI–1, with any specific parameters listed with the figure caption. Assignments of cross peaks in the 2D ^{13}C–^{13}C experiments were based off of the known ^{13}C chemical shift distributions of helical and β–strand conformations.[1] The helical (H) and β–strand (β) peak chemical shift ± standard deviation for Ala $^{13}C\alpha$ are H: 54.8 ± 1.1 ppm and β: 51.5 ± 1.5 ppm, $^{13}C\beta$ are H: 18.3 ± 0.9 ppm and β: 21.1 ± 2.1 ppm, and for ^{13}CO are H: 179.4 ± 1.3 ppm and β: 176.1 ± 1.5 ppm and for Gly $^{13}C\alpha$ are H: 46.9 ± 1.1 ppm and β: 45.2 ± 1.2 ppm, and for ^{13}CO are H: 175.5 ± 1.2 ppm and β: 172.6 ± 1.6 ppm. Ethylenediaminetetraacetic acid copper (II) disodium salt (CuEDTA) was purchased from Fluka and purity was greater than 97.0%.

Table AI–1: Typical parameters for the 2D ^{13}C–^{13}C Experiments with CuEDTA added to the samples.

Parameter	**Fig. AI–1 to AI–4**	**Fig. AI–5 to AI–8**
^{1}H $\pi/2$ (pw90H)	3.88 μs	5.2 μs
Contact time (ct)	2.6 ms	1.5 ms
^{1}H CP condition (aHcp)	0.3200	0.2900
^{13}C CP Condition (ramp) (ampmin; ampmax)	0.3500 ± 0.025	0.2300 ± 0.0175
^{1}H decoupling frequency (aHdec)	84.4 kHz	82.6 kHz
^{13}C $\pi/2$ (pw90X)	4.7 μs	5.0 μs
DARR frequency (adHspin value)	12 kHz	12 kHz (Fig. AI–5,6) 0 kHz (Fig. AI–7,8)
MAS frequency	10 kHz	10 kHz
Acquisition time	20.5 ms	20.5 ms
t_1 delay increment	25 μs	25 μs
# t_1 points	300	300
Recycle delay	0.5 s (Fig. AI–1,2) 0.25 s (Fig. AI–3,4)	0.25 s
Sweep width	50 kHz	50 kHz
Temperature at thermocouple	–50 °C	–50 °C

2D ^{13}C–^{13}C experiments were performed with mixing times of 50 ms and 500 ms as previously discussed in Chapters 2 – 4. The 2D ^{13}C–^{13}C parameters are presented in Table AI–1 for the spectra in Figures AI–1 to AI–8. With the addition of the CuEDTA to the sample, the recycle delay between acquisitions can be reduced from 1 s to between 0.25 – 0.5 s. The recycle delay can be reduced because the unpaired electrons from the copper relax the ^{1}H nuclei back to

thermal equilibrium via scalar and dipolar interactions of the nuclei with the unpaired electrons.[2] Since the electron dipole moment is ~3 orders of magnitude larger than the nuclear dipolar moment it will create a local field causing the nuclear spin of the ^{13}C nuclei to relax back to thermal equilibrium.[2] The relaxation of the ^{1}H spins by the unpaired electrons shortens the ^{1}H T_1 value, which in turn allows for the shorter recycle delay between acquisitions.

Sample 1: FP–Hairpin UA6/UG10 at ~25:1 lipid to protein loading

The first sample that will be presented is FP–Hairpin UA6/UG10 at ~25:1 lipid to protein loading which was previously studied by SSNMR and presented in Chapter 3. Figure AI–1A is the 2D ^{13}C–^{13}C DARR 50 ms experiment with a 0.5 s recycle delay and 300 t_1 points with 768 summed acquisitions per t_1 point. The data was acquired in ~35 hrs, which is ~50% less signal averaging time compared to acquiring the data without CuEDTA and a 1 s recycle delay of ~68 hrs which was presented in Figure 3–4. The 50 ms spectrum is used to assign the intra–residue assignments for FP–Hairpin UA6/UG10. Figure AI–1B is a slice through the Ala $^{13}C\beta$ β–strand chemical shift of f_1 = 23.5 ppm with peak signal to noise ratios of 8.4, 2.3, and 2.6 for the Ala $^{13}C\beta$, $^{13}C\alpha$, and ^{13}CO respectively. Peak signal to noise measurements were previously discussed in Chapter 3 section "Initial SSNMR Studies for FP–Hairpin in Cholesterol Containing Membranes".

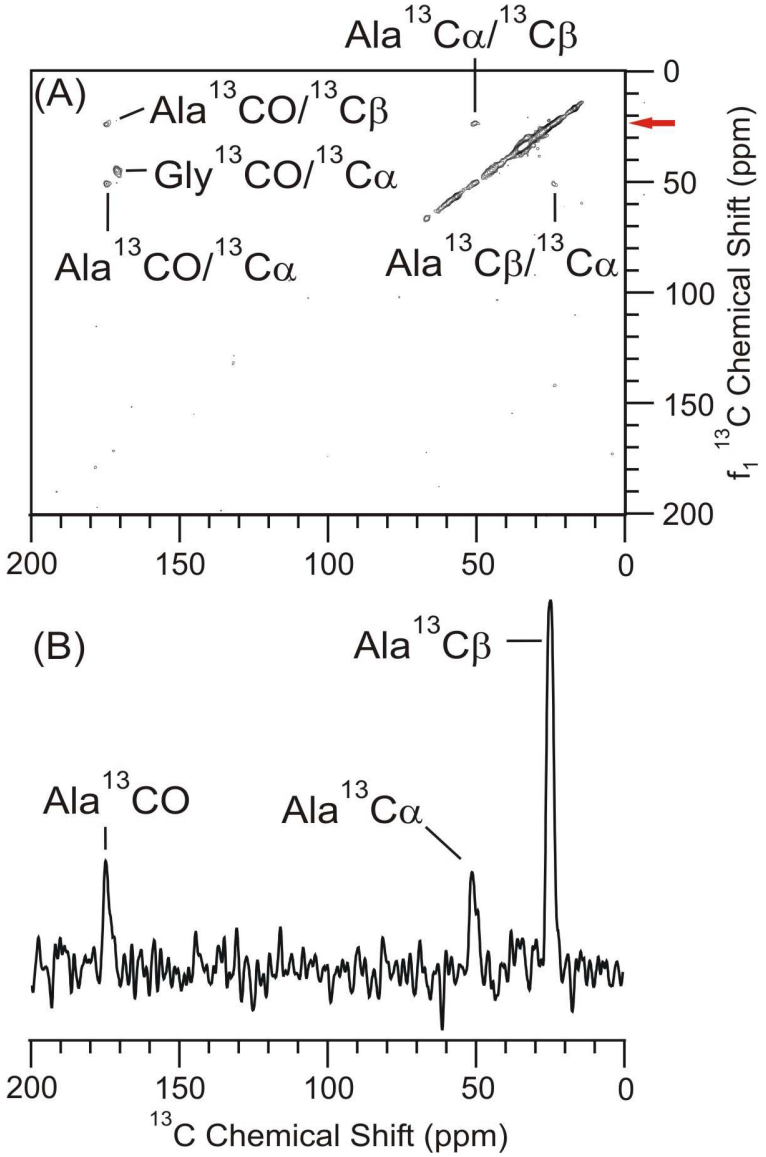

Figure AI–1: 2D DARR ^{13}C–^{13}C spectra at 9.4 T of FP–Hairpin with uniform ^{13}C, ^{15}N labeling at Ala–6 and Gly–10 in the FP region in a POPC/POPG/Chol lipid membrane environment at ~25:1 lipid to protein ratio. Sample was re–hydrated with 10 mM CuEDTA solution and the recycle delay was reduced from 1 s to 0.5 s. (A) The 50 ms mixing time spectrum shows the intra–residue cross peaks. (B) The f_2 slice corresponding to the Ala $^{13}C\beta$ β–strand conformation from f_1 = 23.5 ppm is marked by the red arrow in (A). There were 300 t_1 points with 768 scans summed per t_1 point in a total time of ~35 hrs. Assignments are listed as assignment in f_2 – assignment in f_1. 100 Hz of Gaussian line broadening was applied to each dimension. The MAS frequency was 10 kHz and DARR frequency was 12 kHz.

Interestingly, the FP–Hairpin UA6/UG10 sample in Figure AI–1 had previously shown both helical and β–strand conformations for the A6 and G10 residues, as seen in Figure 3–4. In Figure AI–1, only the β–strand conformation is observed for the sample after the addition of the CuEDTA solution to the sample. The CuEDTA solution was added to the sample after the sample had been prepared, thus the CuEDTA is located in the aqueous solution and not located in the membrane interior. The resulting lack of helical conformations for the cross peaks in Figure AI–1 suggest that the β–strand conformation is membrane inserted and sequestered away from the CuEDTA, where as the helical conformation is probably located outside of the membrane interior, in contact with the copper from the CuEDTA solution. Therefore, it is likely that the precipitated protein is in the helical conformation, and not membrane inserted. The FP–Hairpin UA6/UG10 helical conformation is likely in close contact with the CuEDTA solution, which will relax the nuclei back to thermal equilibrium through the scalar and dipolar interactions between the unpaired electrons of copper and the ^{13}C spins. Any factor that shortens relaxation times, such as the CuEDTA paramagnetic relaxation agent will result in broader lines and reduced resolution.[3] Fourier transforming the quickly decaying signal in the time domain will result in a low, broad signal in the frequency domain, which may be present in the noise level of the spectrum. The main relaxation parameter that is being influenced is the ^{13}C T_2 relaxation time. According to Wickramasinghe and co–workers, the quenched ^{13}C signals of a protein sample may be assigned to residues which are exposed to the CuEDTA solution.[4] It is known that paramagnetic ^{13}C T_2 relaxation rates are proportional to $1 / r^6$, where r is the distance between ^{13}C spin and the paramagnetic ion.[4] For the FP–Hairpin sample presented here, the

helical conformation is likely in close contact with the CuEDTA, resulting in the fast T_2 relaxation, and therefore lack of observable signal in the 2D ^{13}C–^{13}C spectra. As T_2 is the transverse relaxation rate, speeding up the T_2 relaxation rate will result in less signal to detect and therefore lower signal intensity once Fourier transformed from the time to the frequency domain. The CuEDTA doped data fits well with data presented in Chapter 4 where FP–Hairpin UA6/UG10 was prepared with lipid vesicle membranes which were at pH 3 using Method B. This method resulted in only observing the β–strand cross peaks. The pH 3.0 preparation data is presented in Chapter 4, Figure 4–10 for the 50 ms mixing time and Figure 4–11 for the 500 ms data.

Figure AI–2A is the 2D ^{13}C–^{13}C 500 ms DARR experiment for FP–Hairpin UA6/UG10 at ~25:1 lipid to protein loading which had been hydrated with the CuEDTA solution. The recycle delay was 0.5 s, there were 300 t_1 points with 1280 summed acquisitions per t_1 point and was acquired in ~107 hrs compared to ~160 hrs with a 1 s recycle delay translating to ~35% less signal averaging time. Figure AI–2B the f_2 slice through the Ala $^{13}C\beta$ β–strand chemical shift of f_1 = 23.5 ppm with peak signal to noise ratios of 9.6, 2.9, and 4.0 for the Ala $^{13}C\beta$, $^{13}C\alpha$, and ^{13}CO respectively. Only the β–strand conformation is observed.

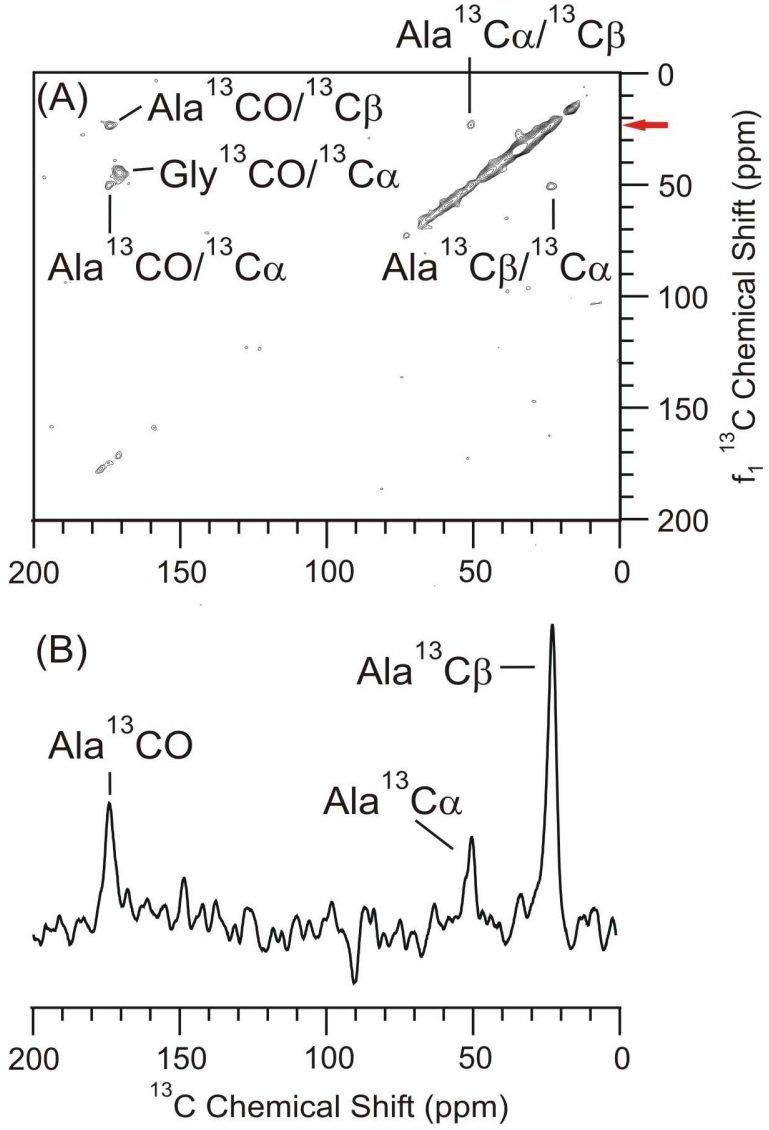

Figure AI–2: 2D DARR ^{13}C–^{13}C spectra at 9.4 T of FP–Hairpin with uniform ^{13}C, ^{15}N labeling at Ala–6 and Gly–10 in the FP region in a POPC/POPG/Chol lipid membrane environment at ~25:1 lipid to protein ratio. Sample was re–hydrated with 10 mM CuEDTA solution and the recycle delay was reduced from 1 s to 0.5 s. (A) The 500 ms mixing time spectrum shows the intra–residue cross peaks, however no inter–residue cross peaks were observed in this sample between A6–G10. (B) The f_2 slice corresponding to the Ala $^{13}C\beta$ β–strand conformation from f_1 = 23.5 ppm is marked by the red arrow in (A). There were 300 t_1 points with 1280 scans summed per t_1 point in a total time of ~107 hrs. Assignments are listed as assignment in f_2 – assignment in f_1. 200 Hz of Gaussian line broadening was applied to each dimension. Only the β–strand conformation is observed for the intra–residue cross peaks.

The same FP–Hairpin UA6/UG10 sample presented in Figures AI–1 and AI–2 was also studied with a recycle delay of 0.25 s. Figure AI–3 is the 2D ^{13}C–^{13}C 50 ms DARR experiment with a 0.25 s recycle delay, 300 t_1 points with 768 summed acquisitions per t_1 point, which was acquired in ~19.2 hrs. Figure AI–3B is the f_2 slice through the Ala $^{13}C\beta$ β–strand chemical shift of f_1 = 23.5 ppm with peak signal to noise ratios of 13.1, 3.5, and 4.0 for the Ala $^{13}C\beta$, $^{13}C\alpha$, and ^{13}CO respectively. Only the β–strand conformations are observed.

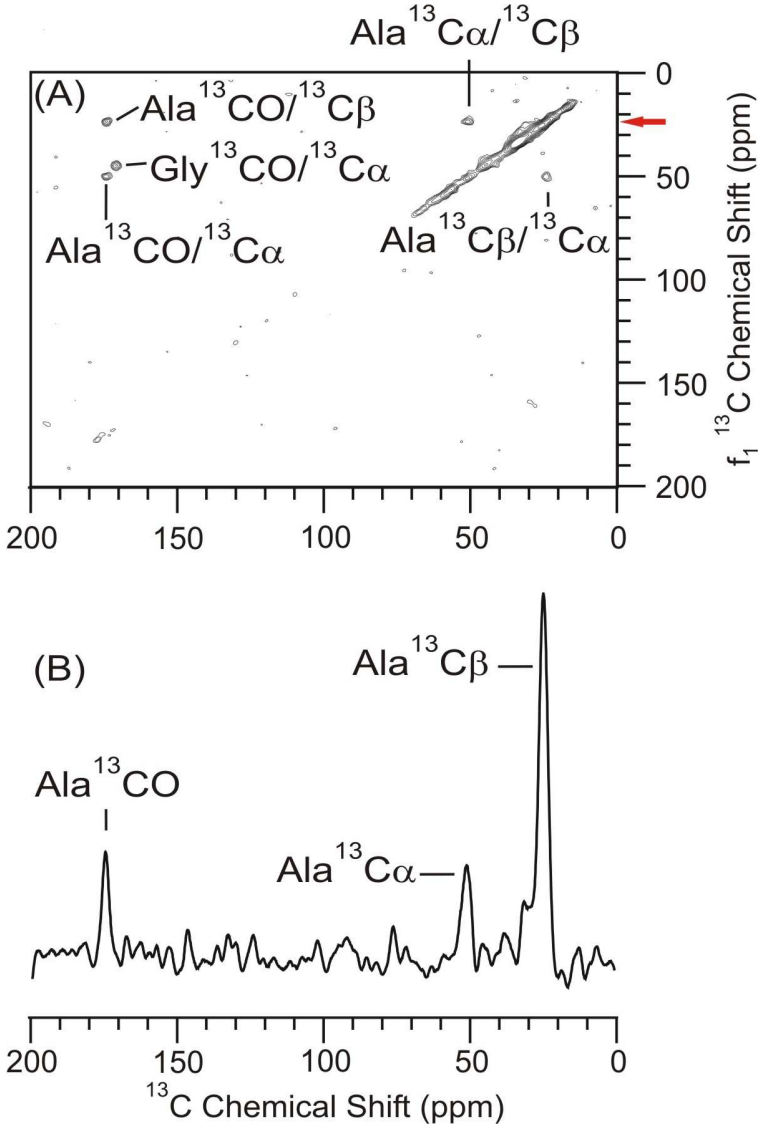

Figure AI–3: 2D DARR ^{13}C–^{13}C spectra at 9.4 T of FP–Hairpin with uniform ^{13}C, ^{15}N labeling at Ala–6 and Gly–10 in the FP region in a POPC/POPG/Chol lipid membrane environment at ~25:1 lipid to protein ratio. Sample was re–hydrated with 10 mM CuEDTA solution and the recycle delay was reduced from 1 s to 0.25 s. (A) The 50 ms mixing time spectrum shows the intra–residue cross peaks. (B) The f_2 slice corresponding to the Ala ^{13}Cβ β–strand conformation from f_1 = 23.5 ppm is marked by the red arrow in (A). There were 300 t_1 points with 768 scans summed per t_1 point in a total time of ~19.2 hrs. Assignments are listed as assignment in f_2 – assignment in f_1. 200 Hz of Gaussian line broadening was applied to each dimension. The MAS frequency was 10 kHz and the DARR frequency was 12 kHz.

Figure AI–4 is the 2D ^{13}C–^{13}C 500 ms DARR experiment with a 0.25 s recycle delay, 300 t_1 points with 1280 summed acquisitions per t_1 point, which was acquired in ~80 hrs. Figure AI–4B is the f_2 slice through the Ala $^{13}C\beta$ β–strand chemical shift of f_1 = 23.5 ppm with peak signal to noise ratios of 4.0, 1.0, and 1.0 for the Ala $^{13}C\beta$, $^{13}C\alpha$, and ^{13}CO respectively. A possible explanation for the absence of the cross peaks in the 500 ms mixing time experiment of Figure AI–4 is that something has occurred to the sample. The data in Figures AI–1 to AI–4 were acquired back to back, such that the 0.5 s recycle delay was preformed first and then the 0.25 s pulse delay was performed. If one looks at Figures AI–5 to AI–8, a 0.25 s pulse delay was used and there are still observable cross peaks in the spectra. As will be discussed next, the sample was rehydrated with CuEDTA solution after the long mixing time of 500 ms with the 0.25 s pulse delay. It is thus possible that the sample may need to be rehydrated in order to observe the cross peaks after being subjected to the heating from the rf pulses in the probe for long periods of time such as this sample was subjected to.

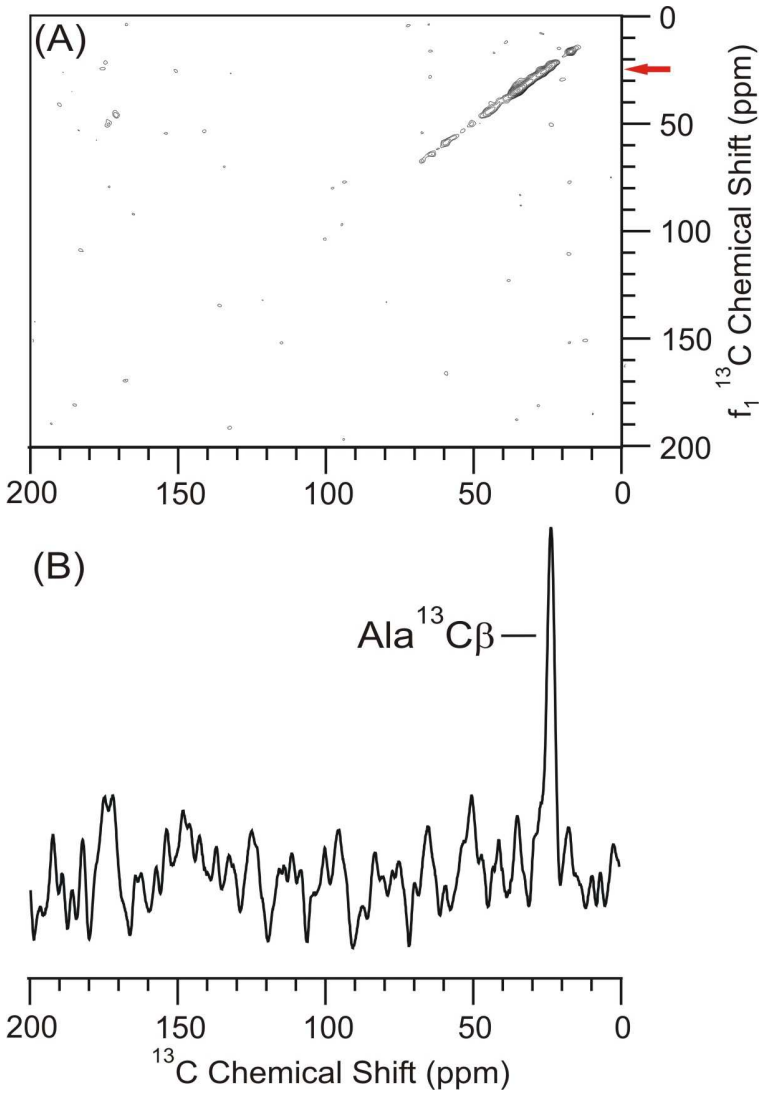

Figure AI–4: 2D DARR ^{13}C–^{13}C spectra at 9.4 T of FP–Hairpin with uniform ^{13}C, ^{15}N labeling at Ala–6 and Gly–10 in the FP region in a POPC/POPG/Chol lipid membrane environment at ~25:1 lipid to protein ratio. Sample was re–hydrated with 10 mM CuEDTA solution and the recycle delay was reduced from 1 s to 0.25 s. (A) The 500 ms mixing time spectrum doesn't show cross peaks which are greater than the noise levels. (B) The f_2 slice corresponding to the Ala ^{13}Cβ β–strand conformation from f_1 = 23.5 ppm is marked by the red arrow in (A). There were 300 t_1 points with 1280 scans summed per t_1 point in a total time of ~80 hrs. 200 Hz of Gaussian line broadening was applied to each dimension.

The difference between the experiments with CuEDTA added and the experiments without CuEDTA added were that the recycle delay was reduce from 1 s without CuEDTA to a shorter recycle delay of either 500 ms or 250 ms in the presence of CuEDTA. The 0.5 s recycle delay provided better quality spectra in terms of ^{13}C peak signal to noise as can be seen in Figures AI–1 and AI–2, especially at the long 500 ms mixing time compared to Figures AI–3 and AI–4. However, it is more beneficial if a shorter recycle delay of 0.25 s can be used resulting in more time savings in terms of signal averaging. The resulting time savings for the 50 ms mixing time experiment by reducing the recycle delay from 1 s can be ~50% and ~70% for the 0.5 s and 0.25 s recycle delay respectively when the same number of acquisitions are acquired. For the 500 ms mixing time experiment with a constant number of acquisitions, reduction of the recycle delay from 1 s to either 0.5 s or 0.25 s results in a time savings of 33% or 50% respectively. A second sample will be discussed next which used a 0.25 s recycle delay obtained quality spectra, shown in Figure AI–5 to AI–8. Table AI–2 lists all the chemical shifts for the spectra presented in Figures AI–1 to AI–4.

Table AI–2: Chemical shift (CS) and relative populations (Pop) for the 2D ^{13}C–^{13}C experiments with FP–Hairpin UA6/UG10 sample with a 25:1 lipid to protein loading in cholesterol containing membranes hydrated with 10 mM CuEDTA solution. The chemical shifts are reported using the (f_2, f_1) convention.

Loading		**~25 : 1 lipid to protein**							
Composition		**POPC / POPG / Chol.**							
Field		**9.4 T**							
Recycle delay		**500 ms**				**250 ms**			
Mixing Time		**50 ms**		**500 ms**		**50 ms**		**500 ms**	
Assignment		**CS**	**Pop (%)**	**CS**	**Pop (%)**	**CS**	**Pop (%)**	**CS**	**Pop (%)**
A Cα / A Cβ	**Helix**	–	–	–	–	–	–	–	–
	β–strand	50.5, 23.7	–	51.0, 23.5	–	51.0, 23.9	–	–	–
A Cα / A CO	**Helix**	–	–	–	–	–	–	–	–
	β–strand	–	–	–	–	–	–	–	–
A Cβ / A CO	**Helix**	–	–	–	–	–	–	–	–
	β–strand	–	–	–	–	–	–	–	–
A CO / A Cα	**Helix**	–	–	–	–	–	–	–	–
	β–strand	174.7, 51.1	–	174.6, 50.5	–	174.6, 50.4	–	173.6, 50.5	–
A CO / A Cβ	**Helix**	–	–	–	–	–	–	–	–
	β–strand	174.8, 24.3	–	174.4, 23.9	–	174.4, 23.8	–	–	–
A Cβ / A Cα	**Helix**	–	–	–	–	–	–	–	–
	β–strand	24.0, 51.2	–	23.9, 51.2	–	24.3, 50.5	–	–	–
G Cα / G CO	**Helix**	–	–	–	–	–	–	–	–
	β–strand	–	–	–	–	–	–	–	–
G CO / G Cα	**Helix**	–	–	–	–	–	–	–	–
	β–strand	171.1, 44.9	–	171.1, 44.8	–	171.0, 45.0	–	170.8, 45.9	–

The tabulated data in Table AI–2 for the 50 ms and 500 ms mixing time with a 0.5 s pulse delay are from the spectra in Figure AI–1 and AI–2 respectively. Figures AI–3 and AI–4 were used for the 0.25 s pulse delay for the 50 ms and 500 ms mixing time experiment in Table AI–2.

The reported chemical shifts of Table AI–2 fit well with the β–strand conformation and also with previous work for FP–Hairpin UA6/UG10 presented in Chapters 3 and 4 and FP23.[5]

Sample 2: "Fresh" FP–Hairpin UA6/UG10 at ~22:1 lipid to protein loading

A second sample containing ~12.3 mg (~1 μmole) of the FP–Hairpin UA6/UG10 in an 8:2:5 molar ratio of POPC/POPG/Chol lipid membranes with a ~22:1 lipid to protein ratio was prepared as described above and in Chapter 2 following Method A. After preparing the sample, it was lyophilized, and then hydrated with CuEDTA prior to being studied by SSNMR. This sample was similar to the ~25:1 lipid to protein loading sample in POPC/POPG/Chol which was presented in Chapter 3. The goal of this data set was to observe if there was an affect from the sample being dehydrated in the rotor prior to being hydrated with the CuEDTA solution. This sample was prepared in the same manner as the FP–Hairpin UA6/UG10 in POPC/POPG/Chol lipid membranes at ~25:1 lipid to protein ratio, which means that we can directly compare the "fresh sample" in CuEDTA solution to the previous 25:1 lipid to protein loading sample which had only been re–hydrated with CuEDTA solution. I would expect that two conformations of helical and β–strand conformation would be observed in the 2D ^{13}C–^{13}C spectra as has been previously observed in Chapter 3 if no CuEDTA solution was present. Figure AI–5A is the 2D ^{13}C–^{13}C 50 ms DARR experiment for the fresh CuEDTA sample with a 0.25 s recycle delay, 300 t_1 points with 768 summed acquisitions per t_1 point, which was acquired in ~19.2 hrs. Figure AI–5B is the f_2 slice through the Ala $^{13}C\beta$ β–strand chemical shift of f_1 = 23.5 ppm with peak signal to noise ratios of 11.3, 4.8, and 4.0 for the Ala $^{13}C\beta$, $^{13}C\alpha$, and ^{13}CO respectively.

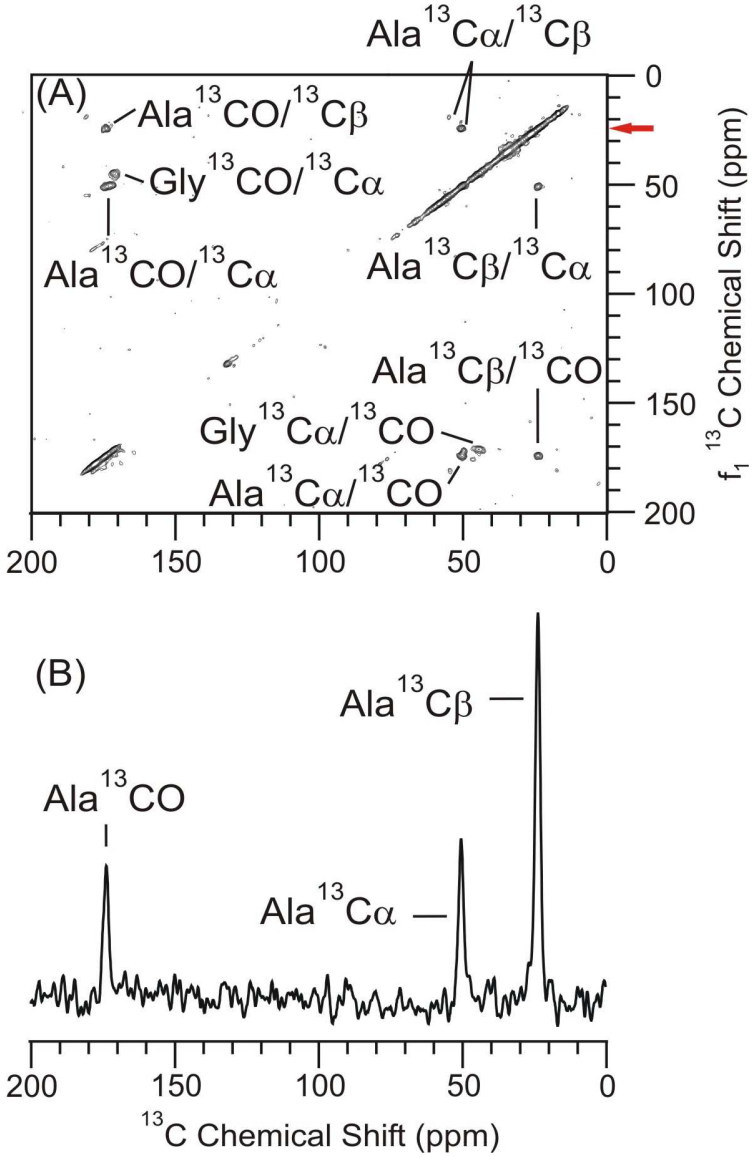

Figure AI–5: 2D DARR ^{13}C–^{13}C spectra at 9.4 T of FP–Hairpin with uniform ^{13}C, ^{15}N labeling at Ala–6 and Gly–10 in the FP region in a POPC/POPG/Chol lipid membrane environment at ~22:1 lipid to protein ratio. This fresh sample was prepared and then hydrated with 10 mM CuEDTA solution and packed into a 4 mm rotor. The recycle delay was 0.25 s. (A) The 50 ms mixing time spectrum shows the intra–residue cross peaks. (B) The f_2 slice corresponding to the Ala $^{13}C\beta$ β–strand conformation from f_1 = 23.5 ppm is marked by the red arrow in (A). There were 300 t_1 points with 768 scans summed per t_1 point in a total time of ~19 hrs. Assignments are listed as assignment in f_2 – assignment in f_1. 100 Hz of Gaussian line broadening was applied to each dimension. The MAS frequency was 10 kHz and the DARR frequency was 12 kHz. The cross peaks predominantly correspond to the β–strand conformation.

Peaks corresponding to the β–strand conformation are predominantly seen in Figure AI–5A, a few minor helical peaks are also observed. The intensity of the helical peaks are ~20% or less of the intensity of the β–strand peaks observed in the 2D spectra. This data is also presented in Table AI–3. Figure AI–6A is the 2D ^{13}C–^{13}C 500 ms DARR experiment for the "fresh" untested CuEDTA sample with a 0.25 s recycle delay, 300 t_1 points with 1152 summed acquisitions per t_1 point, which was acquired in ~72 hrs. Figure AI–6B is a slice through the Ala $^{13}C\beta$ β–strand chemical shift of f_1 = 23.5 ppm with peak signal to noise ratios of 6.2, 1.8, and 1.9 for the Ala $^{13}C\beta$, $^{13}C\alpha$, and ^{13}CO respectively.

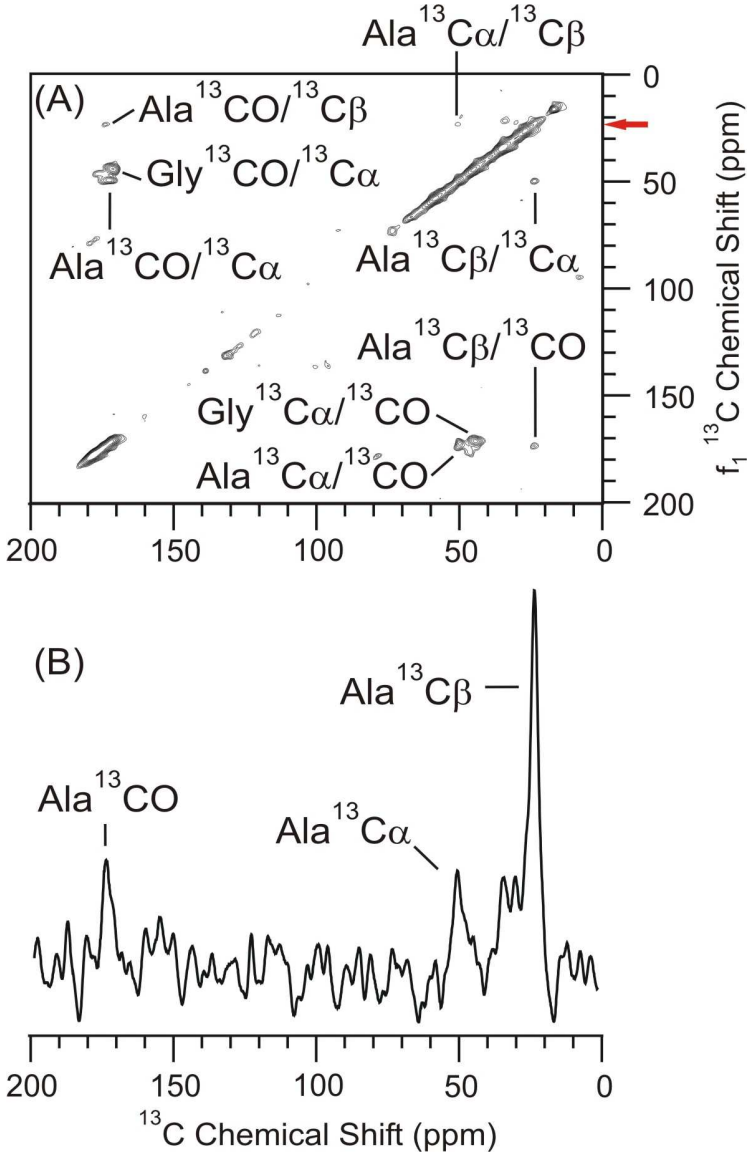

Figure AI–6: 2D DARR ^{13}C–^{13}C spectra at 9.4 T of FP–Hairpin with uniform ^{13}C, ^{15}N labeling at Ala–6 and Gly–10 in the FP region in a POPC/POPG/Chol lipid membrane environment at ~22:1 lipid to protein ratio. This fresh sample was prepared and then hydrated with 10 mM CuEDTA solution and packed into a 4 mm rotor. The recycle delay was 0.25 s. (A) The 500 ms mixing time spectrum shows the intra–residue cross peaks, however no inter–residue cross peaks were observed in this sample between A6–G10. (B) The f_2 slice corresponding to the Ala $^{13}C\beta$ β–strand conformation from f_1 = 23.5 ppm is marked by the red arrow in (A). There were 300 t_1 points with 1152 scans summed per t_1 point in a total time of ~72 hrs. Assignments are listed as assignment in f_2 – assignment in f_1. 200 Hz of Gaussian line broadening was applied to each dimension. Intra–residue cross peaks are predominantly the β–strand conformation.

The spectra in Figures AI–5 and AI–6 show predominantly β–strand conformation for cross peaks. No Ala–6/Gly–10 cross peaks were observed with the long mixing time of 500 ms. The recycle delay of 0.25 s resulted in significant time savings in data acquisitions. For the 50 ms mixing time, the time saving was (0.300 s / 1.050 s), ~29 % of the time and for the 500 ms mixing time experiments the time saving would be (0.750 s/ 1.500 s), 50% of the time needed. This data fits well with the previous spectra presented in Figures AI–1 and AI–2 and also the data presented in Chapters 3 and 4. The 0.25 s recycle delay data for the "fresh sample" is better than the data presented in Figures AI–3 and AI–4 in terms of ^{13}C peak signal to noise ratios and observation of the cross peaks.

Sample 3: Rehydrated "Fresh" FP–Hairpin UA6/UG10 at ~22:1 lipid to protein loading

After the 50 ms and 500 ms tests of FP–Hairpin UA6/UG10 with CuEDTA were finished, the sample was unpacked from the rotor and rehydrated with the CuEDTA solution as described above with one exception, the sample was not lyophilized prior to rehydrating with the CuEDTA solution. Figure AI–7A is the 2D ^{13}C–^{13}C 50 ms DARR experiment for the rehydrated CuEDTA sample with a 0.25 s recycle delay, 300 t_1 points with 768 summed acquisitions per t_1 point, which was acquired in ~19.2 hrs. Figure AI–7B is a slice through the Ala $^{13}C\beta$ β–strand chemical shift of f_1 = 23.5 ppm with peak signal to noise ratios of 13.1, 4.1, and 3.4 for the Ala $^{13}C\beta$, $^{13}C\alpha$, and ^{13}CO respectively.

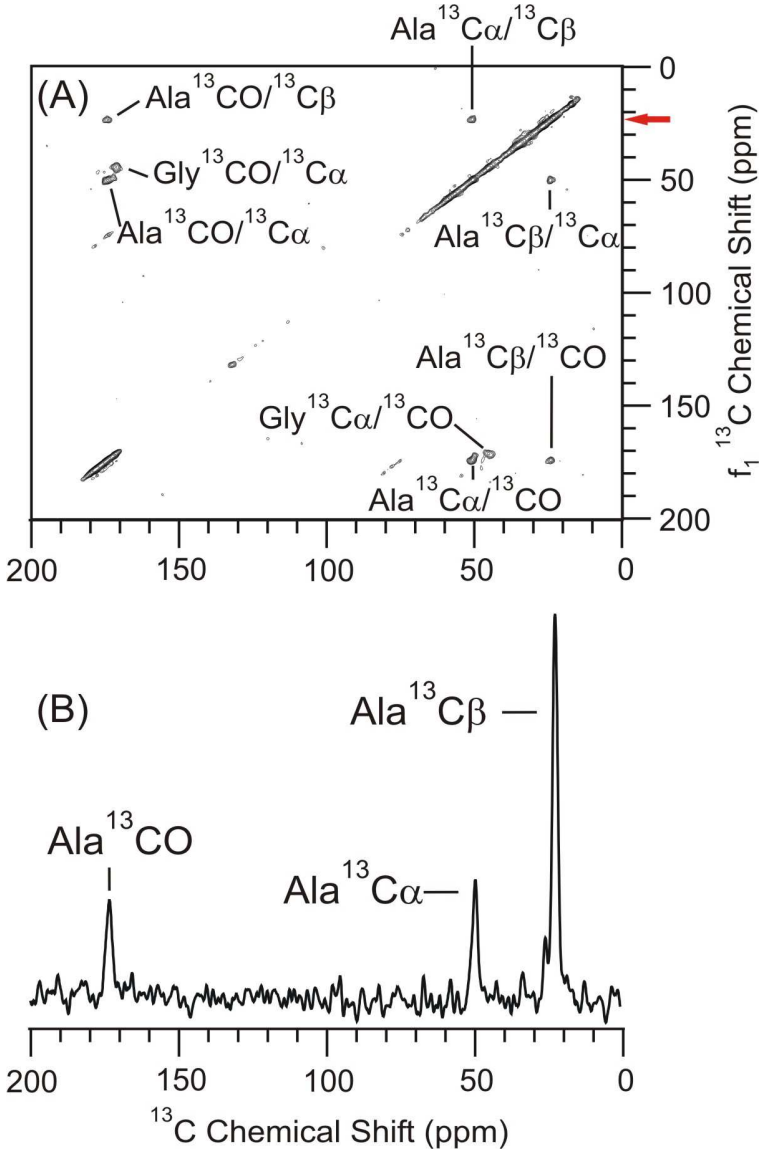

Figure AI–7: 2D PDSD ^{13}C–^{13}C spectra at 9.4 T of FP–Hairpin with uniform ^{13}C, ^{15}N labeling at Ala–6 and Gly–10 in the FP region in a POPC/POPG/Chol lipid membrane environment at ~22:1 lipid to protein ratio. This sample was unpacked from the rotor, rehydrated with the 10 mM CuEDTA solution and then packed into a 4 mm rotor. The recycle delay was 0.25 s. (A) The 50 ms mixing time spectrum shows the intra–residue cross peaks. (B) The f_2 slice corresponding to the Ala $^{13}C\beta$ β–strand conformation from f_1 = 23.5 ppm is marked by the red arrow in (A). There were 300 t_1 points with 768 scans summed per t_1 point in a total time of ~19 hrs. Assignments are listed as assignment in f_2 – assignment in f_1. 100 Hz of Gaussian line broadening was applied to each dimension. The MAS frequency was 10 kHz. The chemical shifts of the intra–residue cross peaks correspond to the β–stand conformation.

Figure AI–8A is the 2D ^{13}C–^{13}C 50 ms PDSD experiment for the rehydrated "fresh" CuEDTA sample with a 0.25 s recycle delay, 300 t_1 points with 1152 summed acquisitions per t_1 point, which was acquired in ~72 hrs. Figure AI–8B is a slice through the Ala $^{13}C\beta$ β–strand chemical shift of f_1 = 23.5 ppm with peak signal to noise ratios of 6.4, 2.4, and 2.9 for the Ala $^{13}C\beta$, $^{13}C\alpha$, and ^{13}CO respectively. The rehydrated sample is the same sample as the "fresh sample" only it was unpacked from the rotor, rehydrated with the 10 mM CuEDTA solution and then packed back into the rotor for SSNMR analysis. Details of the re–hydration are presented above. This set of experiments presented in Figures AI–7 and AI–8 for the 50 ms and 500 ms mixing time experiments showed that similar chemical shifts were observed for the two samples, and that a predominantly β–strand conformation was observed for the Ala–6 and Gly–10 residues. Table AI–3 lists all the chemical shifts for the spectra presented in Figures AI–5 to AI–8 for comparison. No Ala–6/Gly–10 inter–residue cross peaks were observed with the 500 ms exchange time, consistent with previous work for FP–Hairpin UA6/UG10 presented in Chapters 3 and 4.

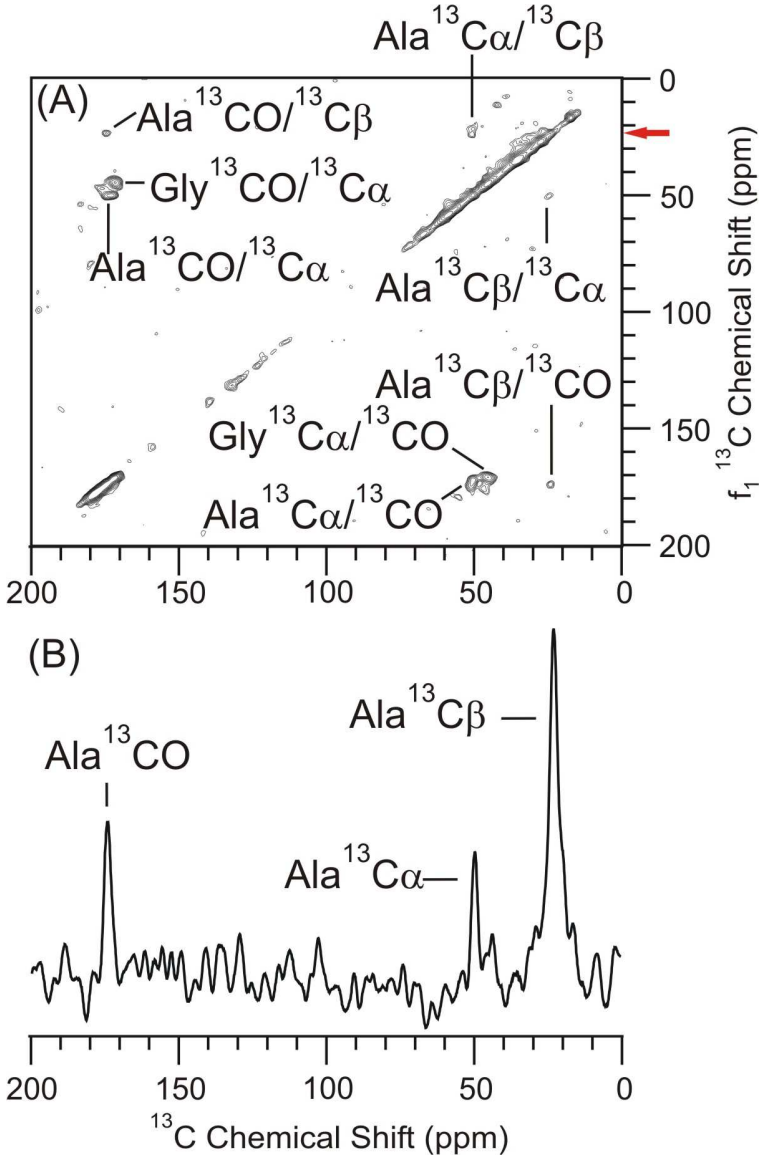

Figure AI–8: 2D PDSD ^{13}C–^{13}C spectra at 9.4 T of FP–Hairpin with uniform ^{13}C, ^{15}N labeling at Ala–6 and Gly–10 in the FP region in a POPC/POPG/Chol lipid membrane environment at ~22:1 lipid to protein ratio. This sample was unpacked from the rotor, rehydrated with the 10 mM CuEDTA solution and then packed into a 4 mm rotor. The recycle delay was 0.25 s. (A) The 500 ms mixing time spectrum shows the intra–residue cross peaks, however no inter–residue cross peaks were observed in this sample between A6–G10. (B) The f_2 slice corresponding to the Ala $^{13}C\beta$ β–strand conformation from f_1 = 23.5 ppm is marked by the red arrow in (A). There were 300 t_1 points with 1152 scans summed per t_1 point in a total time of ~72 hrs. Assignments are listed as assignment in f_2 – assignment in f_1. 200 Hz of Gaussian line broadening was applied to each dimension. Chemical shifts of the intra–residue cross peaks correspond to the β–strand conformation.

Table AI–3: Chemical shift (CS) and relative populations (Pop) for the 2D ^{13}C–^{13}C experiments with FP–Hairpin UA6/UG10 sample with a 22:1 lipid to protein loading in cholesterol containing membranes hydrated with 10 mM CuEDTA solution. The chemical shifts are reported using the (f_2, f_1) convention.

Loading		**~22 : 1 lipid to protein**							
Composition		**POPC / POPG / Chol.**							
Field		**9.4 T**							
Recycle delay		**0.25 s Fresh Sample**				**0.25 s Rehydrated Sample**			
Mixing Time		**50 ms**		**500 ms**		**50 ms**		**500 ms**	
Assignment		**CS**	**Pop (%)**	**CS**	**Pop (%)**	**CS**	**Pop (%)**	**CS**	**Pop (%)**
A Cα / A Cβ	**Helix**	54.9, 18.7	23.9	–	–	–	–	–	–
	β–strand	50.6, 23.9	76.1	–	–	50.3, 23.4	–	50.5, 23.7	–
A Cα / A CO	**Helix**	–	–	–	–	–	–	55.0, 179.8	26.1
	β–strand	50.3, 174.0	–	49.7, 172.7	–	50.2, 174.0	–	50.1, 172.6	73.9
A Cβ / A CO	**Helix**	–	–	23.6, 173.6	–	–	–	–	–
	β–strand	23.9, 174.1	–	–	–	23.7, 174.0		23.9, 174.3	–
A CO / A Cα	**Helix**	–	–	–	–	–	–	–	–
	β–strand	173.6, 50.4	–	172.3, 49.7	–	174.0, 50.3		172.8, 49.9	–
A CO / A Cβ	**Helix**	–	–	–	–	–	–	–	–
	β–strand	173.8, 23.7	–	173.8, 23.9	–	173.9, 23.6		174.4, 23.2	–
A Cβ / A Cα	**Helix**	–	–	–	–	–	–	–	–
	β–strand	23.9, 50.5	–	23.5, 50.2	–	23.9, 50.4	–	24.1, 49.2	–
G Cα / G CO	**Helix**	–	–	–	–	–	–	46.6, 176.2	23.9
	β–strand	44.6, 171.3	–	44.2, 171.4	–	44.8, 171.2	–	45.1, 171.3	76.1
G CO / G Cα	**Helix**	–	–	–	–	–	–	175.7, 47.0	25.8
	β–strand	171.1, 44.4	–	171.0, 44.5	–	171.0, 44.5	–	171.3, 44.3	74.2

The fresh sample data in Table AI–3 for the 50 ms and 500 ms mixing experiment were obtained from Figures AI–5 and AI–6 respectively. The rehydrated data in Table AI–3 for the 50 and 500 ms sample were obtained from Figures AI–7 and AI–8.

Table AI-4 compares the peak signal to noise (peak S/N) and the peak S/N per scan (peak S/N/scan) for the 2D ^{13}C-^{13}C experiments for FP-Hairpin UA6/UG10 sample without the addition of CuEDTA presented in Chapter 3 Figures 3-4 and 3-5 along with the FP-Hairpin UA6/UG10 samples presented in Appendix I in Figures AI-1 to AI-8 which had the CuEDTA added to the sample. The peak S/N was determined from the f_1 = 23.5 ppm slice corresponding to the Ala $^{13}C\beta$ β-strand chemical shift. The total number of acquisitions was determined by the product of the number of scans per slice and the number of slices. The peak S/N/scan number presented in Table AI-4 was divided by 10^{-6} so that all the data can be easily compared.

Comparison of the slices of f_1 = 23.5 ppm from the 2D ^{13}C-^{13}C experiments with a 50 ms mixing time of Figure 3-4B which did not contain the CuEDTA showed that compared to the same sample with the CuEDTA solution added, the $^{13}C\beta$ carbon was affected the most. The peak S/N/scan for the sample without CuEDTA and 1 s recycle delay was 66.5 compared to the same sample with the addition of the CuEDTA solution with the 0.5 s or 0.25 s recycle delay having peak S/N/scan values of 36.5 and 34.1 as seen in Table AI-4. The peak S/N/scan suggests that with the shorter recycle delay and the addition of the CuEDTA, ~50% less signal per scan is obtained. However, this reduction in signal can be compensated by the reduced signal averaging time. The time to acquire data was ~67, ~35, and ~19 hrs for the 1 s, 0.5 s, and 0.25 s respectively. Reviewing the peak S/N for the samples presented in Table AI-4 shows that even

with the CuEDTA added to the sample, peak S/N values for the $^{13}C\alpha$ and ^{13}CO carbons are similar between the two samples. Therefore, the time savings does not come at the expense of the peak S/N for the off diagonal cross peaks. Comparison of the $^{13}C\alpha$ and the ^{13}CO carbons show that the sample without CuEDTA and the samples with CuEDTA are only ~10% different in the peak S/N/scan values.

For the 500 ms data, the FP-Hairpin without CuEDTA showed more fluctuation in the peak S/N/scan values, as shown in Table AI-4. For the $^{13}C\beta$ signals, the sample without CuEDTA had a value of 18.2, where as the addition of the CuEDTA to the sample, and a 0.5 s recycle delay increase the peak S/N/scan to 25.0, but with a 0.25 s recycle delay the value falls off to only 10.4. The increase in the peak signal to noise per scan between the sample without CuEDTA and the sample with CuEDTA and a recycle delay of 0.5 s is observed for the $^{13}C\alpha$ and ^{13}CO carbons, followed by the sharp drop off between the 0.5 s and 0.25 s recycle delay. As discussed above, the fall off between the 0.5 s and the 0.25 s recycle delay data could be due to sample related issues.

For the "fresh" sample and the "rehydrated" sample of FP-Hairpin with CuEDTA added, the data is much more consistent between the differing recycle delays. For the 50 ms data, the $^{13}C\beta$ peak S/N/scan were 49.0 and 56.9 for the "fresh" and "rehydrated" samples respectively. The $^{13}C\alpha$ and ^{13}CO peak S/N/scan values were also higher for these samples compared to the previous data at 50 ms mixing time. The difference between the peak S/N/scan values were < 20% difference between the "fresh" and "rehydrated" values with a 0.25 s recycle day. For the 500 ms mixing time, the peak S/N/scan values of the "fresh" and "rehydrated" sample for the

$^{13}C\beta$ peak, $^{13}C\alpha$ peak, and the ^{13}CO peak all showed an increase in the peak S/N/scan going from the "fresh" sample to the "rehydrated" sample when using the 0.25 s recycle delay. This suggests that shortening the recycle delay with the addition of the CuEDTA to the sample is beneficial, as discussed previously.

Table AI-4: Comparison of the peak signal to noise (Peak S/N) per scan for the FP-Hairpin UA6/UG10 samples at 9.4 T that were used to compare the affect of the addition of the CuEDTA solution to the sample.

Peak	Cβ	Cα	CO
Figure 3-4B: 50 ms mixing time with 1 s recycle delay			
Peak S/N	15.3	2.0	2.4
Total Acquisitions	300 * 768		
Peak S/N/scan [a]	66.4	8.68	10.4
Figure 3-5B: 500 ms mixing time with 1 s recycle delay			
Peak S/N	8.4	0.9	1.1
Total Acquisitions	300 * 1536		
Peak S/N/scan	18.2	1.95	2.39
Figure AI-1B: 50 ms mixing time with 0.5 s recycle delay			
Peak S/N	8.4	2.3	2.6
Total Acquisitions	300 * 768		
Peak S/N/scan	36.5	9.98	11.3
Figure AI-2B: 500 ms mixing time with 0.5 s recycle delay			
Peak S/N	9.6	2.9	4.0
Total Acquisitions	300 * 1280		
Peak S/N/scan	25.0	7.55	10.4
Figure AI-3B: 50 ms mixing time with 0.25 s recycle delay			
Peak S/N	13.1	3.5	4.0
Total Acquisitions	300 * 768		
Peak S/N/scan	34.1	9.11	10.4
Figure AI-4B: 500 ms mixing time with 0.25 s recycle delay			
Peak S/N	4.0	1.0	1.0
Total Acquisitions	300 * 1280		
Peak S/N/scan	10.4	2.60	2.60
Figure AI-5B: 50 ms mixing time with 0.25 s recycle delay (fresh sample)			
Peak S/N	11.3	4.8	4.0
Total Acquisitions	300 * 768		
Peak S/N/scan	49.0	20.8	17.4
Figure AI-6B: 500 ms mixing time with 0.25 s recycle delay (fresh sample)			
Peak S/N	6.2	1.8	1.9
Total Acquisitions	300 * 1152		
Peak S/N/scan	17.9	5.21	5.50
Figure AI-7B: 50 ms mixing time with 0.25 s recycle delay (rehydrated)			
Peak S/N	13.1	4.1	3.4
Total Acquisitions	300 * 768		
Peak S/N/scan	56.9	17.8	14.8
Figure AI-8B: 500 ms mixing time with 0.25 s recycle delay (rehydrated)			
Peak S/N	6.4	2.4	2.9
Total Acquisitions	300 * 1152		
Peak S/N/scan	18.5	6.94	8.39

Table AI-4 (cont'd)

a = All peak S/N/scan values are divided by 10^{-6} to remove the exponent.

The calculations for the peak S/N/scan were based on the way they were done in Chapter 4, section "Low pH Sample Preparation Technique for FP-Hairpin UA6/UG10", subsection " pH swapped FP-Hairpin UA6/UG10 from pH 3 to pH 7 at 21.1 T".

Conclusions to the CuEDTA sample work for FP–Hairpin UA6/UG10

In conclusion from this work, the use of the CuEDTA solution allowed for the reduction of the recycle delay between acquisitions, leading to savings of 35 – 70% in signal averaging time for the 50 ms mixing time and up to 50% time savings for the 500 ms mixing time. A second major finding from this work is that only the β–strand conformation from the 2D ^{13}C–^{13}C experiments was observed, unlike previous work for the same FP–Hairpin UA6/UG10 sample in POPC/POPG/Chol lipid membranes at ~25:1 lipid to protein ratio prepared at neutral pH. There, both the helical and β–strand conformation were observed in the 2D ^{13}C–^{13}C experiments. The data from the CuEDTA samples suggest that the β–strand conformation is inserted into the lipid membrane, away from the CuEDTA solution. The helical conformation is likely located on the membrane exterior in close proximity to the CuEDTA solution which allows for the helical conformation to be relaxed back quickly and thus not observed by the 2D ^{13}C–^{13}C experiments. One possibility that agrees with the pH 3 sample presented in Chapter 4 is that the helical conformation is due to precipitated protein.

Testing a fresh FP–Hairpin UA6/UG10 sample in POPC/POPG/Chol at ~22:1 lipid to protein loading by hydrating it with the CuEDTA solution and then re–hydrating the sample again with the CuEDTA solution after the 50 ms and 500 ms 2D ^{13}C–^{13}C experiments were performed showed two observations. First, only the β–strand conformation for the Ala–6 and Gly–10 labeled residues for the FP–Hairpin UA6/UG10 sample were observed, which is consistent with the work where FP–Hairpin without CuEDTA hydration was studied, and then hydrated with CuEDTA. Second, the spectra for the fresh FP–Hairpin UA6/UG10 sample with CuEDTA is nearly identical to the rehydrated CuEDTA sample, as seen by comparing Figures AI–5 and AI–7 for the 50 ms experiment and Figures AI–6 and AI–8 for the 500 ms data along with the tabulated data of Table AI–3. Finally, the CuEDTA data fits well with the data presented in Chapter 4 where FP–Hairpin UA6/UG10 was prepared with lipid membranes and the protein both at pH 3. The take home message from these experiments is that the CuEDTA likely is in contact with the helical component resulting in the absence of the helical cross peaks in the CuEDTA sample spectra. The β–strand conformation is likely sequestered away in the membrane, resulting in the observation of β–strand cross peaks and not the helical cross peaks. Thus, the helical conformation is likely due to the precipitated protein. By preparing the "fresh sample" this was tested, and the lack of the helical cross peaks confirms this thought.

Wickramasinghe and co–workers measured the ^{1}H T_1 relaxation times of the proteins ubiquitin and lysozyme in a microcrystal state, finding that without the addition of CuEDTA the ^{1}H T_1 times of ubiquitin were ~820 ms in D_2O and ~300 ms in H_2O, and the ^{1}H T_1 times of Lysozyme were ~350 ms in D_2O and ~280 ms in H_2O.[4] With the addition of 10 mM CuEDTA solution, the ^{1}H T_1 values of ubiquitin and lysozyme were reduced to 73 ms and 59 ms

respectively.[4] From this data, it is likely that the ^{1}H T_1 of the sample which is exposed to the CuEDTA are significant reduced. It is likely that the ^{1}H T_1 is reduced to various degrees in the sample, where the ^{1}H closest to the CuEDTA have the shortest ^{1}H T_1 values, and the ^{1}H which are located in the membrane farthest from the CuEDTA will have the longest ^{1}H T_1 values.

Section 2: 1D, 2D, and 3D supplemental data from 21.1 T for U–NAL and FP–Hairpin UA6/UG10

This section contains supplemental data from experiment performed at the 21.1 T spectrometer with the U–NAL and FP–Hairpin UA6/UG10 samples. The experiments that will be presented below include the 1D ^{15}N CP Ramp for U–NAL; 2D NCA / NCO heteronuclear correlation experiments for both samples; 2D ^{13}C–^{13}C experiments for FP–Hairpin; and 3D NCACX experiments for both U–NAL and FP–Hairpin. Most of the data being presented in this section were the first attempts at the experiment using at the high field spectrometer, and the data fit better here than in Chapter 4. This section lays the ground work for future experiments.

1D ^{15}N CP ramp of U–NAL at 21.1 T

The file location for the U–NAL ^{15}N CP is listed in Appendix IV, Table IV–10. The ^{15}N CP parameters are the same as Table 2–5 in Chapter 2. The ^{15}N spectrum was referenced as described in Chapter 2 and Appendix III.

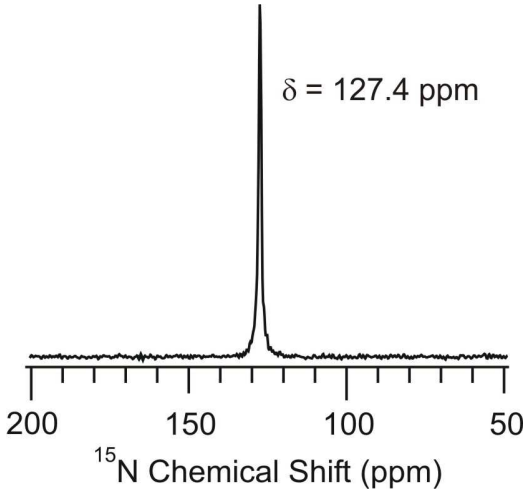

Figure AI–9: The ^{15}N CP for U–NAL properly referenced as described in Chapter 2 and Appendix III. The chemical shift for the referenced ^{15}N amide is δ = 127.4 ppm. The ^{15}N CP is the result of 256 acquisitions with a 3 second recycle delay and no line broadening applied.

2D ^{13}C–^{13}C experiments for FP–Hairpin UA6/UG10 at 21.1 T

Supplemental data for the FP–Hairpin UA6/UG10 which was at ~15:1 lipid to protein loading in a lipid membrane environment of POPC/POPG/Chol in a 8:2:5 molar ratio. Parameters for the 2D ^{13}C–^{13}C experiment were consistent with those presented in Table 2–7 of Chapter 2 unless noted in the figure caption. The mixing times were changed for the different figures, with Figure AI–10, AI–11, AI–12, and AI–13 having mixing times of 10 ms, 50 ms, 100 ms, and 1000 ms. The purpose of this set of experiments was to determine if there was any difference between a mixing time of 10 ms, 50 ms, 100 ms, or 1000 ms for the intra–residue assignments.

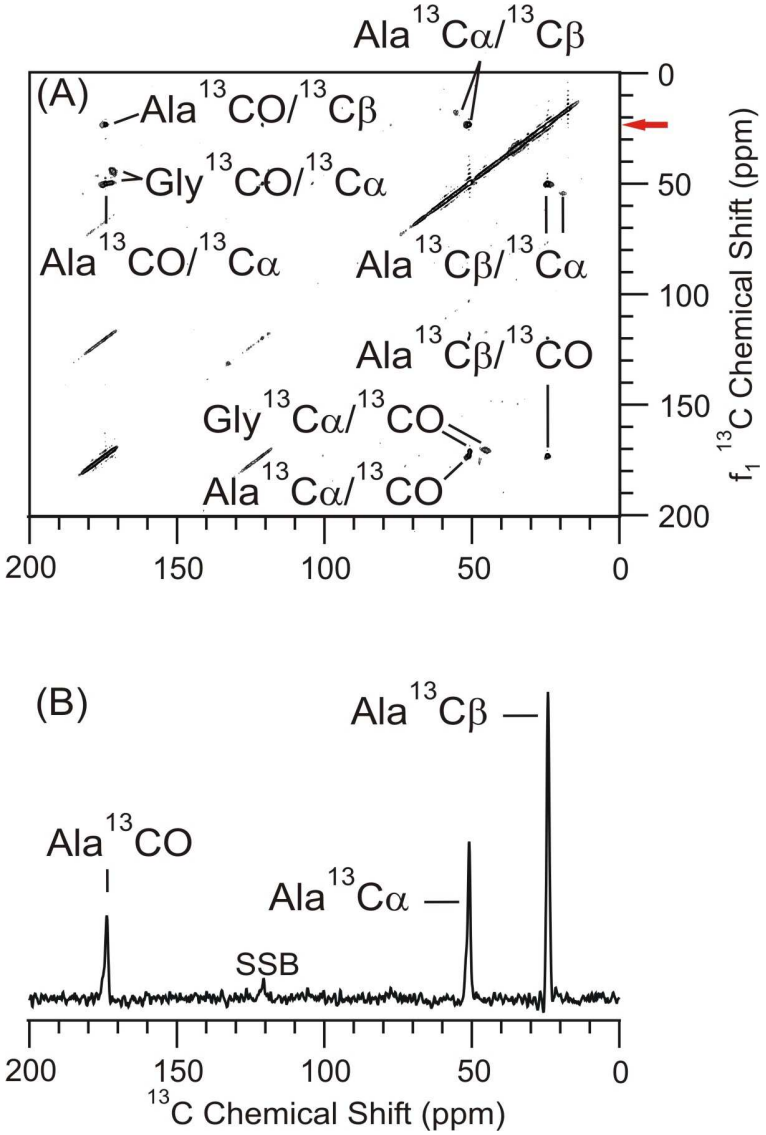

Figure AI–10: The 2D DARR ^{13}C–^{13}C spectra at 21.1 T of FP–Hairpin with uniform ^{13}C, ^{15}N labeling at Ala–6 and Gly–10 in the FP region in an 8:2:5 mole ratio of POPC/POPG/Chol in a lipid membrane environment at ~15:1 lipid to protein ratio. (A) The 10 ms mixing time spectrum shows the intra–residue cross peaks. (B) The f_2 slice corresponding to the Ala $^{13}C\beta$ β–strand conformation from f_1 = 23.5 ppm is marked by the red arrow in (A). There were 256 t_1 points and 128 scans summed per t_1 point in a total time of ~16 hrs. Assignments are listed as assignment in f_2 – assignment in f_1. 100 Hz of Gaussian line broadening was applied to each dimension. A spinning sideband for the ^{13}CO peak is labeled as SSB.

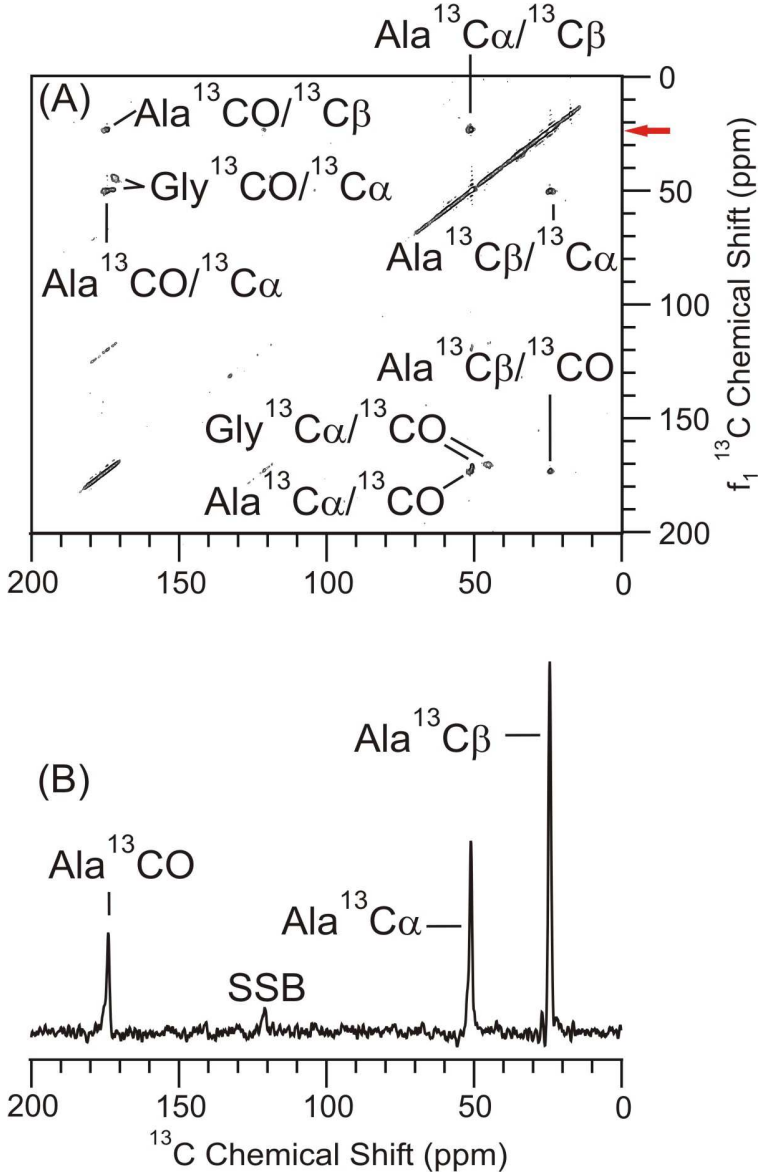

Figure AI–11 The 2D DARR ^{13}C–^{13}C spectra at 21.1 T of FP–Hairpin with uniform ^{13}C, ^{15}N labeling at Ala–6 and Gly–10 in the FP region in an 8:2:5 mole ratio of POPC/POPG/Chol in a lipid membrane environment at ~15:1 lipid to protein ratio. (A) The 50 ms mixing time spectrum shows the intra–residue cross peaks. (B) The f_2 slice corresponding to the Ala $^{13}C\beta$ β–strand conformation from f_1 = 23.5 ppm is marked by the red arrow in (A). There were 256 t_1 points and 128 scans summed per t_1 point in a total time of ~16 hrs. Assignments are listed as assignment in f_2 – assignment in f_1. 100 Hz of Gaussian line broadening was applied to each dimension. A spinning sideband for the ^{13}CO peak is labeled as SSB. The slice (B) is scaled to the same noise level as the slice in Figure AI–10B.

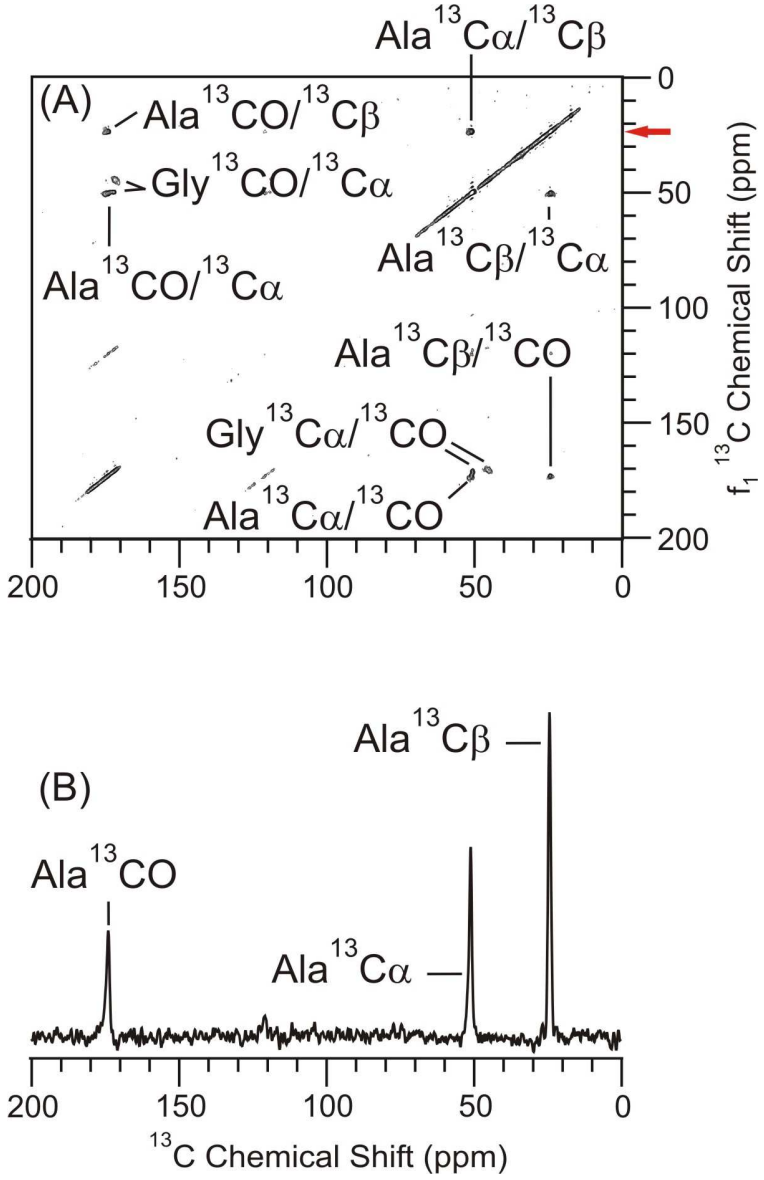

Figure AI–12 The 2D DARR ^{13}C–^{13}C spectra at 21.1 T of FP–Hairpin with uniform ^{13}C, ^{15}N labeling at Ala–6 and Gly–10 in the FP region in an 8:2:5 mole ratio of POPC/POPG/Chol in a lipid membrane environment at ~15:1 lipid to protein ratio. (A) The 100 ms mixing time spectrum shows the intra–residue cross peaks. (B) The f_2 slice corresponding to the Ala $^{13}C\beta$ β–strand conformation from f_1 = 23.5 ppm is marked by the red arrow in (A). There were 256 t_1 points and 128 scans summed per t_1 point in a total time of ~16 hrs. Assignments are listed as assignment in f_2 – assignment in f_1. 100 Hz of Gaussian line broadening was applied to each dimension. The slice (B) is scaled to the same noise level as the slice in Figure AI–10B.

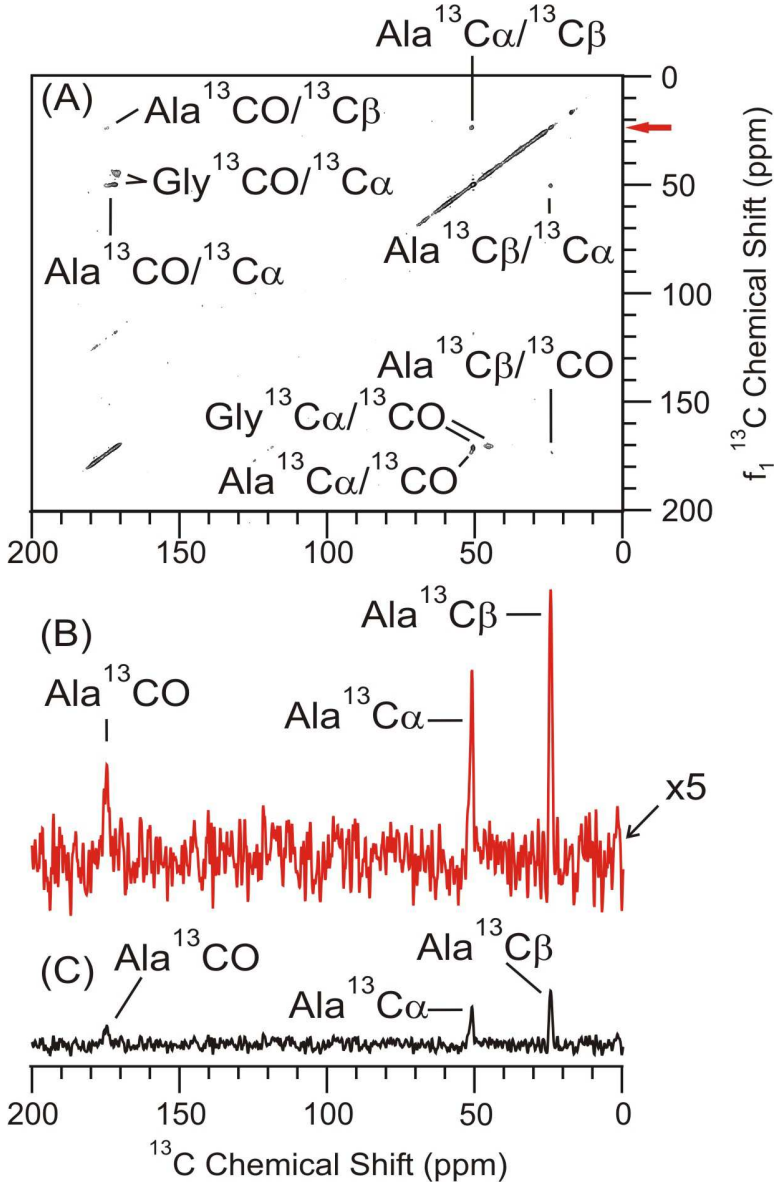

Figure AI–13: The 2D DARR ^{13}C–^{13}C spectra at 21.1 T of FP–Hairpin with uniform ^{13}C, ^{15}N labeling at Ala–6 and Gly–10 in the FP region in an 8:2:5 mole ratio of POPC/POPG/Chol in a lipid membrane environment at ~15:1 lipid to protein ratio. (A) The 1000 ms mixing time spectrum shows the intra–residue cross peaks. (B, C) The f_2 slice corresponding to the Ala $^{13}C\beta$ β–strand conformation from f_1 = 23.5 ppm is marked by the red arrow in (A). The slice in (B) is fivefold (x5) the size of the slice in (C). The slice in (C) is scaled to the same noise level as Figure AI–10B. There were 256 t_1 points and 128 scans summed per t_1 point in a total time of ~16 hrs. Assignments are listed as assignment in f_2 – assignment in f_1. 100 Hz of Gaussian line broadening was applied to each dimension.

The 2D ^{13}C–^{13}C spectra presented in Figures AI–10 to AI–13 are all scaled to the same contour levels in the 2D plots and also in the slices. The slices are scaled to the noise level as the slice in Figure AI–10B for ease of comparison. In Figure AI–13B, the top slice in red corresponds to a fivefold scaling compared to the black slice below (Figure AI–13C). The bottom black slice of Figure AI–13C is scaled to the same noise level as the previous slices, and the red (top) slice of Figure AI–13B is expanded fivefold for ease of visualization. As the mixing time increases from 10 ms to 1000 ms, the magnetization is allowed to diffuse out away from the starting carbons. At the short mixing times of 10 – 100 ms most of the magnetization will be within 1 – 2 bonds of the initial ^{13}C nuclei, and as seen above, results in intense off diagonal peaks in the 2D plot and the slice. As the mixing time approaches 1000 ms, the magnetization continues to diffuse out, and spread amongst the further away carbons, leaving less magnetization on the closer carbons, and resulting in a less intense off diagonal cross peak. Work by Castellani and co–workers used the build up of the cross peaks to identity distance constraints which were used to develop a 3D model of a fully labeled protein, which was previously discussed in Chapter 1 of this dissertation.[6]

Figure AI–14 is the 2D ^{13}C–^{13}C experiment for FP–Hairpin which was acquired in ~7 hrs for the 50 ms mixing time which is the spectrum that resulted in the finding of the reduced signal averaging time, increased ^{13}C integrated area and peak signal to noise, and reduced FWHM linewidths discussed in Chapter 4.

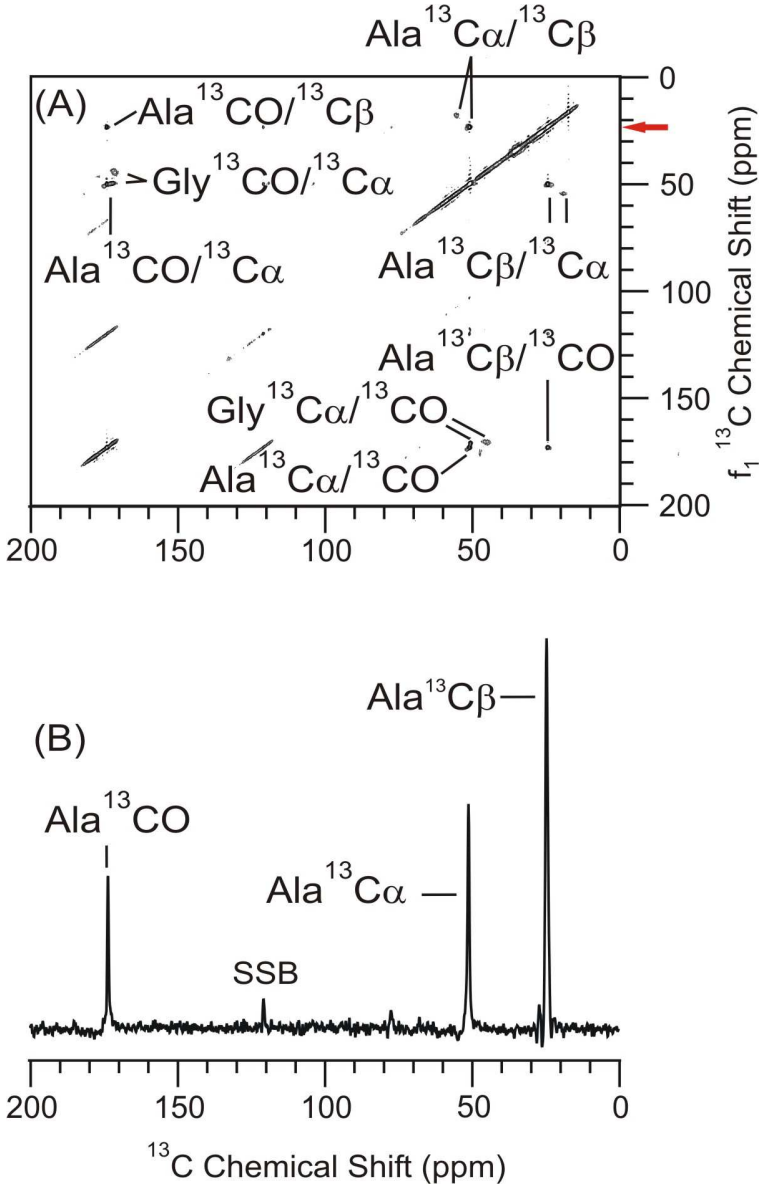

Figure AI–14: The 2D DARR ^{13}C–^{13}C spectra at 21.1 T of FP–Hairpin with uniform ^{13}C, ^{15}N labeling at Ala–6 and Gly–10 in the FP region in an 8:2:5 mole ratio of POPC/POPG/Chol in a lipid membrane environment at ~15:1 lipid to protein ratio. (A) The 50 ms mixing time spectrum shows the intra–residue cross peaks. (B) The f_2 slice corresponding to the Ala $^{13}C\beta$ β–strand conformation from f_1 = 23.5 ppm is marked by the red arrow in (A). There were 256 t_1 points and 64 scans summed per t_1 point in a total time of ~16 hrs. Assignments are listed as assignment in f_2 – assignment in f_1. No Gaussian line broadening was applied. This data was acquired in ~7 hrs, but probably could have been acquired in half that time by reducing the number of scans per t_1 point by half as determined by the signal intensity of the slice presented in Figure AI–14B. A spinning sideband for the ^{13}CO peak is labeled as SSB.

2D NCA / NCO heteronuclear correlation experiments

Two dimensional experiments were performed using U–NAL to setup and determine ^{15}N–^{13}C correlations. The experiments were either the NCA or the NCO experiment. Setup on U–NAL was performed first before attempting the experiment on the FP–Hairpin protein sample. These experiments were performed at 21.1 T using a Bruker spectrometer and a 4 mm MAS E–free probe. Figure AI–14 is the pulse sequence for the 2D NCA / NCO experiments. Table AI–5 contains the parameters for the experiments for U–NAL and the FP–Hairpin sample.

Phase cycling for the 2D ^{15}N–^{13}C experiment is as follows: ^{1}H $\pi/2$ pulse was y, y, y, y, –y, –y, –y, –y; the $^{1}H \rightarrow {}^{15}N$ CP step (p15) had ^{1}H phase of x and ^{15}N phase of x. The $^{15}N \rightarrow {}^{13}C$ CP step (p16) had ^{15}N phase of x, x, –x, –x and ^{13}C phase of x, x. The first ^{13}C $\pi/2$ pulse phase was y; and the second ^{13}C $\pi/2$ read pulse phase was x, y, –x, –y. The receiver phase cycling was x, y, x, y, –x, –y, –x, –y. For experiments which had a PDSD period between the ^{13}C $\pi/2$ pulses, there was no rf irradiation on the ^{1}H channel. For experiments which had a DARR period between the ^{13}C $\pi/2$ pulses, the phase of the ^{1}H rf was x. ^{1}H CW decoupling during the $^{15}N \rightarrow {}^{13}C$ CP step was phase x.

Data processing was done using nmrDraw. The Topspin data was read into the nmrDraw program using the "bruker" conversion program. The 2D script for the 2D ^{13}C–^{13}C experiments was also used for the 2D NCA or NCO experiments. The only difference was the amount of line broadening applied. The macro script is discussed in more detail in Appendix III.

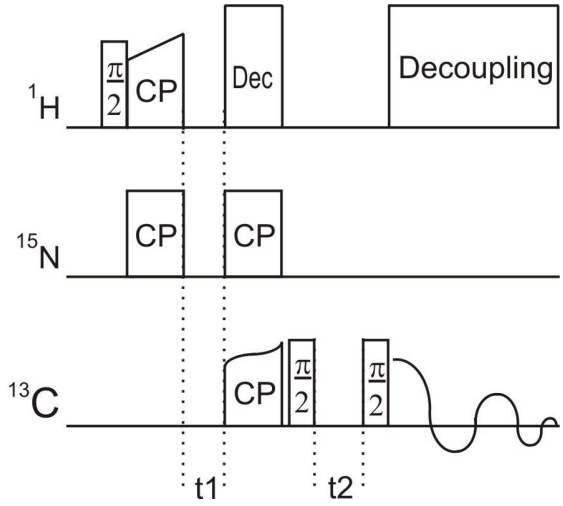

Figure AI–15: Pulse sequence for the 2D ^{15}N–^{13}C heteronuclear correlation experiments performed at 21.1 T. The magnetization is first prepared by a ^{1}H $\pi/2$ pulse which rotates the magnetization from the Z–axis to the transverse plane. A cross polarization step transfers the magnetization from the $^{1}H \rightarrow {}^{15}N$ nuclei. Next, the magnetization is selectively transferred from $^{15}N \rightarrow {}^{13}C$ via a second cross polarization step under high power ^{1}H continuous wave (CW) decoupling. The ^{13}C transverse magnetization is rotated to the Z–axis and exchange occurs during the second mixing time (t_2). A second ^{13}C $\pi/2$ pulse rotates the magnetization back to the transverse plane for detection. Depending on the ^{13}C transmitter location depends on the correlation that will be observed. The 2D NCO experiment has the ^{13}C transmitter at ~165 ppm, and the 2D NCA experiment has the ^{13}C transmitter at ~50 ppm. The PDSD version of the experiment is shown here, with the only difference for the DARR experiment being the addition of rf being applied during t_2 on the ^{1}H channel which is equal to the MAS frequency.

U–NAL: 2D NCA / NCO Experiments

Data locations for the 2D NCA and 2D NCO experiments can be found in Appendix IV, Tables AIV–10 and AIV–15. Table AI–6 presents the chemical shifts for the U–NAL's 2D NCA and NCO experiments corresponding to Figures AI–16 and AI–17. Processing of the data sets were done as discussed above. For the U–NAL spectra, 25 Hz of Gaussian line broadening was applied to each dimension in the 2D plots of the NCO and NCA spectra. Optimized experimental parameters were determined from files 174 (2D NCA: UNAL), 175 (2D UNAL: NCO), and 311 (2D NCA: FP–Hairpin). Files 174 and 175 are listed in Appendix IV, Table IV–10 and IV–15; File 311 is listed in Appendix IV, Table IV–17.

Table AI–5: Parameters for the 2D NCA and NCO experiments for U–NAL and FP–Hairpin.

Parameter [a]	**2D NCA: UNAL**	**2D NCA: FP–Hairpin UA6/UG10**	**2D NCO: U–NAL**
^{1}H π/2 pulse	3.0 μs	3.0 μs	3.0 μs
^{1}H π/2 PL	–2.2 dB (83 kHz)	–2.2 dB (83 kHz)	–2.2 dB (83 kHz)
Initial t_1 delay	0.3 μs	0.3 μs	0.3 μs
t_1 increment	83.3 μs	63.3 μs	63.3 μs
^{1}H→^{15}N CP time	2 ms	2 ms	4.2 ms
^{1}H→^{15}N CP PL	2 dB (51.4 kHz)	2 dB (51.4 kHz)	2 dB (51.4 kHz)
^{15}N→^{13}C CP time	4.6 ms	4.6 ms	4.7 ms
^{15}N→^{13}C CP PL	4.6 dB (38.0 kHz)	4.6 dB (38.0 kHz)	3 dB (45.8 kHz)
^{13}C π/2 pulse	4 μs	4 μs	4 μs
^{13}C π/2 PL	–1.4 dB (62.5 kHz)	–1.4 dB (62.5 kHz)	–0.4 dB (62.5 kHz)
^{1}H decoupling	–2.2 / –2.4 dB (83 – 86 kHz)	–2.2 / –2.4 dB (83 – 86 kHz)	–2.6 dB (87.3 kHz)
Acquisition time	15.05 ms	15.05 ms	15.05 ms
Temperature	250 K	250 K	250 K
MAS	12 kHz	12 kHz	12 kHz
#t_1 points	128	128	128
ns / t_1	32	64	32
Recycle delay	2 s	2 s	2 s
^{1}H offset	7 ppm	7 ppm	7 ppm
^{15}N offset	110 ppm	110 ppm	110 ppm
^{13}C offset	50 ppm	50 ppm	165 ppm
Mixing time	4 ms	5 ms	4 ms
Sweep Width ^{15}N	12 kHz	16 kHz	16 kHz
Sweep Width ^{13}C	68 kHz	68 kHz	68 kHz

a = Optimized experimental parameters were determined from files 174 (2D NCA: UNAL), 175 (2D UNAL: NCO), and 311 (2D NCA: FP–Hairpin).

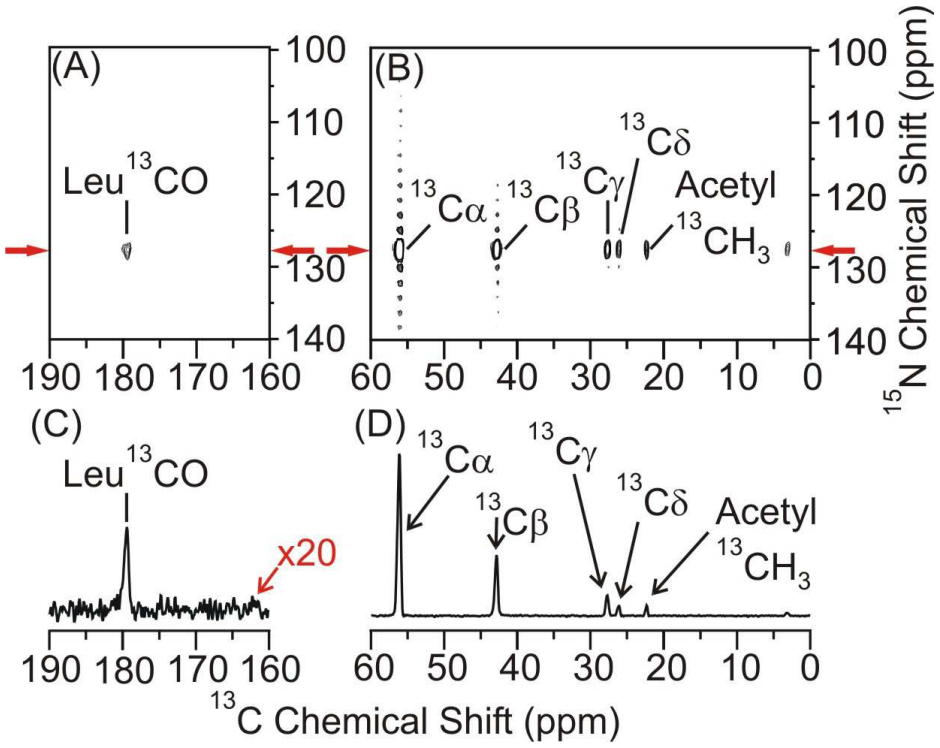

Figure AI–16: 2D NCA experiment for U–NAL. (A) The ^{13}CO region of the 2D NCA experiment. The ^{15}N – Leu ^{13}CO correlation can be observed. (B) The aliphatic region of the ^{13}C spectrum, showing the ^{15}N – ^{13}C correlation for all Leu Cα, Cβ, Cγ, and Cδ carbons along with the acetyl CH_3 group. The acetyl ^{13}CO was not observed in (A). Ringing in the ^{15}N dimension resulted in the vertical peaks in line with the Leu ^{13}Cα peak. (C, D) The 1D slice corresponding to the ^{15}N shift of 127.5 ppm and is marked by the red arrow in (B). The slice bisects all the ^{13}C peaks in (A) and (B). The portion of the slice shown in (C) is blown up by 20–fold compared to (D) to better illustrate the Leu ^{13}CO peak. The 2D results are consistent with the 1D NCA results for Figure 4–20D with the exception being that the Leu ^{13}CO is not observed for the 1D experiment. The chemical shifts are presented in Table AI–5. 25 Hz of Gaussian line broadening was applied to each dimension.

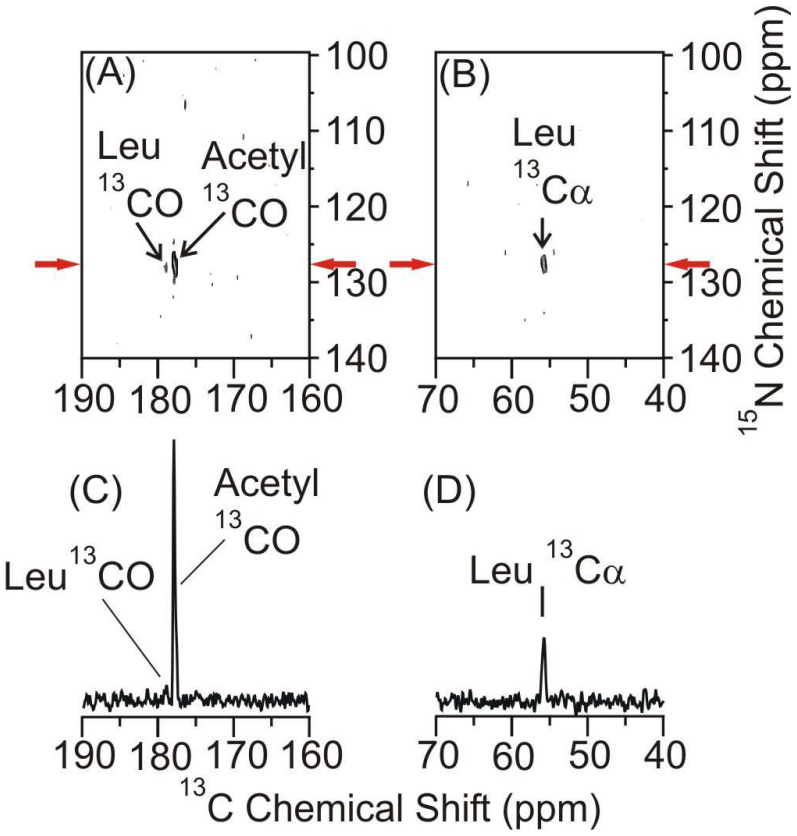

Figure AI–17: 2D NCO experiment for U–NAL. (A) The carbonyl region of the 2D experiment, where the predominate peak is the acetyl ^{13}CO for U–NAL. A slight peak for the Leu ^{13}CO is also seen. (B) The aliphatic region of the 2D plot where the Leu ^{13}Cα carbon is observed. No other ^{13}C peaks are observed in the 2D plot. The slices presented in (C) and (D) correspond to the red arrows in the 2D plot in (A) and (B). The slice was taken at the ^{15}N chemical shift of 128.0 ppm. The Leu ^{13}CO peak is hardly observable in (C). The 2D results are consistent with the 1D NCO results for Figure 4–20B. The chemical shifts are presented in Table AI–6. 25 Hz of Gaussian line broadening was applied to each dimension.

FP–Hairpin: 2D NCA experiment

Data locations for the 2D NCA experiments can be found in Appendix IV, Tables AIV–6 and AIV–17. Table AI–6 presents the chemical shifts for FP–Hairpin's 2D NCA experiment corresponding to Figure AI–18. Data processing was done using nmrDraw as discussed above.

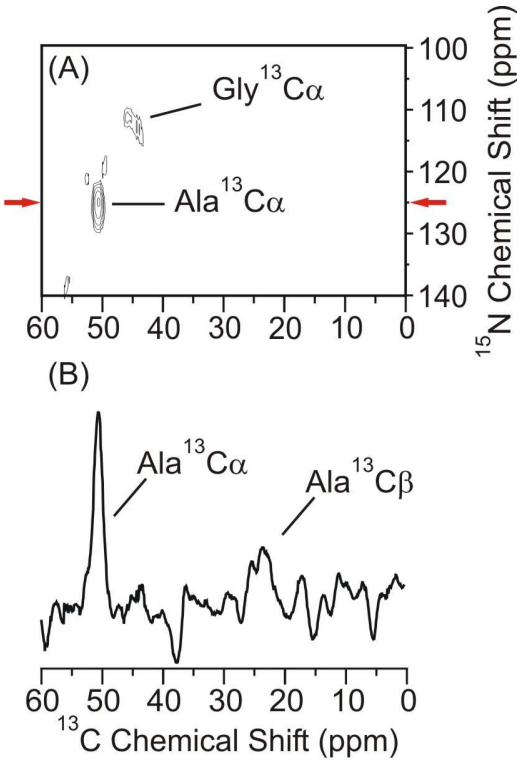

Figure AI–18: The 2D NCA experiment for FP–Hairpin UA6/UG10 prepared at pH 3 with ~1 μmole of protein in a lipid membrane consisting of an 8:2:5 molar ratio of POPC/POPG/Chol. 300 Hz of Gaussian line broadening was applied to each dimension. (A) The 2D NCA plot, where the Ala–6 ^{15}N/^{13}Cα and the Gly–10 ^{13}Cα/^{15}N cross peaks are observed. (B) The slice corresponding to the Ala–6 ^{15}N chemical shift of 125 ppm. The chemical shifts of the cross peaks are presented in Table AI–5. The Ala–6 ^{13}Cβ peak is observed in the slice (B), however it is not seen in the 2D plot due to the chosen contour levels. Lowering the contour levels of the 2D plot would result in the spectrum being filled with noise. The 2D plot is the result of 128 scans per t_1 point, with 128 t_1 points and a 2 s recycle delay. The raw and processed data are listed in Table AIV–6. Parameters for the 2D experiment are presented in Table AI–5.

Figure AI–18 is the result of the co–addition of experiment 311 and 314, each which having 64 scans per t_1 point. See also Table AIV–17 for more information about the individual files. 300 Hz of Gaussian line broadening was applied to each dimension of the 2D NCA plot of FP–Hairpin in Figure AI–18. The 2D NCA work for FP–Hairpin UA6/UG10 is in agreement with previous work by Michelle Bodner for FP23.[7, 8]

Table AI–6: Chemical shifts for the 2D NCA and NCO experiments for U–NAL and for the 2D NCA experiment of FP–Hairpin UA6/UG10 at 21.1 T.

(^{13}C, ^{15}N) System [a]	**2D NCA: U–NAL**	**2D NCO: U–NAL**	**2D NCA: FP–Hairpin UA6/UG10** [b]
^{13}Cα / ^{15}N	(56.0, 127.5)	(55.8, 127.6)	**Ala6:** (50.7, 124.9) **Gly10:** (45.7, 111.4)
^{13}Cβ / ^{15}N	(42.8, 127.5)	–	**Ala6:** –
^{13}Cγ / ^{15}N	(27.7, 127.5)	–	–
^{13}Cδ / ^{15}N	(26.1, 127.4)	–	–
^{13}CO / ^{15}N	(179.4, 127.8)	(178.9, 128.2)	–
Acetyl ^{13}CO / ^{15}N	–	(177.9, 127.4)	–
Acetyl ^{13}CH$_3$ / ^{15}N	(22.3, 127.5)	–	–

a = listed in the (f_2, f_1) convention
b = "–" means not observed.

3D NCACX experiments at 21.1 T

The 3D experiments were N–CA–CX experiments, which will initially prepare the magnetization on the ^{1}H nuclei, then a cross polarization transfer from ^{1}H→^{15}N occurs,

followed by the $^{15}N \rightarrow {}^{13}C\alpha$ diffusion and finally $^{13}C\alpha \rightarrow {}^{13}Cx$ transfer occurs, where Cx is any other ^{13}C bonded to the $^{13}C\alpha$, such as $^{13}C\beta$ or ^{13}CO. Parameters for the 3D experiment were determined from optimized ^{13}C CP, ^{15}N CP, and 2D ^{13}C–^{13}C experiments. Some parameters from the optimized NCA / NCO double cross polarization experiments were also used. Optimized parameters for the 3D experiment are presented in Table AI–7. Figure AI–19 is the pulse sequence for the 3D NCACX experiment.

The phase cycling for the 3D NCACX experiment is as follows: ^{1}H $\pi/2$ pulse was y, –y; the $^{1}H \rightarrow {}^{15}N$ CP step (p15) had ^{1}H phase of x and ^{15}N phase of x. The $^{15}N \rightarrow {}^{13}C$ CP step (p16) had ^{15}N phase of x, x, x, x, –x, –x, –x, –x and ^{13}C phase of x, x, x, x, y, y, y, y, –x, –x, –x, –x, –y, –y, –y, –y. The first ^{13}C $\pi/2$ pulse phase was y, y, y, y, –x, –x, –x, –x, –y, –y, –y, –y, x, x, x, x; and the second ^{13}C $\pi/2$ read pulse phase was –y, –y, –y, –y, x, x, x, x, y, y, y, y, –x, –x, –x, –x. The receiver phase cycling was x, –x, x, –x, –y, y, –y, y, –x, x, –x, x, y, –y, y, –y. For experiments which had a PDSD period for t_3, there was no rf irradiation on the ^{1}H channel. For experiments which had a DARR period for t_3, the phase of the ^{1}H rf was x. ^{1}H CW decoupling during the $^{15}N \rightarrow {}^{13}C$ CP step was phase x.

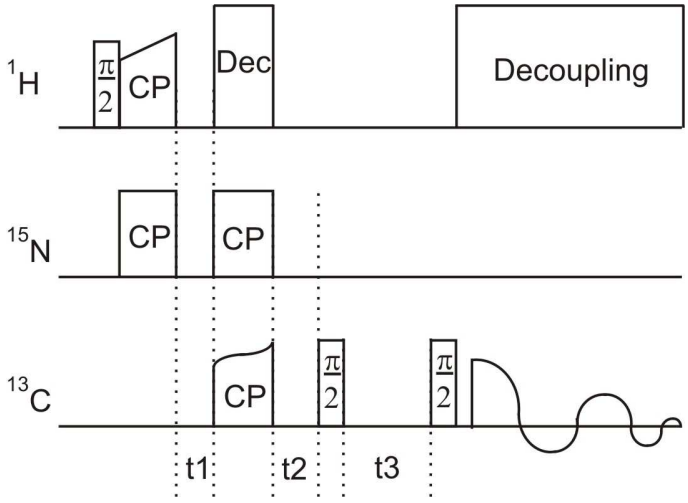

Figure AI–19: Pulse sequence for the Bruker 3D NCACX experiment at 21.1 T. The magnetization is initially prepared by a π/2 pulse on ^{1}H, after a delay (t_1) the magnetization is selectively cross polarized from the ^{1}H→^{15}N nuclei. After a second delay (t_2), the magnetization is selectively cross polarized from the ^{15}N→^{13}Cα nuclei with a tangent ramp for the ^{13}C nuclei (see Figure 2–10 for more information). The transverse magnetization is then rotated to the Z axis by a ^{13}C π/2 pulse where a third delay (t_3) exchanges the magnetization among the nearby ^{13}C nuclei. Following the t_3 mixing, the ^{13}C magnetization is rotated back to the transverse plane by a ^{13}C π/2 pulse and then detection occurs on the ^{13}C channel. This variant of the pulse sequence uses a PDSD mixing for the t_3 period. A DARR t_3 period can also be used by applying ^{1}H rf during the t_3 mixing time if desired, much like the 2D ^{13}C–^{13}C experiment (Figure 2–13B).

Table AI–7: Parameters for the 3D NCACX experiment for U–NAL and FP–Hairpin using the 21.1 T Bruker spectrometer.

Parameter [a]	**3D NCACX: UNAL**	**3D NCACX: FP–Hairpin UA6/UG10**
^{1}H π/2 pulse	3 μs	3 μs
^{1}H π/2 PL	–2.2 dB (83.3 kHz)	–2.2 dB (83.3 kHz)
Initial t_1 delay	0.3 μs	0.3 μs
t_1 increment (F1)	63 μs	63 μs
^{1}H→^{15}N CP time	2 ms	2 ms
^{1}H→^{15}N CP PL	2.0 dB (51.4 kHz)	2.0 dB (51.4 kHz)
t_2 time delay	0 μs	0 μs
t_2 increment (F2)	20.8 μs	20.8 μs
^{15}N→^{13}C CP time	4.6 ms	4.6 ms
^{15}N→^{13}C CP PL	4.6 dB (38.0 kHz)	4.6 dB (38.0 kHz)
^{13}C π/2 pulse	4 μs	4 μs
^{13}C π/2 PL	–1.40 dB (62.5 kHz)	–1.40 dB (62.5 kHz)
^{1}H decoupling	–2.2 / –2.4 dB (83 – 86 kHz)	–2.2 / –2.4 dB (83 – 86 kHz)
Acquisition time	15.05 ms	15.05 ms
Temperature	250 K	250 K
MAS	12 kHz	12 kHz
#t_1's	32	32
#t_2's	64	64
Recycle delay	1.5 s	1.5 s
^{1}H offset	7 ppm	7 ppm
^{15}N offset (F1)	110 ppm	110 ppm
^{13}C offset (F2)	50 ppm	50 ppm
^{13}C offset (F3)	50 ppm	50 ppm
DARR Mixing	120 dB	120 dB
^{13}C–^{13}C mix time	4 ms	4 ms

Table AI–7 (cont'd)

F1 Sweep Width ^{15}N	16 kHz	16 kHz
F2 SW ^{13}C	48 kHz	48 kHz
F3 SW ^{13}C	68 kHz	68 kHz
ns / t_1	14	14

a = Optimized experimental parameters were determined from files 25 (3D NCACX: UNAL), and 35 (3D NCACX: FP–Hairpin). Files 25 and 35 are listed in Appendix IV, Table IV–21.

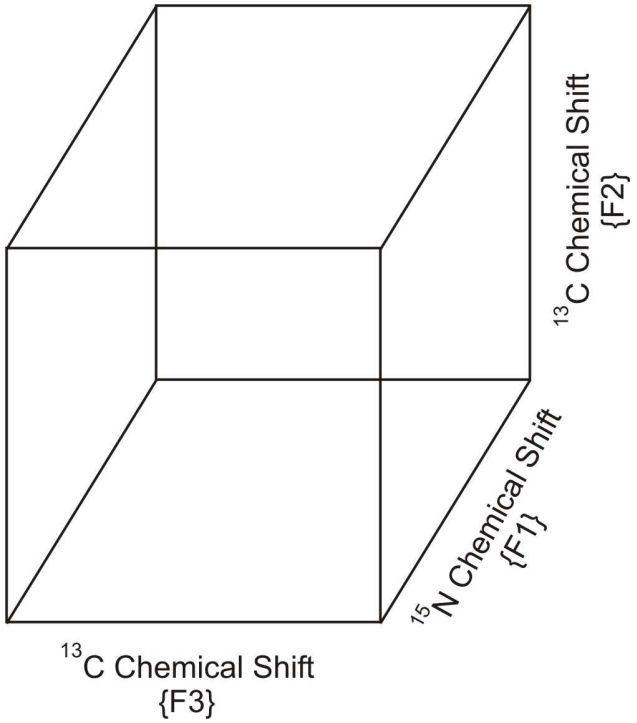

Figure AI–20: Visual presentation of the 3D box. For the experiments discussed here, the F1 dimension is the ^{15}N chemical shift, the F2 dimension is the ^{13}C chemical shift, and the F3 dimension is the ^{13}C chemical shift. The 2D planes obtained from the 3D experiments corresponding to the F1–F2 or the F2–F3 can be visually seen in the cube. The F1–F2 plane corresponds to the ^{15}N–^{13}C correlation, the F2–F3 plane corresponds to the ^{13}C–^{13}C correlation, and the F3–F1 plane corresponds to the ^{13}C–^{15}N correlation. Only the F1–F2 and the F2–F3 planes will be presented below.

Data processing was done in Topspin for the 3D experiments following information from the NESG website in reference [9]. Briefly, after acquisition of the 3D data set, the 3D data needed to be referenced and phased, which was done by extracting 2D planes. First, the F2–F3 and the F1–F3 planes were extracted and processed using the "xfb" command.[9] The phasing and referencing were done as previously described for the 2D data sets. After phasing and storing it in the 3D spectrum, the data needed to be transformed using the "tf3", "tf2", and "tf1" commands.[9] After this time, extraction of relevant 2D planes could be done and presented as 2D ^{13}C–^{13}C spectra or 2D ^{15}N–^{13}C spectra. 3D boxes can also be used for visualization of the data, as presented in Figure AI–21 for U–NAL's 3D experiment.

U–NAL: 3D NCACX Experiments

Data locations for these experiments can be found in Table AIV–15 and Table AIV–21 in Appendix IV. The sample was uniformly labeled N–acetyl leucine (U–NAL) which was a powder and had been packed in a 4 mm rotor.

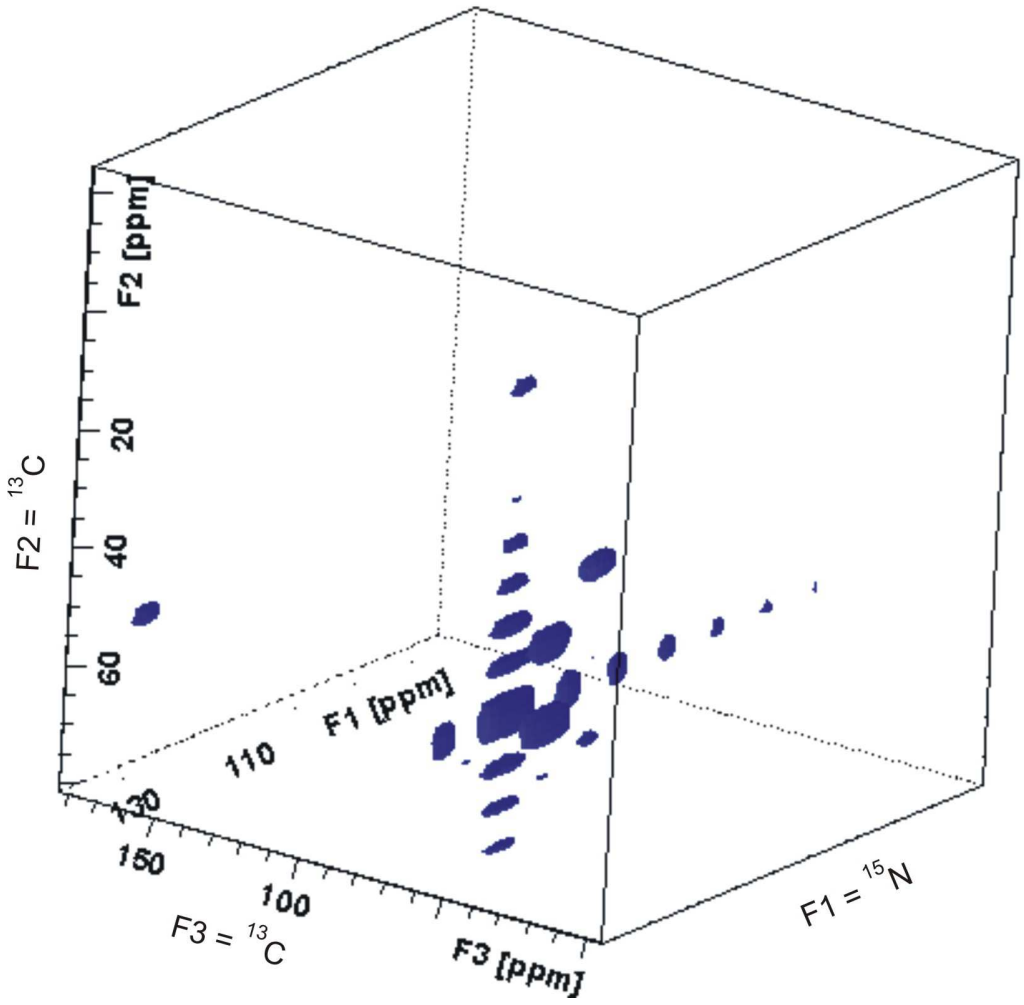

Figure AI–21: 3D data presentation for U–NAL with 0 Hz of line broadening applied to the three dimensions. The F1 dimension is the ^{15}N chemical shift, the F2 and F3 dimensions are the ^{13}C chemical shifts. The spots in the box correspond to the 3D location of the specific peaks from the experiment, and will be illustrated in Figures AI–22 and AI–23 with the 2D planes from the 3D box. Referencing of the three dimensions were done in the 2D planes, referencing the F1–F3 plane's ^{15}N/^{13}Cα cross peak to 127.5 ppm / 56.0 ppm. The F2–F3 plane was referenced using the ^{13}Cα/^{13}Cα cross peak at 56.0 ppm / 56.0 ppm. The referencing values were obtained from the 2D NCA experiment presented in Table AI–6 for U–NAL. There were 14 scans per t_1 point, and there were 32 t_1 points, and a total of 64 2D planes were acquired using a 1.5 s recycle delay. The experimental time was determined by: (t_1 points)*(ns/t_1)*(t_2 points)*(recycle delay) divided by 3600 s to yield ~12 hrs for data acquisition.

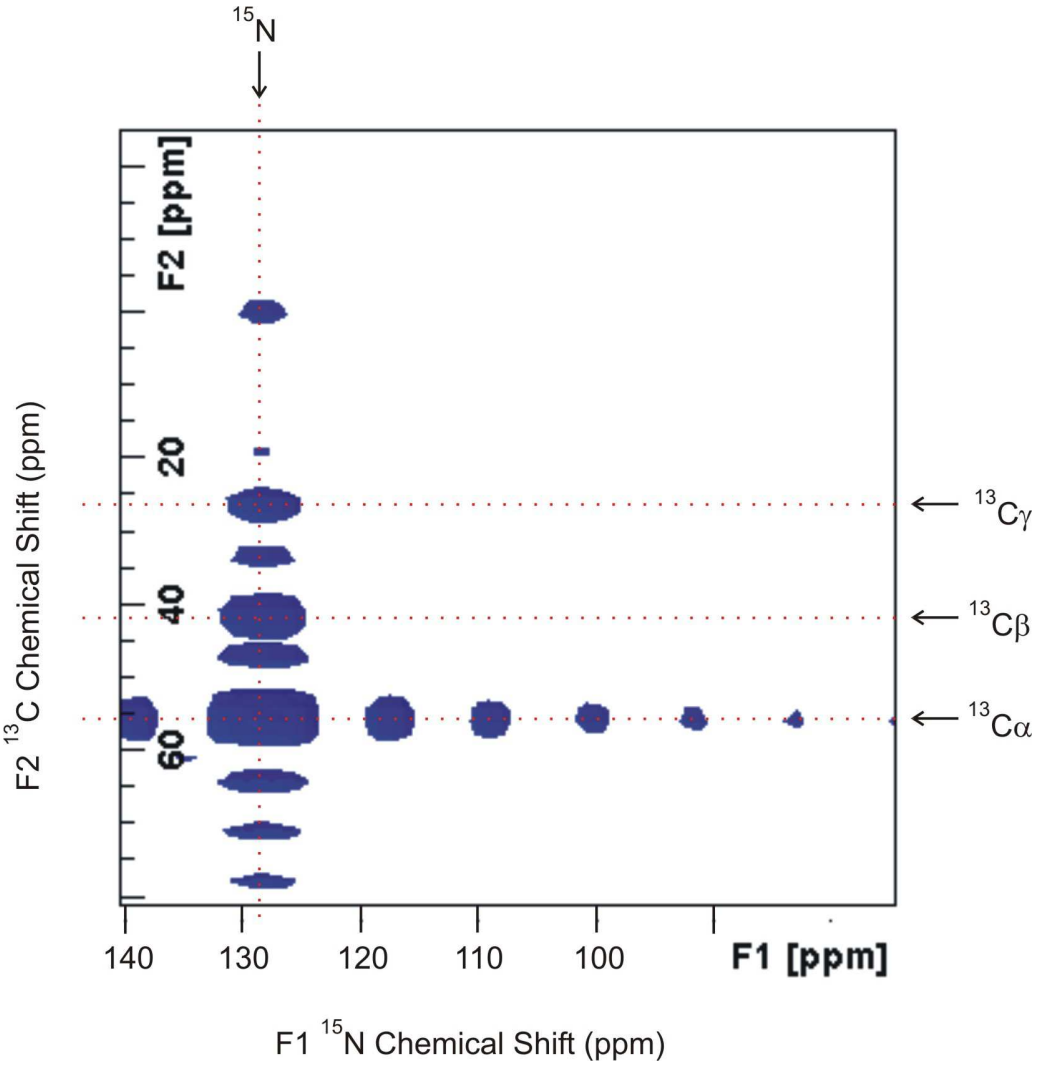

Figure AI–22: A 2D ^{15}N–^{13}C plane representative of the F1–F2 dimension of the 3D plot presented above for U–NAL. The blue cross peaks are shown. The red dashed lines are a visual guide to highlight the $^{15}N/^{13}C$ cross peaks. Extra cross peaks are observed (not marked by the intersection vertical and horizontal lines) which correspond to the ringing in the spectrum's ^{15}N dimension. Similar results were seen in the 2D NCA experiments for U–NAL presented in Figure AI–16. The same processing and acquisition parameters as those listed in Figure AI–21 were used in Figure AI–22.

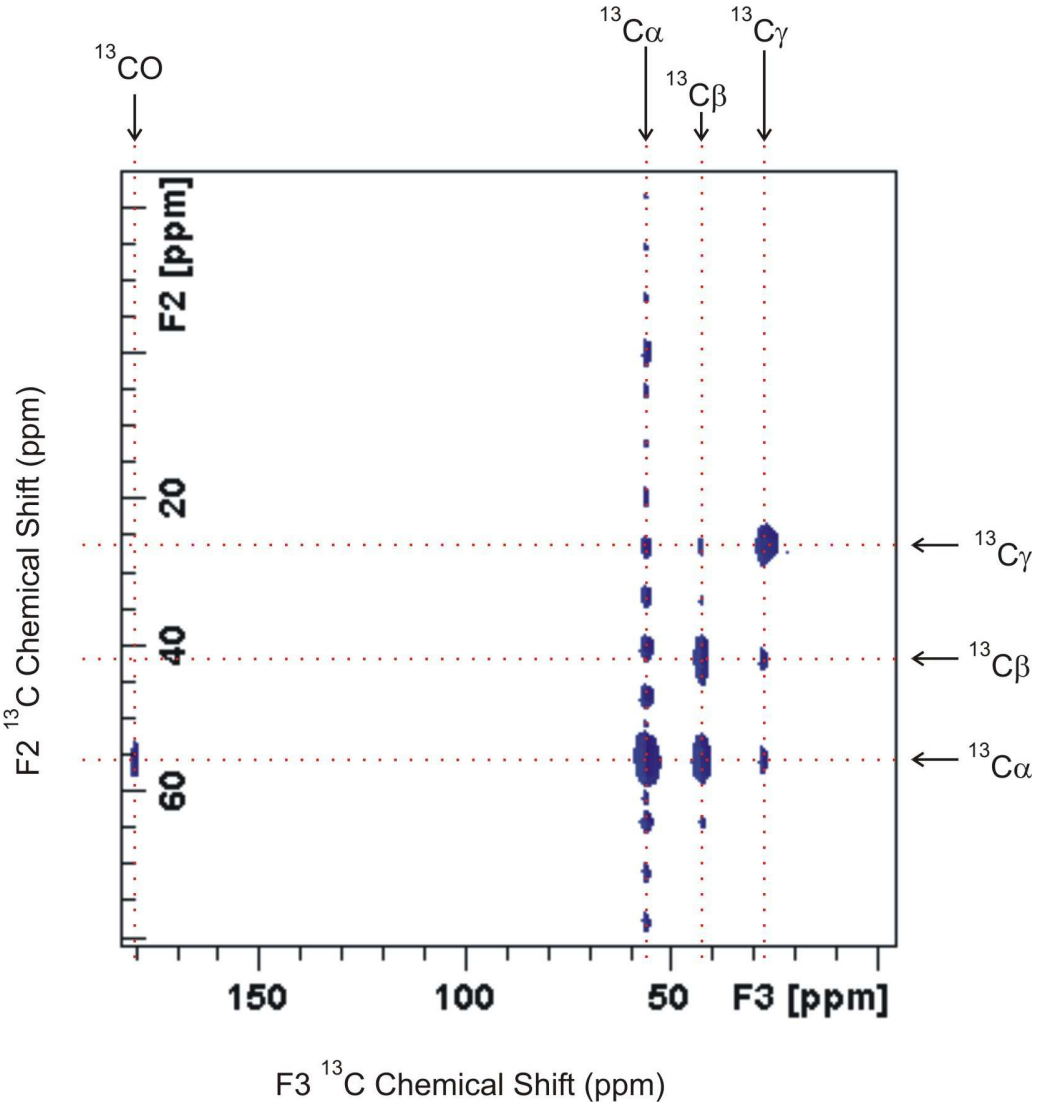

Figure AI–23: A 2D ^{13}C–^{13}C plane representative of the F2–F3 plane from the 3D experiment presented in Figure AI–21 for U–NAL. The blue cross peaks are shown. The red dashed lines are a visual guide to highlight the ^{13}C/^{13}C cross peaks. Extra cross peaks are observed (not marked by the intersection vertical and horizontal lines) which correspond to the ringing in the spectrum. The same processing and acquisition parameters as those listed in Figure AI–21 were used in Figure AI–23. The mixing of the ^{13}C magnetization between the different spin systems is observed by the ^{13}CO/^{13}Cα cross peak and the ^{13}Cα/^{13}Cβ and ^{13}Cα/^{13}Cγ cross peaks. The mixing of the ^{13}C magnetization with the same nuclei such as ^{13}Cα/^{13}Cα, ^{13}Cβ/^{13}Cβ, and ^{13}Cγ/^{13}Cγ are also observed. The ^{13}C–^{13}C mixing time was 4 ms.

FP–Hairpin: 3D NCACX experiments

FP–Hairpin 3D experiments can be found in Table AIV–16 for the FP–Hairpin UA6/UG10 in POPC/POPG/Chol lipid membranes at ~15:1 lipid to protein ratio. Table AIV–21 of Appendix IV also contains data for the FP–Hairpin UA6/UG10 at ~15:1 lipid to protein ratio. The optimized parameters are listed in Table AI–7.

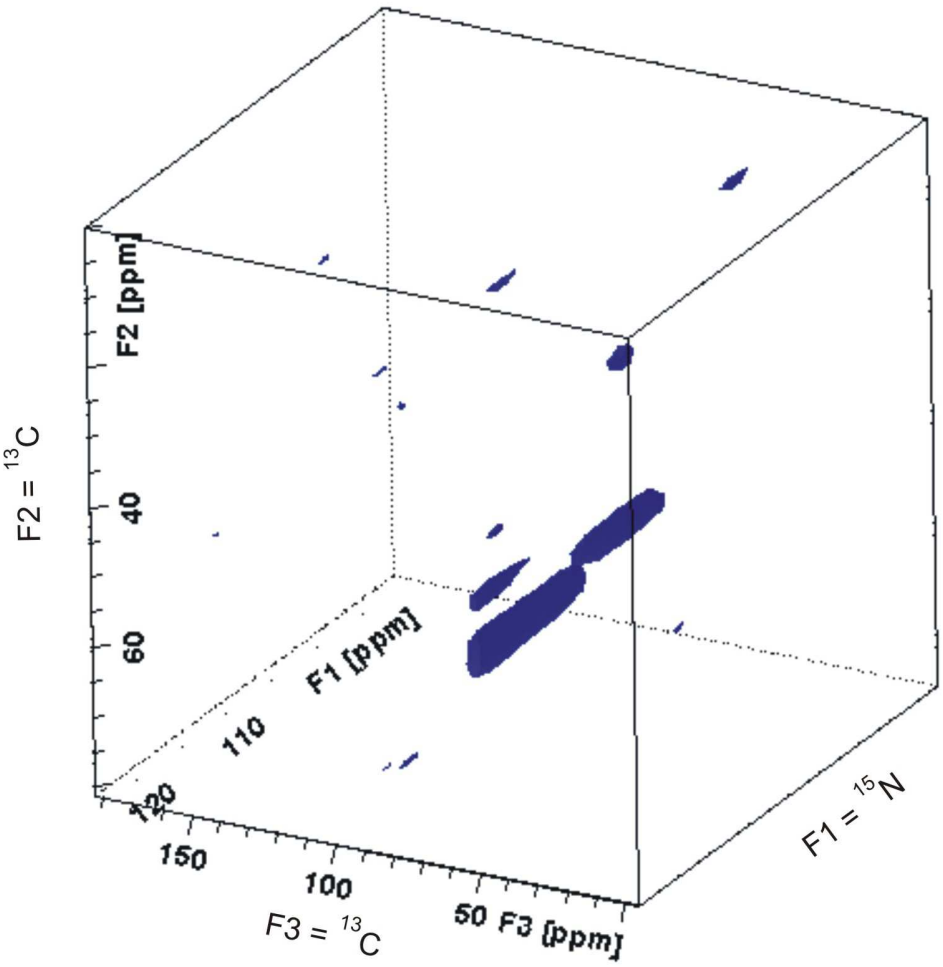

Figure AI–24: 3D data presentation for FP–Hairpin UA6/UG10 prepared at pH 3. No line broadening applied to the three dimensions. The F1 dimension is the ^{15}N chemical shift, the F2 and F3 dimensions are the ^{13}C chemical shifts. The spots in the box correspond to the 3D location of the specific peaks from the experiment, and will be illustrated in Figures AI–25 and AI–26 with the 2D planes from the 3D box. There were 14 scans per t_1 point, and there were 32 t_1 points, and a total of 64 2D planes were acquired using a 1.5 s recycle delay. The experimental time was determined by: (t_1 points)*(ns/t_1)*(t_2 points)*(recycle delay) divided by 3600 s to yield ~12 hrs for data acquisition.

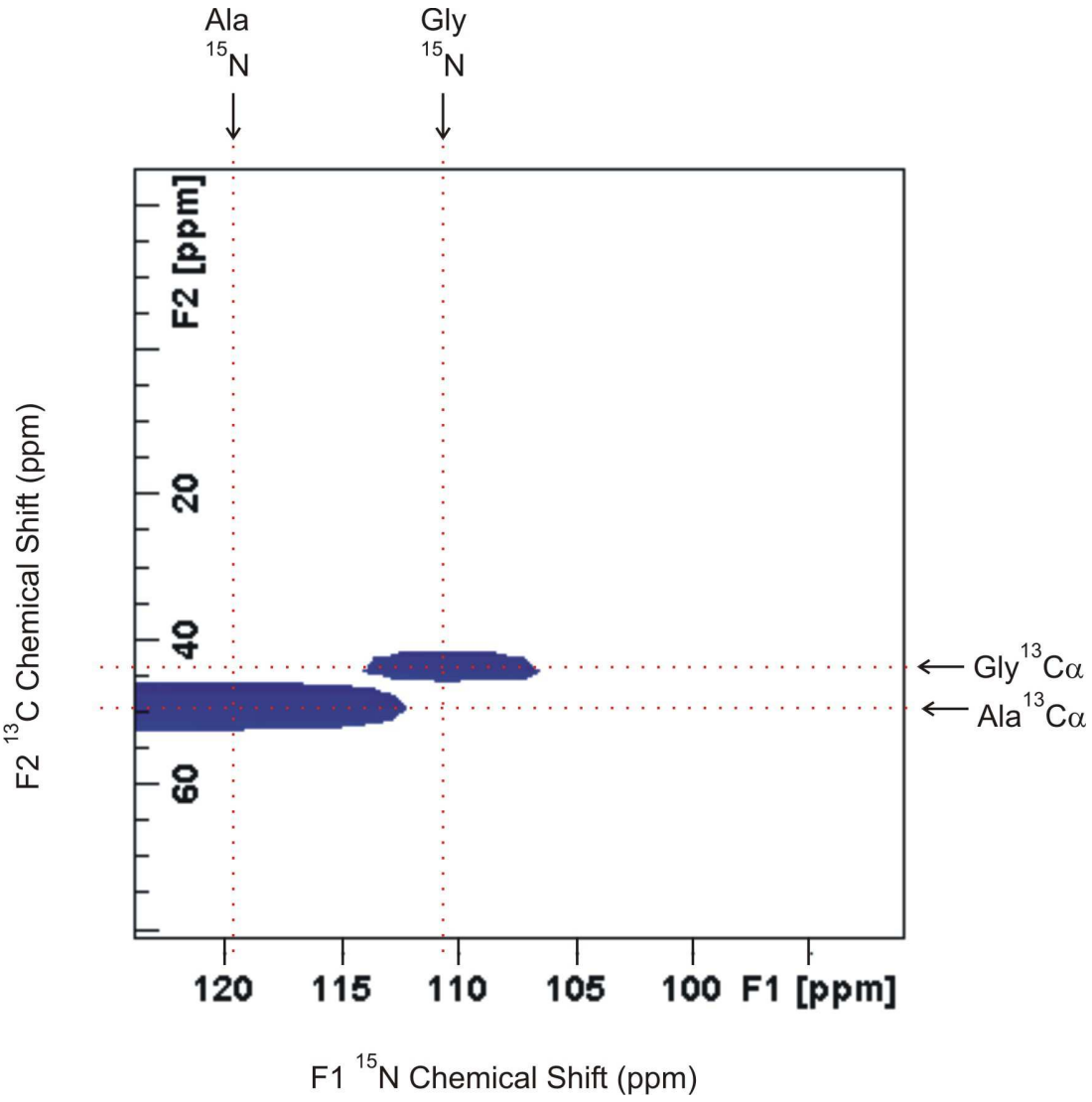

Figure AI–25: A 2D ^{15}N–^{13}C plane representative of the F1–F2 dimension of the 3D plot presented above for FP–Hairpin. The blue cross peaks are shown. The red dashed lines are a visual guide to highlight the $^{15}N/^{13}C$ cross peaks. The same processing and acquisition parameters as those listed in Figure AI–24 were used in Figure AI–25. As previously seen for the 2D NCA experiment of FP–Hairpin UA6/UG10 in Figure AI–18 and the ^{15}N CP of FP–hairpin, the ^{15}N chemical shift for the protein was ~20 ppm wide, which is why the spots in the 2D plot are broad as well. The sample when probed by 2D ^{13}C–^{13}C experiments (Figure 4–10) was found to be predominantly β–strand, which these shifts would correspond with predominantly.

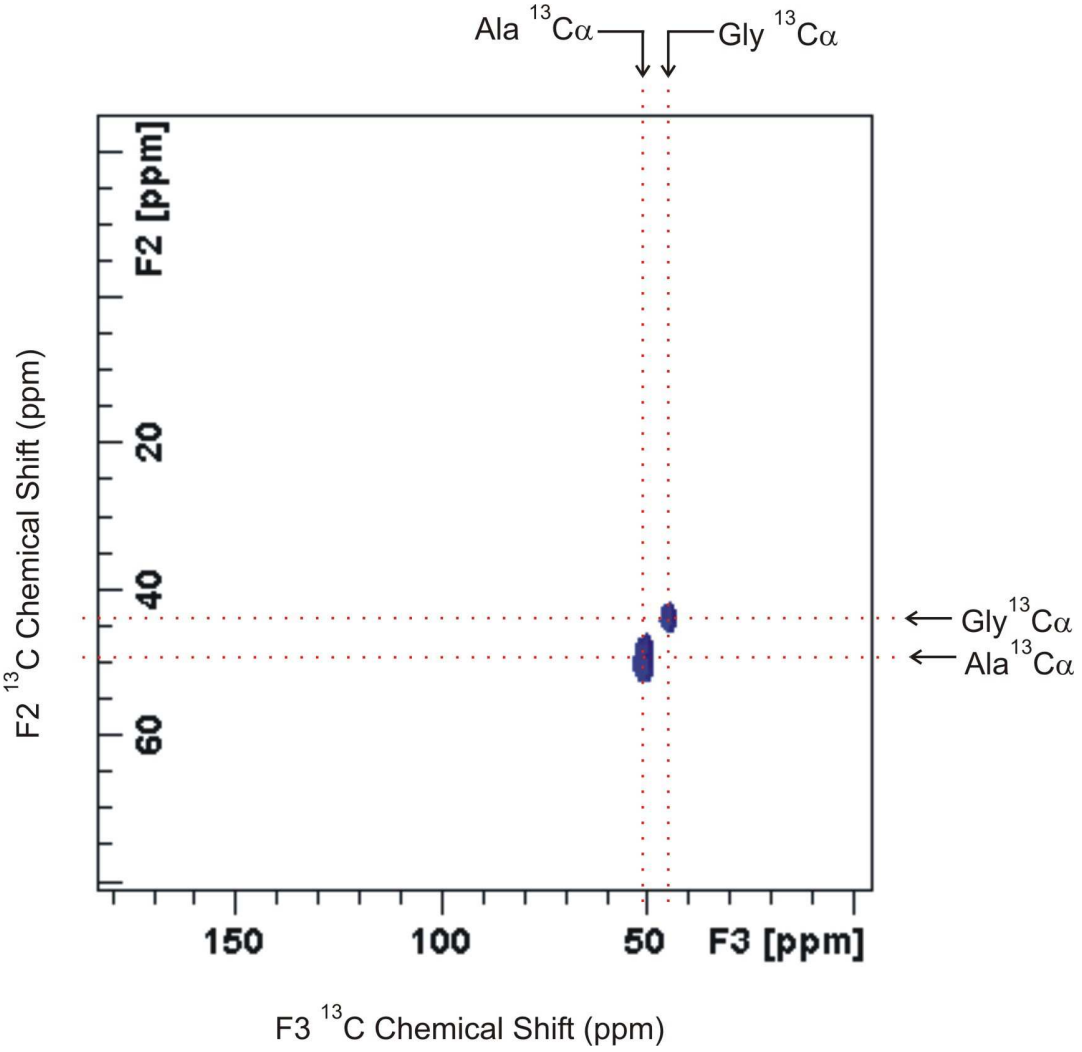

Figure AI–26: A 2D ^{13}C–^{13}C plane representative of the F2–F3 plane from the 3D experiment presented in Figure AI–24 for FP–Hairpin UA6/UG10. The blue cross peaks are shown. The red dashed lines are a visual guide to highlight the $^{13}C/^{13}C$ cross peaks. The same processing and acquisition parameters as those listed in Figure AI–24 were used in Figure AI–26. The mixing of the ^{13}C magnetization between the different spin systems is observed by the Ala $^{13}C\alpha/^{13}C\alpha$ and Gly $^{13}C\alpha/^{13}C\alpha$ cross peaks. The lack of signal is due to only 14 acquisitions per t_1 resulted in the inability to observe other $^{13}C/^{13}C$ interactions, such as the Ala $^{13}C\alpha/^{13}C\beta$ cross peak.

The 3D experiments were successful at the 21.1 T spectrometer for the U–NAL sample, however more work and understanding of the experiment and how to implement the experiment is needed in order to be able to routinely perform the 3D NCACX experiments. This is obvious from the results of the FP–Hairpin UA6/UG10 sample where there is low peak signal to noise resulting in the lack of observable ^{13}C–^{13}C cross peaks in the F2–F3 plane. Future experimentation with the 3D experiments may require different labeling schemes and longer acquisition times. Due to these limitations, it may be more beneficial to perform the 1D double cross polarization experiments and 2D ^{13}C–^{13}C or ^{15}N–^{13}C correlation experiments with the protein samples instead of the 3D experiments. The time required to collect the 1D or 2D experiments will be less than the time required to acquire a signal 3D experiment. Also, the Weliky group is knowledgeable in the acquisition and processing of the 1D and 2D data currently whereas the 3D data is a new frontier for the group. Finally, due to the limited amount of solids time at the 21.1 T spectrometer per year (~1 – 2 months), it is important to make the most of the time, which is why the 1D and 2D experiments should have priority over the 3D experiments.

Section 3: Supplemental data for 9.4 T experiments of FP–Hairpin and FP34

FP–Hairpin UA6/UG10 sensitivity tests at 9.4 T

As presented in Chapter 4, studies with the FP–Hairpin UA6/UG10 sample in POPC/POPG/Chol lipid membranes at ~15:1 lipid to protein ratio were performed at 9.4 T and 21.1 T to determine the affect of field and probe design on the increased peak signal to noise ratios of the ^{13}C resonances. Chapter 4 only focused on comparison of the optimized setup of the

^{13}C CP experiment at 9.4 T with the cooling gas temperature at –50 °C at the thermocouple located about 1" away from rotor in the probe for the 9.4 T instrument and in the flow of the cooling gas [10] to the optimized ^{13}C CP experiment at 21.1 T with the cooling gas temperature at –23 °C at the thermocouple located on the post supporting the stator and is directly in the path of the bearing and VT gas flow (Brian Andrew, Bruker Biospin Corp., personal communication). The thermocouple is therefore ~1" away from the rotor for the E–free probe used at 21.1 T and in the flow of the cooling gas. Other experiments were performed at 9.4 T where the recycle delay was changed from 2 s to 1 s, and the cooling gas temperature at the thermocouple was either –50 °C, –23 °C, or –10 °C and the spinning frequency was either 10 or 12 kHz. The sample was the ~15:1 lipid to protein sample of FP–Hairpin UA6/UG10 for all experiments. All experiments were performed within one day of starting, without unpacking the rotor. Table 4–3 lists the standard parameters for the experiments, and Table AI–8 lists the specific parameters, values, and file names for the spectra acquired which were varied for the ^{13}C peak signal to noise measurements. File locations are listed in Table AIV–28 in Appendix IV.

Table AI–8: Parameters that were varied for the ^{13}C CP ramp experiment and file names which were used in the measurement of the ^{13}C signal for the ^{13}C sensitivity measurements when comparing the 9.4 T and 21.1 T spectrometers. Files listed are for the 9.4 T data only.

Spectra / File Name	Temperature	MAS Frequency	Recycle Delay
SenTest_12a	–50 °C	12 kHz	2 s
SenTest_12b	–50 °C	12 kHz	1 s
SenTest_12c	–23 °C	12 kHz	2 s
SenTest_12d	–23 °C	12 kHz	1 s
SenTest_12e	–10 °C	12 kHz	2 s
SenTest_12f	–10 °C	12 kHz	1 s
–	–	–	–
SenTest_10a	–50 °C	10 kHz	2 s
SenTest_10b	–50 °C	10 kHz	1 s
SenTest_10c	–23 °C	10 kHz	2 s
SenTest_10d	–23 °C	10 kHz	1 s
SenTest_10e	–10 °C	10 kHz	2 s
SenTest_10f	–10 °C	10 kHz	1 s

Temperature was the nominal temperature of the N_2 cooling gas as measured at the thermocouple. The sample temperature was likely warmer due to reasons which were presented in Chapter 4. Figure AI–27 provides a comparison of the spectra with either a 1 s or 2 s pulse delay at 9.4 T for the FP–Hairpin UA6/UG10 at 15:1 lipid to protein loading sample. All spectra are scaled to the same noise level. Visual comparison of the spectra show that the 2 s pulse delay had an increase in the observed peak signal to noise ratio. Table AI–9 provides a comparison of the integrated areas for the six spectra presented in Figure AI–27 at 9.4 T.

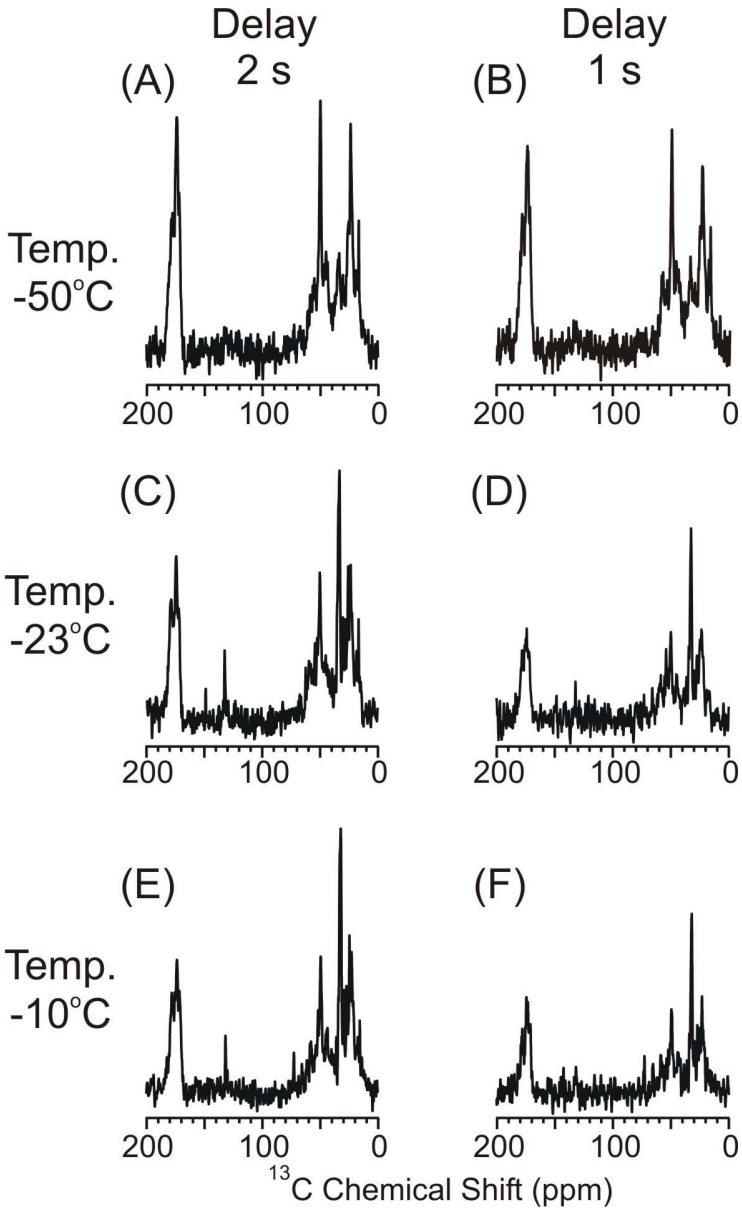

Figure AI–27: Comparison of the CP–Ramps at 9.4 T for the FP–Hairpin UA6/UG10 sample at 15:1 lipid to protein loading in a 8:2:5 molar ratio of POPC/POPG/Chol. The MAS spinning frequency was 10 kHz, and 512 acquisitions were acquired for each spectrum. The pulse delay was either 1 s (B, D, F) or 2 s (A, C, E). The nominal temperature as measured at the thermocouple was –50 °C (A, B), –23 °C (C, D) or –10 °C (E, F). All spectra are scaled to a common noise level for clear visual comparison on the affect of the pulse delay. The 2 s pulse delay spectra show higher signal to noise than for the 1 s pulse delay. All spectra were processed with 50 Hz of Gaussian line broadening. The integrated areas are presented in Table AI–9 for the six spectra.

Table AI–9: Parameters that were varied for the ^{13}C CP ramp experiment and file names which were used in the measurement of the ^{13}C signal for the ^{13}C sensitivity measurements when comparing the 9.4 T and 21.1 T spectrometers. Data presented is for the 9.4 T comparison only.

Figure AI-27	Aliphatic Region Integrated Area	Carbonyl Region Integrated Area
A: 2 s delay	95.85	42.26
B: 1 s delay	79.85	37.17
% increase 1 s → 2 s delay	**20.04 %**	**13.69 %**
C: 2 s delay	87.11	33.55
D: 1 s delay	47.23	16.94
% increase 1 s → 2 s delay	**84.44 %**	**98.05 %**
E: 2 s delay	93.41	32.99
F: 1 s delay	50.79	19.15
% increase 1 s → 2 s delay	**83.91 %**	**72.27 %**

Integrated area was determined using the Spinsight software. The integrated regions were 168 – 186 ppm for the carbonyl region and 8 – 68 ppm for the aliphatic region. The percent increase in the integrated areas of the aliphatic or the carbonyl region were calculated by taking the difference between the integrated area with the 2 s delay from the integrated area with the 1 s delay and then dividing the difference by the integrated area at 1 s. The largest increase in integrated area was observed for the spectra acquired at a nominal temperature of –23 °C for both the aliphatic and the carbonyl region. At –50 °C the increase in integrated area is only ~20% when using the 2 s pulse delay instead of a 1 s pulse delay. At the –50 °C temperature, shortening the pulse delay from 2 seconds to 1 second will be more beneficial. At the warmer temperatures the longer pulse delay can be applied or twice as many acquisitions could be obtained which will probably result in similar results as determined by the comparison of the integrated areas.

REDOR for FP–Hairpin and FP34 at 9.4 T

The rotational echo double resonance (REDOR) experiment allows for determining the distances between nuclei by measuring the dipolar interactions between two coupled spins.[11] The Weliky group has used REDOR extensively to determine distances between the ^{13}C and ^{15}N labels in the peptide backbone of the fusion peptide [5, 12-15] or ^{13}C and ^{31}P labels in the lipids [16, 17]. REDOR can also be used to obtain the filtered ^{13}C chemical shift for the nuclei as well, and this approach has been used in the FP peptides as well as in larger protein constructs that were expressed recombinantly in order to determine if the chemical shift of the ^{13}C falls within the helical, β–strand, or loop region based on the chemical shift of the RefDB database.[1, 5, 12, 13, 18-29] The REDOR pulse sequence is shown in Figure AI–28, where the "Y" channel can be either the ^{15}N, ^{19}F, or ^{31}P nuclei to name a few, depending on the heteronuclear dipolar couplings that want to be measured. The REDOR experiment depends on the dipolar coupling, Equation AI–1:

$$\hat{H}_D = -\left(\frac{\mu_o}{4\pi}\right)\frac{\gamma_I \gamma_S \hbar}{R_{IS}^3}\left(3\cos^2\theta_{IS} - 1\right)\hat{I}_z\hat{S}_z \qquad \text{(AI–1)}$$

Where $\hat{H}_D$ is the dipolar Hamiltonian which was explained in Chapter 1's section "Magic angle spinning for SSNMR" subsection "The dipolar coupling Hamiltonian" with Equation 1–25.

My initial work in the Weliky group dealt with preparing samples for solid state NMR analysis which utilized the REDOR pulse sequence. Three samples were made, two for FP34 and one for FP–Hairpin. This section is to briefly mention the samples that were made, the conditions for sample preparation, and the outcome of the sample. File locations are listed in Table AIV–29

in Appendix IV. Four samples were studied, which were (1) FP34 A14/A15, (2) FP34 I4/G5, (3) FP–Hairpin L7/F8, and (4) FP–Hairpin UA6/UG10. Labeling for the samples were $^{13}CO/^{15}N$ for samples (1–3), and uniformly labeled ^{13}C, ^{15}N at Ala–6 and Gly–10 for sample (4). Samples (1–3) were studied using the $^{1}H/^{13}C/^{15}N$ REDOR pulse sequence to determine the chemical shift of the ^{13}CO labeled residue for (1) A14, (2) I4, and (3) L7. For sample (4), the $^{1}H/^{13}C/^{31}P$ pulse sequence was used, where the ^{31}P nuclei where from the natural abundant phosphorous of the phosphate lipid head group. Two dephasing times of 2 ms and 24 ms were acquired. The ^{1}H amplifier turned off during acquisition of the 2 ms data resulting in the S_0 and S_1 data being the same, and of low peak signal to noise (~2:1). Parameters for the REDOR experiment are listed in Table AI–10 for the $^{1}H/^{13}C/^{15}N$ data and Table AI–11 for the $^{1}H/^{13}C/^{31}P$ experiments.

The phase cycling for the 9.4 T $^{1}H/^{13}C/^{15}N$ and $^{1}H/^{13}C/^{31}P$ REDOR experiments were: ^{1}H $\pi/2$ pulse was x, –x; ^{1}H CP condition was y; ^{13}C CP (x mix) was –y, –y, –x, –x; ^{13}C π pulse phase was x, y, x, y, y, x, y, x; ^{15}N π pulse was x, y, x, y, y, x, y, x; receiver phase cycling was –x, x, y, –y. The only difference between the $^{1}H/^{13}C/^{15}N$ and $^{1}H/^{13}C/^{31}P$ REDOR experiments is that the ^{15}N pulses were replaced by ^{31}P pulses. The S_0 experiment (Figure AI–28A) did not utilize the ^{15}N or ^{31}P pulses, the S_1 experiment (Figure AI–28B) had the ^{15}N or ^{31}P pulses applied.

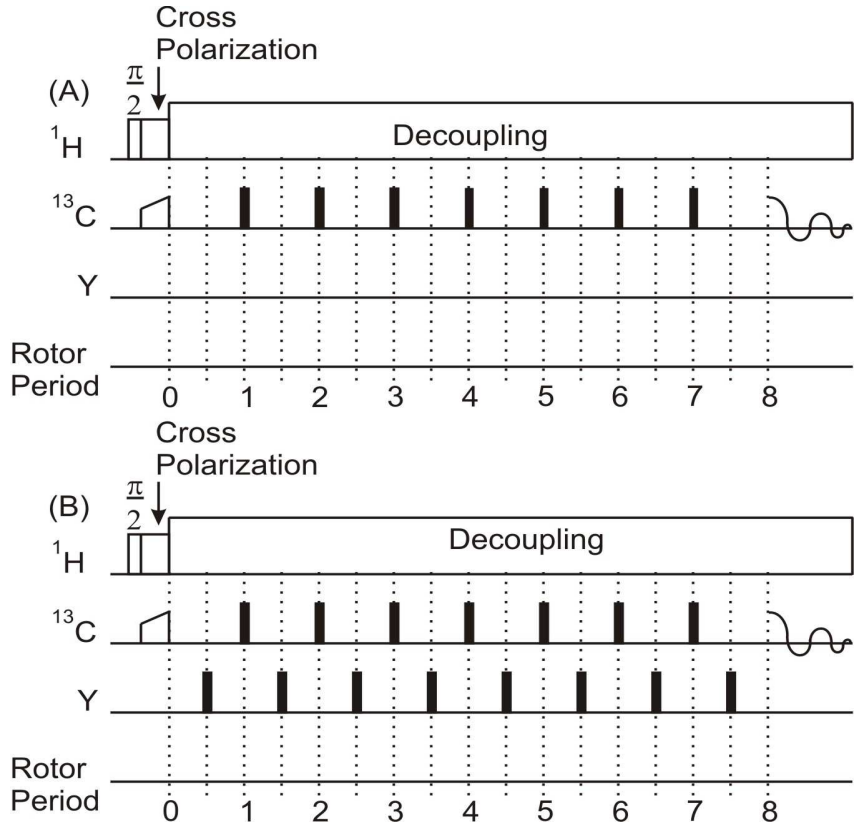

Figure AI–28: Pulse sequence for the rotational echo double resonance (REDOR) experiment for either the $^{1}H/^{13}C/^{15}N$ or the $^{1}H/^{13}C/^{31}P$, where the "Y" channel is either the ^{15}N or the ^{31}P nucleus. The $^{1}H/^{13}C/^{15}N$ REDOR experiment that was used had a 2 ms dephasing time (16 rotor periods at 8 kHz MAS) and was used for observation of directly bonded $^{13}C–^{15}N$ nuclei. The pulse sequence in (A) is the S_0 experiment where all the ^{13}C nuclei in the sample will be observed. (B) is the S_1 experiment where only the ^{13}C nuclei which will be observed are those which are directly bonded to the ^{15}N. Modification of the pulse sequence for the $^{1}H/^{13}C/^{31}P$ experiment required that the dephasing time (number of rotor periods) be varied from 2 ms to 48 ms (20 to 480 rotor periods at 10 kHz MAS) to establish the REDOR dephasing curve. An attempt to study the FP–Hairpin UA6/UG10 sample with $^{1}H/^{13}C/^{31}P$ REDOR only probed two dephasing periods, 2 ms and 24 ms. Due to spectrometer related issues and demand for spectrometer time, the project was tabled. The spectrometer issue was that the proton amplifier would randomly turn off during data acquisition. The Varian pulse sequence and the Bruker pulse sequence are similar with the following differences. (1) The Varian CP ramp is on the ^{13}C channel and the Bruker CP ramp is on the ^{1}H channel. (2) The Varian pulse sequence has been modified so that the S_0 and S_1 spectra are acquired alternating, and then during processing the two data sets are separated by running the "Jun_REDOR_sub" macro in Spinsight. The Bruker pulse sequence is not interwoven at this time (Feb. 2012), requiring instead that the user acquire blocks of S_0 and S_1 spectra separately.

Table AI–10: Parameters for the $^{1}H/^{13}C/^{15}N$ REDOR experiment for FP34 I4/G5, FP34 A14/15, and FP–Hairpin L7/F8 in lipid membrane environments at 9.4 T.

Parameter	FP34 I4/G5	FP34 A14/A15	FPH L7/F8
^{1}H π/2 (pw90H)	5.70 μs	5.70 μs	4.85 μs
Contact time (ct)	1.600 ms	1.600 ms	1.600 ms
^{1}H CP condition (aHcp)	0.4300	0.4300	0.4300
^{13}C CP Condition (ramp) (ampmin; ampmax)	0.1600 ± 0.0070	0.1600 ± 0.0070	0.1600 ± 0.0030
^{1}H decoupling frequency (aHdec) **a**	0.4000	0.4000	0.5100
MAS frequency	8 kHz	8 kHz	8 kHz
Acquisition time	5.12 ms	5.12 ms	10.24 ms
Pulse delay	1 s	1 s	0.8 s
Sweep width	50 kHz	50 kHz	50 kHz
Temperature at thermocouple	–10 °C	–10 °C	–50 °C
^{13}C π pulse	8.10 μs	8.10 μs	8.40 μs
^{15}N π pulse	17.80 μs	17.80 μs	8.50 μs
Acquisitions	78,016	81,600	101,775
Dephasing time	2 ms	2 ms	2 ms
^{13}C π pulse amp. **b**	0.1150	0.1150	0.1150
^{15}N π pulse amp. **c**	0.7500	0.7500	0.7500

a, b, c = Do not know the value in kHz as the voltage associated with the parameter was not recorded. However the ^{1}H, ^{13}C, and ^{15}N forward voltages for I4/G5 and A14/A15 were 395, 635, and 465 mV respectively. For L7/F8 the ^{1}H, ^{13}C, and ^{15}N forward voltages were 940, 450, and 408 mV. The ^{1}H decoupling for L7/F8 was ~85 kHz.

The dephasing time was equal to a constant times the rotor period. The rotor period is simply 1 over the MAS rotation frequency. For 8 kHz rotation frequency, the rotor period is 125 μs. A dephasing time of 2 ms requires 16 rotor periods. The acquisition time was determined by the product of the dwell time (dw) and acquisition length (al). For the a dwell time of 20 μs and an acquisition length of 256, the acquisition time is: 20 μs * 256 = 5.12 ms. The operating frequencies were 400.78 MHz, 100.79 MHz, and 40.62 MHz for the ^{1}H, ^{13}C, and ^{15}N nuclei respectively.

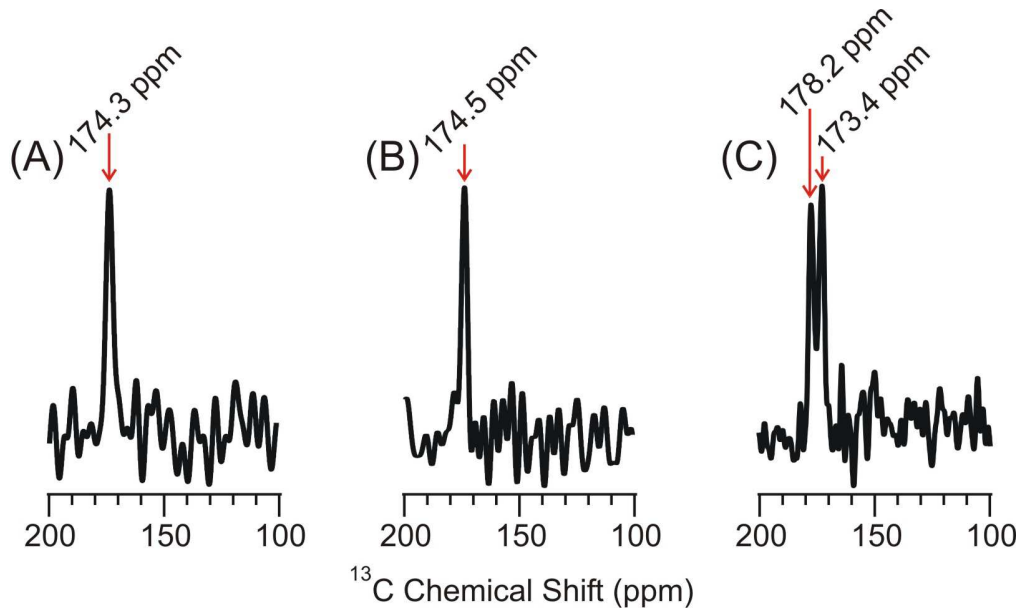

Figure AI–29: ^{1}H/^{13}C/^{15}N REDOR filtered spectra at 9.4 T for (A) FP34 I4/G5, (B) FP34 A14/15, (C) FP–Hairpin L7/F8 where the first labeled residue is the ^{13}CO and the second labeled residue is the ^{15}N amide. 100 Hz of Gaussian line broadening was applied to each spectrum. The difference signal is the result of (A) 78,016; (B) 81,600; and (C) 101,217 S_0 and S_1 acquisitions. The peak chemical shifts for (A) 174.3 ppm, (B) 174.5 ppm, (C) 173.4 ppm all correspond to the β–strand chemical shift. The 178.2 ppm chemical shift of (C) corresponds to the helical chemical shift.

Assignments for conformations were based off of known values for the ^{13}C chemical shift distributions of helical and β–strand conformations.[1] The helical (H) and β–strand (β) peak chemical shift ± standard deviation for the Ile ^{13}CO are H: 177.7 ± 1.3 ppm and β: 174.9 ± 1.4 ppm; Ala ^{13}CO are H: 179.4 ± 1.3 ppm and β: 176.1 ± 1.5 ppm; and Leu ^{13}CO are H: 178.3 ± 1.3 ppm and β: 175.7 ± 1.5 ppm. The chemical shifts for the FP34 peptide's of Figure AI–29 (A, B) correspond well with the β–strand chemical shift. Figure AI–29C has a distribution of both the β–strand and the helical conformation. Deconvolution of the two peaks resulted in ~46.1 % β–strand and ~53. 9 % helical for the Leu–7 ^{13}CO.

Table AI–11: Parameters for the $^{1}H/^{13}C/^{31}P$ REDOR experiment for FP–Hairpin UA6/UG10 in a lipid membrane environment at 9.4 T.

Parameter	**FP–Hairpin UA6/UG10** [a]
^{1}H π/2 (pw90H)	5.00 μs
Contact time (ct)	2.600 ms
^{1}H CP condition (aHcp)	0.3200
^{13}C CP Condition (ramp) (ampmin; ampmax)	0.3600 ± 0.01800
^{1}H decoupling frequency (aHdec) [b]	0.4500
MAS frequency	10 kHz
Acquisition length (time)	10.24 ms
Pulse delay	1 s
Sweep width	50 kHz
Temperature at thermocouple	–50 °C
^{13}C π pulse	10.00 μs
^{31}P π pulse	10.00 μs
Acquisitions	2 ms: 63,052 24 ms: 100,000
^{13}C π pulse amp. [c]	0.4700
^{31}P π pulse amp. [d]	0.4000

a = dephasing time of either 2 ms (L0 = 20) with 63,052 acquisitions, or dephasing time of 24 ms (L0=240) with 100,000 acquisitions.

b, c, d = Do not know the value in kHz as the voltage associated with the parameter was not recorded. However the ^{1}H, ^{13}C, and ^{31}P forward voltages were not recorded, but were based off of experiments performed in Feb. 2009.

The dephasing time was equal to a constant times the rotor period. For 10 kHz rotation frequency, the rotor period is 100 μs. A dephasing time of 2 ms requires 20 rotor periods and a dephasing time of 24 ms requires 240 rotor periods. The operating frequencies were 398.70 MHz, 100.27 MHz, and 161.39 MHz for the ^{1}H, ^{13}C, and ^{31}P nuclei respectively.

Section 4: Scott Schmick's HFP V2E peptide sample studied by SSNMR at 21.1 T

Solid state NMR data at the 900 MHz spectrometer was acquired for a sample provided by Scott Schmick (SDS) which are listed in Tables AIV–19 and AIV–21 of Appendix IV. The sample was the FP peptide containing the V2E mutant with isotopic labeling at F8 ^{13}CO (F8C) and G13 ^{15}N (G13N) in ether linked lipids. The experiments performed were $^{1}H/^{13}C/^{15}N$ REDOR, ^{13}C CP, and ^{15}N CP experiments. Scott produced the produced the sample and I performed the SSNMR experiments at 21.1 T and subsequent data analysis for this sample.

Experimental conditions

The SSNMR experimental conditions for this sample were 12 kHz rotation frequency, cooling gas temperature of 250 K as measured at the thermocouple, and a 4 mm MAS rotor. ^{13}C ramps were used to reference the spectra. ^{13}C ramp spectra confirmed the ^{13}C carbonyl label and the ^{15}N spectra confirmed the ^{15}N amide label. Dephasing times and total number of acquisitions summed together are presented in Table AI–14 below. The REDOR pulse sequence is displayed in Figure AI–14, with the main difference between the one presented (modified for Varian spectrometer) and the Bruker pulse sequence being that the CP ramp is on the ^{13}C

channel for the Bruker software. The phase cycling for the Bruker pulse sequence was the following: ^{1}H π/2 pulse was x, x, –x, –x; ^{1}H CP condition was x; ^{13}C CP was x, y, x, y; ^{13}C π pulse phase was x, y, x, y, y, x, y, x; ^{15}N π pulse was x, y, x, y, y, x, y, x; the last ^{13}C refocusing pulse phase was x, y, x, y; and the receiver phase cycling was x, y, –x, –y.

Table AI–12: Scott Schmick's ^{13}C and ^{15}N CP ramp parameters for experiments at 21.1 T for HFP V2E peptide labeled at F8C and G13N.

Parameter [a]	**^{13}C CP Ramp**	**^{15}N CP Ramp**
π/2 pulse ^{1}H	3.00 μs	4.66 μs
π/2 power level ^{1}H	–2.2 dB (83.3 kHz)	2 dB (53.6 kHz)
^{1}H CP condition	–1.3 dB (75.1 kHz)	–0.8 dB (74.0 kHz)
X CP condition	–0.4 dB (67.7 kHz)	0.40 dB (64.5 kHz)
^{1}H decoupling	–2.2 dB (83.3 kHz)	2.0 dB (53.6 kHz)
^{1}H→X CP time	2 ms	2.2 ms
Acquisition time	15.05 ms	12.8 ms
Temperature	250 K	250 K
MAS frequency	12 kHz	12 kHz
Recycle delay	2 s	3 s
X offset location	100 ppm	110 ppm
^{1}H transmitter offset	2 ppm	6 ppm
Dwell time	7.35 μs	12.5 μs
ns	256	256

[a] = X refers to either the ^{13}C or the ^{15}N nuclei depending on the experiment performed. (^{13}C CP ramp, X = ^{13}C)

Table AI–13: Scott Schmick's $^{1}H/^{13}C/^{15}N$ REDOR parameters for experiments at 21.1 T for HFP V2E peptide labeled at F8C and G13N.

Parameter	FP V2E [a]
^{1}H π/2 (pw90H)	2.9 μs
π/2 power level ^{1}H	–2.6 dB (86.2 kHz)
Contact time (P15)	2.0 ms
^{1}H CP condition	–1.2 dB (73.3 kHz)
^{13}C CP Condition	0.0 dB (57 kHz)
^{1}H decoupling frequency	–2.6 dB (86.2 kHz)
MAS frequency	12 kHz
Acquisition length (time)	15.05 ms
Pulse delay	3 s
Sweep width	68 kHz
Temperature at thermocouple	250 K
^{13}C π pulse	8.00 μs
^{15}N π pulse	11.00 μs
Dwell time (dw)	7.350 μs
^{13}C π pulse PL	–0.80 dB (62.5 kHz)
^{15}N π pulse PL	On: 0.0 dB (45.5 kHz) Off: 120 dB

[a] = Number of rotor periods in the dephasing time is listed in Table AI–13 with the specific dephasing times. The listed parameters were used for all the REDOR experiments, only changing the L0 loop to change the dephasing time.

Table AI–14: Scott Schmick's REDOR data at 21.1 T for HFP V2E peptide labeled at F8C and G13N.

Dephasing Time (ms) {L0 value} [a]	**S_0 acquisitions**	**S_1 acquisitions**	**Total acquisitions**
2.0 ms {3}	2048	2048	2096
8.7 ms {13}	4096	4096	8192
16.6 ms {25}	10240	10240	20480
24.7 ms {37}	10240	10240	20480
32.7 ms {49}	12288	12288	24576
40.7 ms {61}	28672	28672	57344
48.7 ms {73}	28672	28672	57344

a = The dephasing time is determined by the product of the rotor period, the L0 value, and the phase cycling value of 8. Taking L0*8*(1/MAS frequency) will equal the dephasing time presented in this column.

Figure AI-30 presents the S_0 and S_1 spectra for Scott Schmick's HFP sample with dephasing time of either 8.7 ms (Figure AI-30A, B) or 40.7 ms (Figure AI-30C, D). The spectra were processed with 100 Hz of Gaussian line broadening. Table AIV-30 lists the file locations for the data in Figure AI-30. Table AIV-19 in Appendix IV contains all the data for Scott Schmick's samples.

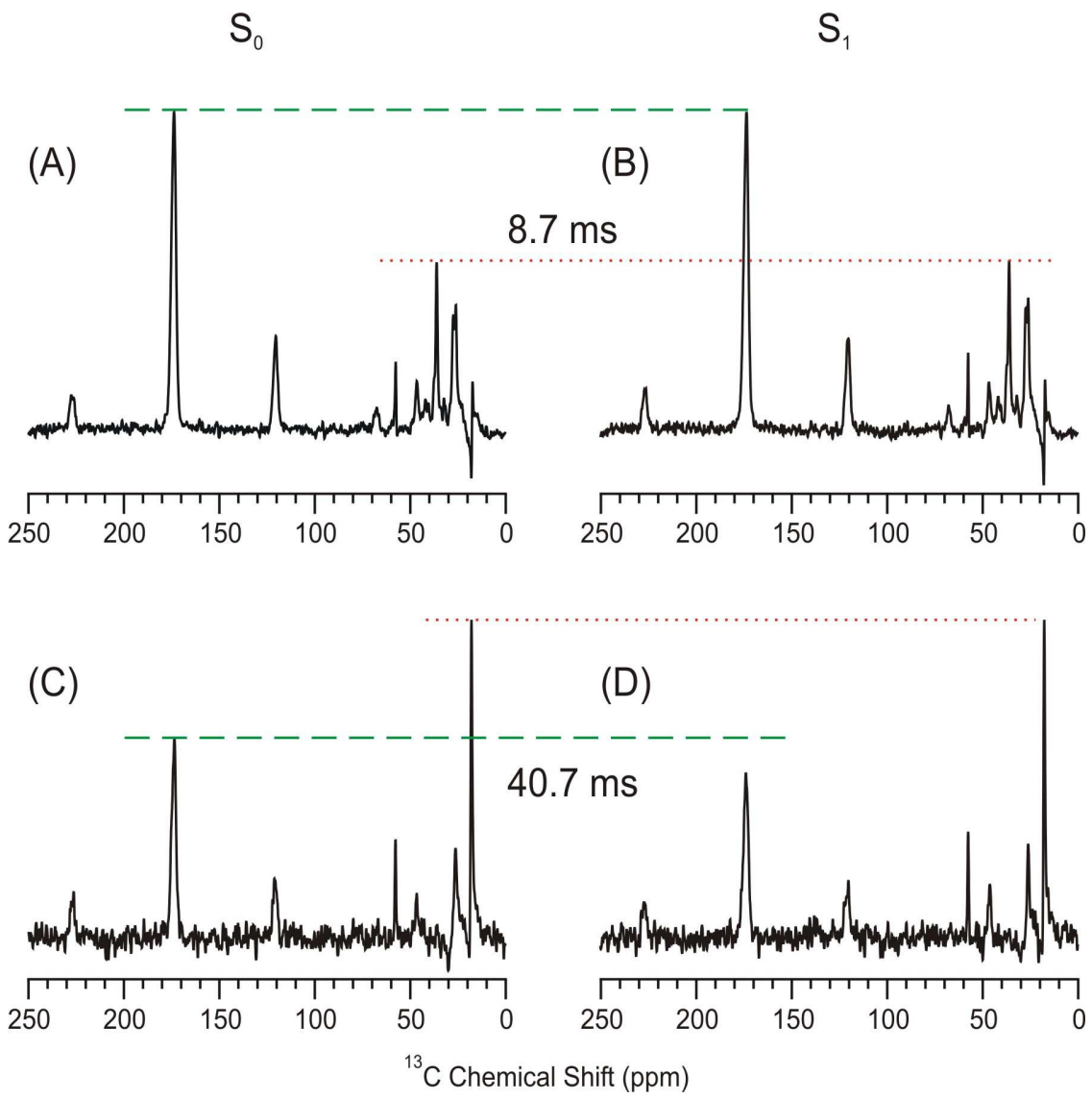

Figure AI-30: REDOR spectra at 21.1 T for Scott Schmick's HFP V2E sample with the ^{13}CO isotopic label at F8 and the ^{15}N isotopic label at G13. (A) S_0 spectra (no ^{15}N pulses applied) with a dephasing time of 8.7 ms, and 4096 acquisitions. (B) S_1 spectra (^{15}N pulse applied) and 4096 acquisitions. (C) S_0 spectra (no ^{15}N pulses applied) with a dephasing time of 40.7 ms, and summation of 28672 acquisitions. (D) S_1 spectra (^{15}N pulse applied) and 28672 acquisitions. All spectra had 100 Hz of Gaussian line broadening applied during processing. The red dotted line is for visual comparison of the aliphatic region, and the green dashed line is for visual comparison of the carbonyl region. The spectra in A and B are scaled to the same noise level. The spectra in C and D are scaled to the same noise level.

Results and conclusions

There is no significant advantage of using the 21.1 T spectrometer for the REDOR experiment with the isotopically labeled peptide samples. The full width at half maximum (FWHM) linewidths for similar samples at 9.4 T reported by Schmick were 3 – 4 ppm, which correspond to 300 – 400 Hz for the carbonyl peak.[15] For the spectra presented in Figure AI-30, the FWHM linewidths were ~3 ppm, which is ~675 Hz for the carbonyl peak. At 21.1 T, the linewidths are nearly twice as broad as those obtained at 9.4 T for the carbonyl peak. The main issue with REDOR at the 21.1 T spectrometer is that the S_0 and S_1 data is not interwoven, requiring the setup of blocks of S_0 or S_1 acquisitions. This could be problematic due to the drift of the spectrometer not being constant or trivial. One way around the problem is to setup multiple S_0 and S_1 programs and enter them into a queue. Also, one could write the program so that the S_0 and S_1 acquisitions are combined like the Varian (now Agilent) pulse sequence. Currently the system is setup and optimized on the 9.4 T spectrometer, and more work needs to be done at the 21.1 T spectrometer to make the system fully operational and run smoothly like at the 9.4 T spectrometer. In my opinion, use of the high field instrumentation would be better utilized for the larger protein constructs which do not have the ability to achieve high peak signal to noise like the peptide samples can at 9.4 T.

Section 5: Erica Vogel's whole cell samples studied by SSNMR at 21.1 T

SSNMR data at the 900 MHz was acquired for samples provided by Erica Vogel (EPV) and are listed in Tables AIV–20 and AIV–24 of Appendix IV. Her samples were the fully hydrated whole cell samples corresponding to doubly labeled LL Fgp41, and experiments

performed were the 1D ^{13}C CP, 1D ^{15}N CP, 1D $^{1}H/^{13}C/^{15}N$ REDOR, and the 1D NCO double cross polarization experiments. Figure AI–14 shows the REDOR pulse sequence, and the phase cycling for the Bruker REDOR pulse sequence was discussed in above in "Section 4: Scott Schmick's HPF V2E peptide sample studied by SSNMR at 21.1 T" subsection "Experimental conditions". The parameters for the 1D ^{13}C or 1D ^{15}N CP Ramp are listed in Table AI–15. The parameters for the $^{1}H/^{13}C/^{15}N$ REDOR are listed in Table AI–16. The REDOR dephasing period was set to 2 ms by using a L0 value of 3, as discussed below Table AI–16. The ^{13}C or ^{15}N CP ramp spectra and the REDOR spectra were acquired at nominal temperatures of either 270 K or 250 K, with the 250 K data having more observable signal, especially for the ^{15}N signal.

Table AI–15: Erica Vogel's ^{13}C and ^{15}N CP ramp parameters for experiments at 21.1 T for the fully hydrated whole cell samples corresponding to doubly labeled LL Fgp41 samples.

Parameter [a]	**^{13}C CP Ramp**	**^{15}N CP Ramp**
$\pi/2$ pulse ^{1}H	3.00 μs	4.66 μs
$\pi/2$ power level ^{1}H	–2.2 dB (83.3 kHz)	2 dB (53.6 kHz)
^{1}H CP condition	–1.3 dB (75.1 kHz)	–0.8 dB (74.0 kHz)
X CP condition	–0.4 dB (67.7 kHz)	0.40 dB (64.5 kHz)
^{1}H decoupling	–2.2 dB (83.3 kHz)	2.0 dB (53.6 kHz)
$^{1}H \rightarrow X$ CP time	2 ms	2.2 ms
Acquisition time	15.05 ms	12.8 ms
Temperature	250 K or 270 K	250 K or 270 K
MAS frequency	12 kHz	12 kHz
Recycle delay	2 s	3 s
X offset location	100 ppm	110 ppm
^{1}H transmitter offset	2 ppm	6 ppm
Dwell time	7.35 μs	12.5 μs
ns	256	256

a = X refers to either the ^{13}C or the ^{15}N nuclei depending on the experiment performed. (^{13}C CP ramp, X = ^{13}C)

Table AI–16: Erica Vogel's $^{1}H/^{13}C/^{15}N$ REDOR parameters for experiments at 21.1 T for the fully hydrated whole cell samples corresponding to doubly labeled LL Fgp41 samples.

Parameter	LL Fgp41 Samples
^{1}H π/2 (pw90H)	2.9 μs
π/2 power level ^{1}H	–2.6 dB (86.2 kHz)
Contact time (P15)	2.0 ms
^{1}H CP condition	–1.2 dB (73.3 kHz)
^{13}C CP Condition	0.0 dB (57.0 kHz)
^{1}H decoupling frequency	–2.6 dB (86.2 kHz)
MAS frequency	12 kHz
Acquisition length (time)	15.05 ms
Pulse delay	3 s
Sweep width	68 kHz
Temperature at thermocouple	250 K
^{13}C π pulse	8.00 μs
^{15}N π pulse	11.00 μs
Dwell time (dw)	7.350 μs
^{13}C π pulse PL	–0.80 dB (62.5 kHz)
^{15}N π pulse PL	On: 0.0 dB (45.5 kHz) Off: 120 dB
L0 parameter **a**	3

a = Number of rotor periods in the dephasing time which was the product of L0*(rotor period)*8. The 8 was for the phase cycling and is written in the pulse sequence.

Erica Vogel's double cross polarization parameters for experiments at 21.1 T for the fully hydrated whole cell samples corresponding to doubly labeled LL Fgp41 samples are the same as

the 1D double cross polarization NCO parameters listed in Table 2–6 of Chapter 2. The two differences are the $^{1}H \rightarrow ^{15}N$ contact time of 2 ms and the $^{15}N \rightarrow ^{13}C$ contact time of 5 ms instead of the 4.2 ms and 4.7 ms contact times listed in the table. No observable signal was seen for her samples, even though the pulse program had been optimized using the U–NAL setup compound, and ^{13}CO signal had been observed from the U–NAL setup compound. This result was the same as the FP–Hairpin sample discussed in Chapter 4 which also showed no signal for the NCO double cross polarization experiment.

Results and conclusions

The ^{15}N signal was stronger at T = 250 K vs. T = 270 K. This is important because it resulted in the REDOR experiment preforming better at the T = 250 K, likely as there is less motional averaging which could result in the loss of ^{15}N magnetization, and also more efficient cross polarization from $^{1}H \rightarrow ^{15}N$ at the lower temperatures. The double cross polarization NCO experiment did not work for the LL Fgp41 sample. The DCP experiment was first setup and optimized using the U–NAL sample as discussed in Chapter 4. However, as was also discussed in Chapter 4, the DCP experiment did not work for a FP–Hairpin sample with the NCO labeling, just as it did not work for this sample either. Finally, these samples were fully hydrated, meaning that once they were grown in the LB media, they were spun down and packed into the rotor. After performing the SSNMR experiments, the samples were still fluid like, and not a dried out powder. This suggests that the E–free probe is able to handle the biological samples and not dehydrate them like what is observed for the non E–free probes. In the future, to confirm the retention of the sample's hydration, the sample should be weighted before and after running on

the spectrometer. Do to the fluid like consistency of these samples, extra care should be taken when packing the rotor and spinning the rotor up to speed. When packing the rotor, make sure to place the top spacer in before sealing the rotor with the drive tip. The fluid like consistency has the possibility to lubricate the drive tip and cause it to loosen or come off completely in the stator. When spinning up the sample, it is best to go up slowly from 5 kHz to the targeted speed by 1 – 2 kHz at a time. Also allow some equilibration time at the desired temperature and 5 kHz spinning frequency before jumping right up to the desired spinning frequency (such as 12 kHz).

Section 6: Dr. Ronny Priefer's insoluble polymers requiring SSNMR analysis

A collaboration with Dr. Ronny Priefer from Niagara University (Lewiston, NY) resulted in performing SSNMR analysis of insoluble polymer samples. These polymers are not homopolymers, as they were synthesized from a mixture of starting amine and amides, with the exact ratio determined from elemental analysis.[30]

Sample preparation for SSNMR analysis

The samples were first ground up using a mortar and pedestal to a uniform consistency, usually 5 – 10 minutes of grinding. The ground up sample (~35 mg) was then scrapped onto a clean piece of weight paper and funneled into a 4 mm MAS pencil rotor, where it was confined to the central 2/3 of the rotor.[12] The sample was compressed into the rotor volume using a packing tool, and then a top spacer was inserted into the rotor. Samples were stored at room temperature, packed at room temperature, and analyzed at room temperature unless otherwise noted. Recovery of the sample was done by removing the drive tip and bottom spacer from the rotor and pushing the sample out. In some cases a small 3 mm drill bit was used to dig out the

samples. The rotors were washed with water, ethanol, water, and then dried with a Kimwipe between sample packing.

The samples only contained natural abundance ^{13}C. A ^{13}C CP ramp experiment was performed to observe all the ^{13}C signals in the sample. Figures AI–31 and AI–32 are the polymers which were sent to me for analysis. Table AIV–26 in Appendix IV lists the file locations for all the samples and any parameters which differed from the general parameters listed below. Samples were prepared by Paolo Grenga, in the lab of Dr. Ronny Priefer at Niagara University.[30]

Solid state NMR parameters

Solid state NMR spectra were collected on a 9.4 T spectrometer (Varian Infinity Plus, now Agilent, Palo Alto, CA), using a 4 mm MAS probe in triple resonance probe tuned to ^{13}C and ^{1}H nuclei at 100.8 MHz and 400.8 MHz respectively. Spectra were externally referenced to the methylene resonance of adamantane at 40.5 ppm,[31] and the ^{13}C transmitter was placed at 100 ppm. Sample rotation was 12000 ± 2 Hz, and spectral data were collected at room temperature (~20 °C) and with cooling of the VT gas to –50 °C. Uniformly ^{13}C, ^{15}N labeled N–acetyl leucine was used as a model compound to optimize the parameters for the ^{13}C CP ramp. The parameters included a 5 μs ^{1}H $\pi/2$ pulse (50 kHz Rabi frequency), a 1.6 ms CP contact time, a 49 – 69 kHz ramped ^{13}C CP, a 2 s recycle delay, 10 ms acquisition time, 2048 scans, and ^{1}H decoupling of 77 kHz. 100 or 200 Hz Gaussian line broadening was applied during

processing. Some samples required more signal averaging time and that is listed in Table AIV–26. Chemical structures corresponding to the SSNMR data are listed in Figures AI–31 and AI–32.

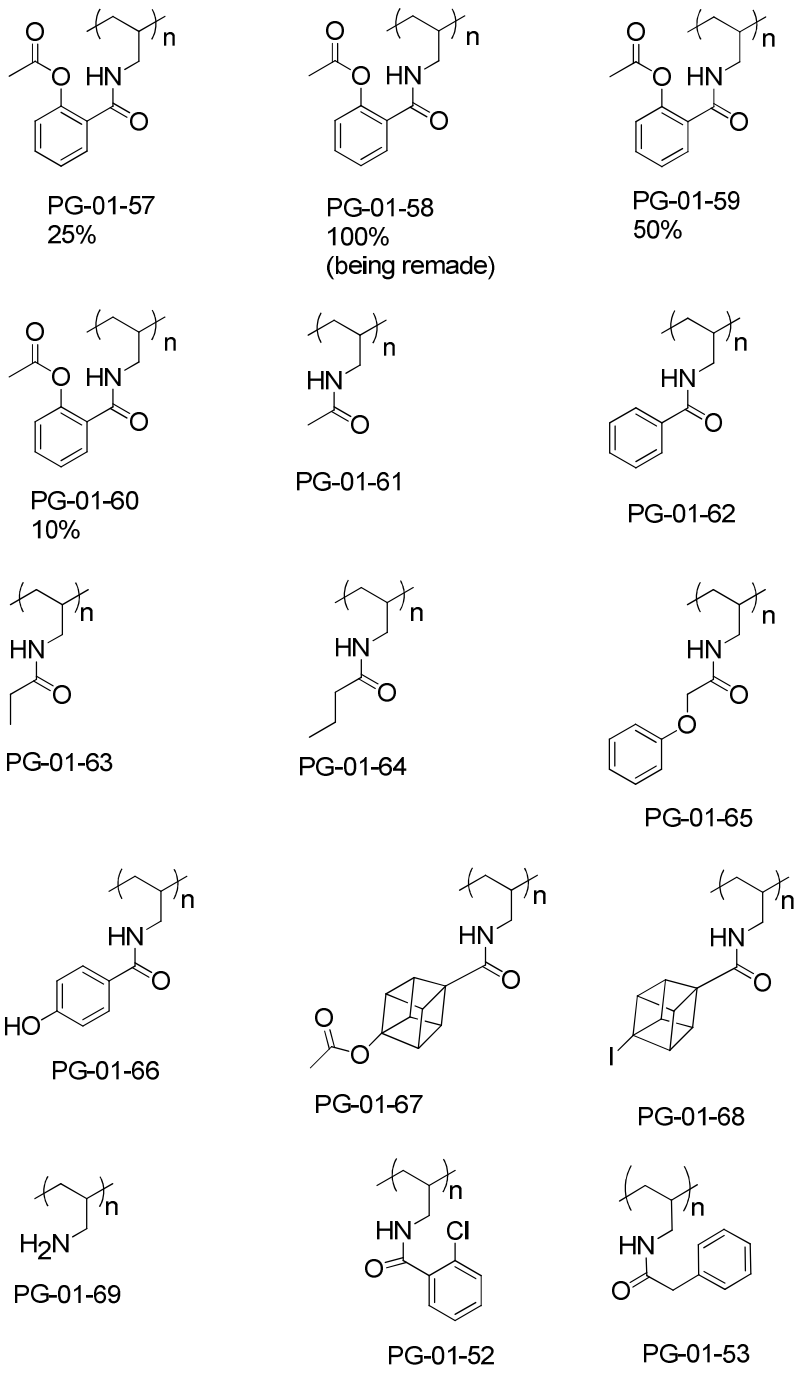

Figure AI–31: Compounds characterized in shipment 1 and 2 which were synthesized by Paolo Grenga.[30] Samples were packed in a 4 mm MAS rotor and a ^{13}C CP Ramp experiment was used to analyze the samples at 9.4 T.

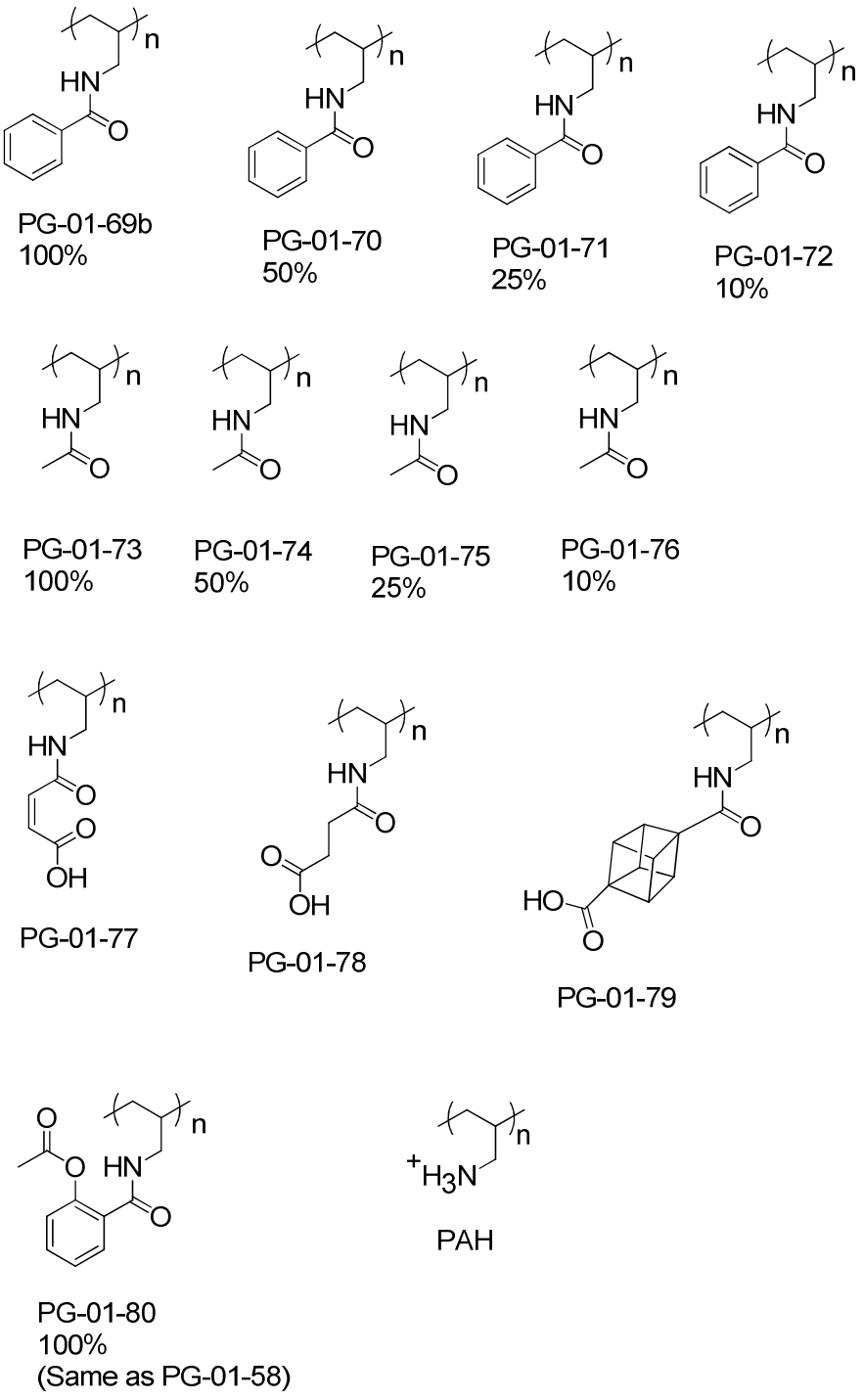

Figure AI–32: Compounds characterized in shipment 3 which were synthesized by Paolo Grenga.[30] Samples were packed in a 4 mm MAS rotor and a ^{13}C CP Ramp experiment was used to analyze the samples at 9.4 T.

Data Processing

Once the 1D ^{13}C spectra were acquired, they were processed in the following manor. First, each spectrum was processed using 100 Hz or 200 Hz of Gaussian line broadening, 5th order polynomial baseline correction and Fourier transformed. After Fourier transforming the spectrum, it was phased and the new values applied. Each spectrum was referenced to the methylene peak of adamantane at 40.5 ppm.

The important data for these samples was to determine the relative populations of the carbons from the 1D ^{13}C CP ramp by deconvolution the 1D ^{13}C spectra. The deconvolution was performed using the deconvolution panel in Spinsight. First, auto peak picking was used to obtained the peaks in the processed spectrum. Next, the processed spectrum was selected and then the "Deconv Panel" was selected. There, the option to "use peak list" was selected which generated a number of Gaussian curves equal to the number of peaks. By interactively fitting each peak to the whole spectrum, some peaks could be eliminated and a good overall fit could be obtained. The goodness of fit was determined by visually comparing the original data to the spectrum that resulted from the individual deconvoluted curves. Comparison of the amplitude percentage of the curves corresponding to the different carbons will result in determining the composition of the system. The processed and deconvoluted data were saved separately in Spinsight, and are listed in Table AIV–26 as well.

REFERENCES

References

1. Zhang, H.Y., S. Neal, and D.S. Wishart, *RefDB: A database of uniformly referenced protein chemical shifts.* Journal of Biomolecular Nmr, 2003. **25**(3): p. 173-195.

2. Weliky, D.P. *Chemistry 988 Lecture Notes*. [website containing pdf file of notes] May 3, 1999 [cited 2011 19 December 2011]; Available from: http://www2.chemistry.msu.edu/courses/CEM988NMR/cem988nmr.htm.

3. Pochapsky, T.C. and S.S. Pochapsky, *NMR for Physical and Biological Scientists*. 2007, New York: Taylor & Francis Group. 372.

4. Wickramasinghe, N.P., et al., *Sensitivity enhancement in 13C solid-state NMR of protein microcrystals by use of paramagnetic metal ions for optimizing 1H T1 relaxation.* Journal of Magnetic Resonance, 2007. **184**(2): p. 350-356.

5. Qiang, W., M.L. Bodner, and D.P. Weliky, *Solid-state NMR spectroscopy of human immunodeficiency virus fusion peptides associated with host-cell-like membranes: 2D correlation spectra and distance measurements support a fully extended conformation and models for specific antiparallel strand registries.* J Am Chem Soc, 2008. **130**(16): p. 5459-71.

6. Castellani, F., et al., *Structure of a protein determined by solid-state magic-angle-spinning NMR spectroscopy.* Nature, 2002. **420**(6911): p. 98-102.

7. Bodner, M.L., *Solid state nuclear magnetic resonance of the HIV-1 and influenza fusion peptides associated wtih membranes*. 2006, Michigan State University: East Lansing, MI.

8. Bodner, M.L., et al., *13C-13C and (15)N-(13)C correlation spectroscopy of membrane-associated and uniformly labeled human immunodeficiency virus and influenza fusion peptides: amino acid-type assignments and evidence for multiple conformations.* J Chem Phys, 2008. **128**(5): p. 052319.

9. *Bruker Data Processing*. [webpage] 2012 5 Jan. 2010 [cited 2012 7 Feb 2012]; website with useful nmr processing information for the bruker software]. Available from: http://www.nmr2.buffalo.edu/nesg.wiki/Bruker_Data_Processing.

10. Bodner, M.L., *Temperature dependence, structural plasticity, and resonance assignment of uniformly labeled HIV-1 fusion peptides associated with membranes*. 2003, Michigan State University. Dept. of Chemistry 2003. p. xi, 55 leaves.

11. Gullion, T., *Introduction to rotational-echo, double-resonance NMR.* Concepts in Magnetic Resonance, 1998. **10**(5): p. 277-289.

12. Yang, J. and D.P. Weliky, *Solid-state nuclear magnetic resonance evidence for parallel and antiparallel strand arrangements in the membrane-associated HIV-1 fusion peptide.* Biochemistry, 2003. **42**(40): p. 11879-90.

13. Balbach, J.J., et al., *Probing hydrogen bonds in the antibody-bound HIV-1 gp120 V3 loop by solid state NMR REDOR measurements.* J Biomol NMR, 2000. **16**(4): p. 313-27.

14. Zheng, Z., et al., *Conformational flexibility and strand arrangements of the membrane-associated HIV fusion peptide trimer probed by solid-state NMR spectroscopy.* Biochemistry, 2006. **45**(43): p. 12960-75.

15. Schmick, S.D. and D.P. Weliky, *Major Antiparallel and Minor Parallel beta Sheet Populations Detected in the Membrane-Associated Human Immunodeficiency Virus Fusion Peptide.* Biochemistry, 2010. **49**(50): p. 10623-10635.

16. Qiang, W. and D.P. Weliky, *HIV fusion peptide and its cross-linked oligomers: efficient syntheses, significance of the trimer in fusion activity, correlation of beta strand conformation with membrane cholesterol, and proximity to lipid headgroups.* Biochemistry, 2009. **48**(2): p. 289-301.

17. Qiang, W., Y. Sun, and D.P. Weliky, *A strong correlation between fusogenicity and membrane insertion depth of the HIV fusion peptide.* Proc Natl Acad Sci U S A, 2009. **106**(36): p. 15314-9.

18. Vogel, E.P., et al., *Solid-State Nuclear Magnetic Resonance (NMR) Spectroscopy of Human Immunodeficiency Virus gp41 Protein That Includes the Fusion Peptide: NMR Detection of Recombinant Fgp41 in Inclusion Bodies in Whole Bacterial Cells and Structural Characterization of Purified and Membrane-Associated Fgp41.* Biochemistry, 2011. **50**(46): p. 10013-10026.

19. Yang, J., et al., *Application of REDOR subtraction for filtered MAS observation of labeled backbone carbons of membrane-bound fusion peptides.* J Magn Reson, 2002. **159**(2): p. 101-10.

20. Yang, R., J. Yang, and D.P. Weliky, *Synthesis, enhanced fusogenicity, and solid state NMR measurements of cross-linked HIV-1 fusion peptides.* Biochemistry, 2003. **42**(12): p. 3527-35.

21. Bodner, M.L., et al., *Temperature dependence and resonance assignment of C-13 NMR spectra of selectively and uniformly labeled fusion peptides associated with membranes.* Magnetic Resonance in Chemistry, 2004. **42**(2): p. 187-194.

22. Yang, J., et al., *Oligomeric beta-structure of the membrane-bound HIV-1 fusion peptide formed from soluble monomers.* Biophys J, 2004. **87**(3): p. 1951-63.

23. Yang, R., et al., *A trimeric HIV-1 fusion peptide construct which does not self-associate in aqueous solution end which Has 15-fold higher membrane fusion rate.* Journal of the American Chemical Society, 2004. **126**(45): p. 14722-14723.

24. Wasniewski, C.M., et al., *Solid-state nuclear magnetic resonance studies of HIV and influenza fusion peptide orientations in membrane bilayers using stacked glass plate samples.* Chem Phys Lipids, 2004. **132**(1): p. 89-100.

25. Curtis-Fisk, J., et al., *Solid-state NMR structural measurements on the membrane-associated influenza fusion protein ectodomain.* J Am Chem Soc, 2007. **129**(37): p. 11320-1.

26. Curtis-Fisk, J., R.M. Spencer, and D.P. Weliky, *Isotopically labeled expression in E-coli, purification, and refolding of the full ectodomain of the influenza virus membrane fusion protein.* Protein Expression and Purification, 2008. **61**(2): p. 212-219.

27. Curtis-Fisk, J., R.M. Spencer, and D.P. Weliky, *Native conformation at specific residues in recombinant inclusion body protein in whole cells determined with solid-state NMR spectroscopy.* J Am Chem Soc, 2008. **130**(38): p. 12568-9.

28. Gabrys, C.M., et al., *Nuclear magnetic resonance evidence for retention of a lamellar membrane phase with curvature in the presence of large quantities of the HIV fusion peptide.* Biochimica Et Biophysica Acta-Biomembranes, 2010. **1798**(2): p. 194-201.

29. Sackett, K., et al., *Comparative analysis of membrane-associated fusion peptide secondary structure and lipid mixing function of HIV gp41 constructs that model the early pre-hairpin intermediate and final hairpin conformations.* J Mol Biol, 2010. **397**(1): p. 301-15.

30. Grenga, P., *Work Toward the Synthesis and Characterization of Novel Amide Tethered Cubyl Polymers*. 2011, Niagara University: Niagara University, NY.

31. Morcombe, C.R. and K.W. Zilm, *Chemical shift referencing in MAS solid state NMR.* Journal of Magnetic Resonance, 2003. **162**(2): p. 479-486.

Appendix II:

Collaborations for DNP and Crystallography

Dynamic Nuclear Polarization Collaboration with Bruker BioSpin

Sample Preparation

Sample preparation was the same as described in Chapter 2, following Method A for the lipid preparation where the POPC/POPG/Chol lipids (8:2:5 mole ratio) were hydrated with 2 mL of 25 mM HEPES Buffer, pH 7.6 for 15 minutes. 8.1 mg (0.63 µmoles) FP–Hairpin UA6/UG10 at a concentration of 117 µM were added 0.5 mL at a time through a narrow 22 gauge needle to the 200 nm lipid vesicles. The pH was maintained no lower than 7.0 and continuously stirred at room temperature until all FP–Hairpin was added and then allowed to stir at room temperature for 30 minutes before placement at 4 °C overnight. The lipid to protein ratio was ~25:1. The sample was pelleted at 4,000g for 3–5 minutes, decanted, and lyophilized.

The lyophilized sample was then rehydrated with the dynamic nuclear polarization (DNP) solution containing 20 mM 1–(TEMPO–4–oxy)–3–(TEMPO–4–amino)propan–2–ol (TOTAPOL, MW = 399.58 g/mol, Figure AII–1) in a 60:30:10 (v:v:v) of deuterated glycerol : D_2O : H_2O solution. The D_2O/H_2O was first used to create the 20 mM TOTAPOL solution and then the deuterated glycerol was added in. The FP–Hairpin UA6/UG10 sample was rehydrated with ~30 µL of the DNP solution, mixed to a homogenous consistency in an eppendorf tube and then transferred to a Bruker 3.2 mm rotor. Sample packing was similar to that described in

Chapter 2. The drive tip sealed the sample in the rotor, and the sample was shipped to Bruker BioSpin (Billerica, MA).

DNP Parameters and Experiments

A Bruker BioSpin 263 GHz ADVANCE DNP–NMR Spectrometer (Billerica, MA) having a 9.4 T magnet operating at a ^{1}H and ^{13}C frequency of 399.8 MHz and 100.5 MHz respectively equipped with a 3.2 mm LT–MAS (Low Temperature Magic Angle Spinning) $^{1}H/^{13}C/^{15}N$ probe was used in acquiring the spectra for FP–Hairpin UA6/UG10. General experimental conditions were nominal temperature of ~100 K at the thermocouple, MAS rotation of 8 kHz, ^{1}H Rabi frequency of 55.6 kHz (P1), 100 kHz Spinal64 decoupling, 1 ms contact time (P15), 10% ramp for CP, and 32 scans (ns). For the CP Ramp experiment the recycle delay was 5 s. Spectra were either acquired with the microwaves on (Figure AII–3A) or the microwaves off (Figure AII–3B). For the 2D $^{13}C–^{13}C$ DARR experiments, all conditions were the same as the ^{13}C CP experiment except for the recycle delay was 3.5 s, 32 scans per t_1 point, and 200 t_1 points were acquired for mixing times of 15 ms, 50 ms, or 500 ms which are shown in Figures AII–4A,
AII–5A, and AII–6A respectively. 0 Hz of line broadening was applied to the spectra and Topspin 2.0 or 3.1 were used for data processing. ^{13}C referencing set the methylene resonance of solid adamantane to 40.5 ppm, as described in Chapter 2.[1] Appendix IV contains file locations of both raw and processed spectra.

DNP Results

Figure AII–1 is the molecular structure of the biradical polarizing agent TOTAPOL that was added in with the deuterated glycerol for the DNP experiments.

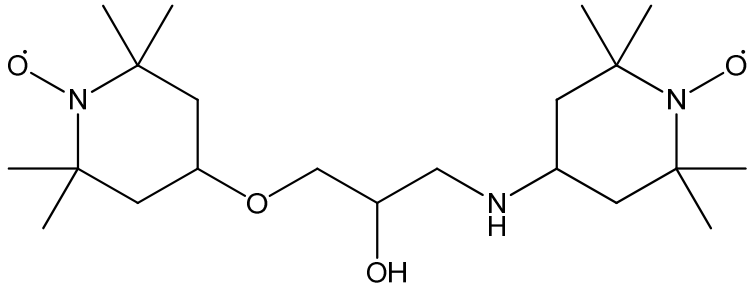

Figure AII–1: Molecular structure of the biradical TOTAPOL, MW = 399.58 g/mol.[2]

Figure AII–2 highlights the modified pulse sequence for the DNP experiments. They are similar to those for the solid state NMR with the only addition being the electron channel where the microwave irradiation is applied.

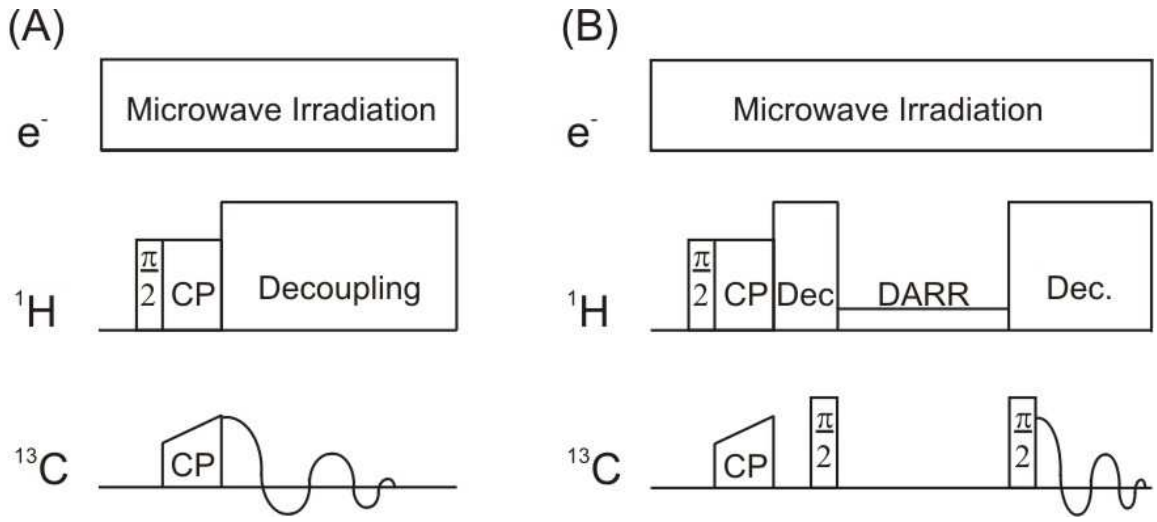

Figure AII–2: Dynamic nuclear polarization (DNP) pulse sequence for the (A) ^{13}C CP Ramp and (B) 2D ^{13}C–^{13}C DARR experiments. As seen in reference[2] the microwaves (MW) are on the whole time, and usually have a buildup period prior to the ^{1}H $\pi/2$ pulse.

Figure AII–3 illustrates the increase in ^{13}C peak signal to noise per scan. Initially, an ~22–fold increase in ^{13}C signal per scan was determined when matching up the signal intensities. However, a better comparison is to integrate the area under the peaks for the two spectra and compare the total area. The area of the curve was first determined for the MW on spectrum, and then the same integrated regions were used to determine the area under the peaks for the MW off spectrum. The ratio of the areas for MW on / MW off provides a measure of the increased ^{13}C signal per scan. Comparing the areas under the curve resulted in determining that the microwaves on spectrum is ~39–fold greater than when there are no microwaves. Table AII–1 provides the integrated region and the area of the integral for the MW on and the MW off spectra. Figure AII–3 shows the MW on and the MW off spectra for FP–Hairpin UA6/UG10.

The red (x1) spectrum in Figure AII–3B is scaled to the same noise level as the microwaves on spectrum of Figure AII–3A. The blue (x10) spectrum in Figure AII–3B is scaled up 10x to better show the features of the ^{13}C CP with microwaves off.

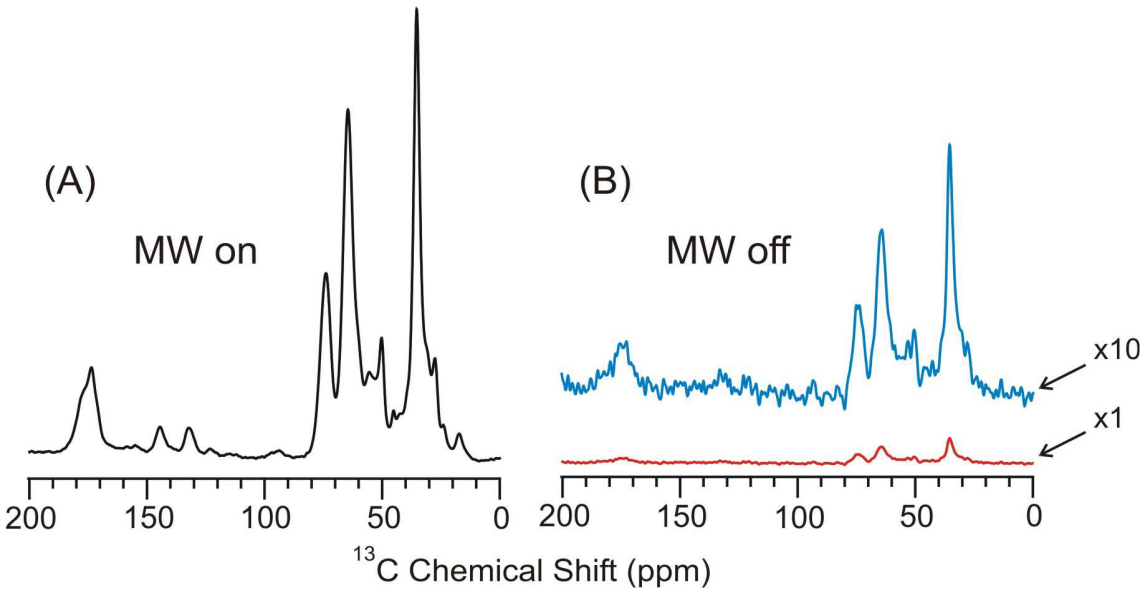

Figure AII–3: Comparison of FP–Hairpin UA6/UG10 (A) with microwaves on and (B) with microwaves off in a POPC/POPG/Chol lipid environment. Comparing the ^{13}C CP of (A) microwaves on and (B) microwaves off (red, x1 spectrum) shows that a ~39–fold enhancement is achieved when comparing the integrated area of the peaks. The red (x1) spectrum in (B) is scaled to the same noise level as the spectrum in (A). The blue (x10) spectrum in (B) is scaled 10x greater than the red one in (B) to better highlight the observed peaks for the microwave off spectrum. 100 Hz of Gaussian line broadening was applied to both spectra. The non–flat baseline of the blue x10 spectrum in (B) is not observed for the other spectra, suggesting that it is an artifact from the scaling up of the spectrum.

Table AII–1: Comparison of the integrated areas of the ^{13}C CP ramp experiment for FP–Hairpin UA6/UG10 with either the microwaves on or the microwaves off.

Integral #	Integrated Region (ppm)	Integrated Area MW on	Integrated Area MW off	$\frac{\text{MW on}}{\text{MW off}}$ Ratio
1	Start: 187.13 Stop: 167.29	2852300	35029	81.427
2	Start: 82.97 Stop: 69.49	4349000	128350	33.884
3	Start: 69.49 Stop: 57.72	8550600	298940	28.603
4	Start: 57.72 Stop: 47.06	3027200	85895	35.243
5	Start: 47.06 Stop: 40.93	770970	26421	29.180
6	Start: 40.93 Stop: 25.25	9340600	339540	27.510
			Average:	39.308

When calculating the average and standard deviation, the data was skewed due to the 81.5 value producing a standard deviation of 20.86. If the 81.5 value is excluded, the new average ± standard deviation is 30.88 ± 3.44. Visually in Figure AII–3, the CO region is not well defined for the MW off spectrum, and could be the main reason why the ratio of the integrated areas has such a discrepancy compared to the other data presented in Table AII–1.

The following three figures present the 2D ^{13}C–^{13}C data for FP–Hairpin UA6/UG10 with the microwaves on. Table AII–2 lists the chemical shifts for the cross peaks in the 2D spectra which is presented after the figures.

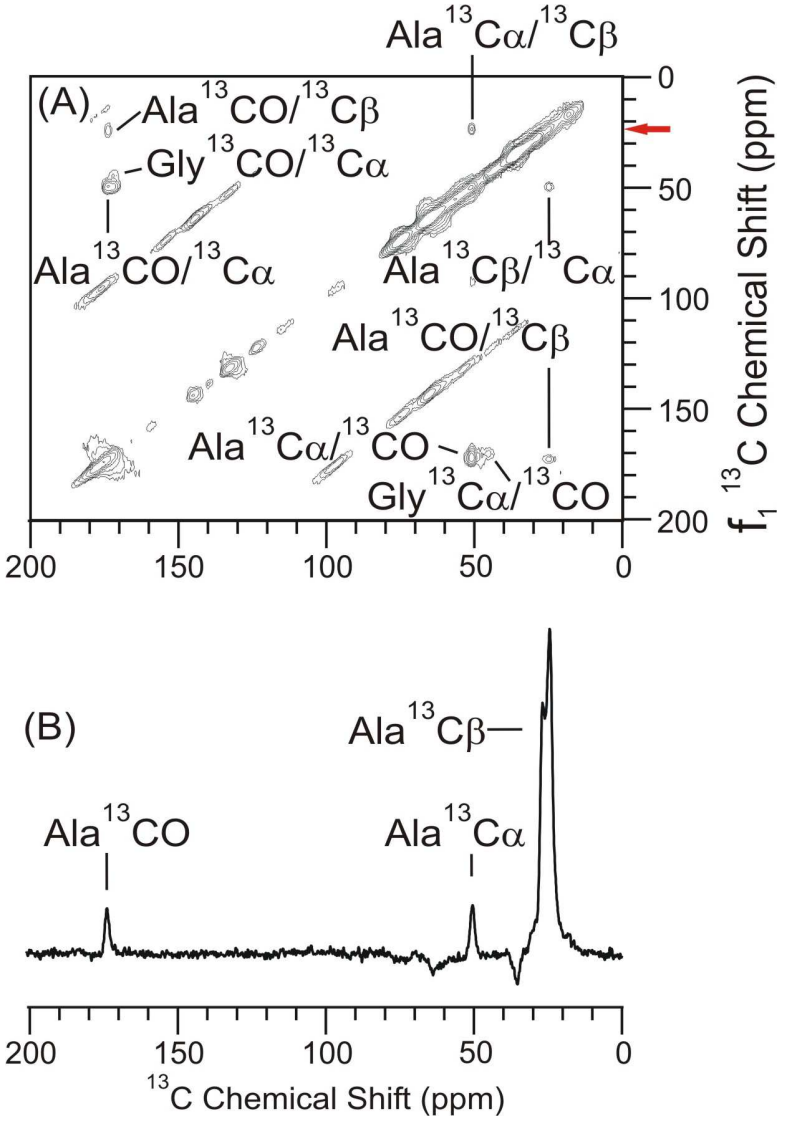

Figure AII–4: 2D ^{13}C–^{13}C spectra at 9.4 T of FP–Hairpin with uniform ^{13}C, ^{15}N labeling at Ala–6 and Gly–10 in the FP region in a POPC/POPG/Chol lipid membrane environment. (A) The 15 ms showing the cross peaks are starting to be observed even at short mixing times and arising from intra–residue connections. (B) The f_2 slice corresponding to the Ala ^{13}Cβ β–strand conformation from f_1 = 23.5 ppm is marked by the red arrow in (A) showing where the Ala6/Gly10 cross peaks would be expected at longer mixing times. There were 200 t_1 points and 32 scans summed per t_1 point in a total time of ~6.3 hrs. Assignments are listed as assignment in f_2 – assignment in f_1 convention. No line broadening was applied to the spectra.

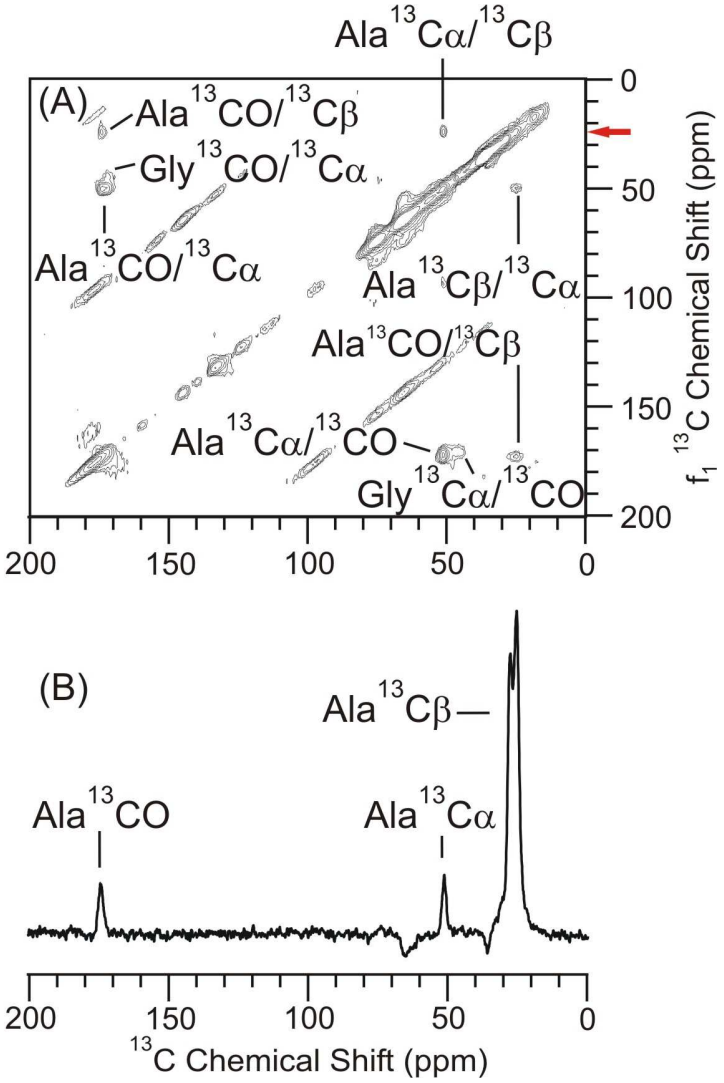

Figure AII–5: 2D ^{13}C–^{13}C spectra at 9.4 T of FP–Hairpin with uniform ^{13}C, ^{15}N labeling at Ala–6 and Gly–10 in the FP region in a POPC/POPG/Chol lipid membrane environment. (A) The 50 ms showing the cross peaks arising from intra–residue connections. (B) The f_2 slice corresponding to the Ala $^{13}C\beta$ β–strand conformation from f_1 = 23.5 ppm is marked by the red arrow in (A) showing where the Ala6/Gly10 cross peaks would be expected at longer mixing times. There were 200 t_1 points and 32 scans summed per t_1 point in a total time of ~6.3 hrs. Assignments are listed as assignment in f_2 – assignment in f_1 convention. No line broadening was applied to the spectra.

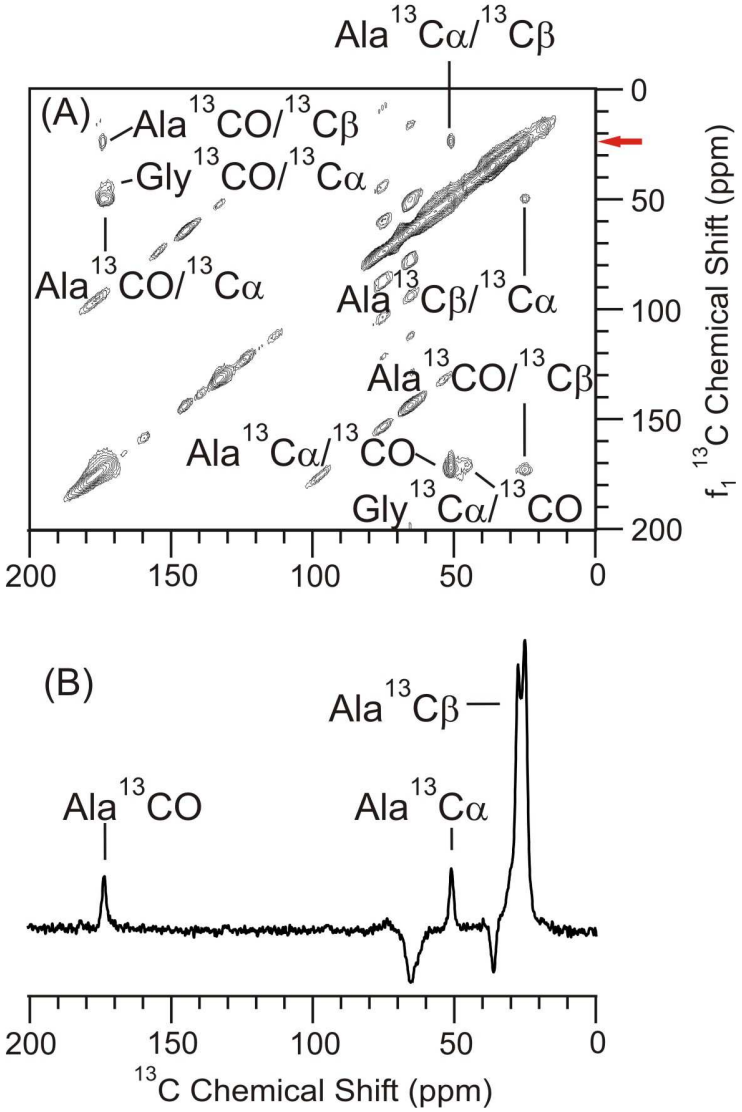

Figure AII–6: 2D ^{13}C–^{13}C spectra at 9.4 T of FP–Hairpin with uniform ^{13}C, ^{15}N labeling at Ala–6 and Gly–10 in the FP region in a POPC/POPG/Chol lipid membrane environment. (A) The 500 ms spectra for inter–residue assignment and probing the through space connectivity. (B) The f_2 slice corresponding to the Ala $^{13}C\beta$ β–strand conformation from f_1 = 23.5 ppm is marked by the red arrow in (A) showing where the Ala6/Gly10 cross peaks would be expected. There were 200 t_1 points and 32 scans summed per t_1 point in a total time of ~7.1 hrs. Assignments are listed as assignment in f_2 – assignment in f_1 convention. No line broadening was applied to the spectra. No Ala6/Gly10 cross peaks are observed, consistent with work presented in Chapters 3 and 4 for FP–Hairpin with the UA6/UG10 labeling scheme.

Table AII–2: Chemical shift (CS) and relative populations (Pop) for the FP–Hairpin UA6/UG10 sample with loading at ~25:1 in cholesterol containing lipid membranes studied by DNP. Shifts are reported as the (f_2, f_1) convention.

Loading		**25 : 1**					
Composition		**POPC / POPG / Chol**					
Field		**9.4 T**					
Pulse Sequence		**DARR**					
Mixing Time		**15 ms**		**50 ms**		**500 ms**	
Assignment		**CS**	**Pop (%)**	**CS**	**Pop (%)**	**CS**	**Pop (%)**
A Cα / A Cβ	**Helix**	–	–	–	–	–	–
	β–sheet	49.8, 23.7	–	49.9, 23.7	–	50.1, 23.7	–
A Cα / A CO	**Helix**	–	–	–	–	–	–
	β–sheet	49.8, 171.2	–	49.9, 171.2	–	49.9, 171.2	–
A Cβ / A CO	**Helix**	–	–	–	–	–	–
	β–sheet	23.7, 172.4	–	23.5, 172.4	–	23.7, 172.4	–
A CO / A Cα	**Helix**	–	–	–	–		–
	β–sheet	171.3, 48.9	–	172.6, 48.9	–	172.7, 48.9	–
A CO / A Cβ	**Helix**	–	–	–	–	–	–
	β–sheet	172.8, 23.7	–	172.7, 23.7	–	172.7, 23.7	–
A Cβ / A Cα	**Helix**	–	–	–	–	–	–
	β–sheet	23.7, 48.9	–	23.7, 48.9	–	23.9, 48.9	–
G Cα / G CO	**Helix**	–	–	–	–	–	–
	β–sheet	44.2, 170.0	–	44.5, 170.0	–	44.2, 170.0	–
G CO / G Cα	**Helix**	–	–	–	–	–	–
	β–sheet	171.0, 44.1	–	170.2, 44.1	–	170.8, 44.1	–

Populations were not determined for the samples due to the lack of observable helical cross peaks. The chemical shifts for the 15 ms, 50 ms, and 500 ms data are presented in Table AII–2. The chemical shifts for the peaks were determined by selecting the region of interest of the spectra using the Topspin 3.1 software and then allowing the software to automatically pick the peaks. The software generated a numbered list corresponding to the numbered cross peak. The chemical shifts of Table AII–2 agree well with previous work for FP–Hairpin UA6/UG10 presented in Chapters 3 and 4. The Ala ^{13}CO peaks are observed ~2 ppm lower chemical shift as observed with the DNP experiment than when observed using the non–DNP SSNMR experiments at 9.4 T presented in Chapter 3. The Ala ^{13}Cα, ^{13}Cβ and the Gly ^{13}Cα and ^{13}CO chemical shifts are in agreement between the DNP and the non–DNP experiments with less than 1 ppm difference in their reported chemical shifts.

Table AII–3 highlights the comparison of linewidths between the DNP experiments at 400 MHz and 100 K to linewidths for a similar sample at 400 MHz and 223 K nominal temperatures and no line broadening applied. The trade off between running the DNP experiment at ~100 K compared to the SSNMR experiments at ~223 K is that a ~39–fold increase in ^{13}C was observed. Comparison between the sample at ~100 K and the sample at ~223 K shows that the linewidths for the Ala ^{13}Cα are within error, where as the ^{13}Cβ FWHM are ~40% larger linewidth from the DNP experiment and the Ala ^{13}CO peaks are ~10% broader in the non–DNP experiment. Comparing the DNP FWHM linewidths to the FP–Hairpin UA6/UG10 15:1 lipid to protein sample presented in Table 4–4, the DNP linewidths values in Hertz are ~25 – 60% broader than the narrowest linewidths achieved with the FP–Hairpin protein sample at 21.1 T.

The increased linewidths would make it difficult to resolve peaks into the helical or the β–strand conformation.

Table AII–3: Comparison of the linewidths for the 50 ms slices when FP–Hairpin UA6/UG10 is studied using SSNMR at ~223 K vs. DNP at ~100 K. FWHM measurements were performed on the f_2 slice corresponding to the Ala $^{13}C\beta$ β–strand conformation from f_1 = 23.5 ppm.

	$^{13}C\alpha$		**$^{13}C\beta$**		**^{13}CO**	
	Hz	**ppm**	**Hz**	**ppm**	**Hz**	**ppm**
DNP 50 ms	209.0	2.08	268.3	2.67	217.1	2.16
400 MHz NMR	206.6	2.05	192.5	1.91	247.0	2.45

The 400 MHz NMR slice FWHM was determined for the 25:1 lipid to protein loading sample in POPC/POPG/Chol lipid membranes corresponding to Figure 3–4. 25 Hz of Gaussian line broadening was applied to the spectra in each dimension so that the ^{13}C peaks could be distinguished from the noise more easily. The 25:1 sample from Figure 3–4 was chosen as it closely resembled the DNP sample for protein loading and lipid composition of POPC/POPG/Chol in an 8:2:5 molar ratio. There was ~12 mg (~1 μmole) FP–Hairpin UA6/UG10 in the 400 MHz NMR sample.

DNP Conclusions

DNP provides an increase in the ^{13}C peak signal to noise ratio per scan, as is clearly demonstrated in Figure AII–3 by comparing the CP ramp with and without microwaves. For the FP–Hairpin sample, no Ala6/Gly10 cross peaks were observed for this sample which is consistent with the results from the 9.4 T and 21.1 T SSNMR experiments for various loading conditions presented in Chapters 3 and 4. The linewidths were broader than what we are able to obtain using either the 9.4 T or 21.1 T spectrometer which can lead to ambiguity in peak assignment. In conclusion, while DNP can be utilized on samples containing less protein, the increase in ^{13}C peak signal to noise ratio per scan alone doesn't out weigh the broader lines that are associated with it. Cross peaks were observed as early as 15 ms, which provided the intra–residue assignment like the 50 ms mixing time does for the SSNMR experiments. The 500 ms mixing time of Figure AII–6A does not contain any cross peaks that would correlate with the Ala6 $^{13}C\beta$ / Gly10 $^{13}C\alpha$ chemical shift as evidenced by the slice in Fig. AII–6B. The slice goes through the β–strand chemical shift of the Ala $^{13}C\beta$, which is where Ala $^{13}C\beta$ / Gly $^{13}C\alpha$ cross peak would be observed. These results are consistent with the results presented in Chapters 3 and 4 for FP–Hairpin UA6/UG10 labeling in cholesterol containing membranes.

The lower temperature of ~100 K did not affect the chemical shifts of the peaks as seen in Table AII–2, which is consistent with previous reports from the Weliky group.[3] The chemical shifts presented in Table AII–2 for FP–Hairpin with the 15 ms, 50 ms, and 500 ms DNP spectra are consistent with the reported chemical shifts of FP–Hairpin in Chapters 3 and 4 with the exception of the Ala ^{13}CO β–strand peak being observed ~2 ppm lower than the other Ala ^{13}CO β–strand chemical shifts.

Significant savings in signal averaging time can be achieved when comparing samples of comparable lipid to protein loadings and with the total amount of protein in the sample. This is directly proportional to the increased ^{13}C signal that is achieved from DNP experiments by transferring the magnetization from the electron to the proton before transferring to the ^{13}C nuclei. DNP may have benefits for experiments that suffer from a lack of peak signal to noise per scan from the low gamma nuclei such as the ^{13}C or ^{15}N nuclei, however it will first need to get around the broad linewidths that seem to be associated with it.

Crystallization of Hairpin and FP–Hairpin with Arizona State University

Crystallography Sample Preparation

Hairpin and FP–Hairpin were sent to Arizona State University (ASU) for crystallization in the laboratory of Dr. Petra Fromme with assistance from graduate student "Jane" Gong Zhen. Samples were prepared as described in Chapter 2 for Hairpin and FP–Hairpin with the following modifications. Protein solutions were shipped overnight to ASU on ice. As mentioned earlier, there are crystal structures for gp41 representing the SHB[4–9] and of the SIV gp41 protein[10, 11], but none for this exact construct of "Hairpin" and none that contain the fusion peptide region. Thus, our motivation for crystallization is to try and obtain a crystal structure of a FP region containing construct.

Hairpin Sample Preparation

A pellet of the lyophilized Hairpin which was previously purified as described in Chapter 2 was dissolved in a 15% acetonitrile / water solution, with 2 mM TCEP added, tip sonicated,

and repurified on a C18 semi–preparative RP–HPLC column. Only the central portion of the Hairpin peak was collected, and the acetonitrile was removed under a stream of N_2 gas, and dialyzed against low pH water with TFA added (1:2000 v/v) at pH 3.0. Three buffer changes occurred, obtaining a dialysis ratio of 125,000:1. The Hairpin sample was quantified and concentrated on a vivaspin concentrator until the desired concentration of 1 mg/mL was achieved. The protein was stored under an argon atmosphere and kept at 4°C until shipment to Arizona State University. Hairpin has a molecular weight of 10.724 kDa which was confirmed by mass spectrometry and quantification was done by A_{280}. [12]

FP–Hairpin Sample Preparation

FP–Hairpin was created and purified as described in Chapter 2. Following RP–HPLC purification, the pooled fractions had sodium formate pH 3 buffer added so that after removal of ACN by a stream of N_2 gas the final concentration would be between 10 – 20 mM sodium formate. The FP–Hairpin solution was then dialyzed against 20 mM sodium formate pH 3.0 and no reducing agent was added. Dialysis was used to refold FP–Hairpin and remove any co–eluted FP23(linker). Following three buffer exchanges, the FP–Hairpin solution was then subjected to a low pH water solution, which was DDW with ~0.05% TFA and pH 3. The FP–Hairpin solution was dialyzed against this for three buffer changes. The solution was quantified and concentrated to the 1 mg/mL concentration requested by ASU for crystallography. After concentration, the FP–Hairpin sample was stored under an argon environment and at 4°C until shipped.

Crystallography Conclusions

The samples have been shipped however to date no crystals of diffraction quality have been produced. The attempts to crystallize Hairpin have been halted since similar constructs have been crystallized. Progress on FP–Hairpin is very slow as well and no crystals have been observed yet for this construct. The idea of sending Hairpin along with FP–Hairpin to ASU was so that Hairpin would be able to give some insight into possible crystallographic conditions for FP–Hairpin, the more interesting construct since no gp41 protein constructs with the FP region has been crystallized to date. One possible issue could be that the Hairpin construct, and likely the FP–Hairpin construct are aggregated in solution. Using gel filtration to separate the proteins into their different oligomeric states might increase the chances of observing crystals of the proteins. Several attempts to get gel filtration to work for Hairpin and FP-Hairpin have been unsuccessful to date. Work by Caffrey and co–workers shows evidence for gp41 to be associated as either trimers or aggregates.[13] A pH 2.5 solution containing 50 mM sodium formate buffer shows the HIV gp41 construct was trimeric, whereas at pH 8.0 with 100 mM sodium bicarbonate buffer the protein was observed in both trimer and aggregated oligomeric states. The construct Caffrey was using contained the NHR, native loop, and CHR domains corresponding to residues 27 – 154, but lacking the FP region.[13] While the constructs presented here for Hairpin and FP–Hairpin contain only a minimal linker instead of the native loop, it is still possible that there is aggregation from (1) the free N–terminal cysteine of Hairpin or (2) aggregation of the FP regions of FP–Hairpin.

REFERENCES

References

1. Morcombe, C.R. and K.W. Zilm, *Chemical shift referencing in MAS solid state NMR.* Journal of Magnetic Resonance, 2003. **162**(2): p. 479–486.

2. Song, C.S., et al., *TOTAPOL: A biradical polarizing agent for dynamic nuclear polarization experiments in aqueous media.* Journal of the American Chemical Society, 2006. **128**(35): p. 11385–11390.

3. Bodner, M.L., et al., *Temperature dependence and resonance assignment of 13C NMR spectra of selectively and uniformly labeled fusion peptides associated with membranes.* Magn Reson Chem, 2004. **42**(2): p. 187–94.

4. Weissenhorn, W., et al., *Atomic structure of the ectodomain from HIV–1 gp41.* Nature, 1997. **387**(6631): p. 426–30.

5. Chan, D.C., et al., *Core structure of gp41 from the HIV envelope glycoprotein.* Cell, 1997. **89**(2): p. 263–273.

6. Tan, K., et al., *Atomic structure of a thermostable subdomain of HIV–1 gp41.* Proc. Natl. Acad. Sci. U. S. A., 1997. **94**(23): p. 12303–12308.

7. Shu, W., H. Ji, and M. Lu, *Interactions between HIV–1 gp41 core and detergents and their implications for membrane fusion.* J. Biol. Chem., 2000. **275**(3): p. 1839–1845.

8. Shi, W., et al., *Structural characterization of HIV gp41 with the membrane–proximal external region.* J Biol Chem, 2010. **285**(31): p. 24290–8.

9. Buzon, V., et al., *Crystal Structure of HIV–1 gp41 Including Both Fusion Peptide and Membrane Proximal External Regions.* PLoS Pathogens, 2010. **6**(5): p. e1000880.

10. Yang, Z.N., et al., *The crystal structure of the SIV gp41 ectodomain at 1.47 angstrom resolution.* Journal of Structural Biology, 1999. **126**(2): p. 131–144.

11. Caffrey, M., et al., *Three–dimensional solution structure of the 44 kDa ectodomain of SIV gp41.* Embo J, 1998. **17**(16): p. 4572–4584.

12. Sackett, K., et al., *Hairpin folding of HIV gp41 abrogates lipid mixing function at physiologic pH and inhibits lipid mixing by exposed gp41 constructs.* Biochemistry, 2009. **48**(12): p. 2714–22.

13. Caffrey, M., et al., *Biophysical characterization of gp41 aggregates suggests a model for the molecular mechanism of HIV–associated neurological damage and dementia.* J. Biol. Chem., 2000. **275**(26): p. 19877–19882.

Appendix III:

Setting up and Running on the 900 MHz NMR: A Users Guide

Introduction

This appendix is meant serve as a reference for operating the 21.1 T NMR spectrometer with the solids probes, and should be used in conjunction with the solids manual from Bruker.[1] Below are details on setting up the spectrometer, troubleshooting and tips and tricks to making the most of your time at the 21.1 T NMR spectrometer which I have learned during my time with the Bruker instrument.

Starting at the 900 MHz Facility

When the probes are switched from the cryoprobe for liquid state NMR to the solid state NMR probes, it will usually take about a half a day to warm up the cryoprobe and install the solids probe. This has traditionally been handled by Mr. Kermit Johnson and Dr. Dan Holmes. Once the probes are switched and the cabling is correct, you will want to do the following before performing your experiments. Setup airflow going into the bottom of the probe and the top of the magnet bore, check the magic angle to ensure that it is set correctly, set and adjust the drift correction and make sure that the peaks from a ^{13}C adamantane spectrum are well shimmed. Make sure that the probe is tuned to the correct nuclei, and that the experiments are optimized. Gas flow to the bottom of the probe is controlled by "probe flush" which needs to be turned on at the console.

The BSMS controller allows you to adjust the shims, drift correction and field setting. Setting the drift correction needs to be saved once entered to take affect. In order to save the drift correction, you will need to go into a menu on the BSMS controller and enter a security code. The security code's last four digits are 1964, after which a beep will sound letting you know that the code is correct and allow you to save the values for the shims and the drift correction.

Packing samples for the 900 MHz NMR are similar to the 400 MHz NMR samples. Once your sample is packed, make sure to place a top spacer in the rotor, this helps to seal the contents into the rotor and prevents it from leaking out around the drive tip. Leakage around the drive tip could result in loss of sample, instability with spinning, or the drive tip coming completely off inside the probe and possibly damaging the probe. Unpacking the Bruker rotors is easily done by inserting the rotor without the drive tip or top spacer upside down in a 1.7 mL eppendorf tube and spinning in the microfuge at maximum speed for 2–3 minutes. Remove the rotor, clean off the sample that has been centrifuged out and repeat until all the sample is out.

Samples at the 900 MHz NMR are inserted through the top of the magnet, with the drive tip facing up. Before inserting the sample, press eject on the interactive screen at the console. This will eject the rotor from the probe and will position the stator to receive the next rotor. Once the gas flow stops from eject, drop in the new rotor, and press "insert" on the console. Watch to make sure that MAS unit under the probe moves upwards. If it doesn't move up, then the rotor is not fully inserted. Eject the sample, and then re–insert it. Make sure that the airflow from the BCU unit is at 135 L/hr or less. A high gas flow can cause a cushion of air for the rotor to sit on, and prevents it from sliding fully into the stator. Once the rotor is in the stator and the MAS unit moves up, start spinning the rotor. If the rotor doesn't spin then remove it, re–mark it, and try again. Also check and make sure the drive pressure (DP) and bearing pressure (BP) are set to

zero prior to inserting the rotor. If they aren't, then manually decrease them to zero and try re–inserting the sample. Spinning problems in auto mode are indicated by the inability to get above 800 – 900 Hz and extremely high pressures causing the system to shutdown automatically. Once spinning is above 1200 Hz, you can start to slowly increase the cooling gas flow from 135 L/hr to the desired value.

Setting the magic angle is an important process that needs to be done properly and checked both at room temperature and the temperature your experiments are to be conducted at. Setting of the magic angle should be done first followed by checking and optimizing the shim files for the probe.

Setup Samples

Setup samples at the 900 facility include: (i) adamantane / KBr, (ii) U–NAL, (iii) natural abundance glycine, and (iv) ^{15}N ammonium sulfate (AMS). The adamantane / KBr sample is used for setting the magic angle and for referencing the chemical shift of the ^{13}C spectra, and is also useful for shimming the ^{13}C line shapes, and setting the drift correction. The U–NAL sample is uniformly ^{13}C, ^{15}N labeled N–acetyl leucine and is used for optimizing pulse program parameters for ^{1}H, ^{13}C, and ^{15}N. The natural abundance glycine sample can also be used for optimizing the pulse program, however I opted for the U–NAL sample as it easily allows for ^{15}N, where as the ^{15}N signal from glycine is nonexistent. The ^{15}N ammonium sulfate sample can be used for optimizing the ^{15}N parameters and also for referencing of ^{15}N spectra. Referencing of the ^{13}C and ^{15}N spectra will be discussed below.

Setting the Magic Angle

Setting the magic angle is achieved by using the setup rotor containing adamantane / KBr. After inserting the rotor into the probe, spin up to 5000 Hz. At the computer, open up a previous zg pulse program file, copy the file to a new directory by typing "edc" and filling in the information needed. Typing "edasp" will open up the cabling of the experiment along with the base frequencies of the different nuclei. Hit the "default" button which will update nuclei frequencies and highlight the correct cabling which you should double check, then click "save" and "close". Type "wobb" in the topspin command bar. The ^{13}C channel will be tuned to the frequency of the ^{79}Br nucleus. Acquire a spectrum for of the KBr rotational resonance for future comparison, and then systematically adjust the MAS rod beneath the probe by making a small 1/8 turn, acquire a new spectrum and compare the results. Continue this until the central rotational resonance peak is the maximal height possible and the first order rotational resonance peak is less than 10% of the central peak. It is best to check the magic angle setting at room temperature first, and then lower the temperature and re–check the setting of the angle. After setting the angle at the lower temperature, eject the rotor and then re–insert the rotor and check the angle one last time to confirm it is set correctly. It is advisable to check the angle again before running actual samples to confirm proper setting of the angle.

Tuning

With a sample in the probe, type "wobb" in the topspin command line with a pulse program open that you want to use. This will allow for the low power tuning, starting with the lowest gamma nuclei for that pulse program and work to the highest gamma nuclei. For ^{13}C,

^{15}N, and ^{79}Br you do not need to disconnect any cables, however for proton, you will need to disconnect the cable from the filter and attach it to the HPPR pre–amplifier for tuning. I advise you to tune all nuclei with the cabling setup for that the experiment. Tuning of the ^{13}C circuit is affected by whether the proton cable is connected to the HPPR pre–amplifier resulting in improper tuning of the ^{13}C channel. Once the nuclei are all tuned, perform a second check to confirm optimal tuning of the circuits have been achieved. Two ways to determine if the circuit is tuned: (1) using the LED lights on top of the HPPR pre–amplifier or (2) watching the low power tuning parabola on the computer screen, trying to get the parabola's vertex centered on the red vertical line and making the parabola go the farthest down possible.

Adjustment of the circuit is done by adjusting the tune "T" and match "M" rods beneath the probe using the hanging screwdriver. The LED lights change from red to orange to green as you approach the resonance condition. Make sure that all the LED lights are in the green before running the experiments, as failure to do so can result in damage to the probe. After tuning the probe, make sure to reconnect the ^{1}H cable from the HPPR to the ^{1}H filter. Check probe tuning between samples. The tuning of the circuit will be affected by the match condition and as the match is adjusted, the tuning will be affected requiring an iterative process of adjusting the match and the tune until the best tuning of the circuit is achieved. My experience has shown that the tuning is rather consistent over long periods of time for the same sample. Switching between a standard sample and a biological sample will result in significantly different tuning conditions and the need to retune the probe.

Shimming

Shimming the spectrometer should be done using the adamantane sample. First, write the current shim files to the hard drive as a restore point using the "wsh" command. It is a good idea to acquire and save a spectrum before starting, so that you can compare the before and after results to determine which are better. By typing "gs" an interactive window will open, and allow for real time adjustment of the shimming. The Bruker manual contains more information on how to specifically adjust the shims. Briefly a few tricks are to set the recycle delay (d1) to 1.5 – 2 seconds, either shim the FID or look at the Fourier transformed spectrum and zoom in around the adamantane peaks. Starting at the Z1 shim (press "axis on" button and then "Z1" button), use the spinning knob on the BSMS controller to adjust the value. Once the shape of the FID or spectrum has been adjusted move on to the Z2 shims until a narrow peak and well shimmed peak is obtained. For more information check out the document available on shimming at the Max T. Rogers NMR facility.[2]

After adjusting the shimming, write the shim files again. Date and reference what probe the shim files are associated with so that they are distinguishable from the other files without overwriting previous ones. This is something that should be performed at the beginning of the solids time for the spectrometer. If the BSMS controller is reset when working at the 900 MHz NMR, the shim values may be reset to default values, which will affect your shimming. Either re–read the saved values or re–shim the magnet.

Optimization of Pulse Programs

Optimization of pulse programs and checking the magic angle are important steps that need to be accomplished before starting to run your samples. In the directory listed there is a

folder which contains the pulse programs that I optimized in Jan 2011 for the E–free probe. This is an ideal starting point to check the parameter set and make sure the experiment is working properly. The directory is: /home/data/Nethercott/nmr/Jan2011–2. Table AIII–1 shows the directory for each optimized pulse sequence.

Table AIII–1: Directory of optimized experiments for the 900 MHz NMR

Experiment Number	Pulse Program Name	Notes [a]
10	cp90 (^{13}C)	Optimized 1D ^{13}C CP90 experiment.
11	cp90 (^{15}N)	Optimized 1D ^{15}N CP90 experiment.
12	doubcp.av.jos	Optimized 1D NCA experiment
13	doubcp.av.jos	Optimized 1D NCO experiment
14	cpdarr.av.jos	Optimized 2D ^{13}C – ^{13}C experiment
15	doubcp2ddarr.jos	Optimized 1D NCA experiment, and used to optimize the 2D experiment.
16	doubcp2ddarr.jos	Optimized 1D NCO experiment, and used to optimize the 2D experiment.
17	doubcp2ddarr.jos	2D NCA experiment optimized from the 1D experimental setup.
18	doubcp2ddarr.jos	2D NCO experiment optimized from the 1D experimental setup
19	cpredxy8.av.jos	1D REDOR experiment, No ^{15}N Pulses (pL3=120). L0 = dephasing time parameter. See note in "title" of program. (S0 file) Want maximal signal from this one.
20	cpredxy8.av.jos	1D REDOR experiment, ^{15}N Pulses (pL3 ≠ 120). L0 = dephasing time parameter. See note in "title" of program. (S1 file). Want minimal signal from this one.
21	cpredorxy8i.av.jos	Interwoven 2D REDOR experiment. Acquires all S0, then all S1 for specific dephasing time, and then moves onto a new dephasing time point. X–axis = ^{13}C, y–axis = dephasing time.
22	doubcp3d.jos	3D NCACX experiment. Optimized from best parameters of 1D and 2D experiments.
23	zg	1 pulse experiment to determine Magic Angle. Uses the ^{79}Br signal from KBr in the Adamantane/KBr rotor. See Mar2011 exp. 4 for best results.

[a] Unless noted, pulse programs are optimized for T = 250 K, and MAS of 12 kHz.

When optimizing the pulse program, use one of the standard samples such as adamantane / KBr or the U–NAL sample. Start by optimizing the 1D ^{13}C and ^{15}N CP experiments and then using the best parameters from the CP experiments to optimize the other 1D and 2D experiments. Load the pulse program, tune the probe and acquire 8 scans for the pulse program, which will give you a metric for comparison of your optimization of the pulse program. Looking at the pulse program, it is best to follow the path of events, and optimize in the order that they happen. Optimization of a specific parameter is achieved by typing the command "paropt" or "popt", which will bring up a new window. This window will specify the parameter, values to optimize between, step size, and what type of value you are looking for, such as positive max (posmax), negative maximum (negmax), or zero crossing (zero). The optimization will be saved in that experiment as number 999, and works its way down towards 0. Perform a course optimization first to find the region to focus on for fine tuning. Once an optimal value has been determined, place that value in the pulse program and move to the next parameter to optimize. After all the parameters have been optimized acquire a new spectrum of the sample and compare the two spectra. It is best to start optimization with the ^{13}C and ^{15}N CP ramps first and then move onto the more complicated ones (REDOR, 1D NCA/NCO, 2D and 3D experiments) since the more complicated experiments will build off of the optimized parameters from the 1D ^{13}C and ^{15}N CP's. For example, the 2D ^{13}C–^{13}C PDSD experiment uses all the optimized parameters from the ^{13}C CP experiment, and the DARR experiment only requires optimization of one more parameter, the decoupling field for ^{1}H during the mixing period. Therefore, significant time savings is achieved by spending the time to optimize the simpler experiments first. One

command for converting the power levels associated with pulses to Rabi frequencies is the "pulse" command. This command should be performed in a 1 pulse experiment setup (zg), where you supply the power level and pulse length of a 90° and then get out the a power level or pulse length for a new 90°. This command works well for determining decoupling fields.

MAS and Temperature Control

After setting up the probe, make sure that the BCU–XTREME is turned on and connected to the probe. This is what will allow you to cool the samples in the probe to the desired temperature. Once the sample is in the rotor and spinning, you can adjust the cooling gas flow to achieve a desired temperature. Currently, 250 K works well for most experiments. This is achieved by setting the temperature panel (command: edte) to the desired temperature of 250 K, and then increasing the gas flow. The higher the gas flow, the quicker you can obtain your desired temperature. Also, as you run for longer periods of time, the higher gas flow of up to 2000 L/hr is needed to maintain temperature. Ice tends to build up at the connection of the probe and the cooling unit tube, so it is a good idea once every 10 days or so to let the ice thaw and melt off overnight or for a few hours. Over longer periods of time it will be difficult to maintain the cold temperature and the temperature will start to drift towards room temperature. Initial cooling of your sample is best achieved when the MAS frequency is around 5 kHz. I suggest that you cool down the sample at the lower spinning frequency and then once you have reached or are near your target temperature increase to the final MAS frequency.

Warming up the probe from the cold temperatures for running at warmer temperatures is done by applying heating, which is best to keep below 12 – 16%. If you want to remove the ice build up beneath the probe, then turn off the BCU–Xtreme unit. With the BCU–Xtreme unit on,

there is still cold gas flowing to the probe. There is a setting in the edte window that will allow you to change the maximum heating percentage. When warming up or cooling down the probe it is best if you have a standard sample spinning to prevent the build up of condensation. During cooling of a sample, I would set the maximum heating to 1 – 2%, thus allowing the sample to cool down faster without being exposed to excess heating in the probe. Once I had reached the target temperature and spinning frequency I would adjust the maximum heating to 5% and adjust the gas flow appropriately.

Understanding the Pulse Sequence Notation

As stated earlier, it is best to start from the simpler pulse programs and move onto the more complicated pulse programs. Common abbreviations in the pulse sequences are the following: PL for power level, P for pulse length, and d for delay. On the topspin pulse sequence, the power level will be in decibels (dB) and the pulse length will be in time (ms or μs). Setting the 90° pulses are performed by setting the PL for a specific nuclei to the probe limits and then arraying the pulse to determine the 180° or 360° pulse, which is where the signal is zero. The 180° or 360° pulse is divided by 2 or 4 respectively to achieve the value for the 90° pulse. Do not try to optimize the PL level, as you can easily exceed the safe power levels for the probe. The range of values goes from –6 dB to 120 dB, where a value of 120 dB is affectively off. When using the E–free probe the safe power levels for ^{1}H, ^{13}C, and ^{15}N were –2.2 dB, –0.4 dB, and 0.4 dB respectively or higher towards 120 dB. The topspin software will reject values that input too much power into the probe for a certain nucleus.

Data Processing

There are three separate sections to this, (1) Topspin on the computer at the 900 MHz facility; (2) Topspin on Hydra (remote data processing / Chemistry building); and (3) converting data from Topspin to nmrDraw. It is highly desirable to process the data at the 900 MHz facility as you acquire it to confirm the results and so that referencing can be done to compensate for the drift of the magnet. It is highly advisable in the "Title" tab to put notes on what sample, conditions and even when it was ran and referenced. Placing the SR value in here allows for easily checking the sample later and confirming that the proper referencing was performed.

Topspin on the Computer at the 900 MHz Facility

Processing data at the 900 MHz facility is quite easy and straight forward. The main problem with Topspin lies in the data processing when you want to apply Gaussian line broadening. The software does not make it easy to apply this type of line broadening. Processing the data is rather straight forward, and most of the commands have been discussed above. Printing from Topspin allows you to either print a hardcopy of the file or you can save it as a post script file which can be opened with a drawing program such as CorelDraw. For more information on Topspin processing, refer to the solids user manual.[1]

Topspin on Hydra (Remote Data Processing)

In order to remotely process your data, you need to do several steps. First, you need to get an account on the Chemistry supercomputer "Hydra" which has Topspin installed on it. Second, you need to have Topspin installed to your account. The computer support staff in Chemistry will be able to help with this. Once you have an account, you need to deposit the files there and

then open them with Topspin. The general operation of Topspin is the same when you remote process or are at the 900 MHz facility with two exceptions. First, there is a disk quota on Hydra, which after processing 2D and 3D files will fill up fast and prevent you from processing more until you remove some of the data. Second, remote processing on Hydra is much slower as there is a considerable lag time between telling the program to do something and when it will be preformed. It is advisable to try and do as much processing at the 900 MHz facility as possible.

In order to transfer your data you can use a file transfer program to connect to the 900 MHz NMR computer and get your data and save it to your computer. From there you can transfer the data to Hydra for processing with Topspin remotely or you can transfer it to the UNIX NMR computer for processing with nmrDraw. The required information for connecting to the computers are the following.

900 Computer: **Host:** NMRL11.EGR.MSU.EDU; **username:** data; **password:** 900nmr; **port:** 22. For the host login use all lowercase letters.

Hydra: **Host:** HYDRA.CEM.MSU.EDU; **username:** MSUNETID; **password:** your password; **port:** 22. Your username is going to be your MSU NetID, and the password will be unique as well. I connect to Hydra using a free program called Putty.

UNIX NMR Computer: **Host:** IP Address; **username:** mb4c; **password:** mb4c00; **port:** 22. The IP address will be for one of the computers, such as Hapi (35.8.24.135). I used mb4c because this account has access to the nmrDraw program.

Converting Topspin Data to nmrDraw

After transferring the needed files from the 900 MHz NMR computer to the UNIX NMR computer, you will need to log into the UNIX NMR computer and locate the files you deposited.

I used Exceed to tunnel into the computer from my laptop and then login with the mb4c account. To start the conversion process open a terminal window and navigate to the folder containing the Bruker ".ser" file you want to convert into the ".ft2" format. Once you have reached the folder, type "bruker" in the command line. This will open the conversion program "bruk2pipe". Click on the "read parameters" button which will read in the file and display values for different parameters. The boxes in yellow need to have their parameters changed / verified. Check that all parameters are correct. If you type in a value make sure to hit enter otherwise the change will not be recorded. After adjusting the parameters, hit "save" and it will ask if you want to save "fid.com" click yes. Next either select the "execute" button or close the Bruker conversion program. If you don't execute the "fid.com" file, then in the terminal window type "fid.com" and hit enter. This will execute the file creating "test.fid".

In order to visualize the file, there are two options. For 1D experiments you can type "nmrDraw" in the terminal window and then File → Select and choose the "test.fid" file and hit "Read/Draw". After this, the FID will be shown on the screen, go to the Proc menu → "Auto–Process 1D". This will Fourier transform the file. The other way to do this, and more appropriate for the long term use is to use the "macro1D.com" or "macro2D.com" file located in the directory: /home/mb4c/Matt/Organized_Files. The macro files should be moved to the folder where your data is, and then run the file producing a new ".ft2" file. This file can be read by the nmrDraw program and will do all the processing for you before it is visualized in nmrDraw.[3] The macro allows you to zero fill, baseline correction, line broadening and phasing. The two files are reproduced below. For more information on nmrDraw refer to the manual on the shelf or the yahoo support group.[4]

Typical 1D processing macro (macro1D.com)

```
#!/bin/csh

#
# Basic 1D Phase–Sensitive Processing:
#   Use of "ZF –auto" doubles size, then rounds to power of 2.
#   Use of "FT –auto" chooses correct Transform mode.
#   Imaginaries are deleted with "–di" in each dimension.
#   Phase corrections should be inserted by hand.

nmrPipe –in test.fid \
| nmrPipe  –fn GM –g2 0                      \
| nmrPipe  –fn ZF –auto                      \
| nmrPipe  –fn ZF –auto                      \
| nmrPipe  –fn FT –auto                      \
| nmrPipe  –fn PS –p0 0.0 –p1 0.0 –verb –di       \
| nmrPipe  –fn POLY –auto –ord 4 \
  –ov –out test_0.ft2
```

Typical 2D processing macro (macro2D.com)

```
#!/bin/csh

#
# Basic 2D Phase–Sensitive Processing:
#   Use of "ZF –auto" doubles size, then rounds to power of 2.
#   Use of "FT –auto" chooses correct Transform mode.
#   Imaginaries are deleted with "–di" in each dimension.
#   Phase corrections should be inserted by hand.

nmrPipe –in test.fid \
| nmrPipe  –fn GM –g2 0                    \
| nmrPipe  –fn ZF –auto                    \
| nmrPipe  –fn ZF –auto                    \
| nmrPipe  –fn FT  –auto                    \
| nmrPipe  –fn PS –p0 0.0 –p1 0.0  –verb –di       \
| nmrPipe  –fn POLY –auto –ord 4 \
| nmrPipe  –fn TP                          \
| nmrPipe  –fn GM –g2 0 –c 0.5                \
| nmrPipe  –fn ZF –auto                    \
| nmrPipe  –fn ZF –auto                    \                        \
| nmrPipe  –fn SIGN –i                     \
| nmrPipe  –fn FT –neg –alt                      \
| nmrPipe  –fn PS –p0 0.0 –p1 0.0   –verb        \
| nmrPipe  –fn POLY –auto –ord 4 \
  –ov –out test_0.ft2
```

The parameters in the scripts are Gaussian line broadening (GM), zero filling (ZF), Fourier Transform (FT), phasing (PS) for zero order (p0), and first order (p1), and polynomial baseline correction (POLY) of a specific order (ord). Additional parameters for the 2D script are transpose spectrum (TP), and sign manipulation (SIGN). The top half of the script refers to the f_2 dimension, and the bottom half refers to the f_1 dimension. These scripts need to be executed anytime they are adjusted. Referencing is done using the "fid.com" file, so if the offset is changed, the file needs to be saved and executed again followed by a new execution of the

"macro1D.com" or "macro2D.com" file. If the macro file is not executed again then the new changes will not be observed.

Referencing the Spectrum

In Topspin external referencing for ^{13}C spectra are done using the adamantane sample, and setting the methylene peak to 40.5 ppm, which is a standard SSNMR protocol in the Weliky group and IUPAC convention.[5, 6] After correctly referencing adamantane, the new SR value can be applied to the ^{13}C spectra for referencing. ^{15}N referencing is performed indirectly from a properly referenced ^{13}C spectra as detailed below and from reference.[7]

^{15}N referencing on the Bruker instrument requires knowledge of the base frequency of ^{13}C and ^{15}N along with the SR value for ^{13}C. First determine the BF_{13C} by typing "BF1" in the referenced ^{13}C experiment and do the same for the ^{15}N by typing the appropriate number, such as "BF2". Knowing BF_{13C} and the SR_{13C}, use Equation AIII–1. It is important to maintain the sign associated with the SR_{13C} value.

$$BF_{13C} + SR_{13C} = V_{13C} \quad \text{(AIII–1)}$$

$$V_{13C} * 0.402979946 = \mu_{15N} \quad \text{(AIII–2)}$$

$$\mu_{15N} - BF_{15N} = SR_{15N} \quad \text{(AIII–3)}$$

Equation AIII–2 uses the ratio of gyromagnetic ratios of ^{13}C and ^{15}N you get 0.402979946 which is multiplied by the V_{13C} to give you the corrected frequency for the ^{15}N spectrum, μ_{15N}.[7] Equation AIII–3 is used to determine the SR value in MHz for the ^{15}N spectrum. Converting the SR_{15N} value from MHz to Hz by multiplying by 10^6.

Shortcut commands to Acquire Data

To reach the temperature window, type "edte" into the Topspin command line. This will open up the temperature window where you can adjust gas flow, cooling and set the desired temperature.

The "multizg" command allows you to setup a number of runs into a queue system, and run them. This works in two ways. Experiments can either have been pre–defined and you can run that batch, or Topspin will take the last experiment that you have pre–defined and keep making new copies until all the multizg experiments are performed. Once an experiment is finished, it will move onto the next one. To my knowledge, all experiments will be performed at the spinning frequency and temperature defined for the first one, and it is not able to be varied from one experiment to the other. An alternative to multizg is the "zg" option which allows you to open up a data set and type "zg" adding that experiment to the queue. This avoids having to have all experiments in a row, and it also easily allows for modifications to experiments that have not run yet without having to kill all the other experiments.

The "wobb" and "wobb high" commands are used to perform low power tuning for the desired nuclei. "Wobb" will start at the lowest gamma nuclei and proceed to the highest gamma nuclei (^{15}N, ^{13}C, ^{1}H). "Wobb high" will only turn on the low power tuning for the proton nuclei.

The "edc" command will take the data set that you are viewing and allow you to copy it to a new file. This is quite useful when you set up an experiment with your parameters and want to block average it, requiring multiple experiments of the same file.

Phasing can be called up by typing ".ph" into the command bar, or by clicking on the icon in the tool bar. Likewise, referencing a spectrum can be performed by typing ".cal" or clicking on the associated icon. When referencing the spectrum, reference the adamantane file first, copy the SR (spectrum reference) value and adjust the file set as needed. Peak picking can be done by typing ".pp" or clicking on the icon. To get out of the interactive modes, click on the return arrow or type ".ret" and it will return you to the spectrum. Typing ".sret" will save what you just did when in an interactive window such as phasing or peak picking. Not selecting or typing the ".sret" but rather just the ".ret" brings you back to the data without saving the changes.

Troubleshooting

While running on the 900 MHz NMR you will probably run into a few common problems. Those problems are going to be (1) spinning related, (2) pulse programs, and (3) software issues. Spinning related issues have been discussed above in the "Starting at the 900 MHz Facility" section. Other advice for spinning problems includes trying to spin a different sample and try using a different drive tip and / or a different rotor.

Issues with the pulse sequence can be the root cause to several issues including poor peak signal to noise, no observable FID for a specific nucleus, and parameters that will cause damage to the probe. First the poor peak signal to noise issue. Make sure that the pulse program is optimized that you are using. Also, confirm that the cabling to the probe is correct. Typing "edasp" into the command line will open the cabling window, confirm that the defaults are

correct and select save. Finally, check that the magic angle is set properly. If the angle is off significantly from 54.7°, then this could be contributing to the poor peak signal to noise and broad peaks. The best way to confirm that it is a spectrometer issue and not a sample issue is to run a standard sample and determine the peak signal to noise of the spectrum and compare it to previous work. Checking the parameters to confirm that they are correct is important to do. There may be a case where an unoptimized parameter is still in the pulse program or a value that would cause damage to the probe. The second case will be easy to spot, a popup window with a warning will be seen on the screen telling you that a specific parameter is not appropriate and that it was set back to the safe default value.

The third set of issues that you might run into are software issues. Examples of this include the inability to process data, open, or start acquiring data using Topspin. A different problem would be the inability to read and write ("rsh" and "wsh") the shim files. In the shim file case, you will probably receive a message stating that you do not have permission to perform such operation. The best idea in either case is to exit out of Topspin, and then restart the Topspin software. This should solve most problems. In the case of the shims, it is better to restart the Topspin software and not the BSMS controller. Restarting the BSMS controller will result in the loss of the shim values and the saved drift correction.

Topspin Abbreviations

Below is a list of common abbreviations found in Topspin. This list is not comprehensive, but is representative of most of the ones you will encounter when performing the standard 1D and 2D experiments.

Table AIII–2: Topspin abbreviations, commands and meanings

Abbreviation	Meaning	Abbreviation	Meaning
edte	Open temperature window	wobb	Open low power tuning
edc	Copy data set to new location with parameters	wobb high	Low power tuning for ^{1}H
ns	Number of scans	expt	Experiment
lb	Line broadening	efp	Apply exponential LB, Fourier transform, phase
.ph	Interactive phase correction	.cal	Interactive calibration of spectrum
.pp	Interactive peak picking	xf2	Fourier transform F2 dimension
xfb	Fourier transform F2 and F1	sr	Spectral reference (for calibration)
re "x"	Call a specific experiment number	slice	Command to obtain a slice from a 2D data set
.md	Multiple display, overlay spectra	.hr	Command to show entire horizontal scale
.vr	Show entire vertical scale	peakw	command to calculate the peak width at half height
sinocal	Calculate the peak signal to noise of a spectrum	ft	Fourier transform
multizg	Acquire a number of experiments	gs	Interactive acquisition mode without storing data
tr	Save file while running 1D experiment	abs	Automatic baseline subtraction used in 1D experiment
masrset	Set the spinning frequency at the computer	mash	Stop sample spinning from the computer

Conclusions

In conclusion, I hope that this manual ends up providing some clarity to operation of the Bruker instrument, the quirks of the instrument, and the processing associated with the collected data. I ended up teaching myself the system and how to utilize it from the Bruker solids manual and from emailing other people I had met to ask questions. In the end, once you understand the pulse sequence and what everything means you can optimize the experiments quickly. As for the data processing with nmrDraw, once you understand how to convert the Bruker data to the ".ft2" file format the processing is rather straight forward as highlighted above and provides more functionality than what is achieved with the Topspin software in my opinion. Hopefully the next person that works with this software and instrument will have an easier time.

REFERENCES

References

1. Foerster, H., et al., *Solid State NMR AVANCE Solids User manual*. 2009, Bruker Biospin: Rheinstetten, Germany.

2. Holmes, D.H., *How to Shim on a Varian*. 2004, Michigan State University: East Lansing, MI.

3. Delaglio, F., et al., *NMRPIPE – A Multidimensional Spectral Processing System Based on UNIX Pipes.* Journal of Biomolecular Nmr, 1995. **6**(3): p. 277–293.

4. Delaglio, F. *NMRPipe Spectral Processing and Analysis System*. [website] 2011 [cited 2011 26 September 2011]; Available from: http://spin.niddk.nih.gov/NMRPipe/.

5. Morcombe, C.R. and K.W. Zilm, *Chemical shift referencing in MAS solid state NMR.* Journal of Magnetic Resonance, 2003. **162**(2): p. 479–486.

6. Wasniewski, C.M., et al., *Solid–state nuclear magnetic resonance studies of HIV and influenza fusion peptide orientations in membrane bilayers using stacked glass plate samples.* Chem Phys Lipids, 2004. **132**(1): p. 89–100.

7. Bodner, M.L., et al., *13C–13C and (15)N–(13)C correlation spectroscopy of membrane–associated and uniformly labeled human immunodeficiency virus and influenza fusion peptides: amino acid–type assignments and evidence for multiple conformations.* J Chem Phys, 2008. **128**(5): p. 052319.

Appendix IV:

Location of NMR Data Files

Table AIV–1: 400 MHz SSNMR Data of FP–Hairpin at 15:1 Loading

Fig.	File Location	Type of Experiment	Membranes	pH Condition
4–5A 4–6A	**Raw:** /SenTests/SenTest_12a/ **Proc:** /SenTests/SenTests12a/ SenTest_12a_proc_50lb/	^{13}C CP Ramp	POPC/ POPG/ Chol	Method A; pH 7.0
3–10	**Raw:** /FPH_6Feb10_50ms/ FPH_6Feb10_50ms.fid **Proc:** /FPH_6Feb10_50ms/ FPH_6Feb10_50ms_100lb.ft2	2D ^{13}C–^{13}C PDSD	POPC/ POPG/ Chol	Method A; pH 7.0
3–11	**Raw:** /FPH_MS_500ms/FPH_MS _9Feb10_500ms_sum12/FPH_MS _9Feb10_500ms_sum12.fid **Proc:** /FPH_MS_500ms/FPH_MS _9Feb10_500ms_sum12/FPH_MS _9Feb10_500ms_sum12_200lb.ft2	2D ^{13}C–^{13}C PDSD	POPC/ POPG/ Chol	Method A; pH 7.0
3–12	**Raw:** /FPH_19Feb10–50ms– 2/FPH_19Feb10–50ms–2.fid **Proc:** /FPH_19Feb10–50ms– 2/FPH_19Feb10–50ms– 2_100lb.ft2	2D ^{13}C–^{13}C DARR	POPC/ POPG/ Chol	Method A; pH 7.0
3–13 & 3–14 B	**Raw:** /FPH_MS_500ms_DARR_ sum1467/FPH_MS_500ms_ DARR_sum1467.fid **Proc:** /FPH_MS_500ms_DARR_ sum1467/FPH_MS_500ms_ DARR_sum1467_200lb.ft2	2D ^{13}C–^{13}C DARR	POPC/ POPG/ Chol	Method A; pH 7.0

Table AIV–1 (cont'd)

3–14 A	**Raw:** /FPH_noDARR_12kHz/FigS4/ FPH_sum1234/FPH_MS_500ms_ PDSD_sum1–4.fid **Proc:** /FPH_noDARR_12kHz/FigS4/ FPH_sum1234/FPH_MS_500ms_ PDSD_sum1–4_200lb.ft2	2D ^{13}C–^{13}C PDSD	POPC/ POPG/ Chol	Method A; pH 7.0
3–15	**Raw:** /MassSamp_50ms/FPH_MS _50ms_sum12/FPH_MS_50ms_ sum12.fid **Proc:** /MassSamp_50ms/FPH_MS _50ms_sum12/FPH_MS_50ms_ sum12.fid_100lb.ft2	2D ^{13}C–^{13}C DARR	POPC/ POPG/ Chol	Method A; pH 7.0
3–16	**Raw:** /MassSamp_500ms/FPH_ MS_500ms_sum123/FPH_MS_ 500ms_sum123.fid **Proc:** /MassSamp_500ms/FPH_ MS_500ms_sum123/FPH_MS_ 500ms_sum123_100lb.ft2	2D ^{13}C–^{13}C DARR	POPC/ POPG/ Chol	Method A; pH 7.0

Raw and Proc Data Directory:
/home/mb4c/Matt/Organized_Files/PC_PG_Chol_Files/15to1/

Table AIV–2: 400 MHz SSNMR Data of FP–Hairpin at 25:1 Loading

Fig.	File Location	Type of Experiment	Membranes	pH Condition
3–4 & 3–9	**Raw:** /50ms/3Jun09/50ms_POPCPOPGChol /sum_all_3Jun09/3Jun09_sum50ms.fid **Proc:** /50ms/3Jun09/50ms_POPCPOPGChol /sum_all_3Jun09 /3Jun09_sum50ms_200.ft2	2D ^{13}C–^{13}C DARR	POPC/ POPG/ Chol	Method A; pH 7.0
3–5	**Raw:** /500ms/7Jun09_sum1–6 /7Jun09_sum1–6.fid **Proc:** /500ms/7Jun09_sum1–6 /7Jun09_sum1–6_200.ft2	2D ^{13}C–^{13}C DARR	POPC/ POPG/ Chol	Method A; pH 7.0
3–7 & 3–9	**Raw:** /50ms/8Mar09_FPH–50ms–sum123/8Mar09_sum_50ms.fid **Proc:** /50ms/8Mar09_FPH–50ms–sum123/8Mar09_sum_50ms_200.ft2	2D ^{13}C–^{13}C DARR	POPC/ POPG	Method A; pH 7.0
3–8	**Raw:** /500ms/15Jun09_500ms_sum1234 /15Jun09_sum_500ms.fid **Proc:** /500ms/15Jun09_500ms_sum1234/ 15Jun09_sum_500ms_200.ft2	2D ^{13}C–^{13}C DARR	POPC/ POPG	Method A; pH 7.0

Raw and Proc Data Directory for PC/PG/Chol Files:
/home/mb4c/Matt/Organized_Files/PC_PG_Chol_Files/25to1/
Raw and Proc Data Directory for PC/PG Files:
/home/mb4c/Matt/Organized_Files/PC_PG_ Files/25to1/

Table AIV–3: 400 MHz SSNMR Data of FP–Hairpin at 40:1 Loading

Fig.	File Location	Type of Experiment	Membranes	pH Condition
3–2	**Raw:** /12082008_PCPGCHOL/ 50_ms_sample/FPH_50ms_PCPG Chol_sum/FPH_50ms_PCPGChol _sum.fid **Proc:** /12082008_PCPGCHOL/ 50_ms_sample/FPH_50ms_PCPG Chol_sum/FPH_50ms_PCPGChol _sum_200.ft2	2D ^{13}C–^{13}C DARR	DTPC/ DTPG/ Chol	Method A; pH 7.0
3–3	**Raw:** /12082008_PCPGCHOL/ 1000_ms_sample/FPH_1s_sum /FPH_1s_sum.fid **Proc:** /12082008_PCPGCHOL/ 1000_ms_sample/FPH_1s_sum /FPH_1s_sum_200.ft2	2D ^{13}C–^{13}C DARR	DTPC/ DTPG/ Chol	Method A; pH 7.0
3–6	**Raw:** /12142008_PCPG/50_ms_ data/FPH_PCPG_50ms_sum/FPH _PCPG_50ms_sum.fid **Proc:** /12142008_PCPG/50_ms_ data/FPH_PCPG_50ms_sum/FPH _PCPG_50ms_sum_200.ft2	2D ^{13}C–^{13}C DARR	DTPC/ DTPG	Method A; pH 7.0

Raw and Proc Data Directory for PC/PG/Chol Files:
/home/mb4c/Matt/Organized_Files/PC_PG_Chol_Files/40to1/
Raw and Proc Data Directory for PC/PG Files:
/home/mb4c/Matt/Organized_Files/PC_PG_ Files/40to1/

Table AIV–4: 900 MHz SSNMR Data of FP–Hairpin 15:1 loading

Fig.	File Location	Type of Experiment	Membranes	pH Condition
4–1	**Raw:** /2D_Exps/50ms/sum50ms/test.fid **Proc:** /2D_Exps/50ms/sum50ms/ test_100.ft2	2D ^{13}C–^{13}C DARR	POPC/ POPG/ Chol	Method A; pH 7.0
4–2	**Raw:** /2D_Exps/500ms/sum500ms /sumtest3.fid **Proc:** /2D_Exps/500ms/sum500ms /test_100.ft2	2D ^{13}C–^{13}C DARR	POPC/ POPG/ Chol	Method A; pH 7.0
4–5C 4–6C	**Raw:** /900_SenTest/1/test.fid **Proc:** /900_SenTest/1/CP_50.ft2	^{13}C CP	POPC/ POPG/ Chol	Method A; pH 7.0
4–19A	**Raw:** /1D_Exps/Aug2011/1/test.fid **Proc:** /1D_Exps/Aug2011/1/test_100.ft2	^{15}N CP	POPC/ POPG/ Chol	Method A; pH 7.0
AI–10	**Raw:** /2D_Exps/10ms/sum10ms /sum_10ms.fid **Proc:** /2D_Exps/10ms/sum10ms /test_100.ft2	2D ^{13}C–^{13}C DARR	POPC/ POPG/ Chol	Method A; pH 7.0
AI–11	**Raw:** /2D_Exps/50ms/sum50ms /sumtest2.fid **Proc:** /2D_Exps/50ms/sum50ms /test_100.ft2	2D ^{13}C–^{13}C DARR	POPC/ POPG/ Chol	Method A; pH 7.0
AI–12	**Raw:** /2D_Exps/100ms/ sum_100ms/sum_100ms.fid **Proc:** /2D_Exps/100ms/ sum_100ms/test_100.ft2	2D ^{13}C–^{13}C DARR	POPC/ POPG/ Chol	Method A; pH 7.0
AI–13	**Raw:** /2D_Exps/1000ms/ sum_1000ms/sum_1000ms.fid **Proc:** /2D_Exps/1000ms/ sum_1000ms/test_100.ft2	2D ^{13}C–^{13}C DARR	POPC/ POPG/ Chol	Method A; pH 7.0
AI–14	**Raw:** /2D_Exps/50ms/51/test.fid **Proc:** /2D_Exps/50ms/51/ test_100.ft2	2D ^{13}C–^{13}C DARR	POPC/ POPG/ Chol	Method A; pH 7.0
AI-24* to AI-26*	**Raw:** */FPH_15to1/3D_NCACX/35	3D NCACX	POPC/ POPG/ Chol	Method A; pH 7.0

Table AI-4 (cont'd)

Raw and Proc Data Directory:
/home/mb4c/Matt/Organized_Files/900MHz_Data/FPH_15to1/

* = different directory:
/home/mb4c/Matt/Organized_Files/All_900_Data/Mar2011/*
Data was processed in Topspin 3.1 only!

Table AIV–5: 900 MHz SSNMR Data of FP23_DimerD

Fig.	File Location	Type of Experiment	Membranes	pH Condition
4–16	**Raw:** /50ms_Data/sum50ms/sumtest2.fid **Proc:** /50ms_Data/sum50ms/ sumtest2_50ms_100.ft2	2D ^{13}C–^{13}C DARR	LM3	pH 7
4–17	**Raw:** /500ms_Data/sum500ms_Data/ sumtest_1234.fid **Proc:** /500ms_Data/sum500ms_Data /sumtest_1234_200.ft2	2D ^{13}C–^{13}C DARR	LM3	pH 7

Raw and Proc Data Directory:
/home/mb4c/Matt/Organized_Files/900MHz_Data/FP23_DimerD/

Table AIV–6: 900 MHz SSNMR Data of FP–Hairpin for pH 3.0 Prep

Fig.	File Location	Type of Experiment	Membranes	pH Condition
4–9 & 4–21A	**Raw:** /1D_Exps/280/test.fid **Proc:** /1D_Exps/280/test_100.ft2	^{13}C CP	POPC/ POPG/ Chol	Method B; pH 3.0
4–19B	**Raw:** /1D_Exps/281/test.fid **Proc:** /1D_Exps/281/test_100.ft2	^{15}N CP	POPC/ POPG/ Chol	Method B; pH 3.0
4–21B	**Raw:** /1D_Exps/283/test.fid **Proc:** /1D_Exps/283/test_100.ft2	1D NCA DCP	POPC/ POPG/ Chol	Method B; pH 3.0
4–10	**Raw:** /2D_Exps/50ms/ sum2_50ms/testsum292293.fid **Proc:** /2D_Exps/50ms/ sum2_50ms/sum2_100.ft2	2D ^{13}C–^{13}C DARR	POPC/ POPG/ Chol	Method B; pH 3.0
4–11	**Raw:** /2D_Exps/500ms/sum500ms /sumtest5A.fid **Proc:** /2D_Exps/500ms/sum500ms /test_200.ft2	2D ^{13}C–^{13}C DARR	POPC/ POPG/ Chol	Method B; pH 3.0
AI–18	**Raw:** /2D_Exps/2D_NCA/311314/test.fid **Proc:** /2D_Exps/2D_NCA/311314 /test _300.ft2	2D NCA	POPC/ POPG/ Chol	Method B; pH 3.0

Raw and Proc Data Directory:
/home/mb4c/Matt/Organized_Files/900MHz_Data/lowpH/

Table AIV–7: 900 MHz SSNMR Data of FP–Hairpin pH 3.0 Prep Swapped to pH 7.0

Fig.	File Location	Type of Experiment	Membranes	pH Condition
4–12	**Raw:** /1D_Exps/325/test.fid **Proc:** /1D_Exps/325/test_100.ft2	^{13}C CP	POPC/ POPG/ Chol	pH 7.0
4–13	**Raw:** /2D_Exps/50ms/sum50ms/ sumtest2.fid **Proc:** /2D_Exps/50ms/sum50ms/ test_100.ft2	2D ^{13}C–^{13}C DARR	POPC/ POPG/ Chol	pH 7.0
4–14	**Raw:** /2D_Exps/500ms/sum500ms /sumtest5A.fid **Proc:** /2D_Exps/500ms/sum500ms /test_200.ft2	2D ^{13}C–^{13}C DARR	POPC/ POPG/ Chol	pH 7.0

Raw and Proc Data Directory:
/home/mb4c/Matt/Organized_Files/900MHz_Data/highpH/

Table AIV–8: 700 MHz SSNMR Data of FP–Hairpin at 15:1 loading

Fig.	File Location	Type of Experiment	Membranes	pH Condition
4–4	**Raw:** /28/test.fid **Proc:** /28/test_100.ft2	2D ^{13}C–^{13}C PDSD	POPC/ POPG/ Chol	Method A; pH 7.0
4–5B 4–6B	**Raw:** /700MHz_EFree_edit/sum/ sumtest_512.fid **Proc:** /700MHz_EFree_edit/sum/ test_50lb.ft2	^{13}C CP Ramp	POPC/ POPG/ Chol	Method A; pH 7.0

Raw and Proc Data Directory:
/home/mb4c/Matt/Organized_Files/700MHz_Data/700MHz_Proc/
***** Slices extracted from file 28.
***** Figures 4–5B and 4–6B are the result of co–added files 20 and 22, with 256 acquisitions each.

Table AIV–9: 400 MHz DNP Data of FP–Hairpin

Fig.	File Location	Type of Experiment	Membranes	pH Condition
AII–3A	**Raw:** /2/test.fid **Proc:** /2/test_100.ft2	^{13}C CP Ramp	POPC/ POPG/ Chol	Method A; 7.0
AII–3B	**Raw:** /1/test.fid **Proc:** /1/test_100.ft2	^{13}C CP Ramp	POPC/ POPG/ Chol	Method A; 7.0
AII–4A	**Raw:** /23/pdata/1/***** **Proc:** /23/pdata/1/*****	2D ^{13}C–^{13}C DARR	POPC/ POPG/ Chol	Method A; 7.0
AII–5A	**Raw:** /22/pdata/1/***** **Proc:** /22/pdata/1/*****	2D ^{13}C–^{13}C DARR	POPC/ POPG/ Chol	Method A; 7.0
AII–6A	**Raw:** /21/pdata/1/***** **Proc:** /21/pdata/1/*****	2D ^{13}C–^{13}C DARR	POPC/ POPG/ Chol	Method A; 7.0

Raw and Proc Data Directory:
/home/mb4c/Matt/Organized_Files/DNP/
***Note:** The 2D data sets are not compatible with nmrPipe that is currently installed. Processing was all done in Topspin for those files.

Table AIV–10: 900 MHz SSNMR Data for U–NAL

Fig.	File Location	Type of Experiment	Membranes	pH Condition
4–20B	**Raw:** /16/test.fid **Proc:** /16/test_50.ft2	1D NCO	–	–
4–20C	**Raw:** /13/test.fid **Proc:** /13/test_50.ft2	^{13}C CP	–	–
4–20D	**Raw:** /15/test.fid **Proc:** /15/test_50.ft2	1D NCA	–	–
AI–9	**Raw:** /14/test.fid **Proc:** /14/test_0.ft2	^{15}N CP	–	–
AI–16	**Raw:** /2D_Exps/174/test.fid **Proc:** /2D_Exps/174/test_25.ft2	2D NCA	–	–
AI–17	**Raw:** /2D_Exps/175/test.fid **Proc:** /2D_Exps/175/test_25.ft2	2D NCO	–	–
AI-21 * to AI-23*	**Raw:** /2D_Exps/175/test.fid **Proc:** /2D_Exps/175/test_25.ft2	3D Exp.	–	–

Raw and Proc Data Directory:
/home/mb4c/Matt/Organized_Files/900MHz_Data/UNAL/

* = different directory:
/home/mb4c/Matt/Organized_Files/All_900_Data/Mar2011/U-NAL/3D_NCACX/25
Data was processed in Topspin 3.1 only!

Directory of all 900 MHz NMR Data not listed here. Located on computer at 900 MHz NMR.
Master List of All solid state NMR Data for 900 MHz NMR
Dates: 12/2009 – 8/2011

Table AIV–11: Dec2009 Data for FPH_UA6UG10_MassiveSample acquired at the 900 MHz NMR facility.

Exp. #	Type	Information	Junk or Good?
1	cp90	13C – FPH MS UA6/UG10, T=250K, MAS = 12kHz, ns=512, 12/4/09	G
2	cp90	15N – FPH MS UA6/UG10, T=250K, MAS = 12kHz, ns=512	J
3	cp90	15N – FPH MS UA6/UG10, T=250K, MAS = 12kHz, ns=512	G
4	cp90	15N – FPH MS UA6/UG10, T=250K, MAS = 12kHz, ns=512	G
5	doubcp.av.jos	1D NCA experiment of FPH MS UA6/UG10, o1p = 50 ppm, T=250K, MAS = 12 kHz, ns=512	G
6	doubcp.av.jos	1D NCA experiment of FPH MS UA6/UG10, o1p = 50 ppm, T=250K, MAS = 12 kHz, ns=4096	G
7	cpredorxy8i.av.jos	2D REDOR of FPH MS UA6/UG10, not fully processed, T = 250K, MAS = 12 kHz	G / J?
8	doubcp2ddarr.jos	1D NCO experiment of FPH MS UA6UG10, o1p = 165 ppm, ns = 512, T = 250K, MAS = 12 kHz	J
9	doubcp2ddarr.jos	1D NCO experiment of FPH MS UA6UG10, o1p = 165 ppm, ns = 4096, T = 250K, MAS = 12 kHz; there is signal, just how believable though?	J
10	doubcp2ddarr.jos	1D NCA experiment of FPH MS UA6UG10, o1p = 50 ppm, ns = 512, T = 250K, MAS = 12 kHz	G
11	doubcp2ddarr.jos	1D NCA experiment of FPH MS UA6UG10, o1p = 50 ppm, ns = 4096, T = 250K, MAS = 12 kHz	G
12	cpdarr.av.jos	2D 13C–13C of FPH MS UA6/UG10, SSB's cut through the CO since not setup symmetrically. T=250K, MAS = 12 kHz, tau = 50 ms	J
13	cpdarr.av.jos	2D 13C–13C of FPH MS UA6/UG10, SSB's cut through the CO since not setup symmetrically. T=250K, MAS = 12 kHz, tau = 500 ms	J
14	cp90	13C – FPH MS UA6/UG10, ns=512, T=250K, MAS = 12 kHz,	G
15	cp90	13C – FPH MS UA6/UG10, ns=512, T=250K, MAS = 12 kHz, post 2D DARR (50 ms mixing experiment)	G

Table AIV–11 (cont'd)

16	cp90	13C – FPH MS UA6/UG10, ns=512, T=250K, MAS = 12 kHz, post 2D DARR (50 ms mixing experiment), re–tuned	G
17	cpdarr.av.jos	Junk – No Data	J
18	cp90	13C – FPH MS UA6/UG10, ns=128, T=250K, MAS = 12 kHz, optimize pulse delay	G
19	cp90	13C – FPH MS UA6/UG10, ns=128, T=250K, MAS = 12 kHz, optimize pulse delay, 1s delay (d1)	G
20	cp90	15N – FPH MS UA6/UG10 – ns=32, T=250K, MAS = 12 kHz, optimize 15N recycle delay	G
21	cp90	15N – FPH MS UA6/UG10 – ns=32, T=250K, MAS = 12 kHz, optimize 15N recycle delay = 3s	G
22	cpdarr.av.jos	2D 13C–13C of FPH MS UA6/UG10, SSB's cut through the CO since not setup symmetrically. T=250K, MAS = 12 kHz, tau = 50 ms	J
23	cp90	15N – FPH MS UA6/UG10 – ns = 512, T=250K, MAS = 12 kHz,	G
24	cp90	13C – FPH MS UA6/UG10 – T=250K, MAS = 12kHz, d1 = 2s, ns = 256	G
25	cpdarr.av.jos	2D 13C–13C of FPH MS UA6/UG10, SSB's cut through the CO since not setup symmetrically. T=250K, MAS = 12 kHz, tau = 500 ms	J
26	cpdarr.av.jos	No Data	J
27	doubcp2ddarr.jos	1D NCO of FPH MS UA6UG10, T=250K, MAS = 12 kHz, ns = 512,	J
28	doubcp2ddarr.jos	No data	J
29	doubcp2ddarr.jos	No data	J
30	cpdarr.av.jos	2D 13C–13C of FPH MS UA6/UG10, T=250K, MAS = 12 kHz, tau = 50 ms	G
31	cpdarr.av.jos	2D 13C–13C of FPH MS UA6/UG10,. T=250K, MAS = 12 kHz, tau = 500 ms	G
32	cpdarr.av.jos	2D 13C–13C of FPH MS UA6/UG10, T=250K, MAS = 12 kHz, tau = 50 ms	G
33	cpdarr.av.jos	2D 13C–13C of FPH MS UA6/UG10, T=250K, MAS = 12 kHz, tau = 50 ms	G
34	doubcp2ddarr.jos	2D NCA experiment, FPH MS UA6/UG10, o1p = 50 ppm, 15N = 110 ppm	J
35	doubcp2ddarr.jos	No Data	J
36	cp90	13C – FPH MS UA6UG10 – T=250K, MAS = 12 kHz, ns = 256,	G
37	cp90	15N – FPH MS UA6UG10 – T=250K, MAS = 12 kHz, ns = 256	G

Table AIV–11 (cont'd)

38	cpdarr.av.jos	2D 13C–13C of FPH MS UA6/UG10, T=250K, MAS = 12 kHz, tau = 50 ms, ns = 64, SR = (–787.05, –737.89) , 256 slices.	G
39	cpdarr.av.jos	2D 13C–13C of FPH MS UA6/UG10, T=250K, MAS = 12 kHz, tau = 500 ms, ns = 128, SR = (–779.74, –747.70) , 256 slices.	G
40	cpdarr.av.jos	2D 13C–13C of FPH MS UA6/UG10, T=250K, MAS = 12 kHz, tau = 500 ms, ns = 128, SR = (–794.76, –778.03) , 256 slices.	G
41	cp90	13C – FPH MS UA6UG10 – T=250K, MAS = 12 kHz, ns = 128,	G
42	cpdarr.av.jos	2D 13C–13C of FPH MS UA6/UG10, T=250K, MAS = 12 kHz, tau = 500 ms, ns = 128, SR = (–847.98, –815.39) , 256 slices.	G
43	cpdarr.av.jos	2D 13C–13C of FPH MS UA6/UG10, T=250K, MAS = 12 kHz, tau = 50 ms, ns = 64; SR = (–809.34, –786.37), 256 slices.	G
44	cpredxy8.av.jos	1D REDOR of FPH MS UA6UG10, pl3=0 db = N15 pulses ON, ns = 4096. MAS = 12 kHz, T = 250K, Complete Junk.	J
45	doubcp.av.jos	2D NCA experiment of FPH MS UA6UG10, o1p = 50 ppm, T=250K, MAS = 12 kHz, junk?	J
46	doubcp.av.jos	2D NCA experiment of FPH MS UA6UG10, o1p = 50 ppm, T=250K, MAS = 12 kHz, junk?	J
47	cpredorxy8i.av.jos	2D REDOR of FPH MS UA6UG10, T=250K, MAS = 12 kHz, Junk?	J
48	cpredorxy8i.av.jos	2D REDOR of FPH MS UA6UG10, T=250K, MAS = 12 kHz, Junk? Only did the first 2 points so that I got the S0 and S1.	J?
49	cp90	13C – FPH MS UA6UG10, ns = 128, T=250K, MAS=12kHz,	G
50	cpredorxy8i.av.jos	2D REDOR of FPH MS UA6UG10, T=250K, MAS = 12 kHz, Junk?	J?
51	cpdarr.av.jos	2D 13C–13C of FPH MS UA6/UG10, T=250K, MAS = 12 kHz, tau = 50 ms, ns = 64, SR = (–965.27, –954.02), 256 slices.	G

- Co–added experiments: 39, 40, 42. Yields 384 scans for the 2D Experiment. Referenced the Ala $^{13}C\alpha$/Ala$^{13}C\beta$ β–strand peak as 50.5, 23.5 ppm and got back the correct SR value. (500 ms mixing time FPH 15:1 loading sample). Co–added file = 394042.
- Used experiment 51 as the 50 ms mixing time for the FPH 15:1 loading sample.
- Files: 1 (CP90 at 900 MHz) used to compare in sensitivity test to 400 MHz, file 6: 1D NCA with 4k scans.

Table AIV-11 (cont'd)

File locations:
900 Computer:
/opt/topspin216/data/Nethercott/nmr/From_laptop/FPH_UA6UG10_MassiveSample/
Linux computer:
/home/mb4c/Matt/Organized_Files/900MHz_Data/All_900_Data/Dec2009_FPH_15to1
/FPH_UA6UG10_MassiveSample/

Table AIV–12: July 2010 Data at the 900 MHz NMR Facility.

Exp. #	Type	Information	Junk or Good?
1	cp90	13C – adamantane – T= 250K, MAS = 5kHz, ns = 32, 7/7/10	G
2	cp90	13C – adamantane – T= 250K, MAS = 5kHz, ns = 32, 7/7/10	G
3	cp90	13C – gly sample, T = 250K, MAS = 12 kHz, ns = 512	G
4	cp90	15N of glycine, T = 250 K, MAS = 12 kHz	J
5	cp90	13C – gly sample, T = 250K, MAS = 12 kHz, ns = 4096	G
6	cp90	15N of glycine, T = 250 K, MAS = 12 kHz; ns = 4096	G
7	doubcp.av.jos	Glycine Natural abundance, 1D NCA exp. ns = 4096, T = 250 K, MAS = 12 kHz	J
8	doubcp2ddarr.jos	Glycine Natural abundance, 1D NCO exp. ns = 4096, T = 250 K, MAS = 12 kHz	J
9	cp90	13C – adamantane – 7/8/10; T = 250 K, MAS = 12 kHz	G
10	cp90	13C of AMS sample – no 13C signal, T = 250 K, MAS = 12 kHz, ns = 32 – no signal in sample	G / J
11	cp90	15N of AMS sample – T = 250 K, MAS = 12 kHz, ns = 32	G
12	cp90	13C – U–NAL – T = 250K, MAS = 12 kHz, ns = 512	G
13	cp90	15N – U–NAL – T = 250K, MAS = 12 kHz, ns = 512	G
14	doubcp.av.jos	1D NCA experiment on U–NAL; T= 250 K, MAS = 12 kHz, ns = 1024	G
15	doubcp.av.jos	1D NCO experiment on U–NAL; T= 250 K, MAS = 12 kHz, ns = 1024	G
16	doubcp2ddarr.jos	1D NCO experiment on U–NAL; T= 250 K, MAS = 12 kHz, ns = 1024	G

Table AIV–12 (cont'd)

17	cpredorxy8i.av.jos	2D REDOR of U–NAL, T=250K, MAS = 12 kHz. No optimization of anything.	J?
18	cpredxy8.av.jos	1D REDOR of U–NAL with N15 pulses. L0 = 3 = ~2ms dephasing time. Ns = 128, MAS = 12 kHz, T = 250 K	G
19	cptoss.av	U–NAL (13C signal), MAS = 12 kHz, T=250K, ns = 32	G?
20	doubcp.av.jos	No Data	J
21	doubcp.av.jos	No Data	J
22	cpredxy8.av.jos	U–NAL, T=250K, MAS = 12kHz, ns = 128; with N15 pulses (S1) (pl3 = 0 dB)	G
23	cpredxy8.av.jos	U–NAL, T=250K, MAS = 12kHz, ns = 128; with no N15 pulses (S0) (pl3= 119dB)	G
24	cp90	13C – adamantane – 7/8/10 – ns = 32, T=250K, MAS = 12 kHz	G
25	cp90	13C – adamantane – 7/8/10 – ns = 32, T=273K, MAS = 12 kHz	G
26	cp90	13C – adamantane – 7/9/10 – ns = 32, T=250K, MAS = 12 kHz	G
27	cp90	No data	J
28	cp90	13C – adamantane – 7/22/10 – ns = 4, T=250K, MAS = 12 kHz	G
29	cp90	13C – adamantane – 7/22/10 – ns = 32, T=250K, MAS = 12 kHz – no signal	J
30	zg	No data	J
31	cp90	13C – adamantane – 7/22/10 – ns=32, MAS = 12 kHz, T=250K – starting conditions prior to shimming	G
32	cp90	13C – adamantane – 7/22/10 – ns=32, MAS = 12 kHz, T=250K – post shimming	G
33	cp90	13C – adamantane – 7/22/10 – ns=32, MAS = 12 kHz, T=250K – post shimming, changing field so that SR = 0	G
34	cp90	15N CP of AMS, T=250K, MAS = 12 kHz, 7/22/10, ns = 32	G
35	cp90	15N – AMS – ns = 32, T=250K, MAS = 12kHz	G
36	zg	Testing out MAS on 7/23/10, ns=1, MAS = 6kHz, T=250K	G
37	cp90	13C – adamantane – T=250K, MAS = 12 kHz, post re–insertion of probe. 1150am on 7/23/10; ns=32	G
38	cp90	13C – FPH MS UA6/UG10 – ns=256; T=250K, MAS = 12kHz	G
39	cp90	15N CP of FPH MS UA6UG10, ns = 256 MAS = 12 kHz, T=250 K	J

Table AIV–12 (cont'd)

40	cp90	15N CP of FPH MS UA6UG10, ns = 256 MAS = 12 kHz, T=250 K	G
41	cp90	15N CP of FPH MS UA6UG10, ns = 512, MAS = 12 kHz, T=250 K	G
42	cp90	13C – FPH MS UA6/UG10 – ns=256; T=250K, MAS = 12kHz	G
43	doubcp.av.jos	1D NCA of FPH MS UA6/UG10; MAS = 12 kHz, T=250 K; ns = 4096	G
44	cp90	13C – adamantane – MAS = 12 kHz, T=250 K, ns=8	G
45	cp90	13C – adamantane – MAS = 12 kHz, T=250 K, ns=8; trying to optimize	G
46	cp90	13C – adamantane – MAS = 12 kHz, T=250 K, ns=8; trying to optimize	J
47	cp90	Junk	J
48	cp90	13C – adamantane – MAS = 12 kHz, T=250 K, ns=8	G
49	cp90	13C – adamantane – MAS = 12 kHz, T=250 K, ns=8	G
50	cp90	13C – adamantane – MAS = 12 kHz, T=250 K, ns=8	G
51	cp90	13C – adamantane – MAS = 12 kHz, T=250 K, ns=8	G
52	cp90	13C – adamantane – MAS = 12 kHz, T=250 K, ns=8	G
53	cp90	13C – adamantane – MAS = 12 kHz, T=250 K, ns=8; trying to optimize	G
54	cp90	13C – adamantane – MAS = 12 kHz, T=250 K, ns=32; trying to optimize	G
55	cp90	13C – FPH MS UA6/UG10, MAS=12kHz, T=250K, ns=512	G
56	cp90	13C – adamantane – MAS = 12 kHz, T=250 K, ns=8	G
57	cp90	13C – adamantane – MAS = 12 kHz, T=296 K, ns=8; 7/26/10; trying to optimize?	G
58	cp90	13C – adamantane – MAS = 12 kHz, T=296 K, ns=8; 7/26/10; trying to optimize?	G
59	cp90	13C – adamantane – MAS = 12 kHz, T=296 K, ns=8; 7/26/10; trying to optimize?	G
60	cp90	13C – FPH MS UA6/UG10 – T=250K, MAS =12kHz, ns=512	G
61	cp90	15N FPH MS UA6/UG10, T=250K, MAS=12kHz, ns=512	G
62	doubcp.av.jos	1D NCA experiment, FPH MS UA6/UG10, ns=8192 (8k), T=250 K, MAS = 12 kHz	G

Table AIV–12 (cont'd)

63	cpredorxy8i.av.jos	2D REDOR of FPH MS UA6UG10, T=250K, MAS = 12kHz. Not very impressive of data.	G / J?
64	cpdarr.av.jos	13C – 13C 2D experiment with DARR mixing, tau = 50 ms, FPH MS UA6UG10, T=250K, MAS = 12 kHz	G
65	cpdarr.av.jos	13C – 13C 2D experiment with DARR mixing, tau = 500 ms, FPH MS UA6UG10, T=250K, MAS = 12 kHz	G
66	cp90	13C – FPH MS UA6/UG10 – ns=512, T=250K, MAS = 12 kHz,	G
67	cp90	13C – adamantane – ns=32, T=250K, MAS = 12 kHz	G
68	cp90	13C – U–NAL,. T=250 K, MAS = 12kHz, ns=32	G
69	cp90	13C – U–NAL,. T=250 K, MAS = 12kHz, ns=512	G
70	cp90	15N – UNAL – T=250K, MAS = 12kHz, ns= 512	G
71	doubcp.av.jos	1D NCA of U–NAL, T=250K, MAS = 12 kHz, ns = 512	G
72	doubcp.av.jos	1D NCA of U–NAL, T=250K, MAS = 12 kHz, ns = 4096	G
73	doubcp.av.jos	1D NCO of U–NAL, T=250K, MAS = 12 kHz, ns = 512	G
74	doubcp.av.jos	1D NCA of U–NAL, T=250K, MAS = 12 kHz, ns = 4096	G
75	cpredorxy8i.av.jos	2D REDOR of U–NAL, T=250K, MAS = 12kHz	G / J?
76	cpredorxy8i.av.jos	2D REDOR of U–NAL, T=250K, MAS = 12kHz	G / J?
77	cpredorxy8i.av.jos	2D REDOR of U–NAL, T=250K, MAS = 12kHz	G / J?
78	cpredorxy8i.av.jos	2D REDOR of U–NAL, T=250K, MAS = 12kHz	G / J?
79	cpredorxy8i.av.jos	2D REDOR of U–NAL, T=250K, MAS = 12kHz	G / J?
80	cp90	13C – adamantane – T=250K, MAS = 12 kHz, ns=32	G
81	cp90	13C of Fgp41, T=250K, MAS = 12kHz, ns = 32; 7/29/10	G
82	cp90	13C of Fgp41, T=250K, MAS = 12kHz, ns = 512, 7/29/10	G
83	cp90	15N of Fgp41, T=250K, MAS = 12kHz, ns = 512, 7/29/10	G
84	doubcp.av.jos	1D NCA experiment, Erica's Fgp41, o1p = 50 ppm, ns=512, T=250K, MAS=12kHz	J
85	doubcp.av.jos	1D NCO experiment, Erica's Fgp41, o1p = 165 ppm, ns=512, T=250K, MAS=12kHz	J
86	doubcp.av.jos	1D NCO experiment, Erica's Fgp41, o1p = 165 ppm, ns=4096, T=250K, MAS=12kHz	J

Table AIV–12 (cont'd)

87	cpredorxy8i.av.jos	2D REDOR of Erica's Fgp41 sample, T=250K, MAS=12kHz,	G / J?
88	cpredorxy8i.av.jos	2D REDOR of Erica's Fgp41 sample, T=250K, MAS=12kHz,	G / J?
89	cpredorxy8i.av.jos	2D REDOR of Erica's Fgp41 sample, T=250K, MAS=12kHz,	G / J?
90	cpredorxy8i.av.jos	2D REDOR of Erica's Fgp41 sample, T=250K, MAS=12kHz,	G / J?
91	cpredorxy8i.av.jos	2D REDOR of Erica's Fgp41 sample, T=250K, MAS=12kHz,	G / J?
92	cp90	13C – adamantane – T= ~270K, MAS=12kHz, ns=32	G
93	cp90	13C – adamantane – T= ~270K, MAS=12kHz, ns=32	J

Summary of this work: Multiple issues arose during the time at the 900 MHz NMR facility including the "Bird Rack Flush Error" and having to swap out parts to determine the source of the error messages. This prevented us from getting anything meaningful really accomplished.

File locations:
900 Computer: /opt/topspin216/data/Nethercott/nmr/July2010/
Linux computer: /home/mb4c/Matt/Organized_Files/900MHz_Data/All_900_Data/July2010/

Table AIV–13: Jan. 2011 + Feb. 2011 data at the 900 MHz NMR Facility: Adamantane files.

Exp. #	Type	Information	Junk or Good?
3	cp90	13C of adamantane – 1/5/11	G
4	cp90	13C of adamantane	G
5	cp90	13C of adamantane	G
6	cp90	13C of adamantane – test of parameters from 12/4/09	J
7	cp90	13C of adamantane	J
8	cp90	13C of adamantane	G
9	cp90	Attempt to calibrate 1H	J
10	cp	13C of adamantane	G
11	cp	13C of adamantane	G
12	cp90	13C of adamantane	G
32	cp90	13C adamantane – 1/10/2011	G
33	cp90	13C adamantane – 1/10/2011 (Li's learning)	G
47	cp90	13C adamantane; opt of CP conditions	G
48	cp90	13C adamantane; opt of CP conditions	G
49	cp90	13C adamantane;	G
50	cp90	13C adamantane;	G
87	cp90	13C adamantane – 1/14/11	G
93	cp90	13C adamantane – 1/17/11	G
94	cp90	13C adamantane – 1/17/11; popt dB	G
104	cp90	13C adamantane – 1/19/11	G
105	cp90	13C adamantane – 1/19/11; o1p=0 ppm	G
117	cp90	13C adamantane – 1/20/11	G
118	zg	Setup HH conditions on adamantane	J
119	cp90	13C adamantane; ns=8	J?
120	cp90	13C adamantane; ns=2	G?
121	cp90	13C adamantane; ns=2	J
122	cp90	13C adamantane; ns=2; optimizations	G
123	cp90	13C adamantane; ns=2; popt d1	G
124	cp90	13C adamantane; ns=2; popt p1	G?
125	cp90	13C adamantane; ns=2;	G?
126	cp90	13C adamantane; ns=2; setup 13C pi/2 pulse; popt p1	G
127	cp90	13C adamantane; ns=2	G?
128	cp90	13C adamantane; ns=8	G
129	cp.av.jos	13C adamantane; ns=8	G
130	cp.av.jos	13C adamantane; ns=2; popt pl1; popt p3	G?
131	cp.av.jos	13C adamantane; ns=2; post–popt of pl1 and p3	
132	cp.av.jos	13C adamantane; ns=8	G
200	cp90	13C adamantane – 1/22/11	G
228	cp90	13C – adamantane – 1/24/11	G

Table AIV–13 (cont'd)

231	cp90	13C – adamantane – o1p=0ppm	G
243	cp90	13C – adamantane – 1/26/11	G
277	cp90	13C – adamantane – 1/30/11	G
289	cp90	13C – adamantane – 2/1/11	G
294	cp90	13C – adamantane – 2/3/11	G
318	cp90	13C – adamantane – 2/7/11	G
324	cp90	13C – adamantane 2/9/11	G
334	cp90	13C – adamantane 2/12/11	G
343	cp90	13C – adamantane 2/14/11	G

File locations:
900 Computer: /opt/topspin216/data/Nethercott/nmr/Jan2011/
Linux computer:
/home/mb4c/Matt/Organized_Files/900MHz_Data/All_900_Data/Jan2011/Adamantane

Table AIV–14: Jan. 2011 + Feb. 2011 data at the 900 MHz NMR Facility: AMS, Glycine and KBr

Exp. #	Type	Information	Junk or Good?
Folder: Ammonium Sulfate (AMS)			
244	Cp90	15N CP AMS sample; ns=32; T=250K	G
Folder: Natural Abundance Glycine (Glycine)			
133	cp.av.jos	13C Glycine; ns=8; popt o2	G
134	cp.av.jos	13C Glycine; ns=4	G
135	cp90	13C Glycine; ns=2	G
136	cp90	13C glycine; ns=2; popt p3	G
137	cp90	13C glycine; ns=2; optimize	G
138	cp90	13C glycine; ns=2; popt p15	G
139	cp90	13C glycine; ns=8	G
140	cp90	15N CP glycine; ns=8	J
Folder: Potassium Bromide (KBr)			
1	zg	1/5/11 – KBr to test angle of E-free	G
2	zg	Adjustment of angle	G

File locations:
900 Computer: /opt/topspin216/data/Nethercott/nmr/Jan2011/
Linux computer: /home/mb4c/Matt/Organized_Files/900MHz_Data/All_900_Data/Jan2011/

Table AIV–15: Jan. 2011 + Feb. 2011 data at the 900 MHz NMR Facility U–NAL

Exp. #	Type	Information	Junk or Good?
1D_13C_CP			
40	cp90	13C U–NAL; ns=512; 1/11/11	G
43	cp90	13C U–NAL; ns=8	G
44	hpdec	13C U–NAL; ns=4	J
45	cp90	13C U–NAL; ns=8	J
46	cp90	13C U–NAL; ns=4 (pre–opt)	G
51	cp90	13C U–NAL; ns=32; 1/11/11	G
52	cp90	13C U–NAL; ns=512; 1/11/11	G
53	cp90	13C U–NAL; ns=512; rga, ran again 1/11/11	G
106	cp90	13C of U–NAL; pre–opt; ns=512	G
116	cp90	13C U–NAL; pre–opt (1/20/11); ns=8; T=250K	G
141	cp90	13C U–NAL; ns=8; pre–opt	G
143	cp90	13C U–NAL; ns=2; attempt to opt. optimize: p3, pl12, p1, p15.	G
149	cp90	13C U–NAL; ns=2; popt d1	G
150	cp90	13C U–NAL; ns=2; popt pl2	G
151	cp90	13C U–NAL; ns=8; best of all parameters	G
157	cp90	13C U–NAL; best of parameters; ns=512; T=250K	G
182	cp90	13C U–NAL, best conditions for setting up REDOR	G
184	cp90	13C U–NAL, popt pl11 for REDOR	G
185	cp90	13C U–NAL, popt p1 for REDOR	G
186	cp90	13C U–NAL, best parameters, ns=512	G
218	cp90	13C U–NAL; ns=8; T=250K	G
1D_15N_CP			
41	cp90	15N U–NAL; ns=512	G
54	cp90	15N CP U–NAL; optimization of CP	G
79	cp90	15N CP U–NAL; ns=32; pre–opt	J
80	cp90	15N CP U–NAL; ns=32; pre–opt	J
107	cp90	15N CP of U–NAL; ns=512; T=250K	G
142	cp90	15N U–NAL; ns=8	G
144	cp90	15N U–NAL; ns=2; optimize: p3 and pl2	G
145	cp90	15N U–NAL; ns=2; optimize p1 and pl1	G
146	cp90	15N U–NAL; ns=2; optimize p15	G
147	cp90	15N U–NAL; ns=2; optimize d1	G
148	cp90	15N U–NAL; ns=8; best of all parameters	G
158	cp90	15N CP U–NAL; best of parameters; ns=512; T=250K	G

Table AIV–15 (cont'd)

183	cp90	15N CP U–NAL, best conditions for setting up REDOR	G
1D_DCP_NCA			
42	doubcp.av.jos	1D NCA U–NAL; ns=256	J
55	doubcp.av.jos	1D NCA; U–NAL; ns=32; o1p=50 ppm	G
56	doubcp.av.jos	1D NCA; U–NAL; ns=32; o1p=150 ppm	J
57	doubcp.av.jos	1D NCA; U–NAL; ns=256; o1p=50 ppm	G
58	doubcp.av.jos	1D NCA; U–NAL; ns=32; o1p=50 ppm	G
60	doubcp2ddarr.jos	1D NCA; U–NAL; ns=32; 01p=50 ppm	G
108	doubcp.av.jos	1D NCA of U–NAL; T=250K; ns=512;	G
109	doubcp2ddarr.jos	1D NCA of U–NAL; T=250K; ns=512;	G
152	doubcp.av.jos	1D NCA U–NAL; ns=8; starting parameters	G
153	doubcp.av.jos	1D NCA U–NAL; ns=8; optimize pl2, p15, pl5, p16, pl1, pl13, d1	G
154	doubcp.av.jos	1D NCA U–NAL; ns=8; best of all parameters	G
159	doubcp.av.jos	1D NCA U–NAL, best of parameters; ns=512; T=250K	G
166	doubcp2ddarr.jos	1D NCA U–NAL, prior to opt. ns=8	G
167	doubcp2ddarr.jos	1D NCA U–NAL, prior to opt. ns=8; optimize: pl12, pl11	G
168	doubcp2ddarr.jos	1D NCA U–NAL, best parameters ns=8	G
177	doubcp2ddarr.jos	1D NCA U–NAL, ns=512; best parameters	G
222	doubcp.av.jos	1D NCA U–NAL; ns=8; T=250K;	G
1D_DCP_NCO			
59	doubcp2ddarr.jos	1D NCO; U–NAL; ns=32; 01p=165 ppm	G?
110	doubcp2ddarr.jos	1D NCO of U–NAL; T=250K; ns=512;	G
111	doubcp.av.jos	1D NCO of U–NAL; T=250K; ns=512;	G
160	doubcp.av.jos	1D NCO U–NAL, prior to opt. ns=8	J
161	doubcp.av.jos	1D NCO U–NAL, prior to opt. ns=8; edc from #111	J
162	doubcp.av.jos	1D NCO U–NAL, work to optimize	J
163	doubcp.av.jos	1D NCO U–NAL, optimize: pl2, p15, p16, pl1, pl13	G
164	doubcp.av.jos	1D NCO U–NAL, best of all parameters, ns=8	G
165	doubcp.av.jos	1D NCO U–NAL, best of all parameters, ns=512	G
169	doubcp2ddarr.jos	1D NCO U–NAL, trying best parameters from exp. 168 with o1p = 165 ppm	J
170	doubcp2ddarr.jos	1D NCO U–NAL, optimizing pl11; ns=8	G
171	doubcp2ddarr.jos	1D NCO U–NAL, best parameters; ns=8	G
176	doubcp2ddarr.jos	1D NCO U–NAL, ns=512; best parameters	G
223	doubcp.av.jos	1D NCO U–NAL; ns=8; T=250K;	G
1D_REDOR			
178	cpredxy8.av.jos	1D REDOR pl3=0 (N15 pulse), U–NAL, ns=8, prior to opt.	G

Table AIV–15 (cont'd)

179	cpredxy8.av.jos	1D REDOR pl3=120 (N15 pulse), U–NAL, ns=8, prior to opt.	G
180	cpredxy8.av.jos	1D REDOR pl3=0 (N15 pulse), U–NAL, ns=8, attempt to optimize	G
181	cpredxy8.av.jos	1D REDOR U–NAL, with N15 pulse, optimization: pl1, pl3, pl12, pl1, pl3, pl2, p15, pl11, p2	G
187	cpredxy8.av.jos	1D REDOR, U–NAL, ns=16, pl3=0dB; prior to opt.; N15 pulse	G
188	cpredxy8.av.jos	1D REDOR, U–NAL, ns=16, pl3=120dB; prior to opt.; no N15 pulse	G
189	cpredxy8.av.jos	1D REDOR, U–NAL, ns=8, pl3=0dB; prior to opt.; N15 pulse	G
190	cpredxy8.av.jos	1D REDOR, U–NAL, ns=8, pl3=120dB; no N15 pulse; optimization of pl1, pl12, pl2, p15, pl11	G
191	cpredxy8.av.jos	1D REDOR, U–NAL, ns=8, pl3=120dB; best parameters.; no N15 pulse	G
192	cpredxy8.av.jos	1D REDOR, U–NAL, ns=16, pl3=120dB; best parameters.; no N15 pulse	G
193	cpredxy8.av.jos	1D REDOR, U–NAL, ns=16, pl3=0dB; best parameters from 192 prior to opt. of N15; N15 pulse	G
194	cpredxy8.av.jos	1D REDOR, U–NAL, ns=8, pl3=0dB; best parameters from 192 prior to opt. of N15; N15 pulse; popt pl3	G
195	cpredxy8.av.jos	1D REDOR, U–NAL, ns=64, pl3=0dB; best parameters from 192, now N15 opt is done; N15 pulse	G
196	cpredxy8.av.jos	1D REDOR, U–NAL, ns=16, pl3=0 dB = N15 pulse, l0=21 (for dephasing)	G
197	cpredxy8.av.jos	1D REDOR, U–NAL, ns=16, pl3=120 dB = no N15 pulse, l0=21 (for dephasing)	G
198	cpredxy8.av.jos	1D REDOR, U–NAL, ns=64, pl3=0 dB = N15 pulse, l0=3 (for dephasing)	G
199	cpredxy8.av.jos	1D REDOR, U–NAL, ns=64, pl3=120 dB = no N15 pulse, l0=3 (for dephasing)	G
219	cpredxy8.av.jos	1D REDOR, U–NAL; ns=8; pl3=0 dB (N15 pulses); l0=3 → 2ms dephasing; T=250K	G
220	cpredxy8.av.jos	1D REDOR, U–NAL; ns=8; pl3=120 dB (no N15 pulses); l0=3 → 2ms dephasing; T=250K	G
221	cpredxy8.av.jos	1D REDOR U–NAL; opt. pl3 (N15 powerlevel); ns=8	G
2D_13C–13C			
63	cpdarr	13C–13C U–NAL; tau=10ms	G?
155	cpdarr	13C–13C U–NAL; prior to optimization	G

Table AIV–15 (cont'd)

156	cpdarr	13C–13C U–NAL; post optimization, done by putting in best parameters from 13C CP ramp	G
2D_NCA			
62	doubcp	2D NCA experiment – don't work	J
64	doubcp2ddarr.jos	2D NCA exp. U–NAL	G
113	doubcp2ddarr.jos	2D NCA of U–NAL; T=250K	G
114	doubcp2ddarr.jos	2D NCA of U–NAL; T=250K	G?
115	doubcp2ddarr.jos	2D NCA of U–NAL; T=250K	G
172	doubcp.av.jos	2D NCA U–NAL, ns=32; best from 1D experiment	J
174	doubcp2ddarr.jos	2D NCA U–NAL, used best parameters from 1D experiment	G
2D_NCO			
61	doubcp	2D NCO experiment – don't work	J
173	doubcp.av.jos	2D NCO U–NAL, ns=32; best from 1D experiment	J
175	doubcp2ddarr.jos	2D NCO U–NAL, used best parameters from 1D experiment	G
2D_REDOR			
224	cpredorxy8i.av.jos	2D REDOR U–NAL; T=250K; prior to optimization	J?
225	cpredorxy8i.av.jos	2D REDOR U–NAL; T=250K; attempt to optimize	J
226	cpredorxy8i.av.jos	2D REDOR U–NAL; T=250K; trying to understand XY loops	J
227	cpredorxy8i.av.jos	2D REDOR U–NAL; T=250K; trying to figure out if this will give max dephasing of 10 ms?	J?
3D_NCACX			
112	doubcp3d.jos	3D N–CA–CX of U–NAL; T=250K	Unk.

File locations:
900 Computer: /opt/topspin216/data/Nethercott/nmr/Jan2011/
Linux computer: /home/mb4c/Matt/Organized_Files/900MHz_Data/All_900_Data/Jan2011/U–NAL/

Table AIV–16: FP–Hairpin UA6/UG10 experiments from Jan and February 2011 at ~15:1 lipid to protein loading.

Exp. #	Type	Information	Junk or Good?
1D_13C_CP			
13	cp90	13C FPH–MS–UA6/UG10; T=250K, ns=512	G
17	cp90	13C FPH–MS–UA6/UG10; T=250K, ns=16	G
19	cp90	13C FPH–MS–UA6/UG10; T=250K, ns=64	G
20	cp90	13C FPH–MS–UA6/UG10; T=250K, ns=256	G
21	cp90	13C FPH–MS–UA6/UG10; T=250K, ns=512	G
22	cp90	13C FPH–MS–UA6/UG10; T=250K, ns=512	G
23	cp90	13C FPH–MS–UA6/UG10; T=250K, ns=256	G
24	cp90	13C FPH–MS–UA6/UG10; T=250K, ns=128	G
39	cp90	13C FPH–MS–UA6/UG10; T=250K, ns=4k	G
65	cp90	13C FPH–MS–UA6/UG10; T=250K, ns=512	G
71	cp90	13C FPH–MS–UA6/UG10; T=250K; ns=4k	G
76	cp90	13C FPH–MS–UA6/UG10; T=250K; ns=6k	G
92	cp90	13C FPH–MS–UA6/UG10; T=250K; ns=512	G
209	cp90	13C FPH–MS–UA6/UG10; ns=512; T=250K	G
1D_15N_CP			
14	cp90	15N CP of FPH–MS–UA6/UG10	J
18	cp90	15N CP FPH–MS–UA6/UG10;	J
34	cp90	15N CP – FPH–MS–UA6/UG10; T=250, ns=256	G
35	cp90	15N CP – FPH–MS–UA6/UG10; T=250, ns=512	G
36	cp90	15N CP – FPH–MS–UA6/UG10; T=250, ns=1024	G
66	cp90	15N CP FPH–MS–UA6/UG10; T=250K, ns=512	J
74	cp90	15N FPH–MS–UA6/UG10	J
78	cp90	15N CP FPH–MS–UA6/UG10; pre–opt	J
81	cp90	15N CP FPH–MS–UA6/UG10; ns=1k; pre–opt	G
82	cp90	15N CP FPH–MS–UA6/UG10; ns=512; pre–opt	G
83	cp90	15N CP FPH–MS–UA6/UG10; ns=4k; pre–opt	G
210	cp90	15N CP FPH–MS–UA6/UG10; ns=512; T=250K	G
1D_DCP_NCA			
15	doubcp.av.jos	NCA of FPH–MS–UA6/UG10	J
37	doubcp.av.jos	1D NCA FPH–MS–UA6/UG10; ns=4k	J
38	doubcp2ddarr.jos	1D NCA; FPH–MS–UA6/UG10; ns=4k	J
67	doubcp.av.jos	1D NCA; FPH–MS–UA6/UG10; T=250K; ns=512; pre–optimization	J?

Table AIV–16 (cont'd)

68	doubcp2ddarr.jos	1D NCA; FPH–MS–UA6/UG10; T=250K; ns=512; pre–optimization	J?
72	doubcp.av.jos	1D NCA FPH–MS–UA6/UG10; T=250K; ns=4k; pre–optimization	G
73	doubcp2ddarr.jos	1D NCA FPH–MS–UA6/UG10; T=250K; ns=4k; pre–optimization	G
75	doubcp.av.jos	1D NCA FPH–MS–UA6/UG10; T=250K; ns=6k; pre–opt	G?
77	doubcp2ddarr.jos	1D NCA; FPH–MS–UA6/UG10; T=250K; ns=6k; pre–opt	G?
211	doubcp.av.jos	1D NCA FPH–MS–UA6/UG10; ns=512; T=250K	G
212	doubcp.av.jos	1D NCA FPH–MS–UA6/UG10; ns=4k; T=250K	G
1D_REDOR			
213	cpredxy8.av.jos	1D REDOR FPH–MS–UA6/UG10; ns=4k; pl3=120 dB (no N15 pulse); l0=3 → 2ms dephasing	G
214	cpredxy8.av.jos	1D REDOR FPH–MS–UA6/UG10; ns=4k; pl3=0 dB (N15 pulse); l0=3 → 2ms dephasing	G
215	cpredxy8.av.jos	1D REDOR FPH–MS–UA6/UG10; ns=4k; pl3=120 dB (no N15 pulse); l0=21 → ~16ms dephasing	G
216	cpredxy8.av.jos	1D REDOR FPH–MS–UA6/UG10; ns=4k; pl3=0 dB (N15 pulse); l0=21 → 16ms dephasing	G
2D_DARR_10ms			
25	cpdarr	13C–13C FPH–MS–UA6/UG10; tau=10ms	G
30	cpdarr	13C–13C FPH–MS–UA6/UG10; tau=10ms	G
2D_DARR_50ms			
16	cpdarr	13C–13C of FPH–MS–UA6/UG10; tau=50ms	G
217	cpdarr	13C–13C; FPH–MS–UA6/UG10; tau=50ms; T=250K	G
2D_DARR_100ms			
26	cpdarr	13C–13C FPH–MS–UA6/UG10; tau=100ms	G
31	cpdarr	13C–13C FPH–MS–UA6/UG10; tau=100ms	G
2D_DARR_1000ms			
27	cpdarr	13C–13C FPH–MS–UA6/UG10; tau=1000ms	G
28	cpdarr	13C–13C FPH–MS–UA6/UG10; tau=1000ms	G
29	cpdarr	13C–13C FPH–MS–UA6/UG10; tau=1000ms	G
2D_NCA			
69	doubcp2ddarr.jos	2D NCA; FPH–MS–UA6/UG10; T=250K; pre–optimization	J?
70	doubcp2ddarr.jos	2D NCA; FPH–MS–UA6/UG10; T=250K; pre–optimization	J?
91	doubcp2ddarr.jos	2D NCA; FPH–MS–UA6/UG10; pre–opt	G?

Table AIV–16 (cont'd)

2D_REDOR			
86	cpredorxy8i.av.jos	2D REDOR (HCN) FPH–MS–UA6/UG10	J
3D_NCACX			
84	doubcp3d.jos	3D N–CA–Cx; FPH–MS–UA6/UG10; pre–opt; process still?	Unk.
85	doubcp3d.jos	3D N–CA–Cx; FPH–MS–UA6/UG10; pre–opt; process still?	Unk.
88	doubcp3d.jos	3D N–CA–Cx; FPH–MS–UA6/UG10; pre–opt; process still?	Unk.
89	doubcp3d.jos	3D N–CA–Cx; FPH–MS–UA6/UG10; pre–opt; process still?	Unk.
90	doubcp3d.jos	3D N–CA–Cx; FPH–MS–UA6/UG10; pre–opt; process still?	Unk.

File locations:
900 Computer: /opt/topspin216/data/Nethercott/nmr/Jan2011/
Linux computer: /home/mb4c/Matt/Organized_Files/900MHz_Data/All_900_Data/Jan2011/FPH_UA6UG10_Jan+Feb2011/FPH_15to1/

Table AIV–17: FP–Hairpin UA6/UG10 experiments from Jan and February 2011 at ~33:1 lipid to protein loading pH 3 (low pH sample)

Exp. #	Type	Information	Junk or Good?
1D_13C_CP			
278	cp90	13C FPH–UA6/UG10– pH 3.0 prep (1.11 µmole); ns=512; T=250K	G
280	cp90	13C FPH–UA6/UG10– pH 3.0 prep (1.11 µmole); ns=4k; T=250K	G
288	cp90	13C FPH–UA6/UG10– pH 3.0 prep (1.11 µmole); ns=256; T=250K	G
310	cp90	13C FPH–UA6/UG10– pH 3.0 prep (1.11 µmole); ns=256; T=250K	G
1D_15N_CP			
279	cp90	15N CP FPH–UA6/UG10– pH 3.0 prep (1.11 µmole); ns=512; T=250K	G
281	cp90	15N CP FPH–UA6/UG10– pH 3.0 prep (1.11 µmole); ns=4k; T=250K	G
287	cp90	15N CP FPH–UA6/UG10– pH 3.0 prep (1.11 µmole); ns=256; T=250K	G
1D_NCA			
282	doubcp.av.jos	1D NCA FPH–UA6/UG10– pH 3.0 prep (1.11 µmole); ns=512; T=250K	G
283	doubcp.av.jos	1D NCA FPH–UA6/UG10– pH 3.0 prep (1.11 µmole); ns=4k; T=250K	G
2D_DARR_50ms			
284	cpdarr	13C–13C FPH–UA6/UG10– pH 3.0 prep (1.11 µmole); tau=50 ms; T=250K	G
292	cpdarr	13C–13C FPH–UA6/UG10– pH 3.0 prep (1.11 µmole); tau=50 ms; T=250K	G
293	cpdarr	13C–13C FPH–UA6/UG10– pH 3.0 prep (1.11 µmole); tau=50 ms; T=250K	G
2D_DARR_500ms			
285	cpdarr	13C–13C FPH–UA6/UG10– pH 3.0 prep (1.11 µmole); tau=500 ms; T=250K	G
286	cpdarr	13C–13C FPH–UA6/UG10– pH 3.0 prep (1.11 µmole); tau=500 ms; T=250K	G
290	cpdarr	13C–13C FPH–UA6/UG10– pH 3.0 prep (1.11 µmole); tau=500 ms; T=250K	G
291	cpdarr	13C–13C FPH–UA6/UG10– pH 3.0 prep (1.11 µmole); tau=500 ms; T=250K	G

Table AIV–17 (cont'd)

319	cpdarr	13C–13C FPH–UA6/UG10– pH 3.0 prep (1.11 μmole); tau=500 ms; T=250K (2/7/11)	G
2D_NCA			
311	doubcp2ddarr.jos	2D NCA FPH–UA6/UG10– pH 3.0 prep (1.11 μmole); T=250K; mix = 5 ms	G
312	doubcp2ddarr.jos	2D NCA FPH–UA6/UG10– pH 3.0 prep (1.11 μmole); T=250K; mix = 50 ms	G
313	doubcp2ddarr.jos	2D NCA FPH–UA6/UG10– pH 3.0 prep (1.11 μmole); T=250K; mix = 500 ms	G
314	doubcp2ddarr.jos	2D NCA FPH–UA6/UG10– pH 3.0 prep (1.11 μmole); T=250K; mix = 5 ms	G
315	doubcp2ddarr.jos	2D NCA FPH–UA6/UG10– pH 3.0 prep (1.11 μmole); T=250K; mix = 5 ms; NO DATA! Did not collect here yet.	J
REDOR			
316	cpredxy8.av.jos	1D REDOR FPH–UA6/UG10– pH 3.0 prep (1.11 μmole); T=250K; ns=8k; pl3=0 dB (N15 pulses); l0=3 → ~2ms dephasing; 2/6/11	G
317	cpredxy8.av.jos	1D REDOR FPH–UA6/UG10– pH 3.0 prep (1.11 μmole); T=250K; ns=8k; pl3=120 dB (no N15 pulses); l0=3 → ~2ms dephasing; 2/6/11	G

File locations:
900 Computer: /opt/topspin216/data/Nethercott/nmr/Jan2011/
Linux computer: /home/mb4c/Matt/Organized_Files/900MHz_Data/All_900_Data/Jan2011/FPH_UA6UG10_Jan+Feb2011/lowpH/

Table AIV–18: FP–Hairpin UA6/UG10 experiments from Jan and February 2011 at ~33:1 lipid to protein loading pH swapped to pH 7 sample (high pH sample)

Exp. #	Type	Information	Junk or Good?
1D_13C_CP			
325	cp90	13C FPH–UA6/UG10; 1.11 µmole, low pH prep swapped to higher pH; ns=256; T=250K	G
1D_15N_CP			
326	cp90	15N CP FPH–UA6/UG10; 1.11 µmole, low pH prep swapped to higher pH; ns=256; T=250K	G
2D_DARR_50ms			
327	cpdarr	13C–13C FPH–UA6/UG10; 1.11 µmole, low pH prep swapped to higher pH; ns=256; T=250K; tau = 50 ms; d1=1.5s	G
328	cpdarr	13C–13C FPH–UA6/UG10; 1.11 µmole, low pH prep swapped to higher pH; ns=256; T=250K; tau = 50 ms; d1=1.5s	G
2D_DARR_500ms			
329	cpdarr	13C–13C FPH–UA6/UG10; 1.11 µmole, low pH prep swapped to higher pH; ns=256; T=250K; tau = 500 ms; d1=1.5s	G
330	cpdarr	13C–13C FPH–UA6/UG10; 1.11 µmole, low pH prep swapped to higher pH; ns=256; T=250K; tau = 500 ms; d1=1.5s	G
331	cpdarr	13C–13C FPH–UA6/UG10; 1.11 µmole, low pH prep swapped to higher pH; ns=256; T=250K; tau = 500 ms; d1=1.5s	G
332	cpdarr	13C–13C FPH–UA6/UG10; 1.11 µmole, low pH prep swapped to higher pH; ns=256; T=250K; tau = 500 ms; d1=1.5s	G
333	cpdarr	13C–13C FPH–UA6/UG10; 1.11 µmole, low pH prep swapped to higher pH; ns=256; T=250K; tau = 500 ms; d1=1.5s	G

File locations:
900 Computer: /opt/topspin216/data/Nethercott/nmr/Jan2011/
Linux computer: /home/mb4c/Matt/Organized_Files/900MHz_Data/All_900_Data/Jan2011/FPH_UA6UG10_Jan+Feb2011/highpH/

Table AIV–19: Scott Schmick's REDOR Data from 900 MHz NMR for V2E Sample.

Exp. #	N15 on NS	Information	Dephasing Time
2_ms			
237	NO N15 2k	1D REDOR Scott's Sample: F8C G13N; V2E; ns=2k; 12kHz rotation; no N15 pulse (pl3=120 dB); l0=3 → 2ms dephasing	2 ms
238	YES N15 2k	1D REDOR Scott's Sample: F8C G13N; V2E; ns=2k; 12kHz rotation; N15 pulse (pl3=0 dB); l0=3 → 2ms dephasing	2 ms
Total	2K S0; 2k S1		2 ms
8_7ms			
245	NO N15 2k	1D REDOR Scott's Sample: F8C G13N; V2E; ns=2k; 12kHz rotation; no N15 pulse (pl3=120 dB); l0=13 → ~8.7 ms dephasing	8.7 ms
246	YES N15 2k	1D REDOR Scott's Sample: F8C G13N; V2E; ns=2k; 12kHz rotation; N15 pulse (pl3=0 dB); l0=13 → ~8.7 ms dephasing	8.7 ms
251	NO N15 2k	1D REDOR Scott's Sample: F8C G13N; V2E; ns=2k; 12kHz rotation; no N15 pulse (pl3=120 dB); l0=13 → ~8.7 ms dephasing	8.7 ms
252	YES N15 2k	1D REDOR Scott's Sample: F8C G13N; V2E; ns=2k; 12kHz rotation; N15 pulse (pl3=0 dB); l0=13 → ~8.7 ms dephasing	8.7 ms
Total	4K S0; 4k S1	245–200; 246–200 = summations	8.7 ms
16_6ms			
239	NO N15 4k	1D REDOR Scott's Sample: F8C G13N; V2E; ns=4k; 12kHz rotation; no N15 pulse (pl3=120 dB); l0=25 → ~16.6 ms dephasing	16.6 ms
240	YES N15 4k	1D REDOR Scott's Sample: F8C G13N; V2E; ns=4k; 12kHz rotation; N15 pulse (pl3=0 dB); l0=25 → ~16.6 ms dephasing	16.6 ms
241	NO N15 6k	1D REDOR Scott's Sample: F8C G13N; V2E; ns=6k; 12kHz rotation; no N15 pulse (pl3=120 dB); l0=25 → ~16.6 ms dephasing	16.6 ms
242	YES N15 6k	1D REDOR Scott's Sample: F8C G13N; V2E; ns=6k; 12kHz rotation; N15 pulse (pl3=0 dB); l0=25 → ~16.6 ms dephasing	16.6 ms
Total	10k S0; 10k S1	239–200; 240–200 = summations	16.6 ms

Table AIV–19 (cont'd)

24_7ms			
247	NO N15 4k	1D REDOR Scott's Sample: F8C G13N; V2E; ns=4k; 12kHz rotation; no N15 pulse (pl3=120 dB); l0=37 → ~24.7 ms dephasing	24.7 ms
248	YES N15 4k	1D REDOR Scott's Sample: F8C G13N; V2E; ns=4k; 12kHz rotation; N15 pulse (pl3=0 dB); l0=37 → ~24.7 ms dephasing	24.7 ms
320	NO N15 6k	1D REDOR Scott's Sample: F8C G13N; V2E; ns=6k; 12kHz rotation; no N15 pulse (pl3=120 dB); l0=37 → ~24.7 ms dephasing;	24.7 ms
321	YES N15 6k	1D REDOR Scott's Sample: F8C G13N; V2E; ns=6k; 12kHz rotation; N15 pulse (pl3=0 dB); l0=37 → ~24.7 ms dephasing;	24.7 ms
Total	10k S0; 10k S1		24.7 ms
32_7ms			
249	YES N15 4k	1D REDOR Scott's Sample: F8C G13N; V2E; ns=4k; 12kHz rotation; N15 pulse (pl3=0 dB); l0=49 → ~32.7 ms dephasing	32.7 ms
250	NO N15 4k	1D REDOR Scott's Sample: F8C G13N; V2E; ns=4k; 12kHz rotation; no N15 pulse (pl3=120 dB); l0=49 → ~32.7 ms dephasing	32.7 ms
322	NO N15 8k	1D REDOR Scott's Sample: F8C G13N; V2E; ns=8k; 12kHz rotation; no N15 pulse (pl3=120 dB); l0=49 → ~32.7 ms dephasing;	32.7 ms
323	YES N15 8k	1D REDOR Scott's Sample: F8C G13N; V2E; ns=8k; 12kHz rotation; N15 pulse (pl3=0 dB); l0=49 → ~32.7 ms dephasing;	32.7 ms
Total	12k S0; 12k S1		32.7 ms
40_7ms			
261	YES N15 4k	1D REDOR Scott's Sample: F8C G13N; V2E; ns=4k; 12kHz rotation; N15 pulse (pl3=0 dB); l0=61 → ~40.7 ms dephasing;	40.7 ms
262	NO N15 4k	1D REDOR Scott's Sample: F8C G13N; V2E; ns=4k; 12kHz rotation; no N15 pulse (pl3=120 dB); l0=61 → ~40.7 ms dephasing;	40.7 ms
263	YES N15 4k	1D REDOR Scott's Sample: F8C G13N; V2E; ns=4k; 12kHz rotation; N15 pulse (pl3=0 dB); l0=61 → ~40.7 ms dephasing;	40.7 ms
264	NO N15 4k	1D REDOR Scott's Sample: F8C G13N; V2E; ns=4k; 12kHz rotation; no N15 pulse (pl3=120 dB); l0=61 → ~40.7 ms dephasing;	40.7 ms

Table AIV–19 (cont'd)

273	YES N15 4k	1D REDOR Scott's Sample: F8C G13N; V2E; ns=4k; 12kHz rotation; N15 pulse (pl3=0 dB); l0=61 → ~40.7 ms dephasing;	40.7 ms
274	NO N15 4k	1D REDOR Scott's Sample: F8C G13N; V2E; ns=4k; 12kHz rotation; no N15 pulse (pl3=120 dB); l0=61 → ~40.7 ms dephasing;	40.7 ms
275	YES N15 4k	1D REDOR Scott's Sample: F8C G13N; V2E; ns=4k; 12kHz rotation; N15 pulse (pl3=0 dB); l0=61 → ~40.7 ms dephasing;	40.7 ms
276	NO N15 4k	1D REDOR Scott's Sample: F8C G13N; V2E; ns=4k; 12kHz rotation; no N15 pulse (pl3=120 dB); l0=61 → ~40.7 ms dephasing;	40.7 ms
335	YES N15 6k	1D REDOR Scott's Sample: F8C G13N; V2E; ns=6k; 12kHz rotation; No N15 pulse (pl3=120 dB); l0=61 → ~40.7 ms dephasing;	40.7 ms
336	NO N15 6k	1D REDOR Scott's Sample: F8C G13N; V2E; ns=6k; 12kHz rotation; N15 pulse (pl3=0 dB); l0=61 → ~40.7 ms dephasing;	40.7 ms
340	YES N15 6k	1D REDOR Scott's Sample: F8C G13N; V2E; ns=6k; 12kHz rotation; N15 pulse (pl3=0 dB); l0=61 → ~40.7 ms dephasing;	40.7 ms
339	NO N15 6k	1D REDOR Scott's Sample: F8C G13N; V2E; ns=6k; 12kHz rotation; No N15 pulse (pl3=120 dB); l0=61 → ~40.7 ms dephasing;	40.7 ms
Total	28k S0; 28k S1		40.7 ms
48_7ms			
265	YES N15 4k	1D REDOR Scott's Sample: F8C G13N; V2E; ns=4k; 12kHz rotation; N15 pulse (pl3=0 dB); l0=73 → ~48.7 ms dephasing;	48.7 ms
266	NO N15 4k	1D REDOR Scott's Sample: F8C G13N; V2E; ns=4k; 12kHz rotation; no N15 pulse (pl3=120 dB); l0=73 → ~48.7 ms dephasing;	48.7 ms
267	YES N15 4k	1D REDOR Scott's Sample: F8C G13N; V2E; ns=4k; 12kHz rotation; N15 pulse (pl3=0 dB); l0=73 → ~48.7 ms dephasing;	48.7 ms
268	NO N15 4k	1D REDOR Scott's Sample: F8C G13N; V2E; ns=4k; 12kHz rotation; no N15 pulse (pl3=120 dB); l0=73 → ~48.7 ms dephasing;	48.7 ms
269	YES N15 4k	1D REDOR Scott's Sample: F8C G13N; V2E; ns=4k; 12kHz rotation; N15 pulse (pl3=0 dB); l0=73 → ~48.7 ms dephasing;	48.7 ms
270	NO N15 4k	1D REDOR Scott's Sample: F8C G13N; V2E; ns=4k; 12kHz rotation; no N15 pulse (pl3=120 dB); l0=73 → ~48.7 ms dephasing;	48.7 ms

Table AIV–19 (cont'd)

271	YES N15 4k	1D REDOR Scott's Sample: F8C G13N; V2E; ns=4k; 12kHz rotation; N15 pulse (pl3=0 dB); l0=73 → ~48.7 ms dephasing;	48.7 ms
272	NO N15 4k	1D REDOR Scott's Sample: F8C G13N; V2E; ns=4k; 12kHz rotation; no N15 pulse (pl3=120 dB); l0=73 → ~48.7 ms dephasing;	48.7 ms
337	YES N15 6k	1D REDOR Scott's Sample: F8C G13N; V2E; ns=6k; 12kHz rotation; no N15 pulse (pl3=120 dB); l0=73 → ~48.7 ms dephasing;	48.7 ms
338	NO N15 6k	1D REDOR Scott's Sample: F8C G13N; V2E; ns=6k; 12kHz rotation; N15 pulse (pl3=0 dB); l0=73 → ~48.7 ms dephasing;	48.7 ms
342	YES N15 6k	1D REDOR Scott's Sample: F8C G13N; V2E; ns=6k; 12kHz rotation; N15 pulse (pl3=0 dB); l0=73 → ~48.7 ms dephasing;	48.7 ms
341	NO N15 6k	1D REDOR Scott's Sample: F8C G13N; V2E; ns=6k; 12kHz rotation; no N15 pulse (pl3=120 dB); l0=73 → ~48.7 ms dephasing;	48.7 ms
Total	28k S0; 28k S1		48.7 ms
1D_13C+15N_CP			
235	cp90	13C Scott's Sample: F8C G13N; V2E Sample; ns=256; T=250K	G
236	cp90	15N CP Scott's Sample: F8C G13N; V2E Sample; ns=256; T=250K	G
No Data: 253 – 260			
Setup_REDOR_for_SDS			
232	cpredxy8.av.jos	1D REDOR U–NAL for Scott, with 20 us N15 Pi pulse; ns=8; T=250K (yes to N15 pulse) rotation = 10kHz	G?
233	cpredxy8.av.jos	1D REDOR U–NAL for Scott, with 20 us N15 Pi pulse; ns=8; T=250K (no N15 pulse) rotation = 10kHz	G?
234	cpredxy8.av.jos	1D REDOR U–NAL for Scott, with 20us N15 pi pulse; no N15 pulses on this one, popt pl1, pl12, pl2	G?

File locations:
900 Computer: /opt/topspin216/data/Nethercott/nmr/Jan2011/
Linux computer:
/home/mb4c/Matt/Organized_Files/900MHz_Data/All_900_Data/Jan2011/SDS_Data/

Table AIV–20: EPV data from the 900 MHz NMR Facility Jan and Feb 2011

Exp. #	Type	Information	Junk or Good?
Fgp41_FullyHydrated/1D_13C_CP			
295	cp90	13C Erica's new Fgp41 fully hydrated whole cell sample LL label; T=270K; ns=256, (weak signal)	G?
300	cp90	13C Erica's new Fgp41 fully hydrated whole cell sample LL label; T=250K; ns=256	G
306	cp90	13C Erica's new Fgp41 fully hydrated whole cell sample LL label; T=250K; ns=1k	G
Fgp41_FullyHydrated/1D_15N_CP			
296	cp90	15N CP Erica's new Fgp41 fully hydrated whole cell sample LL label; T=270K; ns=256, (no observable signal)	G?
299	cp90	15N CP Erica's new Fgp41 fully hydrated whole cell sample LL label; T=270K; ns=1k, (halted, not worth running)	J
301	cp90	15N CP Erica's new Fgp41 fully hydrated whole cell sample LL label; T=250K; ns=256	G
307	cp90	15N CP Erica's new Fgp41 fully hydrated whole cell sample LL label; T=250K; ns=1k	G
Fgp41_FullyHydrated/REDOR			
297	cpredxy8.av.jos	1D REDOR Erica's new Fgp41 fully hydrated whole cell sample LL label; T=270K; ns=12k; pl3=120 dB (no N15 pulse) l0=3 → 2ms dephasing	G
298	cpredxy8.av.jos	1D REDOR Erica's new Fgp41 fully hydrated whole cell sample LL label; T=270K; ns=12k; pl3=0 dB (N15 pulse) l0=3 → 2ms dephasing	G
302	cpredxy8.av.jos	1D REDOR Erica's new Fgp41 fully hydrated whole cell sample LL label; T=250K; ns=4k; pl3=120 dB (no N15 pulse) l0=3 → 2ms dephasing	G
303	cpredxy8.av.jos	1D REDOR Erica's new Fgp41 fully hydrated whole cell sample LL label; T=270K; ns=4k; pl3=0 dB (N15 pulse) l0=3 → 2ms dephasing	G
304	cpredxy8.av.jos	1D REDOR Erica's new Fgp41 fully hydrated whole cell sample LL label; T=250K; ns=8k; pl3=120 dB (no N15 pulse) l0=3 → 2ms dephasing	G
305	cpredxy8.av.jos	1D REDOR Erica's new Fgp41 fully hydrated whole cell sample LL label; T=250K; ns=8k; pl3=0 dB (N15 pulse) l0=3 → 2ms dephasing	G

Table AIV–20 (cont'd)

308	cpredxy8.av.jos	1D REDOR Erica's new Fgp41 fully hydrated whole cell sample LL label; T=250K; ns=4k; pl3=120 dB (no N15 pulse) l0=3 → 2ms dephasing	G
309	cpredxy8.av.jos	1D REDOR Erica's new Fgp41 fully hydrated whole cell sample LL label; T=250K; ns=4k; pl3=0 dB (N15 pulse) l0=3 → 2ms dephasing	G
Old_Fgp41_LL_Sample/1D_13C_CP			
95	cp90	13C Erica's old LL Fgp41 sample; T=250K; ns=4k	G
97	cp90	13C Erica's old LL Fgp41 sample; T=250K; ns=512	G?
201	cp90	13C Erica's old Fgp41 LL sample; ns=256; T=250K	G
Old_Fgp41_LL_Sample/1D_15N_CP			
96	cp90	15N CP Erica's old LL Fgp41 sample; T=250K; ns=4k	G
98	cp90	15N CP Erica's old LL Fgp41 sample; T=250K; ns=512	G?
202	cp90	15N CP Erica's old Fgp41 LL sample; ns=256; T=250K	G
Old_Fgp41_LL_Sample/1D_DCP_NCO			
99	doubcp2ddarr.jos	1D NCO; Erica's old LL Fgp41 sample; w=12kHz; T=250K; ns=512	J
100	doubcp2ddarr.jos	1D NCO; Erica's old LL Fgp41 sample; w=12kHz; T=250K; ns=512 (convert from NCA)	J
203	doubcp.av.jos	1D NCO; Erica's old Fgp41 LL sample; ns=256; T=250K	J
206	doubcp.av.jos	1D NCO; Erica's old Fgp41 LL sample; ns=8k; T=250K	J
Old_Fgp41_LL_Sample/REDOR			
101	cpredxy8.av.jos	1D REDOR w/ N15; Erica's old LL Fgp41 sample; T=250K; ns=8k; pl3=0 dB	G
102	cpredxy8.av.jos	1D REDOR no N15; Erica's old LL Fgp41 sample; T=250K; ns=8k; pl3=120dB	G
103	cpredorxy8i.av.jos	2D REDOR; Erica's old LL Fgp41 sample; T=250K; interwoven S0/S1	J
204	cpredxy8.av.jos	1D REDOR; Erica's old Fgp41 LL sample; ns=256; pl3=120 (no N15 pulse) l0=3 → 2ms dephasing	G
205	cpredxy8.av.jos	1D REDOR; Erica's old Fgp41 LL sample; ns=256; pl3=0 (N15 pulse) l0=3 → 2ms dephasing	G

Table AIV–20 (cont'd)

207	cpredxy8.av.jos	1D REDOR; Erica's old Fgp41 LL sample; ns=4k; pl3=120 (no N15 pulse) l0=3 → 2ms dephasing	G
208	cpredxy8.av.jos	1D REDOR; Erica's old Fgp41 LL sample; ns=4k; pl3=0 (N15 pulse) l0=3 → 2ms dephasing	G
229	cpredxy8.av.jos	1D REDOR of Erica's old Fgp41 LL sample; T=250K; ns=10k; pl3=120 dB (no N15 pulses)	G
230	cpredxy8.av.jos	1D REDOR of Erica's old Fgp41 LL sample; T=250K; ns=10k; pl3=0 dB (N15 pulses)	G

File locations:
900 Computer: /opt/topspin216/data/Nethercott/nmr/Jan2011/
Linux computer: /home/mb4c/Matt/Organized_Files/900MHz_Data/All_900_Data/Jan2011/EPV_Jan+Feb2011/

Table AIV–21: March 2011 data from the 900 MHz NMR Facility

Exp. #	Type	Information	Junk or Good?
Adamantane			
5	cp90	13C – Adamantane – 3/14/11 @ 1310, 6kHz = MAS, T= 250K; SR = –301.15	G
26	cp90	13C – adamantane – 3/15/11 at 0930 am, MAS = 12 kHz, T = 250 K. o1p = 100 ppm; SR = –283.11	G
27	cp90	13C – adamantane – 3/15/11 at 0930 am, MAS = 12 kHz, T = 250 K. Changed a parameter, o1p = 50 ppm	G
28	cp90	13C – adamantane – 3/15/11 at 0930 am, MAS = 12 kHz, T = 250 K. Changed a parameter, o1p = 50 ppm	G
44	cp90	13C – Adamantane – 3/16/11 @ ~1830; copied from exp. 42; ns = 32	G
45	cp90	13C – Adamantane – 3/16/11 @ ~1830; copied from exp. 42; ns = 8	G
46	cp90	13C – adamantane – 3/16/11 at 1835, MAS = 12 kHz, T = 250 K. o1p = 100 ppm; SR = –276.52	G
51	cp90	13C – adamantane – T=250K, MAS = 12kHz, ns=8?; SR = –269.48	G
AMS			
29	cp90	15N – AMS sample; T = 250 K, MAS = 12 kHz, ns = 8, 3/15/11	G
30	cp90	15N – AMS sample; T = 250 K, MAS = 12 kHz, ns = 8, 3/15/11, changed some parameter, it's junk.	J
KBr			
1	zg	Mar. 14, 2011 – Checking the magic angle with KBr. T = 250K	G
2	zg	Mar. 14, 2011 – Checking the magic angle with KBr. T = 250K	G
3	zg	Mar. 14, 2011 – Checking the magic angle with KBr. T = 250K	G
4	zg	Mar. 14, 2011 – Checking the magic angle with KBr. – Best results; T = 250K	G
U–NAL/1D_13C_CP			
6	cp90	13C – U–NAL – MAS = 12 kHz, T = 250 K, ns = 16. wanted to compare to Jan2011 data., SR = –301.15	G

Table AIV–21 (cont'd)

8	cp90	13C – U–NAL – MAS = 12 kHz, T = 250 K, ns = 8. wanted to compare to Jan2011 data., SR = –301.15	G
9	cp90	13C – U–NAL – MAS = 12 kHz, T = 250 K, ns = 16. wanted to compare to Jan2011 data., SR = –301.15	G
13	cp90	13C – U–NAL – MAS = 12 kHz, T = 250 K, ns = 256., SR = –301.15	G
52	cp90	13C – U–NAL – T = 250K, MAS = 12 kHz, ns = 8; SR = –269.48	G
U–NAL/1D_15N_CP			
7	cp90	15N CP – U–NAL, MAS = 12 kHz, T = 250 K, ns = 8. wanted to compare to Jan2011 data., SR = –301.15	G
10	cp90	15N CP – U–NAL, MAS = 12 kHz, T = 250 K, ns = 8. wanted to compare to Jan2011 data., SR = 119.47	G
14	cp90	15N CP – U–NAL, MAS = 12 kHz, T = 250 K, ns = 256, SR = 119.47	G
53	cp90	15N – U–NAL – T=250K, MAS = 12 kHz, ns=8, SR = 131.36	G
U–NAL/1D_DCP_NCA			
11	doubcp.av.jos	1D NCA – U–NAL, T=25K, MAS = 12 kHz, ns = 8, SR = –301.15?	G
15	doubcp.av.jos	1D NCA – U–NAL, T=25K, MAS = 12 kHz, ns = 256, SR = –301.15	G
17	doubcp2ddarr.jos	1D NCA – U–NAL, T=25K, MAS = 12 kHz, ns = 8, SR = –301.15	G
19	doubcp2ddarr.jos	1D NCA – U–NAL, T=25K, MAS = 12 kHz, ns = 256, SR = –301.15	G
U–NAL/1D_DCP_NCO			
12	doubcp.av.jos	1D NCO – U–NAL, T=25K, MAS = 12 kHz, ns = 8, SR = –301.15?	G
16	doubcp.av.jos	1D NCO – U–NAL, T=25K, MAS = 12 kHz, ns = 256, SR = –301.15	G
18	doubcp2ddarr.jos	1D NCO – U–NAL, T=25K, MAS = 12 kHz, ns = 8, SR = –301.15	G / J?
20	doubcp2ddarr.jos	1D NCO – U–NAL, T=25K, MAS = 12 kHz, ns = 256, SR = –301.15	G / J?
U–NAL/3D_NCACX			
21	doubcp3d.jos	3D NCACX experiment, as is from Jochem. U–NAL; T=250K, MAS = 12kHz. Short, ~13 minute experiment. Lack of resolution, but wanted to have a base to compare it to.	G

Table AIV–21 (cont'd)

22	doubcp3d.jos	Same as #21, but with optimized parameters from 1D and 2D experiments.	G
23	doubcp3d.jos	Same as 22, using optimized parameters to figure it all out.	G
24	doubcp3d.jos	Still playing around with it to figure it out. ~13 min experiments	G
25	doubcp3d.jos	At a point where I am satisfied with it, running longer, ~12.5 hrs with U–NAL sample, MAS = 250 K, T = 12 kHz	G
FPH_15to1/1D_13C_CP			
31	cp90	FPH–MS–UA6/UG10 (~2 μmoles protein) – 13C CP, ns = 256; MAS = 12 kHz, T = 250 K, 3/15/11 @ 1009, SR = –283.11	G
47	cp90	FPH–MS–UA6/UG10 (~2 μmoles protein) – 13C CP, ns = 256; MAS = 15 kHz, T = 250 K	G
FPH_15to1/1D_15N_CP			
32	cp90	FPH–MS–UA6/UG10 (~2 μmoles protein) – 15N CP, ns = 256; MAS = 12 kHz, T = 250 K, 3/15/11 @ 1018, SR = 126.73	G
48	cp90	FPH–MS–UA6/UG10 (~2 μmoles protein) – 15N CP, ns = 256; MAS = 15 kHz, T = 250 K	G
FPH_15to1/1D_DCP_NCA			
33	doubcp.av.jos	FPH–MS–UA6/UG10 (~2 μmoles protein) – 1D NCA experiment, ns = 256; MAS = 12 kHz, T = 250 K	G
34	doubcp2ddarr.jos	FPH–MS–UA6/UG10 (~2 μmoles protein) – 1D NCA experiment, ns = 256; MAS = 12 kHz, T = 250 K	G
49	doubcp.av.jos	FPH–MS–UA6/UG10 (~2 μmoles protein) – 1D NCA experiment, ns = 256; MAS = 15 kHz, T = 250 K; don't see signal. Must have miss-mashed parameters.	J
50	doubcp2ddarr.jos	FPH–MS–UA6/UG10 (~2 μmoles protein) – 1D NCA experiment, ns = 256; MAS = 15 kHz, T = 250 K; don't see signal. Must have miss-mashed parameters.	J
FPH_15to1/3D_NCACX			
35	doupcp3d.jos	FPH–MS–UA6/UG10 (~2 μmoles protein) – 3D NCACX experiment, MAS = 12 kHz, T = 250 K; same setup as exp. 25; ~12.5 hrs	G
36	doupcp3d.jos	FPH–MS–UA6/UG10 (~2 μmoles protein) – 3D NCACX experiment, MAS = 12 kHz, T = 250 K; same setup as exp. 25; ~12.5 hrs; same as exp. 35	G

Table AIV–21 (cont'd)

37	doupcp3d.jos	FPH–MS–UA6/UG10 (~2 μmoles protein) – 3D NCACX experiment, MAS = 12 kHz, T = 250 K; same setup as exp. 25; ~12.5 hrs; same as exp. 35, 36.	G
SDS_V2E/1D_13C_CP			
38	cp90	13C CP of Scott's sample V2E, F8C G13N; 256 scans; T=250K, MAS = 12 kHz	G
42	cp90	13C CP of Scott's sample V2E, F8C G13N; 32 scans; T=250K, MAS = 12 kHz	G
SDS_V2E/1D_15N_CP			
39	cp90	15N CP of Scott's sample V2E, F8C G13N; 256 scans; T=250K, MAS = 12 kHz	G
43	cp90	15N CP of Scott's sample V2E, F8C G13N; 32 scans; T=250K, MAS = 12 kHz	G
SDS_V2E/1D_REDOR			
40	cpredxy8.av.jos	1D REDOR of Scott's V2E Data, F8C G13N; 2ms data point, ns = 2k, no N15 pulses (pl3 = 120 dB), T=250K, MAS = 12 kHz	G
41	cpredxy8.av.jos	1D REDOR of Scott's V2E Data, F8C G13N; 2ms data point, ns = 2k, N15 pulses (pl3 = 0 dB), T=250K, MAS = 12 kHz	G

- U–NAL for comparison and referencing:
  - ^{15}N CP = #53
  - ^{13}C CP = #52
  - ^{13}C CP adamantane for initial reference: #51
- Comparing efficiency of 1D NCA / NCO to CP for U–NAL:
  - Exp. 13 = 13C CP, 256 scans
  - Exp. 15 = 1D NCA, 256 scans
  - Exp. 16 = 1D NCO, 256 scans

File locations:
900 Computer: /opt/topspin216/data/Nethercott/nmr/Mar2011/
Linux computer: /home/mb4c/Matt/Organized_Files/900MHz_Data/All_900_Data/Mar2011/

Table AIV–22: August 2011 data from the 900 MHz NMR Facility for FP23UA6UG10

Exp. #	Type	Information	Junk or Good?
1	cp90	U–NAL	G
2	cp90	13C CP of Michelle's Dimer D; ns = 2048	G
3	cp90	15N CP of Michelle's Dimer D; ns = 2048; SR = –8.39 (topspin)	G
4	cpdarr	FP23 Dimer D from Michelle Bodner, tau=50ms, Block 1	G
5	cpdarr	FP23 Dimer D from Michelle Bodner, tau=50ms, Block 2	G
6	doubcp	FP23 Michelle Bodner's Dimer D; ns = 2048	G
7	cp90	15N CP of U–NAL; ns = 8 (for referencing)	G
8	cp90	15N CP of U–NAL; ns = 8 (for referencing)	G
9	cp90	13C CP of U–NAL; ns = 8 (for referencing)	G
10	cp90	13C CP of Michelle's Dimer D; ns = 128	G
11	cp90	15N CP of Michelle's Dimer D; ns = 128	G
12	doubcp	FP23 Dimer D from Michelle Bodner, ns = 128	G
13	cpdarr	FP23 Dimer D from Michelle Bodner, tau=500ms, with 12kHz DARR Block 1	G
14	cpdarr	FP23 Dimer D from Michelle Bodner, tau=500ms, with 12kHz DARR Block 2	G
15	cp90	1D 13C FP23 of Dimer D for referencing	G
16	cp90	1D 13C FP23 of Dimer D for referencing	G
17	cp90	13C CP of Adamantane for referencing	G
18	cp90	13C of UNAL for referencing	G
19	cp90	1D 13C of FP23 Dimer D for referencing	G
20	cp90	1D 13C of FP23 Dimer D for referencing, ns=64	G
21	cp90	1D 13C of FP23 Dimer D for referencing, ns=64	G
22	cpdarr	FP23 Dimer D from Michelle Bodner, tau=500ms, with 12kHz DARR Block 3	G
23	cp90	1D 13C of FP23 Dimer D for referencing, ns=64	G
24	cpdarr	FP23 Dimer D from Michelle Bodner, tau=500ms, with 12kHz DARR Block 4	G
25	cp90	1D 13C of FP23 Dimer D for referencing, ns=64	G
26	cpdarr	FP23 Dimer D from Michelle Bodner, tau=500ms, with 12kHz DARR Block 5	G
27	cp90	1D 13C of FP23 Dimer D for referencing, ns=64	G
28	cp90	13C of Adamantane for referencing	G
29	cp90	13C of U–NAL for referencing	G
30	cp90	1D 13C of FP23 Dimer D for referencing, ns=64	G
31	cpdarr	FP23 Dimer D from Michelle Bodner, tau=500ms, with 12kHz DARR Block 6	G

Table AIV–22 (cont'd)

32	cp90	1D 13C of FP23 Dimer D for referencing, ns=64	G
33	cp90	1D 13C of FP23 Dimer D for referencing, ns=64	G
34	cpdarr	FP23 Dimer D from Michelle Bodner, tau=500ms, with 12kHz DARR Block 7	G
35	cp90	1D 13C of FP23 Dimer D for referencing, ns=64	G
36	cpdarr	FP23 Dimer D from Michelle Bodner, tau=500ms, with 12kHz DARR Block 8	G
37	cp90	1D 13C of FP23 Dimer D for referencing, ns=64	G
38	cpdarr	FP23 Dimer D from Michelle Bodner, tau=500ms, with 12kHz DARR Block 9	G
39	cp90	1D 13C of FP23 Dimer D for referencing, ns=64	G
40	cp90	1D 13C of FP23 Dimer D for referencing, ns=64	G
41	cpdarr	FP23 Dimer D from Michelle Bodner, tau=500ms, with 12kHz DARR Block 10	G
42	cp90	1D 13C of FP23 Dimer D for referencing, ns=64	G
43	cpdarr	FP23 Dimer D from Michelle Bodner, tau=500ms, with 12kHz DARR Block 11	G
44	cp90	1D 13C of FP23 Dimer D for referencing, ns=64	G
45	cpdarr	FP23 Dimer D from Michelle Bodner, tau=500ms, with 12kHz DARR Block 12	G
46	cp90	1D 13C of FP23 Dimer D for referencing, ns=64	G
47	cpdarr	FP23 Dimer D from Michelle Bodner, tau=500ms, with 12kHz DARR Block 13	G
48	cp90	1D 13C of FP23 Dimer D for referencing, ns=64	G
49	cp90	1D 13C of FP23 Dimer D for referencing, ns=64	G
50	cpdarr	FP23 Dimer D from Michelle Bodner, tau=500ms, with 12kHz DARR Block 14	G
51	cp90	1D 13C of FP23 Dimer D for referencing, ns=64	G
52	cpdarr	FP23 Dimer D from Michelle Bodner, tau=500ms, with 12kHz DARR Block 15	G
53	cp90	1D 13C of FP23 Dimer D for referencing, ns=64	G
54	cp90	13C of Adamantane for Referencing	G

Unless noted otherwise, all experiments of FP23 were performed at 12kHz MAS, T = 250 K. For CPDARR: ns=64 / slice; 256 slices, d1 =1.5s,
Adamantane and UNAL had MAS of 6kHz (double check)

File locations:
900 Computer: /opt/topspin216/data/Nethercott/nmr/FP23UA6UG10_Aug2011/
Linux computer: /home/mb4c/Matt/Organized_Files/900MHz_Data/All_900_Data/Aug2011/FP23UA6UG10_Aug2011

Table AIV–23: August 2011 data from the 900 MHz NMR Facility for FPHUA6UG10

Exp. #	Type	Information	Junk or Good?
1	cp90	15N CP of FPH 15:1 Loading in POPC/POPG/Chol membranes. Ns= 2048; T = 250K; d1 = 2s; MAS=12 kHz	G
2	cp90	13C CP of FPH 15:1 Loading in POPC/POPG/Chol membranes. Ns= 2048; T = 250K; d1 = 2s; MAS=12 kHz	G
3	cpdarr	2D 13C–13C of FPH 15:1 Loading in POPC/POPG/Chol membranes. Ns= 64/slice; 256 slices; tau = 50ms T = 250K; d1 = 1s; MAS=12 kHz; DARR experiment (PL14 = 13.9 dB)	G
4	cpdarr	2D 13C–13C of FPH 15:1 Loading in POPC/POPG/Chol membranes. Ns= 64/slice; 256 slices; tau = 50ms T = 250K; d1 = 1.5s; MAS=12 kHz; PDSD experiment (PL14 = 120 dB)	G
5	doubcp	1D NCA experiment: FPH 15:1 Loading in POPC/POPG/Chol membranes. Ns= 2048; T = 250K; d1 = 2s; MAS=12 kHz; 1H → 15N → 13Ca	G
6	cpdarr	2D 13C–13C of FPH 15:1 Loading in POPC/POPG/Chol membranes. Ns= 64/slice; 256 slices; tau = 50ms T = 250K; d1 = 1s; MAS=12 kHz; DARR experiment (PL14 = 13.9 dB)	G

File locations:
900 Computer: /opt/topspin216/data/Nethercott/nmr/FPHUA6G10–AUG2011/
Linux computer: /home/mb4c/Matt/Organized_Files/900MHz_Data/All_900_Data/Aug2011 /FPHUA6G10–AUG2011

Table AIV–24: August 2011 data at the 900 MHz NMR for Erica's samples located in the directory "Vogel"

Exp. #	Type	Information	Junk or Good?
A:	**Folder:**	**Setups**	
1	cp90	13C CP of U–NAL ns= 8; d1 = 3s; 8/15/11 used for referencing when adamantane wouldn't spin.	G
2	cp90	13C CP of U–NAL ns= 8; d1 = 1.5s; 8/15/11 used for referencing when adamantane wouldn't spin.	G
3	cp90	Adamantane, 13C, ns = 8, T=270K, 8/18/11, d1=1.5s, MAS = 6 kHz	G
4	cp90	Adamantane, 13C, ns = 8, T=270K, 8/20/11, d1=1.5s, MAS = 6 kHz	G
5	cp90	Adamantane, 13C, ns = 8, T=270K, 8/22/11, d1=1.5s, MAS = 6 kHz	G
6	cp90	Adamantane, 13C, ns = 8, T=270K, 8/25/11, d1=1.5s, MAS = 6 kHz	G
–	–	–	–
B:	**Folder:**	**WC_labeled_08232011**	
1	cp90	1–13C,15N Leu labeled Fgp41 whole cell fully hydrated sample 8/23/11, 13C CP, ns=256, TD = 512; d1 = 1.5s; T=270 K; not thermally equilibrated yet is the assumption.; MAS = 12 kHz	J
2	cp90	1–13C,15N Leu labeled Fgp41 whole cell fully hydrated sample 8/23/11, 13C CP, ns=256, TD = 512; d1 = 1.5s; T=270 K; not thermally equilibrated yet is the assumption.; MAS = 12 kHz	J
3	cp90	1–13C,15N Leu labeled Fgp41 whole cell fully hydrated sample 8/23/11, 15N CP, ns=256, TD = 512; d1 = 1.5s; T=270 K; not thermally equilibrated yet is the assumption.; MAS = 12 kHz	J
4	cpredxy8.av	1–13C,15N Leu labeled Fgp41 whole cell fully hydrated sample 8/23/11, S0, ns=25,000, TD = 512; d1 = 1.0s; T=270 K; not thermally equilibrated yet is the assumption.; MAS = 12 kHz	J
5	cpredxy8.av	1–13C,15N Leu labeled Fgp41 whole cell fully hydrated sample 8/23/11, S1, ns=25,000, TD = 512; d1 = 1.0s; T=270 K; pl3 = 2.0 dB; MAS = 12 kHz	G
6	cpredxy8.av	1–13C,15N Leu labeled Fgp41 whole cell fully hydrated sample 8/23/11, S0, ns=25,000, TD = 512; d1 = 1.0s; T=270 K; pl3 = 120.0 dB; MAS = 12 kHz	G
7	cpredxy8.av	1–13C,15N Leu labeled Fgp41 whole cell fully hydrated sample 8/23/11, S1, ns=25,000, TD = 512; d1 = 1.0s; T=270 K; pl3 = 2.0 dB; MAS = 12 kHz	G

Table AIV–24 (cont'd)

8	cpredxy8.av	1–13C,15N Leu labeled Fgp41 whole cell fully hydrated sample 8/23/11, S0, ns=25,000, TD = 512; d1 = 1.0s; T=270 K; pl3 = 120.0 dB replaces #4; MAS = 12 kHz	G
9	cpredxy8.av	1–13C,15N Leu labeled Fgp41 whole cell fully hydrated sample 8/23/11, S1, ns=10,000, TD = 512; d1 = 1.0s; T=270 K; pl3 = 2.0 dB; MAS = 12 kHz	G
10	cpredxy8.av	1–13C,15N Leu labeled Fgp41 whole cell fully hydrated sample 8/23/11, S0, ns=10,000, TD = 512; d1 = 1.0s; T=270 K; pl3 = 120.0 dB; MAS = 12 kHz	G
11	cp90	13C CP of 1–13C,15N Leu labeled Fgp41 whole cell fully hydrated sample 8/23/11, ns = 256 (replaces #1 or 2), d1 = 1.5s, T=270K, TD = 512; MAS = 12 kHz	G
12	cp90	15N CP of 1–13C,15N Leu labeled Fgp41 whole cell fully hydrated sample 8/23/11, ns = 256 (replaces #1 or 2), d1 = 1.5s, T=270K, TD = 512; MAS = 12 kHz	G
–	–	–	–
C:	**Folder:**	**Whole_Cell_labeled**	8/15/11 – 8/16/11
1	cp90	1–13C,15N Leu labeled Fgp41 whole cell fully hydrated sample 8/15/11, 13C CP, ns=256, TD = 512; d1 = 1.5s; T=270 K; MAS = 12 kHz	
2	cp90	1–13C,15N Leu labeled Fgp41 whole cell fully hydrated sample 8/15/11, 13C CP, ns=256, d1 = 1.5s; T=270 K; MAS = 12 kHz	
3	cp90	1–13C,15N Leu labeled Fgp41 whole cell fully hydrated sample 8/15/11, 15N CP, ns=512, d1 = 2s; T=270 K; MAS = 12 kHz	
4	hpdec	1–13C,15N Leu labeled Fgp41 whole cell fully hydrated sample 8/15/11, 13C CP, ns=512, d1 = 2s; T=270 K; MAS = 12 kHz	
5	cpredxy8.av	1–13C,15N Leu labeled Fgp41 whole cell fully hydrated sample 8/23/11, S0, ns=18,432, TD = 512; d1 = 1.0s; T=270 K; pl3 = 120.0 dB; MAS = 12 kHz; o1p = 165 ppm	
6	cpredxy8.av	1–13C,15N Leu labeled Fgp41 whole cell fully hydrated sample 8/23/11, S1, ns=18,432, TD = 512; d1 = 1.0s; T=270 K; pl3 = 2.0 dB; MAS = 12 kHz; o1p = 165 ppm	
–	–	–	–
D:	**Folder:**	**Whole_Cell_labeled_Aug192011**	8/19/11
1	cp90	1–13C,15N Leu labeled Fgp41 whole cell fully hydrated sample 8/19/11, 13C CP, ns=512; d1 = 1.5s; T=270 K; MAS = 12 kHz	

Table AIV–24 (cont'd)

2	cp90	1–13C,15N Leu labeled Fgp41 whole cell fully hydrated sample 8/19/11, 15N CP, ns=512, d1 = 2 s; T=270 K; MAS = 12 kHz	
3	cp90	1–13C,15N Leu labeled Fgp41 whole cell fully hydrated sample 8/19/11, 13C CP, ns=36,864; d1 = 1.5s; T=270 K; MAS = 12 kHz	
–	–	–	–
E:	**Folder:**	**Whole_Cell_unlabeled_Aug202011**	8/20/11
1	cp90	Natural Abundance Leu unlabeled Fgp41 whole cell fully hydrated sample 8/19/11, 13C CP, ns=512; d1 = 1.5s; T=270 K; MAS = 12 kHz	
2	cp90	Natural Abundance Leu unlabeled Fgp41 whole cell fully hydrated sample 8/19/11, 15N CP, ns=512, d1 = 2 s; T=270 K; MAS = 12 kHz	
3	cp90	Natural Abundance Leu unlabeled Fgp41 whole cell fully hydrated sample 8/19/11, 13C CP, ns=36,864; d1 = 1.5s; T=270 K; MAS = 12 kHz	

Unless noted otherwise, all experiments were performed at 12kHz MAS, T = 270 K. Adamantane and UNAL had MAS of 6 kHz

File locations:
900 Computer: /opt/topspin216/data/Vogel/nmr/
Linux computer:
/home/mb4c/Matt/Organized_Files/900MHz_Data/All_900_Data/Vogel_Aug2011/nmr/

Table AIV–25: All the 700 MHz NMR data from Dr. Jochem Struppe expect previously listed data in Table AIV–8.

Exp. #	Type	Information	Junk or Good?
20	cp90	FPH UA6UG10 15:1 loading sample. ns=256, T=250K	G
21	cp90	FPH UA6UG10 15:1 loading sample. T=250K, CP90 with flipback pulse, no signal seen, as expected.	G / J?
25	2D ^{13}C–^{13}C PDSD	2D PDSD experiment, 50 ms mixing time. Experiment started at T=250 K, then chiller shut off and warmed to T=296 K. ns = 64/slice, 256 slices. Time ~14 hrs	J
26	2D ^{13}C–^{13}C PDSD	2D PDSD experiment, 50 ms mixing time. T=296 K. ns=64/slice, 256 slices. Time ~14 hrs	J
27	2D ^{13}C–^{13}C PDSD	2D PDSD experiment, 50 ms mixing time. T=250 K. ns=64/slice, 256 slices. Time ~14 hrs	G

File locations:
Linux computer: /home/mb4c/Matt/Organized_Files/700MHz_Data/700Raw_Data/

Table AIV–26: NMR file location and information about samples from Niagara University sent by Dr. Ronny Priefer for solid state NMR analysis. AQ = acquisition length, MAS = sample spinning frequency, pd = pulse delay between acquisitions, temperature was as measured at the thermocouple. Block averaging was used for some samples, which were then co–added together, and nk denotes n*1024 acquisitions for block averaging purposes.

File Name / Sample	Number of Scans	Temperature (°C)	Parameters different from general ones
Initial test conditions. Folder: /Feb2011/PG_01_53–Feb2011			
PG_01_53_1	256	–50	MAS= 10 kHz; pd= 1s; AQ= 20 ms
PG_01_53_2	256	–50	MAS= 10 kHz; pd= 1s; AQ= 10 ms
PG_01_53_3	256	–50	MAS= 10 kHz; pd= 1s; AQ= 5 ms
PG_01_53_4	256	–50	MAS= 10 kHz; pd= 2s; AQ= 10 ms
PG_01_53_5	256	–50	MAS= 8 kHz; pd= 2s; AQ= 10 ms
PG_01_53_6	256	–50	MAS= 12 kHz; pd= 2s; AQ= 10 ms
PG_01_53_7	256	–50	MAS= 12 kHz; pd= 1s; AQ= 10 ms
PG_01_53_8	256	–50	MAS= 12 kHz; pd= 4s; AQ= 10 ms
PG_01_53_9	4000	–50	MAS= 12 kHz; pd= 2s; AQ= 10 ms
PG_01_53_10	24000	–50	MAS= 12 kHz; pd= 2s; AQ= 10 ms
Folder: /Feb2011/PG_01_52–Feb2011			
PG_01_52_1	256	–50	MAS= 12 kHz; pd= 1s; AQ= 10 ms
PG_01_52_2	256	–50	MAS= 12 kHz; pd= 2s; AQ= 10 ms
PG_01_52_3	4000	–50	MAS= 12 kHz; pd= 2s; AQ= 10 ms
Folder: /Mar2011/PG_01_52–Mar2011			
PG_01_52_Mar11–1	256	~ 20	MAS= 12 kHz; pd= 2s; AQ= 10 ms
PG_01_52_Mar11–2	256	~ 20	MAS= 12 kHz; pd= 2s; AQ= 5 ms
PG_01_52_Mar11–3	1024	~ 20	MAS= 12 kHz; pd= 2s; AQ= 10 ms
PG_01_52_Mar11–4	2048	~ 20	MAS= 12 kHz; pd= 2s; AQ= 10 ms
PG_01_52_Mar11–5	256	–50	MAS= 12 kHz; pd= 2s; AQ= 10 ms
PG_01_52_Mar11–6	256	–50	MAS= 12 kHz; pd= 2s; AQ= 5 ms
PG_01_52_Mar11–7	1024	–50	MAS= 12 kHz; pd= 2s; AQ= 10 ms
PG_01_52_Mar11–8	2048	–50	MAS= 12 kHz; pd= 2s; AQ= 10 ms
Folder: /Mar2011/PG_01_53–Mar2011			
PG_01_53_Mar11–1	256	~ 20	MAS= 12 kHz; pd= 2s; AQ= 10 ms

Table AIV–26 (cont'd)

PG_01_53_Mar11–2	256	~ 20	MAS= 12 kHz; pd= 2s; AQ= 5 ms
PG_01_53_Mar11–3	1024	~ 20	MAS= 12 kHz; pd= 2s; AQ= 10 ms
PG_01_53_Mar11–4	2048	~ 20	MAS= 12 kHz; pd= 2s; AQ= 10 ms
PG_01_53_Mar11–5	256	–50	MAS= 12 kHz; pd= 2s; AQ= 10 ms
PG_01_53_Mar11–6	256	–50	MAS= 12 kHz; pd= 2s; AQ= 5 ms
PG_01_53_Mar11–7	1024	–50	MAS= 12 kHz; pd= 2s; AQ= 10 ms
PG_01_53_Mar11–8	2048	–50	MAS= 12 kHz; pd= 2s; AQ= 10 ms
Folder: /April2011/			
PG–01–52	2048	~ 20	
PG–01–53	2048	~ 20	
PG–01–57	2048	~ 20	
PG–01–59	2048	~ 20	
PG–01–60	2048	~ 20	
PG–01–61	2048	~ 20	
PG–01–62	2048	~ 20	
PG–01–63	2048	~ 20	Difficult to get signal. 1 block (file –1 in folder)
PG–01–63	4096	~ 20	Difficult to get signal. 1 block (file –2 in folder)
PG–01–63	20480	~ 20	Difficult to get signal. 1 block (file –3 in folder)
PG–01–64	4096	~ 20	Block averaging: 2 x 2048
PG–01–65	6144	~ 20	Block averaging: 3 x 2048
PG–01–66	6144	~ 20	Block averaging: 3 x 2048
PG–01–67	4096	~ 20	Block averaging: 2 x 2048
PG–01–68	4096	~ 20	Block averaging: 2 x 2048
Folder: /June2011/			
PAH	1024	~ 20	
PG–01–69	2048	~ 20	
PG–01–69b	2048	~ 20	
PG–01–70	2048	~ 20	
PG–01–71	2048	~ 20	
PG–01–72	2048	~ 20	
PG–01–73	2048	~ 20	
PG–01–74	2048	~ 20	
PG–01–75	2048	~ 20	
PG–01–76	2048	~ 20	

Table AIV–26 (cont'd)

PG–01–77	8196	~ 20	Block averaging: 4 x 2048
PG–01–78	12288	~ 20	Block averaging: 2k, 4k, 6k blocks
PG–01–79	4096	~ 20	Block averaging: 2 x 2048
PG–01–80	6144	~ 20	Block averaging: 3 x 2048

File locations:
Linux computer: /home/mb4c/Matt/Organized_Files/Priefer/

Table AIV–27: 400 MHz SSNMR Data of FP–Hairpin at with CuEDTA

Fig.	File Location	Type of Experiment	Membranes	pH Condition
AI–1	**Raw:** /7Jul09–50ms–CuEDTA–sum123/7Jul09–50ms–CuEDTA–sum123.fid **Proc:** /7Jul09–50ms–CuEDTA–sum123/7Jul09–50ms–CuEDTA–sum123_100lb.ft2	2D ^{13}C–^{13}C DARR	POPC/ POPG/ Chol	Method A; pH 7.0
AI–2	**Raw:** /9Jul09–sum1–5/9Jul09–sum1–5.fid **Proc:** /9Jul09–sum1–5/9Jul09–sum1–5_200lb.ft2	2D ^{13}C–^{13}C DARR	POPC/ POPG/ Chol	Method A; pH 7.0
AI–3	**Raw:** /14Jul09–50ms–CuEDTA/14Jul09–50ms–CuEDTA.fid **Proc:** /14Jul09–50ms–CuEDTA/14Jul09–50ms–CuEDTA_200lb.ft2	2D ^{13}C–^{13}C DARR	POPC/ POPG/ Chol	Method A; pH 7.0
AI–4	**Raw:** /16Jul09–500ms–CuEDTA–sum1–5/16Jul09–500ms–CuEDTA–sum1–5.fid **Proc:** /16Jul09–500ms–CuEDTA–sum1–5/16Jul09–500ms–CuEDTA–sum1–5_200lb.ft2	2D ^{13}C–^{13}C DARR	POPC/ POPG/ Chol	Method A; pH 7.0
AI–5	**Raw:** /CuEDTA_50ms_Virgin/FPH_50ms_cuedta–1 /FPH_CuEDTA_50ms.fid **Proc:** /CuEDTA_50ms_Virgin/FPH_50ms_cuedta–1 /FPH_CuEDTA_50ms_100lb.ft2	2D ^{13}C–^{13}C DARR (Fresh Sample)	POPC/ POPG/ Chol	Method A; pH 7.0

Table AIV–27 (cont'd)

AI–6	**Raw:** /CuEDTA_500ms_Virgin/FPH–500–cuedta–sum134/FPH_CuEDTA_500ms–sum134.fid **Proc:** /CuEDTA_500ms_Virgin/FPH–500–cuedta–sum134/FPH_CuEDTA_500ms–sum134_200lb.ft2	2D ^{13}C–^{13}C DARR (Fresh Sample)	POPC/ POPG/ Chol	Method A; pH 7.0
AI–7	**Raw:** /CuEDTA_13Feb–50ms–1/CuEDTA_13Feb10_50ms.fid **Proc:** /CuEDTA_13Feb–50ms–1/CuEDTA_13Feb10_50ms_100lb.ft2	2D ^{13}C–^{13}C PDSD (Re–doped Sample)	POPC/ POPG/ Chol	Method A; pH 7.0
AI–8	**Raw:** /CuEDTA_500ms_noDARR_sum123/CuEDTA_500ms_noDARR_sum123.fid **Proc:** /CuEDTA_500ms_noDARR_sum123/CuEDTA_500ms_noDARR_sum123_200lb.ft2	2D ^{13}C–^{13}C PDSD (Re–doped Sample)	POPC/ POPG/ Chol	Method A; pH 7.0

Raw and Proc Data Directory:
/home/mb4c/Matt/Organized_Files/FPH_CuEDTA_Samples/CuEDTA_Files/

Table AIV–28: Spectra for the ^{13}C CP ramp experiments at 9.4 T for comparison to 21.1 T using FP–Hairpin UA6/UG10 at ~15:1 lipid to protein loading.

File Name	File location
SenTest_12a	**Raw:** /SenTest_12a
SenTest_12b	**Raw:** /SenTest_12b
SenTest_12c	**Raw:** /SenTest_12c
SenTest_12d	**Raw:** /SenTest_12d
SenTest_12e	**Raw:** /SenTest_12e
SenTest_12f	**Raw:** /SenTest_12f
SenTest_10a Figure AI-27a	**Raw:** /SenTest_10a **Proc:** /10kHz_proc/MJN_10a_proc_50lb
SenTest_10b Figure AI-27b	**Raw:** /SenTest_10b **Proc:** /10kHz_proc/MJN_10b_proc_50lb
SenTest_10c Figure AI-27c	**Raw:** /SenTest_10c **Proc:** /10kHz_proc/MJN_10c_proc_50lb
SenTest_10d Figure AI-27d	**Raw:** /SenTest_10d **Proc:** /10kHz_proc/MJN_10d_proc_50lb
SenTest_10e Figure AI-27e	**Raw:** /SenTest_10e **Proc:** /10kHz_proc/MJN_10e_proc_50lb
SenTest_10f Figure AI-27f	**Raw:** /SenTest_10f **Proc:** /10kHz_proc/MJN_10f_proc_50lb

File locations:
Linux computer: /home/mb4c/Matt/Organized_Files/SenTests/

Table AIV–29: Data locations for 1D REDOR for FP34 and FP–Hairpin in lipid membranes.

Sample	File Location	Type of Experiment	Membranes	pH Condition
FP34 I4/G5 Fig. AI-29A	**Raw:** /FP34_I4G5/081107redor **Proc:** /FP34_I4G5/ 081107processedRedor	1D $^{1}H/^{13}C/^{15}N$ REDOR	DTPC/ DTPG/ Chol	Method A; pH 7.0
FP34 A14/A15 Fig. AI-29B	**Raw:** /FP34_A14A15/ 080907redor **Proc:** /FP34_A14A15/080907processedRedor	1D $^{1}H/^{13}C/^{15}N$ REDOR	DTPC/ DTPG/ Chol	Method A; pH 7.0
FP–Hairpin L7/F8 Fig. AI-29C	**Raw:** /FPH_ L7F8/040508 _FPH_L7F8_REDOR/FPH L7F8_040608/FPHairpinL7 F8_PCPG–1_Final **Proc:** /FPH_ L7F8 /processed_L7F8_100108	1D $^{1}H/^{13}C/^{15}N$ REDOR	DTPC/ DTPG	Method A; pH 7.0
FP–Hairpin UA6/UG10 2 ms	**Raw:** /FPH_UA6UG10/REDOR_ 24Feb09/MJN_2ms **Proc: –**	1D $^{1}H/^{13}C/^{31}P$ REDOR	DTPC/ DTPG/ Chol	Method A; pH 7.0
FP–Hairpin UA6/UG10 24 ms	**Raw:** /FPH_UA6UG10/REDOR_ 24Feb09/MJN_24ms **Proc: –**	1D $^{1}H/^{13}C/^{31}P$ REDOR	POPC/ POPG/ Chol	Method A; pH 7.0

* Proton amp kicked off for the 2ms dephasing time point of FP–Hairpin UA6/UG10. Lipid to protein loading was ~ 25:1.

File locations:
Linux computer: /home/mb4c/Matt/Organized_Files/REDOR_Samples/

Table AIV–30: Data locations for 1D REDOR for Scott Schmick's 21.1 T data of HFP V2E sample in lipid membranes presented in Figure AI-30.

Figure	File Location	Comments
AI-30A	**Raw:** /8_7ms/sumS0/sum_S0_4k.fid **Proc:** /8_7ms/sumS0/test_100.ft2	Dephasing time = 8.7 ms.
AI-30B	**Raw:** /8_7ms/sumS1/sum_S1_4k.fid **Proc:** /8_7ms/sumS1/test_100.ft2	Dephasing time = 8.7 ms.
AI-30C	**Raw:** /40_7ms/sumS0/sum_S0_28k.fid **Proc:** /40_7ms/sumS0/test_100.ft2	Dephasing time = 40.7 ms.
AI-30D	**Raw:** /40_7ms/sumS1/sum_S1_28k.fid **Proc:** /40_7ms/sumS1/test_100.ft2	Dephasing time = 40.7 ms.

* See Table AIV-19 for more information.

Raw and Proc Data Directory:
/home/mb4c/Matt/Organized_Files/900MHz_Data/All_900_Data/Jan2011/SDS_Data/